Mathematical modelling of BIPV–micro wind system: production, storage and usages

PETER CLARKE
BEng (Hons) Mechanical Engineering

A thesis submitted in partial fulfilment of the requirements of Edinburgh Napier University, for the award of Doctor of Philosophy

March 2009

ABSTRACT

This thesis deals with the following aspects of renewable energy technology; solar energy modelling within the urban environment, performance of building integrated renewables including solar photovoltaics and micro wind technology. The development of hydrogen technology and electric zero emission transport is also reviewed.

Incident solar irradiation models have been developed to accurately incorporate the effects of shading, in order to enable the detailed simulation and estimation of solar energy systems within the urban environment. Both the Integrated Slope Radiation Model (ISRM) and the Sky Radiance Distribution Model (SRDM) have been developed to use readily available horizontal sub-hourly or hourly solar global and diffuse irradiation data. Shading parameters caused by the surroundings, such as building and trees, can be incorporated into the models. A software package based on these models has been developed to allow the design and simulation of solar energy systems.

Horizontal solar global irradiation data is readily available around the world. However, diffuse irradiation data is available to a lesser extent. To resolve this problem and enable the above mentioned incident solar irradiation models to be used throughout the world a simple regression set was developed between the diffuse ratio, k, and clearness index, k_t, to enable the estimation of horizontal diffuse irradiation from its horizontal global counterpart.

A review of building integrated renewable technology has been carried out. This includes the review of the performance of Edinburgh Napier University photovoltaic facade which has been in operation for over three years. Building mounted micro turbine technology is also reviewed.

Performance analysis of three micro wind turbines installed on the rooftop of Edinburgh Napier University was undertaken, along with an analysis of the available wind regime observed at roof level. A software package was developed to aid the monitoring and analysis of both micro wind turbines and their observed wind regime.

Hydrogen technology is reviewed as part of the development of Napier Hydrogen Research Facility, enabling the demonstration of hydrogen generation, storage and use from renewables.

Finally, an analysis and comparison of a zero emission electric scooter with a conventional petrol car for use as urban transport was carried out. A driving cycle analysis was also undertaken to determine the environmental impact of both vehicles.

ACKNOWLEDGEMENTS

I would like to thank my director of studies, Professor Tariq Muneer. Thank you for your constant support, guidance and motivation, giving me the drive to succeed. In addition I would like to thank my supervisory team, Professor Jorge Kubie and Mr Alan Davidson for the support and advice that you have given me.

I would also like to thank the technical and administrative staff at the Faculty and the school of engineering and built environment: Bill Young, Ian Campbell, Stephen Paterson, Derek Cogle, and all the other technicians who were always so helpful in providing technical insight and support. Many thanks to Ahmad Makkawi for his collaboration in monitoring of the rooftop wind turbine project.

Finally I would like to thank my family, friends and peers for there unconditional support over the years; I am very grateful.

DECLARATION

I hereby declare that the work presented in this thesis was solely carried out by myself at Edinburgh Napier University, Edinburgh, except where due acknowledgement is made, and that it has not been submitted for any other degree.

PETER CLARKE (CANDIDATE)

16/03/2009

Date

TABLE OF CONTENTS

		Page
Abstract		i
Acknowledgements		ii
Declaration		iii
Table of Contents		iv
List of Figures		ix
List of Tables		xiv
Nomenclature		xvi
Glossary of Terms		xviii
CHAPTER 1	**Introduction**	
1.1	An overview of global energy usage	1-20
1.2	Carbon capture and sequestration	
1.3	Sustainable living	
1.4	Building-integrated photovoltaics (BIPV)	
1.5	Building-integrated micro domestic wind turbine technology	
1.6	Energy efficiency	
1.7	Energy supply	
	1.7.1 Fossil fuels	
	1.7.2 Nuclear energy	
	1.7.3 Renewables	
1.8	The role of hydrogen	
1.9	Renewables and transport	
1.10	The present research project aims and objectives	
	1.10.1 Building-integrated solar energy systems	
	1.10.2 Building-integrated micro wind turbine technology	
	1.10.3 The use of hydrogen as an energy storage medium and the development to the Napier hydrogen laboratory	
	1.10.4 Evaluation of the uses of renewable energy for sustainable personal transport	
1.11	Outline of the thesis	
CHAPTER 2	**Review of the Relevant literature**	21-68
	Solar Energy	
2.1	Introduction to photovoltaics	
2.2	Rural electrification	
2.3	Edinburgh Napier University PV facade	
	2.3.2 Performance analysis	
	2.3.3 Energy inputs and outputs	
2.4	Solar radiation models	
2.5	The need for computer-generated solar irradiance data	
2.6	Review and validation of existing solar energy models	
2.7	Development of correlations between diffuse and solar irradiation	
2.8	Solar data collection	

	2.8.1 Meteorological parameter commonly recorded by meteorological stations	
2.9	Source of error associated with solar irradiation measurement	
2.10	Solar quality control of data	
2.11	Evaluation of commercially available solar software	
	2.11.1 PVsyst 4.33	
	Wind Energy	
2.12	Global wind energy	
2.13	European wind energy	
2.14	Britain's wind energy	
2.15	Offshore wind	
2.16	Micro wind turbine technology	
2.17	Domestic wind markets	
2.18	Development of micro wind turbine technology	
2.19	Stand-alone energy systems	
2.20	Grid-connected systems	
2.21	Measurement of wind	
2.22	Wind data collection	
	2.22.1 Turbine direction monitoring	
2.23	The ETSU NOABL wind speed database	
2.24	Case study: Nenthead (Alston) 6kW wind turbine	
2.25	Warwick Wind Trials	
2.26	Available software wind modelling packages	
CHAPTER 3	**Horizontal and diffuse irradiation: data collection, processing and quality control and modelling**	69-100
3.1	Introduction	
3.2	Development of regressions between diffuse and global irradiation	
	3.2.1 Global and diffuse sub-hourly data set used for regression modelling	
	3.2.2 Quality control of solar irradiation data	
	3.2.3 Statistical evaluation tests used to evaluate the model's performance	
3.3	Development of regressions between diffuse ratio and clearness index	
3.4	Horizontal and tilted global irradiance measurement for Napier PV facade analysis and modelling	
	3.4.1 Horizontal, global and diffuse irradiance measurement for Napier PV Facade analysis and modelling	
CHAPTER 4	**Modelling incident solar irradiance in urban environment: Applications for building integrated photovoltaics**	101-131
4.1	Introduction	
4.2	Shading and the effects of shading caused by the surrounding urban environment	
4.3	Ground reflection in the urban environment	
4.4	Statistical evaluation of solar simulation models	
4.5	Integrated slope radiance model (ISRM)	

4.6	Evaluation of ISRM model performance	
4.7	Sky radiance distribution model (SRDM)	
4.8	Sky patch geometries	
4.9	Determining sky patch opacity	
4.10	View factors	
4.11	Beam irradiance	
4.12	SRDM model layout	
4.13	BIPVcalc software	
CHAPTER 5	**Evaluation of slope irradiation models and Edinburgh Napier University photovoltaic outputs using recent measurements**	132-158
5.1	Introduction	
5.2	Validation of modelled tilted global irradiance using measured sub-hourly tilted irradiance data	
5.3	Comparison of SRDM and ISRM solar models with existing solar models	
5.4	Validation of SRDM and ISRM solar models in estimating the performance of the Napier University photovoltaic facade	
CHAPTER 6	**Wind energy potential in urban environments**	159-209
6.1	Development of wind turbine technology	
6.2	Napier turbine trials	
	6.2.1 Zephyr Airdolphin Z1000	
	6.2.2 Ampair 600-230 V	
	6.2.3 Windsave WS1200	
6.3	Measurements of wind regime	
	6.3.1 Analysis of wind regime	
	6.3.2 Factors influencing the power of the wind	
	6.3.3 The Betz limit	
6.4	Factors which reduce available wind speed	
	6.4.1 Capacity factors	
	6.4.2 Wind shear and turbulence	
6.5	Wind data analysis	
	6.5.1 Average velocity	
	6.5.2 Wind velocity distribution	
6.6	Statistical modelling of wind frequency distribution	
	6.6.1 Weibull and Rayleigh distributions	
	6.6.2 Determining Weibull distribution	
	6.6.3 Estimation Weibull parameters	
	6.6.4 Determining Rayleigh distribution	
	6.6.5 Wind roses	
6.7	Windcalc software	
6.8	Results	
6.9	Findings and Conclusions	
	6.9.1 Edinburgh Napier University Merchistion Campus wind regime	
	6.9.2 Analysis of wind regime	
6.10	Airdolphin turbine	
6.11	Ampair 600 turbine	
6.12	Windsave WS1200 turbine	

CHAPTER 7	**Sustainable transport**	210-226
7.1	Introduction	
7.2	Hydrogen vehicle technology	
7.3	Electric vehicle technology	
7.4	Environmental impact of cars	
7.5	Pros and cons of cars and electric scooters	
7.6	The Edinburgh driving cycle	
7.7	Dynamic analyses for scooter	
7.8	Energy and power required for cruise mode	
7.9	Energy and power for travel up a gradient	
7.10	Energy and power required for acceleration	
7.11	Instrumentation, data collection, computer modelling and validation	
7.12	Conclusions	
CHAPTER 8	**Conclusions**	227-234
8.1	Discussions	
8.2	Conclusions	
8.3	Future work	
Bibliography		235-248
Appendix A	The development of the hydrogen research laboratory at Napier-lessons learnt	250-290
A.1	Introduction	
A.2	Hydrogen production	
A.3	Hydrogen from fossil fuels	
	A.3.1 Reforming hydrogen from natural gas	
	A.3.2 Steam reforming of methane	
	A.3.3 Hydrogen production from coal	
A.4	Production of hydrogen by electrolysis	
	A.4.1 Alkaline electrolysers	
	A.4.2 Proton-exchange membrane electrolysers	
	A.4.3 Solid oxide electrolyser	
A.5	Developing future technologies for hydrogen production	
A.6	Hydrogen storage	
	A.6.1 High pressure gas storage	
	A.6.2 Glass microspheres	
	A.6.3 Liquid storage	
	A.6.4 Cryogenic storage	
	A.6.5 Hydrogen storage in chemical hydride solutions	
	A.6.6 Hydrogen storage in organic hydrides	
A.7	Solid hydrogen storage	
	A.7.1 Physisorption of hydrogen	
	A.7.2 Carbon and high surface area materials	
A.8	Rechargeable hydrides	
	A.8.1 Metallic hydrides	
	A.8.2 Alanates and other light hydride	
	A.8.3 Chemical hydrides (H_2O reactive)	
A.9	Hydrogen fuel cells	
	A.9.1 Molten carbonate fuel cells (MCFC)	

A.9.2 Solid oxide fuel cells (SOFC)
A.9.3 Phosphoric acid fuel cells (PAFC)
A.9.4 Alkaline fuel cells (AFC)
A.9.5 Proton exchange membrane fuel cells (PEMFC)
A.10 Napier hydrogen research laboratory
A.11 The integration of a hydrogen storage facility into Edinburgh Napier University's sustainable energy and transport project
A.12 Hydrogen research
A.13 Hydrogen safety
A.14 Laboratory safety
A.14.1 Hydrogen leaks
A.14.2 Leaks detection ventilation
A.15 The hydrogen research laboratory

Appendix B List of Publications 291

LIST OF FIGURES

		Page
CHAPTER 1		1-20
Fig. 1.1.1	World annual energy consumption	
Fig. 1.1.2	UK electricity supplied distribution by fuel type 2007	
Fig. 1.1.3	UK electricity supplied by fuel type 2007	
Fig. 1.1.4	UK renewable Advisory Board's Forecast: cumulative installed renewables capacity by sector	
Fig. 1.1.5	Cost of generating electricity with respect to CO_2 costs	
CHAPTER 2		21-68
Fig. 2.1.1	Cumulative installed PV capacity	
Fig. 2.3.1	Edinburgh Napier University solar facade under discussion	
Fig. 2.3.2	Napier PV facade control board	
Fig. 2.3.2.1	Incident solar irradiation input compared with PV-AC output for Napier PV facade 19 July 2006, 15-minute averaged power	
Fig. 2.3.2.2	Napier PV facade experiencing shading from protruding bay window in the afternoon	
Fig. 2.3.2.3	Loss of power due to shading that occurs mainly in the afternoon for Napier PV facade 19 July 2006, 15-minute averaged power	
Fig. 2.3.3.1	Daily averaged PV-AC and PV-DC energy outputs, Napier PV facade	
Fig. 2.3.3.2	Daily averaged incident solar irradiation and daily averaged PV-AC energy, Napier PV facade	
Fig. 2.8.1	Horizontal and incident pyranometers at Edinburgh Napier University test site	
Fig. 2.12.1	World's cumulative installed wind capacity per year	
Fig. 2.12.2	World's installed wind energy capacity distribution 2007	
Fig. 2.13.1	Europe's installed wind energy capacity distribution 2007	
Fig. 2.15.1	World's offshore wind capacity at the end of 2007	
Fig. 2.15.2	World's offshore wind capacity at the end of 2015	
Fig. 2.19.1	A schematic of a stand-alone sustainable energy system with battery storage	
Fig. 2.20.1	A schematic of a grid-connected sustainable energy system with battery storage	
Fig. 2.22.1	Two wind velocity anemometers and two wind direction vanes	
Fig. 2.22.1.1	Wind turbine direction indicator installed on Airdolphin turbine	
Fig. 2.23.1	ETSU NOABL mean wind velocity for the Edinburgh Napier University site	
Fig. 2.23.2	Annual wind speed map of UK 25m above ground	

	level	
Fig. 2.24.1	Proven turbine WT6000, Nenthead	
Fig. 2.24.2	Proven turbine WT6000, Nenthead	
CHAPTER 3		69-100
Fig. 3.2.2.1	Envelope of acceptance drawn between k-k_t	
Fig. 3.3.1	Annual k-k_t plot, quality-controlled data for Edinburgh data	
Fig. 3.3.2	Summer seasonal k-k_t plot, quality-controlled data for Edinburgh data	
Fig. 3.3.3	Winter seasonal k-k_t plot, quality-controlled data for Edinburgh data	
Fig. 3.3.4	Spring/Autumn seasonal k-k_t plot, quality-controlled data	
Fig. 3.3.5.A	Monthly regressions k-k_t plot, quality-controlled data for Edinburgh data	
Fig. 3.3.5.B	Monthly regressions k-k_t plot, quality-controlled data for Edinburgh data	
Fig. 3.3.6	k-k_t monthly regressions for Edinburgh	
Fig. 3.3.7	k-kt seasonal and annual regressions for Edinburgh	
Fig. 3.3.8	Comparison of k-kt of seasonal regression curve for Edinburgh, Shanwell and the UK.	
Fig. 3.3.9	Comparison of calculated versus measured diffuse irradiation for Edinburgh using monthly regressions	
Fig. 3.4.1	Edinburgh Napier University solar measurement station on the rooftop of Edinburgh Napier University	
Fig. 3.4.2	Horizontal and inclined pyranometers installed at new locations on the rooftop of Edinburgh Napier University to record solar irradiance for the current study	
Fig. 3.4.3	Comparison of horizontal global irradiance recorded using Pyranometer CM11 Pyranometer CM6b for confirmation of correction calibration	
Fig. 3.4.1.1	Horizontal and global irradiation, two BF3 sunshine sensors	
Fig. 3.4.1.2	Horizontal diffuse irradiation, two BF3 sunshine sensors	
CHAPTER 4		101-131
Fig. 4.2.1	Tilted PV array on church roof	
Fig. 4.3.1	Napier PV facade foreground used to calculate ground reflection albedo	
Fig. 4.3.2	Plan view of Napier PV facade, showing PV array and bay windows	
Fig. 4.5.1	Relationship between shaded vertical and horizontal diffuse irradiance	
Fig. 4.6.1	Relationship between measured and modelled slope irradiance using ISRM model in one year's daily averaged hourly irradiance	

Fig. 4.6.2	ISRM model flow cart	
Fig. 4.7.1	Three-dimensional sky patch matrix CAD model developed for current study	
Fig. 4.8.1	Sky patch geometry	
Fig. 4.8.2	Sky patch map	
Fig. 4.8.3	Sky patch global positions	
Fig. 4.9.1	Sky patch map showing sky patches blocked from view	
Fig. 4.9.2	Horizon view from fifth floor	
Fig. 4.9.3	Obstructions on the horizon have been split into strips to simplify description the geometry of sky patches	
Fig. 4.10.1	View-factor schematic demonstrating irradiation being emitted from sky patch and received by PV module surface	
Fig. 4.12.1	Flow chart showing steps taken in the SRDM model	
CHAPTER 5		132-158
Fig. 5.2.1	Relationship between measured and modelled slope irradiance using ISRM model	
Fig. 5.2.2	Relationship between measured and modelled slope irradiance using SRDM model	
Fig. 5.4.1	Edinburgh Napier University PV facade power output. 8th to 10th May 2006	
Fig. 5.4.2	Edinburgh Napier University PV facade power output. 21st to 23rd May 2006	
Fig. 5.4.3	Edinburgh Napier University PV facade power outputs taken for seven days selected for being overcast	
Fig. 5.4.4	Edinburgh Napier University PV facade power outputs taken for seven days selected for being sunny	
Fig. 5.4.5	Monthly averaged daily PV AC energy outputs	
Fig. 5.4.6	Monthly averaged daily PV AC energy outputs	
Fig. 5.4.7	totalled modelled electrical energy outputs versus measured electrical outputs	
Fig. 5.4.8	Daily averaged monthly PV-AC energy outputs	
CHAPTER 6		159-209
Fig. 6.2.1	Visualization of air stream travelling over a flat-roofed building	
Fig. 6.2.2	Edinburgh Napier University Merchistion Campus rooftop test site.	
Fig. 6.2.1.1	Zephyr Airdolphin turbine	
Fig. 6.2.2.1	Ampair 600-230 V	
Fig. 6.2.2.2	Ampair 600 turbine shown with broken blades and loss of tail fin	
Fig. 6.2.2.3	Broken Ampair 600 tail fin	
Fig. 6.2.3.1	Windsave WS1200	
Fig. 6.3.1	Wind turbine swept area	
Fig. 6.4.2.1	Schematic of wind turbulence effects over a building	

Fig. 6.4.2.2	Schematic of wind showing wind flow over smooth topography	
Fig 6.5.2.1	Sample wind velocity probability distribution plot	
Fig 6.5.2.2	Sample cumulative distribution of wind velocity plot	
Fig. 6.6.1	Sample wind velocity frequency distribution	
Fig. 6.6.2.1	Sample wind velocity cumulative frequency distribution	
Fig. 6.6.3.1	Graphical method to estimate Weibull k and c parameters	
Fig. 6.6.5.1	Wind roses, Edinburgh Napier University	
Fig. 6.6.5.2	Three-dimensional wind distribution plot	
Fig. 6.7.1	Windclac software outputs	
Fig. 6.8.1	Monthly frequency roses	
Fig. 6.8.2	Velocity wind roses	
Fig. 6.8.3	Wind power roses for Airdolphin turbine	
Fig. 6.8.4	Energy roses for Airdolphin turbine	
Fig. 6.8.5	Three-dimensional wind distribution plots	
Fig. 6.8.6	Cumulative distribution plots	
Fig. 6.8.7	Frequency distribution plots	
Fig. 6.8.8	Wind-gust frequency duration plots	
Fig. 6.8.9	Airdolphin monthly-averaged daily energy	
Fig. 6.8.10	Ampair monthly-averaged daily energy	
Fig. 6.8.11	Ampair averaged monthly power	
Fig. 6.8.12	Airdolphin averaged monthly power	
Fig. 6.8.13	Ampair mean and weighted wind speed	
Fig. 6.8.14	Shows the frequency which the Ampair turbine generator is producing power, and the frequency the turbine's export inverter is connected to the grid	
Fig. 6.8.15	Frequency at which Ampair turbine is generating, and frequency inverter is grid-connected for exporting	
CHAPTER 7		210-226
Fig 7.3.1	Specific power and energy densities of various energy storage and conversion methods	
Fig. 7.4.1	CO_2 emissions for new cars, and number of cars on the UK roads.	
Fig. 7.4.2	Historical reductions of tail-pipe CO_2 emission achieved via technological developments, g/km.	
Fig. 7.6.1	The city of Edinburgh car driving cycle	
Fig. 7.7.1	Edinburgh Napier University electric demonstration scooter	
Fig. 7.9.1	Free-body diagram for scooter on a level road surface (top) and travelling up a gradient (bottom)	
Fig. 7.11.1	Trace of driven route obtained via on-board GPS sensor	
Fig. 7.11.2	Plot of measured speed, altitude and total distance covered	
Fig. 7.11.3	Measured power and computed acceleration	
APPENDIX A		250-290

Fig. A.4.1	Schematic of simple electrolyser
Fig. A.4.1.1	Schematic of an alkaline electrolyser
Fig. A.4.2	Schematic of a proton exchange membrane electrolyser
Fig. A.4.3	Schematic of a solid oxide electrolyser
Fig. A.6.1	Energy density comparison of select fuels
Fig. A.8.2	Hydrogen atoms stored in the lattice structure of a light metal hydride
Fig. A.9.1	Schematic of a simple fuel cell
Fig. A.9.1.1	Schematic molten carbonate fuel cell
Fig. A.9.2	Schematic of solid oxide fuel cell
Fig. A.9.3	Schematic of the phosphoric acid fuel cell
Fig. A.9.4	Schematic of alkaline fuel cell
Fig. A.9.5	Schematic of the proton exchange membrane fuel cell
Fig. A.11.1	Gas storage cylinder bank located on the University's roof behind the hydrogen lab
Fig. A.15.1	View of Hydrogen research laboratory showing key components
Fig. A.15.2	Second view of hydrogen research laboratory
Fig. A.15.3	LabGas PEM electrolyser
Fig. A.15.4	Water purifying filler and deioniser
Fig. A.15.5	LabGas Palladium membrane hydrogen gas dryer
Fig. A.15.6	Prototype solid oxide fuel cell used for research work and air compressor supply air to fuel cell stack
Fig. A.15.7	A view from above of a solid oxide fuel cell
Fig. A.15.8	Hydrogen alarm and control panel
Fig. A.15.9	Schematic of hydrogen system

LIST OF TABLES

		Page
CHAPTER 1		1-20
Table 1.1	UK energy consumption 2007	
CHAPTER 2		21-68
Table 2.1.1	Installed PV capacity EU-15 2006	
Table 2.8.1	UK Meteorological Office hourly solar radiation stations	
Table 2.9.1	World Meteorological Organisation classification of pyranometers	
Table 2.12.1	World's installed wind energy capacity by region 2007	
Table 2.13.1	Europe's installed wind capacity 2007	
Table 2.22.1	Wind monitoring equipment installed	
CHAPTER 3		69-100
Table 3.2.2.1	Coefficients for use in Eq.(3.2.2.5)	
Table 3.2.3.1	Parameters for presently development regression	
Table 3.2.3.2	Error statistics for cubic regression curves: monthly, seasonal and annual	
Table 3.3.1	Error analysis for presently developed regressions	
Table 3.3.2	Parameters pertaining to regressions developed for 12 UK sites	
Table 3.4.1	Solar horizontal global incident irradiation data set information	
CHAPTER 4		101-131
Table 4.6.1	Statistical tests, relationship between measured and ISRM modelled slope irradiance	
Table 4.7.1	Coefficients for the all-sky model	
Table 4.8.1	The size of sky patches and azimuth angle	
CHAPTER 5		132-158
Table 5.2.1	Horizontal and tilted global irradiance data set used validate modelled tilted data	
Table 5.2.2	Daily totals of modelled tilted global irradiance performance statistics	
Table 5.3.1	Performance statistics for ten transposition models with optimal data input	
Table 5.4.1	SRDM and ISRM solar models statistics using 15-minute averaged horizontal global irradiance diffuse regressions (Pyranometer CM11)	
Table 5.4.2	SRDM and ISRM solar model statistics using 15-minute averaged horizontal global and diffuse irradiance (Delta-T BF3)	
Table 5.4.3	Napier PV facade: monthly systems efficiencies	
Table 5.4.4	Napier PV facade: monthly energy outputs	

CHAPTER 6		159-209
Table 6.2.1	Micro-turbine specifications	
Table 6.8.1	Weibull and Rayleigh coefficients of wind regime observed at Airdolphin turbine and turbine capacity factor	
Table 6.8.2	Airdolphin turbine outputs	
Table 6.8.3	Weibull and Rayleigh coefficients of wind regime observed at Ampair turbine and turbine capacity factor	
Table 6.8.4	Ampair turbine outputs	
CHAPTER 7		210-226
Table 7.5.1	Why own a car	
Table 7.5.2	Merits and demerits of the use of electric scooters as opposed to cars	
Table 7.6.1	Breakdown of the EDC and the ECE-15 driving cycles	
Table 7.6.2	Route undertaken during driving simulation	
Table 7.11.1	Comparative data for the electric scooter and the chosen car	
Table 7.11.2	Validation results and comparison of energy requirements for the car and scooter	
APPENDIX A		250-290
Table A.3.2.1	Comparison of technologies for H_2 production from natural gas	
Table A.13	Properties of hydrogen and other hydrocarbons	
Table A.15	Hydrogen research laboratory specification	

NOMENCLATURES

Abbreviation and symbols

ζ	=	Angle between given point and sun, degrees
INC	=	Angle of incidence, degrees
AST	=	Apparent solar time
A	=	Area, m^2
AZIM	=	Azimuth Angle, degrees
K_B	=	Beam clearness index
r_B	=	Beam conversion factor
I_B	=	Beam irradiance, W/m^2
F	=	Clearness function
k_t	=	Clearness index (ratio of global to extraterrestrial irradiations)
CRM	=	Cloud radiation model
R^2	=	Coefficient of determination
ρ	=	Density, kg/m^3
I_D	=	Diffuse irradiance, W/m^2
DRM	=	Diffuse radiation model
k	=	Diffuse ratio (diffuse irradiations / global irradiations)
DBR	=	Diffuse to beam ratio
T_{rd}	=	Diffuse transmittance
C_d	=	Drag coefficient
H	=	Efficiency
E	=	Energy, Wh
I_E	=	Extraterrestrial irradiance, W/m^2
Γ	=	Gamma function
I_G	=	Global irradiance, W/m^2
GWP	=	Global warming potential
GHA	=	Greenwich hour angle
I_R	=	Ground reflection, W/m^2
IMRM	=	Improved metrological radiation model
ISRM	=	Integrated slope irradiation model
LAT	=	Latitude, degrees
T_L	=	Linke turbidity factor
LONG	=	Longitude, degrees
L_L	=	Lower limit
lm	=	Lumen
I_v	=	Luminance, cd/m^2
L_v	=	Luminance, kcd/m^2
ϕ	=	Luminous flux, lm
m	=	mass, N
MBD	=	Mean bias distribution

K_d	=	mean earth-sun distance correction factor
V_m	=	Mean wind velocity, ms^{-1}
$I_{D\ measured}$	=	Measured diffuse irradiance, W/m^2
MRM	=	Metrological radiation model
P	=	Power, W
δ_r	=	Rayleigh optical depth
c_W	=	Rayleigh scale factor
RMSD	=	Root mean squared distribution
TF	=	Sky clarity
ε	=	Sky clearness
SP	=	Sky Patch
SRDM	=	Sky radiance distribution model
Θ	=	Sky-patch altitude angle, degrees
α	=	Sky-patch altitude, degrees
Ψ	=	Sky-patch azimuth, degrees
SOLALT	=	Solar altitude, degrees
DEC	=	Solar declination angle, degrees
ω	=	Steradian
$I_{B,TilT}$	=	Tilted beam irradiance, W/m^2
$I_{D\ TLT}$	=	Tilted diffuse irradiance, W/m^2
$I_{G\ TLT}$	=	Tilted global irradiations, W/m^2
$I_{R,TilT}$	=	Tilted ground reflection, W/m^2
L_U	=	Upper limit
V	=	Velocity, ms^{-1}
WAZ	=	Wall azimuth angle
c_W	=	Weibull scale factor
k_W	=	Weibull shape factor
L_z	=	Zenith luminance, cd/m^2

Glossary of Terms

Albedo- the fraction of solar radiation which is reflected. The solar energy community defines albedo as the fraction of solar radiation that is reflected from the ground, ground cover, and bodies of water on the surface of the earth. Astronomers and meteorologists include reflectance by clouds and air. To reduce confusion, some solar researchers use the term ground reflectance.

Azimuth Angle- the angle between the sun's beam and a reference direction on a horizontal surface reference direction (usually North, although some solar scientists measure the solar azimuth angle from due South).

Beam Radiation- radiation received directly from the sun without been scatted by the earths atmosphere.

Betz Limit- states that a wind turbine can not convert more than 16/27, (59.3%) of the winds kinetic energy into mechanical energy by turning a rotor.

Capacity Factor- compares a wind turbine's measured energy production for a given period with the amount of energy generated if the turbine was operating at its rated output for the same given period of time.

Clearness Index (k_t)- the ratio of global radiation on a horizontal surface to the horizontal extraterrestrial radiation. It gives the depletion of solar radiation passing through the earth's atmosphere, thus indicating the level of available irradiation incident on the earth's surface and changes of sky conditions.

Declination- defined as the angular position of the sun at noon (AST) with respect to the earth equatorial plane.

Diffuse Ratio (k)- the ratio of diffuse irradiation on a horizontal surface to horizontal global irradiation. It is used to denote the depletion of the diffuse component due to cloud cover and concentrations of aerosols within the atmosphere.

Electrolysis- is separation of chemically bonded elements and compounds by passing an electrical current through the substance. Typically this is water used to produce hydrogen and oxygen.

Extraterrestrial Radiation- is the amount of global radiation which is received at the outermost atmosphere's surface, which would also be received on the earth surface if there were no atmosphere.

Fuel Cell- is an electrochemical conversion device. It produces electricity from fuel and an oxidant, which react in the presence of an electrolyte. The reactants flow into the cell, and the reaction products flow out of it. Electricity and heat are produced as a by-product.

Diffuse Radiation- solar radiation received from the sun after its direction has been changed by scattering by the earth atmosphere.

Global Irradiation- the sum total of beam, diffuse and ground-reflected radiation.

Hour Angle- is the angular displacement of the sun east or west of the local meridian due to the rotation on the earth on its axis; it is equal to 15° per hour, morning is negative and afternoon is positive.

Irradiation- the rate at which incident radiation is incident on a surface, per unit area of surface.

ISRM- Incident slope radiation model.

Latitude- angular distance from the equator to the pole. The equator is 0°, the North pole is 90° North, and the South pole 90° South.

Linke turbidity factor- gives a useful approximation of the atmosphere absorption and scattering effect of solar radiation under clear sky conditions.
Local Apparent Time- the time of day based on the longitude of locality and on time zone time.

Longitude- the East and West angular distance of a locality from the Prime Meridian.

Photovoltaic Array- a photovoltaic model of group of models used to convert solar radiation to electrical energy.

Photovoltaic module- a unit comprising of photovoltaic cells, which are a semi-conducting material that absorbs light or other bands of electromagnetic spectrum and emits electricity.

Sky Patch- an area of sky hemisphere of known dimensional size and position.

Solar Altitude- the angle between the horizontal and the line to the sun.

Solar Radiation- the principle portion of the solar spectrum that spans from approximately 300 nm to 4000 nm in the electromagnetic spectrum.

Solar Time- also known as apparent solar time, it is based on the apparent solar angular motion of the sun across the sky, with solar noon being the it time crosses the meridian. Used in solar geometry calculations.

SRDM- solar radiation distribution model.

Tilt Angle- angle between a given surface and horizontal.

View factor- View factors are used to define the amount of radiation that is exchanged between two surfaces, given the geometry of the two surfaces as a function of both distance and orientation.

Wind Rose- wind rose is a graphic tool used to give a succinct view of how wind velocity and direction are typically distributed at a particular location.

Zenith Angle- the angle between the zenith and the normal to surface of interest.

CHAPTER 1

Introduction

1.1 An overview of global energy usage

Energy is a key element in the survival of life. For this reason, it plays a central role in all of the world's politics and affairs, driving economical growth and social development. Modern life relies upon a cheap, abundant and uninterrupted supply of energy. Currently Europe, as with the rest of the developed world, relies on fossil fuels as its primary energy source.

The UK built its economic wealth on its coal-fired industrial past. Fossil fuels were the key to developing and securing the cheap, reliable and readily available energy supply required for the industrial revolution. Since then, the majority of all energy needs have been met by fossil fuels. Coal was the first major energy resource until the 1930s when oil became the second major contributor to the energy market. This was then joined by natural gas in the 1970s. Until this point, the UK was self-sufficient in all its energy needs, having a stable and secure energy supply. However, in 1973 the world was hit by the oil crisis, when a number of members from the Organization of Petroleum Exporting Countries (OPEC) announced that as a result of the ongoing Yom Kippur War they would no longer supply oil products to nations which supported the conflict. This included the United States and its allies in Europe. This was later followed by OPEC members agreeing to a price-setting mechanism to raise the price of the world's oil supply which resulted in a fourfold increase in oil prices. Many countries then realised the importance of energy security, and introduced initiatives to secure future energy supplies.

At the same time, growing concerns over the environmental impact of fossil fuel emissions lead to the Kyoto Protocol in 2006. Countries agreed to set limits to reduce carbon emissions. The UK agreed to a carbon dioxide emission reduction of 20% of 1990 emissions by the year 2010 and a 60% reduction by 2050. In October 2008 the British government revised its targets of reducing carbon dioxide emissions to 80% by 2050. This agreement has lead many governments to look for alternative energy supplies, such as nuclear and renewable energy.

Concerns over safety issues relating to future fuel supplies, waste storage and security have also lead governments to look to alternatives such as renewable energy and decentralised generation to meet their country's energy needs. According to the Green Paper (European Commission, 2000). Europe imports 50% of its energy needs, which could rise to 70% by 2030 if nothing is done. This would put Europe in a very economically unstable position.

Nuclear energy has proven to be an expensive alternative to fossil fuels. However in January 2008 the British government gave the go-ahead for a new generation of nuclear power stations within the UK. Business Secretary John Hutton presented new plans to streamline the planning process required to install new nuclear plants within the UK. The government itself had no plans to build its own plants, and would not offer any public subsidies for nuclear except within emergencies. Steps put in place were only to encourage private operators to build the nuclear plants. They would also be required to meet the full costs including building, decommissioning and the disposal of nuclear waste.

It is of concern that the government has announced plans for a new regeneration of nuclear power plants yet the government still has not found a permanent solution to storing Britain's nuclear waste. The additional nuclear waste produced from any new power station would continue to be stockpiled above ground at the Sellafield facility in Cumbria until a suitable permanent storage site could be found.

Currently the UK has ten nuclear power stations in operation producing around 18GW of the UK's total 52-57GW electrical supply (Lean & Owen, 2008). A recent report under taken by the Independent newspaper suggests that British nuclear generation is in a poor condition. Out of the ten operating nuclear power stations, two have been shut down for over a year due to corrosion. Another two have had their reactors shut down for over a month, and a further two are operating at part load due to safety concerns. Of the final four still in operation, one is to be decommissioned within two years and another is of concern due to the development of cracks within its reactor (Lean & Owen, 2008).

In 2007 the world's annual energy consumption totalled 129.1 PWh, an increase of 2.4% from 2006. Note that 1PWh (PetaWh) = one billion billion Wh. Fifty-two percent of this growth was due to the growth of China's energy consumption (BP, 2008a). Coal has seen the largest growth of all the fossil fuels in the last year, with a consumption increasing by 4.5%. This is mainly due to the rapid growth of coal-fired power stations in China and India. In the past few years, gas consumption has also increased, but nuclear energy saw a decrease in production by 2%. Figure 1.1.1 shows the world's energy consumption for the five primary energy sources over the period of 2008. Oil has the largest consumption as it is used as a fuel for transportation, whereas coal is the largest energy source for electricity generation. Global energy consumption is set to continue to rise with the development of third-world countries.

In terms of global renewable energy, wind energy capacity increased by 26.5% in 2007, with an increase in installed capacity of 94GW being achieved; this rate of growth is expected to accelerate over the coming years. In 2007 wind energy supplied 194TWh of electricity (BP, 2008b). Solar energy has seen an average growth of 37% over the last ten years, with installed capacity doubling every two years. 2007 saw the largest growth in the PV market, with 2.392GW being installed around the world. The cumulative world installed capacity is 9.162GW. The PV market is expected to continue to grow strongly, with an annual install capacity of 7GW being achieved by 2010. Global predictions of PV growth by 2030 suggest that 8.9% of total global electricity may be supplied by PV, with an installed capacity of 1,864GW generating 2,646TWh annually (European Photovoltaic Industry Association, 2008).

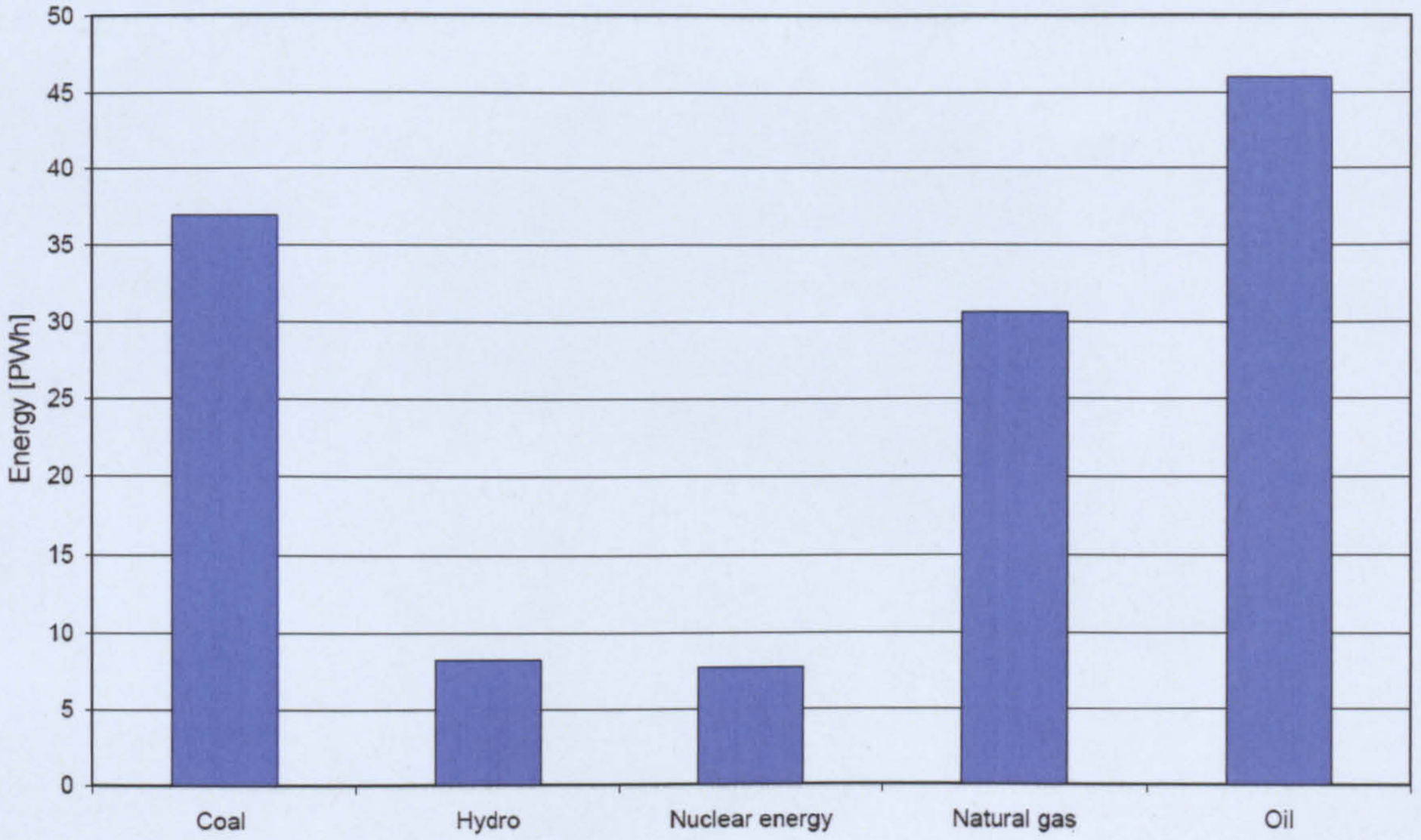

Figure.1.1.1 World annual energy consumption. Source data (BP, 2008a).

The UK electricity mix has also seen a rapid development within recent years. Figure 1.1.2 shows the current UK electricity distribution, with the primary energy been provided by gas and coal fired power plants. Figure 1.1.3 shows the total annual electricity production by each energy sector for 2007. The total electricity generated in the UK was 378.5TWh in 2007, with gas and coal being the main contributors, supplying 161.1TWh and 129.4TWh respectively (Department for Business Enterprise & Regulations Reform, July 2008).

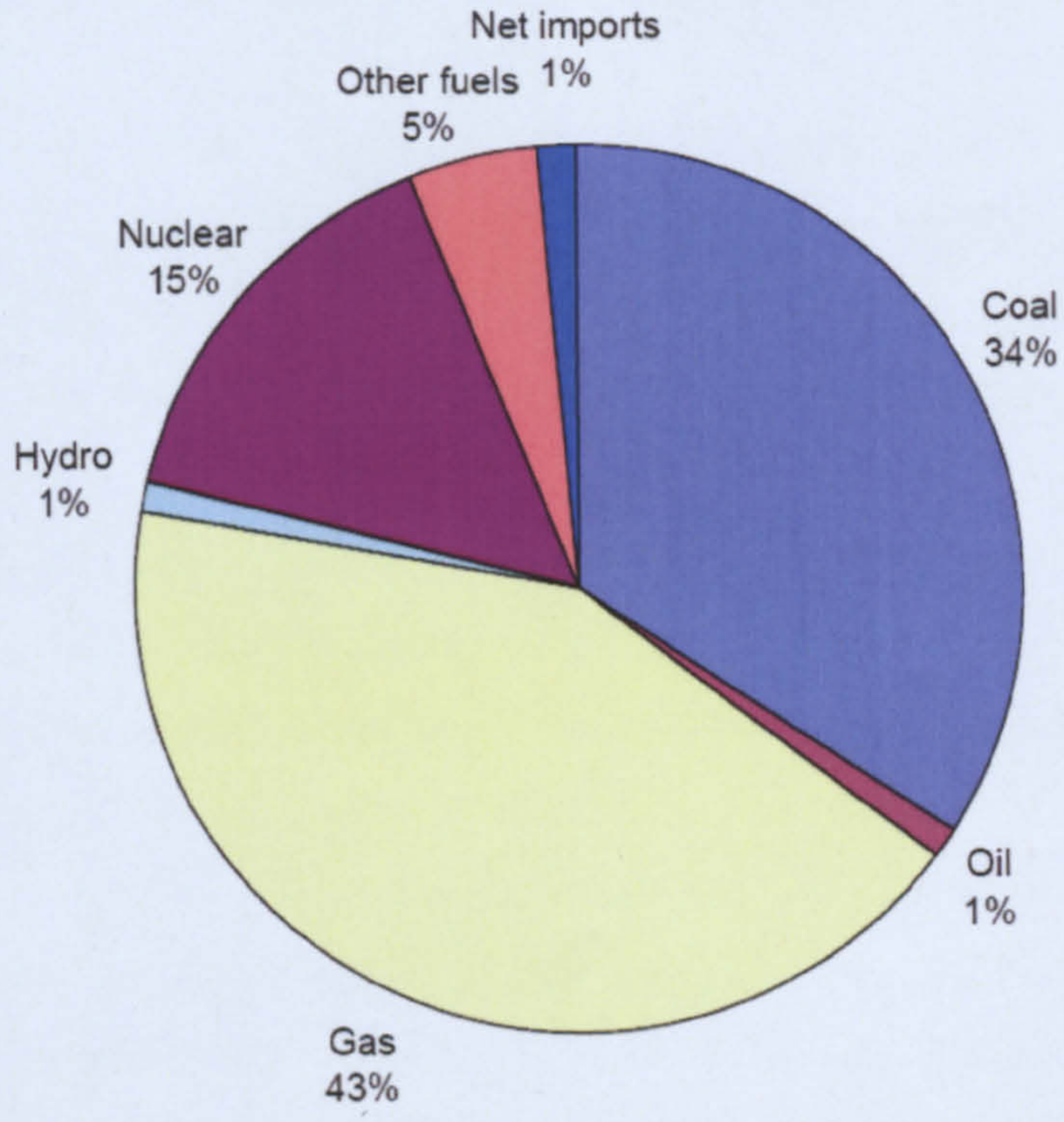

Figure 1.1.2 UK electricity supplied distribution by fuel type 2007. Source data (Department for Business Enterprise & Regulations Reform, July 2008).

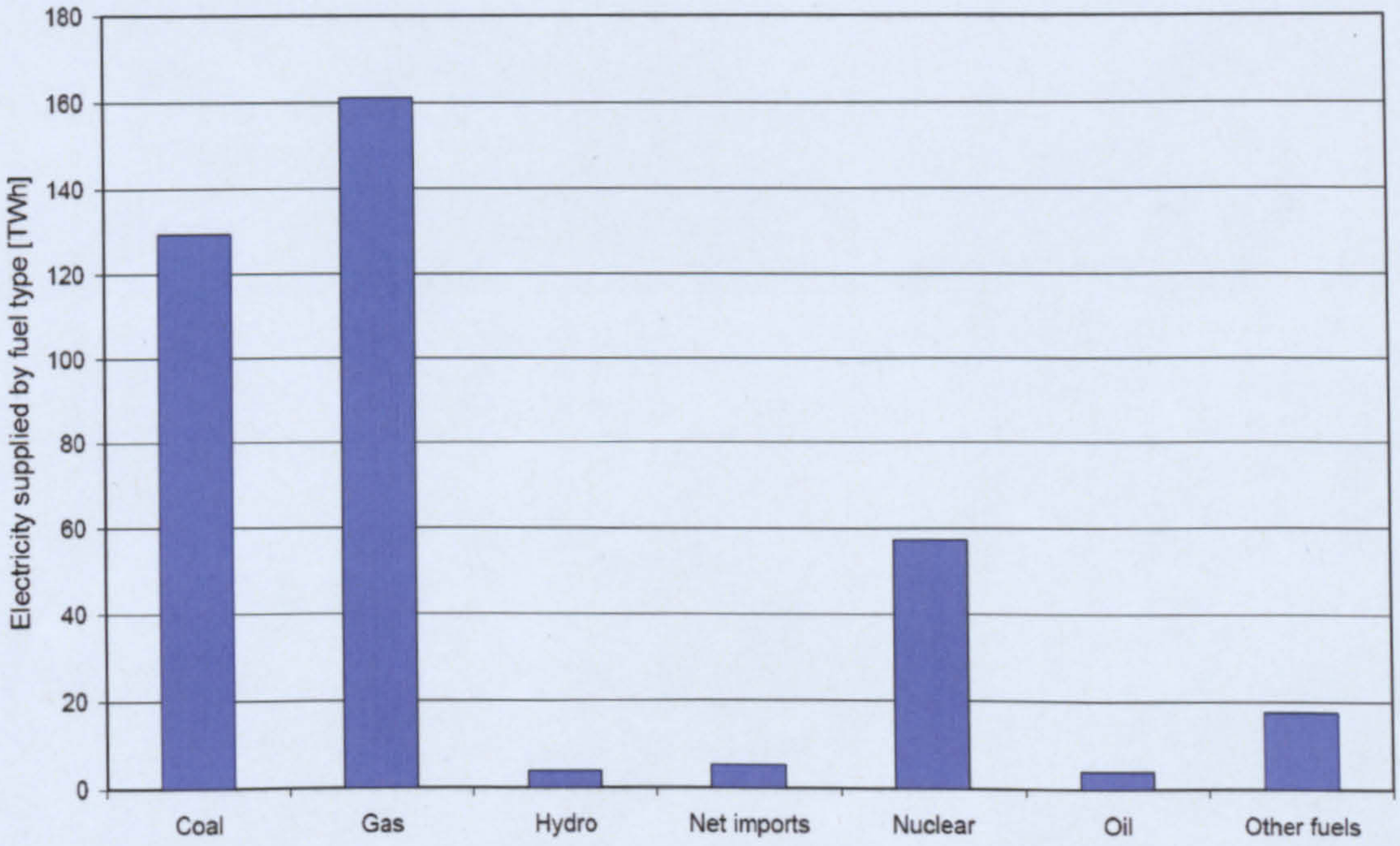

Figure 1.1.3 UK electricity supplied by fuel type 2007. Source data (Department for Business Enterprise & Regulations Reform, July 2008).

The deployment of renewables has been slow in the UK compared with other European countries. Only 6.9GW of installed capacity is expected by the end of 2008. This is not due to poor energy resources. The UK has among the best sustainable resources in the world with the best wind resources in Europe both

on and offshore, as well as having the best tide and wave resources. The UK has plans to install a large capacity of renewables within the coming years, with the bulk being supplied by onshore wind over the next five years. This is because onshore wind energy is a cheaper and more proven technology than offshore wind energy. However, as offshore technology further develops, its cost is expected to fall, and it may become the major energy provider by 2020.

Figure 1.1.4 shows the cumulative forecasted installed capacity of renewables by sector for the coming years. Although both tidal and wave energy can potentially supply very large quantities of renewable energy, this technology is still in the development and testing phase and not expected to be commercially viable in the next decade. Solar thermal technology is already viable and could potentially provide much of the UK thermal water-heating load. Although solar PV technology is proven and well tested, its high manufacturing costs are currently limiting its deployment.

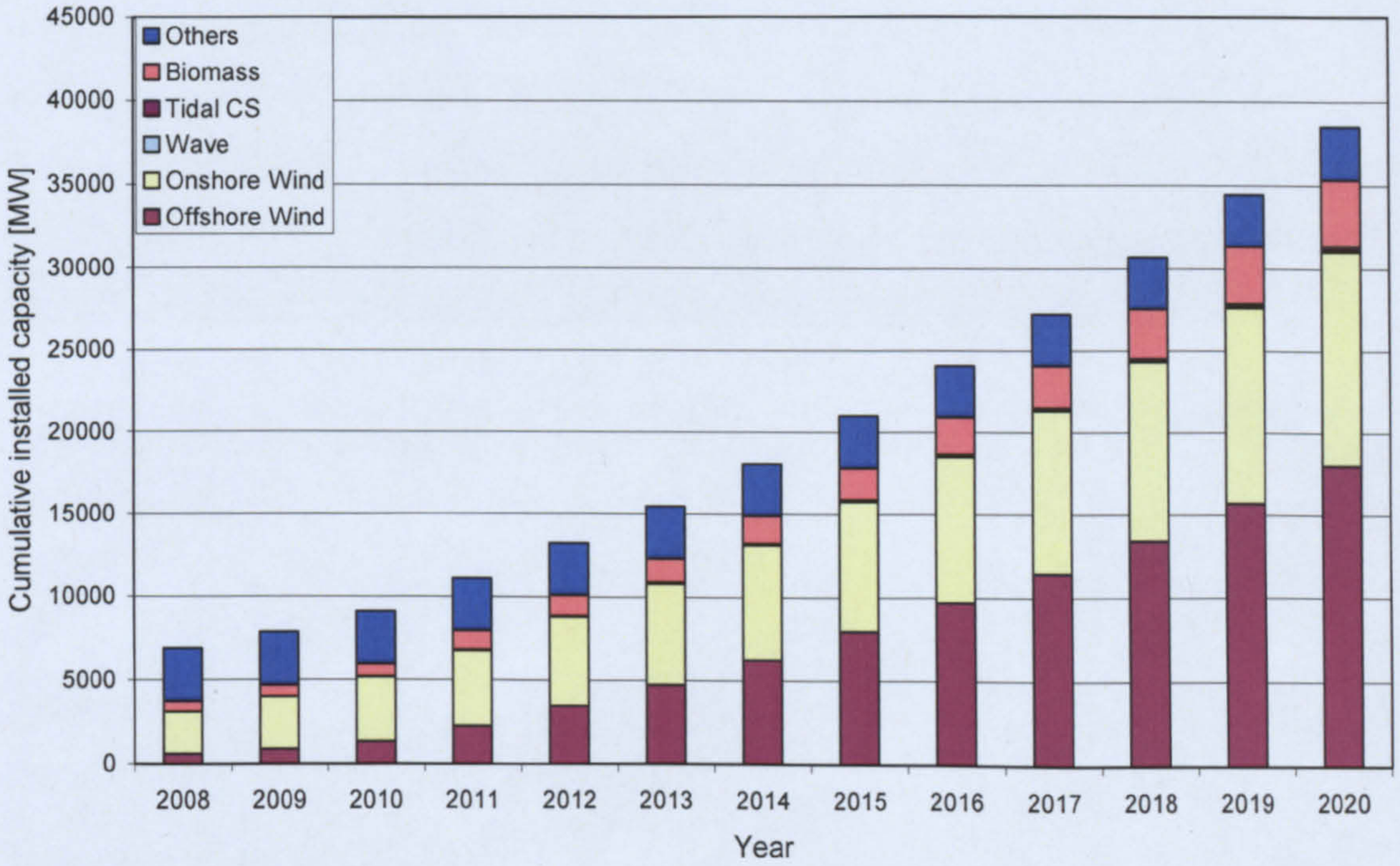

Figure 1.1.4 UK renewable Advisory Board's Forecast: cumulative installed renewables capacity by sector. Source data (Westwood, June 2008).

Table 1.1 shows the energy consumption figures for the UK for all sectors, with the transport and the domestic sectors having the largest energy consumption. Energy conversion losses and distribution losses account for 31.5% of the total energy consumption.

Currently the cost of increasing renewable generation capacity is more expensive than conventional generation technologies, such as fossil fuels; this is reflected in the cost of electricity generated. Figure 1.1.5 shows the costs of electricity generated by both conventional methods of generation and by renewables. It can be seen from Figure 1.1.5 that the cost of electricity generated by nuclear generation is the lowest of all. Although this cost does take into account capital and decommissioning costs, it doesn't include the high waste storage costs. The full extent of these costs are not known yet as the UK has not got a permanent storage solution for storing radioactive waste. The overall cost of nuclear energy is likely to be significantly higher than fossil-fuelled generation.

In the study undertaken by Sandia National Laboratories in Albuquerque put social costs of nuclear power at (4.1 to 8.7 p/kWh) twice that of the cost of fossil fuels of (1.6 to 3.7 p/kWh) (Leggett,1990).
In contrary to common perception nuclear power is no cleaner than renewable technologies such as wind power, in terms of life cycle assessment nuclear power is comparable with wind power, depending upon the fuel enrichment process used; nuclear power has global warming potential of 22-30 g-CO_2/kWh. Wind power and coal fuelled generation have global warming potentials of 20-29 g-CO_2/kWh and 975 g-CO_2/kWh respectively Hondo (2005).

The costs of coal and gas-fired power generation have also been included, with additional costs for carbon dioxide emissions of £30 per tonne. This reflects the probable cost of the capture and sequestration of the carbon dioxide which is produced. This makes the cost of fossil-fuelled generation comparable with renewables.

Table 1.1 UK energy consumption 2007

UK energy consumption 2007	**TWh**
Conversion losses	624.5
Distribution losses and energy industry uses	207.0
Industry	368.7
Domestic sector	511.7
Transport	695.5
Services non agriculture	224.5
Total final energy consumption	**1801.5**
Total inland primary energy consumption	**2628.4**

Source data (Westwood, June 2008)

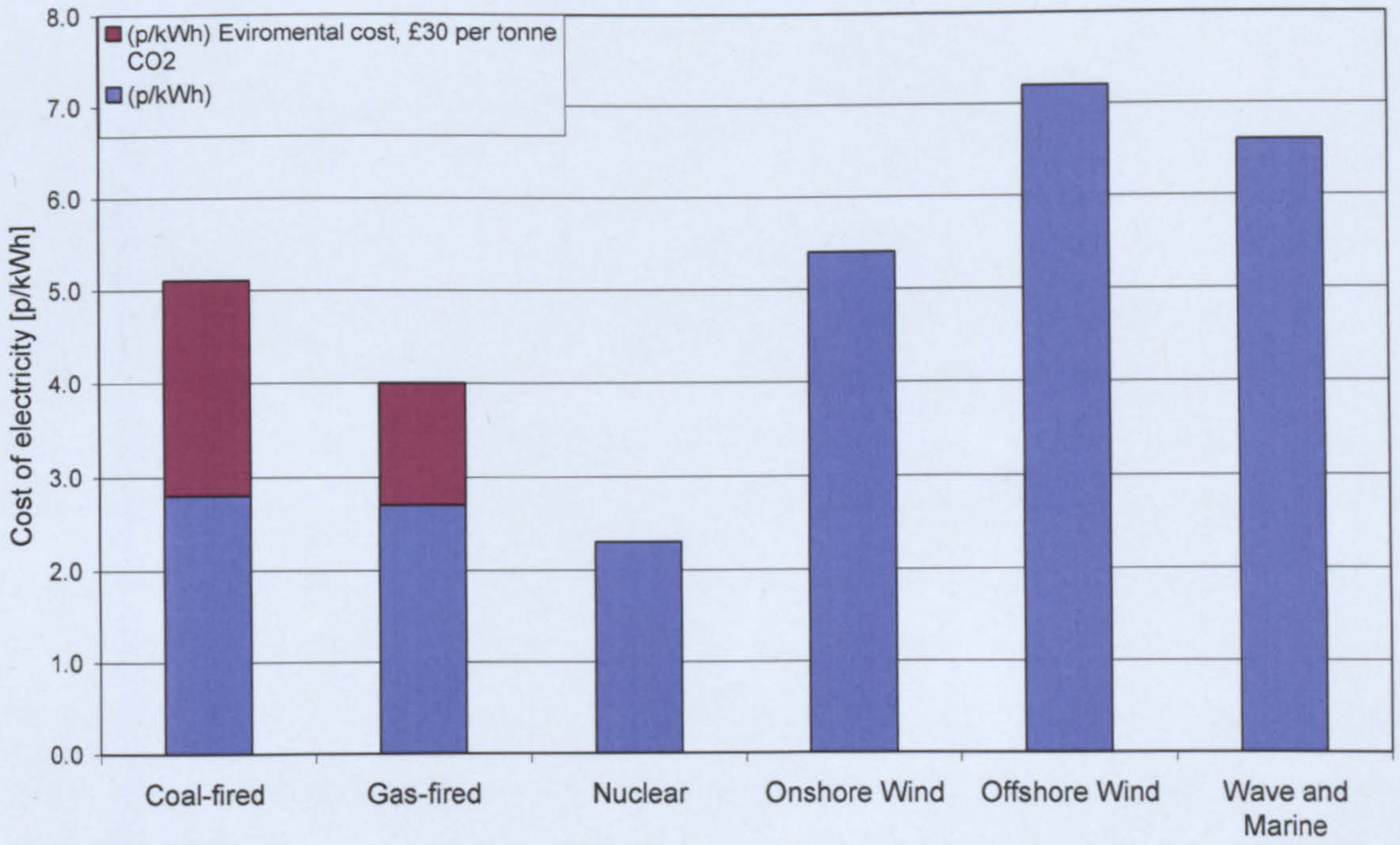

Figure 1.1.5 Cost of generating electricity with respect to CO_2 costs. (Environmental cost £0-£30 per tonne). Source data (Royal Academy of Engineering, March 2004).

1.2 Carbon capture and sequestration

Carbon capture and sequestration could be a possible method of reducing the global carbon dioxide emissions. This could enable the continued use of fossil fuels for energy generation. The principle of carbon capture and storage varies depending on the fuel used. For coal generation, the carbon dioxide is removed at the chimney after the coal has been combusted. Carbon dioxide is removed from the exhaust gases via the use of a chemical scrubber containing amines which bonds to the carbon dioxide enabling it to be removed. For gas-fired power plants carbon dioxide may be removed in a steam reforming process which produces hydrogen which can be cleanly combusted, carbon dioxide can be removed from the synthesis gas before it is combusted. This is already a commonly used commercial process to produce hydrogen gas industrially.

Once captured the carbon dioxide gas is then compressed in to a liquefied state and transported to old gas, coal, or oil fields, or possibly saltwater aquifers below the ground, where the carbon dioxide can be stored indefinitely. In the past similar techniques have been used to inject carbon dioxide into ageing oil fields for increased oil recovery. If saltwater aquifers were to be used, then it could be expected that the carbon dioxide would react with water and minerals

and become a stabilised solid. It has been estimated that there may be enough geological storage to economically store 11,000 billion tonnes of carbon dioxide (Pearce, 2005). The additional cost of carbon capture to conventional fossil fuel generation could be around 30-40 euros per tonne of carbon dioxide.

1.3 Sustainable living

Domestic energy consumption accounts for 30% of the UK's total energy consumption. Space heating accounts for 40% of residential energy consumed, 13% for water heating and 9% for lighting (Department for Business Enterprise & Regulations Reform, July 2002). Between 1971 and 2001 domestic energy consumption increased by 36%. Per household, the energy consumption has increased by 5%. This can be attributed to the increase in the number of houses which have central heating as well as the increased use of electrical appliances in the home. However this has also been partly offset by the increase in energy efficiency within the home. The number of houses being built over the last thirty years has also increased, with changes in modern lifestyle resulting in lower household occupancy (National Statistics, 2004).

Increasing building efficiency by the use of better thermal insulation and improved building design for new buildings can significantly reduce the residential energy requirements. Loft insulation, cavity wall insulation, and double glazing are now incorporated into modern buildings, which substantially improve modern building efficiency. A large proportion of the required heat load can be met by using micro-renewables integrated into the building structure. Solar thermal heating systems have been proved to be able to supply over half of a building's water heating requirements throughout the year. Building-integrated photovoltaic technology can also meet a significant proportion of a building's electrical load.

1.4 Building-integrated photovoltaics (BIPV)

Photovoltaics are one of the most promising future renewable energy technologies. Solid-state electronics make it silent when running, with no obtrusive moving parts. It is the most reliable of all renewable technologies, with few components to fail. Its modular design enables systems to be easily designed and installed. It is also very easy to scale a system from a few watts to

many megawatts in size. The performance of PV is very predictable throughout the year. The only limiting drawback of PV is the current high market price, which is been held high due to the high costs of silicon. One of the possible solutions to this is to use photovoltaic modules as a building material, incorporating PV modules into a new structure's cladding. This can significantly reduce the capital cost of investment in renewables as some of the costs can be absorbed into the cost of the building. Using a building to support PV also eliminates the need for costly and energy-intensive supporting structures to support the PV modules. Electricity generated can be supplied directly into the building's ring main and thus into the national grid, removing the need for any costly grid extensions. The energy is also generated at point of use, reducing transmission losses. BIPV also offers an effective way of significantly reducing a building's carbon footprint.

BIPV technology is very visible but unobtrusive, which makes it a very effective method of raising public awareness and perceptions of renewables. The use of BIPV creates and promotes a high-tech environmentally caring image, which is very desirable for modern industry. Bringing such technology into the workplace and home enables people to see what is possible and achievable. It also makes individuals feel more responsible for their energy consumption and increases energy efficiency. Photovoltaic systems can be retro-fitted to existing building stock, although this is not the practical solution for many installations as it requires additional structural work which is both costly and energy-intensive. In many cases the building's design and location restrict PV facades from achieving optimum performance.

Over the past few years BIPV has progressed from individual demonstration projects to a commercial scale, with PV arrays being installed much more commonly on both commercial and domestic buildings. This is particularly so in Europe, where government incentive feed-in tariffs make BIPV economically attractive. This shift from demonstration projects to small-scale commercialisation has resulted in a rapid growth in the number of small companies who install such technology. Many of these companies are relatively small and do not have the skills or resources to carry out full solar audits before installing the technology. As a result, many systems which have been installed

are operating with outputs below their design specifications. This is mainly a result of BIPV arrays becoming shaded due to obstructions on the horizon and a loss of power at certain times in the day.

A computer software package is required to aid engineers to design, plan and simulate the performance of BIPV systems before they are installed. This would aid designers in installing BIPV systems in optimal locations; it would also allow the design of optimum layouts. For example, if an installed BIPV array is known to receive shading at certain times of the day, then the PV modules which fall under shade at the same time can be connected up into individual strings. Thus when the BIPV array receives shading, only one string of PV modules is affected and the overall affect of shading on the power output is reduced.

1.5 Building-integrated micro-domestic wind turbine technology

The micro-turbine market has grown rapidly in recent years. The technology was previously used for specialised applications such as telecommunications and the marine industry, being used to supply energy to sailing craft and offshore navigation aids. Applications were typically sited in remote locations away from the grid supply, where the cost of extending existing power networks may have added a vast expense or be impossible.

The increasing public awareness of green-house emissions from fossil fuelled power generation and the increased energy costs has resulted in the public considering alternative energy supplies to meet part of their energy needs. This has combined with the UK government's backing, driven by grants and targets to reduce carbon dioxide emissions and ensure 10% of the UK's electricity is generated by renewables by 2010. Thus the micro-domestic renewables market was born.

This new market is small, with many of the installations being educational and demonstration projects set up by community groups and educational establishments. Enthusiasts, who are environmentally aware of the potential effects of global warming resulting from carbon emissions and are willing to pay a premium for sustainable energy, are also installing turbines.

Recent media coverage has suggested that micro-domestic wind turbines installed in urban locations have not been meeting owners' expectations, with turbines supplying little or no energy to the domestic households. As a part of this thesis study, I will review the performance of a range of these commercially available turbines, to determine the available energy yield from a building-integrated micro-turbine as well as determining the available energy from the wind regime. The overall aim is to determine the suitability of the use of micro-wind turbines on buildings as a possible source of energy generation.

1.6 Energy efficiency

The world's energy supply has reached a turning point. Increasing energy demand, growing environmental concerns and future fuel shortages will require sociological, economic and technical challenges to be met. Meeting the future energy demands and reducing carbon emissions is the greatest global and sociological challenge the world has ever faced. This will require a two-directional approach: to reduce energy demand by increasing the efficiency in which energy is used; and to secure a sustainable energy resource for the future.

Improving energy efficiency will require governmental leadership to encourage individuals and industry to reduce energy demands. This can be achieved by improving the energy efficiency of buildings, transport and electrical appliances. This is already possible with today's technologies, although legislation and government incentives are needed to implement the changes. Improving building standards by increasing thermal efficiency and the use of better building design can reduce a building's space heating and cooling load dramatically. Technologies such as combined heat and power plants, building-integrated renewables and the wider adoption of low energy devices can all play a part in reducing a building's energy requirements. Transport accounts for a large segment of energy consumed. This can be addressed by increasing the use of public transport and improving the efficiency of vehicles by better design and the adoption of new technologies.

1.7 Energy supply

Energy supply can be split in to three segments: fossil fuels, nuclear and renewables. Fossil fuels are the country's prime energy source and will remain a prime source for the foreseeable future.

1.7.1 Fossil fuels

In practical terms, fossil fuels are well suited for transport, due to their high chemical energy density which is currently unrivalled by any other energy storage mediums. Fossil fuels can be split in to three classes: oil, gas and coal.

Oil is primarily a fuel used for transport. Currently oil is readily available at an affordable price, with additional resources available for exploitation, although these resources could potentially be limited by political and technical difficulties. Political disputes in the Middle East could block access to the Middle Eastern oil fields. Technical and environmental issues could cause difficulties in accessing the Arctic oil fields.

Gas is a key fuel in terms of electricity generation as the UK government has turned towards gas over coal due to its cleaner emissions. The UK is now a net importer of gas, and is currently enlarging its storage capacity due to concerns about the security of supply from Russia. It is expected that the UK's dependency on gas will continue to grow in the near future. Abundant coal reserves also exist, and these potentially ensure a long-term secure generation capacity if required, although the UK government's policy has been to replace coal with gas for much of its generation capacity due to its lower carbon dioxide emissions. However coal emissions could be reduced with the augmentation of cleaner technology or carbon capture and storage, though the increased economic cost makes it currently uneconomical compared to its alternatives.

1.7.2 Nuclear energy

Nuclear fission is a well-known mature technology, which is likely to continue to play a key role in bulk generation in the future, but there is a large public safety concern based on past accidents. Concerns would have to be addressed before it could be widely accepted by the public. Nuclear fission also has high installation and running costs, partly due to the long licensing process as well as

a lack of companies who will take on the specialist component manufacturing required. Due to the reaction process, nuclear fission is not a flexible form of generation, with reactors taking several days to come on and offline. Therefore nuclear energy can't complement the intermittencies of renewables, and another medium such as a gas-fired power plant would be required to fill the energy gaps.

1.7.3 Renewables

Renewable energy could meet up to 80% of the UK's energy needs by 2050. This would require long-term government incentive schemes to help develop and implement new technologies. Current renewable technologies such as hydro, large-scale wind farms and bio-energy are capable of bulk generation at reasonable economic costs.

Solar thermal energy is also in its maturity and is capable of supplying much of the domestic water-heating load at a cost lower than that of conventional heating systems. Solar PV is also a mature technology, which is capable of supplying a significant segment of the renewable energy market. Unfortunately the high silicon manufacturing costs are holding this technology back. However it is expected that future developments will significantly reduce the costs and PV will become one of the leading renewables.

Marine generation technology is in its infancy, but with the UK's large wave resources this technology could also potentially supply a very large segment of the renewable energy market at very economic costs.

With the increased focus on renewable energy, with its potential of providing energy generation with low carbon emissions, many countries are looking to increase their renewable capacities. Governments are not only working on macro-scale sustainable energy projects, such as large-scale wind farms; it has also been recognised that the use of micro-generation (and in particular the potential of building-integrated renewables) can make a key contribution. It has been acknowledged that, to meet the long-term aims of reducing greenhouse emissions, the situation will have to be addressed in two key ways. Firstly, a large component of the current generation using fossil fuels has to be replaced

by low emission and sustainable technology. Secondly, increased energy efficiency has to be achieved, thus reducing energy demand. Currently global energy consumption is increasing year on year. If energy consumption can be reduced then so can that of the supply.

The key area where efficiency can be increased is within the building environment. A large part of energy consumption is consumed within buildings, so it is necessary to reduce this energy demand. Again this can also be met in two ways. The first is to increase the performance of buildings, resulting in buildings requiring less energy. The second approach is to incorporate measures to enable the building to meet its own energy demands, thus reducing the demand of energy brought into the building.

1.8 The role of hydrogen

The increasingly noticeable affects of global warming, it is now time to find a suitable clean and sustainable fuel replacement. Hydrogen generated from sustainable resources will most likely be the energy carrier used to replace hydrocarbon-based fuels. As part of this study, this thesis will review hydrogen technology, as well as documenting the setting up of a hydrogen research facility to enable the demonstration of the sustainable hydrogen generation, storage and use with fuel-cell technology. The facility will also enable future research into aspects such as environmental impact and sustainability of a hydrogen economy.

1.9 Renewables and transport

Transport is a key part of today's global economy and lifestyle, affecting all aspects of life. Fossil fuels are used to run the majority of all types of transport, accounting for two-thirds of the world's oil consumption. There are currently more than half a billion vehicles on the world's roads; with millions more being added each year as the world economy continues to grow. Transport is one of the main contributors to the world's carbon dioxide emissions.

Transport poses one of the most difficult technical challenges of reducing global greenhouse emissions. This is because transport requires a high energy density fuel which has a relatively small volume to enable it to be easily transported.

Over the last hundred years hydrocarbon fuels have been the ideal fuel. Now the problem arises of finding a new high energy density storage medium which can be used as an energy carrier to replace fossil fuels. Hydrogen gas generated via renewable means is one possible method of replacing fossil fuels as it is a high energy density storage medium. Another possible solution for road transport could be the use of batteries and ultra capacitors for energy storage. As part of this study, this thesis will look into the use of alternative energy storage mediums for use in personal urban transport.

1.10 The present research project aims and objectives

This thesis studies and analyses four key areas of renewable energy systems with practical interest in building integrated renewables, energy storage mediums and sustainable energy for transport. The thesis thus covers the following areas: building-integrated solar energy systems, building-integrated micro wind turbine technology, the use of hydrogen as a sustainable and renewable energy storage medium, and finally the possible use of renewable energy for sustainable transport applications.

The aims of the project for each of these four areas are given below.

1.10.1 Building-integrated solar energy systems

- To develop solar energy models which enable the precise design and accurate simulation of building-integrated photovoltaic arrays within urban locations where the surrounding environment contains objects such as buildings and trees which may cause shading resulting in a loss of performance.

- Solar models should be based on commonly available sub-hourly horizontal irradiance data which is readily available, being recorded at many stations around the world.

- To model and simulate the performance of the Edinburgh Napier University solar PV facade, and determine overall energy losses due to shading.

- To determine the overall performance efficiency of the Edinburgh Napier University PV facade.

- To evaluate the performance of the solar models developed compared with the measured performance of Edinburgh Napier University PV facade.

- To collect and quality control both horizontal and tilted global irradiation measurements as well as Edinburgh Napier University PV facade power output measurements.

- To develop regressions to estimate diffuse irradiance from its global counterpart. Diffuse and beam components of global irradiation are required to accurately simulate solar thermal photovoltaic applications as well as heat gain in buildings.

- To evaluate the performance of regressions developed to estimate diffuse irradiance from its global counterpart using visual and statistical evaluation techniques.

- To evaluate the performance of models compared with the measured performance of the Edinburgh Napier University PV facade using visual and statistical evaluation techniques.

1.10.2 Building-integrated micro wind turbine technology

- To review the performance of micro building-integrated wind turbines for use on domestic properties to generate electricity.

- To compare and evaluate yielded energy generated compared with manufacturers' claimed outputs.

- To install, monitor, and data log rooftop wind turbines on Edinburgh Napier University's rooftop.

- To analyse the performance of Napier's rooftop wind turbines using measured data.

- To compare the performance of both grid-connected and stand-alone systems.

- To determine the available wind resource and wind regime on Edinburgh Napier University's Merchiston campus rooftop.

1.10.3 The use of hydrogen as an energy storage medium and the development of the Napier hydrogen laboratory

- Part of the research project undertaken for this thesis included the design, development and management of the installation of Edinburgh Napier University hydrogen research lab. An operator training scheme and lab safety procedures were also developed. The lab is to serve two purposes: firstly to provide a user-friendly, safe environment to be used for the development and testing of hydrogen fuel cell technology. It will be used for future research projects. Secondly the hydrogen lab is also to be used as an energy storage medium, to enable energy generated via renewable means such as solar and wind to be stored and used to resolve the problems of intermittency in renewables. It will also demonstrate the cycle of generation, storage and uses of renewable energy.

1.10.4 Evaluation of the uses of renewable energy for sustainable personal transport

- To review energy storage mediums suitable for the use with personal transport applications.

- To determine the environmental impact of the current use of personal transport.

- To measure and determine the typical driving cycle taken within the urban environment.

- To determine the energy demand and consumption of both fossil-fuelled and sustainably fuelled personal urban transport.

- To compare the environmental impact of sustainable personal transport with that of fossil fuelled personal transport.

1.11 Outline of the thesis

Chapter 1 gives the introduction to the thesis, which broadly covers the field of energy. The chapter begins with the global energy history before introducing and discussing energy sources such as fossil fuels, nuclear and renewable energy. The chapter also outlines the key areas of renewable energy which this thesis will investigate further.

Chapter 2, the literature review, covers the following areas of interest: the development of world renewable energy; solar energy and irradiation models; Edinburgh Napier University photovoltaic facade; wind energy and wind energy models; and micro and rooftop wind energy.

Chapter 3 examines the collection and quality control of the presently used solar database, and the development of solar energy regressions between horizontal global and diffuse irradiation.

Chapter 4 covers the development of solar irradiation models for use in urban environments, including the development of BIPVcalc software. The models have been developed to incorporate shading from trees and buildings. Statistical tests for the evaluation of solar models are also discussed in this chapter.

Chapter 5 covers the validation of ISRM and SRDM model performance using measured data recorded from the Edinburgh Napier University PV facade and using statistical tests. This chapter also reviews the performance of the Edinburgh Napier University PV facade.

Chapter 6 reviews wind energy within urban environments, the performance analysis of three micro turbines sited on the roof of Edinburgh Napier University,

the rooftop wind regime and the development of Windcalc, a software which has been developed to analyse micro-turbine performances.

Chapter 7 covers the review of hydrogen technologies, and the development of the Napier hydrogen facility.

Chapter 8 compares a conventional petrol car with an electric scooter which is powered by renewably generated energy. The Edinburgh driving cycle has been used as the basis for comparison.

Chapter 9 draws important conclusions from each aspect of the presented work. The potential for future work is also discussed.

CHAPTER 2

Review of the relevant literature

Solar Energy

2.1 Introduction to photovoltaics

Solar PV has the fastest growing market of all the renewables. The main areas of growth are in countries which have government-run incentive programmes. Currently photovoltaics provide a small but significant proportion of the renewable energy's global market. In the early 1990s, growing concerns for the environment and global warming as a result of fossil fuel emissions led many governments to review their energy policies. These new policies promoted the use of renewable energy and over the last ten years the market has rapidly expanded year on year. Until late 1996 the US represented 36% of global market share (BP, 2008). The Japanese government then started a programme to support the manufacture of photovoltaics, and introduced the goal of installing 200MWp of PV systems by 2000 to ensure market growth. This resulted in a large growth in the Japanese market share to 35% [Anon.] (2005).

In1997 the global PV demand was estimated to be 114MWp. Demand grew by 400% in 5 years to 505MWp in 2002 (Mints, 2006). Germany also introduced a new version of its renewable energy law which included a renewable energy feed-in tariff for renewably generated electricity. This enabled renewable energy suppliers to be paid above the market price for energy which was produced by sustainable means. This was the first time any government had tried to implement such a programme on this scale. The original feed-in tariff in 1990 was set at around 8.5 eurocent per kWh, although this only proved economical to wind energy developers, which grew rapidly at the time. The German government, still keen to develop its PV programme, and then introduced its 100,000-roofs programme in 1991, and in addition to the feed-in tariff the government offered cheap low interest loans for installers. At the start of the programme, PV installation capacity grew slowly (around 3MW a year) in the early 1990s. This figure grew year on year, with the increase in public awareness and interest, to around 12MW a year by 1999. The German feed-in tariff has always been kept very simple. A band tariff system has now been

brought in, with smaller systems been paid more per kWh than large systems. All PV systems have to be grid-connected and the utility companies buy every kWh generated at a fixed price for the next 20 years. The loan program ended in 2004, and its success prompted the German government to continue its renewable energy initiative with the introduction of an increased feed-in tariff to compensate, resulting in a 600MWp German PV market in 2005 (Bächler, 2006).

The PV market continued to see strong growth in 2005. Based on the success of the German programme, other European countries including Spain, Italy and Greece have begun to introduce similar incentive programmes. Table 2.1.1 shows key figures for European PV incentive programmes for the EU-15 countries. Figure 2.1.1 shows the global PV market growth from 1996 to 2007. It can be seen that Europe has the fastest growing markets with the largest installed capacity.

Spain has introduced a similar feed-in tariff system after seeing Germany's success. Spain now has the second largest market share in Europe. The Spanish government has set the target of installing a capacity of 150MW (Celik *et al.* 2009). Initially the programme suffered due to a complication in the regulations which limited the size of installations. Larger installations had to be split up and classed separately as smaller systems which resulted in long delays in the permit system. A new tariff is currently being revised and is expected to simplify the process. France has taken a whole new approach to its feed-in tariff. Photovoltaic systems are required to be fully building-integrated, serving another purpose to that of electricity generation. The Italian market already has a large PV capacity installed; the feed-in tariff which is currently being proposed there has a complex structure which will pay between 34-49 eurocent per kWh and is capped at 100MW. Greece, being in the Mediterranean region, has a superb solar resource and has long since had a strong solar thermal industry, but until recently the PV market has been very small. The creation of a new renewable energy law aims for a target of 20% renewables by 2010 and 29% by 2020. The feed-in tariff varies between 40 to 50 eurocents, being adjusted depending on the size and location of the system. Increased rates are paid for islands (Celik et al. 2009).

However these programmes are not likely to expand their country's markets as rapidly as the German market because they are currently capped, which will limit the market growth. It is expected that the rest of the world, lead by China, Taiwan and the Philippines, will surpass Europe in the manufacturing of PV modules by 2008 (Mints, 2006).

Table 2.1.2 shows the installed PV capacity of the EU-15 countries. It shows that Germany has the largest installed capacity of PV, with 87.7% of Europe's installed capacity. Spain has the second largest installed capacity of 4.2%. The PV market is held back by the high cost of silicon, as 90% of current PV production involves crystalline silicon technology. Currently the PV market is also being held back by the short supply of silicon wafers, which has also driven up the market price of silicon. The development of PV technology has tried to compensate for the shortage of silicon, with new designs of PV modules using thinner silicon wafers to reduce the volume of silicon used in each module. However, the rapidly expanding PV market can only be sustained with an increase in silicon production. Thus large-scale investment is required in the silicon industry to increase its production capacity. It is expected that the market will continue to grow strongly in the coming years.

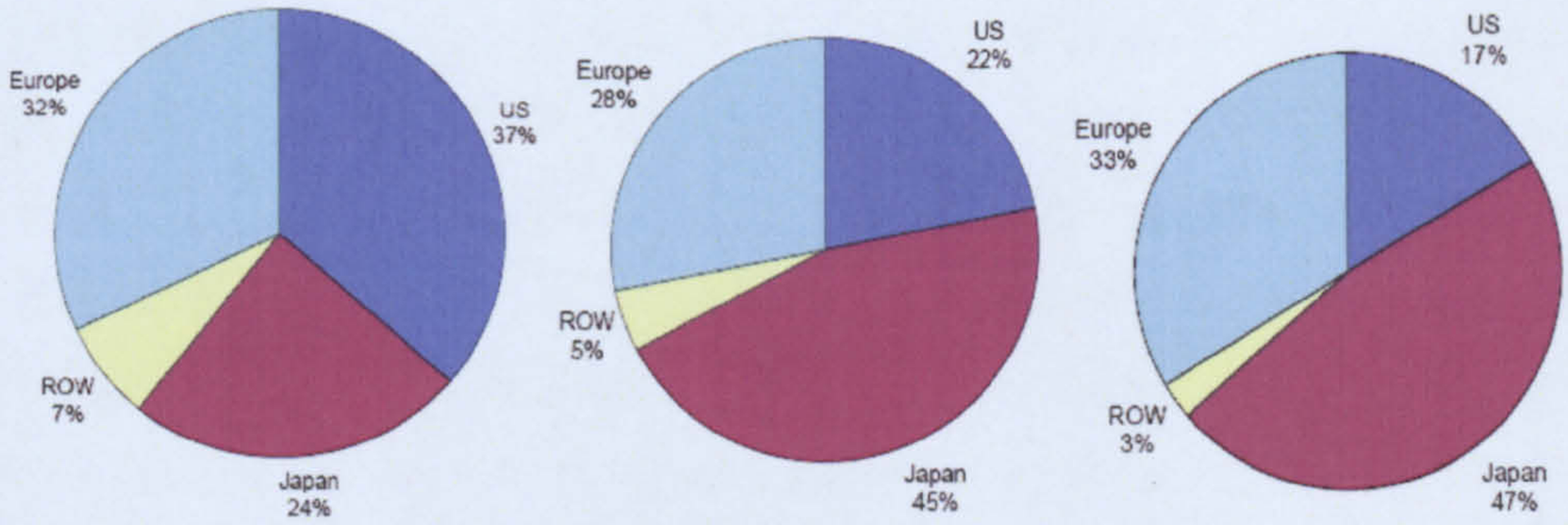

Figure 2.1.1. Cumulative installed PV capacity. Source data: BP, 2008 & Marketbuzz, 2008.

Table 2.1.1 Installed PV capacity EU-15 2006

	Total installed PV capacity, MW_p	Percent, %
Austria	23	0.8
Belgium	3.9	0.1
Denmark	2.9	0.1
Finland	4	0.1
France	43.6	1.5
Germany	2490	87.7
Greece	6.7	0.2
Ireland	0.3	0.0
Italy	48.5	1.7
Luxembourg	23.3	0.8
Netherlands	52.7	1.9
Portugal	3.8	0.1
Spain	118.2	4.2
Sweden	4.8	0.2
United Kingdom	13.9	0.5
Total	**2839.6**	

Source data: Celik *et al.*, 2009.

2.2 Rural electrification

Micro-generation systems such as solar PV can play a crucial role in the development of rural areas in developing countries, where the addition of energy can change the way of life for communities which are too remote for access to the national grid or just too poor to be profitable customers for the power

companies. Off-grid PV can prove to be a cost-effective and reliable energy solution for these areas. A relatively small power supply can make a significant difference to a community's health and economy. The majority of rural communities have been built up around water supplies, but in recent years the changes in weather patterns have resulted in changes in rainfall patterns. It is not uncommon for a community's women and children to have to spend many hours each day travelling on foot to find water for their families. The water supplies are often contaminated and water-born diseases and parasites are a particular problem in the dry seasons. Scarcity of water can force communities to share water supplies used by livestock, causing health problems such as diarrhoea, disease and dehydration. A simple solar PV-driven pump can supply communities with clean safe drinking water. Off-grid PV technology can not only improve basic life standards but can also be used in developing economies. Rural electrification goes far beyond lighting, TVs and water pumps. With the age of digital communication, rural electrification brings information and communication technology as well as services such as finance and insurance, health and education which in turn will enable rural economies to grow (Macias, 2007). In 2005 the UK Finance Minister Gordon Brown at the G8 summit pledged to end poverty in Africa, and to act against climate change (Brown, 2005). The potential of the African PV market has long been recognized by the PV industry. Although markets in Europe, America, Japan and China have rapidly expanded, the African market has remained stagnant. In 1995 Africa accounted for a quarter of the 75 MW world's PV demand (Hankins, 2006). Since this time there has been little growth in Africa's PV market, despite there being around 80 million families off-grid in rural Africa. This has been attributed to several causes, but it is mainly due to the fact that there are virtually no government incentive programmes to subsidise the use of PV technology, resulting in few companies being willing to pursue projects in Africa. The second reason is that PV technology is seen as a poor second-class technology to substitute for the national grid. Governments are not keen to promote the use of off-grid PV as it is politically preferable to make unrealistic promises of grid power. The perception of PV technology is that of the early primitive 12-volt systems with limited power output and not the modern high-performance technology which is on the market today.

2.3 Edinburgh Napier University PV facade

Edinburgh Napier University's School of Engineering and the Built Environment PV facade was set up to demonstrate the viability of solar electricity in high latitude (56°) locations. The University commissioned the medium-sized photovoltaic (PV) electricity generation project in Edinburgh shown in Figure 2.3.1.

Figure 2.3.1 Edinburgh Napier University solar facade under discussion.

Since the installation of the facility in April 2005, the power outputs have been recorded via data-logging at 15-minute intervals. In addition to the photovoltaic facade, the solar energetic inputs into the system have also been monitored. The facility is fully grid-tied, supplying the University with 11.5 MWh of electricity annually.

The array has 192 mono-crystalline silicon BP-Solar BP790 modules, each measuring 0.54m by 1.21m. This equates to a total surface area of 160m^2, with an effective area of 125.5m^2. There are 6 modules on each row of the PV array and the rows are wired together in series, forming "strings" of modules. Each module produces 90W of DC electricity at 22 volts under reference conditions of 1000 W/m^2 irradiance, and stringing modules together in series increases the circuit voltage to a useable voltage. DC power from the strings is then transformed to a stable AC power supply using four inverters. Two larger inverters (6kW peak) are each connected to four strings of 18 modules and two smaller inverters (2kW peak) are each connected to two strings of 12 modules. The voltage rises as soon as the PV modules are irradiated. The maximum output voltage is 500V DC. The inverters turn on as soon as the string voltage exceeds 100V. Under reference conditions, each of the large and small inverters receives a power input of 4.6kW at 20A and 2kW at 7.8A respectively, ensuring a normal generation of 14.4kWp (kW peak) AC power. The inverters consume 12 and 7W of power under operation and 0.15W in night-time stand-by mode (FRONIUS IG, 2005) and are grid-connected, feeding electrical power directly into the University ring main. One of the four inverters contains a data-logger which averages AC and DC voltage, current and cumulative AC power and energy outputs for each inverter. The data-logger is capable of storing six weeks of data (collected at 15-minute intervals). Figure 2.3.2 shows the inverters and power distribution board for the facade.

Figure 2.3.2 Napier PV facade control board.

The PV array has an aspect angle of 37° East of South and a tilt angle 75° from horizontal. Note that due to architectural and planning restrictions, this is not the optimum orientation for the location - the optimum tilt angle for Edinburgh Napier University's facade lies between 35° and 40°.

The total cost of the project was £155,000 and was partly funded (60%) by the UK Government's PV electricity demonstration programme through the office of the Energy Saving Trust.

2.3.2 Performance analysis

Figure 2.3.2.1 represents a good day's performance of the Napier PV facade and, as before, both solar input and PV AC output have been recorded on a 15-minute averaged basis. It can be seen that there is a gradual increase in the incident solar irradiation up to around 10am - this is a regular observation in Edinburgh as the morning sun gradually 'burns' prevailing cloud-cover. From 10am the incident solar irradiation rapidly increases to a peak of 106kW at 11am, followed by a gradual decrease as the impact of the solar radiation decreases. The PV AC power output follows a similar trend to the solar input.

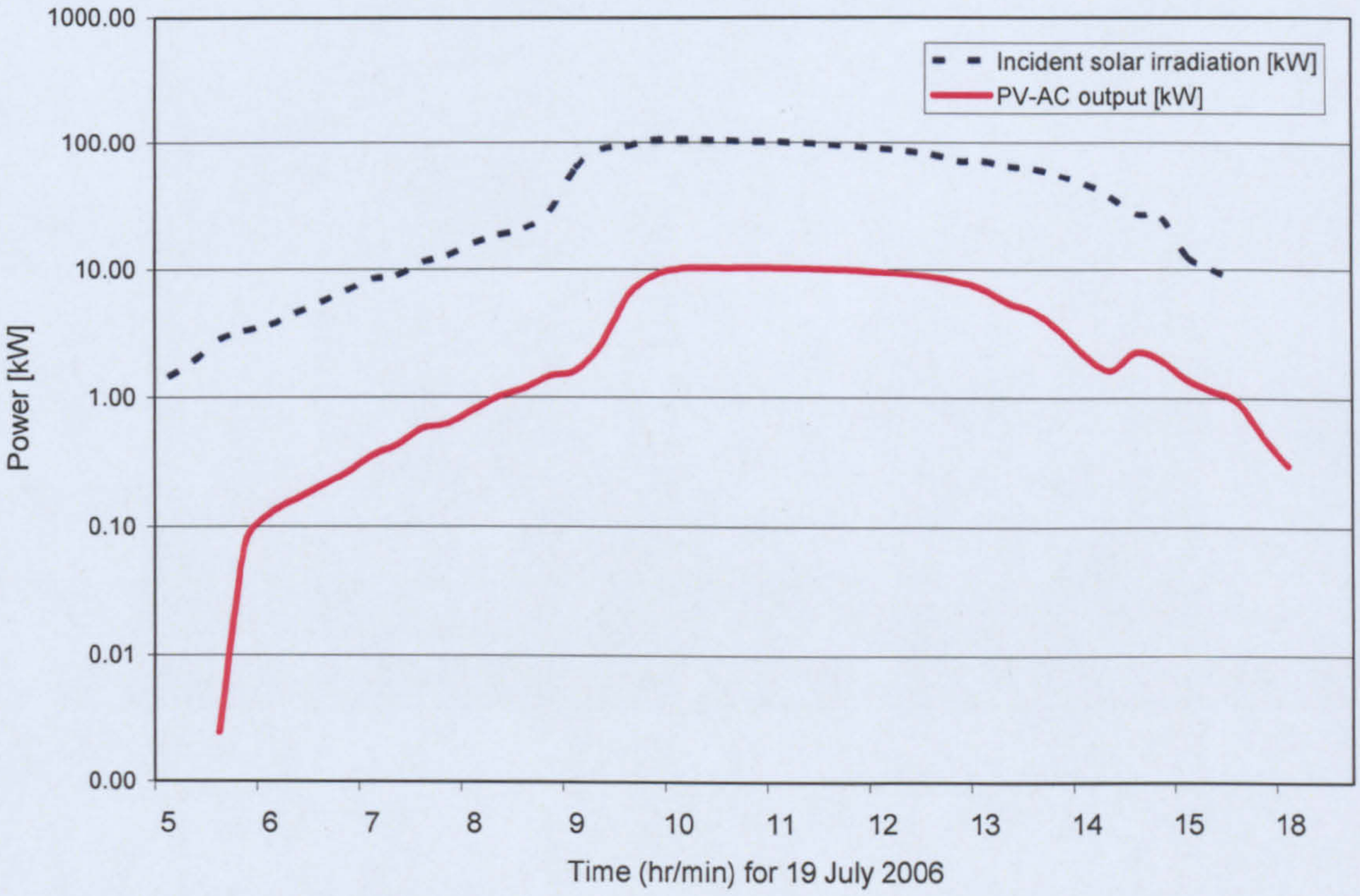

Figure 2.3.2.1 Incident solar irradiation input compared with PV-AC output for Napier PV facade 19 July 2006, 15-minute averaged power. Note: log scale for Y- axis.

It has also been noted that there are certain times in the day, i.e. early morning and early afternoon, when the PV array experiences solar shading, thus reducing the power output and the overall efficiency of the facility. It has been found that there are two causes of shading on the PV facade. In the early morning, lower rows of the PV array can experience shading due to the surroundings such as trees and surrounding buildings. In the afternoon, a protruding bay window casts a shadow across the facade (Figure 2.3.2.2), and by mid-afternoon the facade is fully shaded. For this given , with an aspect

angle of 37° and tilt angle 75°, shading can result in an energy loss of up to 18% of the daily energy output.

Figure 2.3.2.2 Napier PV facade experiencing shading from protruding bay window in the afternoon (08/05/06 at 3:45 PM).

Figure 2.3.2.3 shows a day's data for July 19th 2006 with the energetic incident solar inputs multiplied by the monthly system efficiency (for July, $\eta = 12.4\%$). It shows the loss of power output as a result of solar shading. The shading in the afternoon caused by the bay window has a greater effect on the daily energy output than the morning shading.

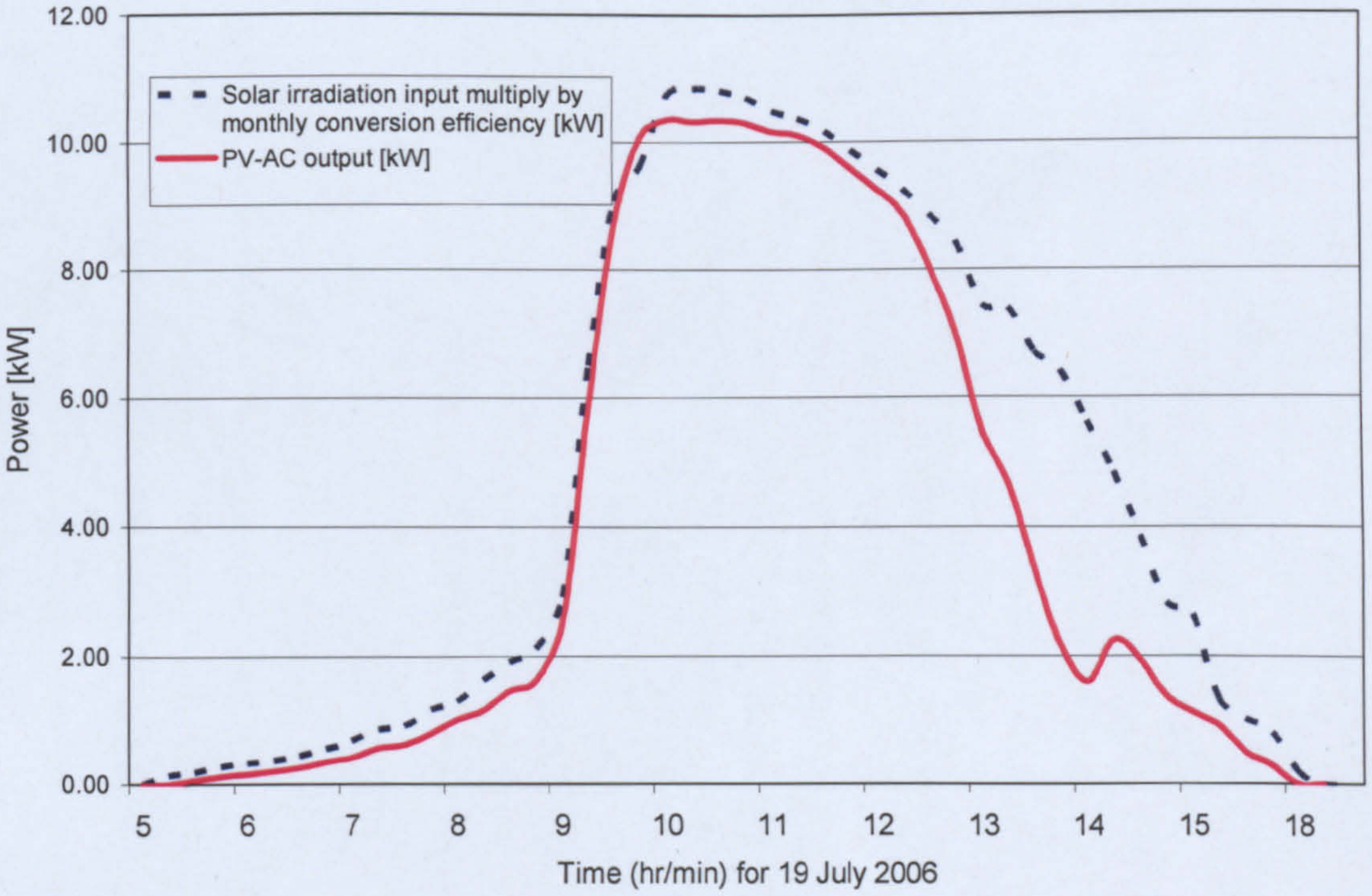

Figure 2.3.2.3 Loss of power due to shading that occurs mainly in the afternoon for Napier PV facade 19 July 2006, 15-minute averaged power.

2.3.3 Energy inputs and outputs

Figure 2.3.3.1 shows the averaged daily energy outputs for both PV-AC and PV-DC since May 2005. The mean averaged daily electrical energy output is 29.5kWh.

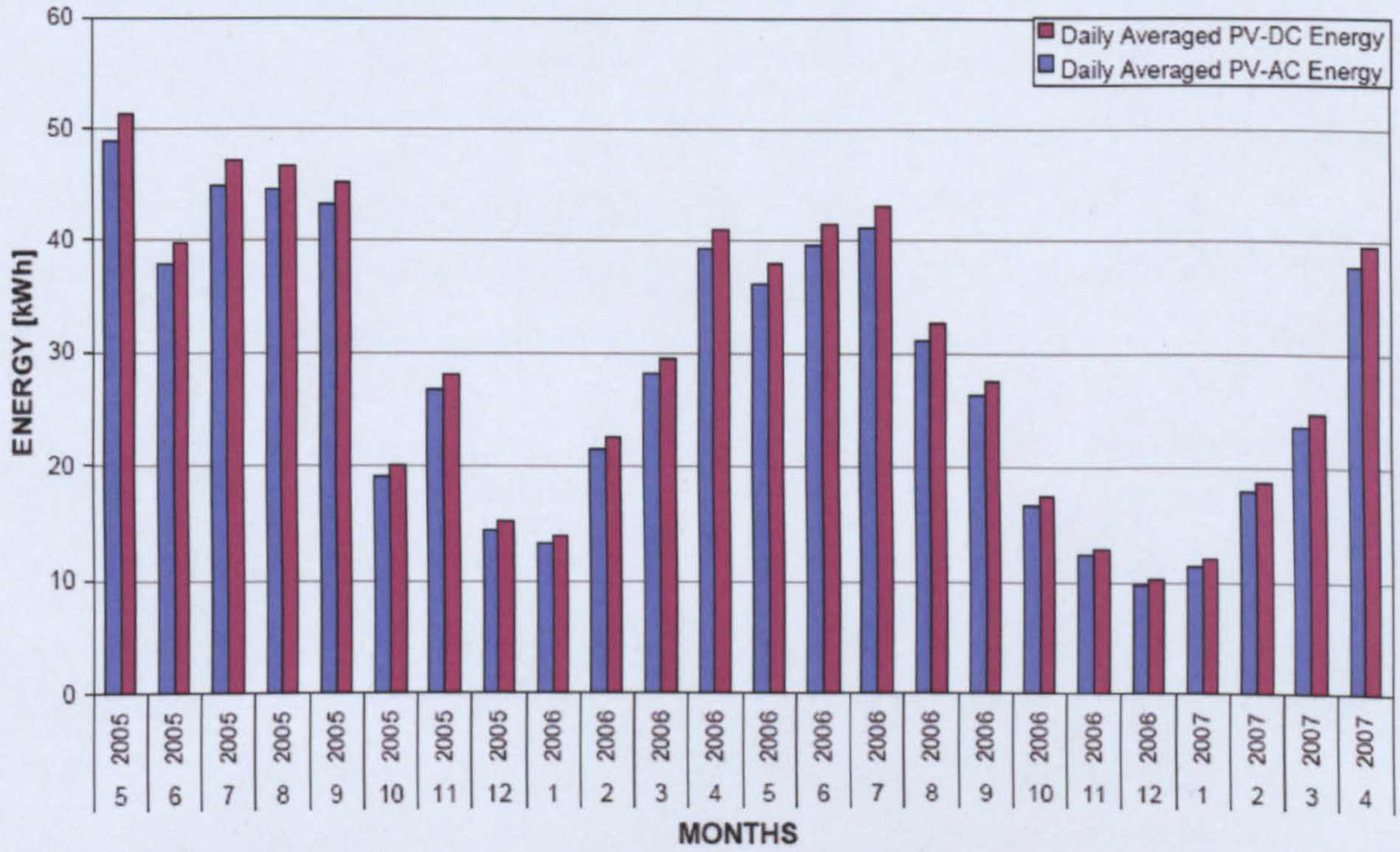

Figure 2.3.3.1. Daily averaged PV-AC and PV-DC energy outputs, Napier PV facade.

Figure 2.3.3.2 shows daily averaged incident solar inputs and PV-AC outputs since May 2005. The mean average daily incident solar irradiance is 307kWh.

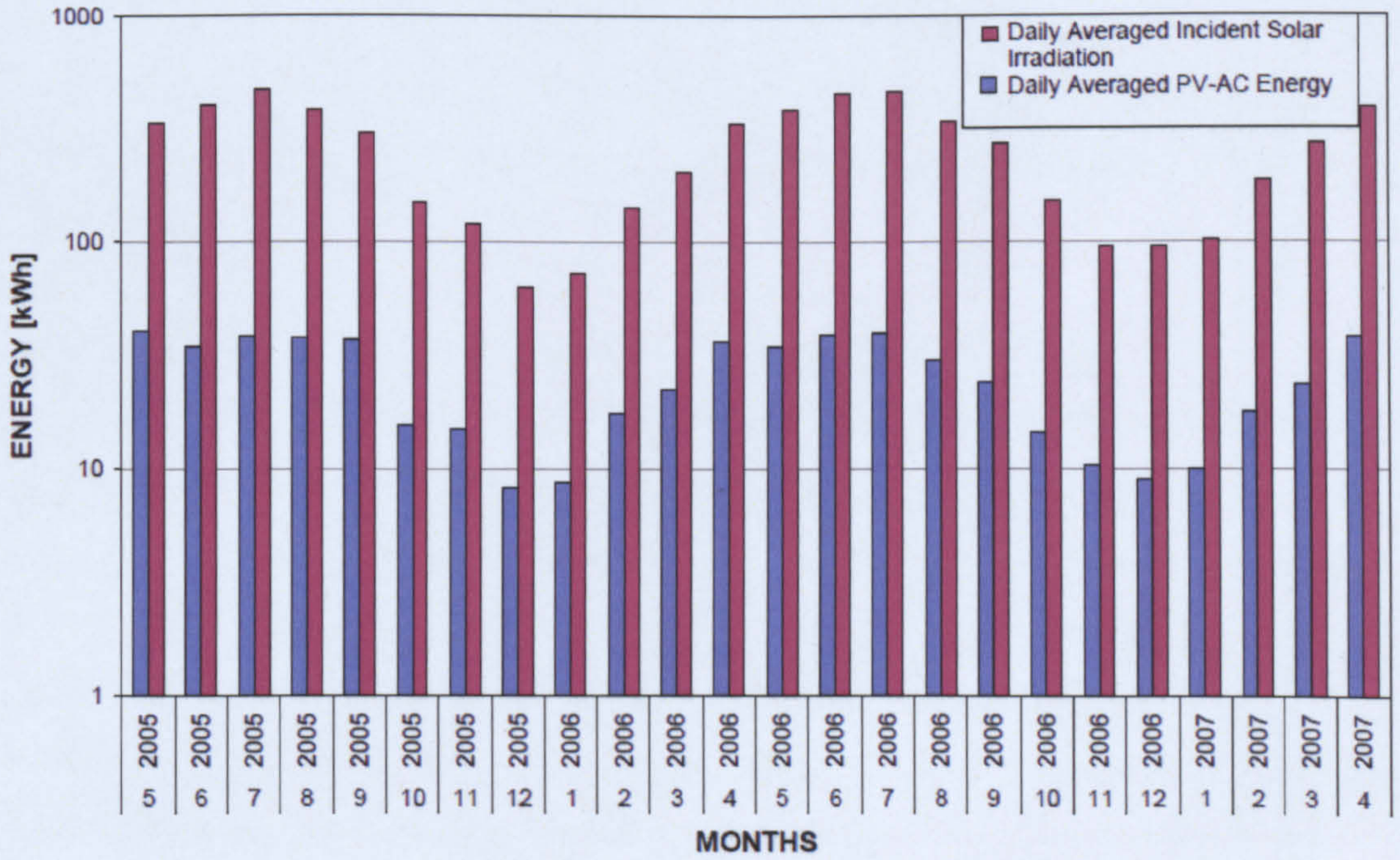

Figure 2.3.3.2 Daily averaged incident solar irradiation and daily averaged PV-AC energy, Napier PV facade.

From Figure 2.3.3.2, it can be seen that the averaged daily energy outputs for the months of June and October 2005 are lower than expected. This was due to the poor weather conditions with above-average cloud cover for these periods. The highest energy output so far was obtained in April 2006 with an average daily output of 45.8kWh. This was due to very low levels of cloud cover and Siberian winds which bring cold dry air to the eastern flank of Britain. This cold dry air has low moisture content and below-average levels of airborne particulate matter resulting in a low diffuse ratio (diffuse irradiation/global irradiation) and hence high levels of incident irradiation.

2.4 Solar radiation models

Much research has been carried out on modelling solar diffuse irradiation. There are many different techniques which have been developed with varying degrees of complexity and accuracy. These models are based on many parameters such as air mass, atmospheric pressure, cloud cover, global irradiation, humidity and sunshine fraction. A review of Muneer *et al.*'s (2005) work was undertaken, and it was concluded that a relatively simple model was required to estimate solar

diffuse irradiation, using data which is easily available from the Building Service Industry CISBE Guides (A & J CIBSE 2004, CIBSE 2006).
An approach developing correlations between diffuse ratio and clearness index was undertaken by Muneer (1987). This simple technique, which only requires measured global irradiance, has proven reliable with reasonable estimation accuracy.

2.5 The need for computer-generated solar irradiance data

Horizontal hourly and sub-hourly diffuse and beam irradiance are required by engineers for the estimation of global irradiance on a given tilted surface. For stations which do not record all these parameters, or for sites which simply do not record any solar irradiation information, a simple but reasonably accurate method is required to estimate diffuse irradiance separately from its more common global counterpart and thus aid designers and engineers in the design of buildings and solar energy systems.

2.6 Review and validation of existing solar energy models

For sites where no solar irradiation information is available but other parameters are available, it is necessary to estimate solar irradiation from available meteorological parameters recorded on site or from nearby meteorological stations. Accurate estimations may also be required just to validate the accuracy of datasets as well as to fill in any gaps within datasets.

There are four main types of model used for estimating solar irradiance from measured meteorological parameters. These models are reviewed by Muneer *et al.* (2005). The first is known as the Meteorological Radiation Model (MRM) and later came the Improved Meteorological Radiation (IMRM), the Cloud Radiation Model (CRM) and the Diffuse Radiation Model (DRM).

The MRM model is a simple broadband solar estimation model which is based on meteorological synoptic measurements, namely atmospheric pressure, dry bulb temperature, wet bulb (or humidity) temperature, and sunshine fraction (or duration) which are readily available, being recorded at many meteorological stations throughout the UK and worldwide locations. The model uses regressions drawn from a relationship between diffuse to beam ratio, DBR= I_D/I_B, and beam clearness index, $K_B= I_B/I_E$, where I_E is the extraterrestrial horizontal

irradiance. Muneer *et al.*, (2000 and 2004) and Gul *et al.*, (1998) expressed the relationship of the dimensionless variables in the form of a power function, and the model was validated using coefficients for UK and Japan. The early MRM model uses 14 coefficients and the later IMRM model uses 35 coefficients, as a result of the coefficients required for the 4^{th} ordered polynomial given for each of the seven sunshine fraction bands.

The Cloud Radiation Model estimates solar irradiance based on cloud cover information. The model was generated using ten years of data collected in Hamburg, Germany. The model is designed to be used when sunshine duration, atmospheric pressure and temperature are not available but cloud information is. Then the horizontal irradiance can be obtained by Page's Clear Sky Model and cloud cover information. The models are based on the relationship between solar irradiance, cloud cover and altitude.

The Diffuse Radiation Model (DRM) is the simplest of all the three models, being based on the relationship drawn between the diffuse to global ratio, k, and the clearness index, k_t. An approach developing correlations between diffuse ratio and clearness index was undertaken by Muneer (1987). This simple technique, which only requires measured global irradiance, has proven reliable with reasonable estimation accuracy.

A hybrid of the above mentioned IMRM and CRM models has been developed by Muneer and Munawwar (2006), further improving the estimation of diffuse irradiance. The hybrid model incorporates additional synoptic information, which was found to play a significant role in improving the model's accuracy in estimating diffuse irradiation. The model incorporates sunshine faction, cloud cover and air mass in addition to clearness index. This model has statistically been found to have improved performances over all other models. However, its drawback lies in the in-depth computation required, as well as the large number of input parameters which are needed to estimate diffuse irradiance. The Diffuse Irradiance Model is the simplest model. It is based on polynomial regressions drawn between the diffuse to global ratio and the clearness index. The model only requires horizontal global irradiance to obtain its diffuse counterpart, thus making the model ideally suitable to be used for solar energy calculations by

non-solar experts. The Muneer and Munawwar hybrid model gives the most precise estimation of diffuse irradiance of all the models, with the best statistical results. This is followed by the MRM and CRM models. The MRM model is also relatively complex compared with the former models. It too gives a precise estimation of diffuse irradiance if synoptic information such as sunshine faction or duration is not available.

The CRM model only requires cloud cover information as a measured input. It is based on Page's Clear Sky Model and also yields reasonable results. For this reason the DRM model was chosen to estimate the diffuse irradiation. Since 2005 Edinburgh Napier University has recorded horizontal global irradiance on site. It is measured sub-hourly at 15-minute intervals which makes it ideally suited for simulating the performance of photovoltaic facilities.

2.7 Development of correlations between diffuse and solar irradiation

The simulation of solar energy systems frequently require the incident hourly and sub-hourly irradiation on inclined surfaces. For the majority of studies this data is not directly available, unless specifically recorded for the purpose of the study. However hourly and sub-hourly global irradiation on a given tilted surface can be calculated from horizontal global and diffuse hourly or and sub-hourly data by the use of a suitable slope irradiation model. In the previous section a variety of solar irradiation models were discussed for the use of obtaining solar diffuse irradiation for a range of other meteorological parameters. The quality and accuracy of the models varied with their complexity and number of input parameters.

It was established early on in the research study that it was necessary to develop a solar energy model suitable for the estimation of incident solar energy. This would be required for simulating the performance of BIPV systems. The model would require a simple diffuse irradiation model which used the minimum number of input parameters to enable the model to be used at the maximum number of sites.

For this reason the Diffuse Radiation Model was chosen for the study. This model is a simple model which only requires hourly or sub-hourly horizontal global irradiance data to estimate its diffuse counterpart.

The Diffuse Radiation Model is based on the polynomial relationship between the diffuse ratio, k, and the clearness index, k_t. The regression fits can be linear, quadratic or cubic depending on the best fit for the location. Correlations between daily diffuse ratio and clearness index were first developed by Liu & Jordan (1960). Muneer & Saluja (1986) further developed the cubic regressions for five sites within the UK, covering the UK's full latitudinal range, based on three years' data. A comparison of these regressions did show some latitudinal dependency. However variations were sufficiently close to enable a single correlation for the whole of the UK. Further work by Muneer (1987) developed hourly correlations for six sites within the UK. On examination of the correlations developed for seasonal dependency, Muneer developed seasonal correlations for winter and summer and for autumn/spring. The correlations showed improvements in the trends for both summer and autumn/spring correlations but winter trends showed more scatter. Seasonal correlations were also developed for the whole of the UK, and statistical evaluations showed good validity.

2.8 Solar data collection

Horizontal hourly and sub-hourly diffuse and beam irradiance are required for the estimation of global irradiance on a given tilted surface. Although horizontal global irradiance is a commonly measured parameter for many sites, horizontal diffuse irradiance is not so readily obtainable. The UK Meteorological Office keeps records of diffuse and global irradiances for 9 stations, but there are a further 84 stations that solely record global irradiance. Hence there is a need to estimate diffuse or beam irradiance for these sites. For the sites that measure global irradiation alone, a simple but reasonably accurate method is required to estimate diffuse irradiance from its global counterpart.

For Edinburgh Napier University, energetic solar inputs are recorded in parallel with the electrical energy outputs for the analysis of the facility. Incident solar irradiation has been recorded using two high quality pyranometers, CM11 and CM6b, manufactured by Kipp and Zonen – both have a low response time of 18 seconds at 95% accuracy (Kipp & Zonen, 2000). Both pyranometers were set up on a horizontal plane for a short period of time to evaluate the accuracy of measurements. Once the quality of data obtained was proven, the CM6b pyranometer was installed at the same aspect and tilt angle as the PV facade,

37° East of South and 75° tilt, recording the irradiance onto the PV facade. The global irradiation was also recorded at 15-minute averaged intervals. The CM11 pyranometer was mounted on a horizontal axis to record horizontal global irradiation. Note that the pyranometers were installed on the rooftop of the building (Figure 2.8.1) to minimise the effect of shading.

Figure 2.8.1 Horizontal and inclined pyranometers at Edinburgh Napier University test site.

To enable the diffuse irradiance regressions to be developed, a data set is required which contains both measured diffuse and global irradiance recorded in parallel. A five-minute-averaged data set recorded in Edinburgh in 1993-94 was obtained from files provided by Muneer *et al.* (2000b) which provided simultaneously recorded data for global and diffuse measurements recorded at five-minute intervals. A clean data set for this study was obtained by using the quality control procedure presented by Younes *et al.* (2005).

2.8.1 Meteorological parameters commonly recorded by meteorological stations

There are many meteorological stations both within the UK and worldwide which record solar irradiance measurements. Typically solar global, direct beam, diffuse irradiation and sunshine duration are being recorded with other parameters such as cloud cover, atmospheric turbidity, humidity and temperature recorded to a lesser extent. Due to the high capital investment and high running costs, many stations only record a fraction of these parameters (Muneer *et al.*, 2005). Muneer noted that within the UK there are 600 sites recording synoptic weather data such as temperature, relative humidity, atmospheric pressure and cloud cover, yet only 230 sites record sunshine duration, and even fewer sites record solar global, beam and direct irradiation. The UK Meteorological Office keeps records of diffuse and global irradiances for 9 stations, but there are a further 84 stations that solely record global irradiance. Table 2.8.1 shows all the meteorological stations within the UK which record solar radiation.

Table 2.8.1 UK Meteorological Office hourly solar radiation stations

STATION	LATITUDE, North	LONGITUDE	ALTITUDE [m]
LERWICK*	60 08'	01 11'W	82
KIRKWALL	58 57'	02 54'W	26
ALTNAHARRA	58 17'	04 26'W	81
KINBRACE	58 14'	03 55'W	103
STORNOWAY*	58 13'	06 19'W	9
GLASCARNOCH	57 43'	04 53'W	265
SKYE (LUSA)	57 15'	05 48'W	18
ABERDEEN	57 10'	02 05'W	35
AVIEMORE	57 08'	03 51'W	228
TULLOCH BRIDGE	56 52'	04 42'W	237
INVERBERVIE	56 51'	02 16'W	134
TIREE	56 30'	06 53'W	9
DUNSTAFFNAGE	56 28'	05 26'W	3
MYLNEFIELD+	56 27'	03 04'W	30
STRATHALLAN	56 19'	03 44'W	35
BISHOPTON	55 54'	04 32'W	59
EDINBURGH	55 51'	03 23'W	57
CHARTERHALL	55 42'	02 23'W	112
PRESTWICK	55 31'	04 35'W	27
ESKDALEMUIR*	55 19'	03 12'W	242
BALLYPATRICK FOREST	55 11'	06 10'W	156
SUNDERLAND	54 54'	01 23'W	56
WEST FREUGH	54 51'	04 57'W	11
DUNDRENNAN	54 48'	04 00'W	114
DURHAM	54 46'	01 35'W	102
ALDERGROVE*	54 39'	06 13'W	68
SHAP	54 30'	02 42'W	255
HILLSBOROUGH	54 27'	06 04'W	38
LECONFIELD	53 87'	00 43'W	6
ST ANGELO	54 24'	07 39'W	47
LEEDS	53 80'	01 55'W	64
LEEMING	54 18'	01 32'W	32
BRAMHAM	53 52'	01 20'W	54
CAWOOD	53 50'	01 08'W	6
CHURCH FENTON	53 50'	01 12'W	8
PRESTON	53 45'	02 40'W	44
MANCHESTER	53 28'	02 15'W	33
VALLEY	53 15'	04 32'W	10
WADDINGTON	53 11'	00 31'W	68
HARWARDEN	53 10'	02 59'W	10
NOTTINGHAM	53 00'	01 15'W	117
HOLBEACH	52 52'	00 09'E	3
SUTTON BONINGTON	52 50'	01 15'W	48
SHAWBURY	52 48'	02 40'W	72
ABERDARON	52 47'	04 44'W	95
COLTISHALL	52 45'	01 21'E	17
LAKE VYRNWY	52 45'	03 28'W	360
WITTERING	52 37'	00 27'W	73
EDGBASTON	52 28'	01 56'W	163
WINTERBOURNE	52 27'	01 55'W	130
GOGERDDAN	52 26'	04 01'W	40
COVENTRY	52 25'	01 32'W	119
MONKS WOOD	52 24'	00 14'W	41

STATION	LATITUDE, North	LONGITUDE	ALTITUDE [m]
CHURCH LAWFORD	52 22'	01 20'W	107
BROOMS BARN	52 16'	00 34'E	75
SHOBDON	52 15'	02 53'W	99
BEDFORD	52 13'	00 29'W	85
ABERPORTH*	52 08'	04 34'W	134
WATTISHAM	52 07'	00 58'E	89
WOBURN	52 01'	00 36'W	89
LITTLE RISSINGTON	51 52'	01 41'W	214
ROTHAMSTED	51 48'	00 21'W	128
HODDESDON	51 47'	00 00'W	47
RYEMEADS	51 47'	00 01'E	29
FILTON	51 31'	02 35'W	59
LONDON*	51 31'	00 07'W	77
LONG ASHTON	51 26'	02 40'W	51
ST. ATHAN	51 24'	03 26'W	49
BRACKNELL MODEL*	51 23'	00 47'W	73
MANSTON	51 22'	01 19'E	44
HERNE BAY	51 21'	01 08'E	40
WISLEY	51 19'	00 28'W	38
KENLEY	51 18'	00 05'W	170
EAST MALLING	51 17'	00 27'E	37
ODIHAM	51 14'	00 57'W	118
CHARLWOOD	51 09'	00 14'W	67
LISCOMBE	51 05'	03 36'W	348
HERSTMONCEUX	50 53'	00 19'E	52
THORNEY ISLAND	50 49'	00 55'W	4
NORTH WYKE	50 46'	03 54'W	177
EFFORD	50 44'	01 34'W	16
BODMIN	50 30'	04 40'W	200
CAMBORNE*	50 22'	05.32'W	87
JERSEY++	49 11'	02 11'W	85

* These stations additionally record hourly sky-diffuse irradiation

+ Only daily integrated global irradiation recorded

++ Only daily integrated global and sky-diffuse irradiation recorded

Source; Muneer *et al.*, 2004.

2.9 Sources of error associated with solar irradiation measurement

When carrying out any scientific measurement there will always be a degree of associated error. For solar irradiation measurements, these errors can be categorized into two groups: errors inherently caused by the equipment used and operational-related errors. Younes *et al.* (2005) state that the most common sources of error arose from the sensors and their construction, with the most general types of error described below:

- Cosine response
- Azimuth response
- Temperature response
- Spectral selectivity
- Stability
- Non-linearity
- Shade-ring misalignment
- Dark offset (nocturnal) long-wave radiation errors.

The largest source of all these errors is the cosine response, caused by low solar altitude at sunrise and sunset. This is due to the way the pyranometers respond when solar irradiance strikes the surface of the sensing area with an acute angle, causing errors to occur, with the greatest error resulting when the altitude is below 6°. This is commonly dealt with by excluding data recorded at sunrise and sunset. Azimuth error yields a similar error percentage as that for cosine response. The general cause of the azimuth error is due to imperfections in the manufacture of the glass dome covering the sensing area. The reflectional properties of the absorber surface can also cause similar errors. Temperature response is an error caused by large or rapid changes in external temperature. This is reduced in pyranometers by the use of a double-glazed dome, which buffers the sensor from large-scale temperature changes. Spectral selectivity is a result of the spectral absorption range of the selective coating which is applied to the surface of the sensing area. It is also caused by the transmission properties and distortion of the double-glazed protective dome. Non-linear response only causes a small error as a result of non-linear outputs over the full range of solar irradiation inputs. Shade-ring misalignment is only an error when measuring diffuse irradiance. This is due to the poor positioning of the shade ring, which is required to be fitted over the pyranometer when measuring shading.

Table 2.9.1 World Meteorological Organisation classification of pyranometers

Characteristic	Secondary standard	First class	Second class
Resolution (smallest detectable change in W/m^2)	±1	±5	±10
Stability (percentage of full scale change/year)	±1	±2	±5
Cosine response (percentage deviation from ideal at 10° solar elevation on clear day)	<±3	<±7	<±15
Azimuth response (percentage deviation from ideal at 10° solar elevation on clear day)	<±3	<±5	<±10
Temperature response (percentage maximum error due to changes of ambient temperature within the operating range)	±1	±2	±5
Non-linear (percentage of full scale)	±0.5	±2	±5
Spectral sensitivity (percentage deviation from mean absorptance 0.3-3 µm)	±2	±5	±10
Response time (99% response)	25s	< 1 min	< 4 min

Source data: Muneer *et al.*, 2004.

Table 2.9.1 provides details of the above-mentioned errors. Other errors which also need to be considered are user errors such as correct positioning of equipment, screening from ground reflectance and shielding of electrical cable from electrical fields (Muneer *et al.*, 2004).

The solar irradiation measurements scale is based up on a reference scale established by the World Meteorological Organisation (WMO) Switzerland. Field sensors are calibrated against this reference scale (Myers, 2003).

2.10 Solar quality control of data

The accuracy of any model can only be assumed to be as accurate as the input parameters on which the model is based. Therefore a quality control model is required to examine input data to ensure that it falls between preset limits of acceptability. If the data falls outside these limits the data is discounted. Younes *et al.* (2005) proposed a new approach to the quality control of solar data by the creation of an envelope of acceptance between the clearness index-diffuse to global irradiance ratio.

2.11 Evaluation of commercially available solar software

Within recent years there have been several commercialized PV and solar thermal modelling packages coming to market these packages were compared with the both the ISRM and SRDM models.

These software packages have been designed to be user-friendly. They enable different types of systems to be simulated and tested. The user is able to select the components which are commercially available from drop-down lists. The programs are generally designed to work on a trial-and-error basis, enabling different systems to be rapidly tested and simulated. All these programs use built-in data sets which are incorporated into the programs. The weakness of these programs is not in their ability to build and model different PV systems but in their ability to simulate the effects of shading, especially in urban environments. More modern programs do enable simple shading parameters to be incorporated into the simulations. These parameters are limited, only taking into account the shading of the beam component and not of the diffuse component. Although this is not shaded, it is reduced if part of the sky hemisphere is blocked from view. This is not taken into account by these simulation programs. Thus it is supposed that the SRDM could be used to simulate the solar radiation components of the above-mentioned commercially available programs, improving their performance, particularly in urban environments where a large area of the horizon may be blocked from view.

2.11.1 PVsyst 4.33

PVsyst 4.33 is commercially available software designed to aid in the sizing, design, simulation and data analysis of photovoltaic systems, for both grid-connected and stand-alone systems. The software includes a range of extensive databases, including metrological data sets for many locations around the world as well as large component databases enabling the user to design and simulate PV systems using commercially available components. In addition, externally sourced data sets can also be imported into the program. If only global irradiation data is available, the software also incorporates the Liu and Jordan model to obtain diffuse irradiation from its global counterpart (Liu & Jordan, 1960).

For the data sets which are included in the software database, diffuse irradiance has been estimated (if it has not been recorded) from its global counterpart using Perez's model (Perez *et al.*, 1990). The software also includes a CAD tool to enable detailed analysis to be carried out on systems by users.

The limitation of the software is in the way in which it calculates the shading parameters. The software treats the sky vault as an isotropic dihedron hemisphere between the tilted surfaces of the PV modules and the horizontal plane. The diffuse component is treated as a uniform spatial distribution across the entire sky hemisphere. Shading of the diffuse component is incorporated as an integral part of the shade factor over the visible sky vault between the PV array and the horizontal plane. Thus the diffuse shading factor is independent from the sun's position within the sky and thus considered to be constant throughout the year. Albedo is included as an integral of the shading factor, if no near obstacles are present to obscure the horizontal plane. Both the diffuse shading and albedo shading components of the shading factor are computed from linear shading factor tables. The spatial distribution of both the diffuse and albedo shading factors are considered to be smooth enough to be assumed equal for all PV modules (PVSYST 4.33, 2008).

Wind Energy

2.12 Global wind energy

Global wind energy has seen rapid growth in recent years. At the end of 2007 the cumulative capacity reached 94GW with a growth rate of 26.5%. A total of 19.7GW of additional capacities were added in 2007. Wind energy now supplies 1.3% of the global electricity supply and the World Wind Energy Association predicts an cumulative installed capacity of 170GW to be installed by 2010 (World Wind Energy Association, 2008).

Wind-powered generation currently supplies 194TWh of electricity annually. Figure 2.12.1 shows the global growth rate of wind energy from 1996 to 2007. The annual average growth rate for this period is 28.5% (BP, 2008b).

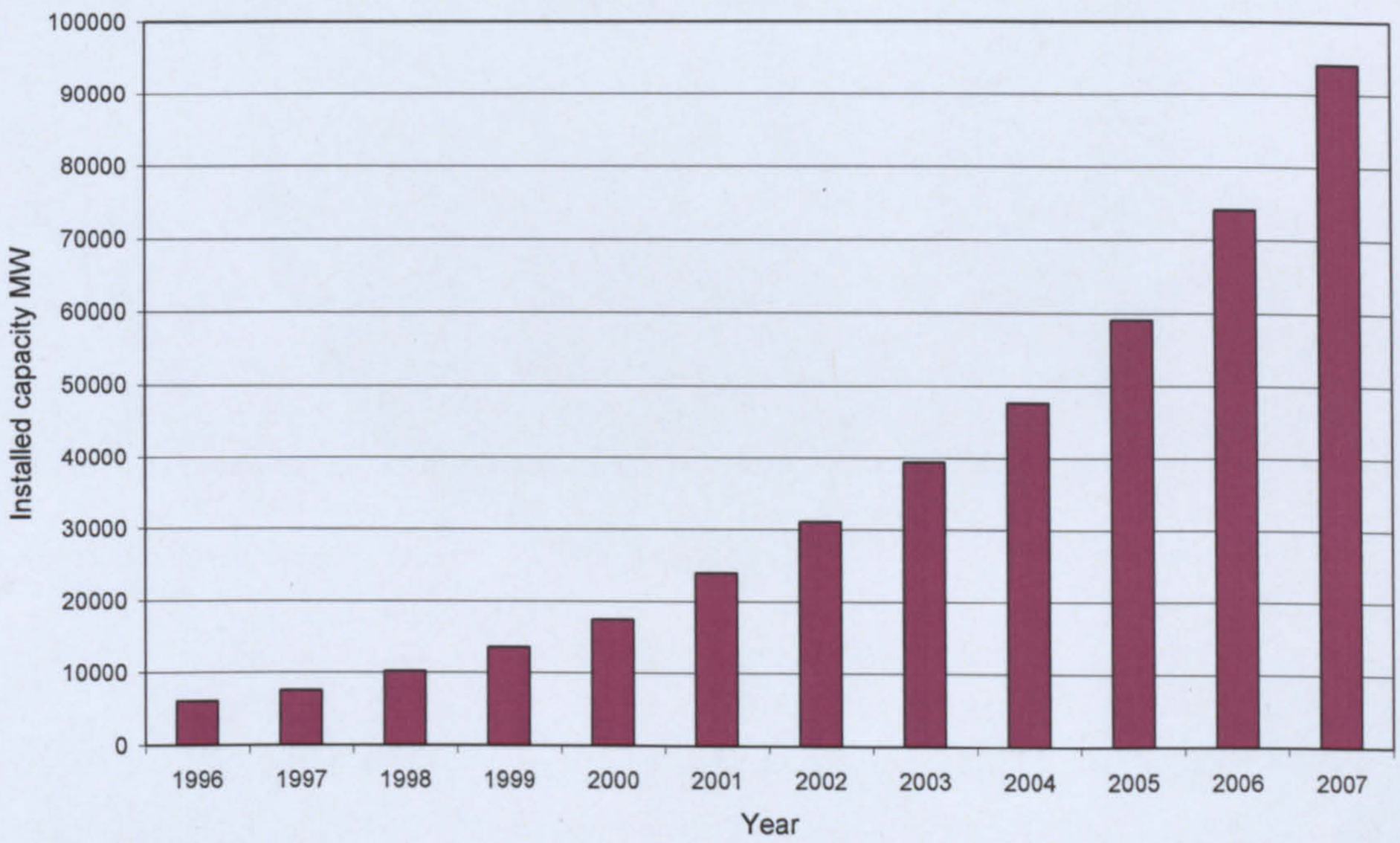

Figure 2.12.1 World's cumulative installed wind capacity per year. Source data: European Wind Energy Association, 2007.

Currently Germany, US and Spain are leading with the largest installed cumulative wind energy capacities, although the US, China and Spain led the world with installed capacity in 2007. Figure 2.12.2 and Table 2.12.1 shows the distribution of the world's wind energy, with Europe having the largest share at 60% and the US having the second largest share at 20%. In 2007 the US saw a 45% growth, with the addition of 5.2GW of new wind capacity begin installed.

Both the Indian and Chinese markets are also saw dramatic growth in 2007, with a rate of growth of 25% and 127% respectively. Both these countries are expected to become dominant competitors in the wind energy market in the coming years.

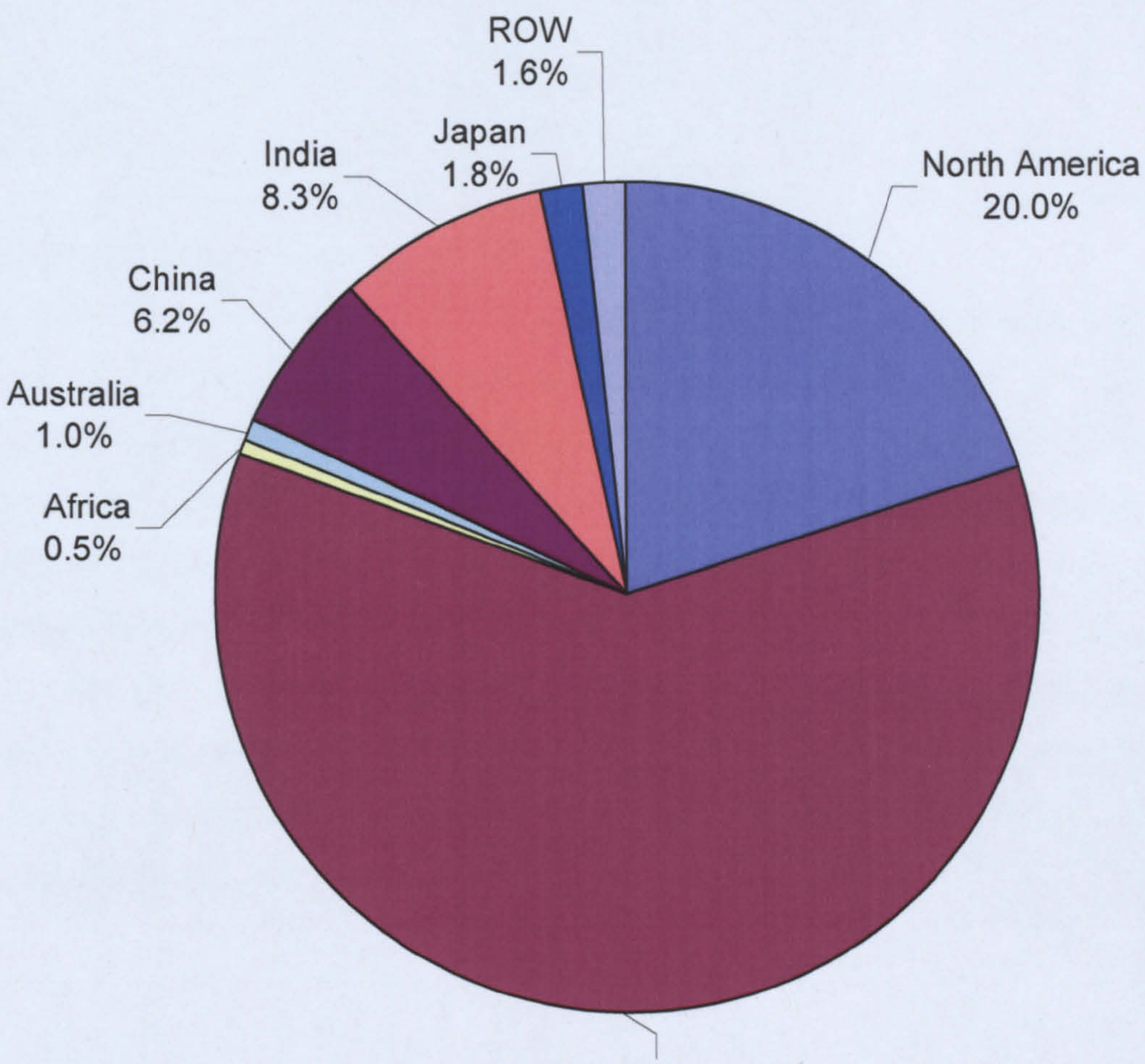

Global cumulative installed wind energy capacity 2007, 94005 MW

Figure 2.12.2. World's installed wind energy capacity distribution 2007. Source data: BP, 2008b.

Table 2.12.1 World's installed wind energy capacity by region, 2007

	Cumulative installed wind turbine capacity [MW]	**Share 2007**
North America	18810	20.0%
Europe & Eurasia	56851	60.5%
Africa	469	0.5%
Australia	972	1.0%
China	5875	6.2%
India	7845	8.3%
Japan	1681	1.8%
ROW	1502	1.7%
Total World	**94005**	

Source data: BP, 2008b.

2.13 European wind energy

Figure 2.13.1 and Table 2.13.1 shows the European installed wind potential. As with solar PV, Germany and Spain are the leaders in Europe with 39% and 26% installed capacities respectively. The German wind market growth slowed in 2007 with its onshore wind markets becoming saturated and the offshore markets being slow to take off. This was due to the increased costs compared with onshore wind. In terms of wind power penetration, 10% of Spain's electricity generation is supplied by wind and 7.5% for Germany. Although Denmark has a relatively small market in wind energy, it has the highest installed capacity *per capita* than any other country, with a 20% penetration of its electricity mix (BP, 2008b).

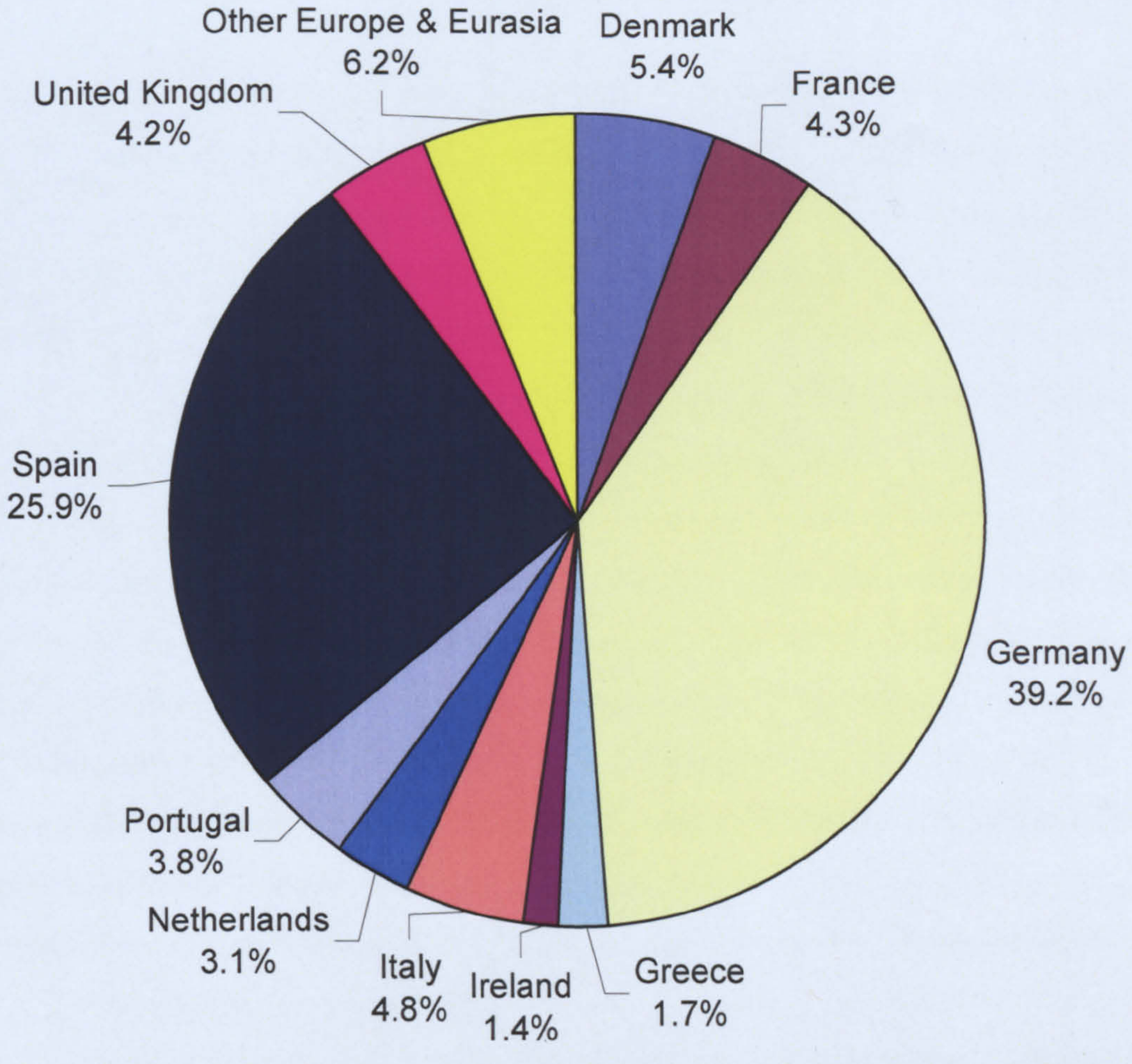

Europe's cumulative installed wind energy capacity 2007, 56851 MW

Figure 2.13.1 Europe's installed wind energy capacity 2007 distribution. Source data: BP, 2008b.

Table 2.13.1 Europe's installed wind energy capacity by region 2007

	Cumulative installed wind turbine capacity [MW]	**Share 2007**
Denmark	3088	5.5%
France	2471	4.3%
Germany	22277	39.2%
Greece	987	1.7%
Ireland	807	1.5%
Italy	2721	4.8%
Netherlands	1745	3.1%
Portugal	2150	3.8%
Spain	14714	26.0%
United Kingdom	2394	4.1%
Other Europe & Eurasia	3499	6.0%
Total Europe & Eurasia	**56851**	

Source data: BP, 2008b.

2.14 Britain's wind energy

Renewable energy contributes over 4.5% of the electricity generated in the UK. Of this, only 1.5% is generated by wind energy. Britain has been slow on the uptake of wind energy in comparison with the rest of Europe. This is not because Britain has a poor wind resource. In reality Britain has the best wind resource in Europe both for on and offshore wind energy. In terms of offshore wind, Britain has a third of Europe's offshore wind potential which, if utilised, could supply the UK's electricity demand three times over.

The UK is currently not on course to meet the government's targets of supplying 4.5% of the electricity supply from onshore wind by 2010. This would require a total of 6,000MW of wind capacity. Currently the UK has around 2,100MW installed from 168 projects, and a further 29 projects are currently under construction with an additional 835MW capacity. There are 128 projects for which planning consent has been approved and are awaiting construction. This should bring the UK's onshore installed capacity up to 5,600MW, still 400MW short of the target (Grimes, 2008).

There are two key factors which have been slowing the UK's policy down. The bureaucracy of the UK's complex and slow planning procedure and the shortage of turbine supply. Typically the given period of time from planning to installation for a wind farm is three years. The UK's planning system is complex, due to the four devolved UK jurisdictions which has resulted in the use of four different legislations, making the whole process slow and often inconsistent.

2.15 Offshore wind

Offshore wind energy is still in its infancy compared with onshore wind, with much of the industry's attention being focused on saturating the onshore wind market as it is currently a more profitable and less risky market. Offshore wind is poised to meet much of the 2020 targets of supplying 20% of all energy supplied within the EU. The first offshore wind farm was installed in 1991 in Denmark. By the end of 2007, the offshore wind energy capacity had grown rapidly to over 1,100MW globally. Europe has taken the lead in offshore wind energy, and this is set to continue in the coming years. Denmark has been the

leader, installing the largest capacity to date, but the UK is set to take over and become world leader in offshore wind energy.

Offshore wind energy is more costly then onshore energy, but it offers much higher capacity factors of up to 40% compared with 30% for onshore wind energy, resulting in higher energy yields. Typically turbines being installed onshore produce 3-5MW. Offshore wind turbines are potentially less limited in their maximum size and thus it is expect that typical offshore turbines will produce between 5-10MW in the future. Figure 2.15.1 shows offshore wind energy capacity at the end of 2007. Demark is the leader, with the UK in a close second place. Figure 2.15.2 shows the cumulative installed offshore capacity for 2015.

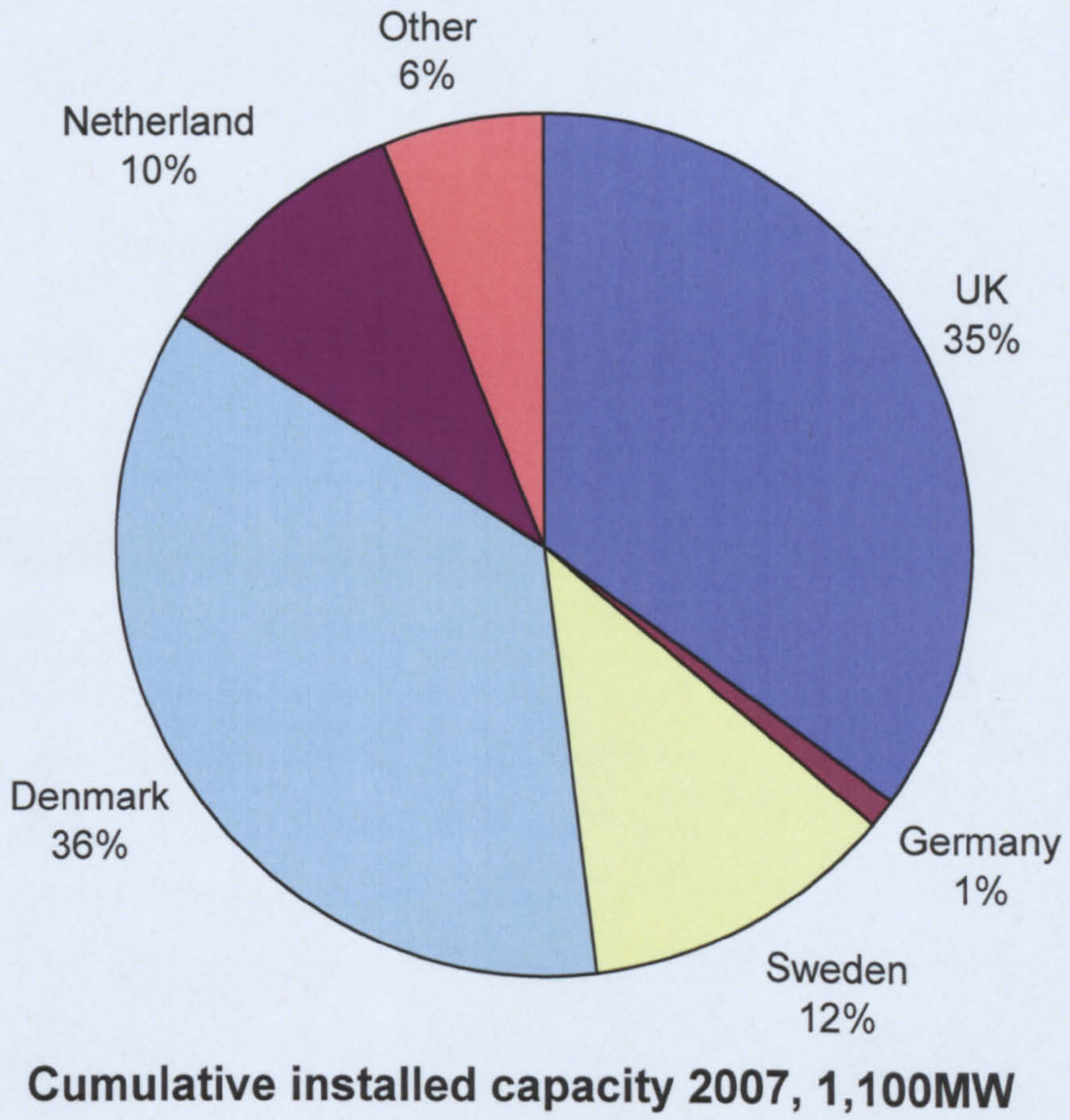

Figure 2.15.1 World's offshore wind capacity at the end of 2007. Source data: BWEA, 2007.

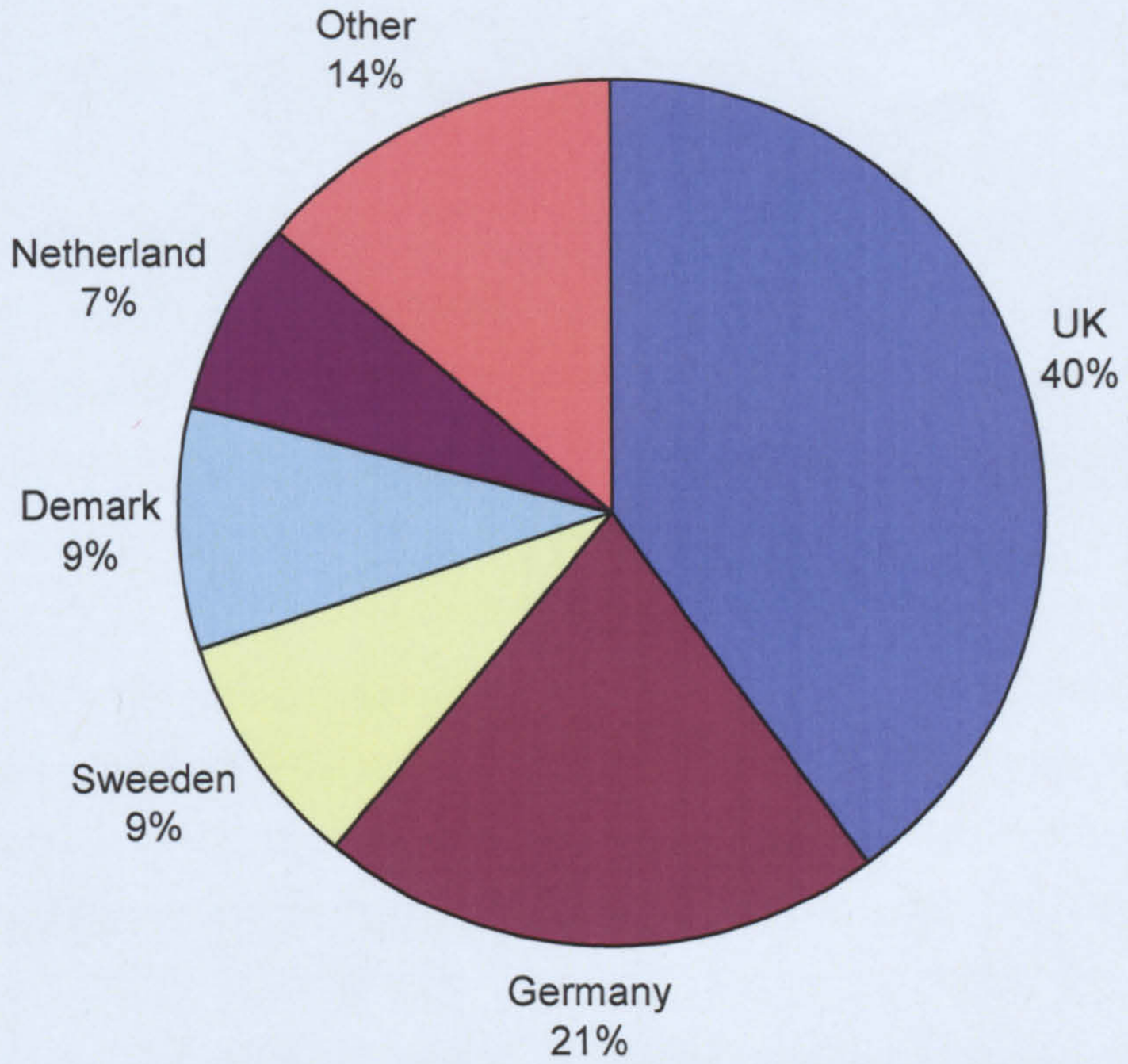

Figure 2.15.2 World's offshore wind capacity at the end of 2015. Source data: BWEA, 2007.

2.16 Micro wind turbine technology

The micro-turbine market has grown rapidly in recent years. Initially micro-turbine technology was used in specialist industries such as communications; However the technology was soon adopted for other applications such as supplying power to rural off-grid dwellings and farms. The technology was also adopted by the marine industry, where it was used to supply energy to sailing craft and offshore navigation aids. The market was limited by cost and the nature of the technology, as it could only supply a low voltage direct current which had limited use.

Advancements made in power control electronics have significantly reduced the cost of turbine technology. In particular, the development of metal oxide semiconductor field-effect transistor technology (MOS-FET) has increased the efficiencies of electronics by overcoming power consumption problems. This in turn enabled the advancement of efficient inverters, used to rectify DC current to AC current, providing the more desirable high voltage mains electricity. There

are many new applications for this technology, such as telecommunications, signalling and environmental monitoring. Increasingly industries such as marketing and retail all require power.

Applications are typically sited in remote locations away from the grid supply, although the reduced cost of this technology has made it economically appealing for applications which may have relatively short life spans or where costs of grid connection (in the majority of cases) is not economically viable or physically not possible.

The cost of extending existing power networks may add a vast expense to such a project. Even extending power networks in urban locations, where the grid may only need extending by a few metres, can be very costly. If cabling needs to be laid through private property or below road and pavement surfaces, costs are further increased. Many of these applications have low power requirements and thus stand-alone renewable energy systems make an attractive alternative to grid connection.

2.17 Domestic wind markets

Increasing public awareness of greenhouse emissions from fossil fuelled power generation and increased energy costs have resulted in the public considering alternative energy supplies to meet part of their energy needs. This has combined with UK government's drive to reduce carbon dioxide emissions and ensure that 10% of the UK's electricity is generated by renewables by 2010 (The National Energy Foundation, 2007). Thus the micro domestic renewables market was born.

This new market is small, with many of the installations being educational and demonstration projects set up by community groups and educational establishments. Enthusiasts, who are environmentally aware of the potential effects of global warming resulting from carbon emissions and who are willing to pay a premium for sustainable energy, are also installing turbines. There is limited funding support through government grant schemes for such installations. Further governmental support along with the rising energy prices could lead to the rapid development of the micro-scale renewables market.

2.18 Development of micro wind turbine technology

There are a growing number of micro wind turbine manufacturers who are developing small-scale turbines for both small business and the domestic market. Initially systems were primarily designed for rural locations with good wind resources. However the majority of domestic homes are located in urban environments where the wind resource is greatly reduced. Only 19.3% of the UK population live in rural areas, compared with 80.7% in urban areas (DEFRA, 2005). To increase potential market size, manufacturers have developed products for the urban market. Since land space is at a premium in urban areas, and to reduce the total cost of systems, many manufacturers are developing building-mounted or rooftop turbines, which are small and light enough to be installed on domestic properties.

Since the rapid development of this new market, there has been little scientific or academic research carried out to validate manufacturers' claims of turbine performance in urban environments. There is a lack of wind data for urban environments, which has meant that many turbines, have been designed using rural wind data which is much higher and less turbulent, yielding a much higher energy potential than can be achieved in urban areas. Nearly all turbine manufacturers who have marketed their product have had to recall their product and cancel orders to make modifications for this reason within the last year (Warwick Wind Trials Interim Report, 2007). Modifications have been made to nearly all aspects of the turbine design. Component strength has been the main area of concern.

2.19 Stand-alone energy systems

A stand-alone system is typically used in rural areas where grid connection is not available or is too costly to extend. A system commonly consists of a low voltage three-phase wind turbine rectified to DC to charge large banks of batteries. Voltage conditioning equipment may be used to regulate charge voltage and turbine load to optimise battery performance. Batteries are used as energy storage for times when the wind resource is not available, or when short-term demand is greater than the available wind resource, acting as a buffer absorbing surplus energy in times of low demand and providing energy at times

of demand when there is little or no supply. Systems are usually low-voltage direct current systems, and electrical loads can either be drawn off as low voltage DC or mains voltage AC equipment can be supplied using inverters. Stand-alone systems are generally smaller than grid-connected systems, typically under 3kW in size. Larger (island) systems are possible, which may use 3-phase high voltage transmission, if there is high power demand or long distance power transmission is required, to reduce transmission losses. Typically these systems are below 100kW in size. Figure 2.19.1 shows a typical layout of a stand-alone energy system.

Advantages

- No grid connection is required, the system can work anywhere
- No power loss as a result of power cuts
- Additional energy does not have to be imported from grid.

Disadvantages

- Increased cost of system due to high costs of batteries
- Batteries have to be replaced periodically
- Loss of power supply over long periods of no wind.

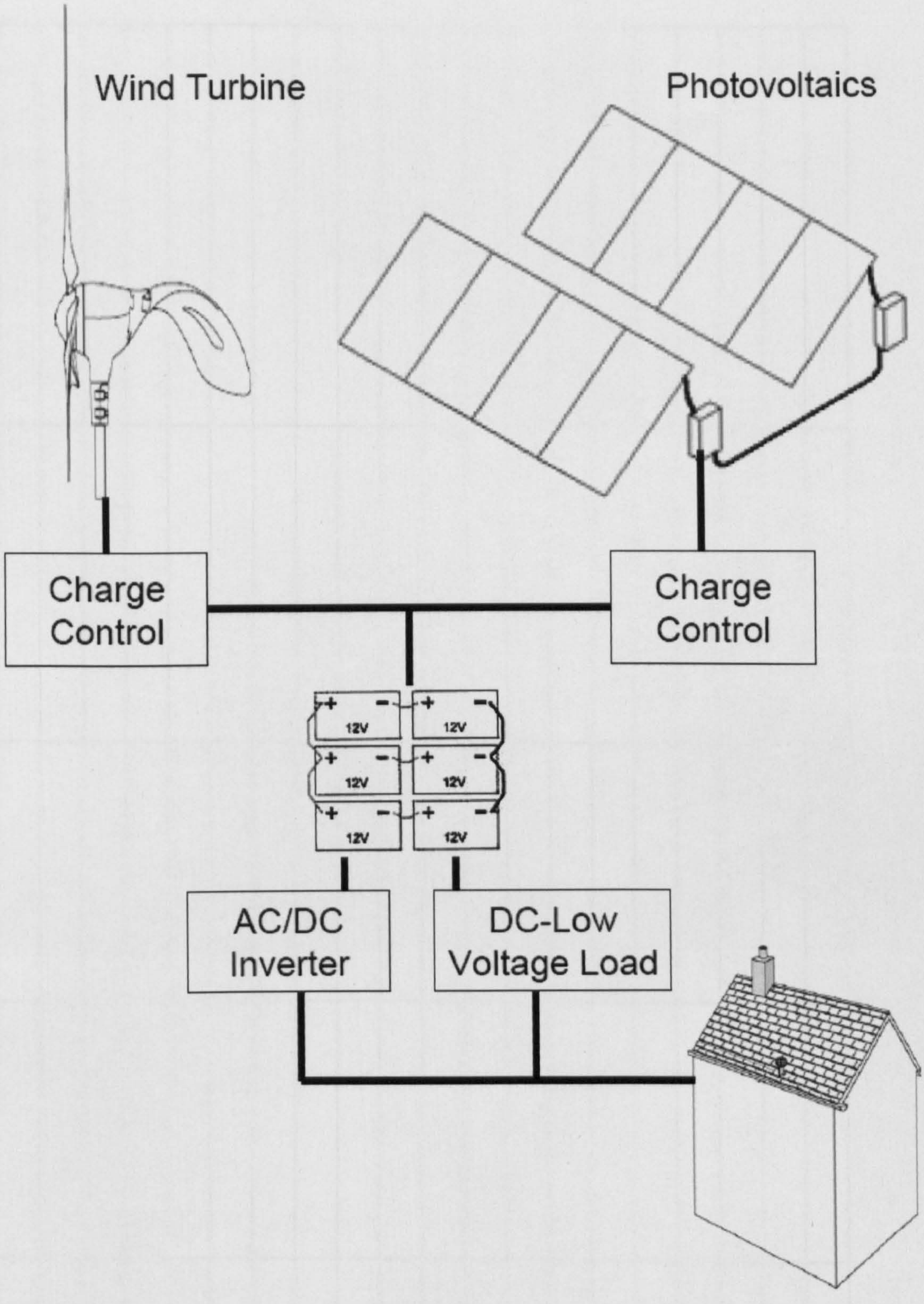

Figure 2.19.1 A schematic of a stand-alone sustainable energy system with battery storage.

2.20 Grid-connected systems

With improvements made in inverter technology, there has been rapid growth in grid-connected systems. Unlike stand-alone systems, grid-connected systems require and rely on a power connection to the national grid. Surplus power supplied from turbine is exported to the grid and additional power is imported at peak demand, providing a continuous power supply. Import-export meters are used to enable energy to be traded via the grid. Typically systems comprise of a high-voltage three-phase wind turbine rectified to direct current which is then inverted to stable single-phase AC and exported to the grid. A grid-connectable inverter is required to monitor the grid voltage for up to three minutes to ensure that the inverter replicates the same voltage and phase angle of power being exported onto the grid. A G-83 protection relay is also legally required in the UK. This automatically disconnects the turbine from the national grid should the grid fail, and this is done to ensure that grid operators can turn off the grid for maintenance. Typical grid-connected systems can vary in size from a few hundred watts upwards to many megawatts. Figure 2.20.1 shows a typical layout of a grid-connected energy system.

Advantages

- Systems are low cost as no costly battery banks are required
- Systems potentially require very little maintenance
- At times of low wind resource, energy is imported from the grid.

Disadvantages

- System automatically shuts down in power cuts
- Time lag from turbine producing power to inverter connecting to grid can result in large quantities of energy being lost
- High long-term running costs as energy is imported from grid.

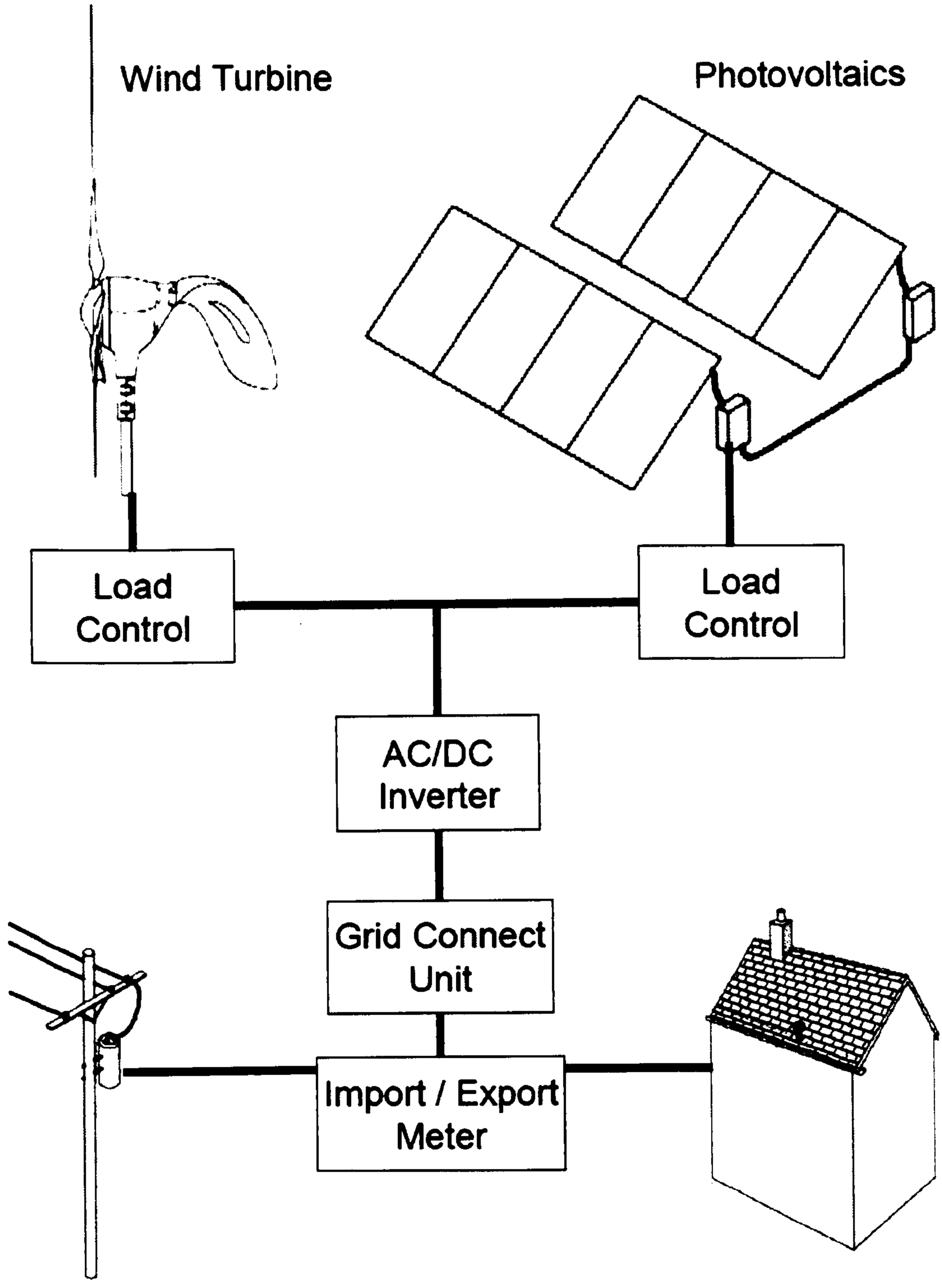

Figure 2.20.1 A schematic of a grid-connected sustainable energy system.

2.21 Measurement of wind speed

A detailed and precise understanding of the wind regime is required for any site before a prospective wind turbine project should be considered. A basic estimation of the wind regime may be obtained using local long-term meteorological data or NOABAL wind data for open rural locations. However, any localised obstructions such as trees and buildings in the vicinity of a proposed location may have a significant influence on the wind-velocity characteristics, which will not be shown in a basic survey. For a precise knowledge of wind speed and direction, measured data for a given site is required. Typically a year's data is recorded to take into account the effects of seasonal changes.

2.22 Wind data collection

A wind monitoring station was set up for the purpose of this study to accurately monitor the wind regime on the roof of Edinburgh Napier University Merchiston Campus. The monitoring station was set up in January 2007 can be seen in Figure 2.22.1. Wind speed and direction were recorded on a sub-minute basis. Two three-cup anemometers and two wind vanes were installed 21.9m above ground level on the Edinburgh Napier University roof, 120m above sea level. The sensors are mounted on a 4.2m mast. Data has been recorded continually since 2007 on a four-second basis, apart from a short period in January 2008 when data was recorded at two-second intervals for a two-week period. Table 2.22.1 shows the instruments used to record wind data at Edinburgh Napier University.

Figure 2.22.1 Two wind velocity anemometers and two wind direction vanes (Wind monitoring station, Edinburgh Napier University).

Table 2.22.1 Wind monitoring equipment installed (Wind monitoring station Edinburgh Napier University)

	Vaisala WM30 Wind Sensor	**NRG #40H Anemometer**
Wind speed		
Measurement range	0.5 to 60m/s	1 to 96m/s
Starting threshold	0.4m/s	0.78m/s
Distance constant	2m	3m
Accuracy		
Wind speed up to 10 m/s	± 0.3m/s	0.1m/s
Wind speed over 10 m/s	± 2%	0.1m/s
Characteristic transfer function	m/s = -0.24 + 0.699 × Hz	m/s = 0.35 + 0.765 x Hz
Wind direction		**W200P Potentiometer Wind Vane**
Measurement range		
Potentiometer	0 to360°	360°
Starting threshold	1.0m/s	0.6m/s
Damping ratio	0.3m	0.2m
Delay distance	0.6m	0.51m
Accuracy	±3°	±3°

Wind speed, wind direction and turbine power output are continually measured at four-second intervals, enabling detailed analysis of turbine performance to be carried out. The turbines have been designed for conditions observed in rural locations where mean winds speed are much higher than urban in areas, resulting in low performances being achieved. Although winds velocities in urban areas are much lower than rural areas, increased turbidity puts greater strain on turbines causing increased premature failures to occur.

2.22.1 Turbine direction monitoring

In September 2007 it was noted that during normal operation the Airdolphin turbine did not always face directly into the wind. The turbine would often yaw out the wind and rapidly slow, reducing the turbine's overall energy yield. To determine the reason for this behaviour an additional sensor was installed on the turbine. A 10kOhm servo potentiometer was mounted on the turbine mast, and a runner installed on the turbine's main body. A rubber contact wheel rotates the potentiometer, giving an electrical resistance reading of the turbine's direction. The exposed location of the turbine made it very difficult to shield the running gear from the environment; water ingression caused corrosion and electrical connection problems. As a result the potentiometer would not remain calibrated over long periods with any degree of accuracy and thus the data collected from the device was not used in the study. Figure 2.22.1.1 shows the device installed on the turbine; it was removed shortly afterwards.

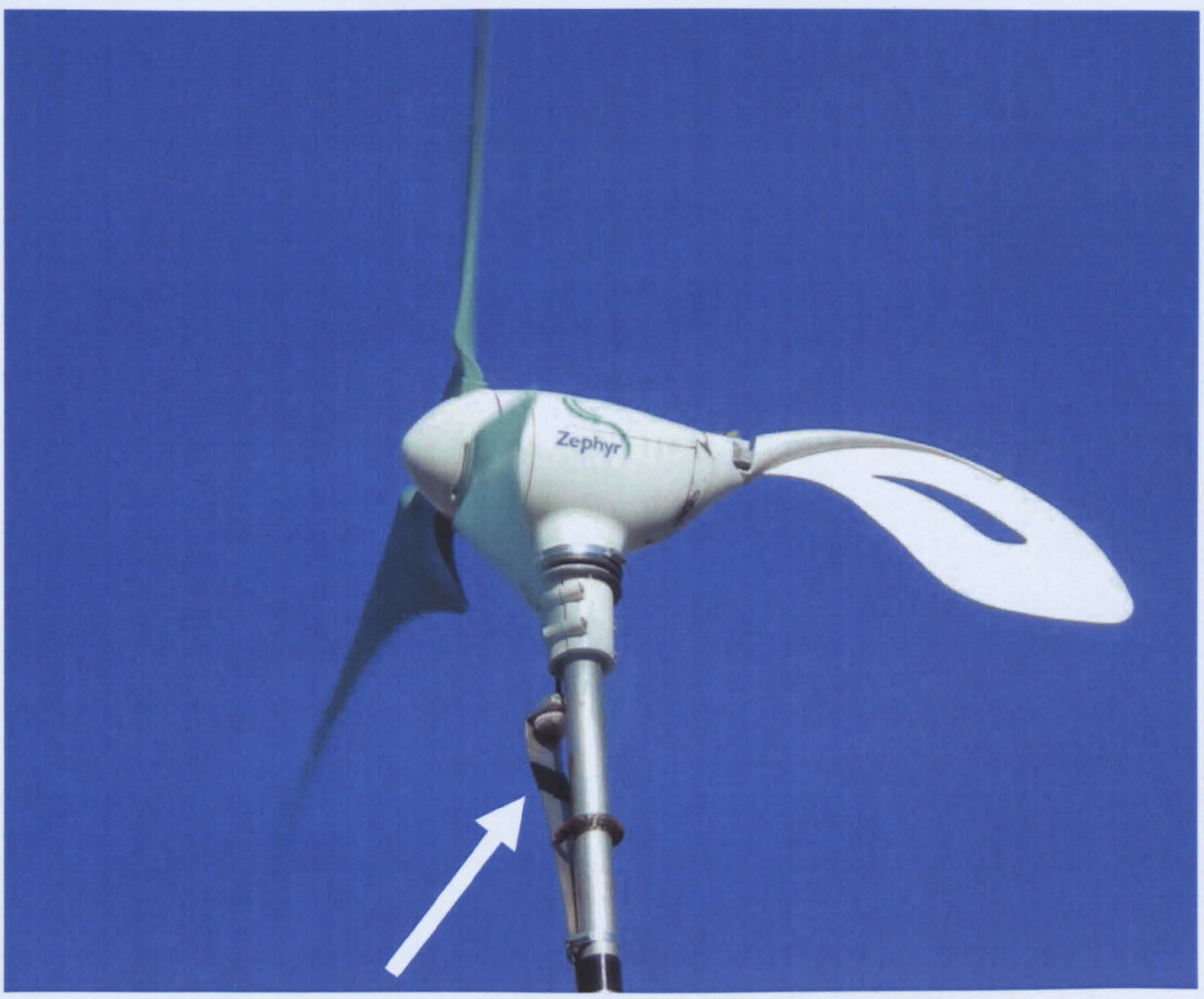

Figure 2.22.1.1 Wind turbine direction indicator installed on Airdolphin turbine (Edinburgh Napier University)

2.23 The ETSU NOABL wind speed database

The Department of Trade and Industry wind velocity database ETSU NOABL (BERR, 2008) contains estimates of the annual mean wind velocities throughout the UK. The database was generated from an airflow model, modelled from a smooth topography at a resolution of 1km square. However, the model database doesn't allow for the effects of localised wind flows, such as thermal flows developed over mountains, valleys or sea breezes. The database also doesn't take account of terrain roughness or topography on a localized scale, for example, terrain surfaces such as crops, trees and the urban landscape which can have a significant effect in reducing the overall mean winds speed for a site (ETSU NOABL, 2008). Winds speeds are given for three heights above ground level: 10m, 25m and 45m. The database uses the Ordnance Survey grid system for England, Scotland and Wales, and the Northern Irish Ordnance Survey grid system for Northern Ireland. Figure 2.23.1 shows the estimated mean wind velocity at a 1km square resolution at the three heights above ground level. Figure 2.23.2 shows a wind speed map of the UK.

Windspeed Database Query Results

for the 1km grid square 324 671 (NT2471)

Wind speed at 45m agl (in m/s)

6.8	**7**	**7.2**
6.9	**7.1**	**7.2**
7.2	**7.3**	**7.4**

Wind speed at 25m agl (in m/s)

6.2	**6.4**	**6.5**
6.2	**6.5**	**6.6**
6.6	**6.7**	**6.7**

Wind speed at 10m agl (in m/s)

5.2	**5.5**	**5.7**
5.4	**5.6**	**5.7**
5.7	**5.8**	**5.9**

Blank squares indicate areas outside the land area of the UK - i.e. areas at sea or of neighbouring countries.
agl = above ground level.
Squares surrounding the central square correspond to wind speeds for surrounding grid squares.

Figure 2.23.1. ETSU NOABL mean wind velocity for the Edinburgh Napier University site.

Courtesy: ETSU NOABL, 2008.

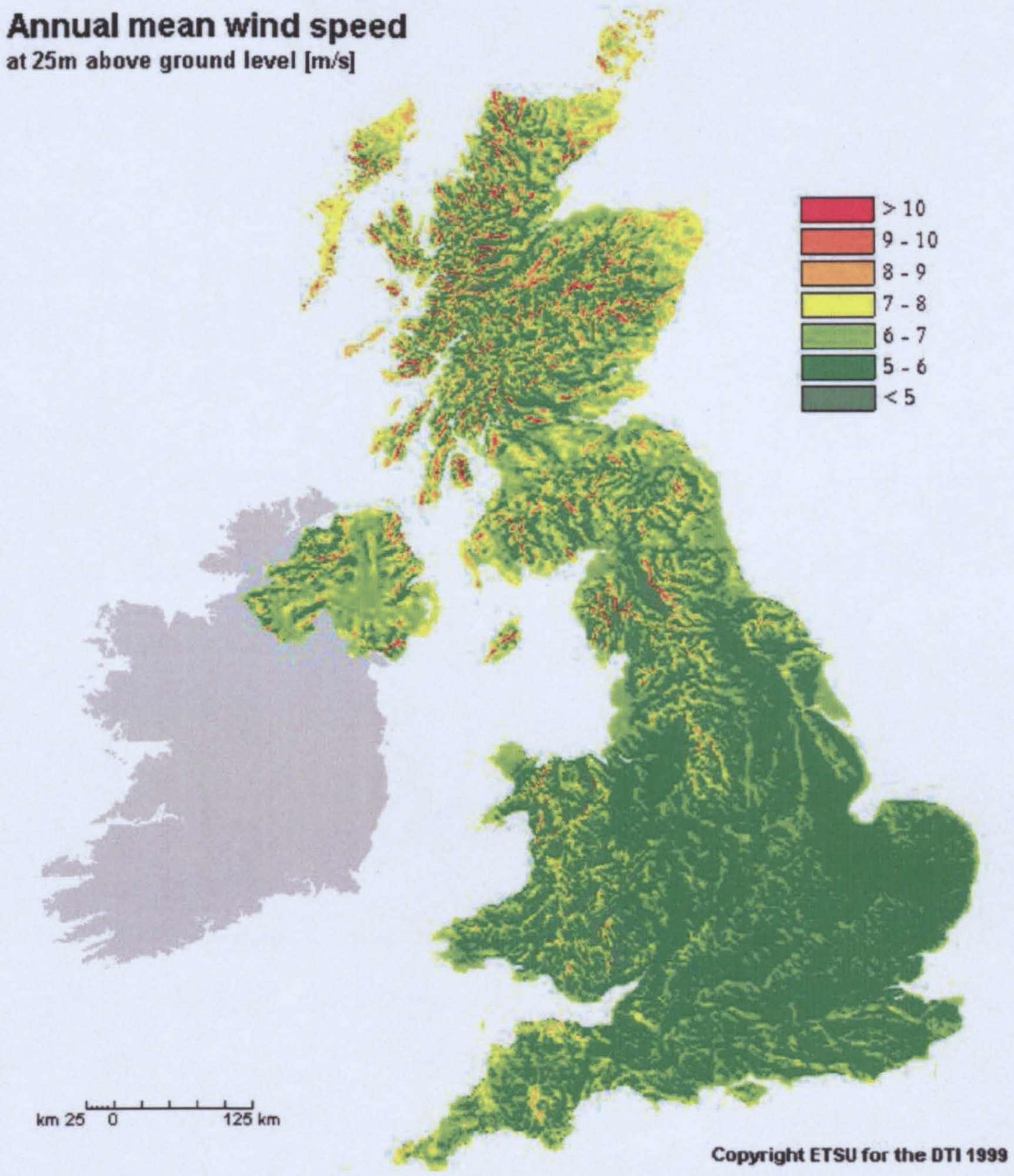

Figure 2.23.2 Annual wind speed map of UK 25m above ground level. Courtesy: BWEA ,http://www.bwea.com/images/misc/noabl_c.gif.

2.24 Case study: Nenthead (Alston) 6kW wind turbine

The Nenthead turbine, located in Cumbria, was installed on the property of a private domestic dwelling. The turbine is located on an exposed hillside at an approximate distance of 100m from the property. The turbine is grid-connected to supply electricity to the property as well as exporting surplus energy to the grid.

Location

Turbine located: Nenthead (Cumbria). Longitude: N54.79879°, latitude: 2.35369°. Altitude: 490m above sea level.

Turbine type

6kW, Proven WT6000 (9.5m mast). Inverter: SMA Windy Boy 6kW.

Planning

- This was the first planning application for a turbine in the Eden district. 13th December 2005: first planning meeting took place.
- 7th March 2006: planning application filed/returned.
- 29th March 2006: completed application submitted. Various objections from neighbours.
- 17th August 2006: installation offer accepted by Turbine Services.
- 26th August 2006: planning application approved.
- 8th November 2006: system commissioned. System was shut down due to over-voltage of national grid (exceeding 260 volts) knocking invertors off line. Grid transformers were adjusted. This time turbine was shut down and the brake was applied. Due to high winds the brake overheated and damaged the generator.
- 13th February 2007: turbine head replaced. System starts to run properly.

Energy generated

Between 13th February 2007 and 19th February 2008, the total number of hours was 7195, with 14,208 kWh produced. The turbine came off line 6-8 times due to grid failure, with an estimated total of 6 days off line. This turbine has a capacity factor of 33% this is typical to that of well placed commercial wind farms within the UK.

Finance

The project received a Clear Skies £5,000 grant and additional funding of £15,000 by the turbine owners.

Figure 2.24.1 Proven turbine WT6000, Nenthead (April 2008).

Figure 2.24.2 Proven turbine WT6000, Nenthead (April 2008).

2.25 Warwick Wind Trials

The Ampair 600 turbine is also being monitored as part of the Warwick Wind Trial. The Warwick Wind Trial is a research project set up in partnership with Action21, Warwick District Council and Warwickshire County Council and run by Encarft. The project is funded by the Pilkington Energy Efficiency Trust and the BRE Trust.

The project's aim is to monitor the performance of 23 rooftop wind turbines in a variety of urban and rural sites over a twelve-month period. Starting in 2007, in addition to monitoring, public opinion surveys are also being conducted before and after the project. The aim of the project is to collect and publish objective data on the performance of systems when used in true-life applications. The project also aims to explore how easy it is to get systems installed on houses and to discover the barriers and real costs. Most importantly, the aim is also to discover what impact installing these systems has on awareness of energy efficiency in households, with the systems installed amongst members of the local community (Warwick Wind Trials Interim Report March, 2007).

To date the Warwick Wind Trails project has produced several interim reports stating their finds. The reports mainly covered findings from public surveys carried out to determine public perception regarding micro-wind turbines. The reports also document the micro-turbine owners' findings regarding the planning and installation process of their turbines (Warwick Wind Trials Interim Report March, 2007). Currently nearly all micro-turbine planning applications and government grant applications approvals are based on data obtained from the ETSU NOABL wind database. However this is solely a synthetic dataset which doesn't take account of land topography and the effects of obstructions such as buildings and trees on the mean wind velocities.

Thus there needs to be a reasonably simple and accurate method of determining the mean winds velocity for a site, without carrying out a costly wind survey which may take a year of recording data before the wind velocity characteristics can the assessed.

2.26 Available software wind modelling packages

WAsP 9.0 is the commercially available software package for modelling wind regimes to aid the design of wind farms. The software is a program for the vertical and horizontal extrapolation of wind climate statistics. The software also includes several models to model different types of terrain, terrain roughness, and the effects of sheltering from obstacles (Wind Atlas Analysis and Application Program, 2008). The software enables the development of detailed wind atlases for use in planning wind farms as well as calculating wind resources, with the addition of turbine performance data the software can also calculate turbine performance and the effects of wakes in turbine arrays.

CHAPTER 3

Horizontal global and diffuse irradiation: data collection, processing and quality control and modelling

3.1. Introduction

A detailed knowledge of incident solar irradiation is required when designing or simulating any solar energy system. Until recent years the main users of solar irradiation information were architects and air conditioning engineers, and the information was used to predict the heating and cooling requirements of building environments in order to maintain constant temperate climates within buildings. Solar irradiance data was also used in agriculture to determine the suitability of growth conditions for different species of crops. But more recently, due to changes in modern building construction techniques and increased pressure to achieve lower energy consumption, as well as the new emphasis on renewable energy systems, there has been a renewed focus on solar energy.

The introduction of the Kyoto Protocol legislation in February 16th 2005 resulted in the implementation of a treaty to enforce its members to reduce their CO_2 emissions. This encouraged the governments of member countries to employ new laws and legislation to economically and socially support the effective utilization of energy efficiency measures in domestic, public and industrial sectors, as well as encouraging the use of renewable energy production over methods using non-sustainable means (Celik *et al.*, 2008).

Modern building techniques have lead to changes in the types of materials used in building construction, with increased use of glazing and lightweight steel construction. This has resulted in modern buildings having a reduced thermal mass, and the use of large glazing facades has increased the effects caused by solar gain. This has increased the technical difficulties of maintaining stable climate conditions within buildings. Engineers have to take into consideration aspects such as glazing with much greater care. The careful placement of shading devices on south-facing facades can reduce solar gain in the summer months, and the use of high performance glazing systems to reduce thermal losses over winter, can help in maintaining a temperate environment.

Movement towards increasing the energy efficiency of buildings has spurred the growth of the renewable energy markets, and in particular the growth of building integrated renewables such as solar thermal and photovoltaics which are

particularly well suited for this task. Building integrated renewables systems offer several advantages over other types of renewable energy systems and can make significant contributions towards reducing energy consumption and thus carbon emissions within buildings. The advantage is that the renewable energy system can be embedded into the building, becoming part of the building fabric, and serving two purposes: as a source of energy generation and as external cladding for the building. This enables some of the high economic costs to be absorbed in the cost of the building. If the building structure can also be used as a support for the renewable energy system, this can also remove the requirements of a costly support structure. Building integrated systems are also attractive in terms of energy, meaning that the source of power generation is located at the same place as the point of use, thus reducing transmission losses and costs.

Their design requires a detailed knowledge and a precise understanding of solar radiation. However in the majority of sites where solar energy systems are installed, there is often little or no data measured on site. Engineers and designers have to rely on data obtained from elsewhere, usually from local metrological stations.

3.2 Development of regressions between diffuse and global irradiation

Regressions are developed monthly between diffuse ratio (k) and clearness index (k_t) to estimate diffuse irradiation. The regressions are based on the previously mentioned Diffuse Radiation Model. Diffuse ratio is the ratio of horizontal diffuse irradiance to horizontal global irradiance. It is used to denote the atmospheric clarity due to cloud cover, and the concentration of aerosols and air-borne particulates within the atmosphere. Clearness index is the global irradiance on a horizontal surface to the horizontal extraterrestrial irradiance. It is used as a measure of normalisation of global horizontal irradiance giving the depletion of horizontal extraterrestrial irradiance to horizontal global irradiance. Thus developing regressions between the k-k_t enables a single regression curve to be fitted to all sky conditions. The regression accuracies of monthly estimations are then compared with seasonal and annual regressions.

$$k = \frac{I_D}{I_G} \tag{3.2.1}$$

$$k_t = \frac{I_G}{I_E} \tag{3.2.2}$$

Monthly regressions were developed using data from an individual month. The annual regression was developed using an entire year's data. Seasonal regressions were based on the approach used by Muneer *et al.*, (2000). The seasonal data was put into three categories, i.e. summer, winter and spring-autumn. A regression was developed for each category. The data was classified as follows: summer data from 1st of May to 30th August, winter from 1st November to 28th February and spring-autumn from 1st of March to 30th April and 1st September to 30th October respectively, combined together to obtain a single regression. The monthly regressions were developed for each calendar month.

3.2.1 Global and diffuse sub-hourly data set used for regression modelling

A sub-hourly data set recorded at Edinburgh Napier University in 1993 was used, although there were two months' data missing from the data set. This was filled with data for February and December recorded at Heriot-Watt University in Edinburgh in 1993/4, which is located approximately 10 km away from the Edinburgh Napier University test site. Both sets of data were obtained from Muneer *et al.*, (2000b) and in both cases the data provided global and diffuse measurements, recorded at 5-minute intervals.

3.2.2 Quality control of solar irradiation data

The accuracy of any model can only be assumed to be as accurate as the input parameters on which the model is based. Therefore a quality control model is required to examine input data to ensure that it falls between preset limits of acceptability. If the data falls outside these limits, the data is then discounted. When measuring or recording any experimental data, the data will always be prone to sources of error for a range of reasons.

The Younes *et al.*, (2005) quality control procedure is used in this study. The procedure is split into multiple steps. The raw data input parameters required are: year, month, day, hour, minute, global irradiance, diffuse irradiance.

1. Test one

Apparent solar time, solar hour angle, declination angle, solar altitude and solar azimuth are calculated. If the solar altitude is less than 7°, the data is discounted.

SOLAT >7°

2. Test two

The day number, horizontal extraterrestrial irradiation, clearness index and diffuse ratio are also calculated. Limits are set for the clearness index between 0 and 1 as well as for the diffuse ratio to ensure that the clearness index and diffuse ratio are between zero and one. If these limits are not met the raw data is discounted.

$0<k_t<1$: $0<k<1$

3. Test three

Page's (1997) quality control procedure is now used to set upper and lower boundaries for diffuse irradiation, as well as an upper boundary for global irradiation. Page's clear-sky model is used for the upper limits and Page's overcast-sky model is used to set the lower limits given by Equation 3.2.2.3. The model is used to calculate hourly beam and diffuse irradiation under clear-sky conditions.

$$I_{B,C} = 1367 K_d \exp\left(-0.8662 m\, T_L \delta_r\right) \sin\ SOLALT \qquad (3.2.2.1)$$

$$I_{D,C} = K_d T_{rd} F\left(SOLALT\right) \qquad (3.2.2.2)$$

$$I_{G,OC} = I_{D,OC} = 572 SOLAT \qquad (3.2.2.3)$$

Equations 3.2.2.1 and 3.2.2.2 compute beam and diffuse irradiances respectively under clear-sky conditions; K_d is the mean earth-sun distance correction factor. The relative air mass takes into account the effects of transmission of the atmosphere, due to its constituent make-up of gases, liquids, and solids. The Linke turbidity factor T_L is independent to air mass, and to standardize its value it is therefore given with a fixed reference value of air mass, m equals 2. It gives a useful approximation of the atmosphere absorption and scattering effect of solar radiation under clear sky conditions. The Linke turbidity uses the Rayleigh optical depth as a function of air mass, which is used to describe the atmosphere's optical thickness. It is based on the absorption effects of water vapour and the scattering effects caused by particulate matter,

given as a function relative to that of a clean dry atmosphere and thus summarizing the turbidity of the atmosphere. This is used for ascertaining the attenuation of direct beam to diffuse radiation ratio. For a clear cloudless blue sky, T_L is equal to 1. Turbidity increases with the presence of cloud cover, water vapour and pollution. Greif & Scharmer (2000) have given information for T_L as well as that for Rayleigh optical depth δ_r in the form of coefficients (for a monthly basis) for many sites in Europe. Like that of the beam, the clear-sky diffuse irradiation is also dependent on air mass 2 Linke turbidity factor as well as solar altitude. The diffuse irradiances increased with the increase of sky turbidity. The diffuse transmittance T_{rd} is the theoretical diffuse irradiance on a horizontal surface when the sun is at its zenith given by Equation 3.2.2.4:

$$T_{rd} = -21.65 + 41.752T_L + 0.51905T_L^2 \quad (3.2.2.4)$$

$$F(SOLALT) = x_0 + x_1 \sin SOLALT + \sin^2 SOLALT \quad (3.2.2.5)$$

Equation 3.2.2.5 for F(SOLALT) are given by Younes *et al.* (2005). The coefficients are given in Table 3.2.2.1.

Table 3.2.2.1 Coefficients for use in Eq.(3.2.2.5)

Coefficients	Sky conditions	
	Clear-skies	Overcast-skies
x_0	3.8175×10^{-2}	-6.7133×10^{-3}
x_1	1.5458	0.78600
x_2	-0.5998	0.22401

The global irradiance for clear-skies is given by Greif & Scharmer (2000). It is the sum of both the global and diffuse components given as Equation 3.2.2.6.

$$I_{G,C} = I_{B,C} + I_{D,C} \quad (3.2.2.6)$$

At this stage the global and diffuse irradiance are compared with that of Page's computed irradiance and are used as upper and lower boundaries of expectance.

$$I_{G,OC} \leq I_G \leq I_{G,C} \quad (3.2.2.7)$$

$$I_{D,OC} \leq I_D \leq I_{D,C} \quad (3.2.2.8)$$

The final stage of the quality control procedure is in the construction of a diffuse ratio and clearness index quality control envelope. This is an envelope drawn between the diffuse ratio k-k_t. The remaining data is controlled by the use of an envelope of acceptance, formed from the banded mean k_t, weighted mean k, and the standard deviation of k. If the data falls outside these boundaries of ± 2 standard deviations of the weighted mean k, the data is discounted. Figure 3.2.2.1 shows the envelope of acceptance created between k-k_t.

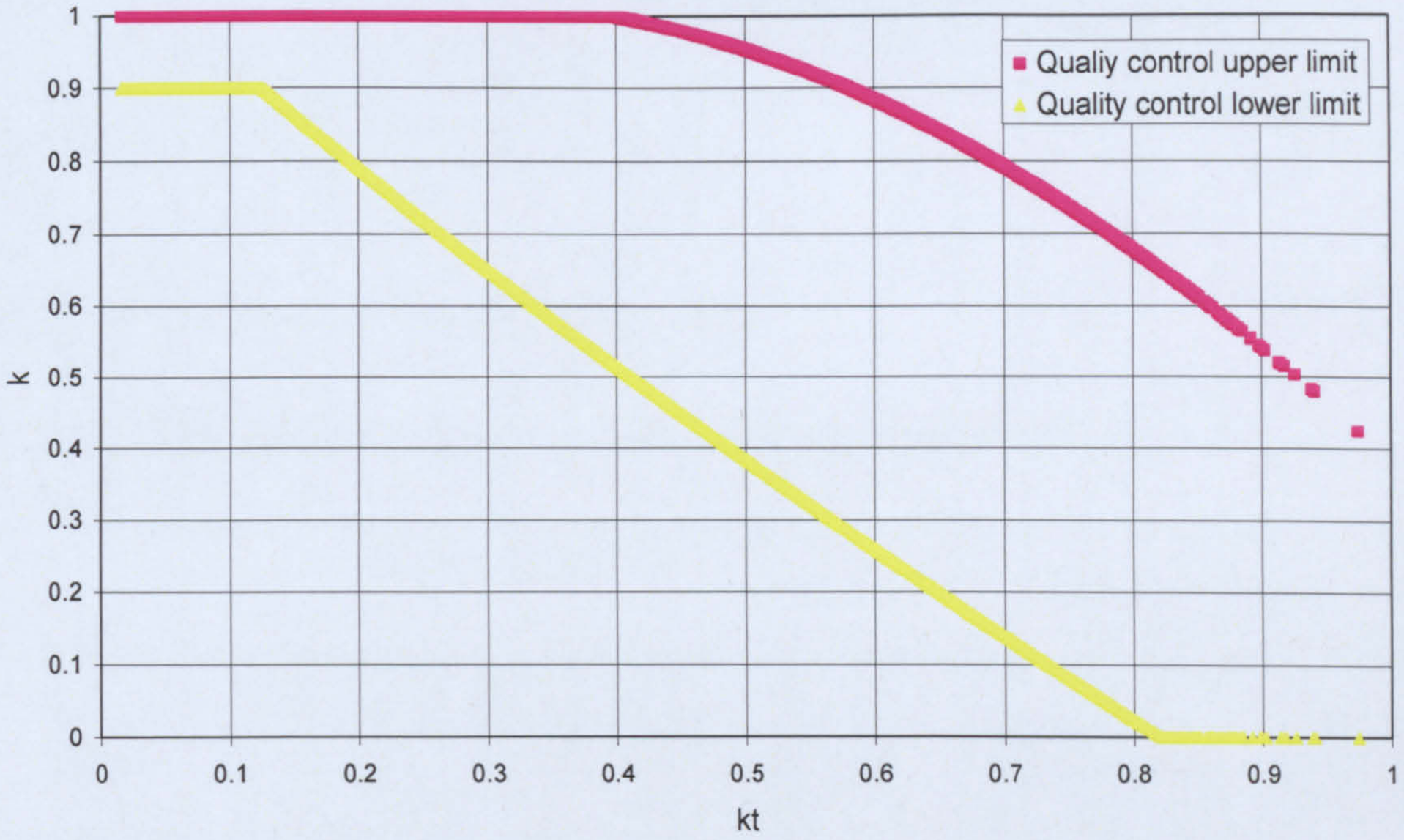

Figure 3.2.2.1 Envelope of acceptance drawn between k-k_t. Note that boundaries of ± 2 standard deviation from mean weighted k, and note that only quality control upper and lower limits are shown.

3.2.3 Statistical evaluation tests used to evaluate the model's performance

The coefficient of determination (R^2) is useful because it gives the proportion of variance of a modelled variable against that of the measured. It is used as a measure to determine the certainty that can be placed on the model in terms of fit, giving a quantitative measure of how well the modelled variable explains the measured. Its value lies between zero and one, with a higher value of R^2 indicating a low variance, which is desired.

$$R^2 = \frac{\sum (Y_C - Y_m)^2}{\sum (Y_O - Y_m)^2} \qquad (3.2.3.1)$$

Note that R^2 listed in Table 3.2.3.1 is the coefficient of determination of a linear regression obtained between calculated and measured diffuse radiation.

Likewise, the Mean Bias Error MBD(s) and Root Mean Bias Error RMSD(s) are also calculated based on error in the estimation of diffuse radiation. They are in the same units as irradiance (W/m^2). An error analysis was carried out for all the regressions to calculate the errors in the estimation of five-minute averaged diffuse irradiance. MBD and RMSD (given by Equations 3.2.3.2 and 3.2.3.3 respectively) have been calculated for all twelve months as well as for annual, seasonal and monthly regressions. Those results are shown in Table 3.2.3.2.

$$MBD = \frac{\sum \left(I_{\text{Dcalculated}} - I_{Dmeasured} \right)}{n} \tag{3.2.3.2}$$

$$RMSD = \left[\sum \left(I_{\text{Dcalculated}} - I_{Dmeasured} \right)^2 / n \right]^{1/2} \tag{3.2.3.3}$$

Table 3.2.3.1 Parameters for presently developed regression

	Regression coefficients				R^2	k_t lower limit	a_0	k_t upper limit	a_5	Number of point used
	a_1	a_2	a_3	a_4						
January	0.8379	2.3590	-8.5929	6.0447	0.84	0.20	0.98	0.65	0.40	861
February	0.8234	2.5252	-8.6825	6.2551	0.74	0.20	0.98	0.72	0.47	1706
March	0.8420	2.1475	-7.7183	5.2648	0.88	0.20	0.98	0.82	0.33	3116
April	0.8788	1.7881	-6.7321	4.5419	0.90	0.20	0.98	0.83	0.33	3580
May	0.8925	1.4524	-4.8990	2.7294	0.86	0.20	0.98	0.85	0.25	4480
June	0.8798	1.7195	-6.1193	3.8769	0.86	0.20	0.98	0.88	0.30	5123
July	0.8656	1.8013	-6.3287	4.0520	0.85	0.20	0.98	0.85	0.31	5362
August	0.8600	1.8965	-6.9659	4.7367	0.87	0.20	0.98	0.82	0.32	3790
September	0.8533	1.9973	-7.4200	5.0490	0.86	0.20	0.98	0.80	0.32	3264
October	0.7895	2.8158	-10.0520	7.4404	0.80	0.20	0.98	0.75	0.38	2506
November	0.8469	2.4528	-9.7624	7.5419	0.91	0.20	0.98	0.64	0.38	2553
December	0.8168	2.3577	-9.2841	7.3998	0.75	0.20	0.98	0.70	0.46	946
Summer	0.8721	1.7619	-6.2135	3.9467	0.86	0.25	1.00	0.80	0.30	19093
Spring/Autumn	0.8575	2.0130	-7.4985	5.1848	0.83	0.20	1.00	0.70	0.43	15836
Winter	0.8163	2.7525	-10.3700	8.0630	0.88	0.25	1.00	0.85	0.32	6066

There are 16 equations altogether: 12 monthly, 3 seasonal and 1 annual regression. Note that R^2 listed in Table 3.2.3.1 is the coefficient of determination of a linear regression obtained between calculated and measured diffuse radiation.

Table 3.2.3.2 Error statistics for cubic regression curves: monthly, seasonal and annual

Month	Range %	Percentage error %		
		Monthly	Seasonal	Annual
January	-15 to 15	81	80	82
	-25 to 25	88	87	86
	-50 to 50	99	100	94
February	-15 to 15	85	79	83
	-25 to 25	90	90	89
	-50 to 50	97	99	98
March	-15 to 15	71	71	70
	-25 to 25	82	82	78
	-50 to 50	97	97	92
April	-15 to 15	76	77	75
	-25 to 25	86	87	83
	-50 to 50	98	100	96
May	-15 to 15	81	79	79
	-25 to 25	88	88	88
	-50 to 50	95	96	96
June	-15 to 15	76	76	75
	-25 to 25	84	84	84
	-50 to 50	94	94	94
July	-15 to 15	72	72	72
	-25 to 25	81	81	81
	-50 to 50	94	94	94
August	-15 to 15	71	71	71
	-25 to 25	82	82	82
	-50 to 50	93	92	92
September	-15 to 15	77	77	73
	-25 to 25	90	89	84
	-50 to 50	100	99	98
October	-15 to 15	76	75	76
	-25 to 25	86	85	82
	-50 to 50	96	95	92
November	-15 to 15	80	66	60
	-25 to 25	93	87	66
	-50 to 50	100	100	95
December	-15 to 15	82	83	84
	-25 to 25	92	91	89
	-50 to 50	98	97	96

Note: table shows error distribution statistics for three separate range distributions.

3.3 Development of regressions between diffuse ratio and clearness index

Using one year's worth of quality-controlled data for the Edinburgh location, regression curves were fitted to the k-k_t quality control envelope for annual, seasonal and monthly data. Quadratic and cubic regression curves were fitted to the data. Figure 3.3.1 shows the annual scatter plot of k-k_t using 5-minute averaged data, with quality control envelope, annual quadratic and cubic regressions fitted.

Careful inspection of Fig 3.3.1 shows that the locus of the cubic equation cuts more centrally through the bulk of the data than that of the quadratic equation. It was found that for values of high k, low k_t, low k and high k_t, the cubic curve had a tendency to overestimate diffuse irradiation. This was also found to be the case for seasonal plots. Figures 3.3.2 to 3.3.3, and monthly plots for Edinburgh shown in Figure 3.3.4 note that there is less data presented in the winter plots due to the short winter days. Therefore visual inspection was used to apply linear cut-offs for each equation to give a reasonable approximation as suggested by Spencer (1982).

Coefficients for cubic regressions are given for all plots in Table 3.2.3.1. It was found that the cubic curve had a significantly higher R^2 compared with its quadratic counterpart for all regressions.

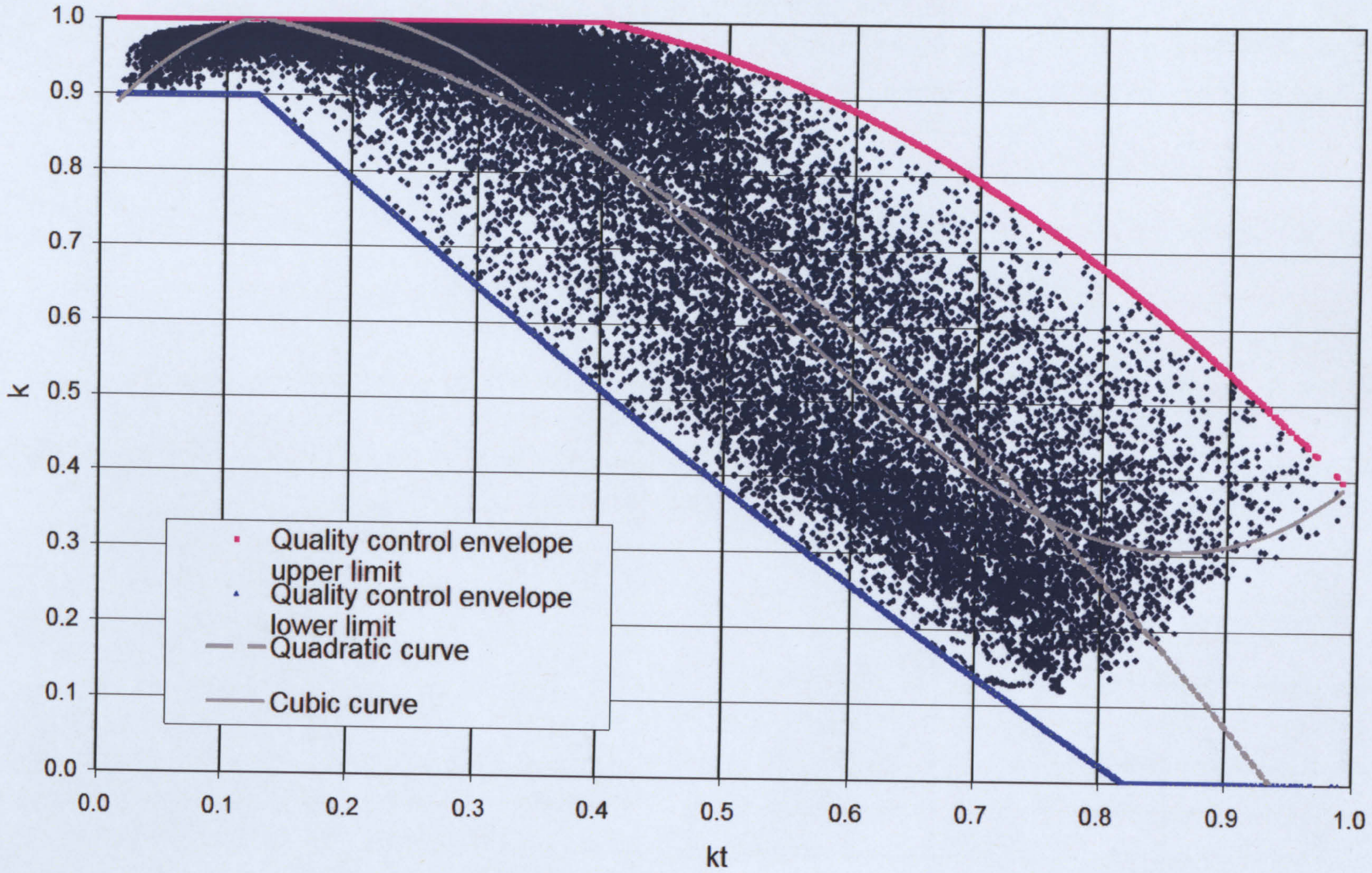

Figure 3.3.1 Annual k-k_t plot, quality-controlled data for Edinburgh data. Note quadratic and cubic equations fitted to data set.

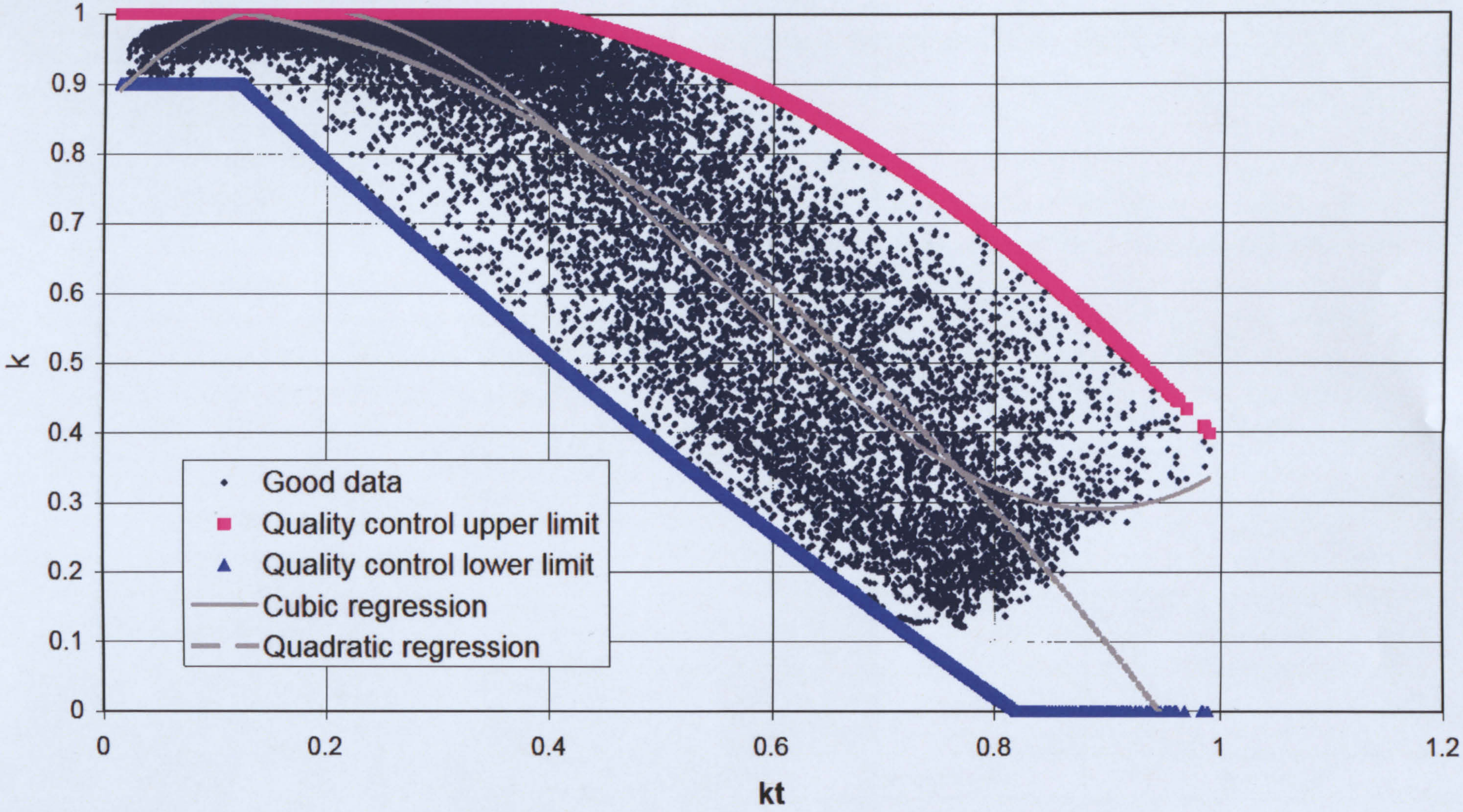

Figure 3.3.2 Summer seasonal k-k_t plot, quality-controlled data for Edinburgh data. Note quadratic and cubic equations fitted to data set.

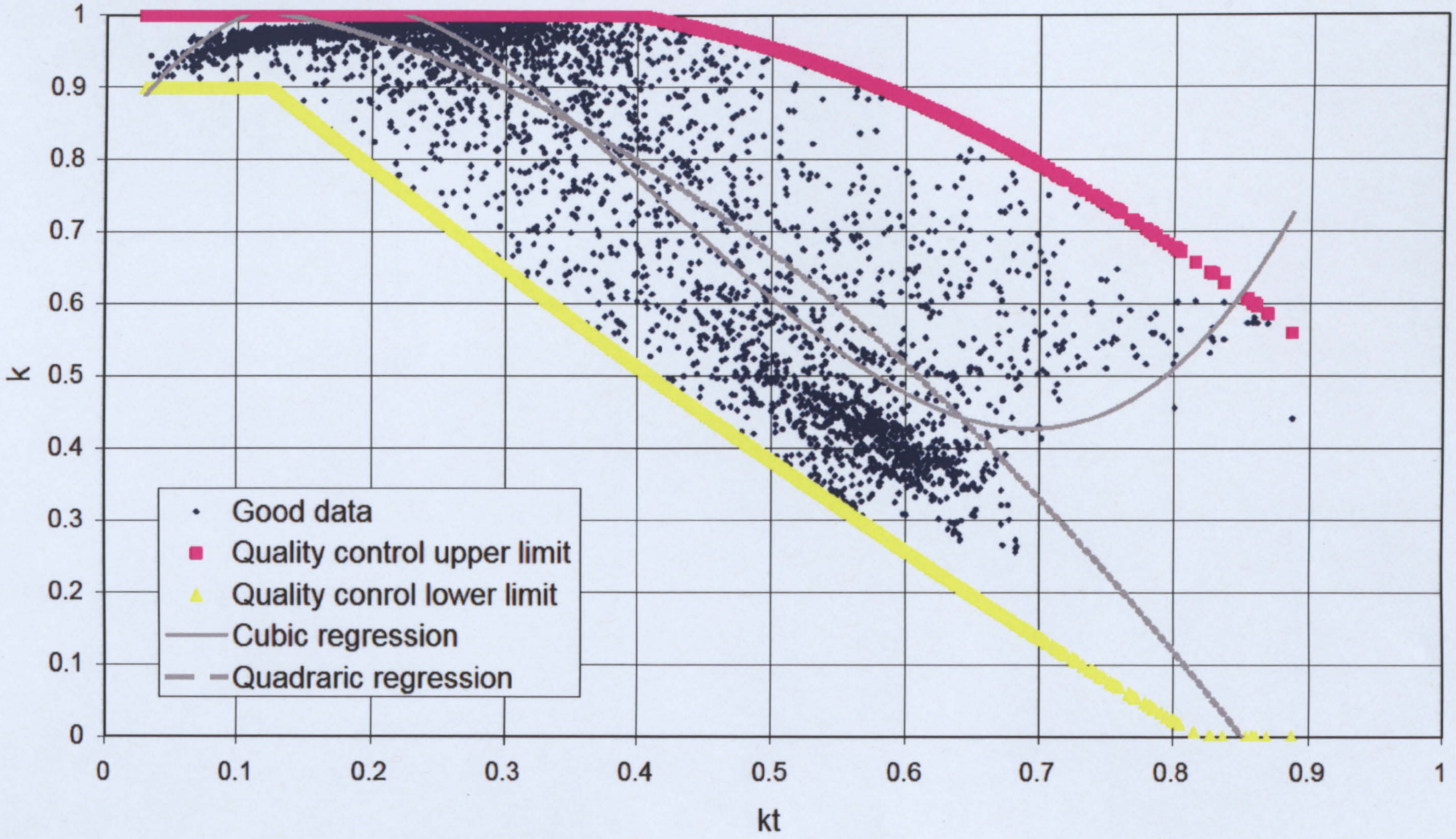

Figure 3.3.3 Winter seasonal k-k_t plot, quality-controlled data for Edinburgh data. Note quadratic and cubic equations fitted to data set.

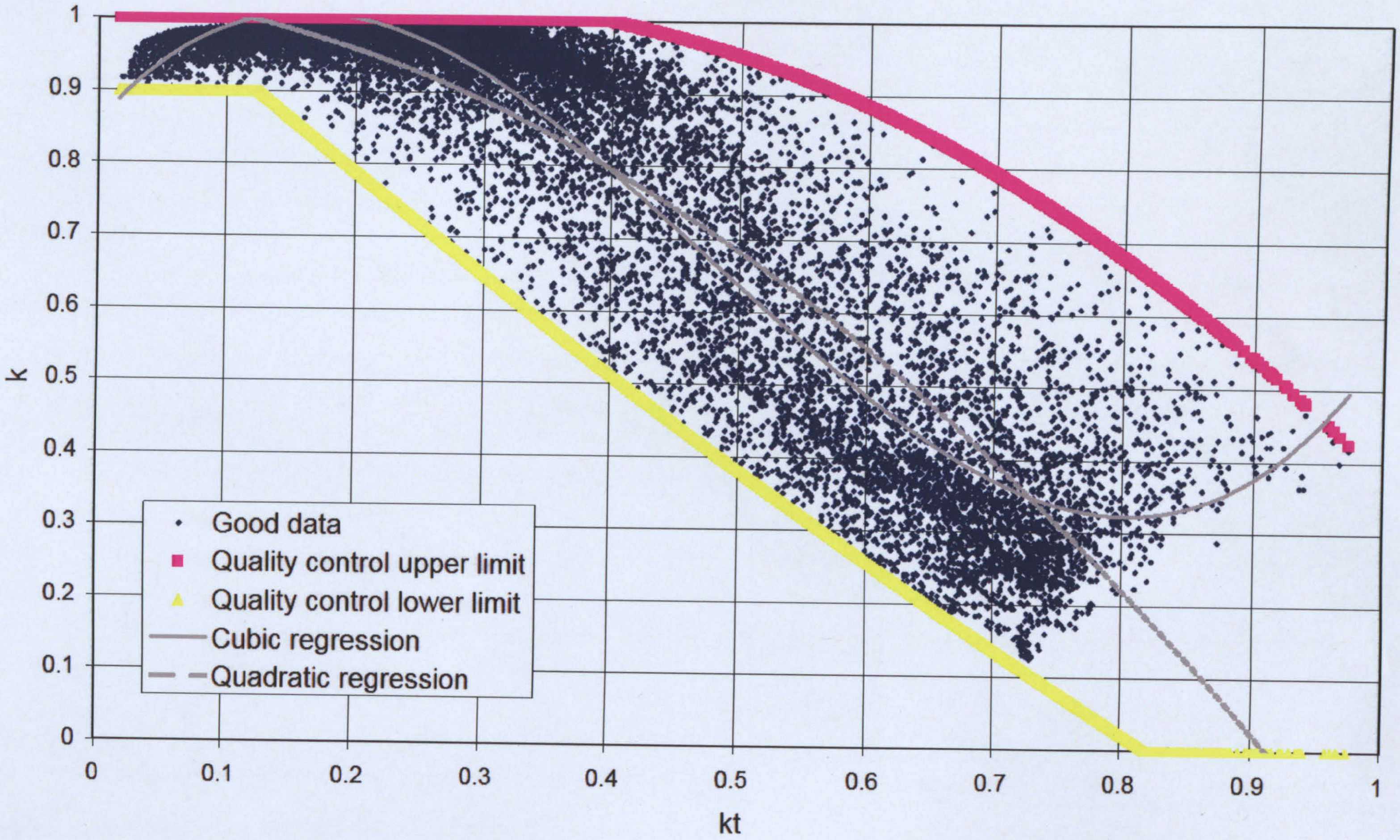

Figure 3.3.4 Spring/Autumn seasonal k-k_t plot, quality-controlled data for Edinburgh data. Note quadratic and cubic equations fitted to data set.

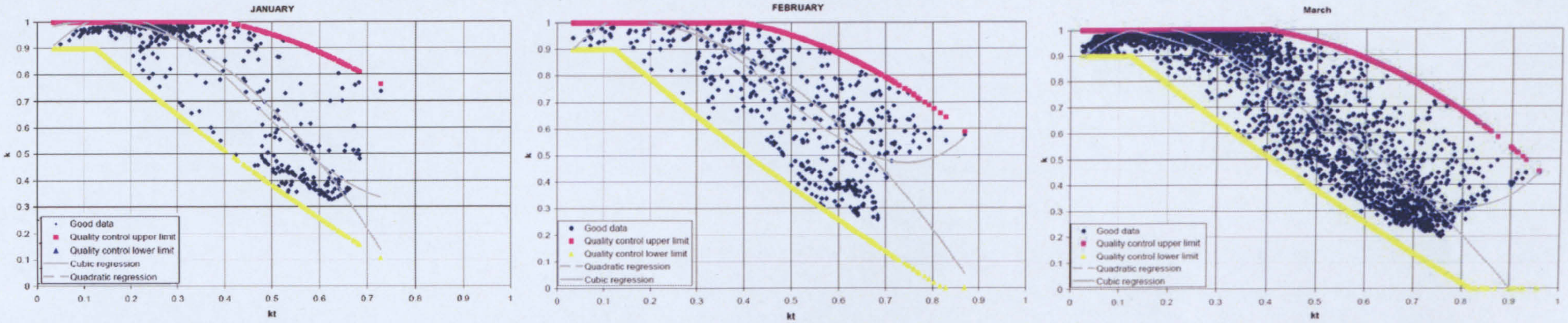

Figure 3.3.5.A. Monthly regressions k-k_t plot, quality-controlled data for Edinburgh data. Note quadratic and cubic equations fitted to data set.

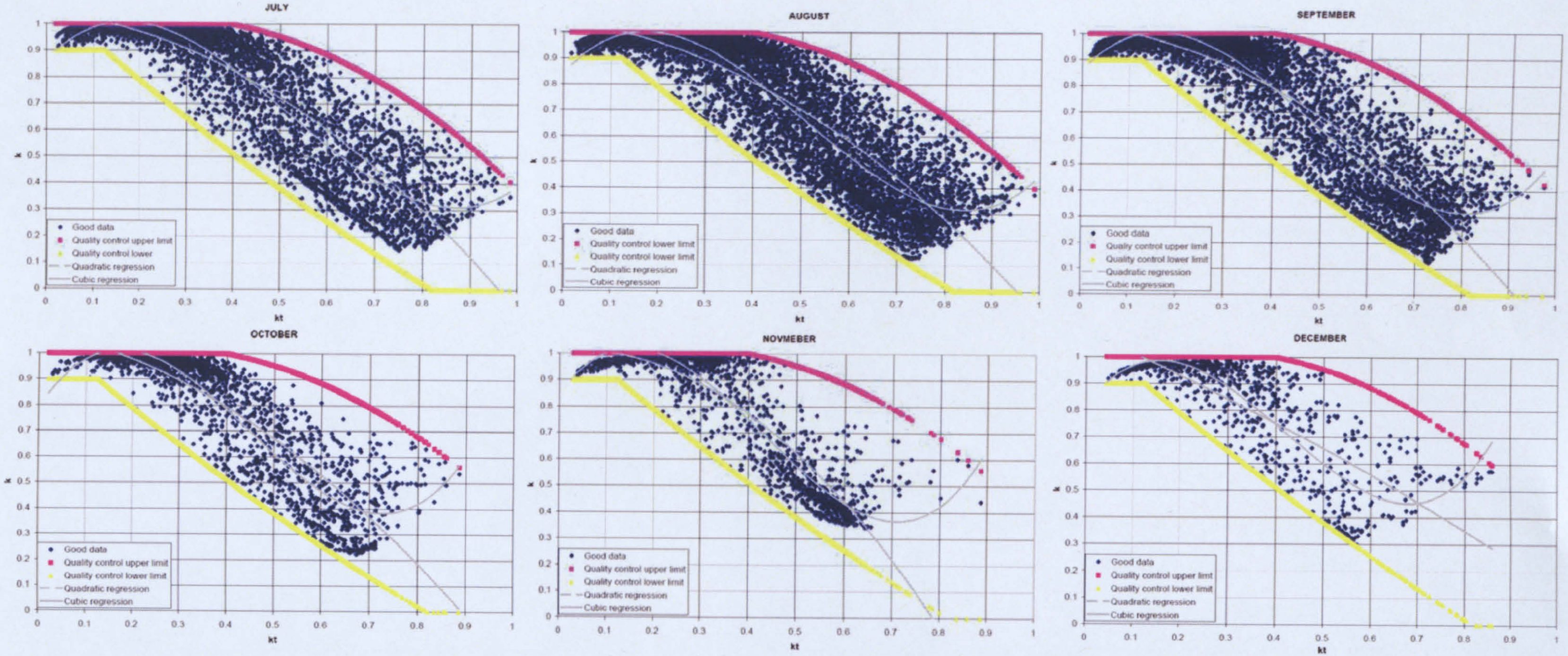

Figure 3.3.5.B. Monthly regressions k-k_t plot, quality-controlled data for Edinburgh data. Note quadratic and cubic equations fitted to data set.

The general regression model for annual, seasonal and monthly is represented by the following set of equations:

$$For\ k_t < \mathrm{L_L}\ k = a_0 \tag{3.3.1a}$$

$$For\ k_t \geq \mathrm{L_L}\ and\ k_t < \mathrm{L_U}, k = a_1 + a_2 k_t + a_3 k_t^{\ 2} + a_4 k_t^{\ 3} \tag{3.3.1b}$$

$$For\ k_t \geq \mathrm{L_U}\ k = a_5 \tag{3.3.1c}$$

Where L_L and L_U, the lower and upper limits respectively of the clearness index k_t, and a_0 to a_5, the regression coefficients, have been obtained for annual, seasonal and monthly regressions. Since a value of k_t of less than 0.3 indicates an overcast sky and a value of k_t of more than 0.7 indicates a clear sky, the lower and upper limits of these values were set in the above correlations. The actual values provide the best fit for the data. Further details are given in Clarke *et al.* (2007).

The coefficients and cut-off values for annual, seasonal and monthly regressions, as given by Equations 3.3.1.a - 3.3.1c, are provided in Table 3.2.3.1, and regression curves are shown in Figures 3.3.1 and 3.3.2. Table 3.2.3.2 shows error analysis statistics for monthly, seasonal and annual regression given for each month.

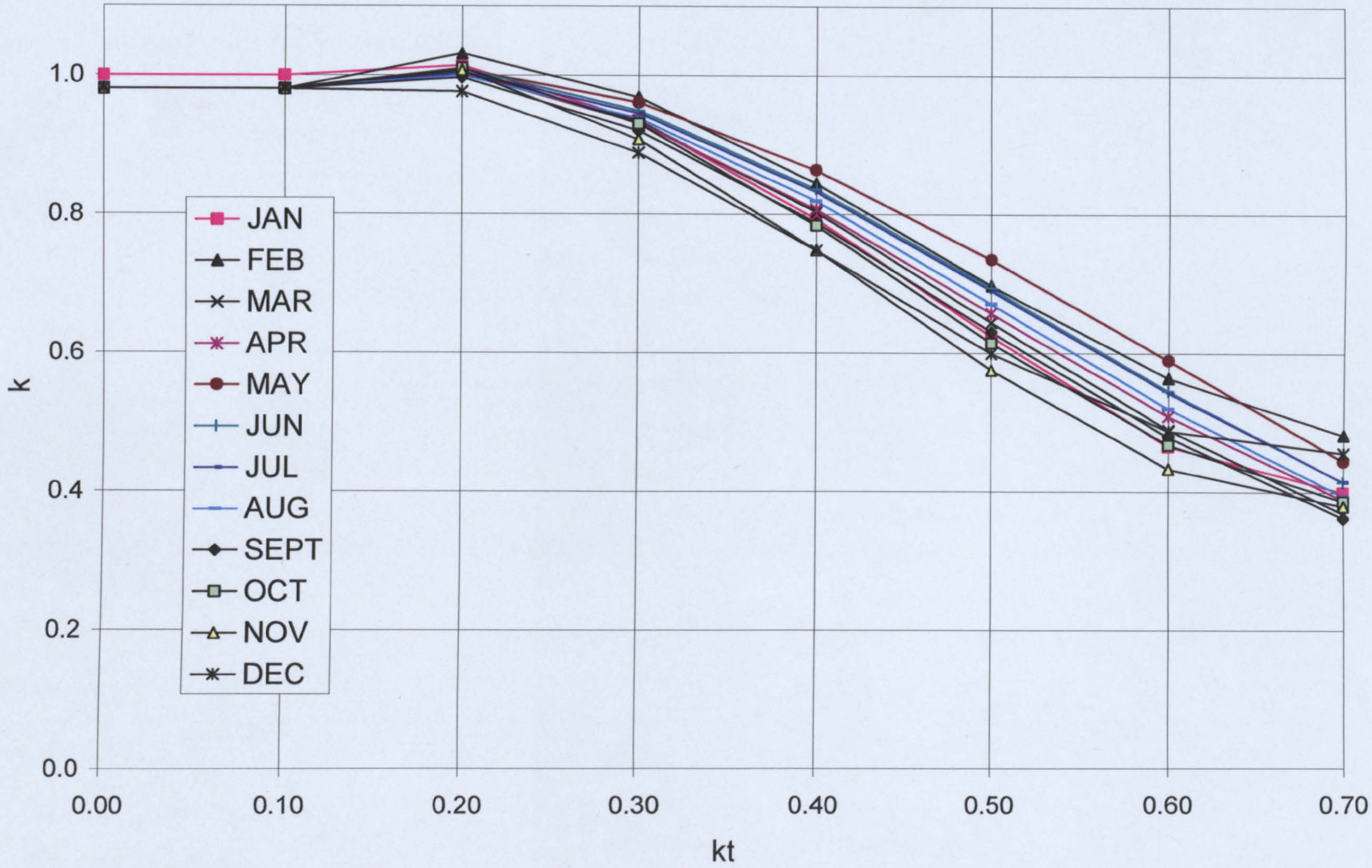

Figure 3.3.6 k-k_t monthly regressions for Edinburgh.

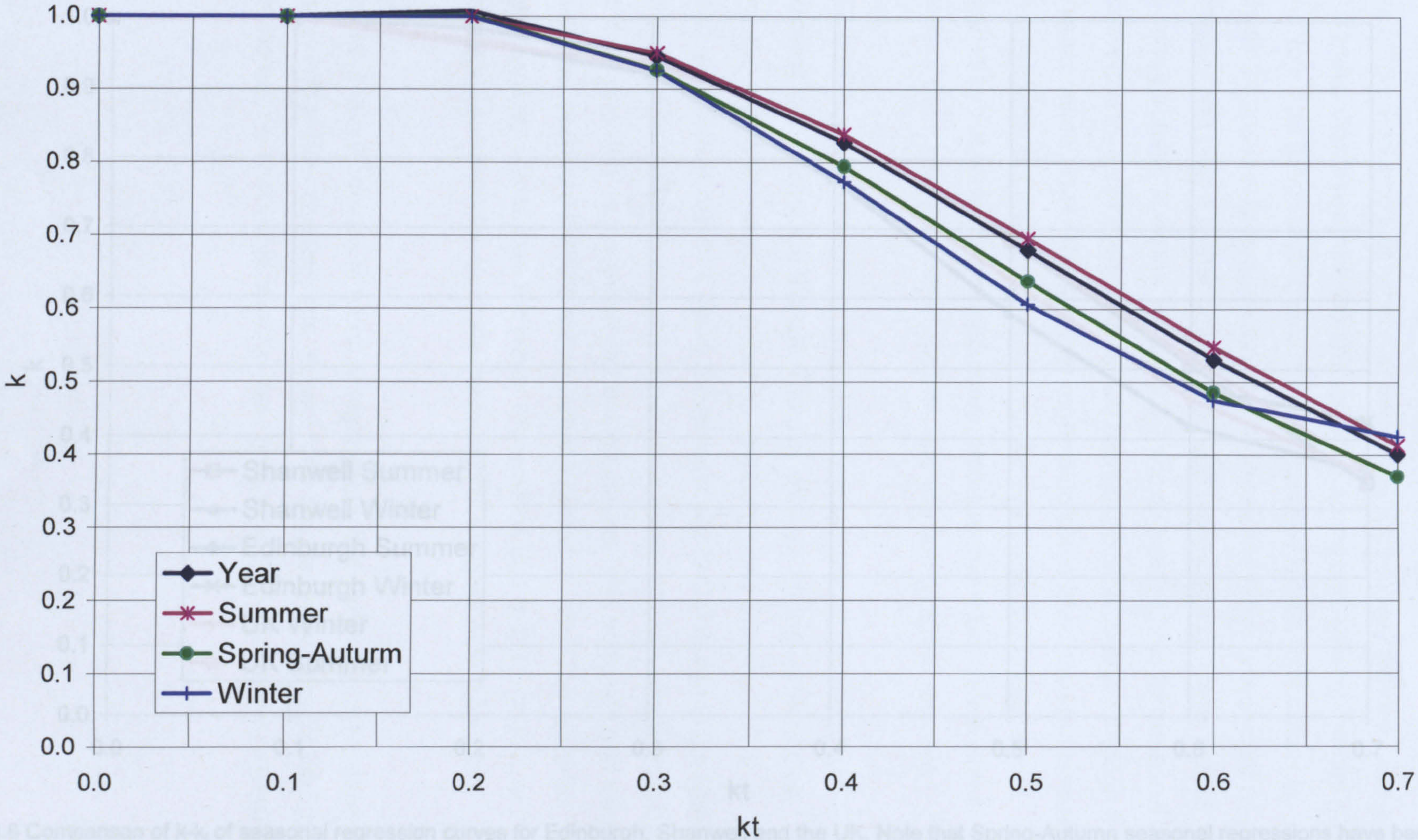

Figure 3.3.7 k-k_t seasonal and annual regressions for Edinburgh. Note order of regression curves Summer, Yearly, Spring-Autumn and Winter regressions. The Annual curve is lower than that of the Summer and above the Spring-Autumn and Winter curves, thus showing a good approximation for all seasons.

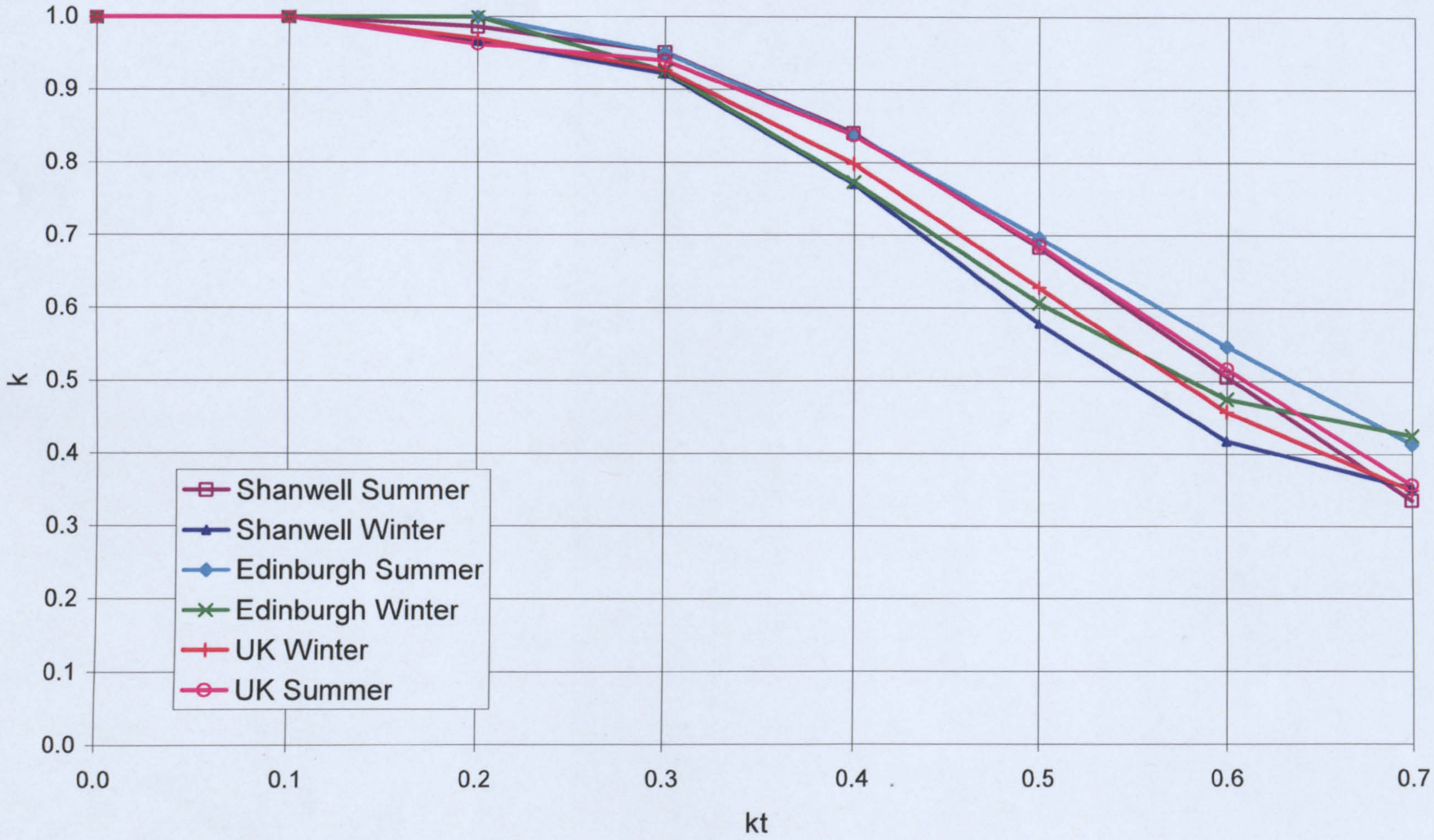

Figure 3.3.8 Comparison of k-k_t of seasonal regression curves for Edinburgh, Shanwell and the UK. Note that Spring-Autumn seasonal regressions have been omitted from the plot due to their close proximity to winter regression curves. Both Summer and Winter curves follow similar trends, validating the accuracy on Edinburgh regressions

Figure 3.3.6 shows twelve monthly regression curves for Edinburgh. All twelve regressions follow the same distinct curve: in general the summer months have a higher diffuse ratio than the winter months, with the spring and autumn months lying in between. Note that the general overall trend of summer month regressions is above both winter and spring-autumn monthly regressions, which is expected as clear summer weather has both a higher diffuse ratio and clearness index than that of winter and spring-autumn seasons. Figure 3.3.7 shows a plot of k-k_t for seasonal and annual regressions for Edinburgh. The annual regression runs centrally through the cluster curve for mixed skies. The summer regression curve lies above the annual regression curve whereas the spring-autumn curve lies below the annual curve, closely followed by the winter regression curve. However this trend differs at the extreme ends of the regression curves, in the clear sky and overcast regimes.

Figure 3.3.8 shows a plot for summer and winter regressions for Edinburgh (55.9° North), Shanwell (56° North) and the UK. The plot shows a strong concordance between the two regression sets, i.e. between Edinburgh and Shanwell. The Shanwell site was chosen due to it being the nearest site to Edinburgh in the previous study by Muneer (1987). Spring-autumn regressions have not been shown in this plot because of their proximity to the winter regression curves. This suggests that winter regression can be used to cover the spring-autumn period of data. The summer curves lie significantly higher than the winter regressions due to the higher turbidity experienced within summer, for example the impact of a higher pollen count in summer.

From Table 3.3.1, the R^2 values of monthly regressions are generally higher than their seasonal and annual counterparts, except for the summer months. However, in terms of R^2 there is no noticeable improvement from seasonal to monthly regressions.

Table 3.3.1 Error analysis for presently developed regressions

Month	R^2			MBD, W/m^2			RMSD, W/m^2		
	Monthly	**Seasonal**	**Yearly**	**Monthly**	**Seasonal**	**Yearly**	**Monthly**	**Seasonal**	**Yearly**
January	0.81	0.81	0.77	-0.02	0.26	3.39	13.2	13.3	15.8
February	0.87	0.87	0.86	-1.16	-6.4	-3.16	18.3	20.6	20
March	0.81	0.8	0.79	0.13	-0.16	7.37	31.3	31.8	34.1
April	0.86	0.86	0.85	0.18	-2.43	5.15	33.6	33.8	35.5
May	0.87	0.88	0.88	-0.92	-3.73	-4.95	42.8	43.2	43.4
June	0.85	0.85	0.85	-1.8	-0.09	-1.33	48.4	48.4	48.4
July	0.85	0.85	0.85	-3.33	-1.58	-2.91	48	47.8	47.8
August	0.82	0.82	0.82	-2.41	2.5	1.45	44.3	44.5	44.2
September	0.87	0.86	0.85	-3.1	-1.59	5.59	28.2	28.6	29.9
October	0.8	0.78	0.77	-0.79	-0.4	5.1	23.2	24.2	25.9
November	0.86	0.86	0.79	1.26	4.96	11.04	11.5	13.1	20.4
December	0.89	0.88	0.85	-1.52	-0.5	1.14	10.1	10	11.1

MBD and RMSD values are lower for monthly regressions compared to annual and seasonal regressions for the majority of months. However, careful inspection reveals that several months (June, July, September, October and December) have lower MBDs for seasonal and annual regressions than for their monthly counterparts. Interestingly, on comparing the RMSDs for these months, they all lie within the same range for monthly, seasonal and annual regressions. There are no significant improvements in MBDs or RMSDs for monthly regressions over seasonal regressions. Considering the fact that estimating diffuse irradiation using monthly regressions requires substantially more computation and shows no evident improvement over seasonal regressions, it is suggested that the latter is used as an optimum solution. It is evident from the statistical indicators that the overall performance of annual regression is poor compared with seasonal and monthly regressions.

The seasonal regression coefficients for 11 sites within the UK and for the country as a whole developed by Muneer *et al.* (2000) are shown in Table 3.3.2; note that the list also includes the Edinburgh regression coefficients developed in the present study.

Table 3.3.2 Parameters pertaining to regressions developed for 12 UK sites

Station	Latitude		Period	No. of hours	Winter					Summer					Spring-Autumn				
	Deg	Min			a_1	a_2	a_3	a_4	R^2	a_1	a_2	a_3	a_4	R^2	a_1	a_2	a_3	a_4	R^2
Lerwick	60	8	Jan'81-Dec'82	12701	0.617	3.668	-11.197	8.352	0.49	0.304	5.768	-14.271	8.840	0.81	0.685	3.143	-9.510	6.184	0.79
Stornoway	58	12	Oct'82-Dec'83	5263	0.539	4.513	-13.254	9.695	0.63	0.524	4.056	-10.106	5.766	0.88	0.576	4.030	-11.701	7.951	0.81
Edinburgh	56	57	~	3732	0.816	2.753	-10.370	8.063	0.88	0.872	1.762	-6.214	3.947	0.86	0.858	2.013	-7.499	5.185	0.83
Shanwell	56	26	Jan'82-Dec'83	9396	0.456	0.456	-15.718	11.469	0.76	0.721	2.722	-7.903	4.614	0.84	0.579	4.148	-12.571	8.767	0.82
Eskdaleemuir	55	19	Jan'81-Dec'83	12723	0.559	0.559	-11.715	7.818	0.72	0.638	3.228	-9.102	5.621	0.80	0.755	2.379	-7.429	4.609	0.78
Aldergrove	54	39	Jan'81-Dec'83	14107	0.664	0.644	-9.220	5.938	0.69	0.513	3.793	-9.739	5.745	0.82	0.679	2.800	-8.396	5.279	0.79
Aughton	53	33	Jan'82-Dec'83	8144	0.758	0.758	-8.839	6.162	0.56	0.777	2.142	-6.224	3.317	0.83	0.786	2.186	-6.891	4.062	0.79
Finningley	53	29	Nov'82-Dec'83	5116	0.312	0.312	-19.263	14.472	0.76	0.744	2.386	-6.796	3.718	0.84	0.752	4.034	-11.966	8.311	0.80
Hemsby	52	51	Jan'82-Dec'83	9006	0.487	0.487	-14.896	10.476	0.80	0.787	2.073	-6.198	3.340	0.83	0.790	2.139	-6.922	4.111	0.83
Aberporth	52	8	Jan'81-Dec'83	11937	0.579	0.579	-12.006	8.058	0.76	0.681	2.821	-7.650	4.260	0.80	0.741	2.628	-8.162	5.088	0.79
Easthampstead	51	23	Jan'81-Dec'83	14058	0.349	0.349	-17.438	12.387	0.80	0.857	1.570	-5.608	3.271	0.82	0.784	2.396	-8.306	5.558	0.83
Camborne	50	13	Jan'82-Dec'83	9109	0.514	0.514	-13.539	9.389	0.80	0.632	3.211	-8.730	5.167	0.80	0.804	2.145	-6.977	4.198	0.84
UK	~	~	~	111552	0.629	0.629	-10.651	7.098	0.79	0.651	3.050	-8.460	5.006	0.81	~	~	~	~	~

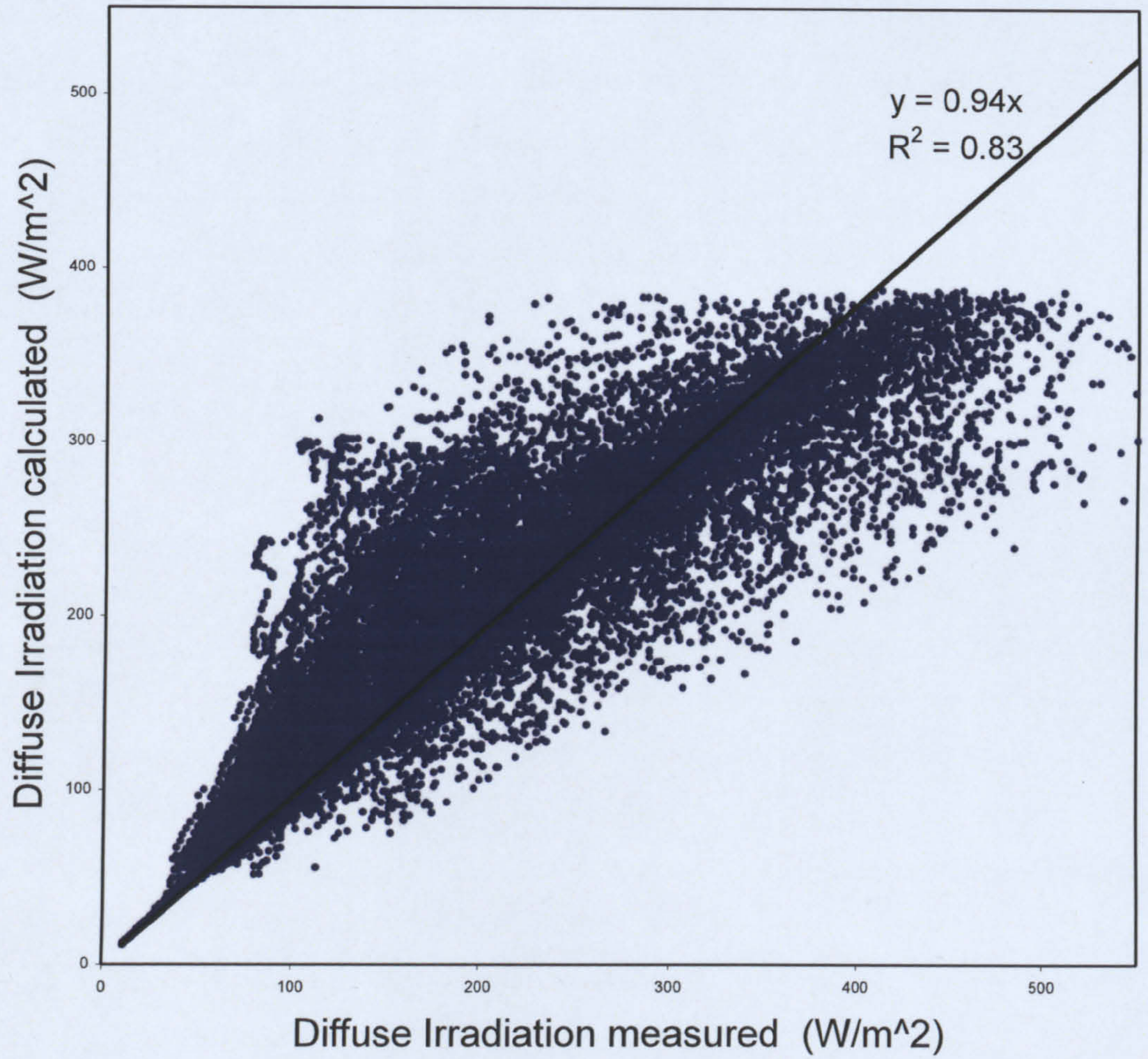

Figure 3.3.9 Comparison of calculated versus measured diffuse irradiation for Edinburgh using monthly regressions. Note that the scatter for low values of measured diffuse irradiance and high values of calculated diffuse irradiance are largely due to shade ring misalignment of measured data.

Figure 3.3.9 shows a plot of measured diffuse irradiance versus calculated diffuse irradiance for Edinburgh. The plot shows a good correlation between the two parameters. Edinburgh, Shanwell and UK summer regression curves coincide for k_t less than 0.5 forming the majority of the data points (77% of the total data). The winter curves of the two locations and the UK curve follow a similar trend and coincide for k_t value of up to 0.4 with the exception of the UK winter curve which deviates from the other two at k_t less than 0.3, representing 58% of the total data. Two very important conclusions can be drawn from this. Firstly, summer regressions appear to be independent of the location or latitude effect for the bulk of the data. Secondly, the latitude effect is more pronounced in winter regression curves. Since Shanwell and Edinburgh are in geographical proximity, their regressions curves lie close together for both winter and summer regimes as expected. It is not suitable to use a single regional regression in winter, unlike summer where the summer UK regression may be used for all sites. This discrepancy can possibly be attributed to the heterogeneous sky conditions prevalent in the UK winter, mainly as result of Siberian winds which bring cold dry air to the eastern flank of Britain. For instance, in winter, winds from Siberia keep the east coast of Scotland cold and dry, whereas the prevailing winds from the Atlantic Ocean keep the west coast of Scotland warm and wet. It is important to note here that Shanwell and UK regressions were developed by Muneer *et al.* (1987) using hourly averaged data, whereas Edinburgh regressions in the current study are developed using a 5-minute (sub-hourly) data set. This helps one conclude that given the closeness of Shanwell and Edinburgh regressions, hourly regressions may be used to estimate sub-hourly data or vice versa, with reasonable approximation.

3.4 Horizontal and tilted global irradiance measurement for Napier PV facade analysis and modelling

Horizontal and inclined solar irradiance data has been recorded at Napier University since the17th May 2005. Early data analysis showed that the diffuse component of the sum global was underestimated. It was determined that this error could be attributed to the location of the measurement station. A building to the north prevented the horizontal pyranometer having a clear view of the sky hemisphere, resulting in the

error of underestimation of the diffused component. Figure 3.4.1 shows the initial location of measurement station. The station was moved to its current location (seen in Figure 3.4.2) in April 2006. The two high-quality pyranometers used for the study, CM11 and CM6b (manufactured by Kipp & Zonen) both have a low response time of 18 seconds at 95 percent accuracy (Kipp & Zonen, 2005). Both pyranometers were set up on a horizontal plane for a short period of time to evaluate the accuracy of measurements. Once the quality of data obtained was proven, the CM6b pyranometer was installed at the same aspect and tilt angle as the PV facade, 37° East of South and 75° tilt, recording the irradiance onto the PV facade. Table 3.4.1 show the total number of hours of data recorded for the study. A Grant Squirrel 1000 series data logger was used to record 15-minute averaged solar irradiance data (Grant, 2008). Solar global irradiance was recorded from 24th March 2006 to 15th May 2007. Within this period, data recording failed during two periods. These were between 9th-22nd June and 12th-25th September 2006. The first failure was to due to a power supply failure within the data logger and the other due to operator error.

Figure. 3.4.1 Edinburgh Napier University solar measurement station on the rooftop of Edinburgh Napier University. Note the building behind the measurement station, found to cause errors in measuring the diffuse component of some global irradiance.

Figure 3.4.2 Horizontal and inclined pyranometers installed at new location on the rooftop of Edinburgh Napier University to record solar irradiance for the current study.

To validate the performance of the pyranometers, the CM6b pyranometer used to record inclined global irradiance was also installed on the horizontal plane for a short period between 28th June to the 20th September 2005. Figure 3.4.3 shows a global irradiance plot for this period. The plot shows a very strong concordance between the two sensors' performances. A linear fit is also shown in the figure with a gradient of one, meaning that both sensors give a precise estimate of global irradiance.

Table 3.4.1 Solar horizontal global incident irradiation data set information

Days	Month	Year	Number of hours
24-31	3	2006	71
1-30	4	2006	284
1-31	5	2006	330
1-9,22-30	6	2006	222
1-31	7	2006	394
1-31	8	2006	320
1-12,25-30	9	2006	147
1-31	10	2006	209
1-30	11	2006	126
1-31	12	2006	101
1-31	1	2007	123
1-28	2	2007	145
1-31	3	2007	267
1-30	4	2007	318
1-15	5	2007	167
Total			3272

Note 15-minute averaged data set recorded using a Kipp & Zonen CM11 pyranometer.

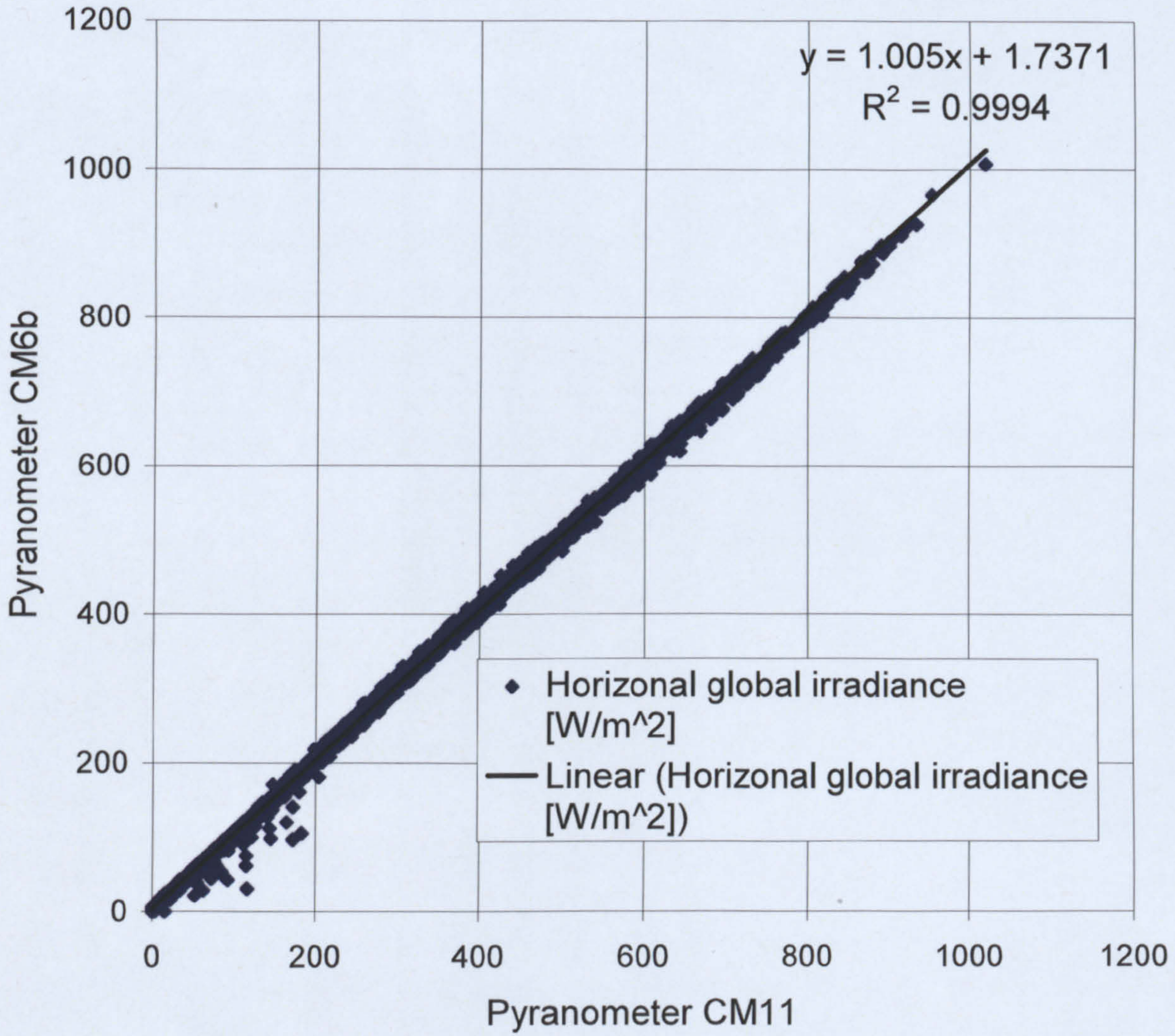

Figure 3.4.3 Comparison of horizontal global irradiance recorded using Pyranometer CM11 and Pyranometer CM6b for confirmation of correct calibration. Period 28/6/2005-20/9/2005, 15-minute averaged data.

3.4.1 Horizontal, global and diffuse irradiance measurement for Napier PV Facade analysis and modelling.

A second data set recording global and diffused irradiances was also recorded at the same location at Edinburgh Napier University Merchiston Campus. The sensors used were BF3 sunshine sensors manufactured by Delta-T Devices.

The sensor is designed to measure global and diffuse irradiance as well as sunshine duration. The sensor relies on an array of photodiodes used with a sophisticated shading pattern ensuring that at least one photodiode is exposed to beam solar radiation, and at least one photodiode is fully shaded by the shade pattern. A microprocessor calculates global, beam components and sunshine duration. The sensor has an accuracy of ±12 %, ±15 % for global and diffuse radiation (W/m^2) respectively and a low response time of <200ms (Delta-T, 2002). The Delta-T has been independently evaluated by Wood *et al.* (2003). The Delta-T sensors were set up in early May 2007, recording horizontal global and diffused irradiance simultaneously for one month, enabling the accuracy of the sensors to be validated. Measured global and diffuse irradiance will also be used to validate the accuracy of solar energy models discussed in Chapter 4. This is because errors generated by previously discussed regressions are transferred to the energy models, and may appear in statistical testing as errors generated by the models being tested.

Figure 3.4.1.1 shows a plot of horizontal global *versus* horizontal global irradiance for two BF3 sensors measured at 15 minute intervals; it shows a good linear relationship between the two sensors and little scattering. The slope is 0.97, which suggests that the sensor being used to collect data slightly overestimates that of the sensor being used for validation. The R^2 of 0.98 shows that there is little scatter between the variance of the two sets of results. This shows that the measured global irradiation is of good quality. Figure 3.4.1.2 shows a similar plot for diffuse irradiation measured using the same two sensors. The slope is 1.03, which suggests that the sensor being used for data collection slightly overestimates the diffuse component compared with that of the sensor used for validation. The R^2 is 0.99, showing that there is very little scatter for diffuse irradiation measurements.

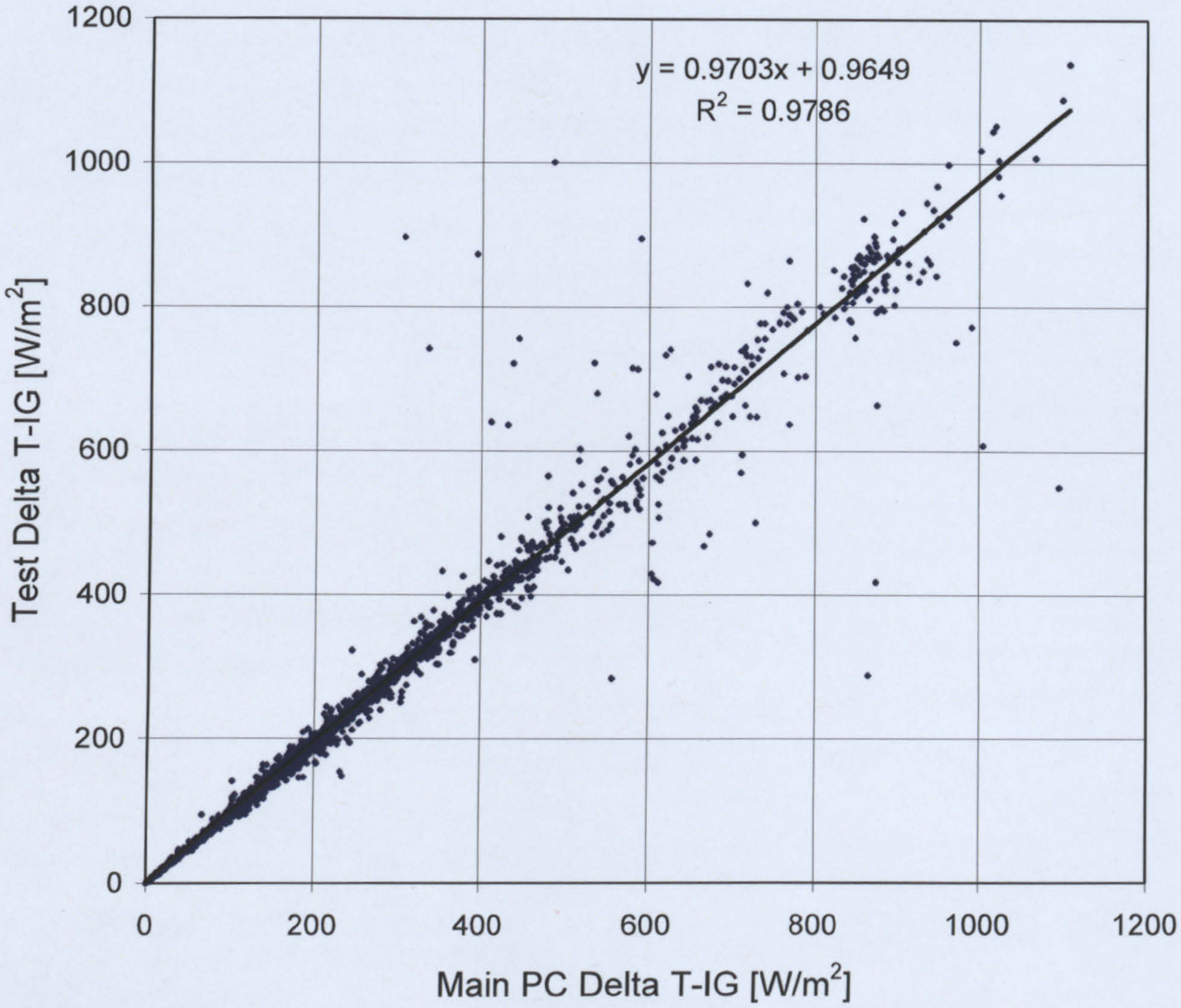

Figure 3.4.1.1 Horizontal and global irradiation, two BF3 sunshine sensors (1/6/2007-15/6/2007).

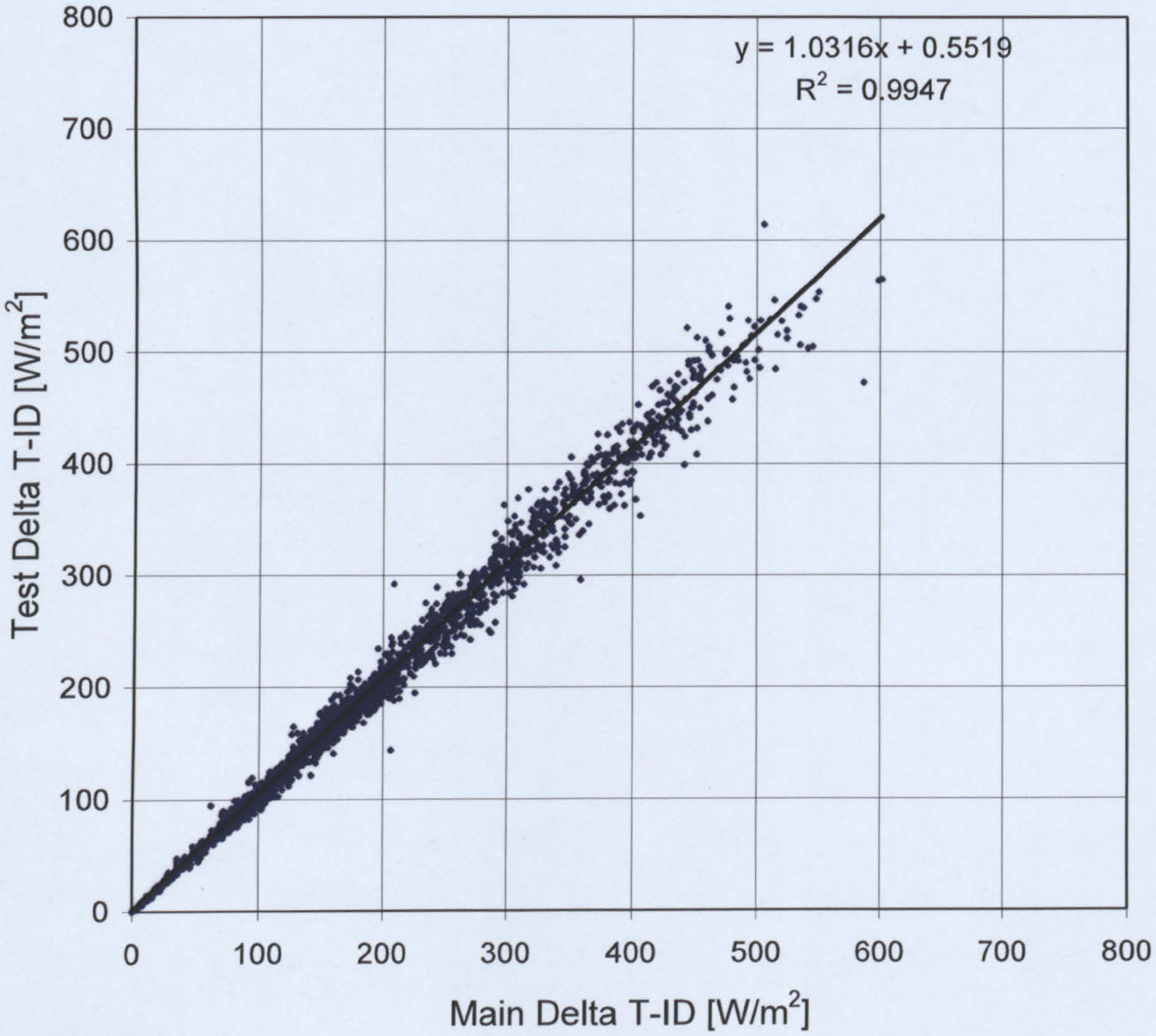

Figure 3.4.1.2 Horizontal diffuse irradiation, two BF3 sunshine sensors (1/6/2007-15/6/2007).

CHAPTER 4

Modelling incident solar irradiance in urban environments: Applications for building integrated photovoltaics

4.1 Introduction

Previously, in the introductory chapter, the importance of the role of building integrated renewables was discussed. It was recognised that building integrated renewables had an important role to play in reducing external energy demands within the building environment. This has been recognised particularly by many of the European countries, resulting in incentives schemes and fiscal measures being introduced across many of the EU countries to encourage the use of micro-generation such as solar thermal, PV and micro-wind.

Solar energy systems are the most suited of all the renewable energy systems to be building integrated. This is because solar availability, unlike wind energy, does not suffer from issues of sheltering in urban environments. Solar energy has good predictability, even within urban locations.

Solar energy systems can also be easily combined into the fabrics of buildings, removing the need for costly and energy intensive support structures. If the system can be incorporated as part of the building's cladding or glazing facade, then some of the high economic costs may be absorbed into the cost of the building structure itself. However, even though solar energy systems are ideally suited for building integration, it is important to recognise that they must be located in the correct location, as described in chapter two with the Napier PV facade.

If a solar energy system is located in a poor situation, the solar income received will be considerably reduced from that which is potentially available. Although solar energy systems do not suffer from the sheltering issues seen with wind energy systems, there are still issues caused by shading. This is a particular problem when considering urban locations where many of the solar energy systems are likely to be installed. Shading can be a very problematic issue for designers and installers to address, particularly where there may be many obstacles in the foreground or on the horizon which may cause shading.

However, these effects will only be noted at certain times of the day. This is an issue not only in terms of shading caused by the loss of the beam component; if the location is in a very built up location such as a city centre which is surrounded by large buildings, then the seen sky hemisphere will be reduced, thus causing an overall dimming effect. Lowering the overall global irradiance received reduces the proportion of the solar diffuse component compared to a non-shaded situation. This has a noticeable effect in reducing the performance of the solar energy system.

Thus there is a need for a model which can be used by designers and installers to accurately simulate and estimate the availability of solar radiation in urban environments. In this chapter, two models are developed to meet this requirement. The second model is much more involved then the first, to enable a far greater accuracy of estimation to be achieved.

4.2 Shading and the effects of shading caused by the surrounding urban environment

Shading causes large losses in solar energy systems resulting in lower energy yields. The first stage in the design process when developing any solar system is to ensure that the system is located in a suitable site where there is little or no shading. This is often a difficult task, especially when considering building integrated systems, as space is often limited and alternative locations are not always available. Thus it is necessary to optimise the use of the location as much as possible using careful design strategies to ensure that maximum performance can be achieved from the available solar resource. This requires a detailed knowledge of all shading patterns formed at that location throughout the day. This is not an easy task as urban locations tend to be full of obstacles which may cause shading at different times.

Energetic losses in PV systems cannot be avoided if PV modules fall under shade. However, steps can be taken to minimise these losses. When a mono-crystalline panel becomes even partly shaded there will be a disproportionately large power loss across the whole module. The reason for this disproportionately large loss is due to the construction of the PV module.

PV modules are made by connecting a number of solar cells in series. Under normal operation the solar cells work in a forward bias, producing energy. However, if a solar cell in the array becomes even partially shaded, electrical mismatching can occur. The shaded solar cells can become reverse biased, in that the energy produced by unshaded solar cells is dissipated as heat across the shaded cells. The potential voltage across the shaded cells can then increase in excess of the cell breakdown voltage, causing the cells to fail (Kovach & Schmid, 1996).

To partly overcome these problems, manufactures install two bypass diodes in each module which are activated should shading occur across the module, thus bypassing the shaded cells within the module. This stops generated energy from the remaining string of modules from being dissipated across the shaded cells, reducing power loss across the string and preventing damage being caused to the shaded cells.

Careful configuration of the module strings within the array can optimise the performance of the array. If the shading parameters are known, then modules can be carefully placed to avoid shaded areas. An example of this is shown in Figure 4.2.1. The PV array is installed on a tilt to avoid shading from the church spire. Shading should also be taken into consideration when wiring strings of modules into the inverter. For example, modules which are known to fall under shade should be placed on separate strings or on strings with other modules which are known to fall under shade at the same time. The careful consideration of string configurations will ensure that only minimum losses occur, thus having a minimal effect on the rest of the PV array's performance.

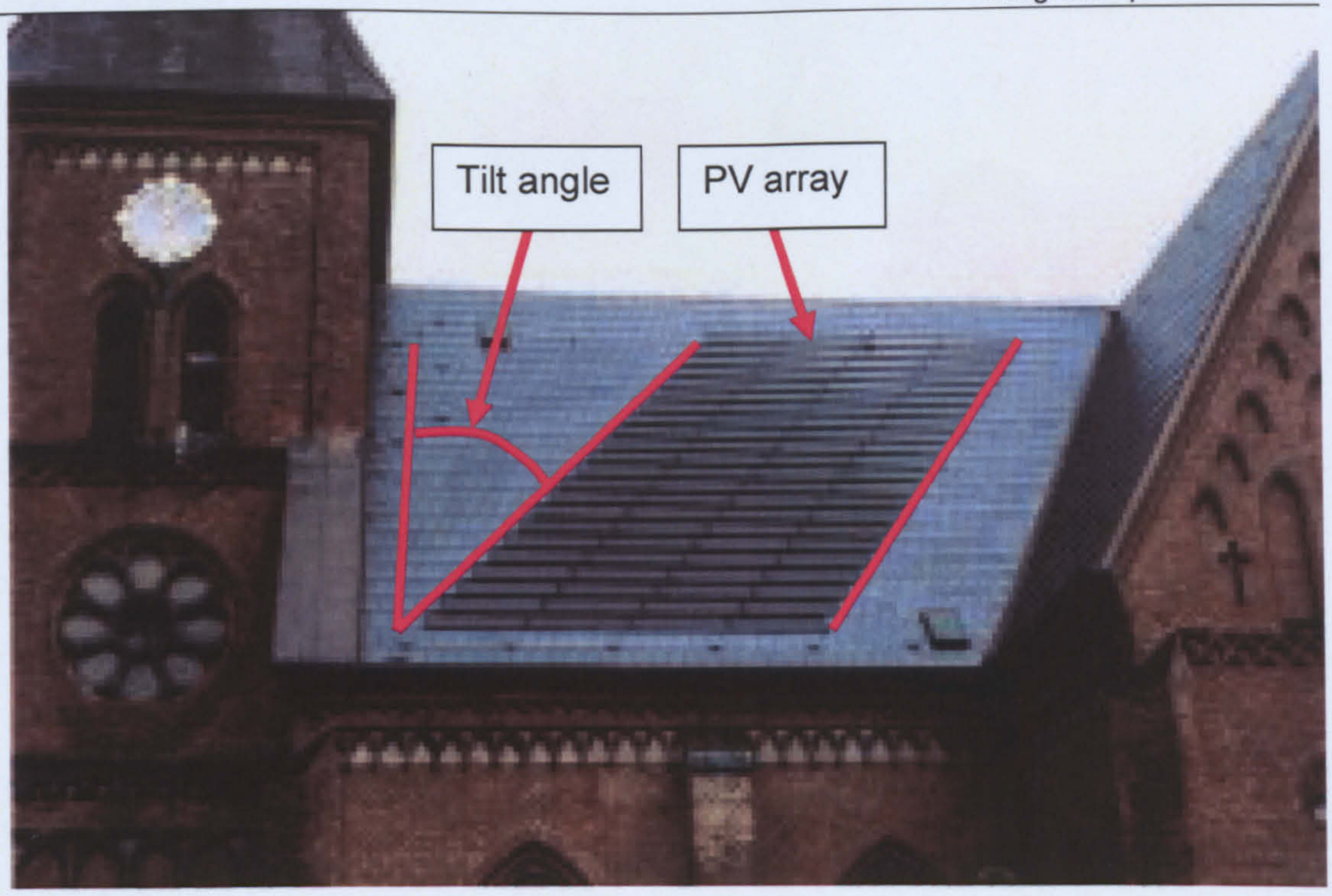

Figure 4.2.1 Tilted PV array on church roof. Note how PV array is tilted away from the church spire to reduce losses caused by shading from spire at certain times of day. (Courtesy: http://www.pfleiderer-dach.de/ Accessed on June 5th 2007).

4.3 Ground reflection in the urban environment

The ground reflection component of global irradiance, also known as the albedo, is the portion of the global irradiance which reflects off surrounding surfaces. Its magnitude is affected by a low solar altitude and the reflectivity of the surrounding surfaces. The main difficulty in measuring ground-based reflection for a given location is in determining the average reflectivity of the foreground and also the inaccuracy of available models. This is mainly due to the difficulties of specifying the properties of reflectivity. Note that the reflectivity of a surface is subject to variations which are dependent on weather and solar altitude.

For this study, the ground reflectivity for various surfaces are based on the work of Kondratyev (1969). The foreground in front of the Edinburgh Napier University PV facade is a non-uniform surface, and an average albedo value was calculated for the entire surface. The surface reflectivity was determined by using a fish-eye lens camera to take a panoramic photograph of the foreground of the PV facade. A 20mm square matrix was overlaid onto the image as seen in Figure 4.3.1. Each element of the overlaid matrix was then given an albedo

value dependent on its surface type which was specified by visual inspection. Following the recommended procedure of Kondratyev (1969), an averaged albedo was calculated for the entire matrix. This value was then used as an overall albedo rating for the PV facade used in all aforementioned solar models. Due to the inaccuracies of applying albedo values to the foreground, and its relatively small contribution to the sum global irradiance, it was considered that an annual value of albedo would be suitable for all seasons.

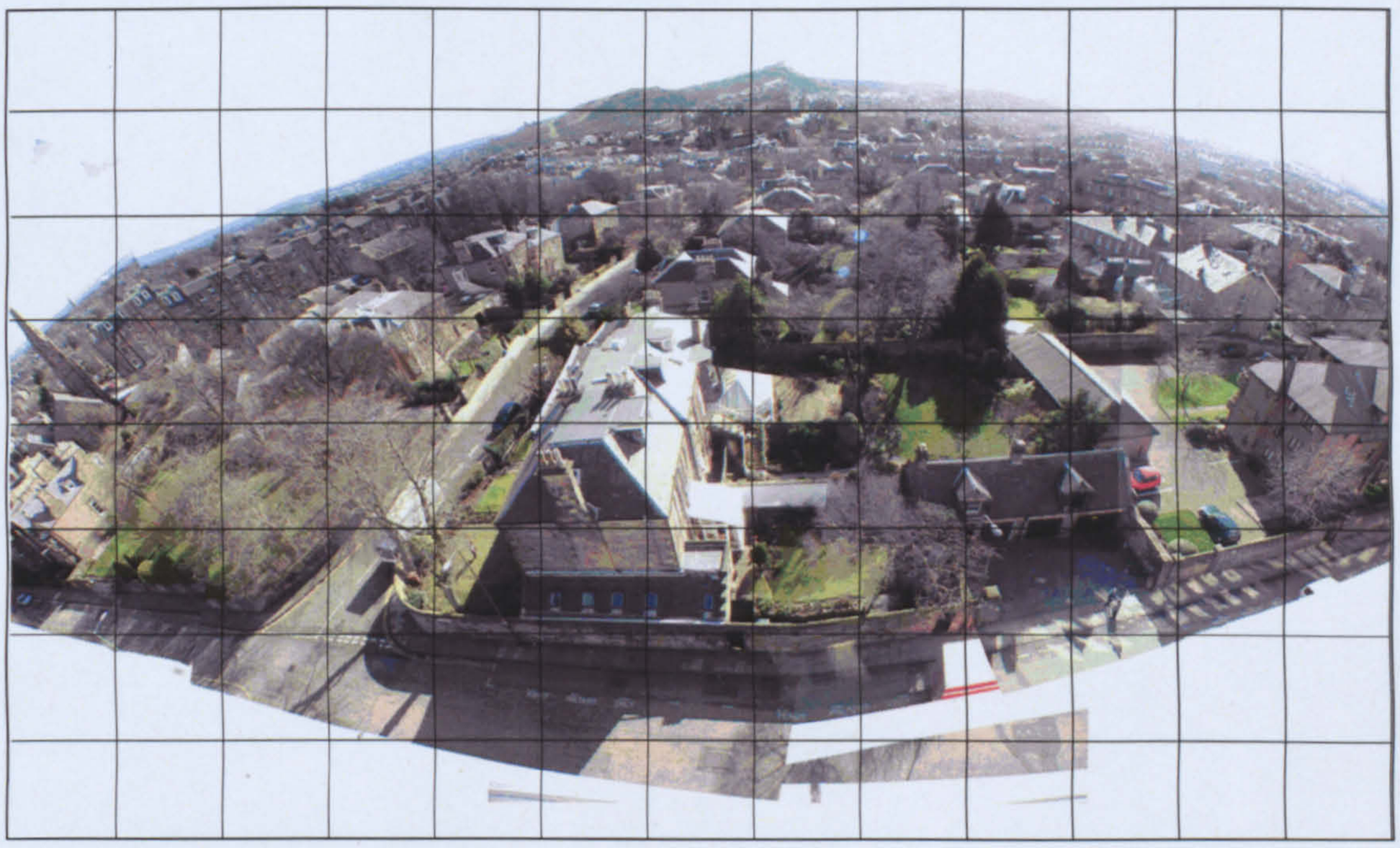

Figure 4.3.1 Napier PV facade foreground used to calculate ground reflected albedo. Image taken from rooftop of Edinburgh Napier University for current study.

Equation 4.5.1 gives global irradiation, incident on a tilted surface. This does not take the effects of shading into account, because the measured horizontal global irradiance which is used by the model does not experience shading.
Architectural plans of the facade were used to calculate the precise position of the bay window in relation to the PV array as seen in Figure 4.3.2, thus enabling the measurement of the full azimuthal range seen by the PV facade. This method shows that when the angle of the sun's azimuth is greater than 216° the bay window will start to cast a shadow across the facade. The shadow propagates across the facade until the facade becomes fully shaded once the sun's azimuth passes 231° from north. This effect has been incorporated into the model. If these parameters are not met, beam irradiance is omitted from the sum global irradiance.

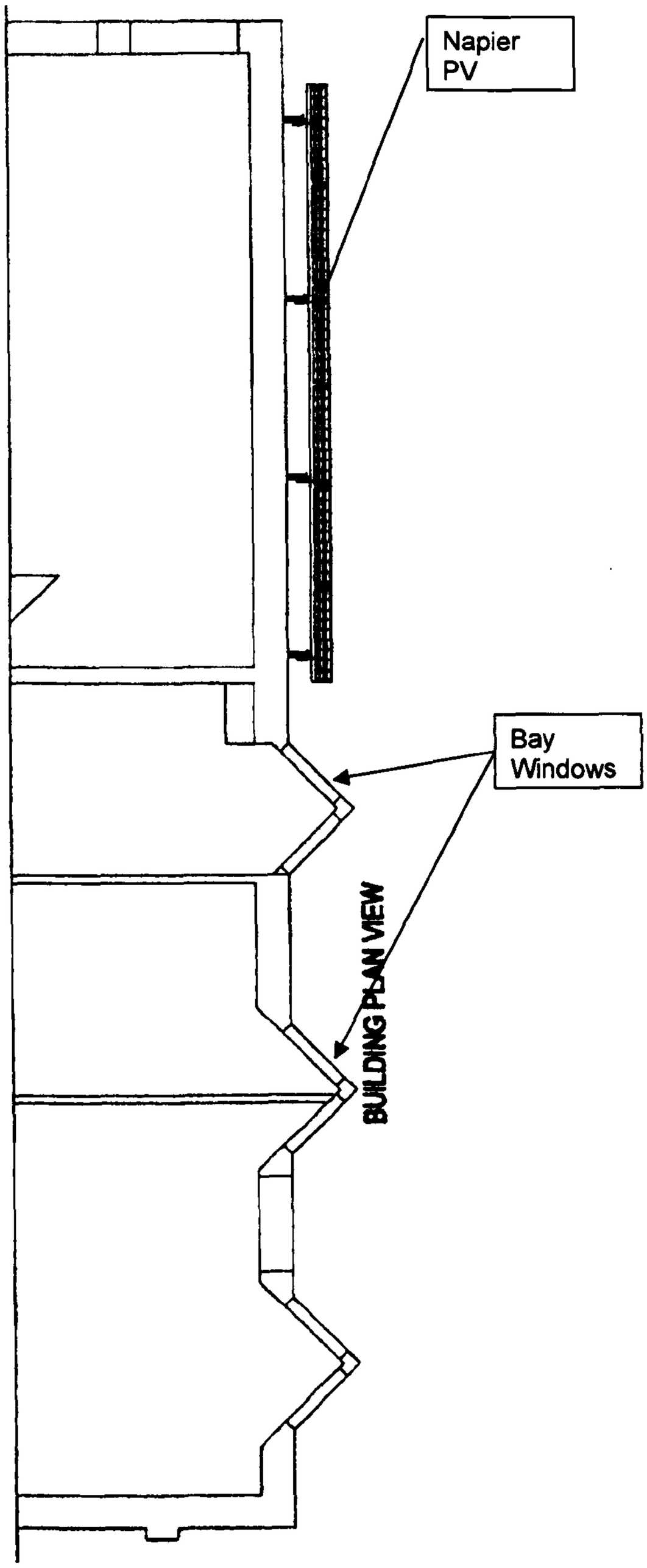

Figure 4.3.2 Plan view of Napier PV facade, showing PV array and bay windows.

4.4 Statistical evaluation of solar simulation models

Following the above observations based on a visual inspection of the two models under discussion, a statistical evaluation was also undertaken. With visual inspection alone, it is often not possible to judge how well a model performs. It may be possible to obtain a general overview of a model's performance in terms of whether a model overestimates or underestimates, or how the model performance is affected by seasonal variations. For this reason, statistical indicators are used to help evaluate the performance of a model.

There are five statistical indicators that are used particularly in assessing the performance of solar models, which often deal with large data sets and wide ranges of input parameters. These statistical indicators are as follows:

- Coefficient of determination (R^2)
- Mean bias deviation (MBD)
- Root mean square deviation (RMSD)
- Slope
- Skewness
- Kurtosis

Coefficient of determination (R^2) is useful because it gives the proportion of variance of a modelled variable against that of the measured. It is used as a measure to determine the certainty that can be placed on the model, in terms of fit, giving a quantitative measure of how well the modelled variable explains the measured. Its value lies between zero and one, with a higher value of R^2 indicating a low variance (which is desired). Note that care is needed when using the R^2 to judge the performance of models which require a large number of parameters, as this can falsely increase the value of R^2.

$$R^2 = \frac{\sum (Y_C - Y_m)^2}{\sum (Y_O - Y_m)^2} \tag{4.4.1}$$

Mean bias deviation (MBD) is the amount by which the model differs from the measured. The difference which occurs is due to the model's inability to account for all the data, which could be accounted for by a more accurate model. It gives

a long-term overall trend of the model's behaviour. A positive value of MBD indicates that the model has underestimated compared with the measured, whereas a negative value indicates overestimation by the model. An MBD closest to zero is desired. However, MBD should be used with care; if a model produces an even distribution of scatter around the mean then the over-estimation of a dataset can be cancelled out by the underestimation within the dataset.

$$MBD = \frac{\sum(Y_O - Y_C)}{n} \tag{4.4.2}$$

Root mean square of deviation (RMSD) is used to provide a comparison of the deviation between the modelled and the measured data. The RMSD will always be positive, thus a lower absolute value is desired.

$$RMSD = \left[\frac{\sum(Y_O - Y_C)^2}{n}\right]^{\frac{1}{2}} \tag{4.4.3}$$

Slope: a least square fit technique is used to determine the slope of the linear regression between the measured and calculated variable. Slope gives a good indication as to whether the calculated underestimates or overestimates the measured variable. A slope lying between zero and one means that the calculated is underestimating that of the measured, whereas if the slope is greater than one the calculated is overestimating that of the measured. It should be noted that RMSD is sensitive to freak observations; a few very large estimates within a data set can significantly increase the value of RMSD.

$$Slope = \frac{\sum(Y_O - \overline{Y_O})(Y_C - \overline{Y_C})}{\sum(Y_O - \overline{Y_O})^2} \tag{4.4.4}$$

Skewness is a measure of the asymmetry of a frequency distribution. If the frequency distribution is symmetrical about its centre point, the skewness will equal zero, indicating perfect symmetry. A positive value of skewness indicates that the frequency distribution will be skewed towards the high end of the scale,

whereas a negative value indicates the distribution will be skewed towards the low end of the scale.

$$Skewness = \frac{n}{(n-1)(n-2)}\sum\left(\frac{(Y_C - Y_O) - \overline{Y_{C,O}}}{\sqrt{\sum\left(\frac{(Y_C - Y_O) - \overline{Y_{C,O}}}{n-1}\right)^2}}\right)^3 \quad (4.4.5)$$

Kurtosis is defined as the measure of peakedness of a frequency distribution relative to its width. In a normal frequency distribution the kurtosis will be mesokurtic and will have a value of zero. A peaked or leptokurtic distribution has a positive value whereas a flat or platykurtic distribution will have a negative value. Higher kurtosis will mean that the majority of the variance will have a lower deviation (which is most desired). Kurtosis is particularly sensitive to the effects of outliers on the outer extremes of sample distribution. This may result in a few outliers on the outer extremities of a distribution having a large effect on the kurtosis.

$$Kurtosis = \left\{\frac{n(n+1)}{(n-1)(n-2)(n-3)}\sum\left(\frac{(Y_O - Y_C) - \left(\overline{Y_O - Y_C}\right)}{\sigma}\right)^4\right\} - \frac{3(n-1)^2}{(n-2)(n-3)} \quad (4.4.6)$$

The statistical tests are used to determine the performance of the models; however, for many cases when comparing the performance of several models to measured values, it is often not straightforward to determine which model performs best. This is due to the fact that not all models behave in the same manner when under the scrutiny of statistical tests. For example a model may have a low RMSD indicating a high degree of accuracy, but this could be offset by a high value of kurtosis. Muneer *et al.* (2007) suggest the accuracy score (AS) procedure. This is a scoring procedure which is based on the above-mentioned statistical tests, and which can give a good picture of a model's performance. A model that yields a high value of R^2 and a score closest to zero for kurtosis would score highest; similarly a model which yields a score closest to one for slope of best fit would also score highly. Thus the maximum score which could be obtained is a score of 6. AS is given by equation (4.4.7).

$$AS = \frac{R_i^2}{R_{i,\max}^2} + \left[1 - \frac{|MBD|_i}{|MBD|_{i,\max}}\right] + \left[1 - \frac{RMSD_i}{RMSD_{i,\max}}\right] + \left[1 - \frac{|Skewness|_i}{|Skewness|_{i,\max}}\right] + \frac{|Kurtosis|_i}{|Kurtosis|_{i,\max}} + SlopeP_i \quad (4.4.7)$$

$$For\ (Slope > 1)\ SlopeP_i = \frac{1}{\max(1, Slope)}$$

$$For\ (Slope < 1)\ SlopeP_i = \min(1, Slope)$$

$SlopeP_i$ is the slope of the best fit line between the modelled and measured components. The subscript i,max is the largest value of the given parameters for all the models.

4.5 Integrated slope radiance model (ISRM)

The integrated slope irradiation model was developed and presented by Saluja & Muneer (1987). The model treats sunlit and shaded surfaces separately and makes further distinctions between overcast and non-overcast conditions for sunlit surfaces. Sloped diffused irradiation for both shaded under overcast skies are given by Equation 4.5.1.

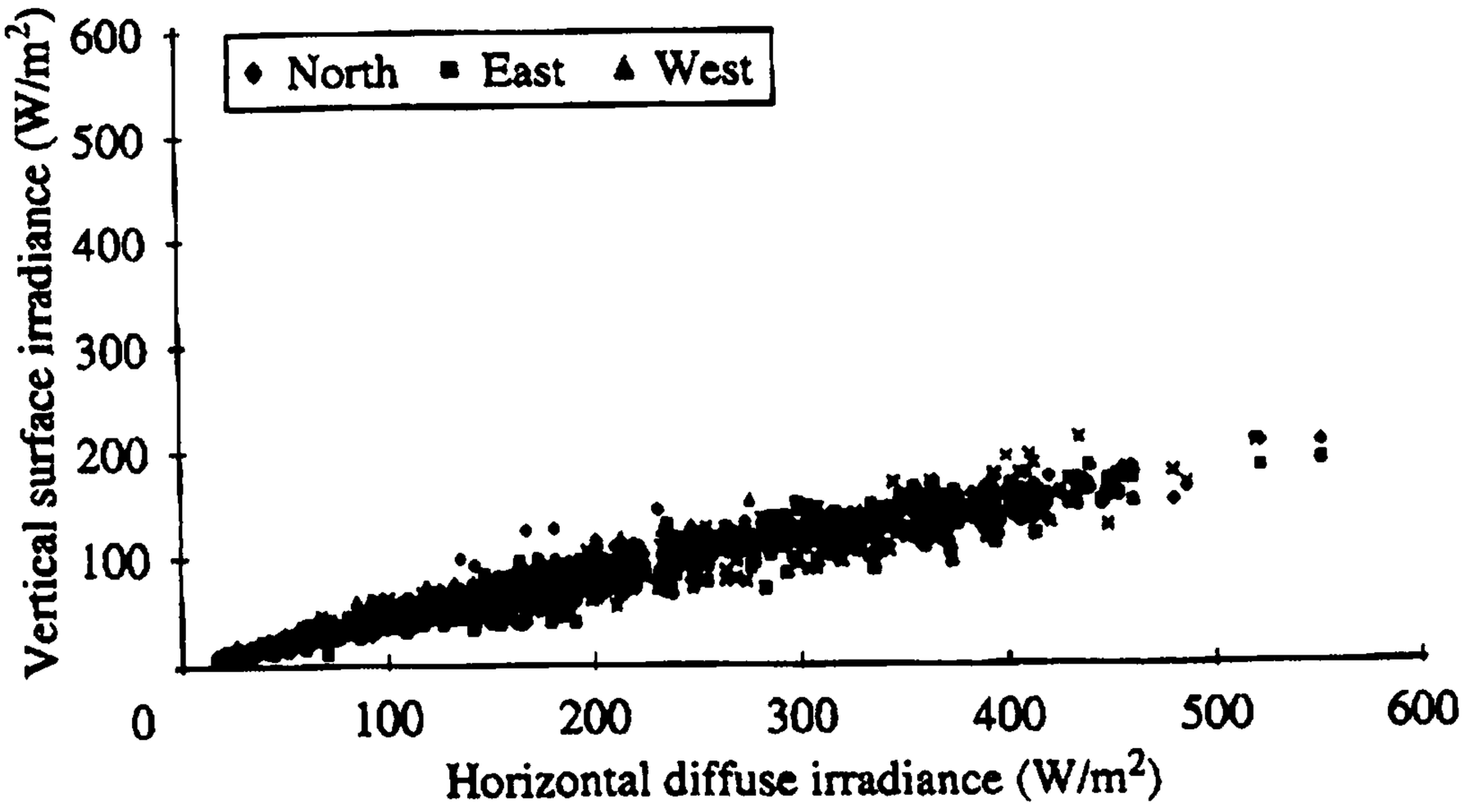

Figure 4.5.1 Relationship between shaded vertical and horizontal diffuse irradiance (Chofu) Courtesy: Muneer *et al.* 2004.

$$I_{D,TLT} = I_D[TF] \tag{4.5.1}$$

The Equation gives the linear relationship between $I_{D,TLT}$ and I_D, for shaded surfaces under overcast skies. Figure 4.5.1 clearly shows that there is a linear relationship between vertical surface irradiance with horizontal diffuse irradiance for shaded surfaces facing North, East and West sited in Chofu (Japan). For sunlit surfaces under overcast skies the model is given as Equation 4.5.2.

$$I_{D,TLT} = I_D[TF(1-F)+Fr_B] \tag{4.5.2}$$

The beam conversion factor, r_B and sky clarity, TF, for a tilted surface is given by Equation 4.5.4 using a value of b which corresponds to the appropriate sky and azimuthal conditions. For northern European regions Muneer givens Equation 4.5.3.

$$2b\{\pi(3+2b)\}^{-1} = 0.00333 - 0.415F - 0.698F^2 \tag{4.5.3}$$

The clarity function F in the above-mentioned equations is a sky clarity index, a function combining both hourly clearness index $k_t=I_G/I_E$, and diffuse ratio $k=I_D/I_G$. It is the horizontal global radiation divided by its extraterrestrial horizontal radiation, giving the depletion of incoming global radiation by the earth's atmosphere. It is used to indicate the available solar radiation on the earth's surface.

A low value of k_t will indicate a site with heavy cloud cover, whereas a high value of k_t will indicate that a site having less or no cloud cover.

Diffuse ratio is the diffuse radiation divided by global radiation used to denote the reduction of the diffuse component caused by the presence of atmospheric pollution and cloud cover. It is also used to describe sky conditions. Note that the clearness index provides an indication of the sky condition, i.e. k_t that is less than 0.3 indicates an overcast sky whereas a k_t of greater than 0.7 indicates a completely clear sky. Sky clarity F is given by Equation 4.5.5.

$$TF = \cos^2 \frac{TLT}{2} + \frac{2b}{\pi(3+2b)}\left[\sin TLT - TLT \cos TLT - \pi \sin^2 \frac{TLT}{2}\right] \quad (4.5.4)$$

$$F = \frac{(I_G - I_D)}{I_E} \quad (4.5.5)$$

Sloped beam irradiance I_B for a tilted surface is given by Equation 4.5.6 below, and the beam conversion factor r_B is given by Equation 4.5.7. The beam conversion factor is used in both Equations 4.5.2 and 4.5.6.

$$I_{B,TLT} = I_B r_B \quad (4.5.6)$$

$$r_B = \max[0, \cos INC / \sin SOLALT] \quad (4.5.7)$$

The global irradiation for the given surface is equal to the sum of components, sloped diffuse, sloped beam and ground reflected irradiation given by Equation 4.5.8.

$$I_{G,TLT} = I_{D,TLT} + I_{B,TLT} + I_{R,TLT} \quad (4.5.8)$$

4.6 Evaluation of ISRM model performance

To ensure good performance of the ISRM model under ranging solar conditions the ISRM model was extensively tested. The modelled outputs were plotted against measured outputs. The 15-minute averaged irradiance data was recorded on both horizontal and tilted surfaces with the same aspect and tilt angle as the Napier PV array. To minimise variation between data sets, the data was averaged daily.

Daily averaged horizontal irradiances were then used to calculate irradiance on a tilted surface. The data set used was taken for the period from the 11th September to the 5th November 2007. Figure 4.6.1 shows ISRM modelled slope irradiance against measured slope irradiance, with a slope angle of 75° degrees and an aspect of 37° degrees East of South. Table 4.6.1 shows the statistical results between the measured and modelled data. It can be seen that there is a strong correlation between the measured and the modelled, with a slope of 0.76

showing that there is a slight underestimation. The R^2 is 0.91. It can be noted from Fig. 4.6.1 that there is a slight scatter. Mean bias deviation is 36.47 W/m^2 showing that the model estimates the measured very well, although there may be some overestimation by the model. The root mean square deviation of 59.03 W/m^2 shows that there is little deviation between the measured and calculated data. Overall the model can be seen to accurately estimate the measured. Figure 4.6.2 is a flow chart showing all steps taken in the ISRM model.

Table 4.6.1 Statistical tests, relationship between measured and ISRM modelled slope irradiance.

Slope	0.76
R^2	0.95
MBD, W/m^2	36
RMSD, W/m^2	59
Skewness	-1.10
Kurtosis	0.50

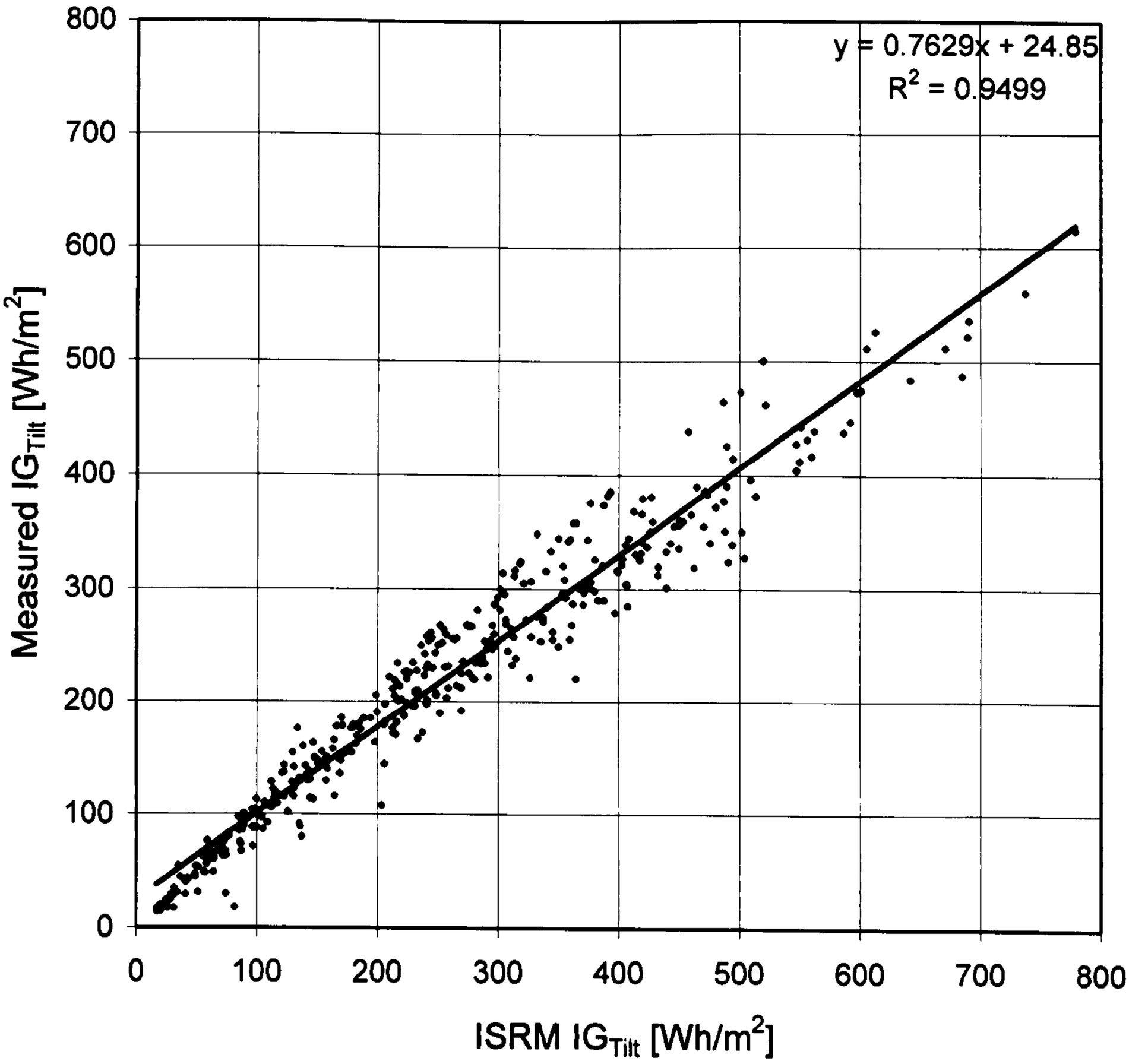

Figure 4.6.1 Relationship between measured and modelled slope irradiance using ISRM model in one year's daily averaged hourly irradiance (Edinburgh 2006/2007).

ISRM Model

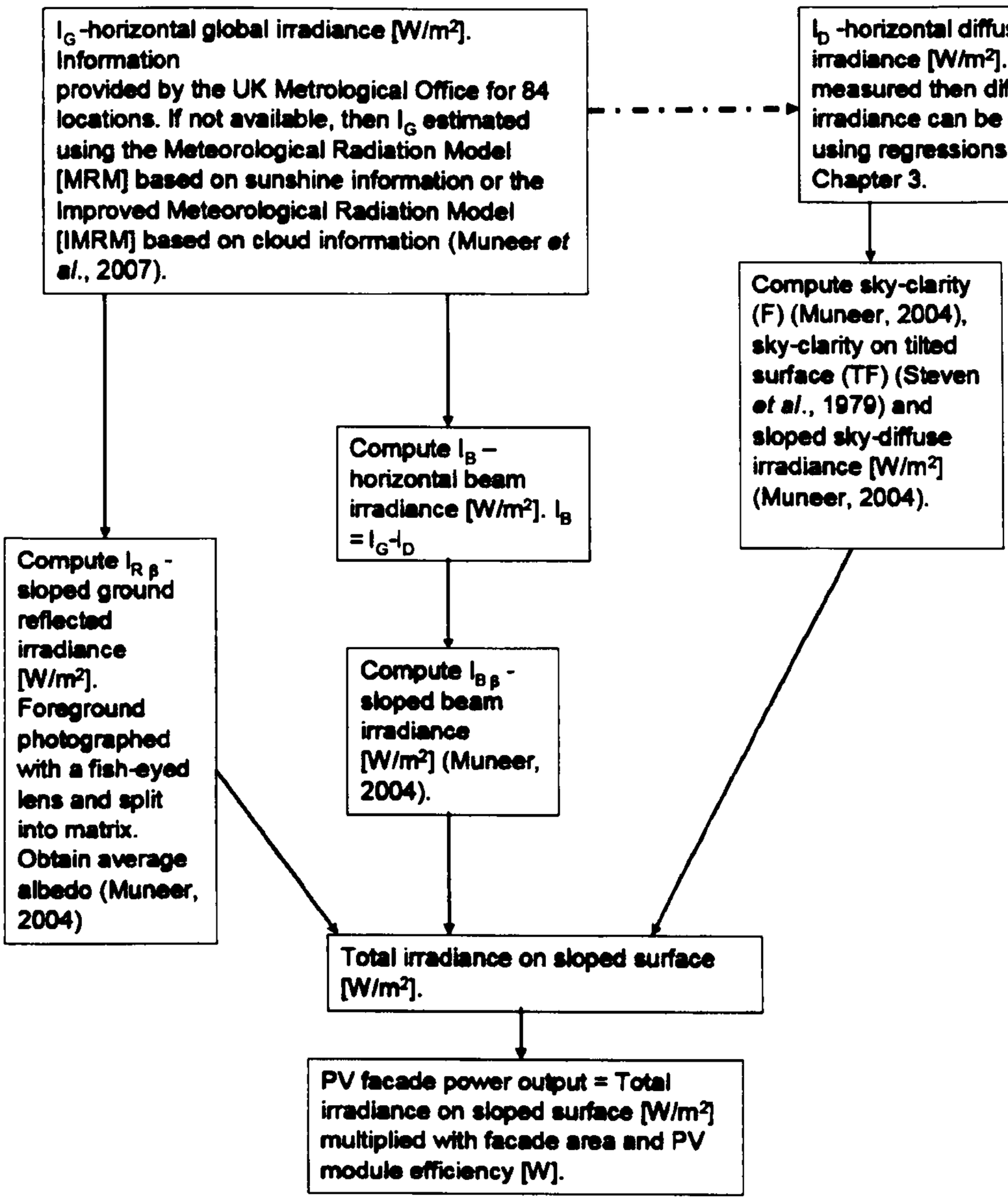

Figure 4.6.2 ISRM model flow chart.

4.7 Sky radiance distribution model (SRDM)

Sky light is a non-uniform extended light source. Its intensity and spatial distribution vary with the sky conditions as well as with sun direction and sky luminance angular distribution (Muneer *et al.*, 2004). The radiance distribution model is based on an all-sky distributions model which considers the sky vault as a matrix. The sky is split into a matrix of 145 individual sky patches, SP. The positions of each sky patch can be seen in Figure 4.7.1.

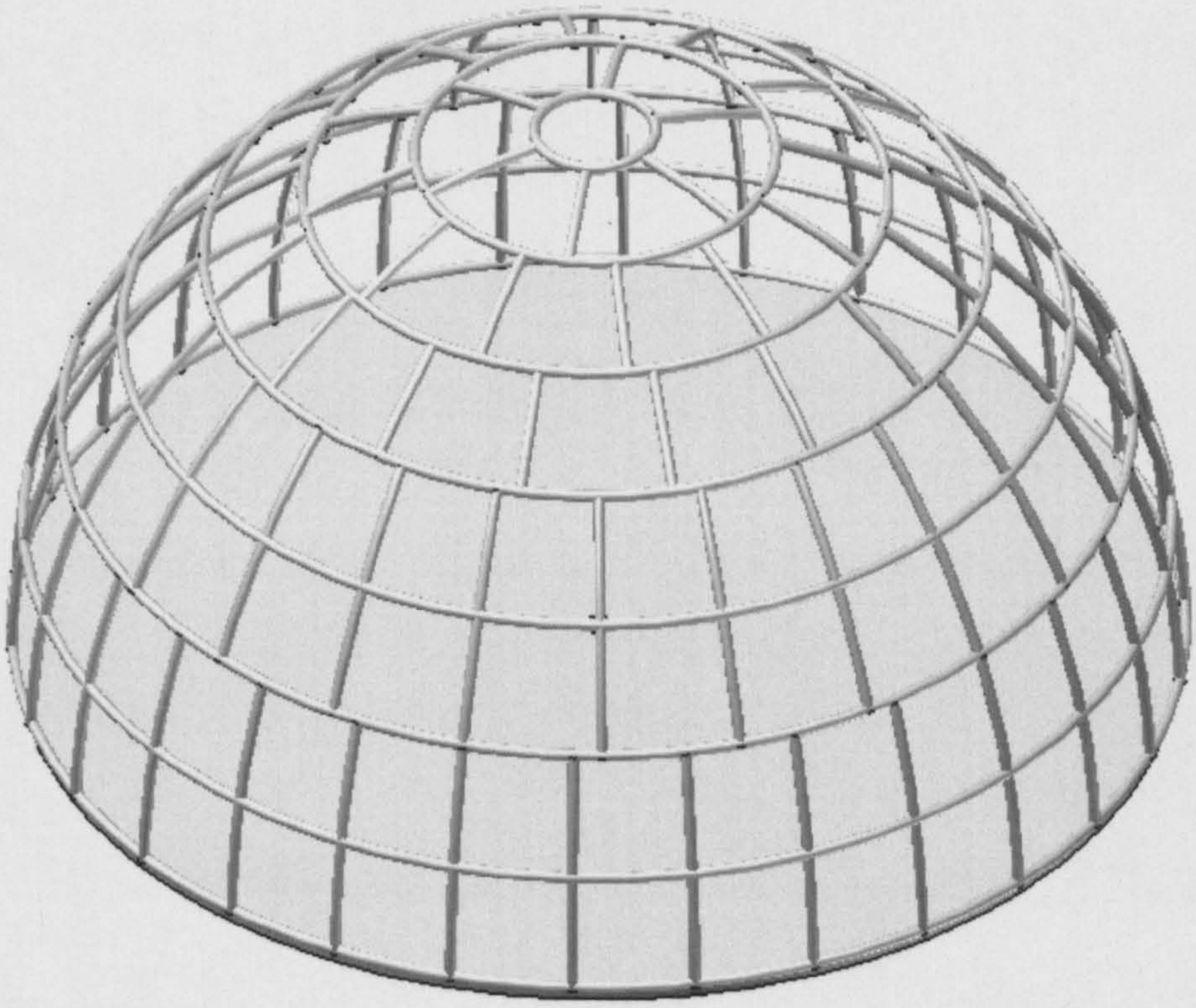

Figure 4.7.1 Three-dimensional sky patch matrix CAD model developed for current study.

The sky-patch matrix is based on an absolute co-ordinate system referenced from the south. The intensity and distribution of the diffuse irradiation over the whole vault is quantified using a mesh covering the entire sky-hemisphere. A fine sky element mesh was adopted in accordance with the work of Nakamura *et al.* (1985). For a PV array of a known size, it is possible to determine which of the sky patches will be in view, and thus determine the amount of diffuse irradiance an individual PV module will receive. Shading is incorporated by measuring the opacity of each sky patch (if a sky patch is obscured from view by a building, for example). Then the diffuse irradiation will be omitted from the sum global irradiation. Sky patch opacity is also used for beam irradiation. If the sun

position moves behind a sky patch which is obscured from view, then the beam component is removed from the sum global irradiance, resulting in the PV modules becoming shaded.

The SRDM model is based on the work of Perez *et al.* (1993), the all-sky model. This model is based the on a mathematical expression that is a generalisation of the CIE standard clear skies (CIE, 1973). The expression takes into account five coefficients which can be adjusted to produce a single model to account for the luminance distribution ranging from totally overcast to clear skies. The model has been further adapted to convert relative luminance l_v, defined as the ratio between the sky luminance at the considered point L_v, (the luminance of given sky patch) and the luminance of an arbitrary reference point, (the zenith luminance), given by Equation 4.7.1.

$$l_v = f(\theta,\xi) = \left[1 + a\exp(b/\cos\theta)\right]\left[1 + c\exp(d\xi) + e\cos\xi^2\right] \qquad (4.7.1)$$

Where θ is the zenith angle of given point and ζ is the angle between given point and the position of the sun. For x = a, b, c, d and e are given by coefficients (see Table 4.7.1).

Table 4.7.1 Coefficients for the all-sky model (sky clearness ε) (Muneer *et al.*, 2004)

Range	From	To								
			a_1	a_2	a_3	a_4	b_1	b_2	b_3	b_4
1	1.000	1.065	1.3525	−0.2576	−0.2690	−1.4366	−0.7670	0.0007	1.2734	−0.1233
2	1.065	1.230	−1.2219	−0.7730	1.4148	1.1016	−0.2054	0.0367	−3.9128	0.9156
3	1.230	1.500	−1.1000	−0.2515	0.8952	0.0156	0.2782	−0.1812	−4.5000	1.1766
4	1.500	1.950	−0.5484	−0.6654	−0.2672	0.7117	0.7234	−0.6219	−5.6812	2.6297
5	1.950	2.800	−0.6000	−0.3566	−2.5000	2.3250	0.2937	0.0496	−5.6812	1.8415
6	2.800	4.500	−1.0156	−0.3670	1.0078	1.4051	0.2875	−0.5328	−3.8500	3.3750
7	4.500	6.200	−1.0000	0.0211	0.5025	−0.5119	−0.3000	0.1922	0.7023	−1.6317
8	6.200	9999.999	−1.0500	0.0289	0.4260	0.3590	−0.3250	0.1156	0.7781	0.0025
			c_1	c_2	c_3	c_4	d_1	d_2	d_3	d_4
1	1.000	1.065	2.8000	0.6004	1.2375	1.0000	1.8734	0.6297	0.9738	0.2809
2	1.065	1.230	6.9750	0.1774	6.4477	−0.1239	−1.5798	−0.5081	−1.7812	0.1080
3	1.230	1.500	24.7219	−13.0812	−37.7000	34.8438	−5.0000	1.5218	3.9229	−2.6204
4	1.500	1.950	33.3389	−18.3000	−62.2500	52.0781	−3.5000	0.0016	1.1477	0.1062
5	1.950	2.800	21.0000	−4.7656	−21.5906	7.2492	−3.5000	−0.1554	1.4062	0.3988
6	2.000	4.500	14.0000	−0.9999	−7.1406	7.5469	−3.4000	−0.1078	−1.0750	1.5702
7	4.500	6.200	19.0000	−5.0000	1.2438	−1.9094	−4.0000	0.0250	0.3844	0.2656
8	6.200	9999.999	31.0625	−14.5000	−46.1148	55.3750	−7.2312	0.4050	13.3500	0.6234
			e_1	e_2	e_3	e_4				
1	1.000	1.065	0.0356	−0.1246	−0.5718	0.9938				
2	1.065	1.230	0.2624	0.0672	−0.2190	−0.4285				
3	1.230	1.500	−0.0156	0.1597	0.4199	−0.5562				
4	1.500	1.950	0.4659	−0.3296	−0.0876	−0.0329				
5	1.950	2.800	0.0032	0.0766	−0.0656	−0.1294				
6	2.800	4.500	−0.0672	0.4016	0.3017	−0.4844				
7	4.500	6.200	1.0468	−0.3788	−2.4517	1.4656				
8	6.200	9999.999	1.5000	−0.6426	1.8564	0.5636				

$$x = x_1 + x_2 z + \Delta[x_3 + x_4 z], \text{(sky clearness } \varepsilon \text{) ranges 2-8} \tag{4.7.2}$$

Else,

$$c = \exp\{(\Delta[c_1 + c_2 z])c_3\}^{-1} \tag{4.7.3}$$

$$d = \exp\{\Delta[d_1 + d_2 z]\} + d_3 + \Delta d_4 \tag{4.7.4}$$

Where solar zenith angle z, the sky clearness ε, and the sky brightness Δ. The coefficients a, b, c, d and e are adjustable functions of irradiance conditions stated by Perez *et al.* (1993) based on an experimental data set which included more than 16,000 full-sky scans from Berkeley, California, covering all sky conditions. The parameter l_v is calculated by Equation 4.7.1 as it is a dimensionless parameter. The luminance distribution of each SP is normalized against the luminance distribution at the zenith position, thus giving the luminance distribution as a ratio of zenith luminance. In the first SRDM model this dimensionless parameter is multiplied with the zenith luminance L_z given by Equation 4.7.5. Thus the luminance distribution is given as a ratio of zenith luminance [cd/m^2]. This dimensionless parameter is divided by diffuse luminous

efficacy. Muneer & Angus (1993) found a strong linear relationship between diffuse luminous efficacy and diffuse irradiance (luminous efficacy = 120 lm/W). De Rosa *et al.* (2008) also carried out a study and found a strong relationship between luminous efficacy, diffuse radiation and diffuse illuminance on vertical surfaces exposed to north, south, east and west for Arcavacata di Rende (Itlay). Values accordingly 107 lm/W, 112 lm/W, 114 lm/W and 108 lm/W for north, south east and west respectively showing a strong concordance with Muneer's value of 120 lm/W. De Rosa *et al.* (2008) also found similar results for Osaka (Japan). Perez *et al.* (1990) developed an all-sky zenith model, given in Equation 4.7.5.

$$L_z / I_D = a_i + b_i \cos z + c_i \exp\left(-3z\right) + d_i \Delta \qquad (4.7.5)$$

The model claims to be site and seasonally dependant, with an overall low error bias (around 1 percent) and RMSDs ranging from 0.7 kcdm^2 for clear skies to 1.5 kcd/m^2 for bright intermediate skies. However, the SRDM model was later improved upon. The current SRDM model uses a slightly different strategy than the above mention step. The dimensionless parameter of luminance distribution, $I_v/I_{v,z}$ as a ratio of the luminance distribution of the zenith is used to obtain zenith irradiance [W/sr-m^2] as a product of the diffuse component divided by the sum luminance distribution of all sky patches. Thus the irradiance of each sky patch may be obtained. The changes made to the improved model reduced the number of calculation steps taken as well as improving the model's performance in terms of thermodynamic basic principles. This can be validated as the sum of all sky-patch irradiances is equal to the diffuse component. Note this is the sum of the total irradiance emanating from each sky patch and not the irradiance being received on a given horizontal surface. In the appendix there is a validation program used to validate that for a horizontal surface the diffuse component is equal to that of the sum irradiance emanating from all 145 sky patches. From here onwards the above-mentioned SRDM model is taken to be the present version of the model.

4.8 Sky patch geometries

In order to obtain the luminance for a given sky patch, its geometry and area must be known. The relative position of an individual sky patch within the sky hemisphere is given from its mid-point. Its geometry co-ordinates are given as an altitude and an azimuth. The altitude is given from the horizontal plane and the azimuth from south as shown in Figure 4.8.1.

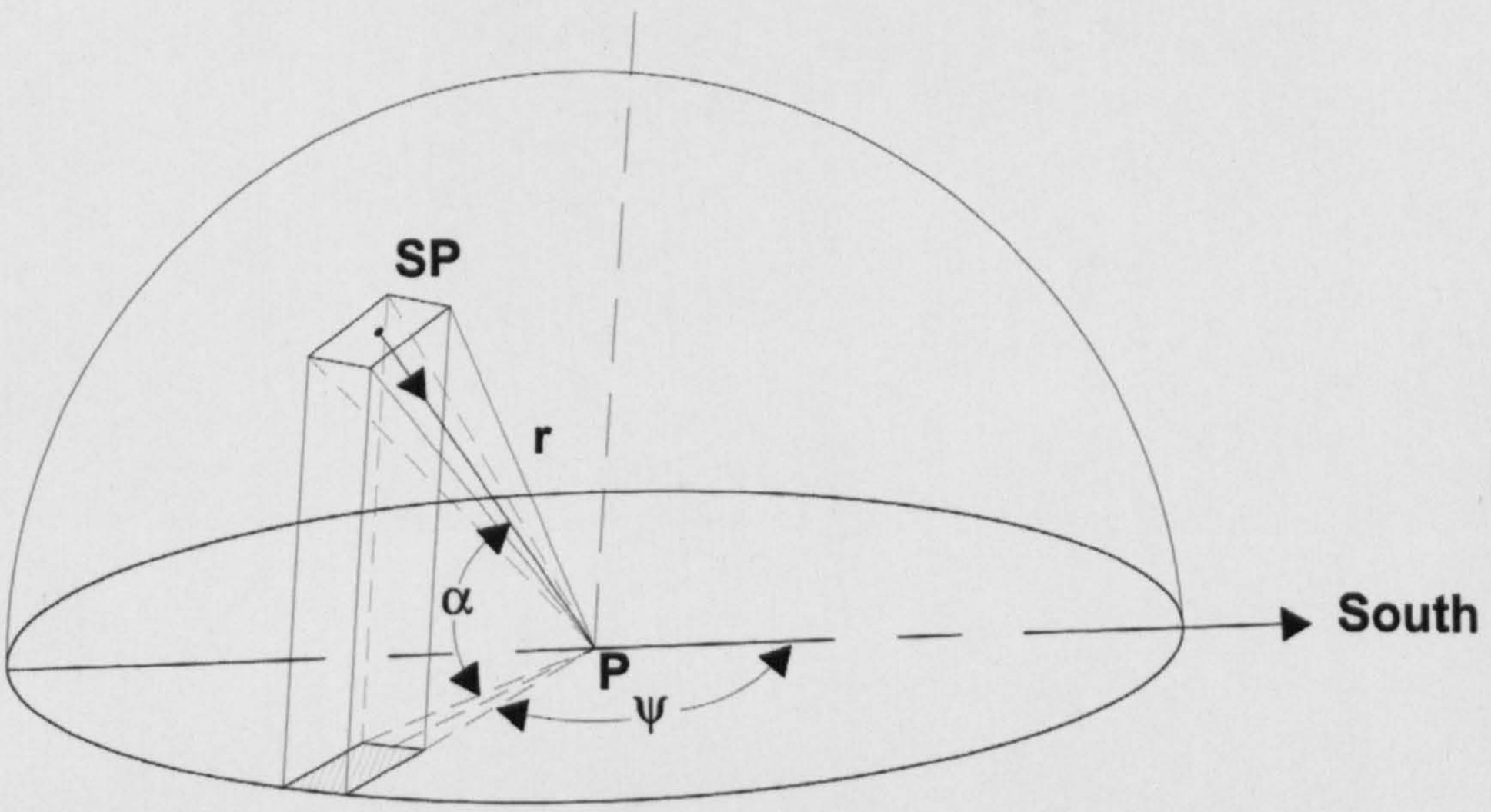

Figure 4.8.1. Sky patch geometry.

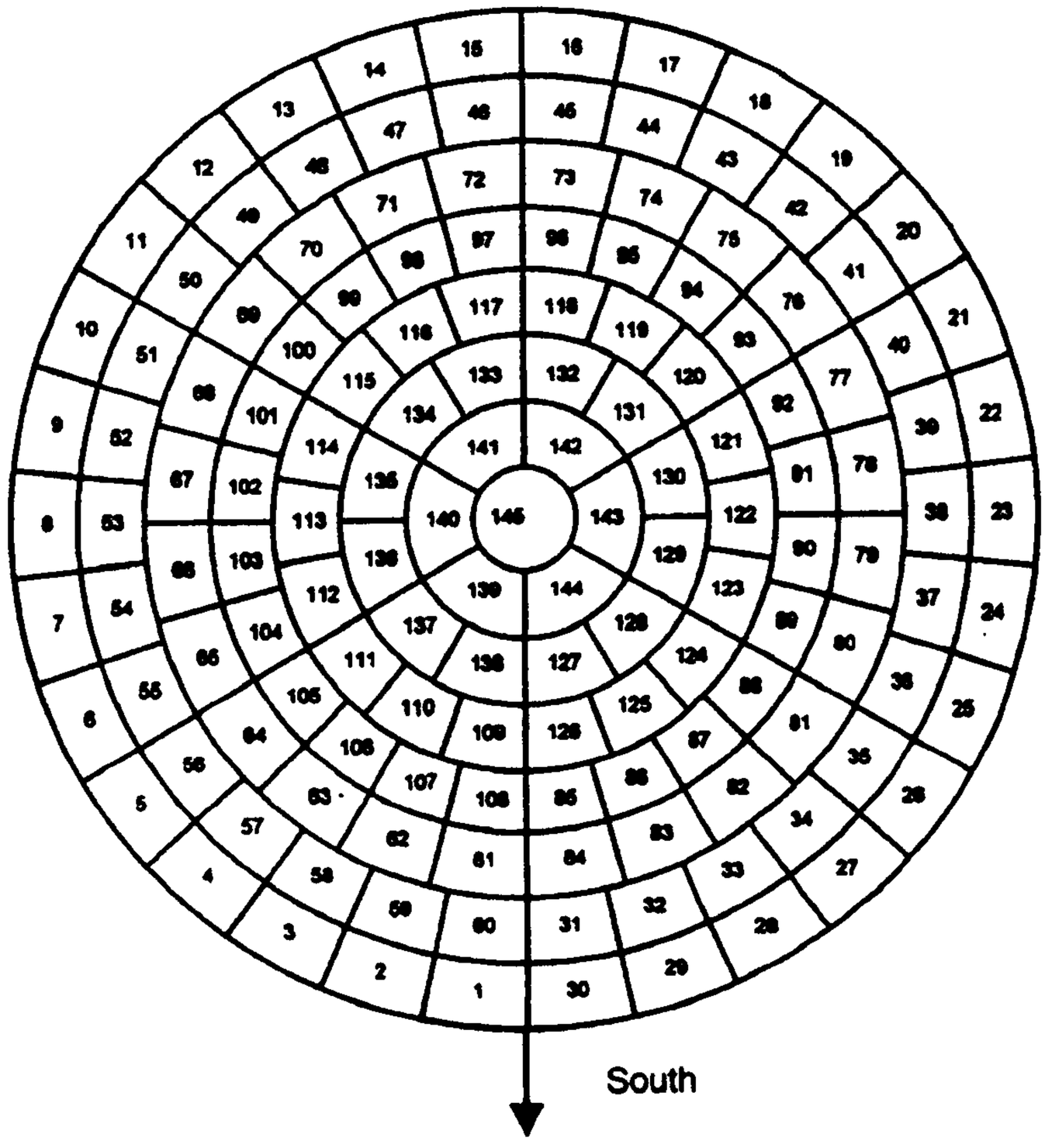

Figure 4.8.2 Sky patch map (Muneer, 2004).

The location and layout of individual sky patches can be seen in Figure 4.8.2. The areas for all but the zenith patch can be obtained from the altitude α height, azimuth ψ width and the azimuth angle θ, given below in Equation 4.8.1. The height, width and azimuth angle for each sky patch is shown in Figure 4.8.3 and their values are given in Table 4.8.1. The sky patch area is given the unit steradian (sr) which is the unit of solid angle used to describe two-dimensional angular spans in three-dimensional space.

$$Area\ of\ sky\ patch = \left(\left(\frac{\pi}{180}\right)^2 \psi\ \alpha\right)\cos\theta \qquad (4.8.1)$$

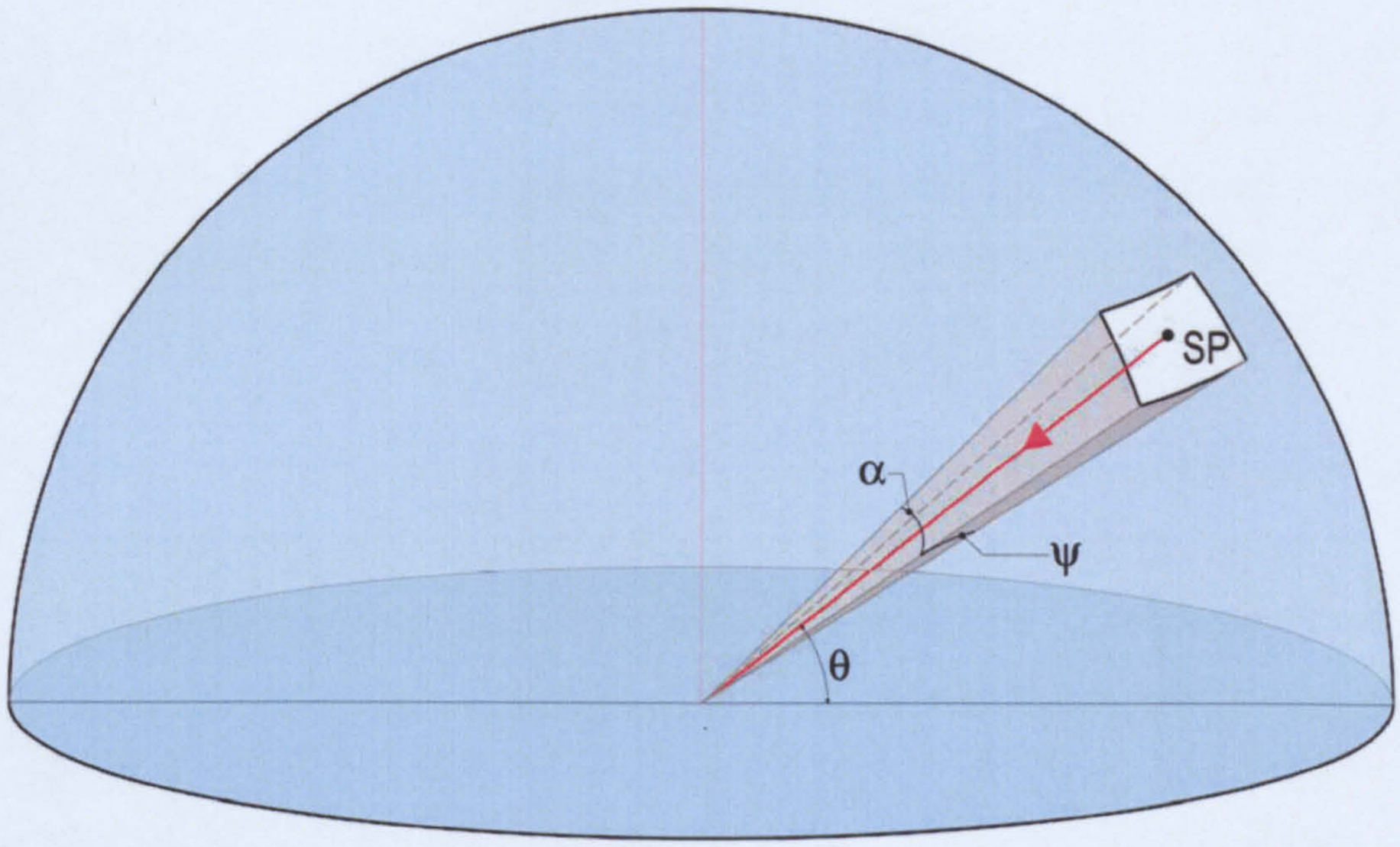

Figure 4.8.3 Sky patch global positions.

The zenith sky patch is circular, and its area is given by Equation 4.8.2 below.

$$Area\ zenith\ sky\ \ patch = 2\pi - \left(2\pi\ \ \sin\theta\right) \tag{4.8.2}$$

Table 4.8.1The size of sky patches and azimuth angle.

Patch No	Altitude Height (degrees), α	Azimuth Width (degrees), Ψ	Azimuth angle, θ
1 to 30	12	12	6
31 to 60	12	12	12
61 to 84	12	15	12
85 to 108	12	15	12
109 to 126	12	20	18
107 to 138	12	30	24
139 to144	6	60	24
145 (Zenith)	6	~	84

4.9 Determining sky patch opacity

Shading is incorporated into the SRDM model by measuring the opacity of each sky patch. For example, if a building obstructs the line of view between a given sky patch and the PV facade, the diffuse irradiation being received from the area of the sky patch will be reduced. If the sun's position moves behind the obstructed sky patch, the sun's beam will also be obstructed, causing shading.

The sky patch's opacity is given as a percentage, with 0% being opaque and 100% being purely transparent. The intensity of both diffused and beam irradiation being radiated from a patch is proportional to the incident radiance received by the patch and that of its opacity. There are 145 sky patches in total. When considering a vertical surface such as the Edinburgh Napier University PV facade, it must be noted that only half of the sky hemisphere can be viewed. Figure 4.9.1 shows the coordinates of all sky patches in relation to the PV Facade. Note that 73 sky patches can potentially be seen by the PV array. To determine which of the sky patches in view of the array are obstructed by the surrounding environment, the horizon must be mapped.

A theodolite was set up to map the altitude and azimuth of every obstruction above the horizontal plane of the horizon, with the azimuth of each blockage being measured from true north, and the altitude from horizontal. An outline of the horizon created is shown in Figure 4.9.2. The skyline outline was split into rectangular strips. The rectangular outline was then transposed over the sky patch coordinates. Figure 4.9.3 shows a representation of the horizon with the obstructions transposed. This procedure was carried out for seven different levels along the facade's height.

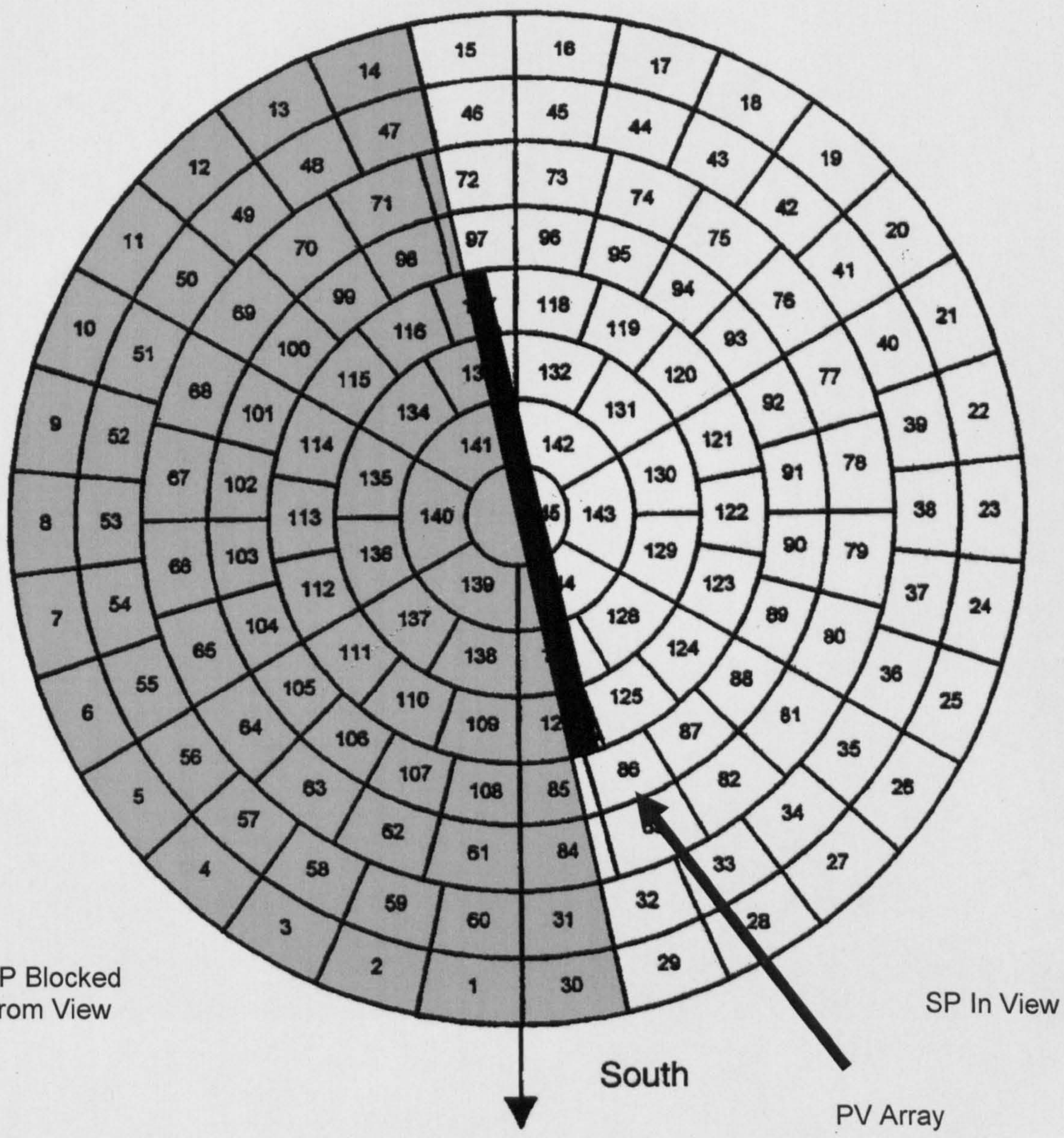

Figure 4.9.1 Sky patch map showing sky patches blocked from view. Note shading blockages have not been included.

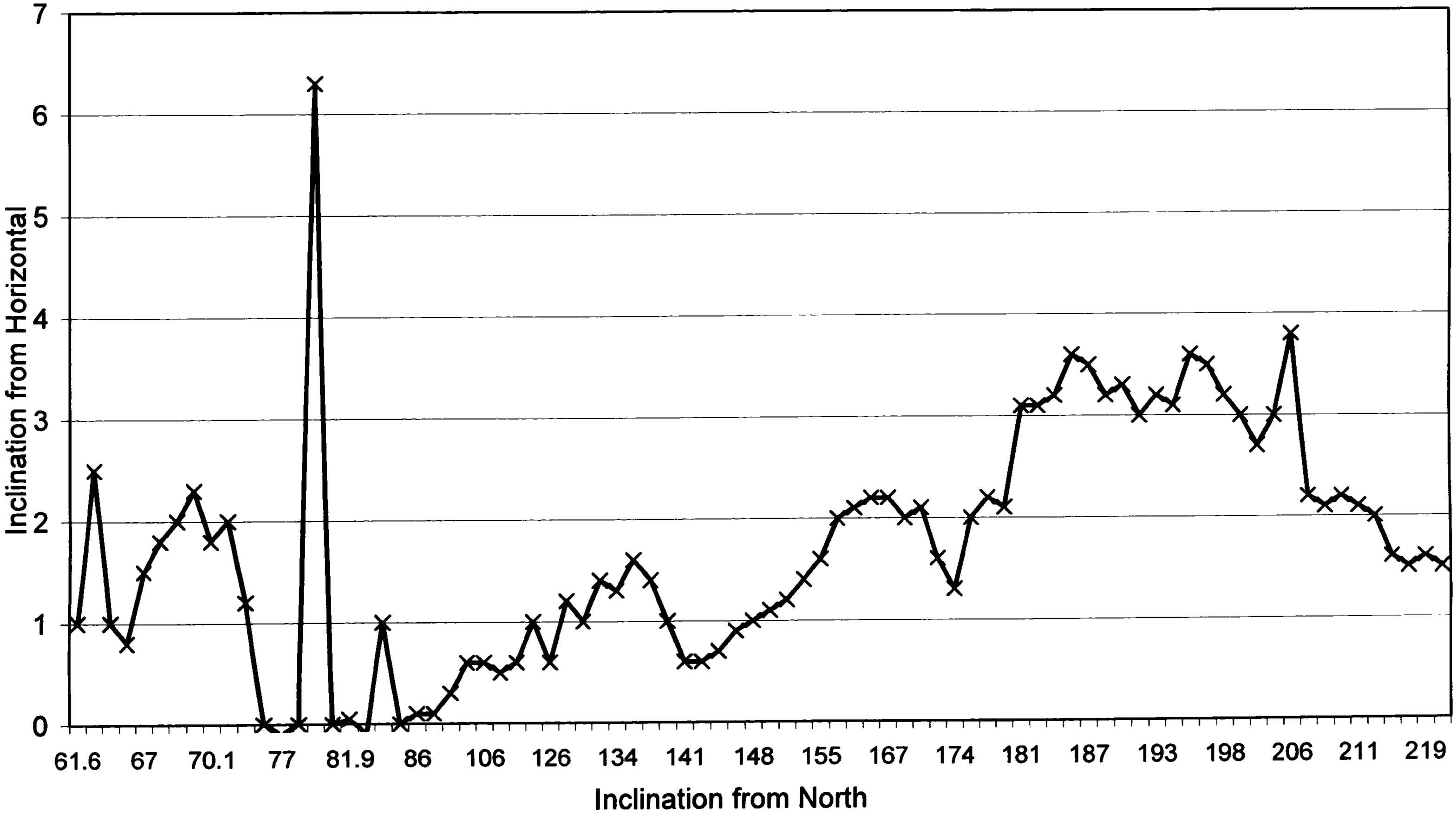

Figure 4.9.2 Horizon view from fifth floor. The scale of obstacles to clear view is shown in this figure. Note the high peak of the church spire.

Figure 4.9.3 Obstructions on the horizon have been split into strips to simplify describing the geometry of sky patches. Image taken for current study.

Horizon measurements were taken from the bay window to the west of the facade. It was not possible to take measurements from the eastern side of the facade. Therefore only one set of measurements was used for both sides of the facade. To evaluate the accuracy of using one set of measurements taken from one side for the whole facade, a simple test was set up. A church spire outline on the horizon was measured using a theodolite at ground level from both sides of the facade. The distance from the spire to either side of the facade was also measured, enabling the solid angle of the spire area to be calculated. The size difference between the two solid angles was found to be less then 2 percent. Thus it was decided that one set of measurements would be suitable for the whole facade. This calculation can be found in appendix. Since shading is a much greater problem on the lower rows of PV modules, the sky-patch opacity was measured from seven levels enabling each string of modules to be accurately simulated.

4.10 View factors

View factors are used to define the amount of radiation that is exchanged between two surfaces. A view factor is simply a term used to calculate the proportion of radiation emitted from one surface which is received by another surface, given the geometry of the two surfaces as a function of both distance and orientation between the surfaces as shown in Figure 4.10.1 (Muneer *et al.*, 2003). In the case of the PV facade, it is the proportion of the diffuse irradiance emitted from a given sky patch which is received by a PV module of a known area, tilt and aspect angle.

From Fig 4.10.1 the two surfaces can be seen (i and j) which represent the surfaces of the sky patch and the PV module. The amount of lumen being exchanged between the surfaces can be shown as Equation 4.10.1.

$$\Delta(R_i) = l_i \cos \theta_i \, dA_i \qquad (4.10.1)$$

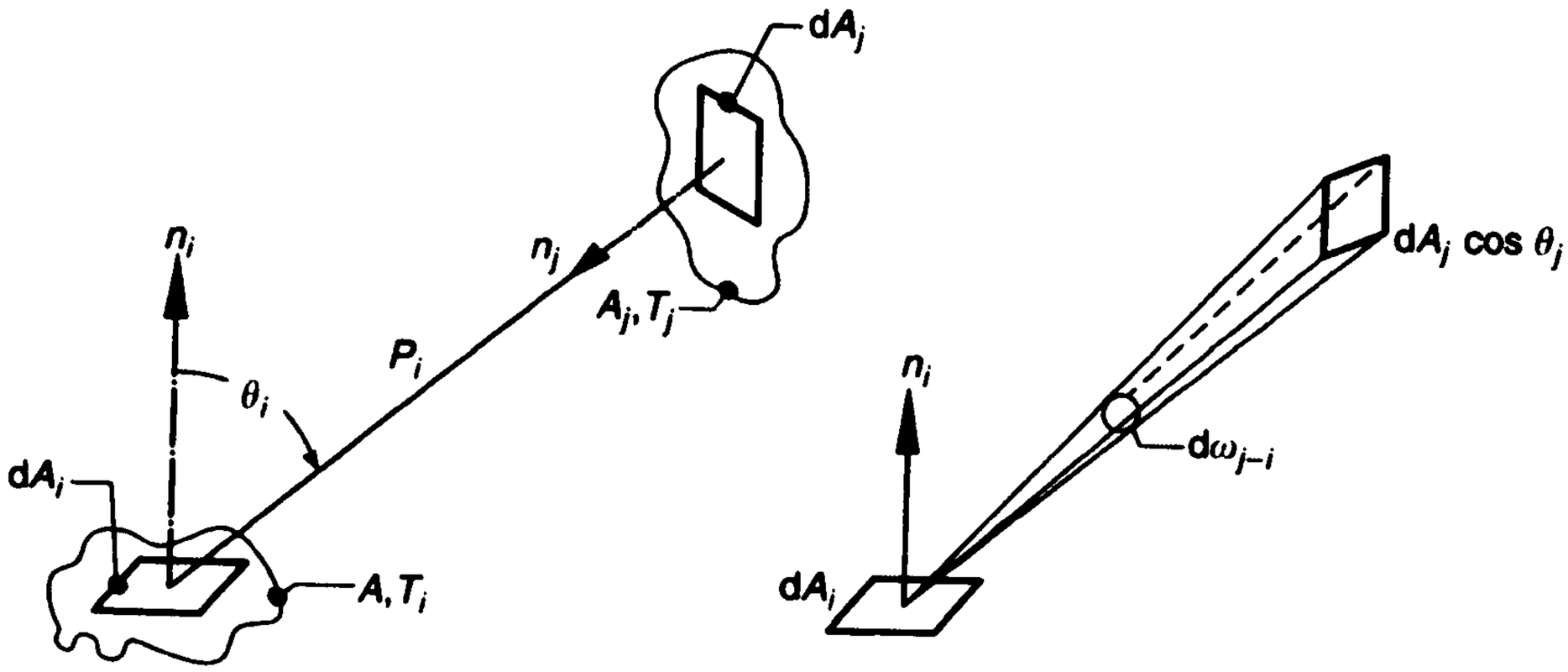

Figure 4.10.1 View-factor schematic demonstrating irradiation being emitted from sky patch and received by PV module surface. Image modified from source image: (Muneer, 2004).

The luminous flux ϕ is defined as the light being emitted from a surface, i.e. a sky patch, and the unit of luminous flux is lumen lm. Lumen is the amount of light emitted from a unit solid angle of one steradian ω, by a source of one candela output, given by Equation 4.10.2 (Muneer, 2004).

$$\phi = I.\omega \tag{4.10.2}$$

For this reason, the radiation exchanged between two surfaces has been measured in lumen.

4.11 Beam irradiance

Beam irradiance is the irradiation that is directly received from the sun. The amount of beam irradiation received on a given tilted surface is given in Equation 4.11.1.

$$I_{B,TLT} = INC\left(\frac{(I_G - I_D)}{\sin(SOLALT)}\right) \tag{4.11.1}$$

The sun's position can be expressed in terms of two angles, solar latitude and solar azimuth. This is required in calculating the angle of incidence of the sun's beam. Solar latitude, SOLALT given by Equation 4.11.2, is dependent on the Greenwich Hour Angle, GHA the latitude, LAT and longitude, LONG of the location and solar

declination, DEC the angular position of the sun at noon and AST with respect to the equatorial plane.

$$\sin SOLALT = \sin LAT \sin DEC - \cos LAT \cos DEC \cos GHA \quad (4.11.2)$$

The angle of incidence, INC, is the angle at which the sun's beam strikes a sloped surface of given tilt, given by Equation 4.11.3. WAZ, the wall azimuth angle, the azimuth of the given surface.

$$INC = \cos^{-1}\left[\begin{array}{l}\cos SOLALT \cos(SOLALT - WAZ)\sin TLT \\ + \cos TLT \sin SOLALT\end{array}\right] \quad (4.11.3)$$

4.12 SRDM model layout

The diffuse irradiances received from each sky patch are summed up with the addition of the beam and ground reflected irradiance to give the global tilted irradiance. The tilted global irradiance is then multiplied by the effective area of the PV array and by the system efficiency to calculate electrical power output. Figure 4.12.1 shows a flow chart of all steps taken in the SRDM model.

SRDM Model Mark 2

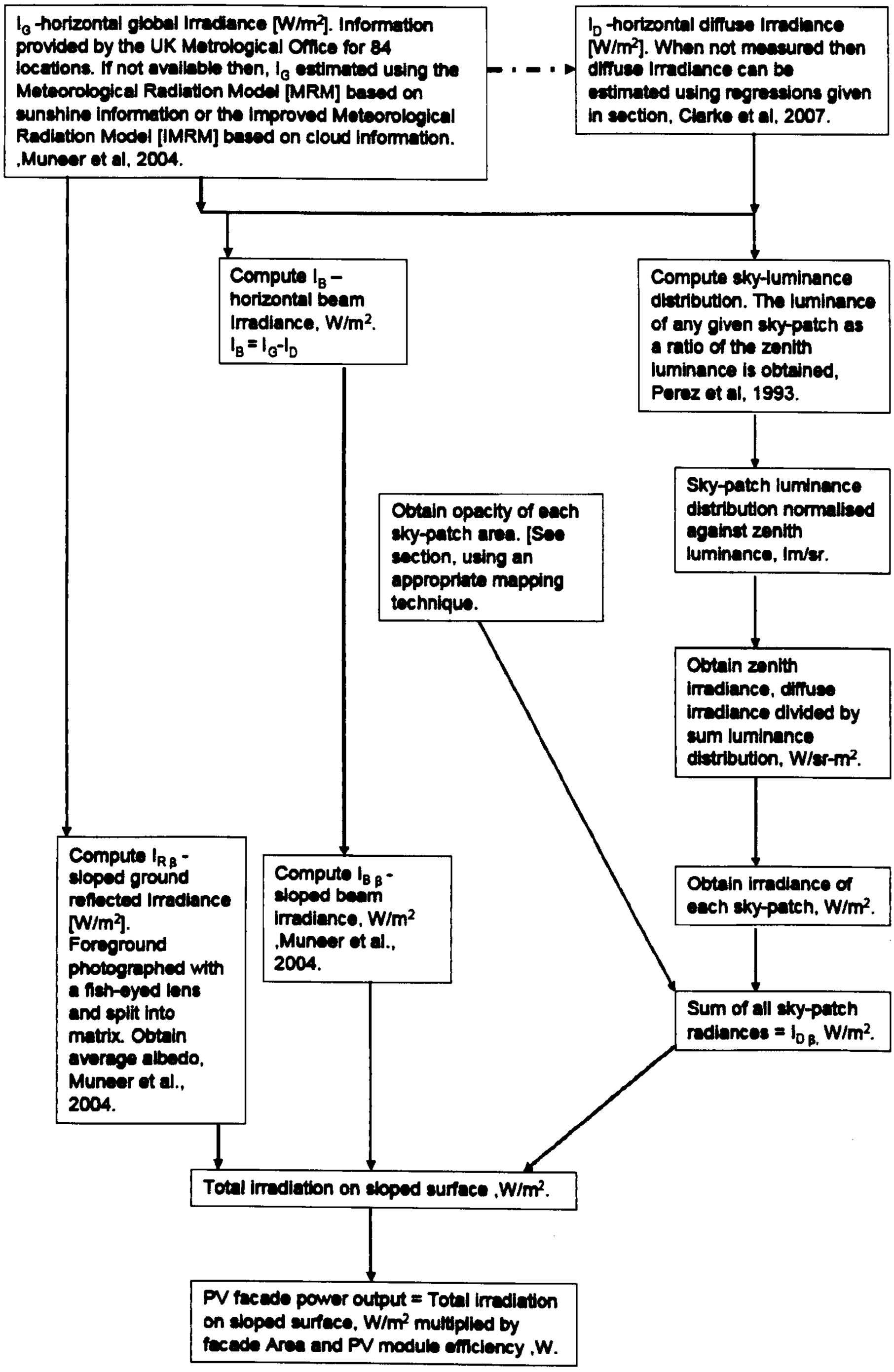

Figure 4.12.1 Flow chart showing steps taken in the SRDM model.

4.13 BIPVcalc software

BIPVcalc is Microsoft Excel-based software based on the SRDM model detailed above. It is used to simulate performance of building integrated photovoltaic systems using measured solar data. The program has been designed specifically for the urban environment, where problems such as shading and global dimming are caused by the surrounding urban environment. This can cause large losses to the potentially available solar irradiation. The software has been designed to calculate incident solar irradiances for each individual module on a PV array. The program requires minimal parameters for operation: time and date, horizontal global irradiance data sub-hourly, horizontal global irradiance data (if available), PV array size and orientation and shading parameters. Shading parameters can be obtained using a fish-eyed lens camera or with a theodolite to measure obstructions in the foreground of the given PV array. The software enables incident global irradiance to be calculated on any surface, taking account of the effects caused by shading of the beam component as well as the effects caused by overall global dimming. This is the result of reduced diffuse irradiance being received from the sky hemisphere, caused by surrounding obstructions. There are many other solar applications for this program, such as solar thermal heating systems. Determining solar thermal gain within buildings is vital to ensure that a temperate climate is maintained. This is particularly problematic in modern buildings which have large expanses of glazed facades. These can potentially lead to rapid temperature changes within buildings, due to the effects of solar gain.

CHAPTER 5

Evaluation of slope irradiation models and Edinburgh Napier University photovoltaic outputs using recent measurements

5.1 Introduction

Before any model can be accepted by the wider research community and used with any certainty of accuracy, it is necessary to extensively test the model using a wide range of methods to prove its validity and robustness in real-life applications. This is also the case for both the ISRM and SRDM solar models. This chapter will extensively test both solar models performance under a full range of prevailing sky conditions.

5.2 Validation of modelled tilted global irradiance using measured sub-hourly tilted irradiance data

To ensure the performance of both the SRDM and ISRM models under ranging solar conditions, the models were extensively tested. One year's worth of 15-minute averaged data (horizontal, global and tilted irradiance data) was simultaneously recorded at Edinburgh Napier University between the 17th May 2005 and 15th May 2007. The tilted irradiance data was recorded at the same aspect and tilt angle as the Edinburgh Napier University PV facade, 37^{o} East of South and 75^{o} tilt. The 15-minute averaged dataset was quality controlled using the procedure developed by Younes *et al.* (2005). The procedure, which has been described in Chapter 3, is used to remove any bad data from the dataset which may cause statistical errors.

Only horizontal and tilted global irradiances are recorded in the above mentioned dataset. Horizontal diffuse irradiance is also needed in order to calculate the tilted global irradiance. Diffuse irradiance is obtained from global irradiance using regressions between diffuse-ratio and clearness index. The regressions were developed using data from the Edinburgh Napier University site and data from Heirot Watt University (10 km west of test site) to fill any missing gaps within the dataset. Further details of how regressions have been developed and performance statistics for regressions can be seen in Chapter 3 or Clarke *et al.* (2007). Table 5.2.1 shows the data used to validate modelled tilted data.

Table 5.2.1 Horizontal and tilted global irradiance data set used validate modelled tilted data

Month	Year	N_o hours data
4	2006	284
5	2006	380
6	2006	222
7	2006	394
8	2006	320
9	2006	147
10	2006	209
11	2006	126
12	2006	101
1	2007	123
2	2007	42
3	2007	267
4	2007	318
Total		**2930**

Note: 15-minute averaged data has been used.

Both the SRDM and ISRM solar models were used to generate a simultaneous 15-minute averaged dataset containing both modelled tilted global irradiance from each model and measured tilted global irradiance. Note that all shading parameters have been removed from both models for validation purposes to enable the performance of both models to be established solely to estimate tilted irradiance. To minimise any phase variations between datasets, the 15-minute averaged irradiance data was then summed to produce daily irradiance totals which were then used for statistical analysis.

Figures 5.2.1 and 5.2.2 show a plot of daily averaged modelled slope irradiance versus measured slope irradiance for ISRM and SRDM models respectively, with a slope angle of 75° and aspect 37° east of South.

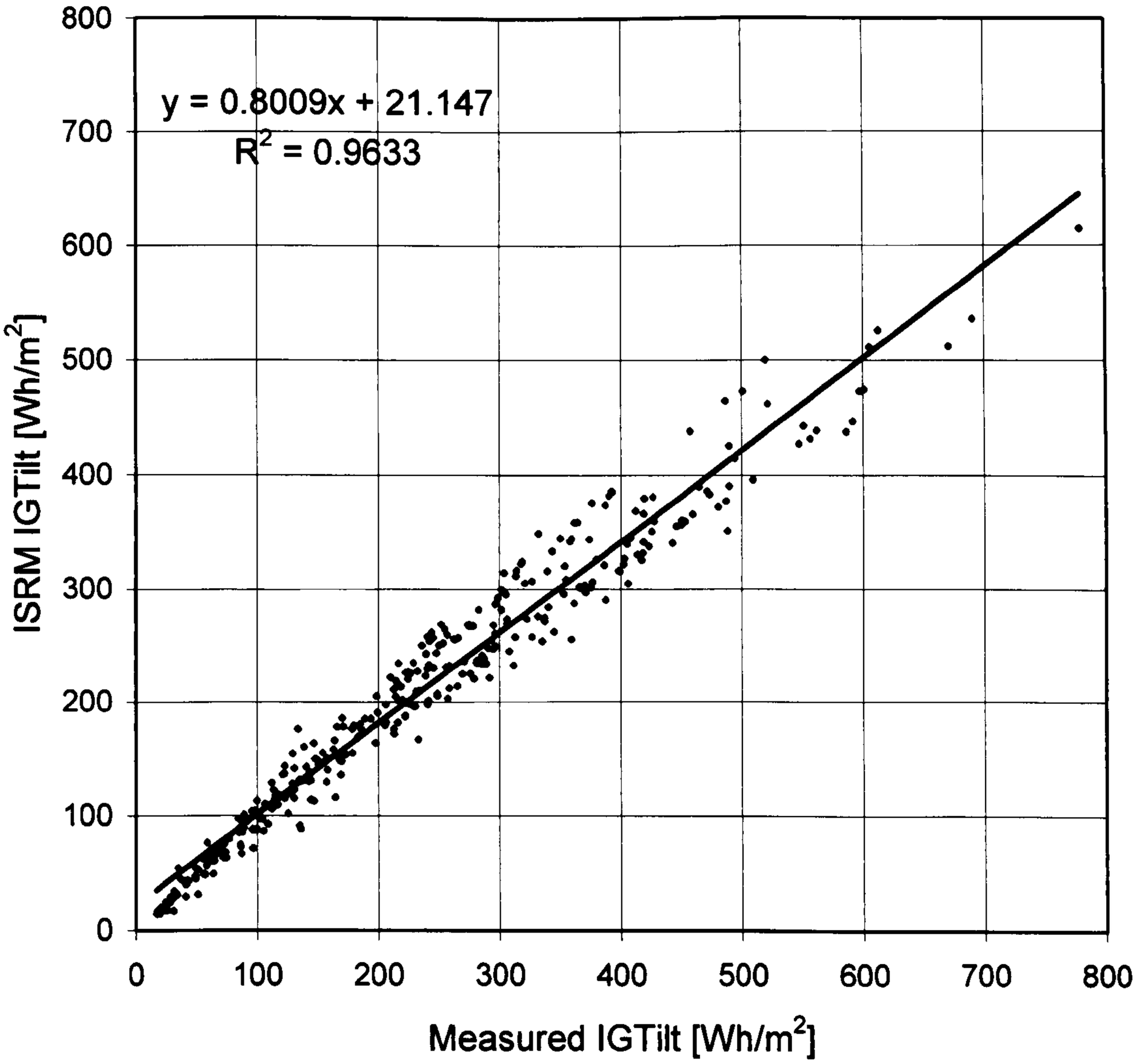

Figure 5.2.1 Relationship between measured and modelled slope irradiance using ISRM model. One year's daily averaged sub-hourly irradiance (Edinburgh 2006/2007).

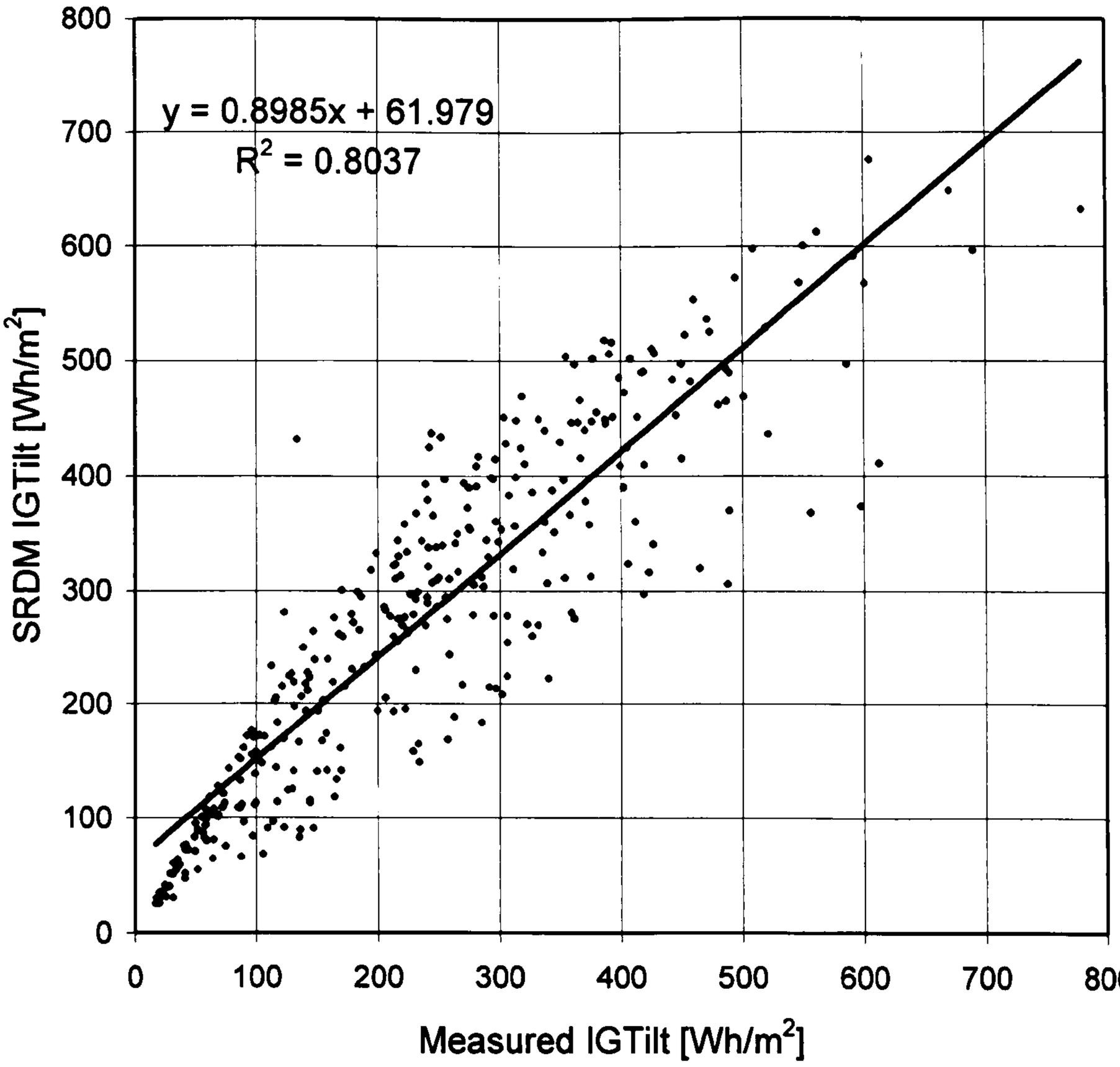

Figure 5.2.2 Relationship between measured and modelled slope irradiance using SRDM model. One year's daily averaged sub-hourly irradiance (Edinburgh 2006/2007).

Figure 5.2.1 shows the linear relationship for ISRM modelled slope irradiance and measured slope irradiance. The plot shows a strong linear relationship with little scatter, and a strong R^2 of 0.96 also verifies this relationship. Figure 5.2.2 shows the results for the SRDM model. The plot shows greater scatter than the previous plot, with a R^2 of 0.80 this can be mainly attributed to the fact the Perez model (on which the SRDM model is based) uses a larger number of coefficients than the ISRM model, and these coefficients have been produced using data from Berkeley, California and not the UK.

Differences between the climatic conditions in the UK and California can cause increased scatter in modelled estimates. It is expected that if a set of coefficients were developed using UK data, the model's performance would be greatly improved. If measured diffuse irradiance data was used and not synthetic data generated from horizontal global irradiance regressions, this could dramatically

increase the performance of both models. This finding has also been reported in the work of Gueymard, (2008).

A study under taken Efim *et al* assessed the performance of 11 models to estimate global solar radiation on a south facing tilted surface in Beer Sheva, Israel. The study showed that Muneer's integrated slope irradiation model used in the ISRM model, performed best out of all the models under all sky, and clear and partially cloudy conditions Efim *et al.*, (2008). This validates that this model is not locality dependant and can be used through-out the world.

Table 5.2.2 Daily totals of modelled tilted global irradiance performance statistics

Model	**SRDM**	**ISRM**
Slope	0.90	0.80
R^2	0.80	0.96
MBD, Wh/m^2	-38	27
RMSD, Wh/m^2	78	46
Skewness	-0.60	-1.27
Kurtosis	1.55	1.20
AS Score	2.36	1.50

Note: Slope angle 75° and aspect 37° East of South (Edinburgh, May-December 2007).

Table 5.2.2 shows performance statistics for both the SRDM and ISRM models. The SRDM model has increased scatter compared with the ISRM model, a fact which concurs with the R^2. Interestingly, further analysis of the statistical results show that the long-term trends of the slope statistic show that the SRDM model underestimates by 10 percent where as the ISRM model underestimates by 20 percent. But a mean bias deviation of -38 shows the overestimation by the SRDM model, and a value of 27 shows that the ISRM model underestimates but to a lesser degree than the SRDM model.

The root mean deviation also shows that the SRDM model has a larger deviation between the modelled and the measured than that of the ISRM model. The accuracy score is a very useful tool to use when comparing the performances of two similar models. Its ability to combine all six statistical indicators into one score enables the validation of the models' performance to be made much more simply. The AS score ranges between one and six, with a higher score being desired. In Table 5.2.2 it can be seen that the AS scores are 2.36 and 1.50 respectively for the SRDM and ISRM models. The SRDM model

gives a better performance than the ISRM model despite the increased scatter shown by the SRDM.

5.3 Comparison of SRDM and ISRM solar models with existing solar models

Recent work has been undertaken by Gueymard to validate the performance of ten transposition models, which are commonly used by engineers in energy and glazing calculations to estimate tilted global irradiances from the more commonly measured horizontal irradiance data (Gueymard, 2008). Gueymard evaluated the ten models' performances for three sets of conditions: fixed-tilt at 40°, south-facing vertical surfaces and 2-axis optimal tracking. Two types of data sets were used within the study, optimal and suboptimal data. Suboptimal data is more commonly used for the majority of sites which require solar irradiation calculations. This is because data is generally not available for the specific site of interest. Thus solar data is usually obtained from nearby meteorological stations which often only record horizontal global irradiance. Therefore a method of separating the diffuse and beam components is required before tilted irradiances can be estimated from the horizontal global irradiance. For the current study this is done using the above-mentioned regressions between the diffuse ratio and clearness index. On the other hand, optimal data generally being global, beam and/or other meteorological parameters also may be available, such as cloud cover. This data may be recorded on site or in very close proximity to the specific site of interest. Gueymard reports that all models give best performances when used with optimal data. The models' performances are reduced with the use of suboptimal data. The main problems arising from the use of suboptimal data are due to the errors produced from obtaining the separation of diffuse and beam components from their global counterpart.

However, the choice of models which can be used for a given application is also reduced, as some models require other metrological parameters which are not always available. For Gueymard's study, a twelve-month dataset covering September 2006 to August 2007 from NREL's Solar Radiation Research Laboratory in Golden, Colorado (latitude 39.74°, longitude 105.18°W) was used. The site is considered to be a sunny site with an annual daily average of 5.65 kWh/m^2. A fix albedo rating was also applied to all models for all four seasons of 0.2 to simplify analysis.

Table 5.3.1 Performance statistics for ten transposition models with optimal data input

Plane	40°S		90°S		Tracking	
Model	MBD (%)	RMSD (%)	MBD (%)	RMSD (%)	MBD (%)	RMSD (%)
	ALL SKY, N= 116,942					
Mean Es, W/m^2	643		432		836	
ASHRAE	-5.1	7.8	6.5	13.4	-8.1	9.6
Gueymard	-0.8	4.3	5.2	10.6	-1	4.2
Hay	-2.1	5.5	-2.7	8.2	-1.9	6.1
HDKR	-1.8	5.3	-0.4	7.7	-1.5	5.9
Isotropic	-5.1	7.8	-5.8	11.6	-8.1	9.6
Klucher	-1.4	4.6	0.3	8.5	-6	7.5
Muneer	-0.4	5.2	2.5	9.5	-5.4	7
Perez	-2.7	6.7	-4.7	12	-2.3	5.8
Reindl	-1.8	5.3	-0.4	7.7	-1.5	5.9
Skartveit	-2.4	5.7	-4.3	9.3	-2.2	6.4

Plane	40°S		90°S		Tracking	
Model	MBD (%)	RMSD (%)	MBD (%)	RMSD (%)	MBD (%)	RMSD (%)
	CLEAR SKY, N= 58,880					
Mean Es, W/m^2	763		524		1020	
ASHRAE	-3.6	4.9	0.1	4.5	-5.5	6.2
Gueymard	-1.1	2.7	-0.2	3.8	-1.2	2.1
Hay	-1	3.2	-2.2	5.2	-0.3	2.7
HDKR	-0.9	3.1	-1.2	4.7	-0.1	2.7
Isotropic	-3.6	4.9	-4.9	8.1	-5.5	6.2
Klucher	-1	2.8	-0.5	5.1	-4	4.8
Muneer	0.4	2.8	2	5.1	-3.3	4
Perez	-0.7	2.6	-0.4	3.9	-1	2.1
Reindl	-0.9	3.1	-1.2	4.7	-0.1	2.7
Skartveit	-1	3.2	-2.2	5.2	-0.3	2.7

Note: Sorce: Gueymard, (2008).

Table 5.3.1 shows the statistical results for all ten transposition models for all planes; tilted 40° south facing, vertical south facing and 2-axis optimal tracking. Statistics are split into two sets: all sky data containing full range of climatic sky conditions and clear sky only. As an overall observation, the models give improved performances in clear sky conditions over those of all skies, which is as expected. Gueymard noted that both the Gueymard and the Perez models perform best compared with the other models when used with optimal data, although by examining the statistical results in Table 5.3.1 it can be concluded that the Muneer model offers improved performance compared with that of the Gueymard model for many cases. It should be noted that the SRDM model is based on the Perez model and the ISRM model is based on the Muneer model. It can be seen from Table 5.2.2 and Table 5.3.1 that both the SRDM model results are similar to the Perez model, MBD indicating overestimation by the model for the majority of cases, whereas the Muneer model underestimated the measured. The RMSD also shows that that the Muneer model produces less deviation from the measured than the more complex Perez model.

5.4 Validation of SRDM and ISRM solar models in estimating the performance of the Edinburgh Napier University photovoltaic facade

Two data sets are used to validate the performance of both the ISRM and SRDM models with measured outputs. Quality controlled horizontal global irradiance data recorded over thirteen months from April 2006 was used with diffuse regressions to generate diffuse irradiance, as previously mentioned in Chapter 3. This was used to evaluate the models' performance for sites which do not record diffuse irradiance. A second dataset also recorded at the same site from May 2007, containing both global and diffuse horizontal irradiance, was also used to evaluate the models. The accuracy of computations was compared with the measured output of the Napier PV facade. Both cumulative monthly energy and instantaneous power outputs were compared.

These results are shown in Tables 5.4.1 and 5.4.2. From the statistical indicators it is not always possible to determine which model performs the best. As an example, Figure 5.4.1 shows the PV AC power output for three days' data from 8th to 10th May 2006. For all of these days the power output rises rapidly from around 7am in the morning and peaks at 12 noon. The peak output

typically lies between 10-11kW for this period. It can be seen that the daily outputs are skewed, i.e. not fitting a Gaussian distribution. In the early afternoon the power output rapidly drops as a result of the PV facade falling under shade. The power output continues to drop, albeit with a shallower gradient, between 3pm and 7pm when the facade is fully shaded and solely receiving diffuse irradiance. Both the ISRM and the SRDM models closely follow the measured PV AC power output. In the early afternoon the SRDM tends to overestimate the PV AC power output, whereas the ISRM model substantially underestimates the peak power output. Figure 5.4.2 shows a similar plot for the 21st to 23rd May 2006. The weather is overcast with broken skies. As a result, the power distribution curves are much more platykurtic, producing less power over these three days. The power output curves are also more uneven as a result of fluctuating changes in cloud cover, which makes it difficult to stipulate which model performs better by visual means alone.

Figures 5.4.3 and 5.4.4 show two sample weeks. The first week is made up of individual days deliberately selected as days with heavily overcast cloud cover, with only diffuse irradiance being received. The second week has also been made up from individually selected days, which are clear and sunny with no cloud cover and little atmospheric pollution, resulting in a high proportion of beam irradiation being received on the surfaces of the PV modules.

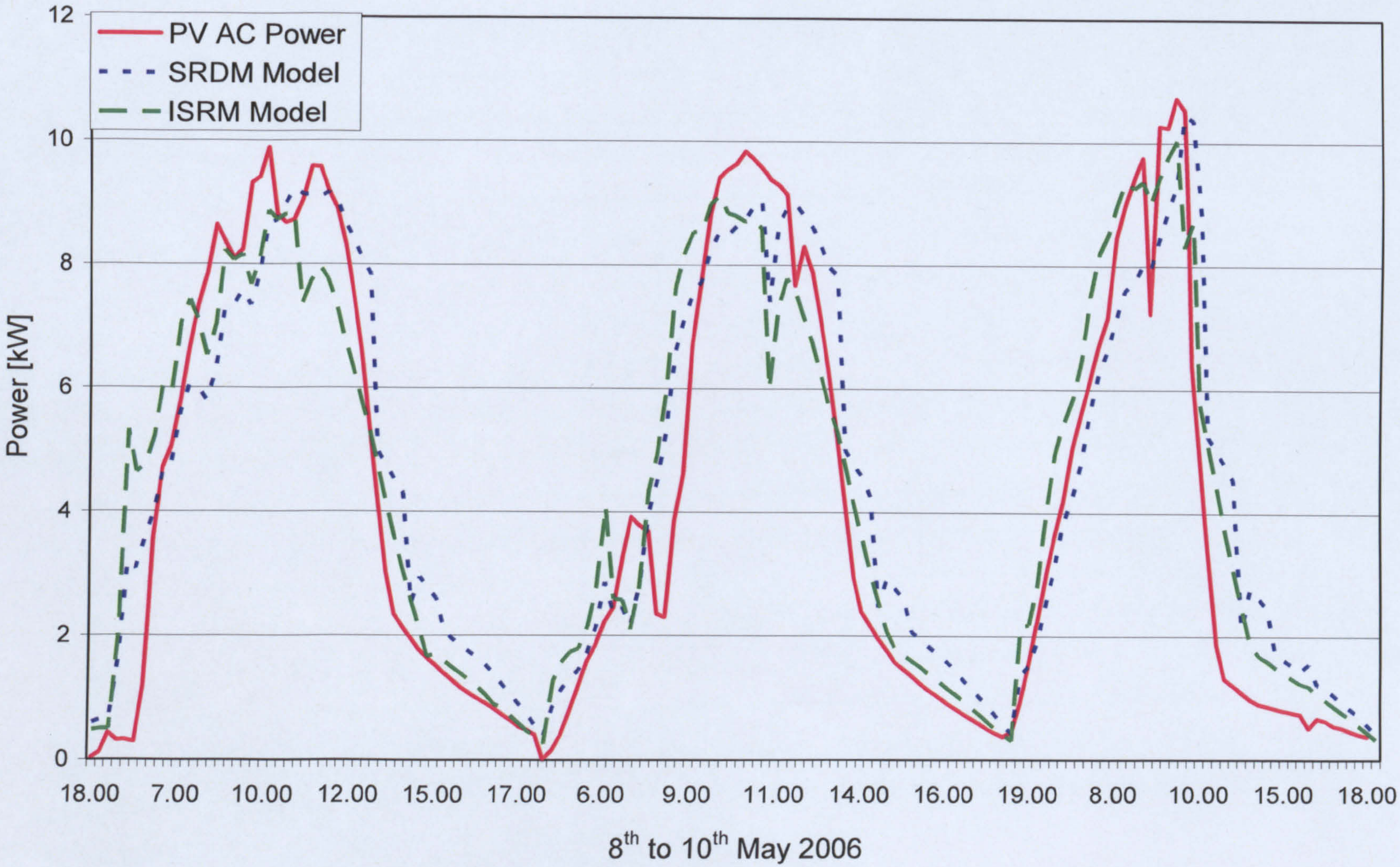

Figure 5.4.1 Edinburgh Napier University PV facade power output. Note: only sunrise to sunset data is shown.

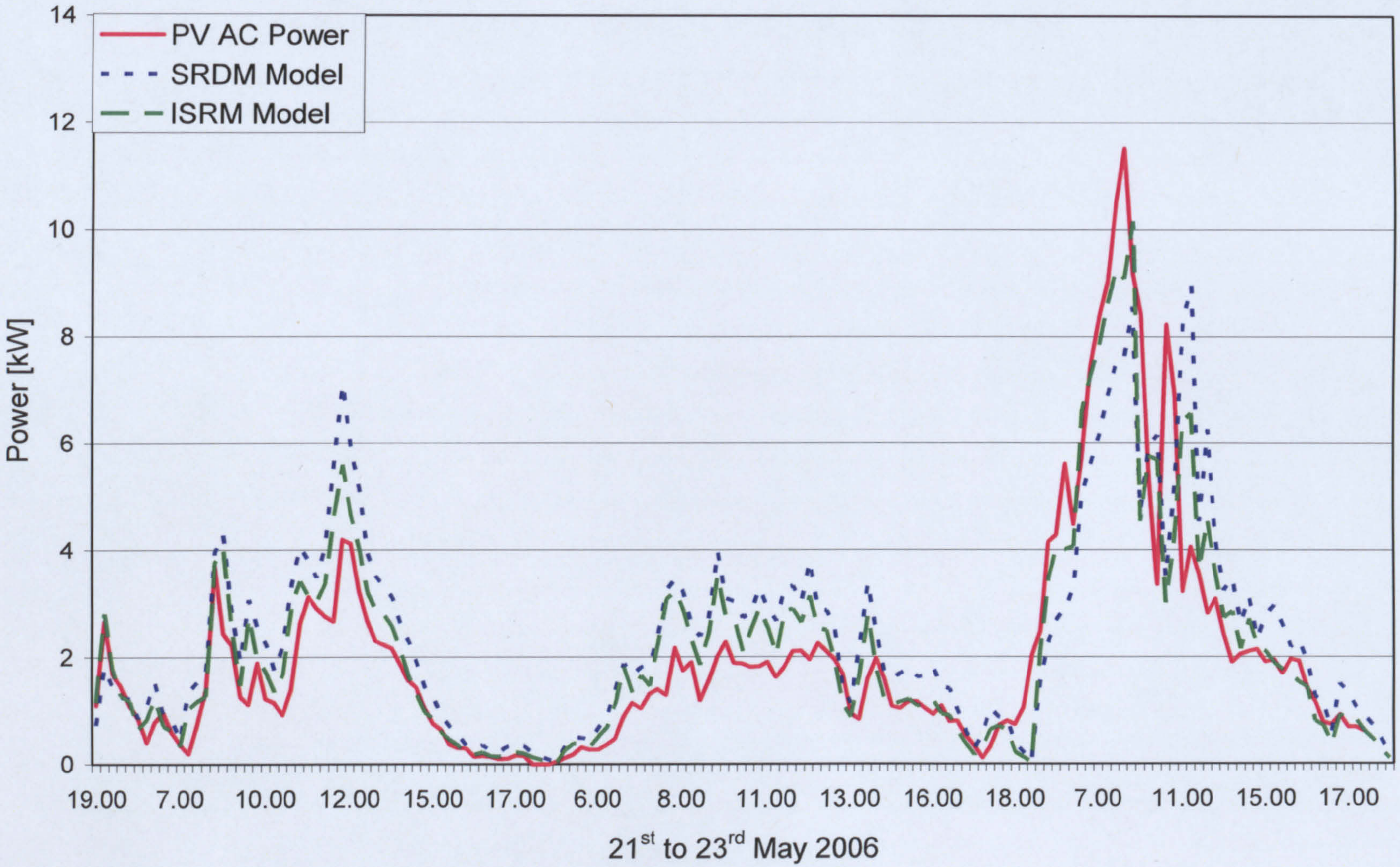

Figure 5.4.2 Edinburgh Napier University PV facade power output. Note: only sunrise to sunset data is shown.

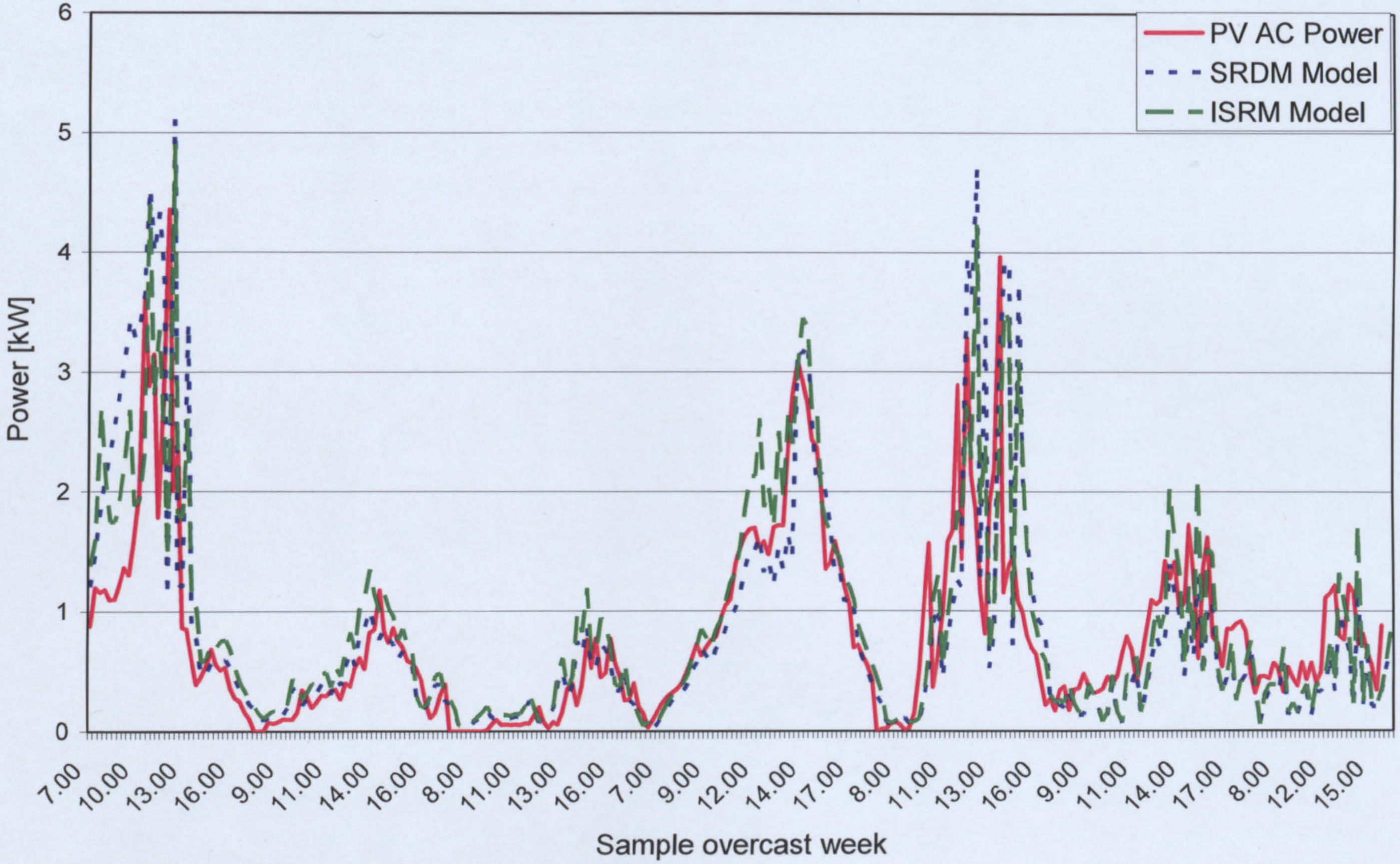

Figure 5.4.3 Edinburgh Napier University PV facade power outputs taken for seven days selected for being overcast. Note: only sunrise to sunset data is shown.

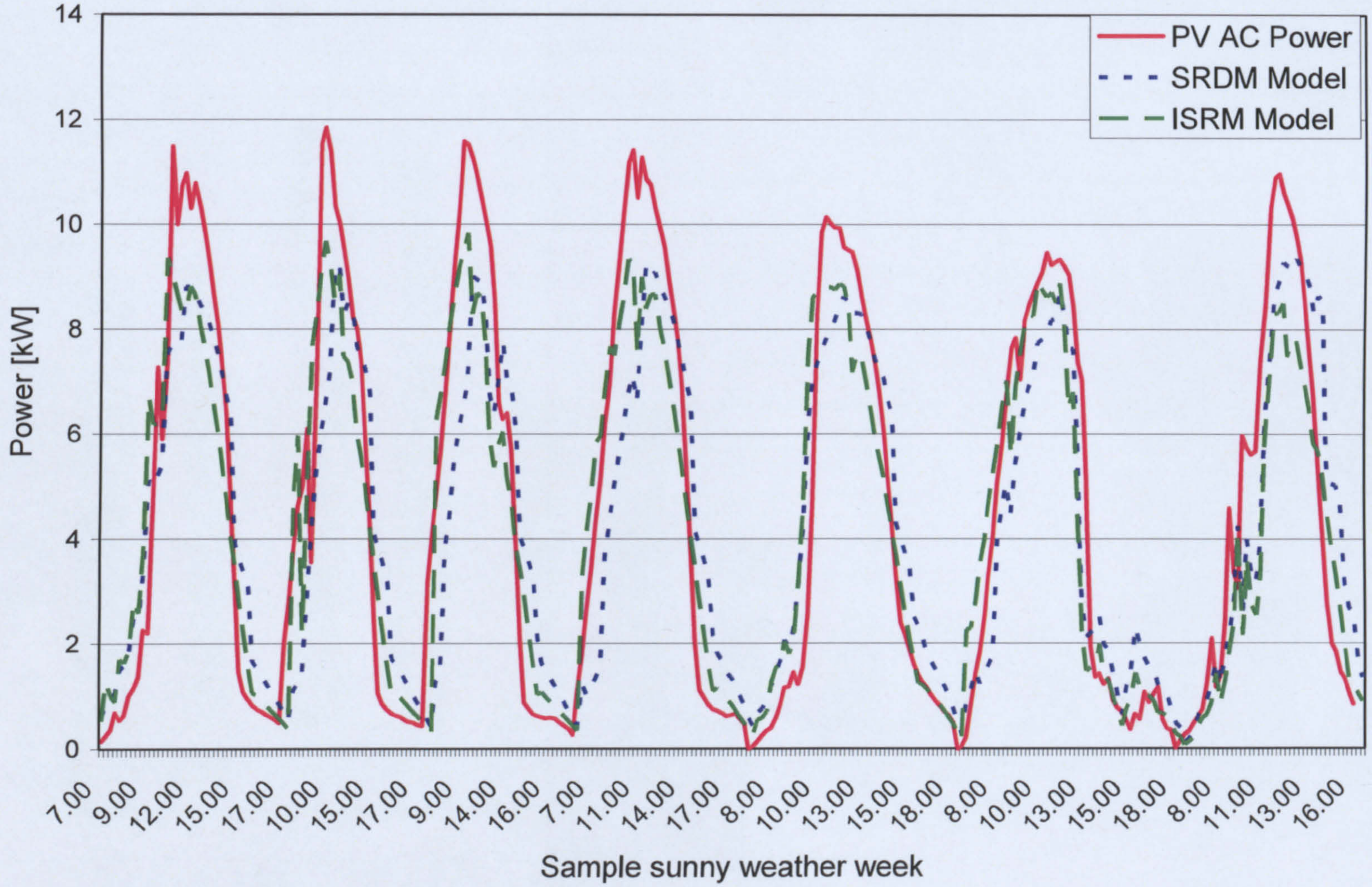

Figure 5.4.4 Edinburgh Napier University PV facade power outputs taken for seven days selected for being sunny. Note: only sunrise to sunset data is shown.

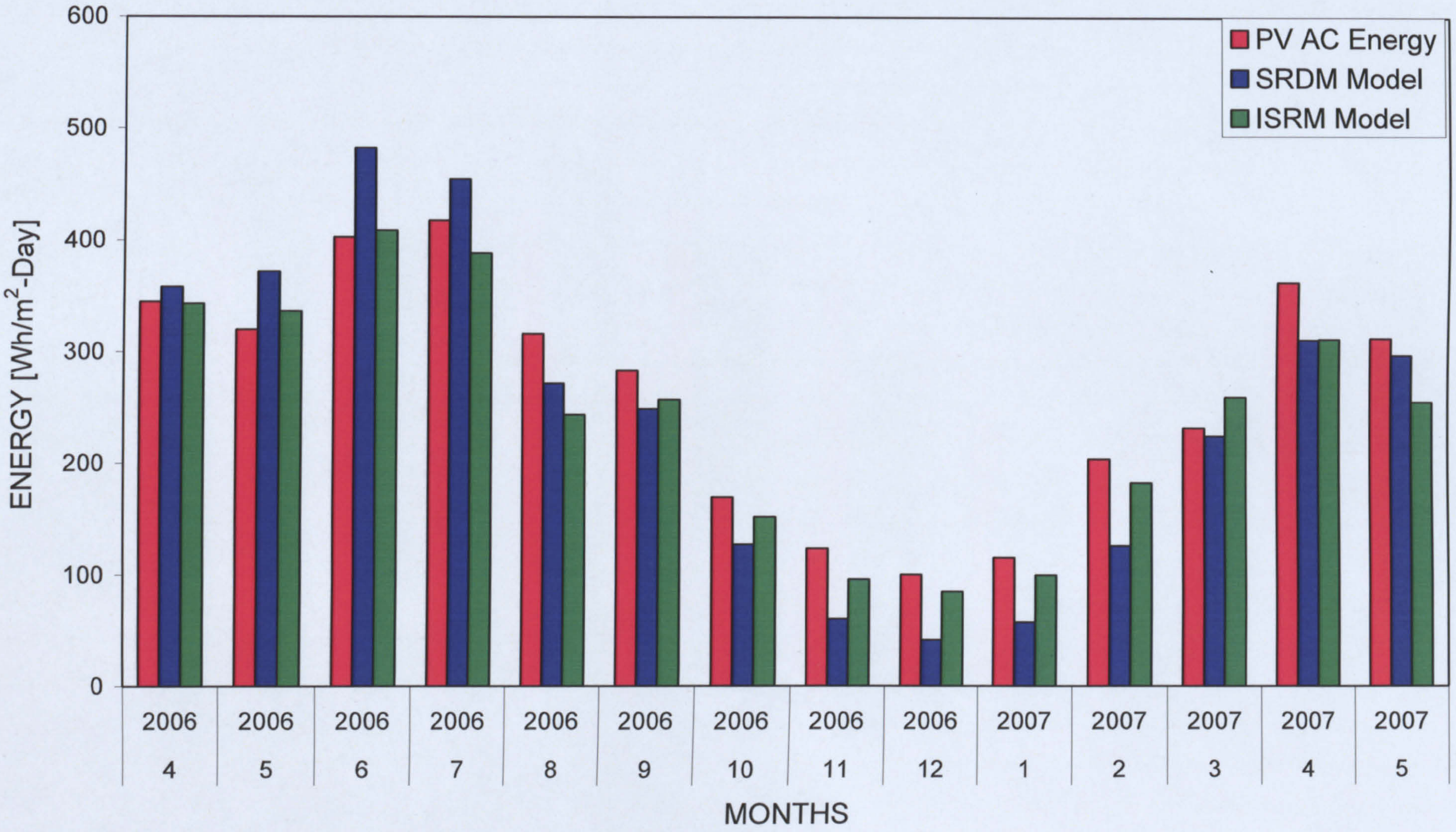

Figure 5.4.5 Monthly averaged daily PV AC energy outputs. Note dataset used contains solely global irradiance data, diffuse component obtained via regressions.

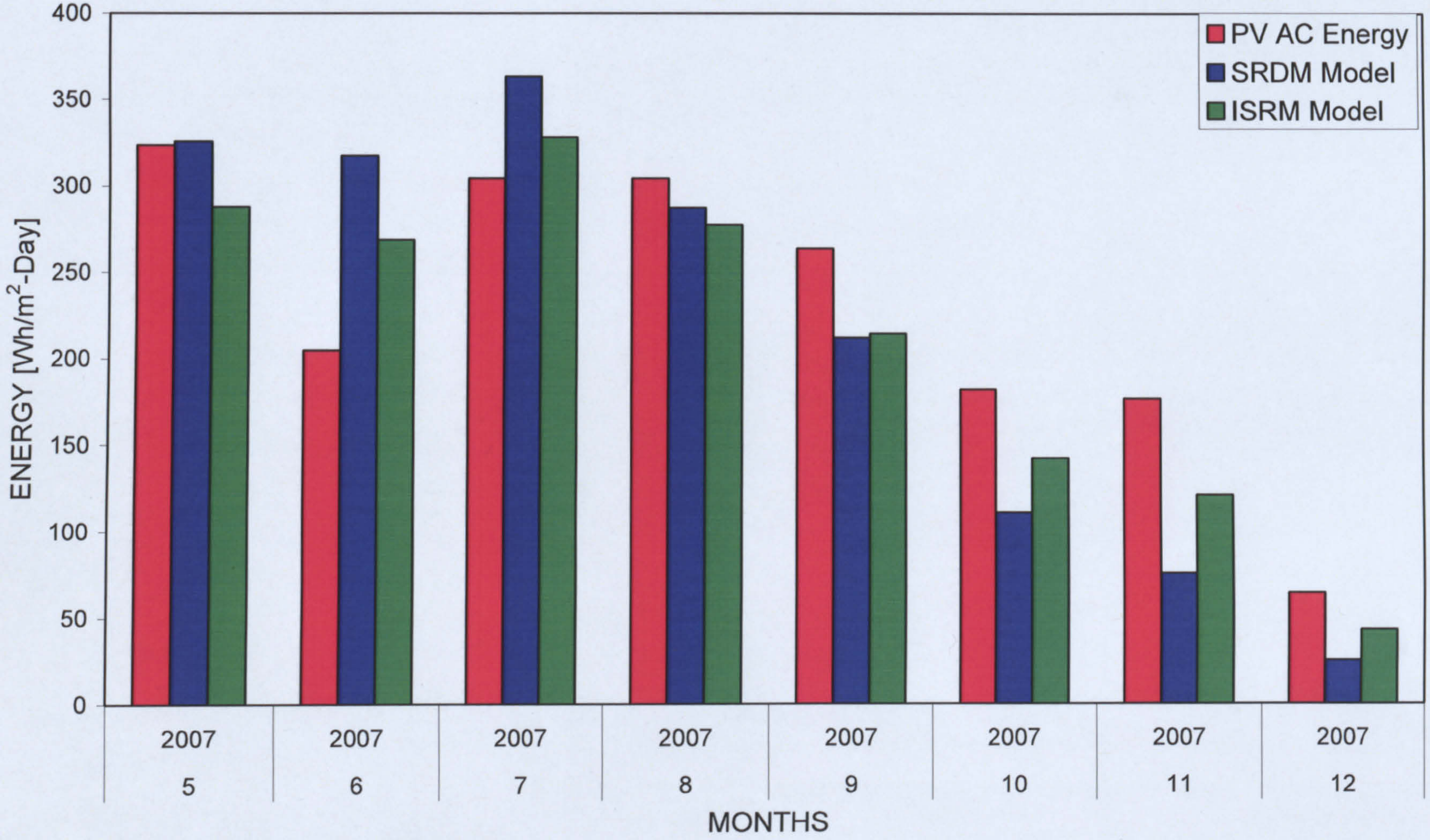

Figure 5.4.6 Monthly averaged daily PV AC energy outputs. Note dataset used contains both global and diffuse components.

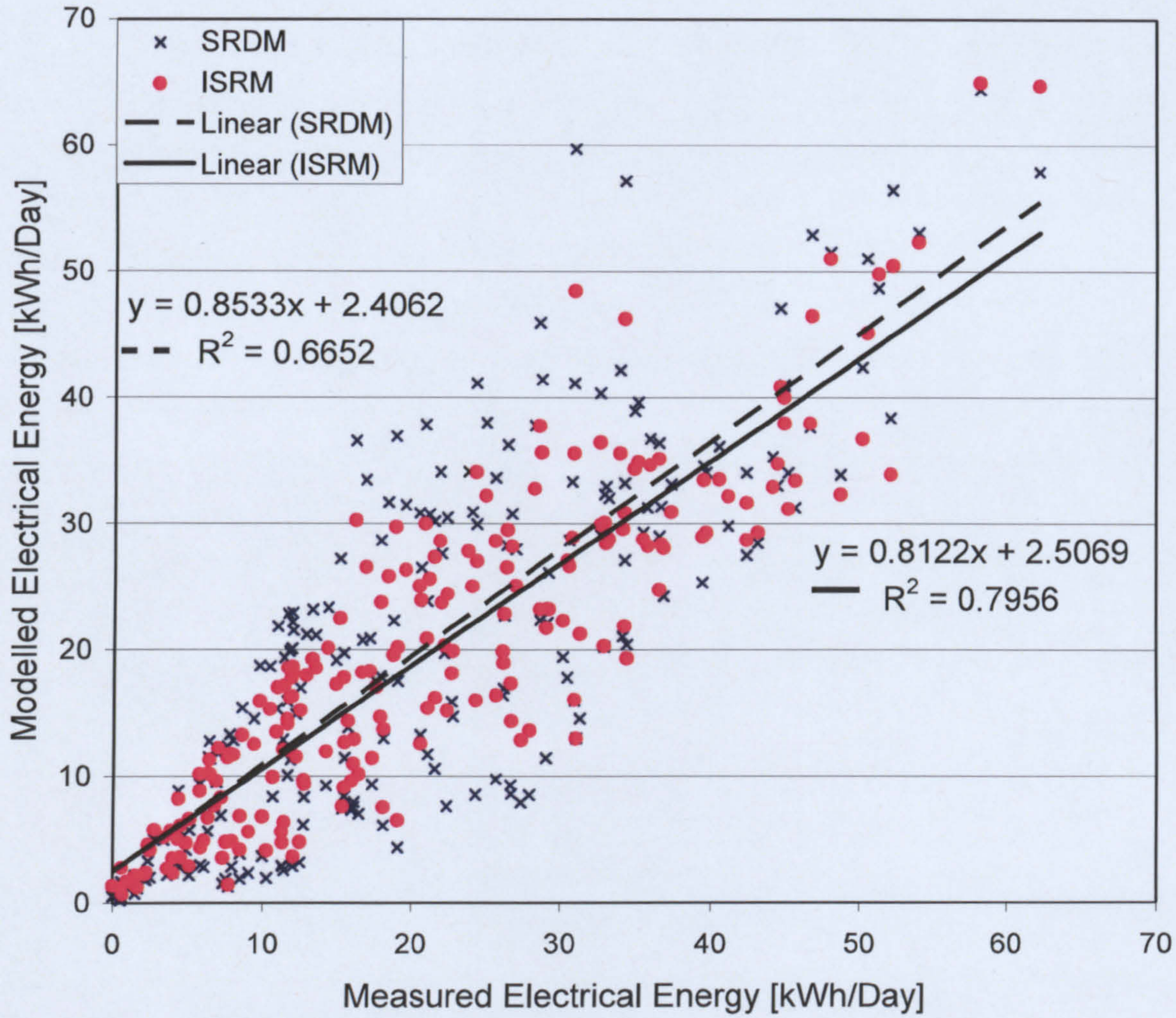

Figure 5.4.7 Daily totalled modelled electrical energy outputs versus measured electrical outputs. Measured 15-minute averaged, ID and IG data used, 7th May to 30th December 2007.

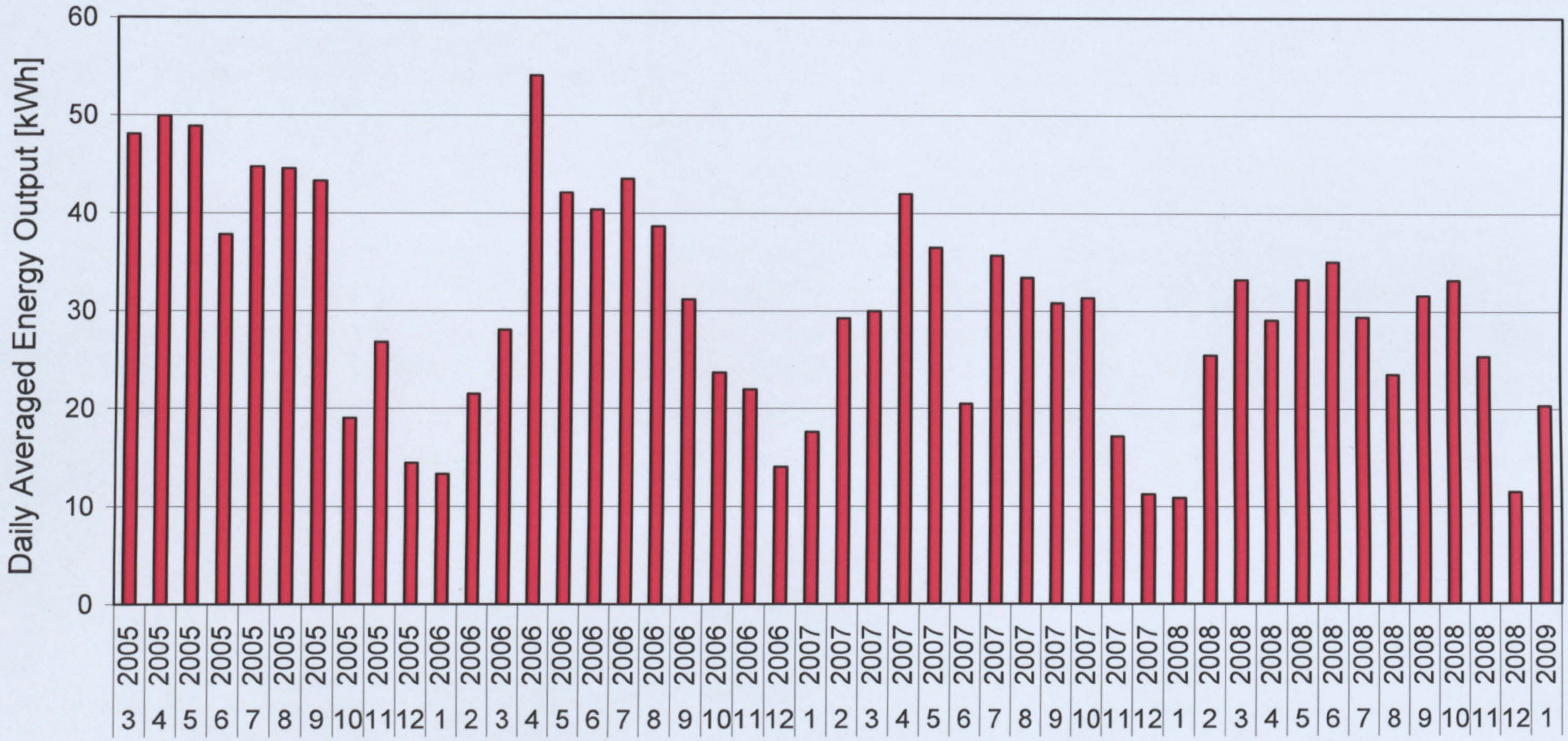

Figure 5.4.8 Daily averaged monthly PV-AC energy outputs. Note: Month numbers at the bottom.

Table 5.4.1 SRDM and ISRM solar model statistics using 15-minute averaged horizontal global irradiance and diffuse regressions (Pyranometer CM 11). Note: the sunny and overcast weather results are single week data with individual days selected by visual inspection

Month	4		5		6		7		8		9		10		11		12		Full Period	
Year	2006		2006		2006		2006		2006		2006		2006		2006		2006		2006	
Model	**SRDM**	**ISRM**	**SRDM**	**ISRM**	**SRDM**	**ISRM**	**SRDM**	**ISRM**	**SRDM**	**ISRM**	**SRDM**	**ISRM**	**SRDM**	**ISRM**	**SRDM**	**ISRM**	**SRDM**	**ISRM**	**SRDM**	**ISRM**
Slope	0.67	0.83	0.86	0.88	0.94	0.88	0.82	0.79	-0.13	-0.16	0.24	0.27	0.44	0.72	0.29	0.65	0.25	0.7	0.85	0.75
R2	0.84	0.88	0.91	0.93	0.94	0.98	0.95	0.98	0.05	0.07	0.12	0.12	0.79	0.96	0.57	0.76	0.9	0.96	0.67	0.71
MBD, W/m²	-1354	649	-4823	-1365	-7347	-513.4	-3498	2821	3446	6113	2879	2087	3784	1542	5362	2151	5103	1497	618.3	1760
RMSD , W/m²	4959	3818	6750	4372	8442	3243	5477	4805	20765	21624	14914	15589	7186	3592	7342	4014	7725	2970	10352	9388
Skewness	0.71	0.09	-0.87	-1.11	-0.28	-0.34	0.02	0.04	-0.13	-0.05	0.41	0.37	-0.54	-0.82	-0.15	-0.04	-0.65	-0.36	-0.56	-0.86
Kurtosis	-0.27	-0.17	1.18	1.39	-0.57	-1.03	-0.56	-1.29	-0.33	-0.34	-0.47	-0.21	-0.81	-0.03	-1.14	-1.03	-1.11	-0.59	3.35	7.67
AS Score	2.62	4.08	2.91	3.95	2.63	4.42	2.79	3.1	2.02	2.45	2.29	2.01	2.6	2.85	2.04	4.36	2.18	3.99	3.25	2.84
PV AC, Wh/m²/day	345.1		319.78		402.52		417.48		316.02		282.89		169.29		123.51		99.91		275.2	
SRDM, Wh/m²/day	357.96		371.81		482.3		454.7		271.44		248.29		127.13		60.1		41.58		268.4	
ISRM, Wh/m²/day	343.09		335.94		408.35		387.96		243.27		257.09		151.85		95.86		84.68		256.5	

Month	1		3		4		5		Full period		Good Weather		Bad Weather	
Year	2007		2007		2007		2007		2007					
Model	**SRDM**	**ISRM**	**SRDM**	**ISRM**	**SRDM**	**ISRM**	**SRDM**	**ISRM**	**SRDM**	**ISRM**	**SRDM**	**ISRM**	**SRDM**	**ISRM**
Slope	0.34	0.75	0.62	0.89	0.63	0.83	0.82	0.76	0.77	0.82	0.61	0.78	0.3	0.62
R2	0.78	0.95	0.85	0.92	0.82	0.9	0.94	0.97	0.84	0.91	0.97	0.98	0.33	0.92
MBD, W/m²	5021	1486	577.6	-2507	4889	5028	1753	5674	3419	1886	467.1	318.6	11279	6080
RMSD, W/m²	7341	2813	6265	4566	7968	6559	4246	6999	7155	5227	8890	5474	12771	6824
Skewness	-1.09	-1	-0.92	1.03	-0.3	-0.19	-0.74	-0.16	-0.59	0.03	-2.28	-1.79	0.31	-0.7
Kurtosis	0.78	0.7	-0.27	1.77	-0.36	-0.72	1.54	-0.22	-0.24	0.66	5.31	3.32	-0.48	0.78
AS Score	2.16	4.06	2.56	3.16	2.06	3.38	3.89	2.68	2.05	4.49	2.61	3.32	1.83	3.54
PV AC, Wh/m²/day	115.01		232.01		362.11		312.41		255.38		466.86		79.69	
SRDM, Wh/m²/day	57		224.35		310.84		297.38		222.39		437.95		85.08	
ISRM, Wh/m²/day	99.48		259.68		311.57		255.52		231.56		432.13		90.95	

Table 5.4.2 SRDM and ISRM solar model statistics using 15-minute averaged horizontal global and diffuse irradiance (Delta-T BF3)

Month	5		6		8		9		9		10		11		12		Full Period	
Year	2007		2007		2007		2007		2007		2007		2007		2007		2007	
Model	**SRDM**	**ISRM**	**SRDM**	**ISRM**	**SRDM**	**ISRM**	**SRDM**	**ISRM**	**SRDM**	**ISRM**	**SRDM**	**ISRM**	**SRDM**	**ISRM**	**SRDM**	**ISRM**	**SRDM**	**ISRM**
Slope	0.62	0.59	1.15	0.97	0.81	0.83	0.70	0.77	0.46	0.54	0.38	0.66	0.25	0.52	0.13	0.35	0.85	0.81
R2	0.77	0.79	0.76	0.82	0.85	0.91	0.88	0.89	0.59	0.72	0.58	0.78	0.55	0.71	0.34	0.63	0.67	0.80
MBD, W/m^2	-245.9	3375.6	-10614.3	-5961.1	-5451.8	-2032.1	1672.5	2661.6	4793.5	4722.7	6410.7	3681.9	9142.7	5222.3	3426.7	1996.7	678.7	1441.8
RMSD, W/m^2	7657.2	8393.0	12425.2	7362.8	7983.0	4974.0	6710.3	6430.6	8577.4	7717.3	8868.0	5644.6	11500.9	7375.8	4788.5	3312.4	8770.7	6514.0
Skewness	-0.26	-0.28	0.83	0.46	-0.55	-0.74	-0.66	-0.63	-0.18	-0.49	-0.40	-0.50	0.04	-0.12	-0.31	-0.50	0.18	-0.25
Kurtosis	-1.07	-1.26	0.75	0.68	0.10	-0.35	-0.85	-1.03	-1.36	-0.81	-0.74	-0.22	-1.58	-1.16	-1.41	-0.74	0.00	-0.06
AS	3.52	2.59	2.79	4.16	2.28	3.84	2.88	2.85	2.92	2.25	2.33	2.74	2.69	3.04	2.06	2.60	2.51	3.07
PV AC, Wh/m^2/day	324.4		204.9		304.2		305.0		263.9		183.3		176.7		64.2		228.3	
SRDM, Wh/m^2/day	325.8		317.6		363.6		287.4		212.1		110.8		75.5		25.1		214.7	
ISRM, Wh/m^2/day	287.8		268.8		328.2		277.5		214.4		142.3		120.8		42.9		210.3	

Table 5.4.3 Napier PV facade: monthly system efficiencies

Period	**Efficiency η**
Apr-06	13.6
May-06	12.4
Jun-06	13.3
Jul-06	12.4
Aug-06	10.3
Sep-06	12.4
Oct-06	13.3
Nov-06	13.3
Dec-06	14.1
Jan-07	13.9
Feb-07	14
Mar-07	13.7
Apr-07	11.2
May-07	11.8
Jun-07	12.9
Jul-07	12.4
Aug-07	11.3
Sep-07	11
Oct-07	11.9
Nov-07	11.7
Dec-07	11.1
Average	12.5

Table 5.4.4 Napier PV facade: monthly energy outputs

Month	Year	kWh
3	2005	106.1
4	2005	441.1
5	2005	1619.3
6	2005	1208.7
7	2005	1482.2
8	2005	1474.3
9	2005	1385.4
10	2005	630.8
11	2005	857.3
12	2005	478.4
1	2006	440.5
2	2006	641.5
3	2006	930.2
4	2006	1731.0
5	2006	1393.8
6	2006	1290.8
7	2006	1439.7
8	2006	1279.7
9	2006	721.8
10	2006	784.2
11	2006	702.6
12	2006	464.0
1	2007	581.9
2	2007	258.2
3	2007	991.8
4	2007	1343.5
5	2007	1207.3
6	2007	655.1
7	2007	1181.1
8	2007	1105.7
9	2007	985.1
10	2007	1037.2
11	2007	549.5
12	2007	754.0
1	2008	359.1
2	2008	787.9
3	2008	1099.9
4	2008	930.9
5	2008	1100.8
6	2008	1122.3
7	2008	882.4
8	2008	706.3
9	2008	917.1
10	2008	995.9
Total Energy		38080.3

Daily-averaged monthly energy outputs for both models and measured PV AC outputs can be seen in Figure 5.4.5 for the period April 2006 to September 2007. Note that global horizontal irradiance data was recorded using a Kipp and Zonen CM11 pyranometer, and estimated diffuse irradiance was obtained using regressions.

The months of June and July 2006 show the highest energy outputs of 402.5 Wh/m^2/day and 417.5 Wh/m^2/day respectively. The lowest monthly-averaged daily energy output was noted to be 99.2 Wh/m^2/day for the month of December 2006. Over the long term, the SRDM model overestimates the measured for the sunny summer months and underestimates for the winter months, whereas the ISRM model underestimates the measured for all but the month of May 2006. This is also observed in the statistical results shown in Table 5.4.1, which corresponds with Figure 5.4.5. For the majority of months, the ISRM model estimates the measured output with more accuracy than the SRDM model in terms of both statistical measurements as well as daily averaged energy yields. The AS score is used as a measure of all statistical tests carried out. The ISRM model scores higher for all the months apart from August 2006 and May 2007 where the SRDM gives an improved score. Over the full period the SRDM model's performance is greatly improved. The reason for this is that the SRDM model tends to overestimate the summer period and underestimate the winter period. Thus over the full period the model's performance is averaged out. The averaged daily output for the full period for the PV facade is 275.2 Wh/m^2/day. The modelled outputs are 268.4 Wh/m^2/day and 256.5 Wh/m^2/day respectively for the SRDM and ISRM models. A closer inspection of the performance of both models in clear sunny skies and overcast skies can be seen in Figures 5.4.3 and 5.4.4, which show instantaneous power plots of a week's data for each weather condition.

For clear skies, the SRDM model follows the measured output with much more precision than the ISRM model for the majority of the day. The peak output each day occurs between 11:00AM and 13:00PM each day, and the highest power outputs achieved are 11.9 kW. The maximum modelled outputs are notably lower, typically around 9 kW at peak. Both models underestimate measured outputs when the facade is operating at peak performance. It is also notable that in the late afternoon the SRDM tends to over estimate the power output when the facade falls under shade.

For the overcast week shown in Figure 5.4.3, it is difficult to determine which model gives improved performance.

The data used for the above-mentioned period was based solely on horizontal global irradiance data. Regressions are used to generate diffuse irradiance from horizontal global measurements. However any errors in the diffused irradiation estimates will affect the performance of the models. To overcome this issue a second data set was also recorded for the same site, recording both horizontal global and diffuse irradiances. The results for this data set can be seen in Figure 5.4.6 and Table 5.4.2. Note that the monthly averaged daily energy outputs seen in Figure 5.4.5 and Figure 5.4.6 can not be compared directly, which is due to the way that the data was combined. Measured PV outputs have been recorded separately to incident solar irradiation datasets. The PV energetic outputs are then merged with the measured solar output data. A quality control procedure is used to ensure that only data recorded from the PV facade that has a corresponding incident solar irradiation measurement is used in the final dataset. However the individual design of each type of sensor, the CM 11 pyranometer and the BF3 Delta-T, is important. The sensors have different threshold limits, meaning the sensor may start and stop recording solar irradiance at different light levels.

This is particularly noticeable in winter, when low irradiation levels may mean that sensors start and stop recording several times a day if there are heavily overcast or broken skies. For the eight months' data shown in Figure 5.4.6 (May to December 2007) both models can estimate the measured with much greater accuracy than seen with the previous dataset. Over the full period the same pattern can be seen: the ISRM model underestimates for all but June whereas the SRDM model overestimates for the summer period and underestimates for the winter period. The statistical results in Table 5.4.2 validate the observed, showing that the AS scoring systems can be used to determine the models' overall statistical performance. The ISRM model scores highest for all months, but for the full period the SRDM model outperforms the ISRM model. This shows that the overall average performance of the SRDM model is better than that of the ISRM model.

Figure 5.4.7 is a scatter plot for measured daily totalled electrical energy outputs versus the modelled electrical energy outputs for 7th May to 30th December 2007. Again it can be seen the SRDM slope of best line of fit is 0.85 (compared

with 0.81 for the ISRM model), showing that over the full period the estimates of the measured are 15% under estimate, where as the ISRM model underestimates by 19%. R^2 is 0.67 and 0.80 for the SRDM model and the ISRM model respectively; the SRDM model has more scatter than the ISRM.

The reason for this varied performance over the year is most likely due to the unique way which the SRDM model estimates the diffuse component. It calculates the intensity and spatial distribution of skylight using Perez's model (Perez *et al.*, 1993). Perez's all sky models uses five coefficients to adjust irradiance conditions and spatial distribution of sky light. The coefficients for the adjustable functions were based on an experimental dataset which included more than 16,000 full-sky scans from Berkeley, California, covering all sky conditions. Sky luminance distributions are only available for a few locations around the world, due to the complex and costly data acquisition equipment required to carry out such sky scans. The data was recorded between June and December 1985 across a wide range of conditions. However the coefficients have been developed for Berkley, California, but it has been assumed that the same coefficients can be used for sites within the UK with reasonable accuracy, although the UK has considerably higher latitude than then California resulting in differing climatic conditions to those of Berkley.

The model has been said to account for most mean anisotropic effects, but not for abnormal climate conditions (Perez *et al.*, 1993). Thus if a set of coefficients were produced for the UK, then the estimated diffused component of the SRDM model may substantially be improved, thus improving the model's overall performance.

From Figure 5.4.8, daily averaged monthly energy outputs can be seen from March 2005 to January 2008. Seasonal effects are clearly seen in monthly outputs. The summer months generally yield twice that of the energy yielded in winter months. There is generally a gradual increase in the energy generated each month throughout spring until the peak energy output is achieved in April. Note that this is not purely due to the PV facade receiving peak incident solar radiation, but rather the combination of high levels of sunshine for long durations each day. Both solar geometry and metrological climate conditions are a factor, and peak incident extraterrestrial radiation will occur at the summer equinox.

However the intensity by which the irradiation will be incident on the surface is greatly affected by the prevailing sky conditions. Cloud cover, moisture content and airborne particulate matter all affect the intensity of incident irradiation on the earth's surface.

This has been attributed to the heterogeneous sky conditions which are seen in the UK over the winter, autumn and spring periods. Siberian winds flank the east coast of Britain, which keeps the east coast of Scotland cold and dry. Skies on the eastern coast contain very little moisture or airborne particulate matter, whereas prevailing winds from the Atlantic Ocean keep the western coast of the UK warm and wet, resulting in higher levels of moisture content than seen on the eastern coast. This phenomenon can result in high sky clarity indices for these periods for the eastern coast. In the summer period, still warm air contains a much higher portion of airborne pollution and moisture content.

This is often seen as a haze in the sky, and as a result of both of these phenomena the peak incident solar irradiation is seen in the month of April. The summer of 2006 can be seen as a typical summer with the month of April producing the highest monthly electrical energy output seen to date. The monthly energy outputs for that period can be seen to fit an even Gaussian distribution. This can be compared with the summer of 2007 which was poor in comparison. Fluctuation in the monthly energy outputs was due to the poor overcast broken skies which occurred for much of the summer period. Studying all three summer periods, it can be observed that the amount of energy being generated each year is steadily reducing. This has been attributed to the gradual build up of dirt on the surfaces of the PV modules. Again this is observed in Table 5.4.3, which shows that monthly efficiencies have an overall tendency to reduce year on year.

It is expected that the level of dirt building up on the surfaces of the PV modules will reach a state of equilibrium where the module efficiency will remain stable. The highest system efficiency which has been achieved by the PV facade is η=14.1% in December 2006 and February 2007. The highest efficiency occurs in the winter months for two reasons. Firstly, PV modules operate with higher efficiencies at lower temperatures. This is because the silicon wafers have a lower internal electrical resistance at lower temperatures, resulting in lower energy losses. Secondly, the high levels of precipitation which occur over winter clean the module's surfaces of dirt and pollution, increasing overall performance.

The overall system efficiency for the full period is η=12.5%. Table 5.4.4 shows the monthly electrical outputs since the facade was installed. In November 2008 the facade has generated a total of 38 MWh of electricity.

In summary it can be concluded that the SRDM model has improved performance over the long term, and that the ISRM model gives improved short term performance. The SRDM model's performance could greatly be improved by the introduction of coefficients based on UK data.

Increasing concerns about global warming have lead to an increase in the number of environmentally considerate buildings being designed. Limiting the solar gain in the summer months can reduce the need for air conditioning, and maximizing the use of solar gain in winter months can displace the heating requirements from non-renewable energy sources. The benefit of the SRDM model is in its ability to be able to precisely incorporate shading effects caused by the surrounding structures. Another application of this model may be in estimating day lighting levels within buildings.

CHAPTER 6

Wind energy potential in urban environments

6.1 Development of wind turbine technology

There are a growing number of micro-wind turbine manufacturers who are developing small-scale turbines for both small business and the domestic market. Initially systems were primarily designed for rural locations with good wind resources. However the majority of domestic homes are located in urban environments where the wind resource is greatly reduced. Only 19.3% of the UK population live in rural areas, compared with 80.7% in urban areas (DEFRA, 2005). To increase potential market size, manufacturers have developed products for the urban market. Since land space is at a premium in urban areas, and to reduce the total cost of systems, many manufacturers are developing building-mounted or rooftop turbines, which are small and light enough to be installed on domestic properties.

Since the rapid development of this new market, there has been little scientific or academic research carried out to validate manufacturers' claims of turbine performance in urban environments. There is a lack of wind data for urban environments, which has meant that many turbines, have been designed using rural wind data which is much higher and less turbulent, yielding a much higher energy potential than can be achieved in urban areas. Nearly all turbine manufacturers who have marketed their product have had to recall their product and cancel orders to make modifications for this reason within the last year (Warwick Wind Trials Interim Report, 2007). Modifications have been made to nearly all aspects of the turbine design. Component strength has been the main area of concern.

The high degree of turbulence observed in the urban environment due to the increased surface roughness of landscape can result in focused and dynamically changing winds. The wind is prone to changing velocity and direction very quickly resulting in high dynamic load forces acting on the turbines and causing increased wear and premature component failure.
Several examples of this have been seen with the turbines installed at Edinburgh Napier University. The Airdolphin needed a replacement mast in

February 2007 when it buckled in high winds. The high degree of turbulence excessively wore the tail fin pivot bearing and a fatigue crack began to develop along the length of the tail fin. This was also replaced in February 2007.

The Ampair 600 turbine also suffered a spate of electrical and mechanical failures within the first few months of installation. The electronic load controller failed twice after being overloaded, and this resulted in damage to the inverter. The electronic load controller and inverter were replaced in November 2007 (one month after being installed) and the electronic load controller was then replaced again with a modified controller in January 2008.
High dynamic load cycling also resulted in fatigue and failure of both the tail fin (figure 6.2.2.2) and the turbine blades (figure 6.2.2.3). Manufacturers are now finding that urban rooftop turbines have to be designed with a greater degree of strength and rigidity than turbines previously designed for use in the rural environment.

The majority of the rooftop turbines installed within the UK are grid-connected systems. Before an inverter can export energy onto the grid, grid regulation states that the inverter is required to monitor the state of the grid for 3 minutes before energy can be exported. While the inverter is connected to the grid it consumes energy, whether or not energy is being exported to the grid. Out of the 30 turbines being tested for the Warwick Wind Trails, inverters were found to consume from 0 to 200Wh of electricity per day, typically 100Wh per day (Warwick Wind Trails Interim Report, 2008).

Two approaches to grid connection have been taken. In the first, which is employed by the Windsave turbine, the inverter remains permanently grid-connected so that any energy generated by the turbine is exported to the grid. However, in long periods of calm the inverter may import more energy than the turbine exports to the grid, with an overall net loss of energy.
In the second approach, which is used by the Ampair 600 turbine, the inverter only connects to the grid when there is an output from the turbine. This reduces the energy required from the grid to run the inverter. However, the disadvantage of this system is that there is a three-minute delay from the turbine starting to generate power to energy being exported to the grid. The energy is dissipated to

a dump load in this period. As soon as the turbine ceases to generate power, the inverter disconnects from the grid.
For sites with turbulent winds, considerable generation may be lost as a result of the high frequency of inverter reconnections to the grid.

6.2 Napier turbine trials

Recently there has been much media attention given to micro-turbine technology. This has varied from unrealistic estimations of the domestic turbines' ability to produce enough energy to make domestic homes carbon neutral to the opposite extreme of the rooftop turbine's embedded carbon payback period being greater than the turbine's design life (Reidy, 2008).

Customers in urban areas are finding that their turbines are not achieving their designed performance. There is also a lack of available data for use by planners and installers to determine site suitability for turbine installations. This may be resulting in poor site locations being chosen for installations.

The Napier study was set up to determine why turbines are underperforming in urban environments. Three micro wind turbines were chosen for this study: the Zephyr Airdolphin, Ampair 600 and Windsave, rated at 1kW, 600W and 1.2 kW respectively, to give a true representation of the UK micro-wind market. There are approximately seven companies within the UK supplying micro turbines to the domestic and rooftop turbine market. The turbines were set up in two configurations to determine the performance of both types of system: a stand-alone system (Figure 2.19.) and a grid-connected system (Figure 2.20.). The Zephyr Airdolphin (Figure 6.2.1.1) was set up to operate as a stand-alone system with a sealed lead-acid battery as an energy storage medium. The Ampair 600 turbine (Figure 6.2.2.1) and the Windsave turbine (Figure 6.2.3.1) are both grid-connected. Both the Zephyr Airdolphin and Ampair 600 turbines are available as grid-connectable or stand-alone systems. The Windsave turbine is only available as a grid-connectable system.

Figure 6.2.2 shows Edinburgh Napier University's rooftop turbine test site located within the city of Edinburgh. The turbines are all located on the southern side of the building. Edinburgh Napier University Merchiston campus is 100m above sea level and all the turbines are approximately 22m above ground level.

Further details can be seen in Fig. 6.2.2. The Windsave, Airdolphin and Ampair turbines are installed on masts 2.5m, 2.2m and 3m above the roofline respectively, and the roof is flat. The University is the highest building in the vicinity with a clear view of the horizon on all but the eastern side, which is flanked by the university teaching block approximately 40 meters away and 15 meters higher than the test site.

The turbines could either be installed on the leading edge to the flat roof, being the up-wind side of the building, or on the trailing edge (down-wind side). There are advantages in siting the turbines in both locations. At the leading edge of the building, the wind shear focuses the air stream, resulting in increased pressure and wind velocities. However, as the wind passes over the building's leading edge the air stream becomes very turbulent. The turbine should be sited at the maximum distance away from this zone, at the trailing edge, to minimise the affects of turbulence. A visualisation of this is shown in Figure 6.2.1. It was concluded that the turbines should be installed on the leading edge of the building so that a smaller mast could be used and the effect caused by the building's wake could still be minimised. Table 6.2.1 gives performance details of all three turbines.

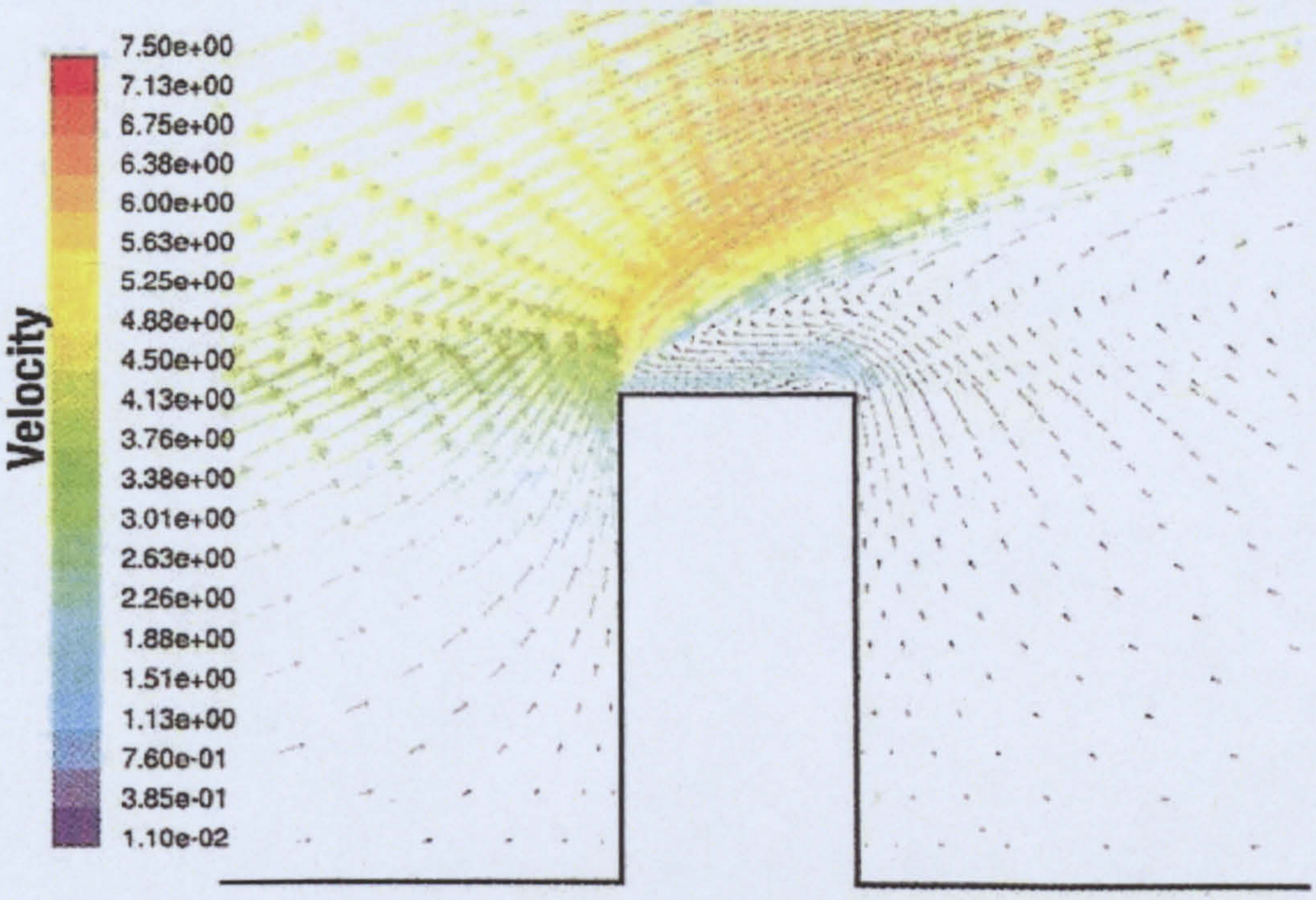

Figure 6.2.1. Visualization of air stream travelling over a flat-roofed building. Courtesy :(Mertens & Vries, 2008).

Figure 6.2.2. Edinburgh Napier University Merchistion Campus rooftop test site. (From the left, Windsave turbine, wind monitoring station, Airdolphin turbine, Ampair 600 turbine and anemometer).

Table 6.2.1 Micro-turbine specifications

Turbine	Airdolphin Z1000	Ampair 600-230V	Windsave WS 1200
Rotor diameter	1.8m	1.7m	1.75m
Mass	17.5kg	16kg	25kg
Number of blades	3	3	3
Generator	Synchronous type, 3-phase, permanent magnet (NeFeBr)	Synchronous type, 3-phase, permanent magnet (NeFeBr)	Asynchronous type, 3-phase, permanent magnet (NeFeBr)
Cut-in wind speed	2.5m/s	3.0m/s	4m/s
Cut-out wind speed	12.5m/s	-	15m/s
Rated power	1kW	698W	1.2kW
Power per square meter	393W/m^2	307W/m^2	571W/m^2

6.2.1 Zephyr Airdolphin Z1000

Figure 6.2.1.1 Zephyr Airdolphin turbine (Edinburgh Napier University).

The Airdolphin turbine seen in Figure 6.2.1.1 was installed in October 2006. The manufacturer claims that it has a rated output of 1kW (12.5m/s). The turbine has been installed in a stand-alone configuration; the turbine has a built-in battery charge management system used to charge deep cycle Absorbed Glass Matt (AGM) batteries. The battery bank consists of four 150Ah 12-volt batteries wired in series/parallel configuration providing 300Ah at 24 volts.

Load is simulated by the use of a 1kW electric dump load heater, used to draw energy from the system. A 2kW modified sine wave 24VDC to 230VAC inverter is used to supply power to the dump load. It was decided that a high voltage load would be used as this reduces the switching current required to operate the dump load air heater and thus reduce the cost of the system. The dump load is operated by a simple flip-flop comparator circuit. The circuit monitors the battery voltage, and once the battery is fully charged to 25.3 volts the dump load is switched on, and remains on until the battery voltage drops to 25 volts,

indicating a 20% state of discharge. At this stage the circuit flips and the load is turned off until the battery recharges back up to 25.3 volts. A flip-flop circuit was chosen to minimise feedback oscillation in the system.

The turbine has a RS-485 communication port, enabling the turbine to be integrated with a PC. The turbine is supplied with software to enable voltage, current, power and cumulative energy data to be recorded at a 1 second resolution.

The turbine has no mechanical furling device, using electronic braking instead. It is controlled by an intelligent load controller to regulate the turbine speed in high winds, and to control the charge voltage, preventing over-charging of the batteries. The turbine also uses a novel power-assist mode to reduce start-up torque in low wind conditions. The turbine automatically rotates the turbine blades for 10 seconds every minute while wind velocity is below the cut-in speed of 2.5m/s. This reduces the start-up torque required to rotate the blades and thus reduces the cut-in wind speed, enabling the turbine to generate at lower wind velocities. The turbine also has very thin slender blades; their surfaces are covered with a number of thin grooves which are design to reduce airflow noise over the blades.

User findings

Since the turbine was installed there have been two faults which have needed to be rectified. The Airdolphin turbine has the narrowest diameter mast of all three turbines in the trial. In early months of operation it was noted that the turbine oscillated by a large degree in high winds. Then in late February 2007 the turbine mast buckled in high winds. The mast was replaced and later it was concluded that the wrong mast was supplied at installation. A mild steel mast had been supplied, whereas the design brief required a high-grade structural steel mast to be installed. The mast was replaced, and at the same time the tail fin was also replaced as fatigue damage was discovered. It has been concluded that the tail fin failed prematurely due to highly turbulent winds observed at the Edinburgh Napier University site. Since the problems have been resolved the turbine has been operating successfully to date.

6.2.2 Ampair 600 – 230 V

Figure 6.2.2.1 Ampair 600-230 V, anemometer can be seen to the right (Edinburgh Napier University).

The Ampair 600 turbine seen in figure 6.2.2.1 was installed in October 2007 and operates as a grid-connected system. The turbine is rated at 600W (11 m/s) producing 230 volts 3-phase, rectified to DC. Its power management system uses a pulse width modulator, and dump load is used to maintain the turbine power output to the required input parameters for the inverter. A Sunny Boy 700W inverter modifies the power output to allow it to be exported onto the national grid. An export meter and G-83 protection relay is also required. The turbine speed is controlled using variable pitched blade control which feathers the turbines blades out of the wind and slows turbine rotational speed. The turbine was installed with an additional wind velocity anemometer two meters from the turbine, and at the same height as the turbine's hub. The turbine and anemometer are data logged, recording averaged data at ten-minute intervals.

User findings

Since the turbine was installed it has experienced a number of electronic and mechanical failures. Early in November 2007 in high winds the interconnection box overloaded and failed in high winds, and as a result the input voltage into the inverter exceeded the input limits and overloaded the inverter. The manufacture claimed this was the first failure of this kind. They concluded it was the result of highly turbulent wind conditions which meant that the turbine did not generate continually for a period more than three minutes, and thus the inverter was unable to connect to the grid. As a result, energy generated was dissipated to the dump load as heat. It was concluded that the internal resistance of the dump load was too high and as a result the turbine output voltage exceeded the system's breakdown voltage and the control system failed. Both the inverter and interconnect box were replaced within two weeks. In mid December the interconnect box failed again for the same reason. The manufacture installed an additional dump load resistor in the replacement interconnect box to lower the turbine output voltage and thus the rotational speed of the turbine when shedding its load to the dump load.

The turbine operated successfully for two months until February 2008, when in a period of high winds the blades and tail fin failed. In this case it was concluded that the alloy tail fin failed due to fatigue in the turbulent winds.

As a result of the turbine tail failure, the turbine became very unstable due to having no mechanism to keep the turbine facing into the wind. The turbine was free to yaw in and out of the wind very rapidly, putting excessive load forces on the blades, resulting in blade failure (Figure 6.2.2.2). The tail fin was manufactured from 4mm thick sheet aluminium. From Figure 6.2.2.3 it can be seen that the three bolts used to secure the tail to the turbine body have pulled through the aluminium. A hairline crack can also be seen, originating from the central securing hole. The turbine blades were manufactured from glass reinforced plastic (GRP) with polyurethane foam cores. A new turbine head was installed late March 2008. The turbine has a modified reinforced tail fin and the blades have been made from carbon fibre instead if GRP for additional strength. Since these modifications have been made the turbine has been operating successfully to date.

Figure 6.2.2.2 Ampair 600 turbine shown with broken blades and loss of tail fin (February 2008).

Figure 6.2.2.3 Broken Ampair 600 tail fin (failed due to fatigue, February 2008).

6.2.3 Windsave WS1200

The Windsave WS 1200 was installed in June 2008. The turbine has a rated power output of 1kW (12.5m/s). The Windsave turbine has been designed and developed specially for the domestic market for urban applications; the turbine is only supplied as a grid-connected system. The turbine uses a permanent magnet asynchronous generator, producing 3-phase. It has a smart controller unit containing the inverter and a G-83 protection unit. The turbine uses a mechanical control to furl the turbine out the wind in high winds. Due to the previously mentioned design modifications which needed to be made to the

Windsave turbine, the turbine took over a year to be installed after the ordered was placed with the company. For this reason there was not enough time left to record the energetic output from the turbine for this study.

Figure 6.2.3.1 Windsave WS1200 (Edinburgh Napier University).

6.3 Measurement of wind regime

6.3.1 Analysis of wind regime

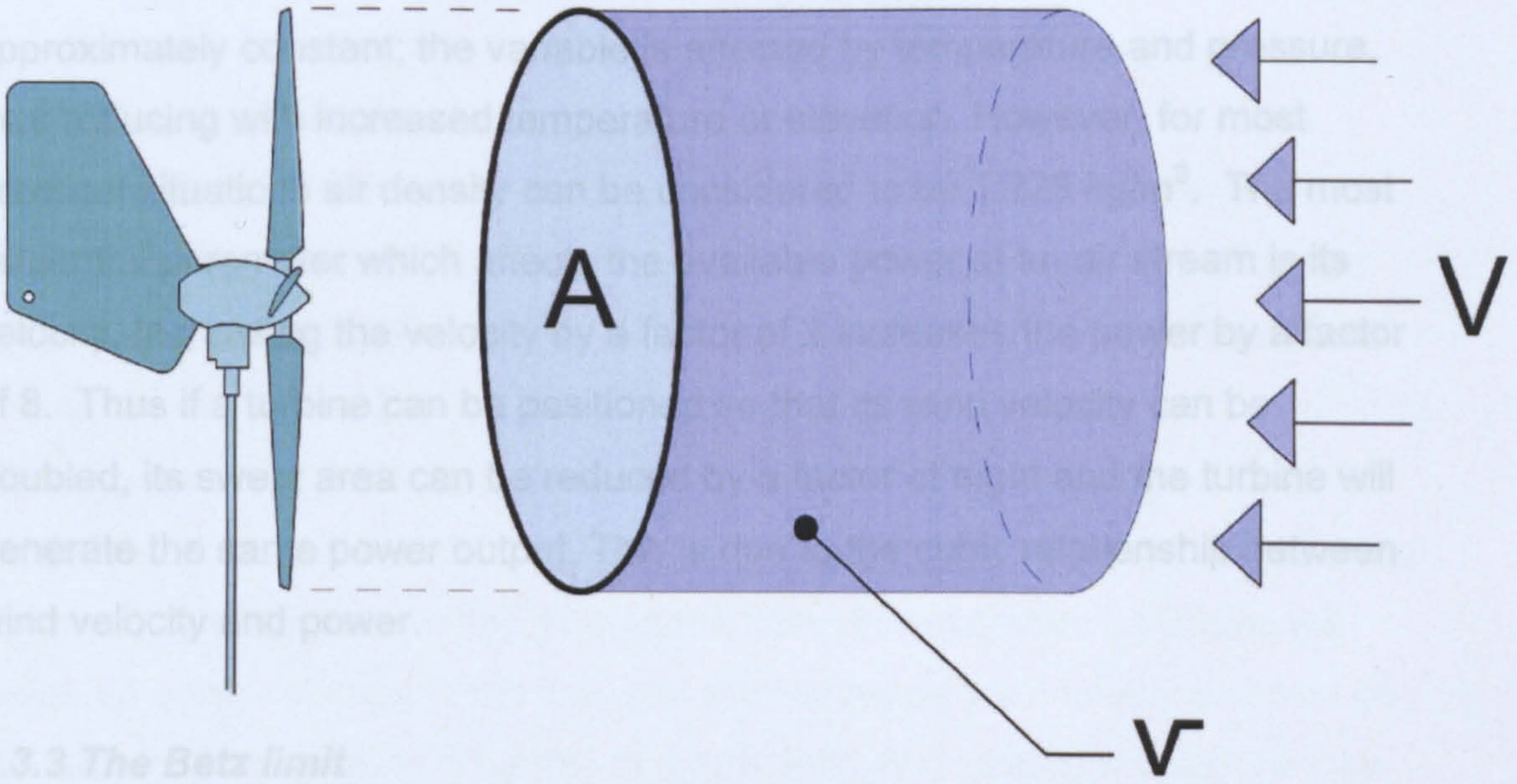

Figure 6.3.1 Wind turbine swept area.

The kinetic energy of a body of air flowing freely within an air stream is dependent on the air mass, m, of the body and its velocity, V, as seen in Figure 6.3.1 and given by Equation 6.3.1.1.

$$E = \frac{1}{2} m V^2 \qquad (6.3.1.1)$$

When considering the energy available for a cross-sectional area, A, of air stream. For example, at the turbines rotor, the kinetic energy available to the turbines rotor blades can be expressed as Equation 6.3.1.2

$$E = \frac{1}{2} \rho v V^2 \qquad (6.3.1.2)$$

for the given time the air stream interacts with turbine rotor. The air stream has a cross-sectional area equal to the turbine swept area. Thus energy per unit of time is known as power, given by Equation 6.3.1.4.

$$P = \frac{1}{2} \rho A V^3 \qquad (6.3.1.4)$$

6.3.2 Factors influencing the power of the wind

The three variables which affect the available power of the wind are air density, cross-sectional area of wind stream and velocity of wind stream. Air density is approximately constant; the variable is affected by temperature and pressure, thus reducing with increased temperature or elevation. However, for most practical situations air density can be considered to be 1.225 kg/m^3. The most influential parameter which affects the available power of an air stream is its velocity. Increasing the velocity by a factor of 2 increases the power by a factor of 8. Thus if a turbine can be positioned so that its wind velocity can be doubled, its swept area can be reduced by a factor of eight and the turbine will generate the same power output. This is due to the cubic relationship between wind velocity and power.

6.3.3 The Betz limit

The Betz limit shows that the maximum amount of available power which can theoretically be extracted from an air stream with a reaction type turbine rotor is 59.3%. When power is extracted from an air stream, its velocity is slowed. If, for example, 100% of the available power in an air stream was extracted, then its velocity would be reduced to zero and thus the air stream would have no energy. Betz's limit determines that the maximum fraction of energy which can be extracted from an air stream is when its velocity is reduced by one third.

6.4 Factors which reduce available wind speed

6.4.1 Capacity factor

In practice a wind stream velocity and direction is never constant; it is continually changing. The capacity factor is a measure used to determine a site's useable wind velocity. For example, if a turbine operated for one whole year producing its rated power output continuously, then the capacity factor would be 100%. However the reality is that the wind does not blow constantly at optimum wind velocity. The majority of the time the wind velocity will be below that of optimum, and turbine output will be below its rated output or even have no output at all. There will also be short periods of time when the wind velocity may exceed the design capacity of the turbine and the turbine may have to shut down.

For much of the UK the mean average wind speed is less than half that of a typical rated wind turbine; as a result the average capacity produced by a turbine is typically 25% of the yearly rated energy output.

6.4.2 Wind shear and turbulence

Wind velocities and directions change rapidly as the wind stream passes over rough surfaces or terrain; for example, hills, trees and buildings can all cause turbulences in its flow. The effects of turbulence are mainly noted downstream and above the obstruction although a smaller disturbance in air flow may also be found upstream of the obstruction as well, as seen in Figure 6.4.2.1. The intensity and magnitude of the effect of turbulence is dependent on the size and shape of the obstruction in the path of the flow. For example, a building will cause an abrupt change in the flow and thus increase the intensity and size of the turbulent zone. Siting a turbine in a turbulent wind stream will both reduce power output and increase fatigue loads on the turbine.

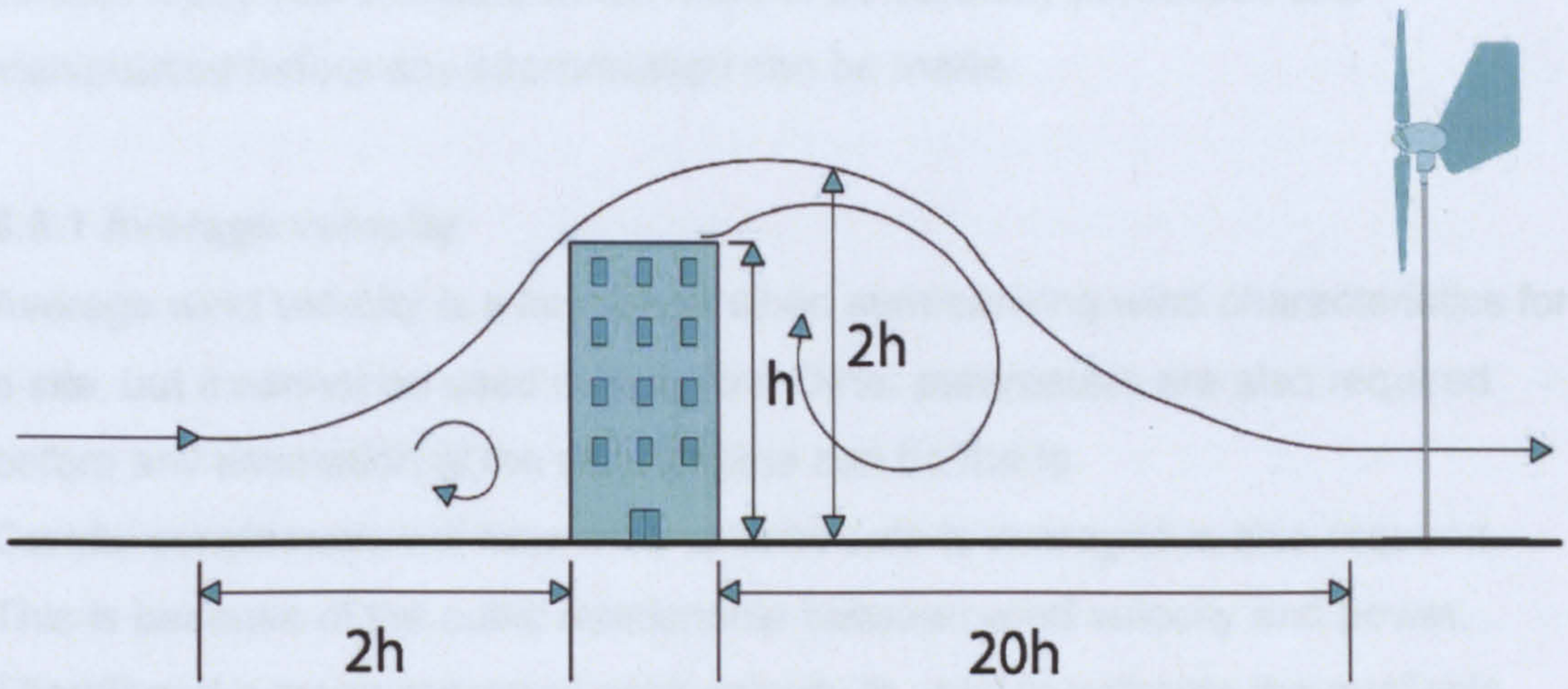

Figure 6.4.2.1 Schematic of wind turbulence effects over a building.

When a smoothly sloped topography is considered, an acceleration affect may be observed at the brow of the hill (Figure 6.4.2.2). An increased pressure zone forms on the ridge of the hill as a result of the boundary layers being pressed together causing the wind velocity to accelerate. Urban environments, crops and forested areas increase the effects of turbulence and reduce wind velocities.

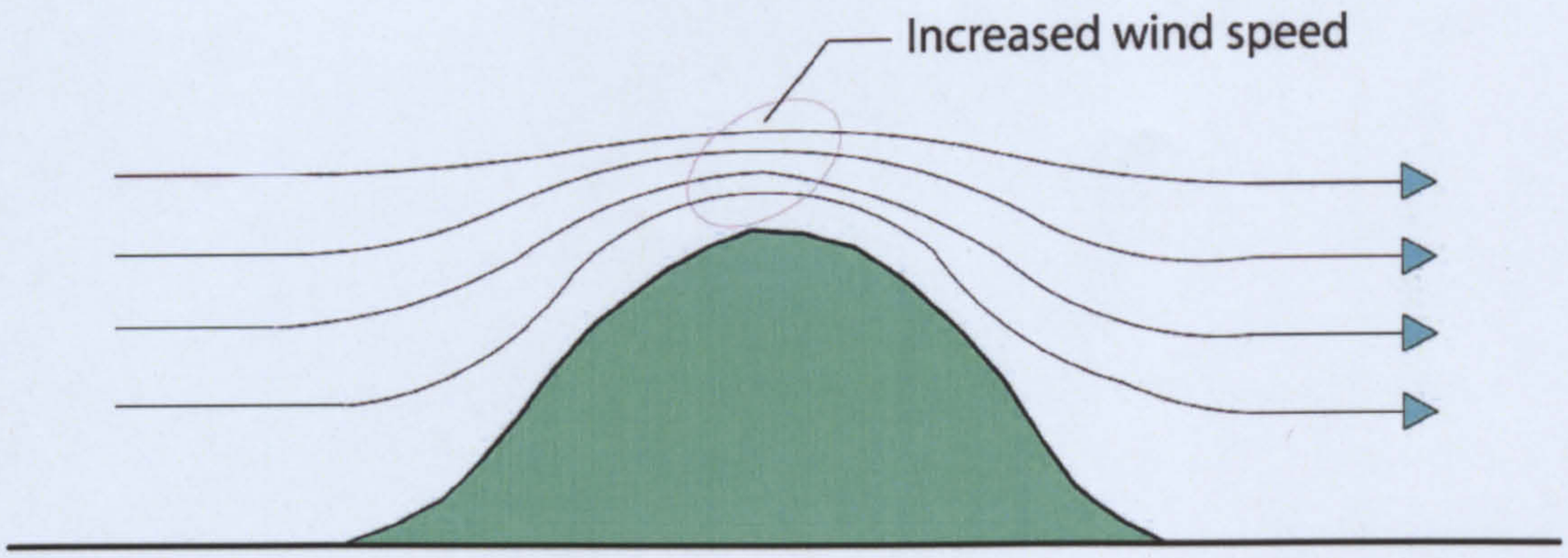

Figure 6.4.2.2 Schematic showing wind flow over smooth topography. Note increased wind velocities at the brow of the hill.

6.5 Wind data analysis

Wind data needs to be analysed in detail before any interpretation of the wind's energy potential can be estimated. Data sets are often very large and may contain many years of data which need to be carefully processed and manipulated before any interpretation can be made.

6.5.1 Average velocity

Average wind velocity is a key factor when summarising wind characteristics for a site, but it cannot be used in isolation. Other parameters are also required before any estimation of the wind regime can be made.

Careful consideration of how wind velocity data is averaged is also required. This is because of the cubic relationship between wind velocity and power. Therefore if a mean averaged wind velocity is used to estimate the available energy of a wind stream, then it will underestimate the output by approximately 20% (Sathyajith, 2006). Sathyajith suggests that a weighted mean wind velocity should be used instead when calculating the available energy of a wind stream.

Equation 6.5.1.1 shows the mean averaged wind speed and Equation 6.5.1.2 shows the weighted wind speed.

$$V_m = \left(\frac{1}{n} \sum_{i=1}^{n} V_i \right) \tag{6.5.1.1}$$

$$V_m = \left(\frac{1}{n} \sum_{i=1}^{n} V_i^3 \right)^{\frac{1}{3}} \tag{6.5.1.2}$$

6.5.2 Wind velocity distribution

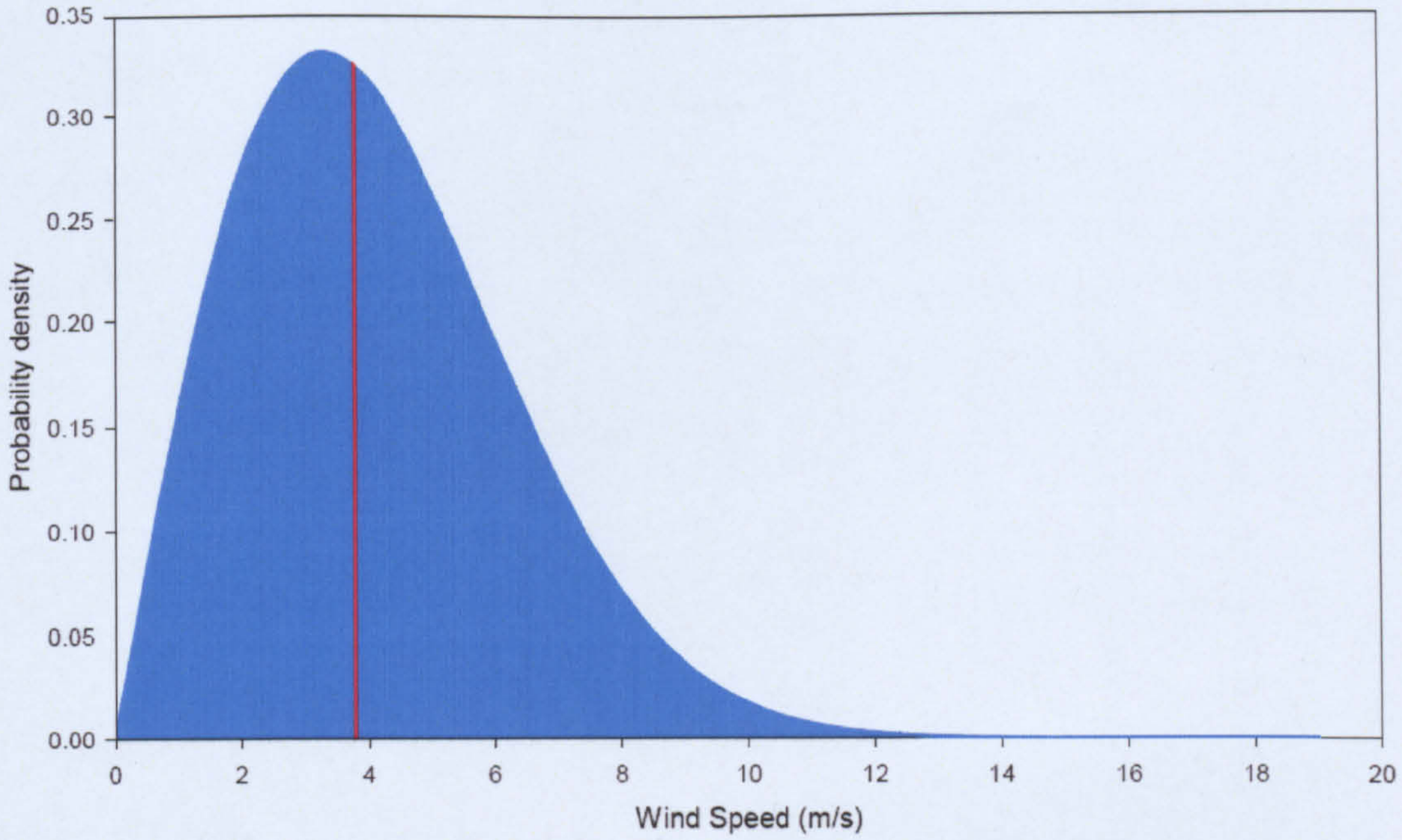

Figure 6.5.2.1 Sample wind velocity probability distribution plot.

Wind data needs to be processed before it can be used to predict wind velocity regimes over a period of time. The wind velocity frequency distribution is used to display the proportion of the time the wind blows at any given wind velocity. For example, if two sites are compared, at the first site the wind could blow at 10m/s continually through out the year. The mean wind velocity would be 10m/s. At the second site the wind regime may differ from the first site: the wind may blow at 20m/s for half of the year and in the second half of the year there may be no wind at all. Again the mean wind velocity would be 10m/s, suggesting that the two sites may have the same wind resource. In reality the two wind resources are very different and would require two different types of turbine to harness the wind energy of each site.

The first site would require a wind turbine with a maximum rated output at the mean wind velocity of 10m/s, whereas the second site would require a turbine with a rated output at 20m/s and not of the mean wind velocity of 10m/s.

Thus the wind speed probability distribution describes the time distribution of the wind's velocity. The area under the probability distribution seen in Figure 6.5.2.1 is equal to 1, as the probability that the wind is blowing with velocity including a velocity of zero is 100%.

If this area is divided into two equal halves along the x-axis, then the vertical line splitting the two areas would occur at a wind velocity of 3.8m/s. 50% of the time the wind velocity is less than 3.8m/s, and 50% of the time the wind velocity would be greater than 3.8m/s. This is known as the median of the distribution. The mean wind velocity for the figure is 5m/s. Note that the plot is skewed as a result of very high wind velocities which are very rarely observed. The most commonly observed wind velocity has the highest frequency; this is at 3.2m/s, which is known as the modal wind velocity.

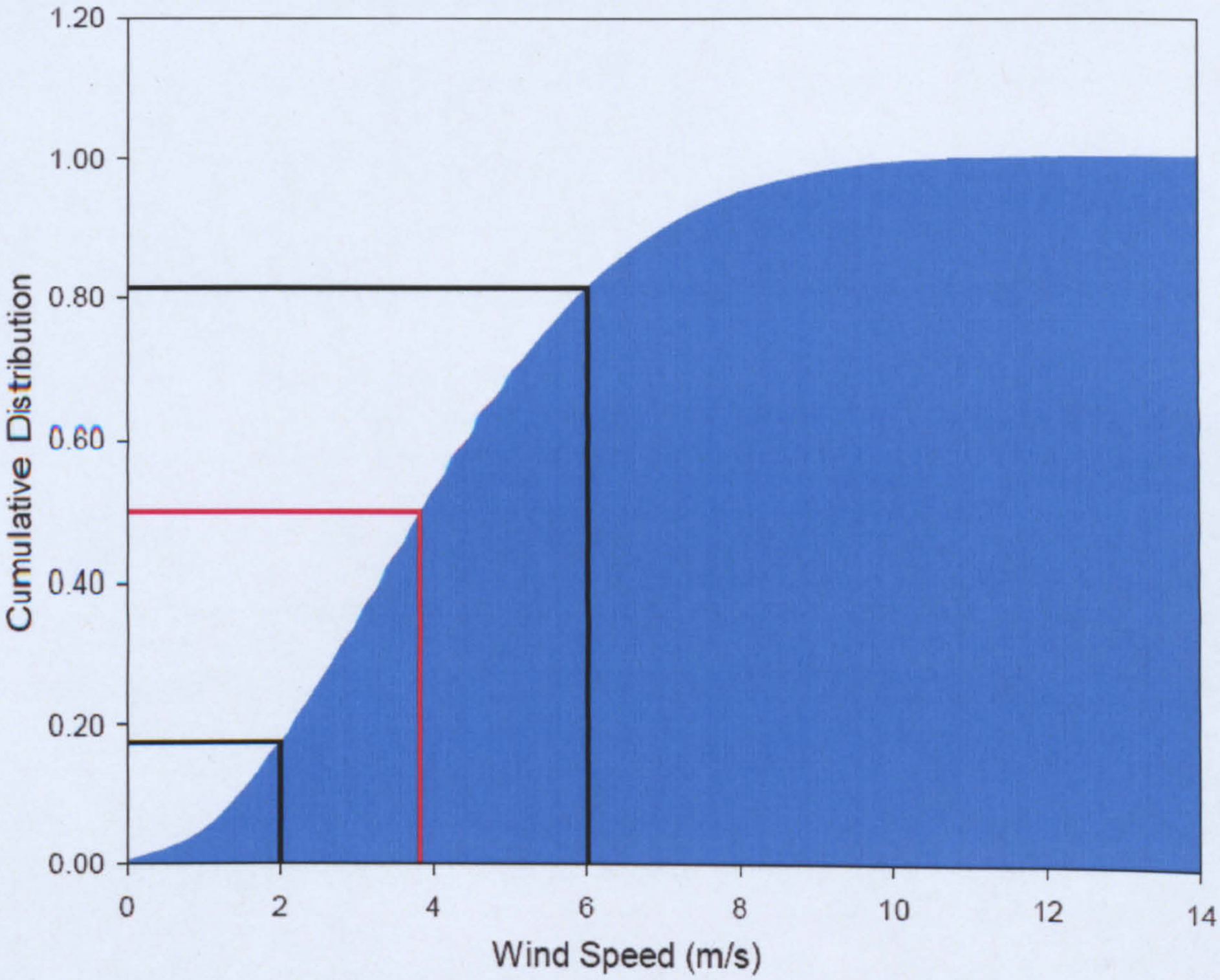

Figure 6.5.2.2 Sample cumulative distribution of wind velocity plot.

The cumulative distribution curve is another plot for presenting the wind velocity distribution, Figure 6.5.2.2. The plot shows measured wind velocity observations in order of wind velocity, which are equal or less than the interval velocity. It can be used to determine the frequencies of winds blowing within given limits. For example, 65% of winds velocities fall between 2m/s and 6m/s. The median wind velocity is also shown at 50% cumulative frequency, measuring 3.8m/s.

6.6 Statistical modelling of wind frequency distribution

Statistical wind frequency distribution models are used to give a representation of the wind velocity distribution for a given location. The advantage of fitting a statistical model to a measured dataset is that it enables the approximation of the measured wind regime characteristics to be represented with a few coefficients. Figure 6.6.1 shows a frequency distribution plot for a sample month's data. The Weibull and Rayleigh distributions have been fitted to the dataset.

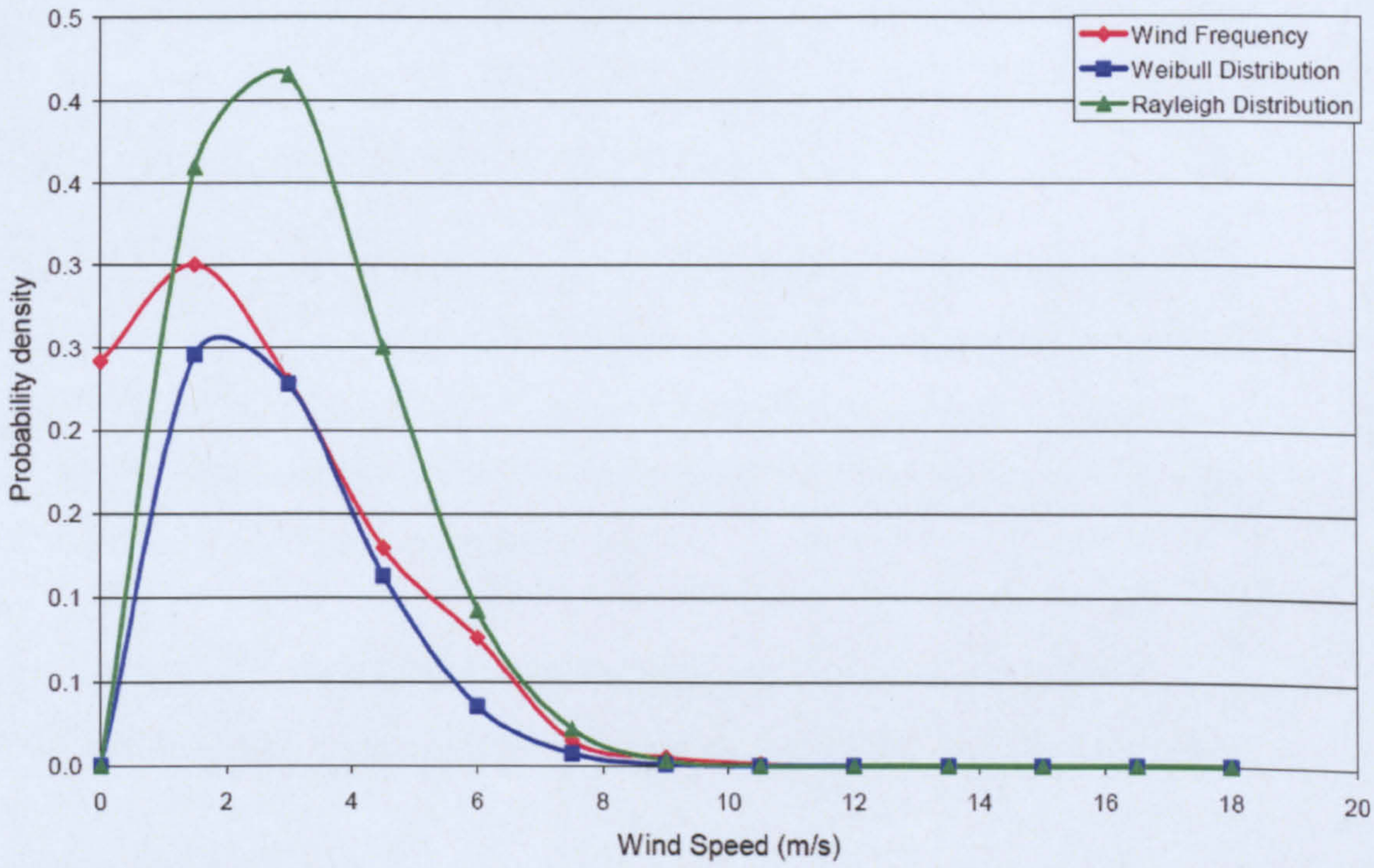

Figure 6.6.1 Sample wind velocity frequency distribution. Note measured distribution shown with Rayleigh and Weibull modelled distributions.

6.6.1 Weibull and Rayleigh distributions

There are two models commonly used by the wind industry to summarise wind regimes, the Weibull and Rayleigh distributions. The Weibull distribution has been derived from the Pierson Class Three distribution. The models represent wind velocity distributions as standard statistical functions. Both the Weibull and Rayleigh distributions have been found to present wind regimes with an acceptable degree of accuracy conforming well to the observed long-term distribution of wind velocities for an extensive range of locations (Sathyajith, 2006).

The Rayleigh distribution is the Weibull distribution where the shape factor is set to equal 2. It is used in circumstances where adequate wind datasets are not available yet long-term mean wind data is available, such as data from local meteorological stations. Thus the Rayleigh distribution can give a good approximation of the wind regime with minimal input data.

6.6.2 Determining Weibull distribution

The Weibull probability density function is used to approximate the wind velocity probability density distribution, expressing the probability $f(V)$ giving the fraction of time which the wind blows at a given frequency (Equation 6.6.2.1).

$$f(V) = \frac{k}{c}\left(\frac{V}{c}\right)^{k-1} \exp\left[-\left(\frac{V}{c}\right)^{k}\right] \qquad (6.6.2.1)$$

The shape factor, k, denotes the wind velocity distribution. A low value of k indicates a relatively broad wind velocity distribution, centred about the mean wind velocity, whereas a high value of k indicates a more narrow distribution about the mean wind velocity. Typically shape factors range from 1 to 3 for most sites. Scale factor is denoted as c.

The cumulative distribution of the wind speed is a function giving the probability of wind speed being equal or less than that of an interval wind velocity. The cumulative distribution is thus an integral of the probability density distribution. The Weibull cumulative distribution F(V) is given as Equation 6.6.2.2. Figure 6.6.2.1 shows a sample wind velocity cumulative frequency plot with the Weibull and Rayleigh functions fitted,

$$F(V) = \int_0^{\alpha} f(V)\, dV = 1 - \exp\left[-\left(\frac{V}{c}\right)^{k}\right] \qquad (6.6.2.2)$$

where the mean wind velocity can be expressed as Equation 6.6.2.3.

$$V_{mean} = c\ \Gamma\left(1 + \frac{1}{k}\right) \qquad (6.6.2.3)$$

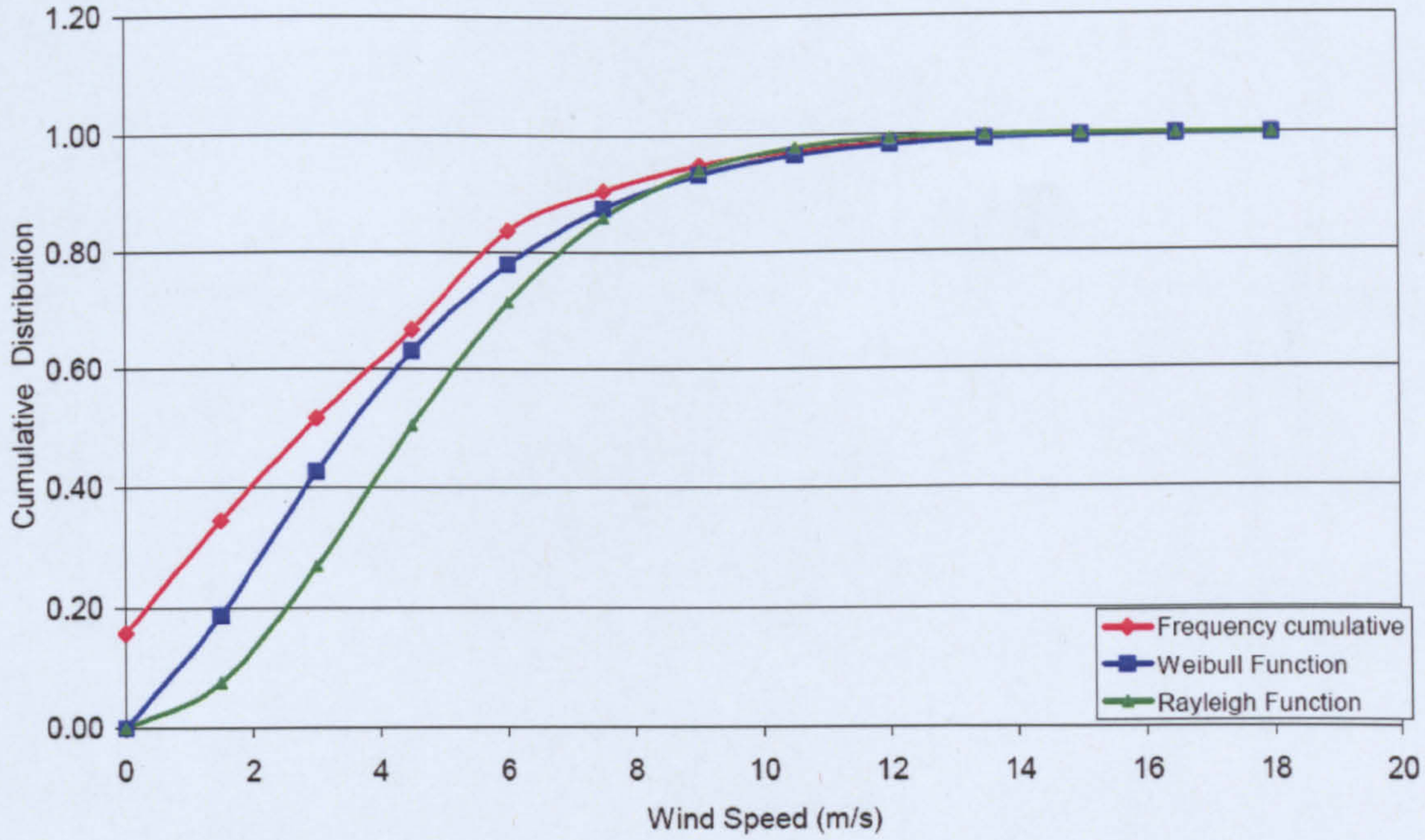

Figure 6.6.2.1 Sample wind velocity cumulative frequency distribution.

The cumulative distribution function can also be used to predict the frequency that the wind velocity blows within a given range, for example between the turbine's cut-in and cut-out speed which can be expressed as Equation 6.6.2.4.

$$P(V_1 < V < V_2) = \exp\left[-\left(\frac{V_1}{c}\right)^k\right] - \exp\left[-\left(\frac{V_2}{c}\right)^k\right] \qquad (6.6.2.4)$$

6.6.3 Estimating Weibull parameters

Before the Weibull distribution can be used, its parameters k and c have to be estimated from the observed measured wind speeds. These parameters can be estimated in a variety of different ways. The method chosen for use in the Windcalc software is the graphical method. This method does not require the use of the statistical gamma function, making programming the model a simpler task.

The graphical method estimates the Weibull coefficients by transforming the cumulative distribution function into a linear form by the use of logarithmic scales (Sathyajith, 2006). If the log of the cumulative distribution function is taken twice it becomes linear, as shown by Equation 6.6.3.1.

$$F(V) = 1 - \exp\left[-\left(\frac{V}{c}\right)^{k}\right] \tag{6.6.3.1}$$

1st log

$$\ln(1 - F(V)) = -\left(\frac{V}{c}\right)^{k} \tag{6.6.3.2}$$

2nd log

$$\ln(-\ln(1 - F(V))) = k\ln(V) - k\ln c \tag{6.6.3.3}$$

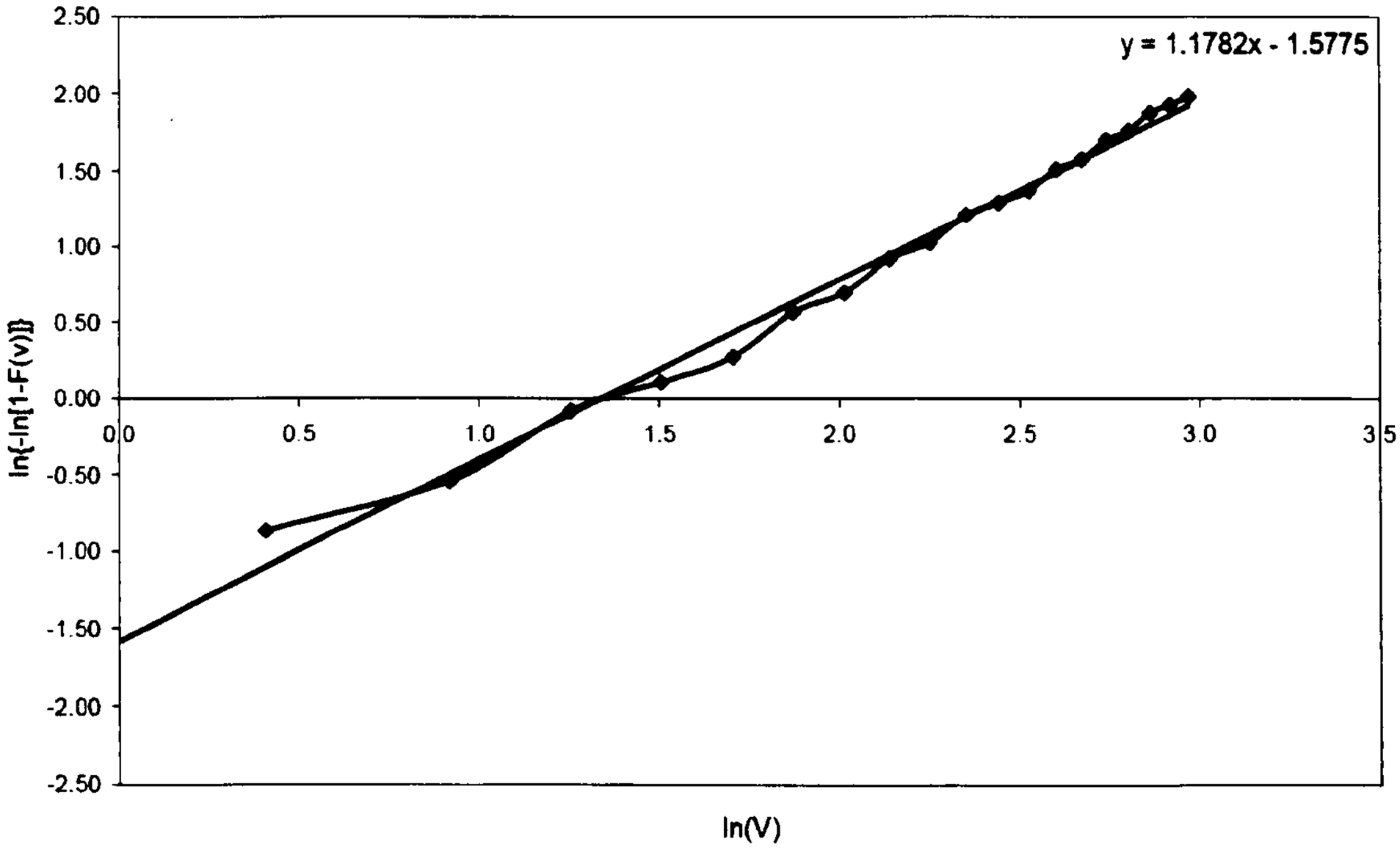

Figure 6.6.3.1 Graphical method to estimate Weibull k and c parameters.

Plotting this function with ln(V) produces a near-linear relationship. Shape factor k is given by the slope of the relationship and scale factor c can be obtained from –k ln c of the intercept.

6.6.4 Determining Rayleigh distribution

Taking the above-mentioned expression of mean wind velocity (Equation 6.6.2.4), and assuming shape factor k to equals 2, then this can be expressed as Equation 6.6.4.1.

$$V_{mean} = c\ \Gamma\left(1 + \frac{1}{2}\right) \tag{6.6.4.1}$$

The above expression can be rearranged and evaluated as Equation 6.6.4.2.

$$c = \frac{2V_{mean}}{\sqrt{\pi}} \tag{6.6.4.2}$$

This can then be substituted in the Weibull probability density function and the Weibull cumulative distribution function to give the Rayleigh frequency distribution, expressed as Equation 6.6.4.3.

$$f(V) = \frac{\pi}{2}\frac{V}{V_{mean}{}^2}\exp\left[-\left(\frac{\pi}{4}\left(\frac{V}{V_{mean}}\right)^2\right)\right] \tag{6.6.4.3}$$

The Rayleigh cumulative distribution is given as Equation 6.6.4.4.

$$F(V) = 1 - \exp\left[-\left(\frac{\pi}{4}\left(\frac{V}{V_{mean}}\right)^2\right)\right] \tag{6.6.4.4}$$

The Rayleigh cumulative distribution function can also be used to predict the frequency of the wind velocity within a given range. For example, between the turbine's cut-in and cut-out speed, given as Equation 6.6.4.5.

$$P(V_1 < V < V_2) = \exp\left[-\left(\frac{\pi}{4}\left(\frac{V}{V_{mean}}\right)^2\right)\right] - \exp\left[-\left(\frac{\pi}{4}\left(\frac{V}{V_{mean}}\right)^2\right)\right] \tag{6.6.4.5}$$

6.6.5 Wind roses

Along with wind velocity, it is also important to measure wind direction for a site, as wind direction can play a significant role in determining power output. A consideration of wind direction can also be used to determine the turbidity of the wind. If the wind direction varies with high frequency then it can be said that the wind is turbulent. This affects the turbine in two ways. If the turbine direction has to continually change to stay facing into the wind its overall energy output is reduced. This is because there is a time lag between the change of wind direction and turbine direction. This is due to the mass and inertia of the turbine and rotating blades, which oppose the force changing the turbine's direction. The turbines blades decelerate as the turbine turns to the wind's new direction, reducing power output. The second reason is the rapid change in load forces acting on the turbine, and the magnitude and frequency of stress cycles increasing fatigue failure rates.

Wind roses can be used to display four different parameters: frequency, velocity, power and energy, as shown in Figure 6.6.5.1. It should be noted that for all four wind roses seen in Figure 6.6.5.1 were recorded at the same site for the same period. The frequency and velocity roses are the most important of the wind roses. These can be used to derive both power and energy for any given turbine. The frequency rose shows the time frequency of the wind blowing in each direction but it does not give the magnitude of wind velocity. The prevailing wind for a site is the wind which is seen most commonly. However the prevailing wind may not yield the largest degree of energy. The velocity rose shows the average wind velocity received from each direction. For example, the highest velocity winds blow from the west-north-westerly direction for the Edinburgh Napier University site. The power rose is directly dependant on wind velocity rose and the turbine blades swept area. Finally the energy rose is possibly the most useful of all the wind roses; it presents the available energy within the wind of given swept area with each direction. It is a combination of both wind frequency and wind power roses. Note that, for this study, the swept area used to calculate the power and energy roses was based on a swept area of 1.8 meters diameter, as used by the Zephyr Airdolphin turbine.

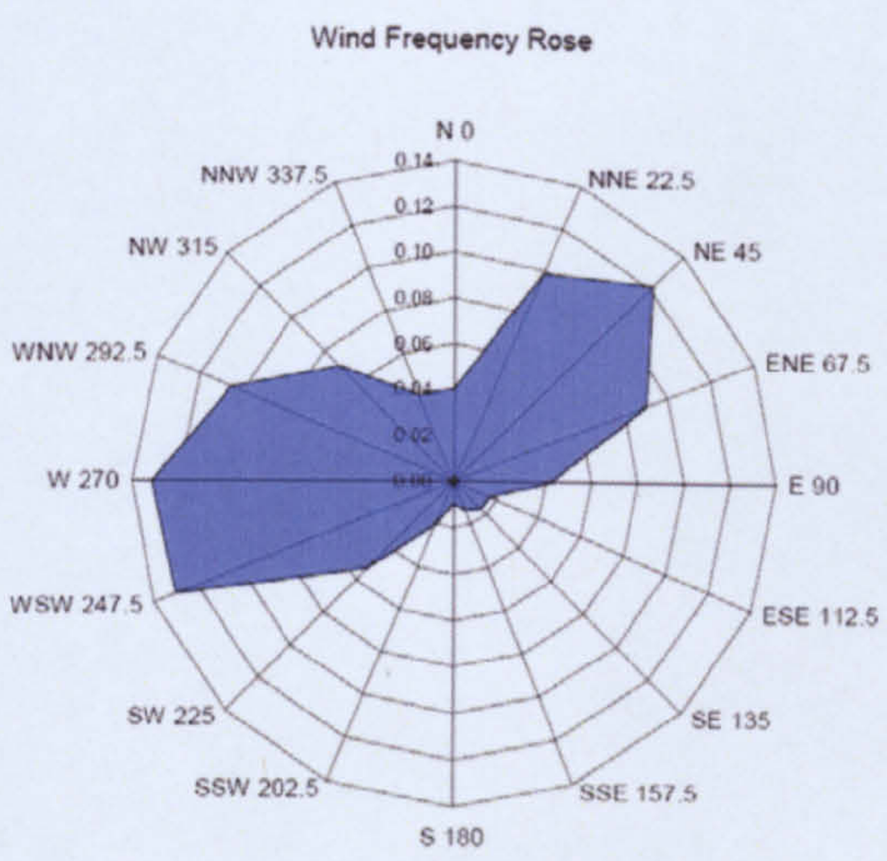

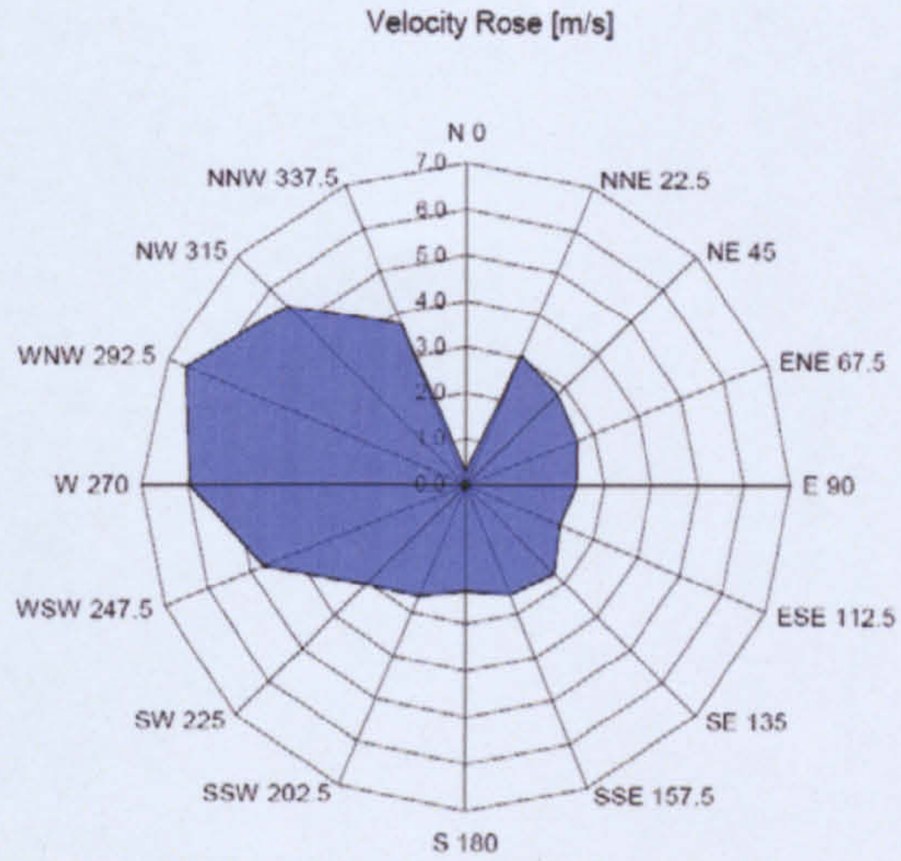

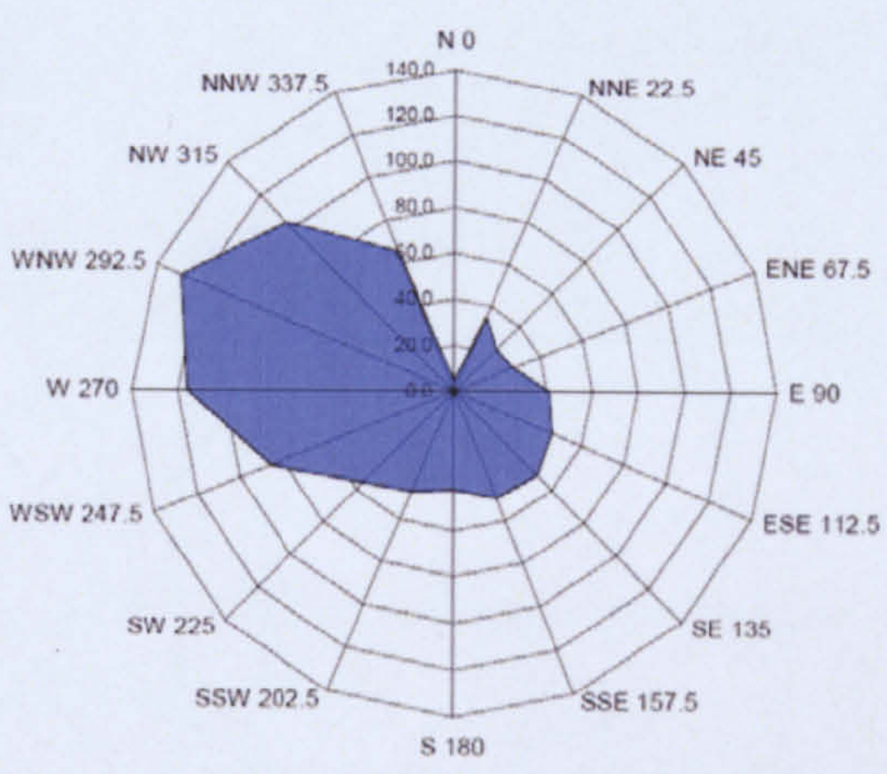

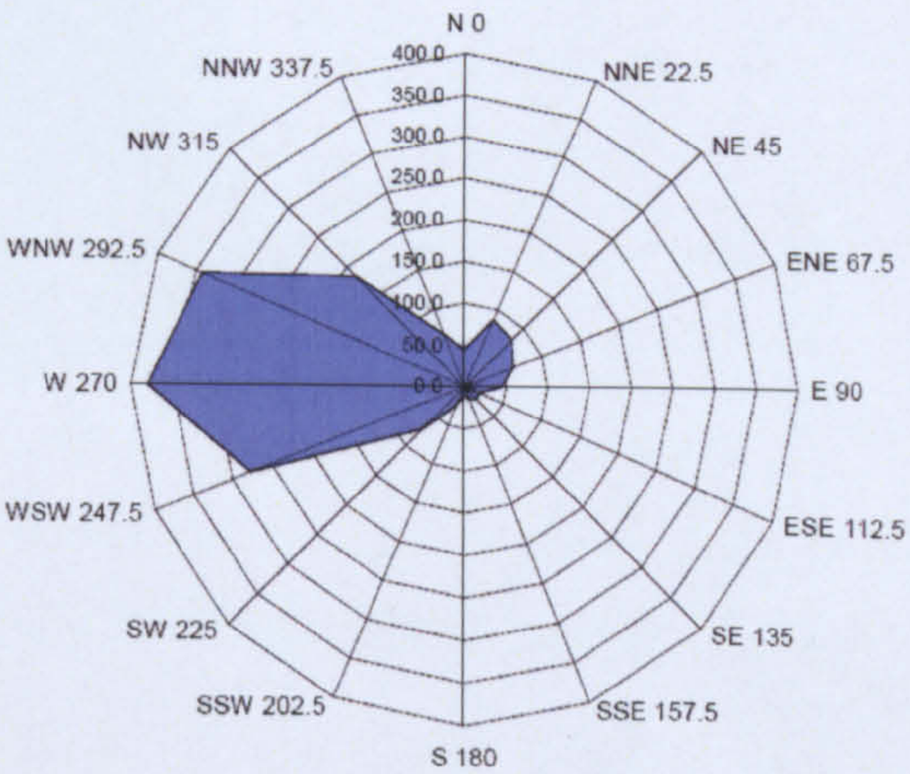

Figure 6.6.5.1 Wind roses, Edinburgh Napier University (January 2008).

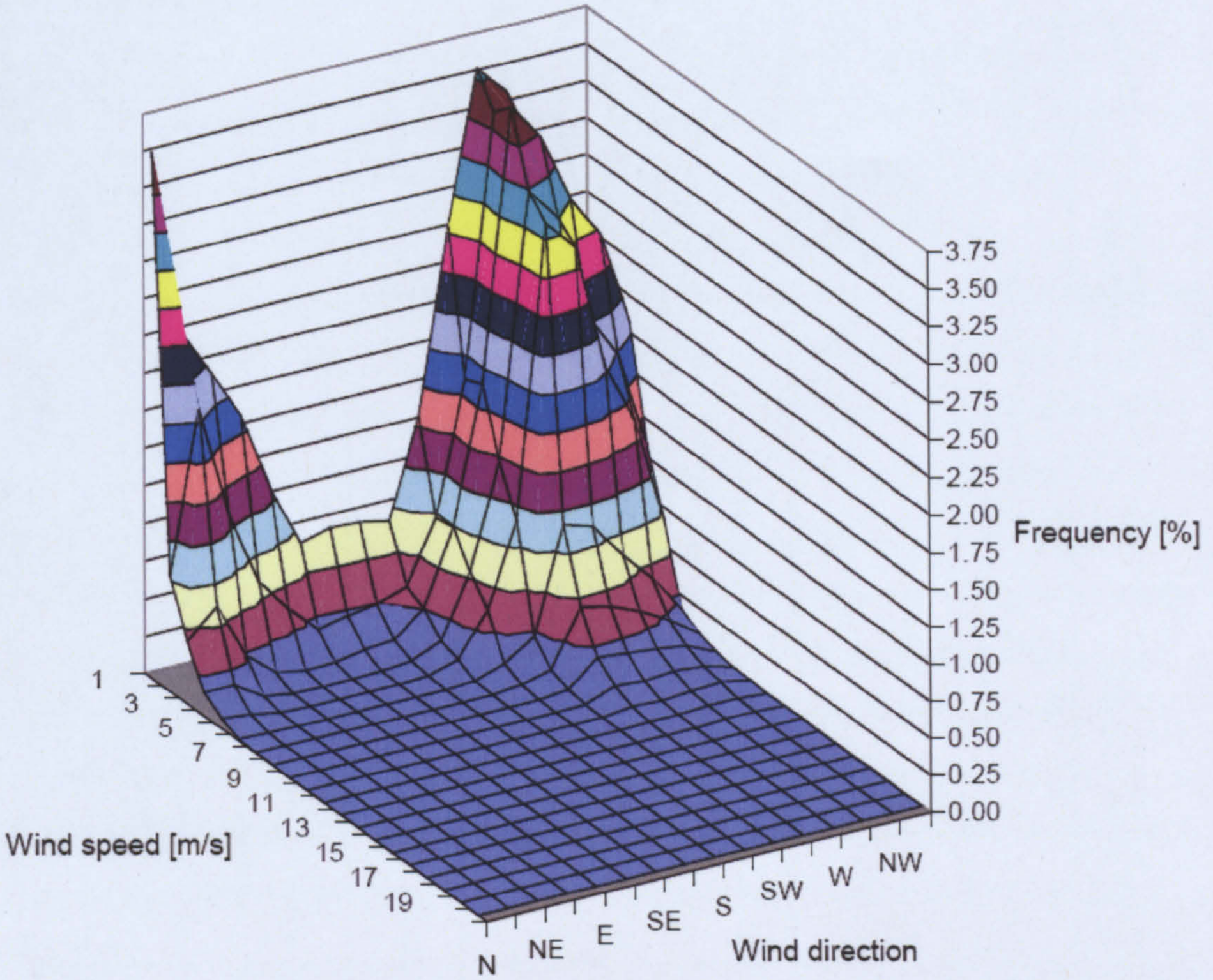

Figure 6.6.5.2 Three-dimensional wind distribution plot, Edinburgh Napier University (January 2008).

The three-dimensional wind distributional plot was produced for this study to display the full wind regime on a single plot, shown in Figure 6.6.5.2. The plot was developed to show the wind velocity, frequency distribution and direction. After reviewing the Ampair turbine's performance at the Edinburgh Napier University site, it was found that the turbine's energy output did not compare well to the energy output rose. This is because of the time required for the inverter to grid-connect before energy can be exported. Therefore wind frequency is a determining factor in energy output.

6.7 Windcalc software

Windcalc is a software package which has been developed as a part of this study to monitor the performance of micro-turbines as well as to determine local wind characteristics. The majority of the rooftop wind turbines installed throughout the UK have not met their performance claimed by the manufacturers. This is partly due to the turbines being installed in poor locations with low wind velocities; it is also due to the lack of available wind data for urban locations, which is required for their design. The majority of turbines which are on the market have been designed to suit typical wind velocity distributions found in rural areas and not for urban areas where the wind resource is greatly reduced. In reality, wind velocity and frequency distributions of urban areas are very different to those of rural locations. Therefore micro-turbines need to be designed accordingly to harness the available winds with maximum efficiency. The Windcalc software package contains two programs. The first program is designed to process the raw data which is then used by the second program to produce the wind report; both programs haven been developed in Microsoft Excel VBA.

The first program, named "Wind Data Processor", has been designed to handle very large high resolution datasets in a range of different file formats. For the Edinburgh Napier University trial, wind velocity and direction data was recorded with a sample rate of four seconds, and the Airdolphin turbine outputs with a sample rate of one second. The wind data is recorded in weekly files, whereas the turbine data is recorded into individual daily files. The program is designed to automatically combine both datasets with minimal human intervention. Firstly the program splits the datasets into individual daily files while also checking for missing data. The program then averages the second-by-second turbine data over the same time period as the wind data. The datasets can then be merged together to form one single dataset. For any period where both datasets are missing this data is omitted from the final dataset.

The Windcalc program itself is then used to process and manipulate the data into a more useful and useable format. The produced output report contains a range of figures such as wind distributions and wind roses. The report also includes statistical analysis on the turbine's performance. Figure 6.7.1 shows all the functions which the Windcalc software can carry out on data.

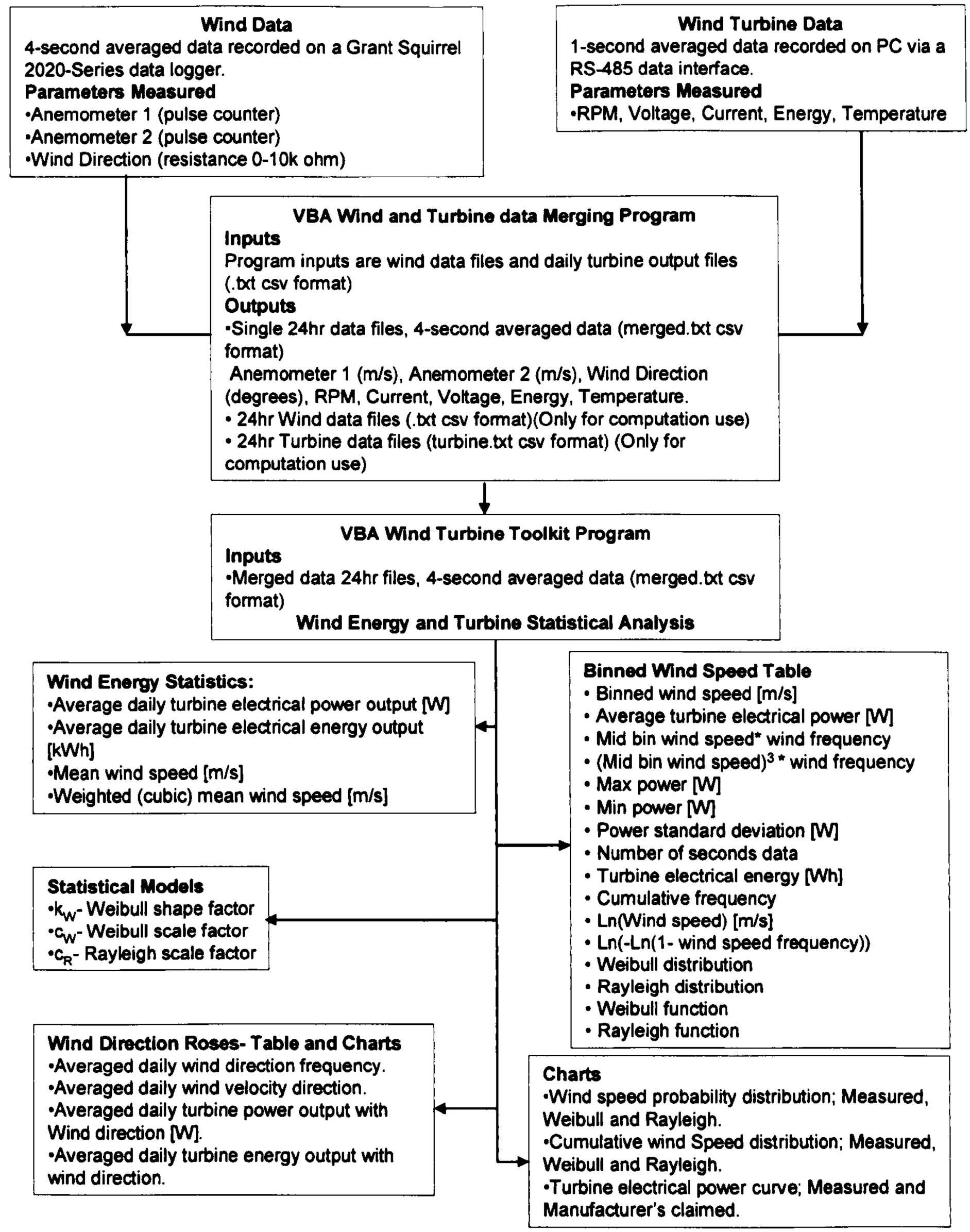

Figure 6.7.1 Windcalc software outputs.

6.8 Results

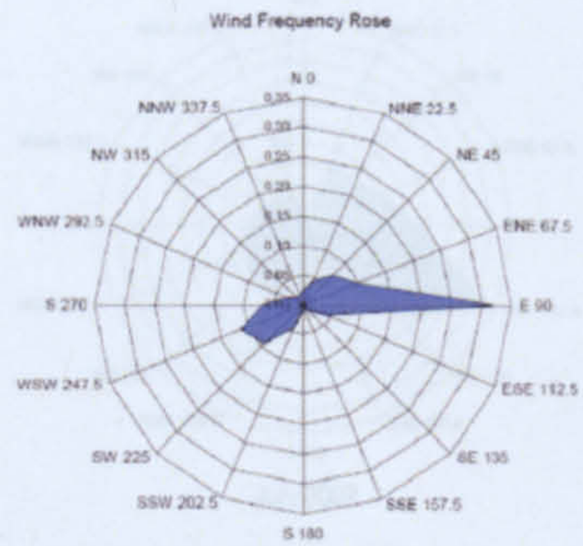

July 2007

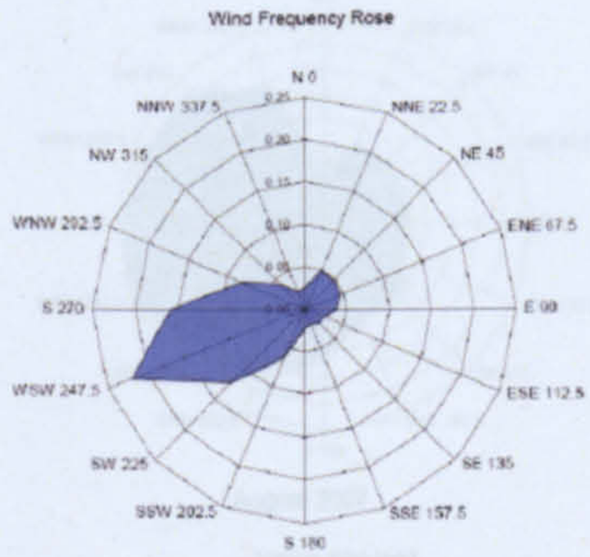

August 2007

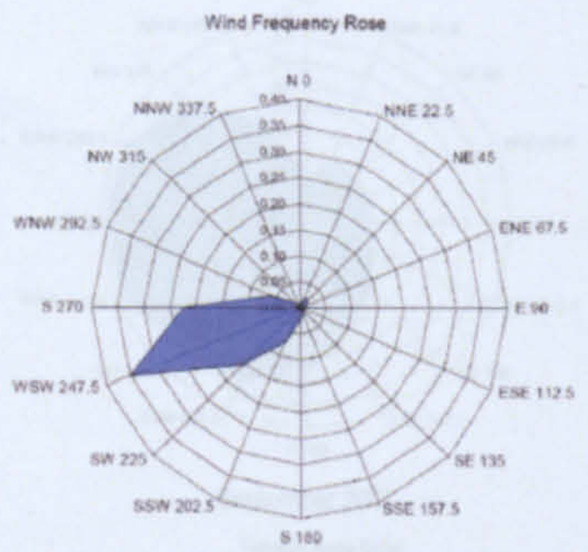

September 2007

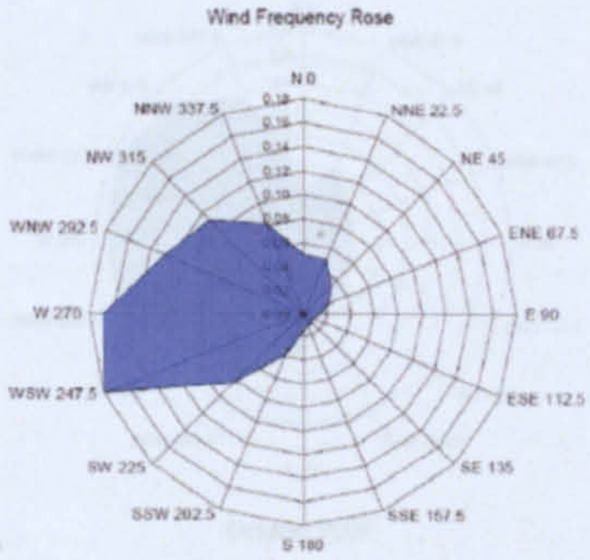

October 2007

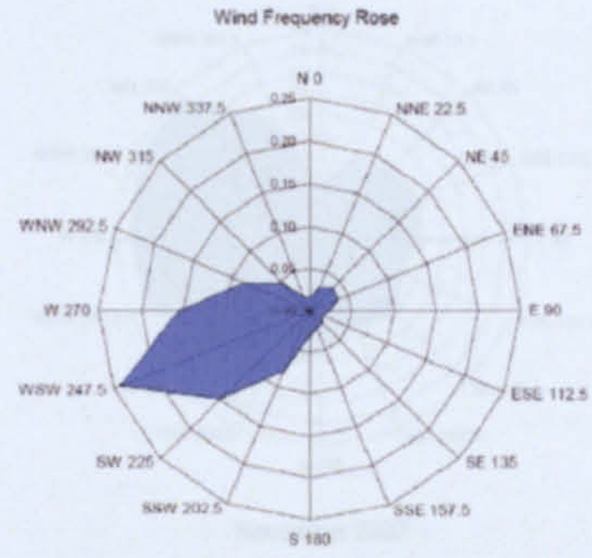

November 2007

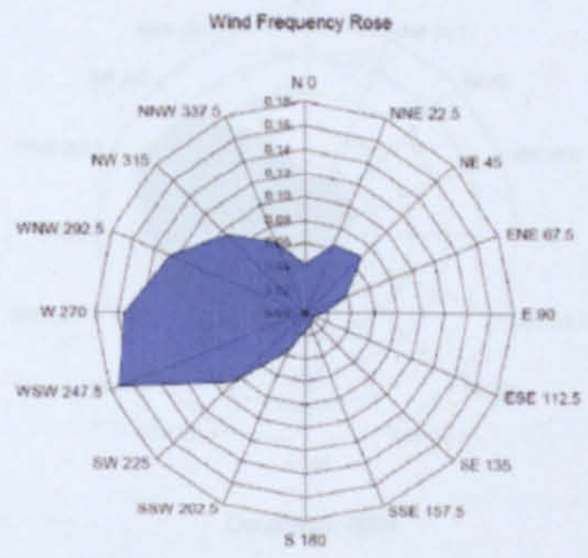

December 2007

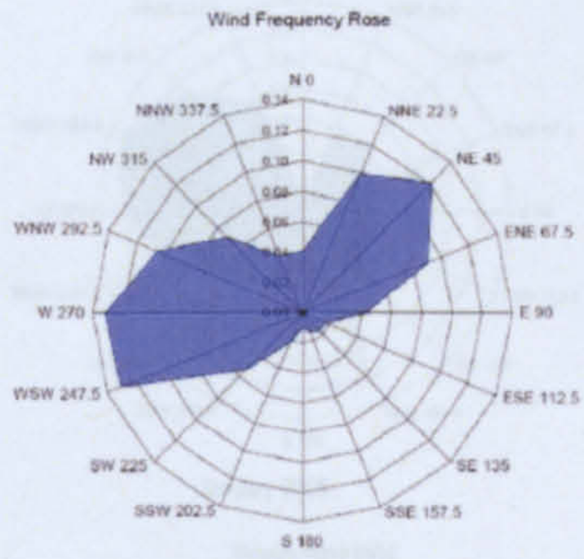

January 2008

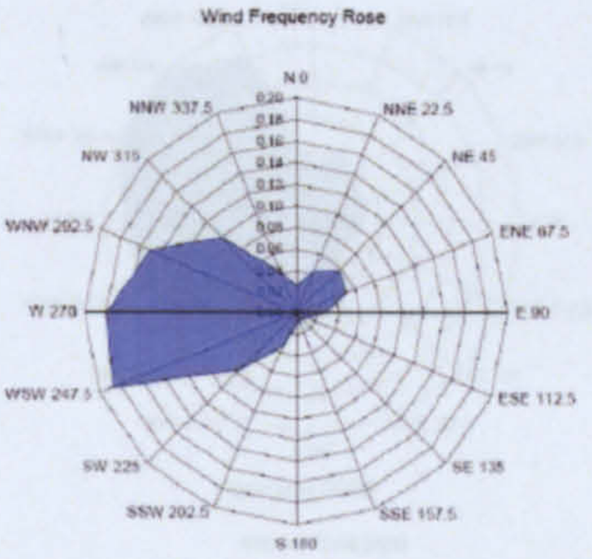

February 2008

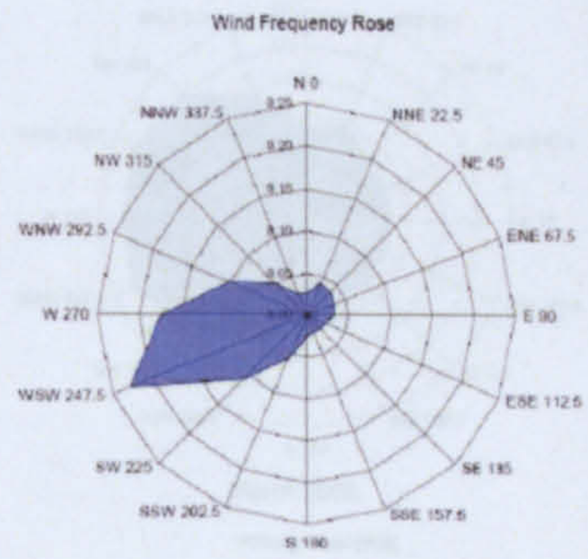

March 2008

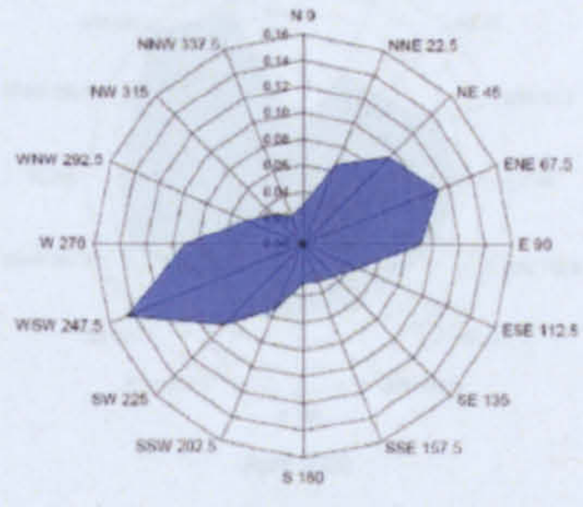

April 2008

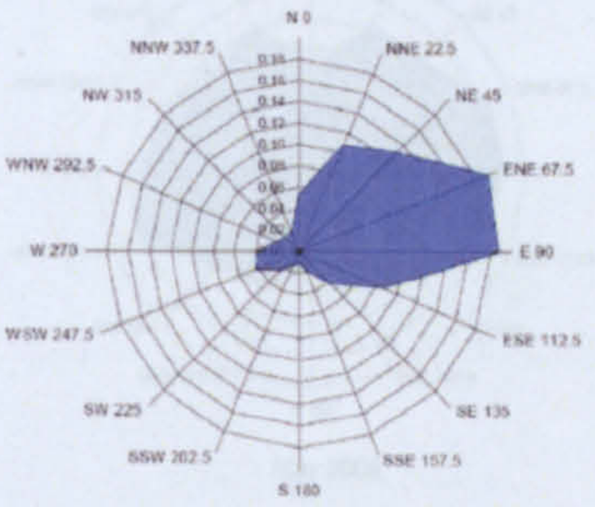

May 2008

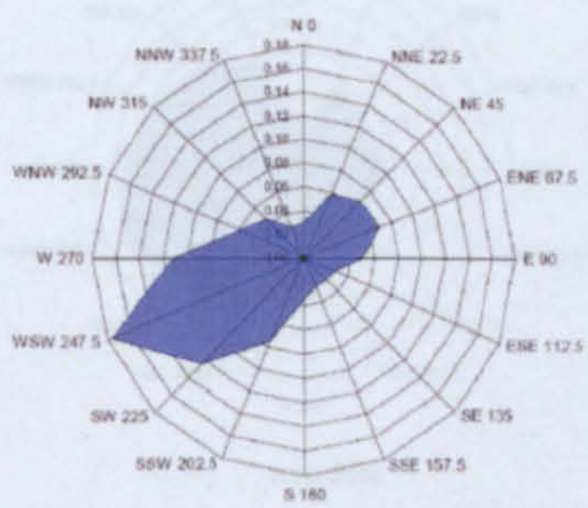

June 2008

Figure 6.8.1 Monthly frequency roses Edinburgh Napier University.

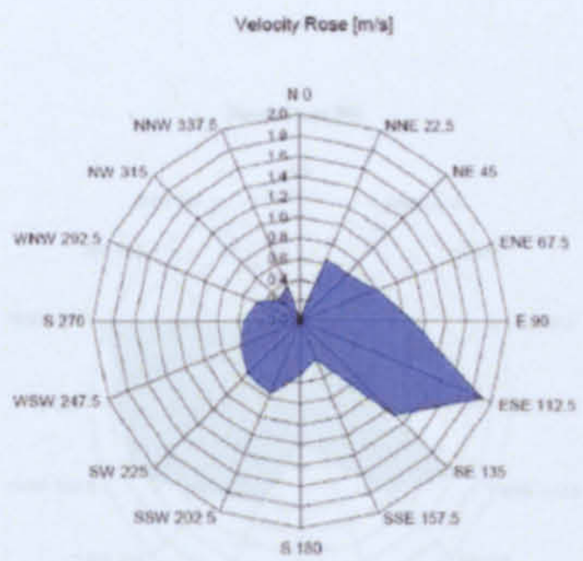

July 2007

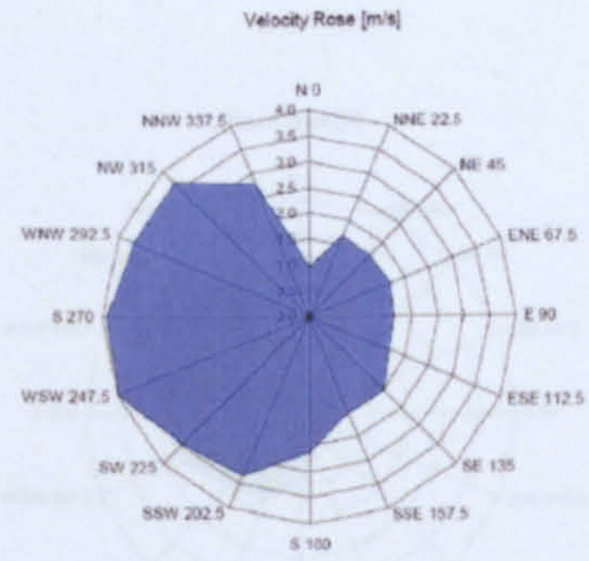

August 2007

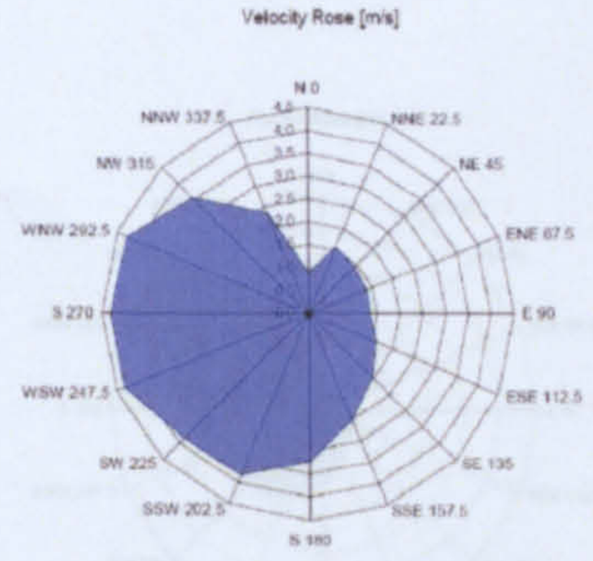

September 2007

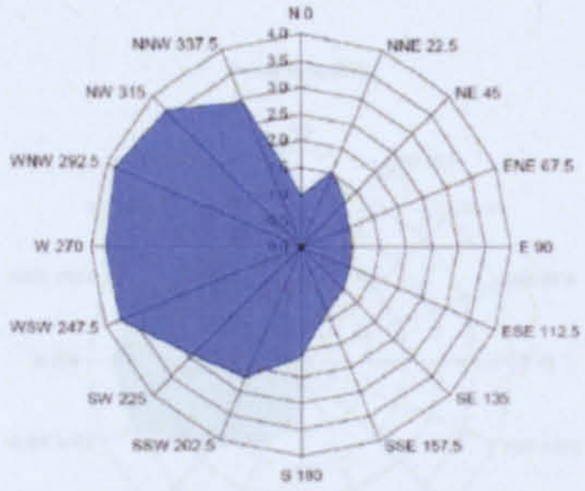

October 2007

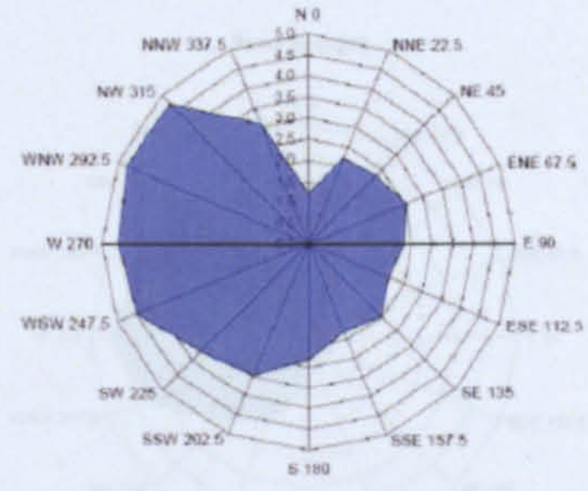

November 2007

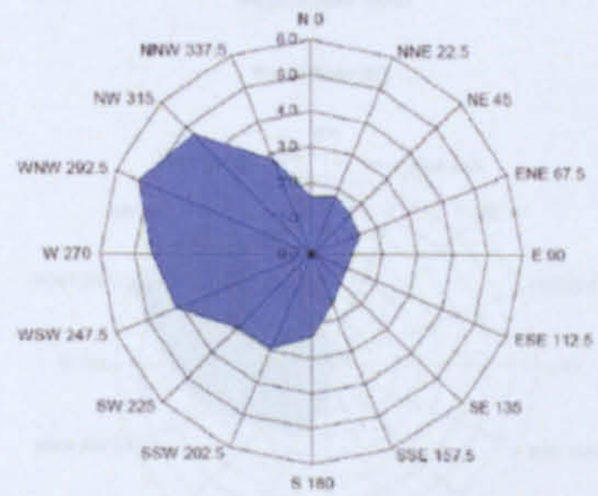

December 2007

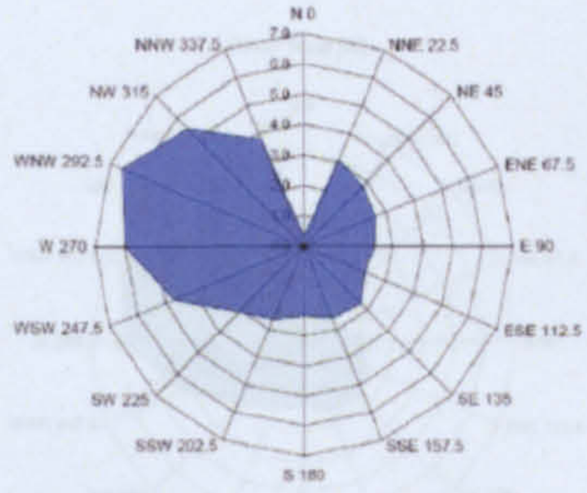

January 2008

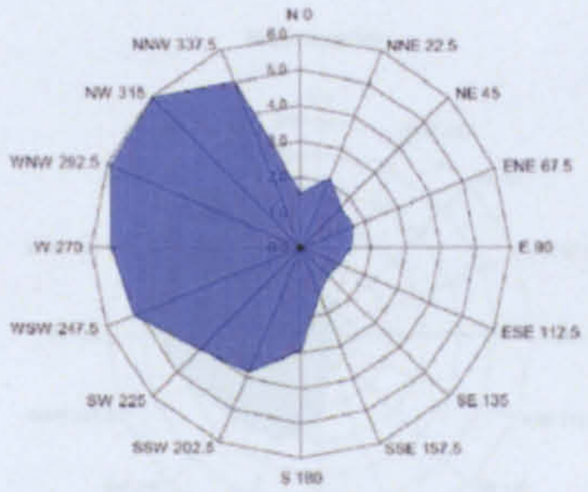

February 2008

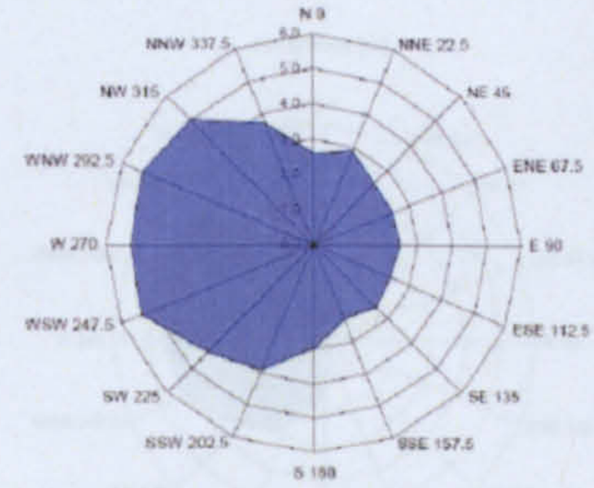

March 2008

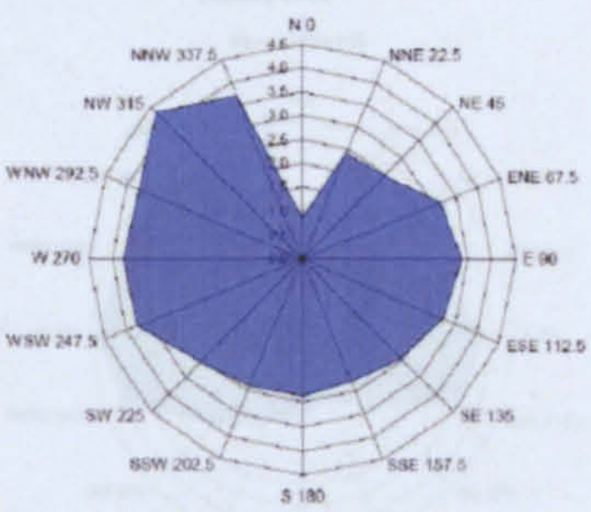

April 2008

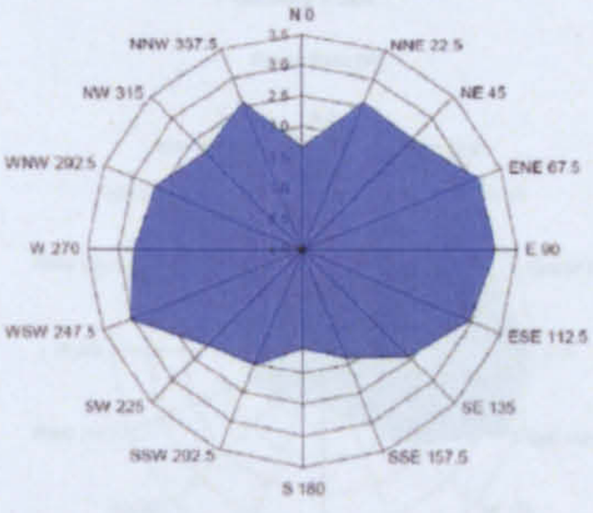

May 2008

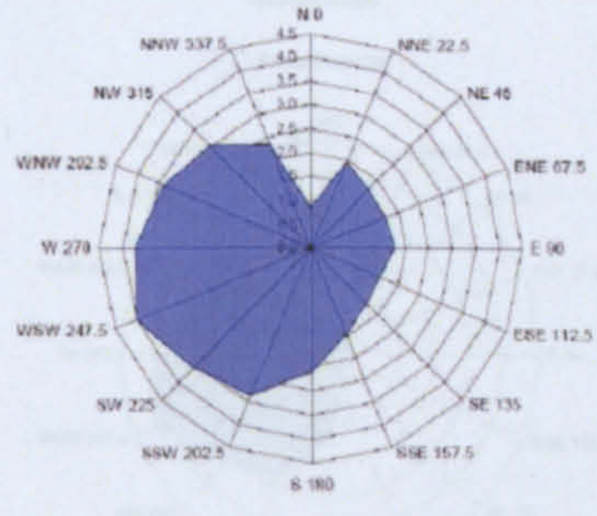

June 2008

Figure 6.8.2 Velocity wind roses Edinburgh Napier University.

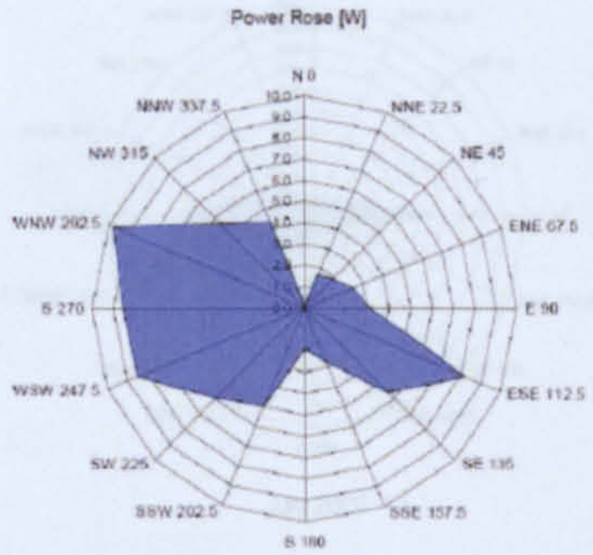

July 2007

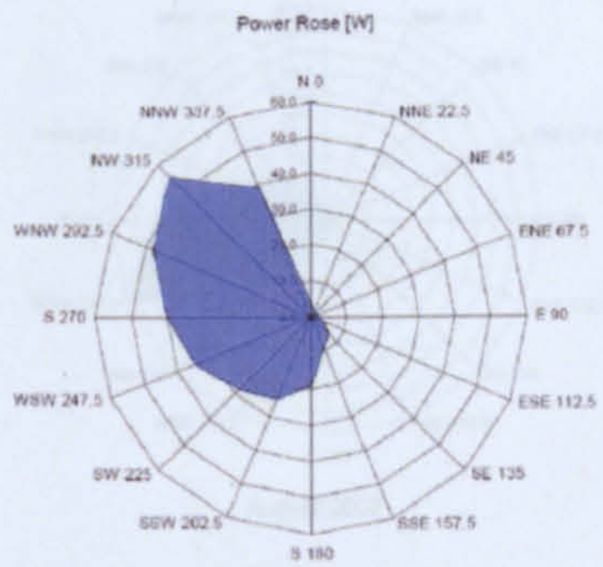

August 2007

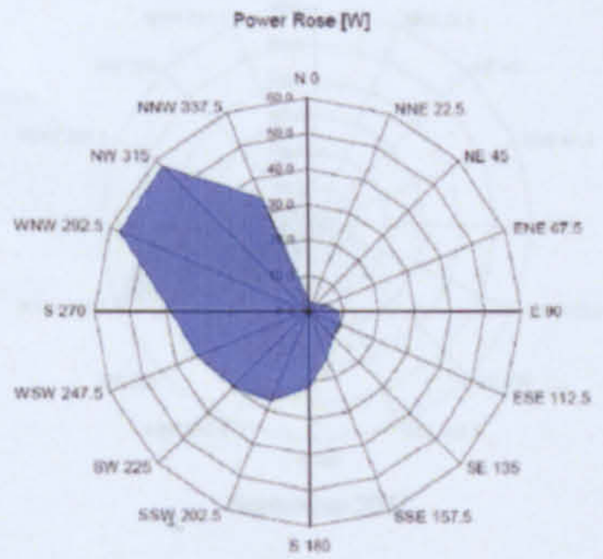

September 2007

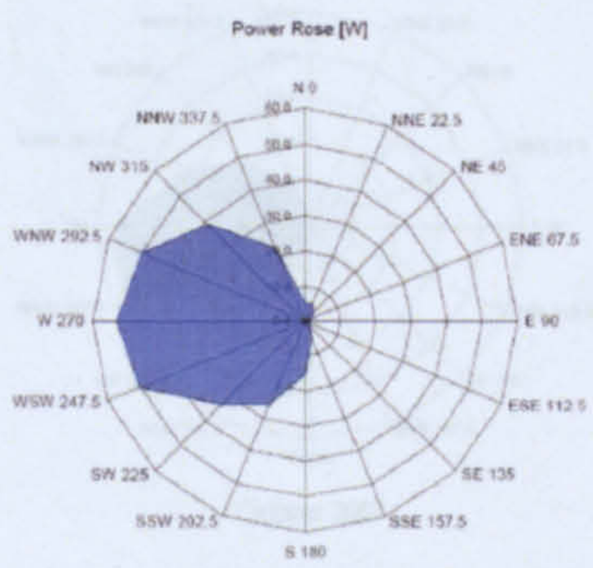

October 2007

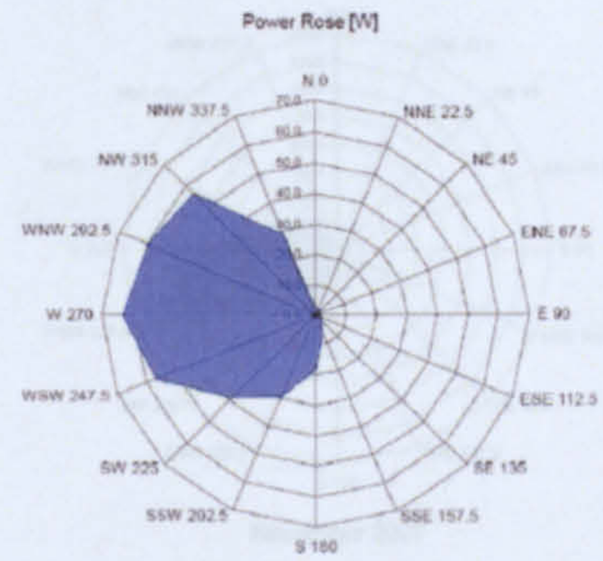

November 2007

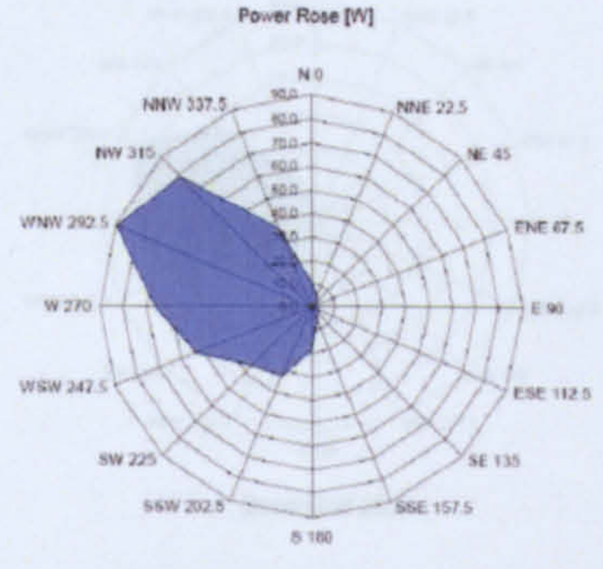

December 2007

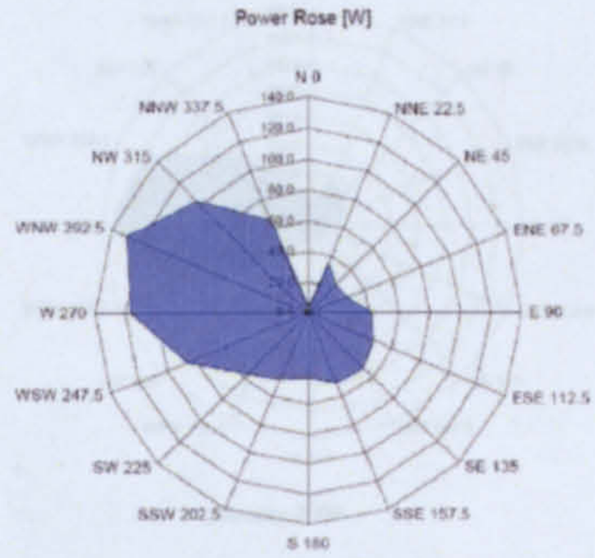

January 2008

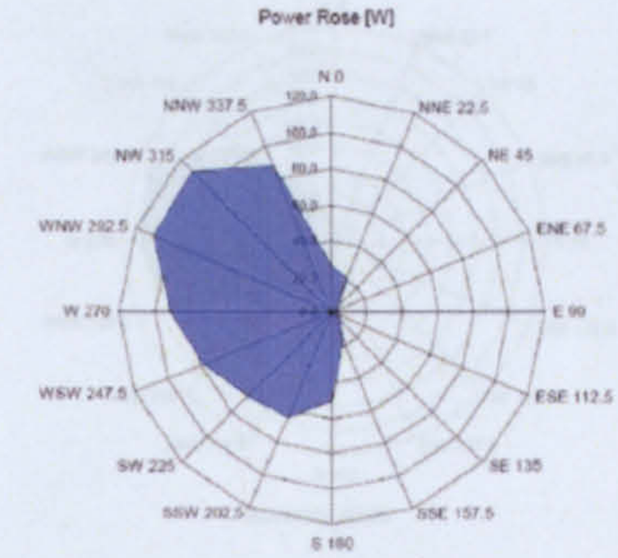

February 2008

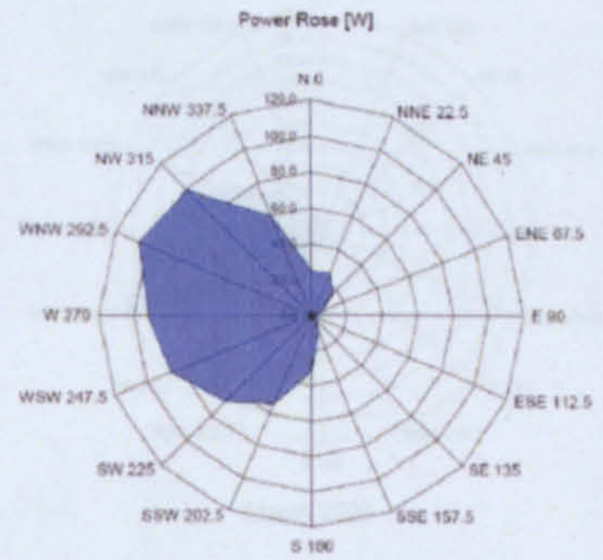

March 2008

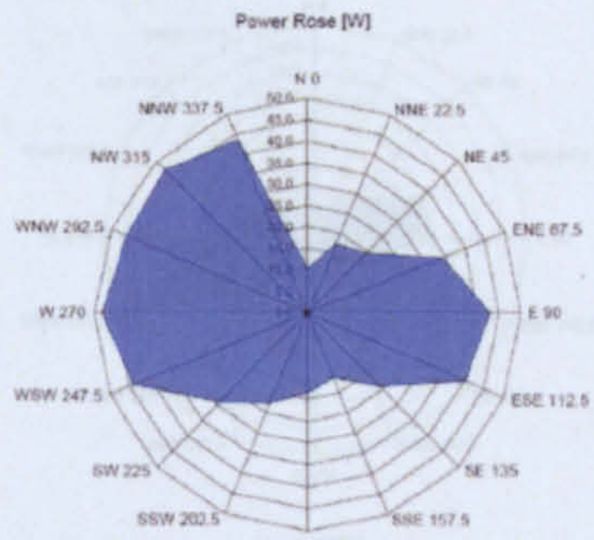

April 2008

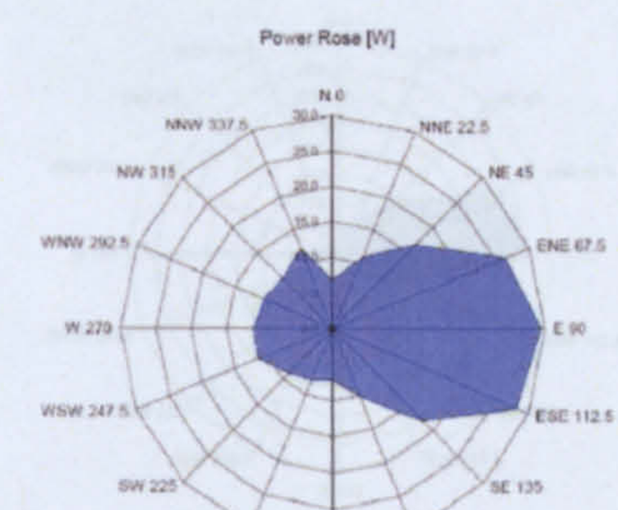

May 2008

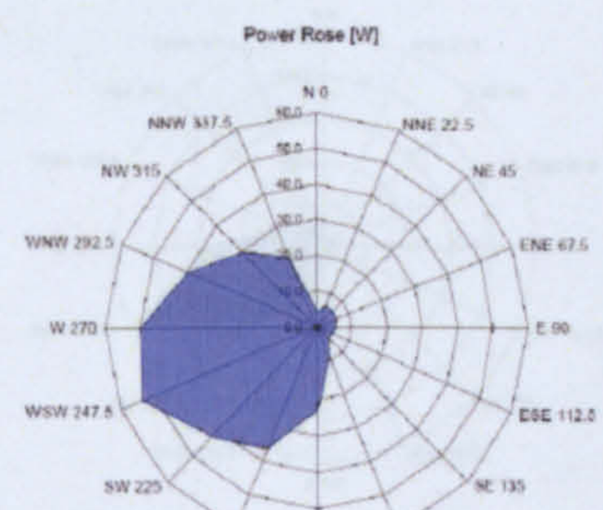

June 2008

Figure 6.8.3 Wind power roses for Airdolphin turbine Edinburgh Napier University.

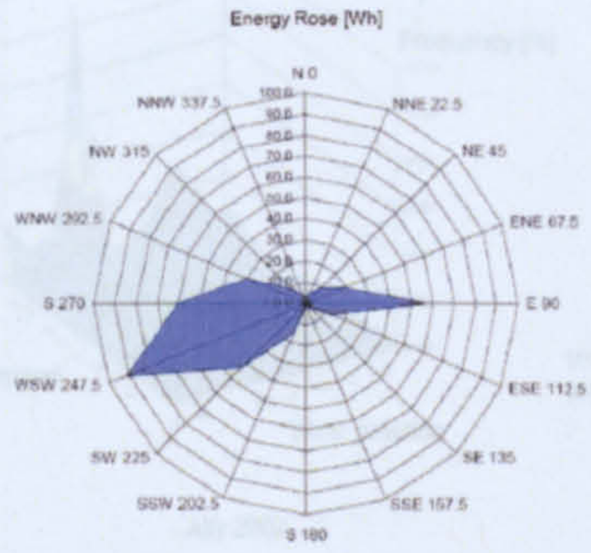

July 2007

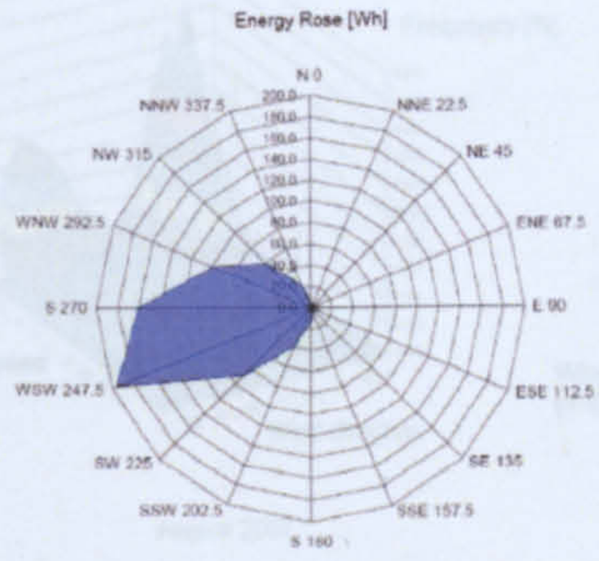

August 2007

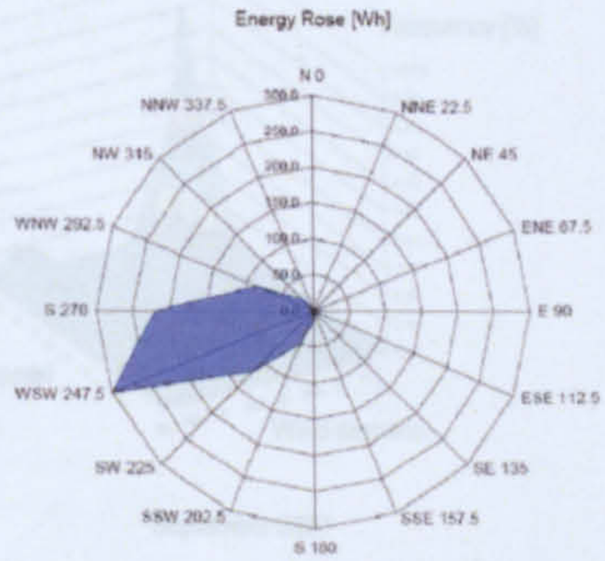

September 2007

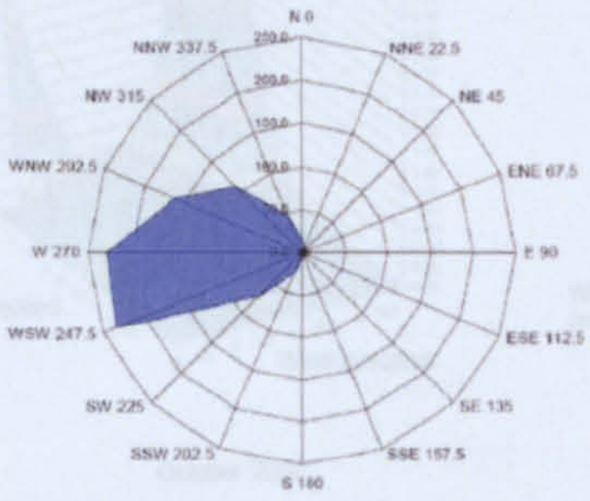

October 2007

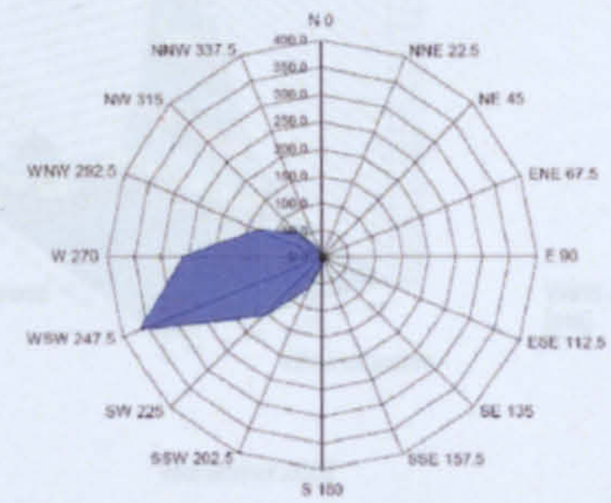

November 2007

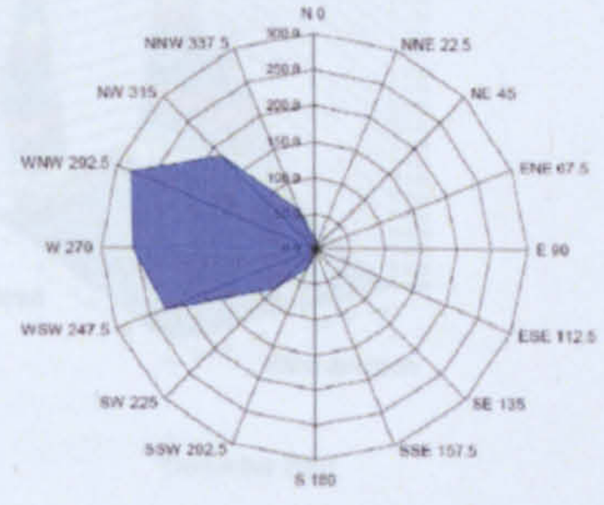

December 2007

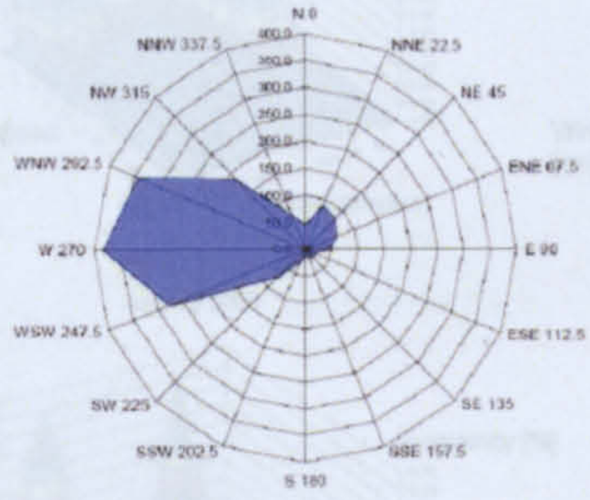

January 2008

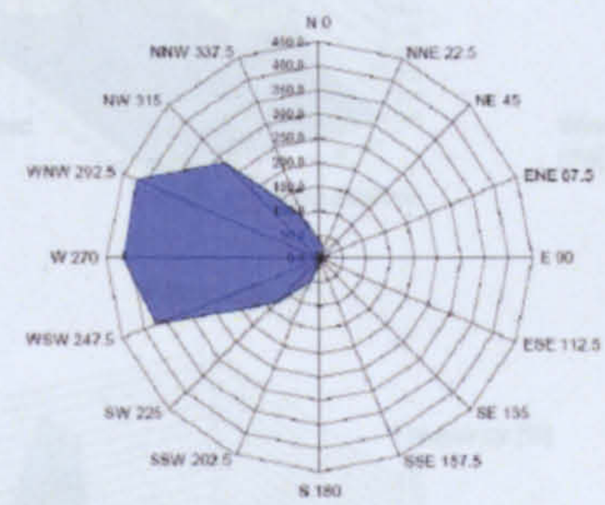

February 2008

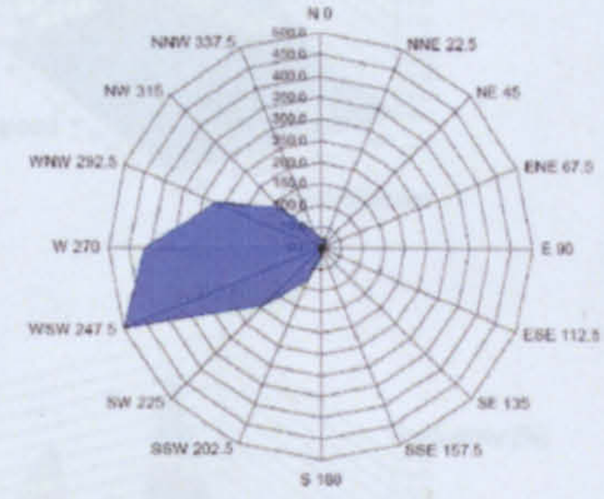

March 2008

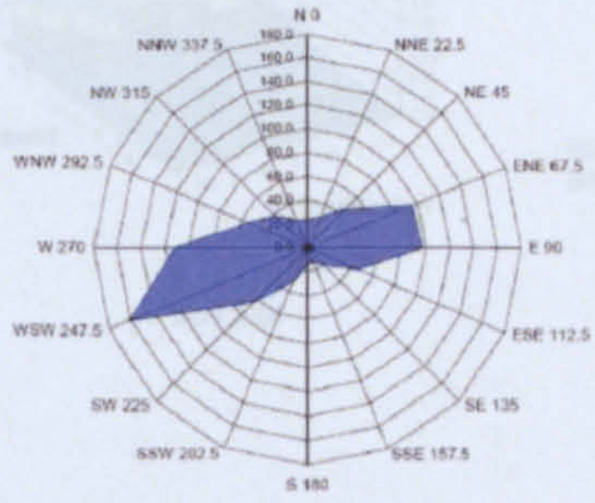

April 2008

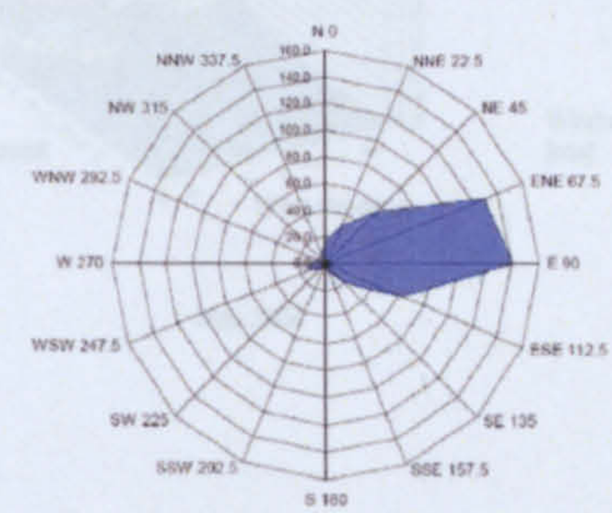

May 2008

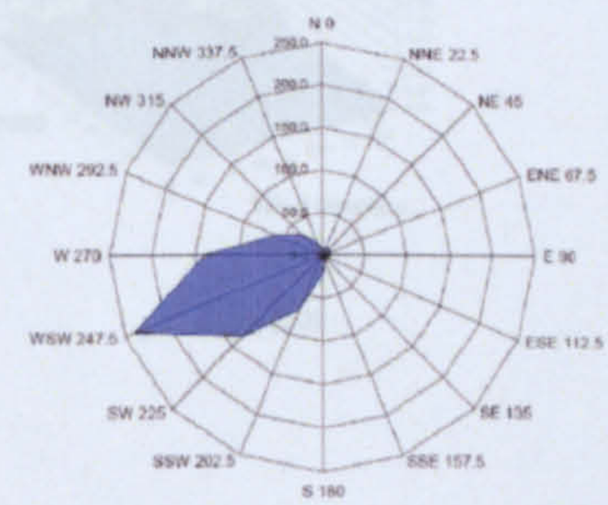

June 2008

Figure 6.8.4 Energy roses for Airdolphin turbine Edinburgh Napier University.

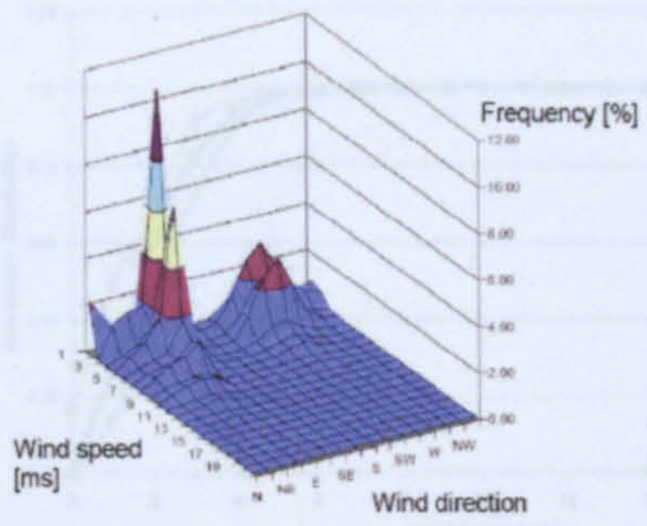

July 2007

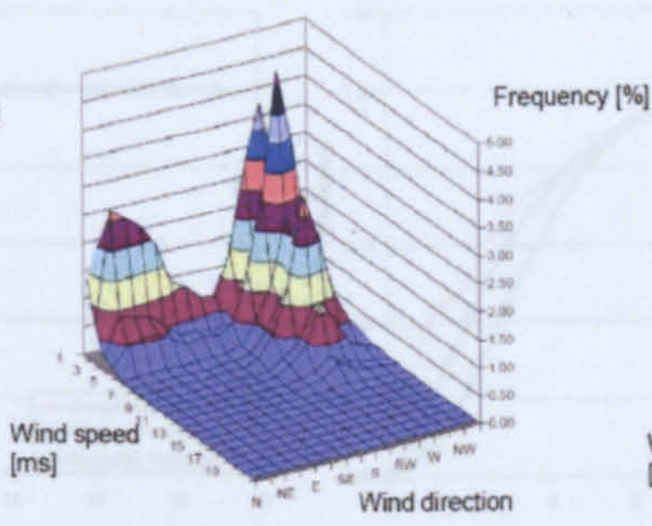

August 2007

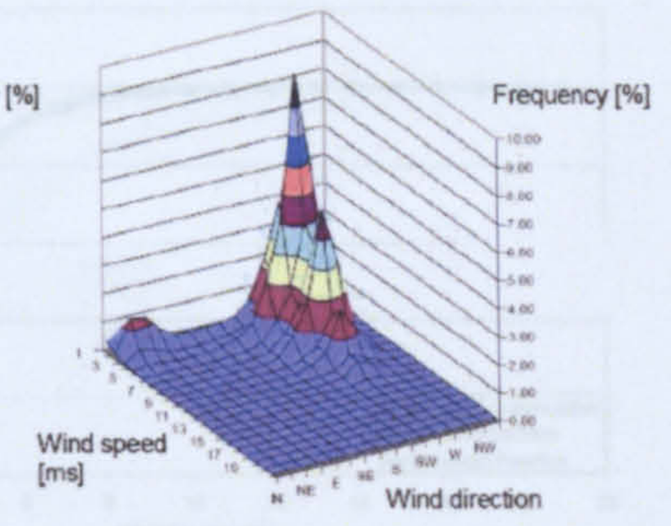

September 2007

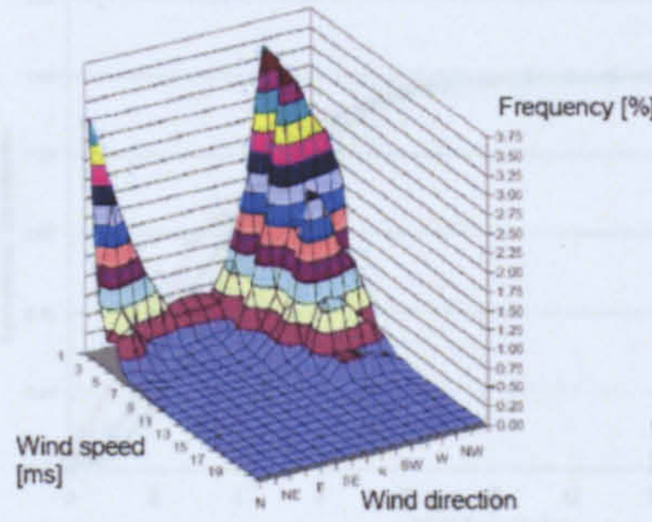

October 2007

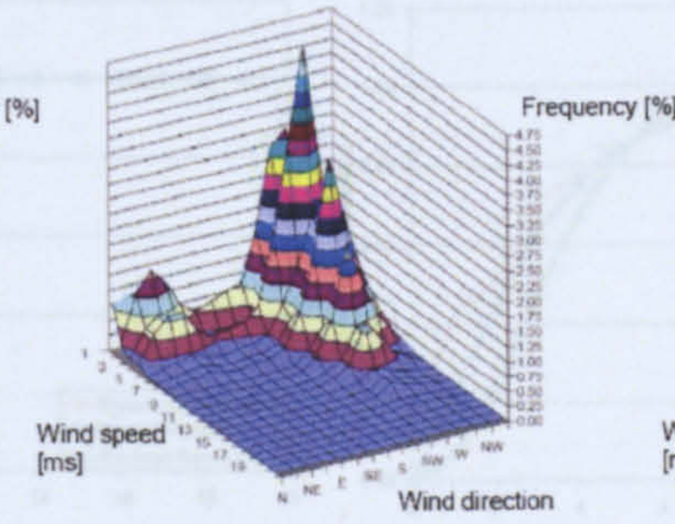

November 2007

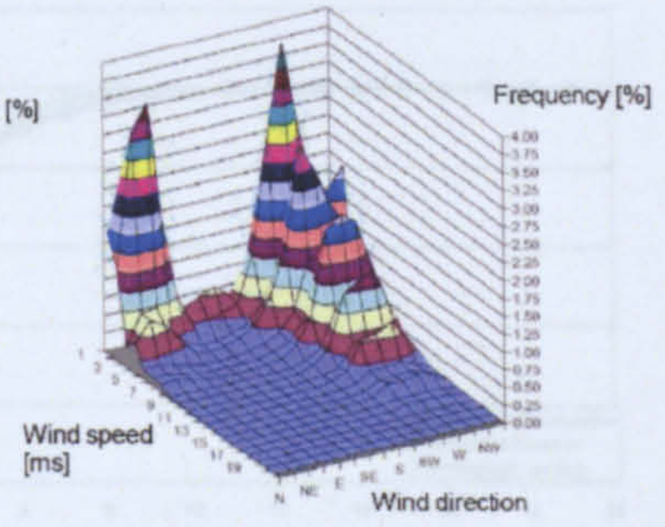

December 2007

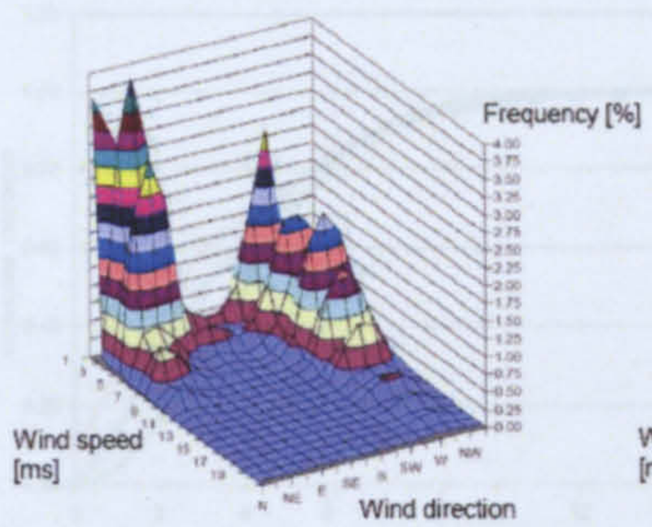

January 2008

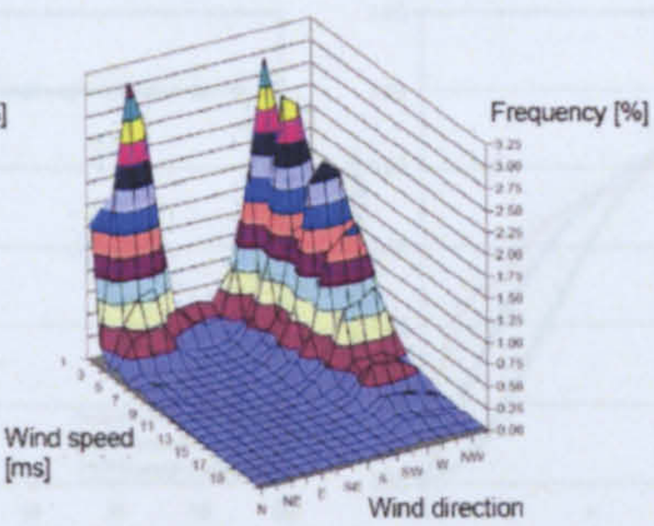

February 2008

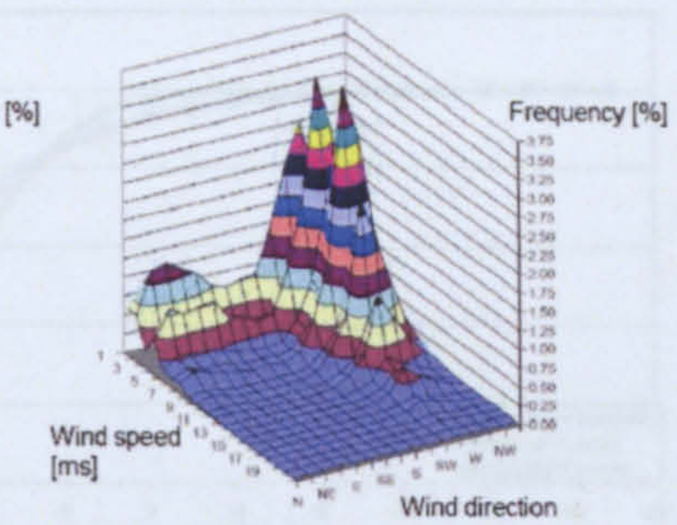

March 2008

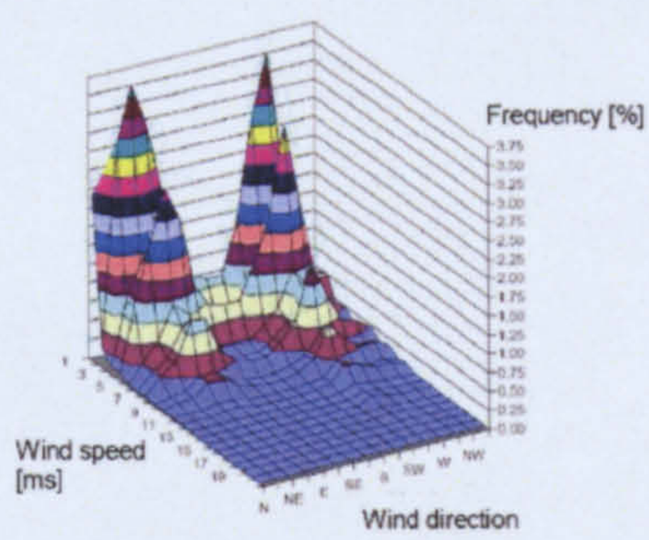

April 2008

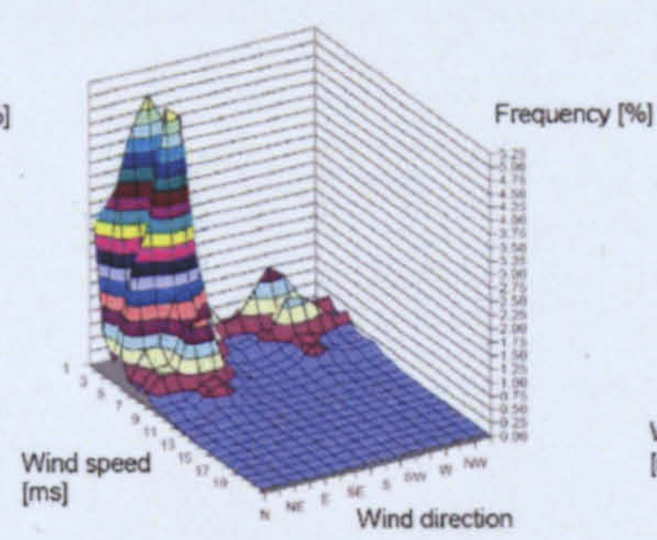

May 2008

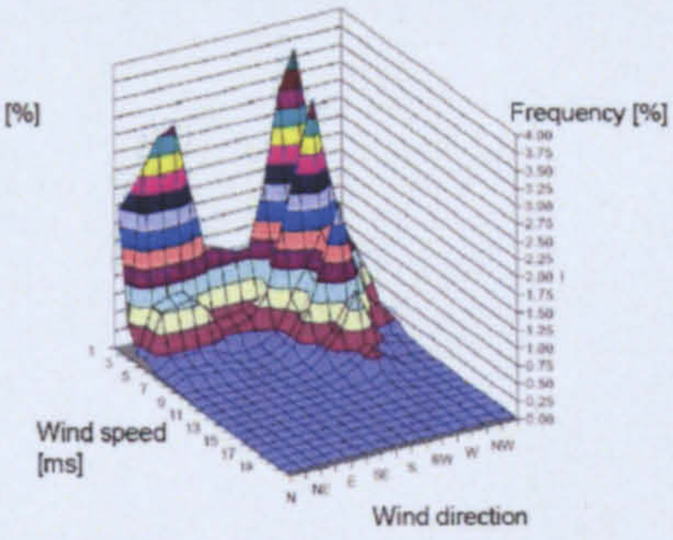

June 2008

Figure 6.8.5 Three-dimensional wind distribution plots for Edinburgh Napier University.

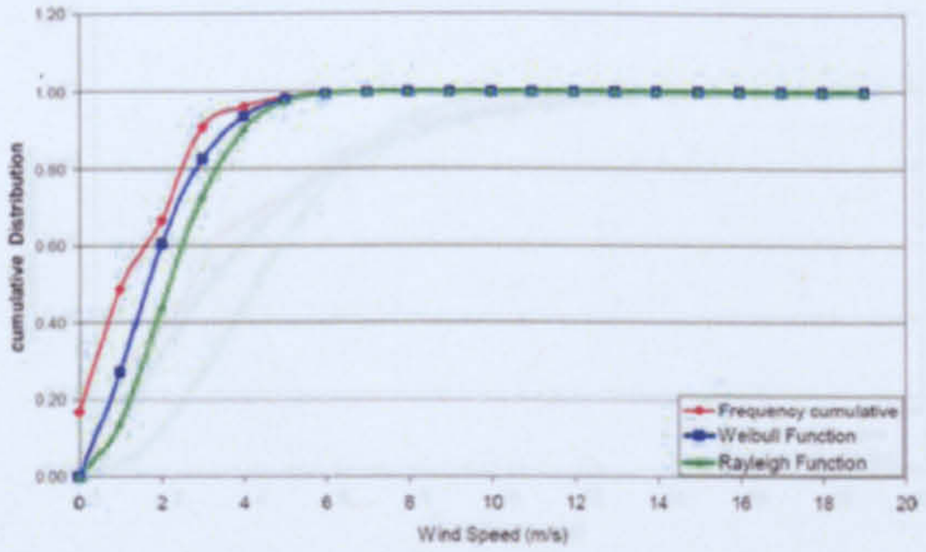

July 2007

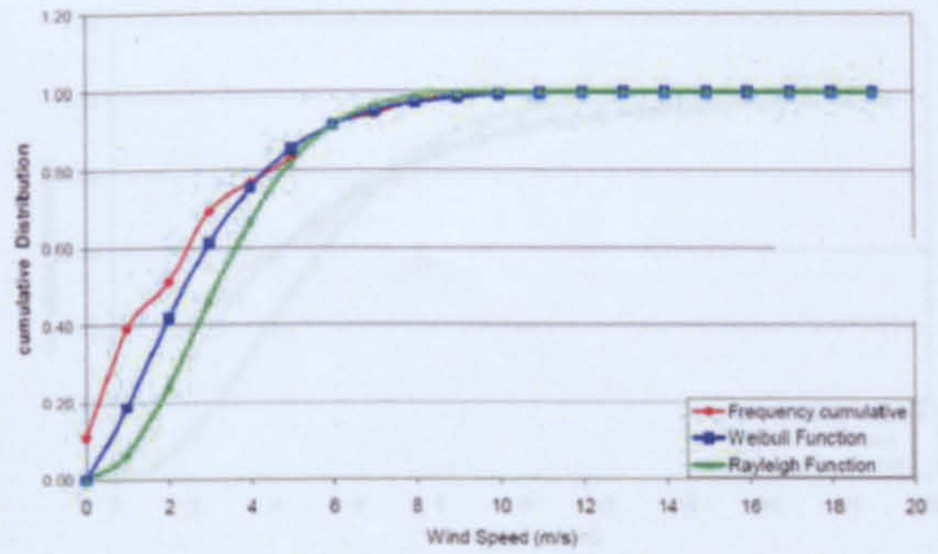

August 2007

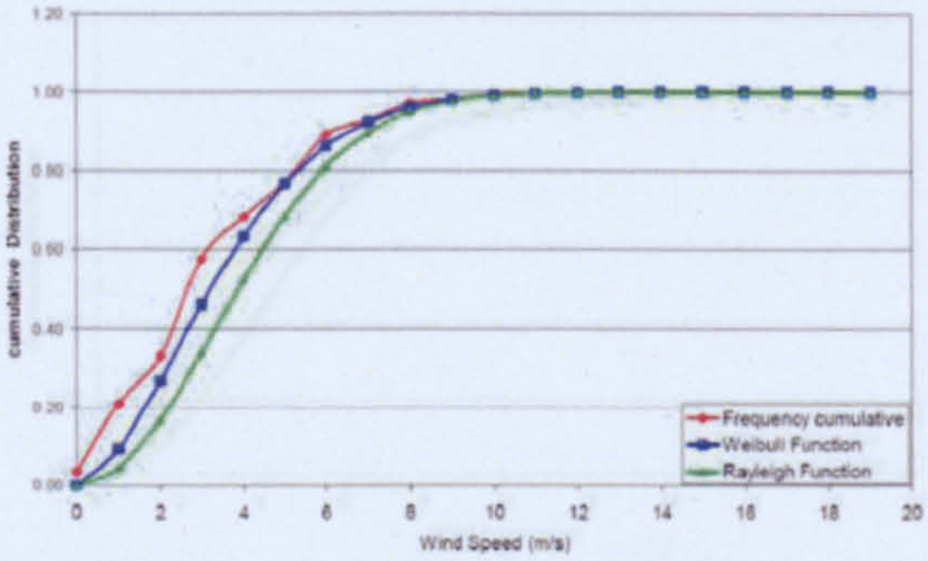

September 2007

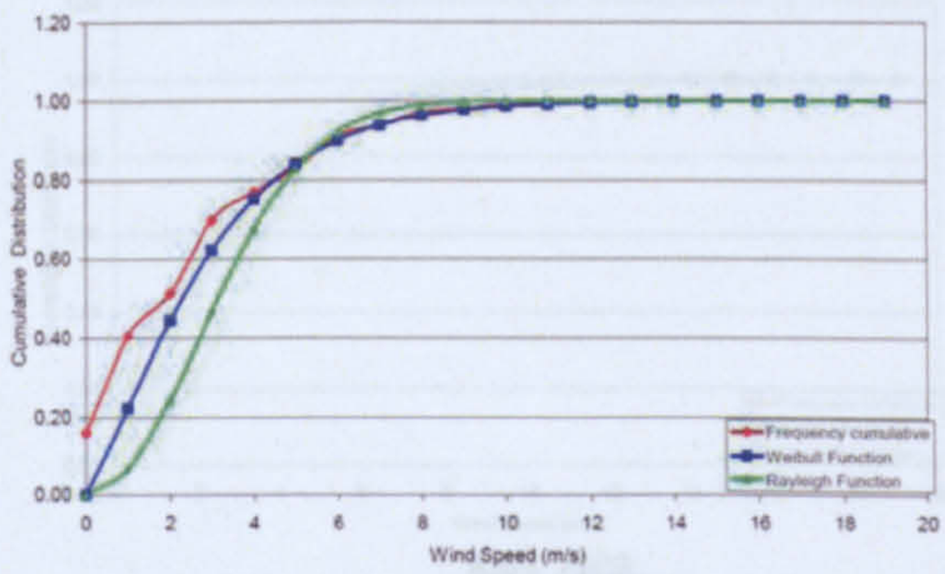

October 2007

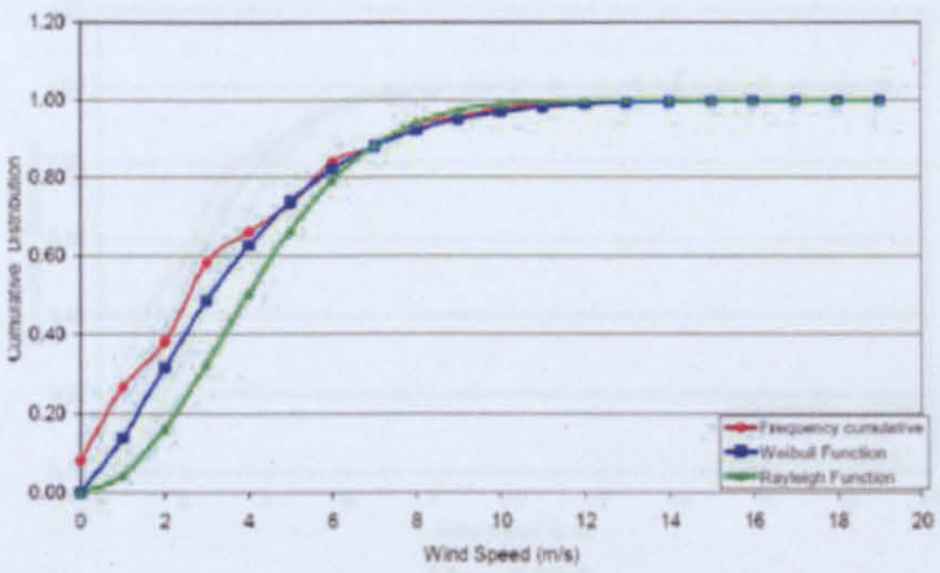

November 2007

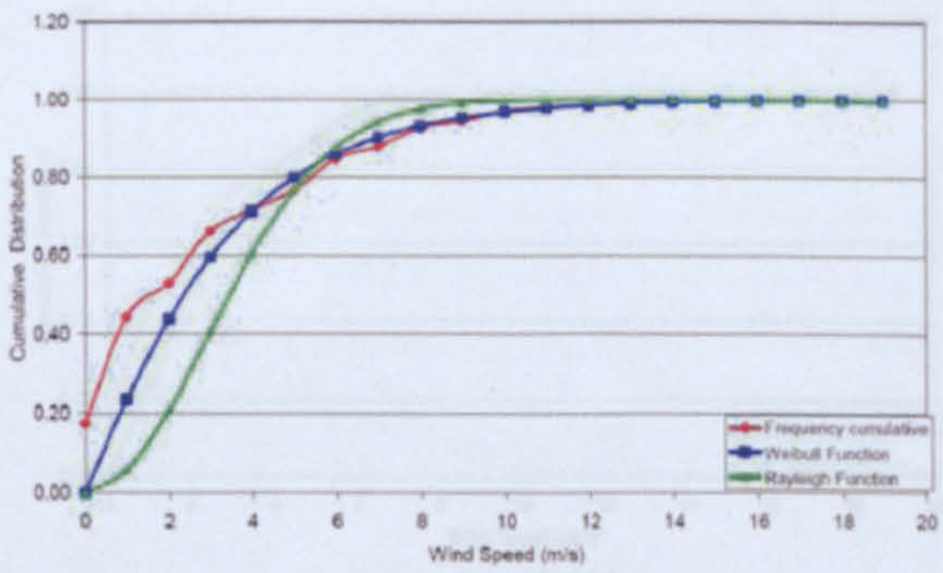

December 2007

Figure 6.8.6 Cumulative wind speed distribution plots for Edinburgh Napier University. Note Red line: measured data, Blue line: Weibull fit, Green line: Rayleigh fit

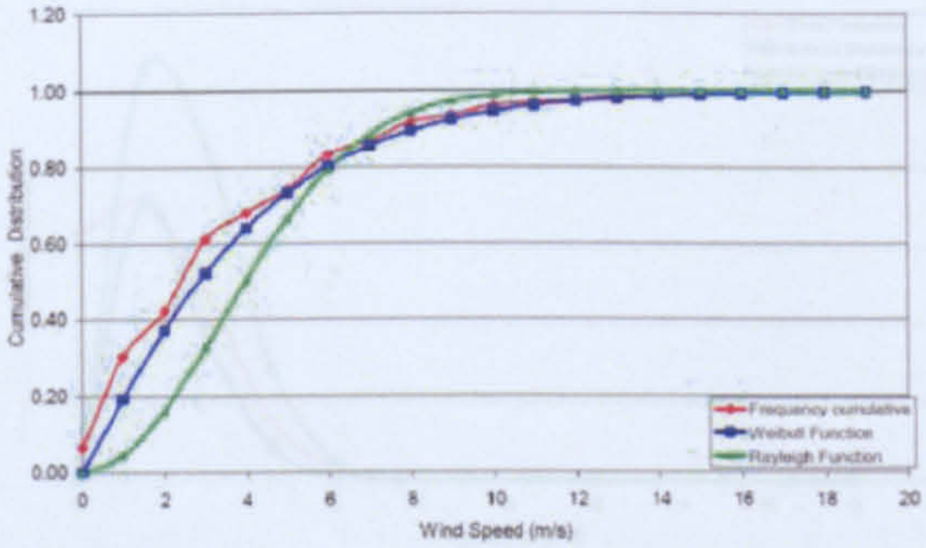

January 2008

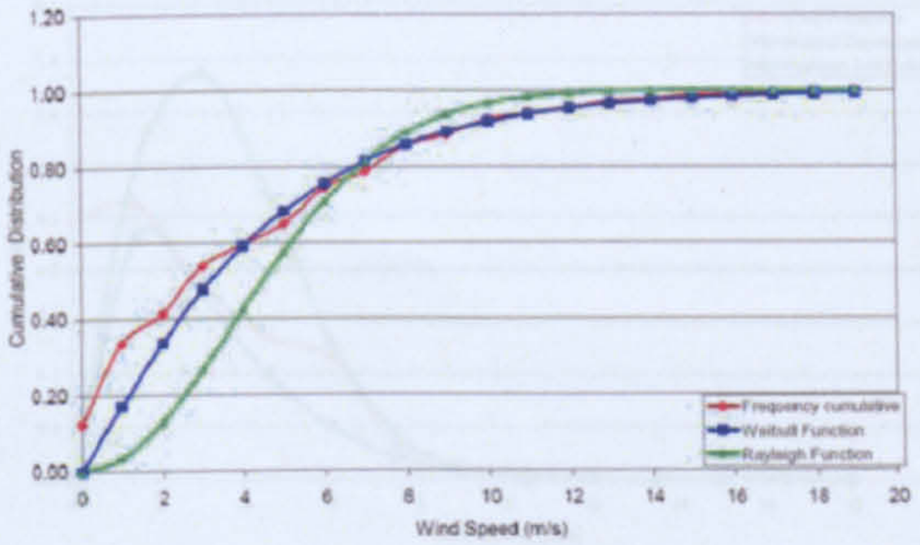

February 2008

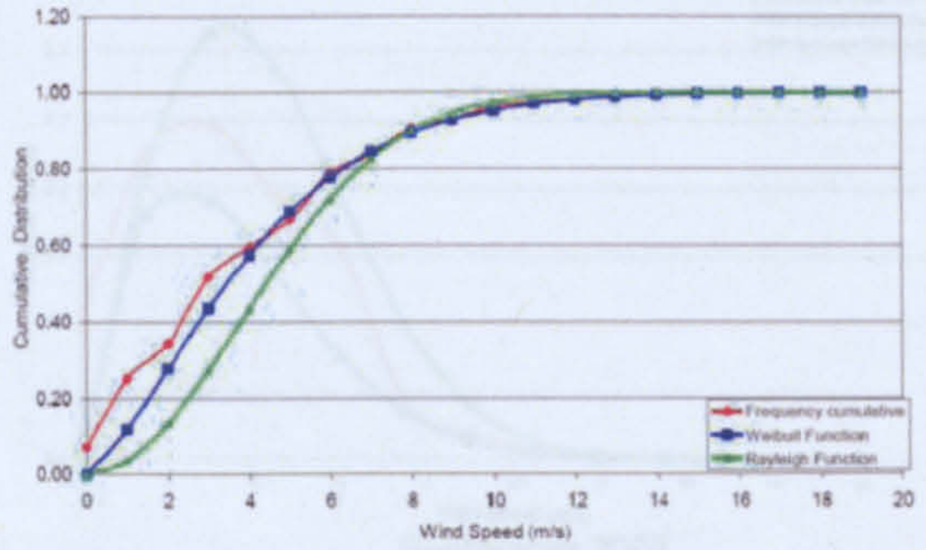

March 2008

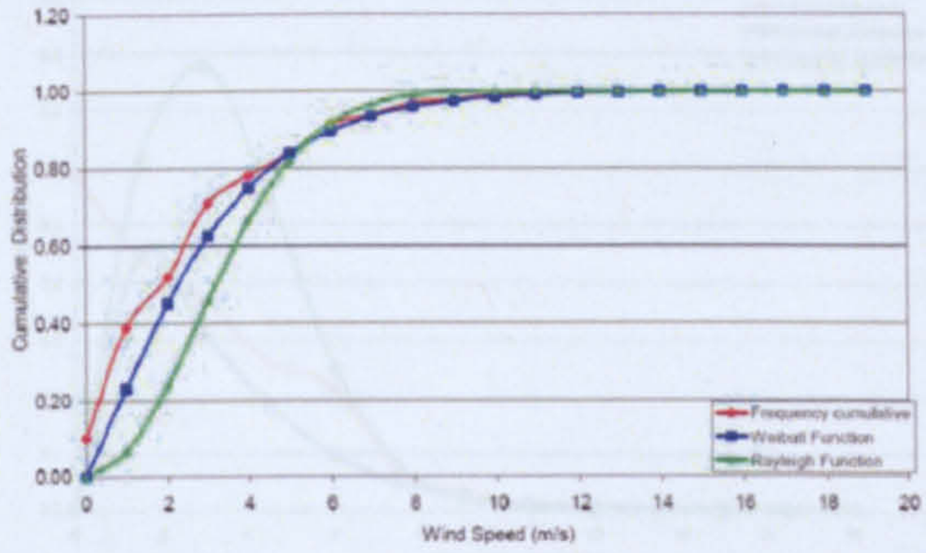

April 2008

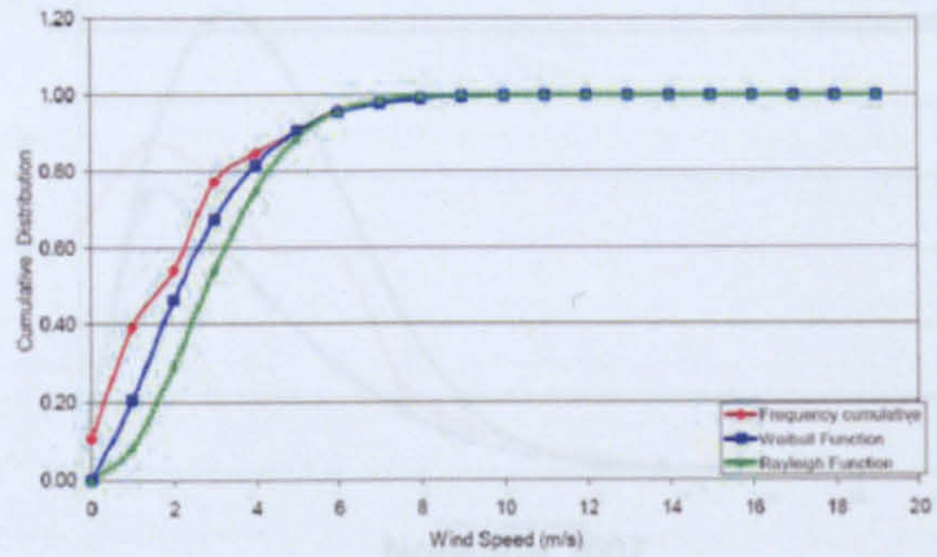

May 2008

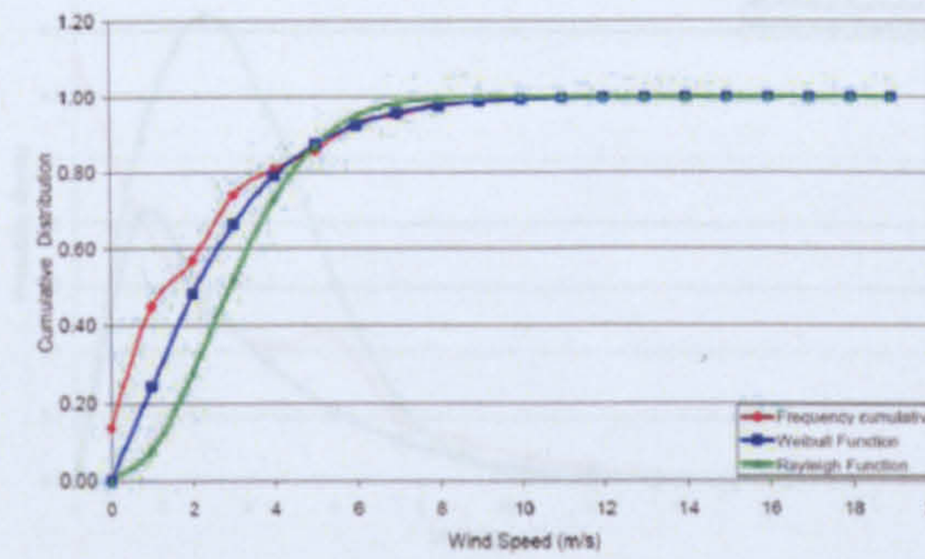

June 2008

Figure 6.8.6 (Continued) Cumulative wind speed distribution plots for Edinburgh Napier University. Note Red line: measured data, Blue line: Weibull fit, Green line: Rayleigh fit.

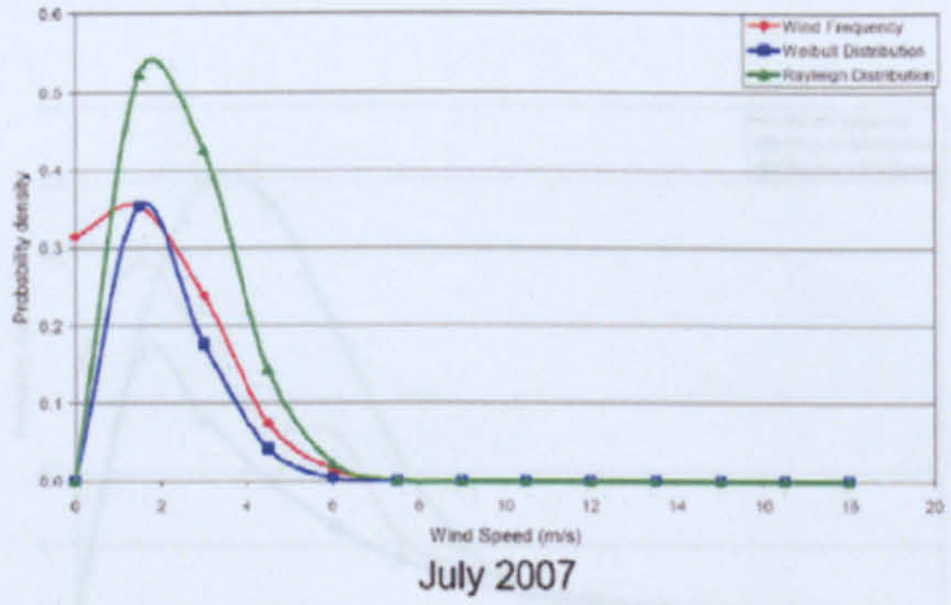

July 2007

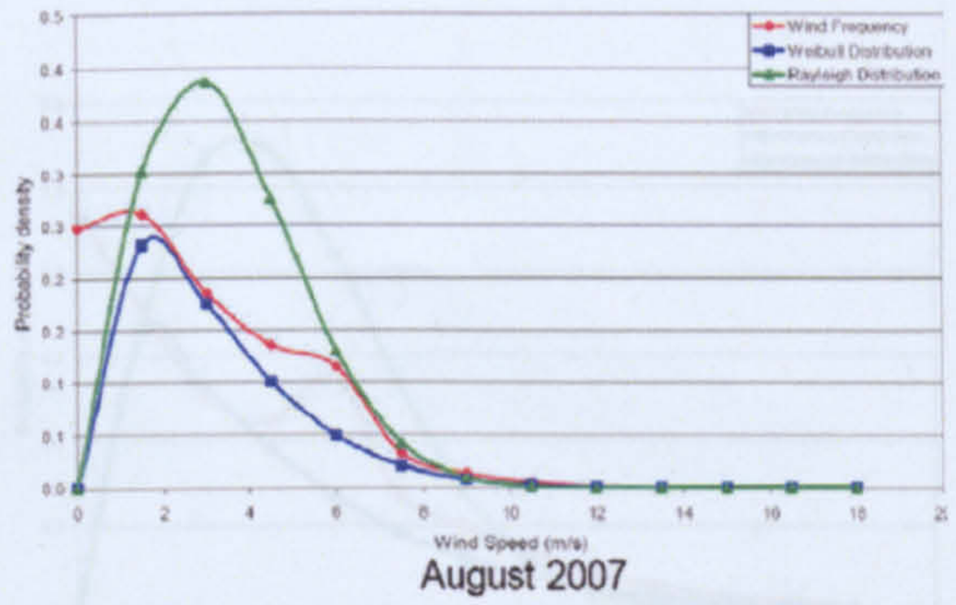

August 2007

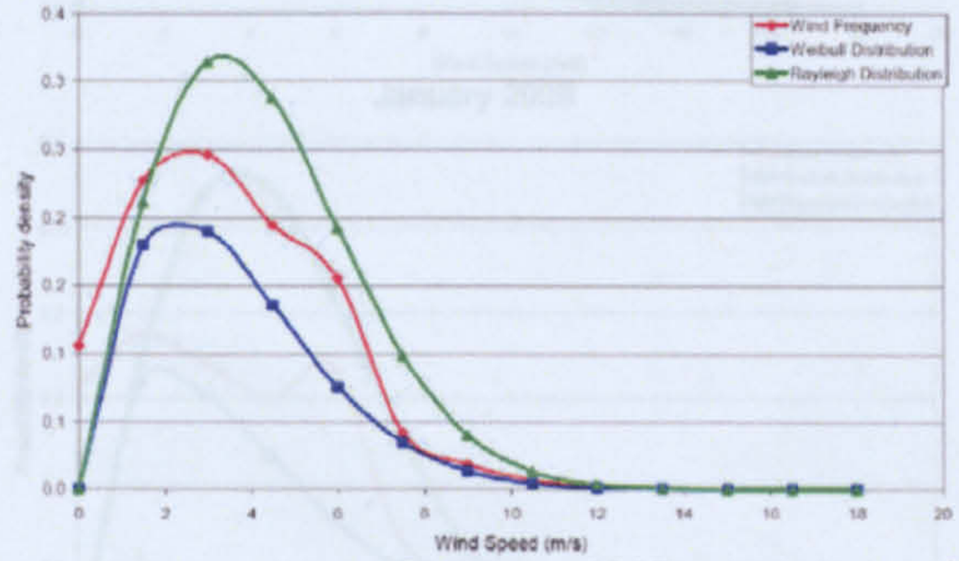

September 2007

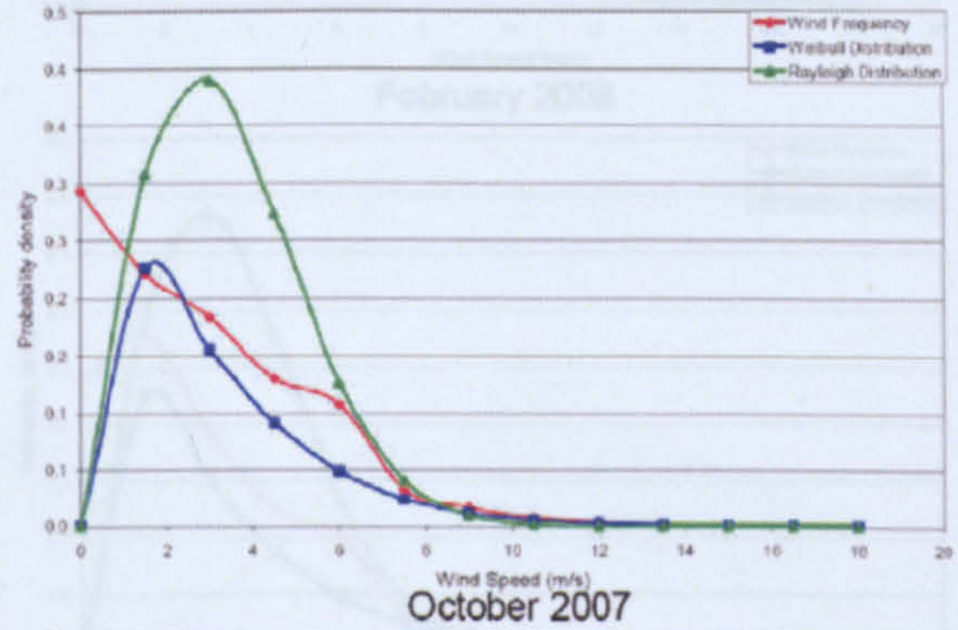

October 2007

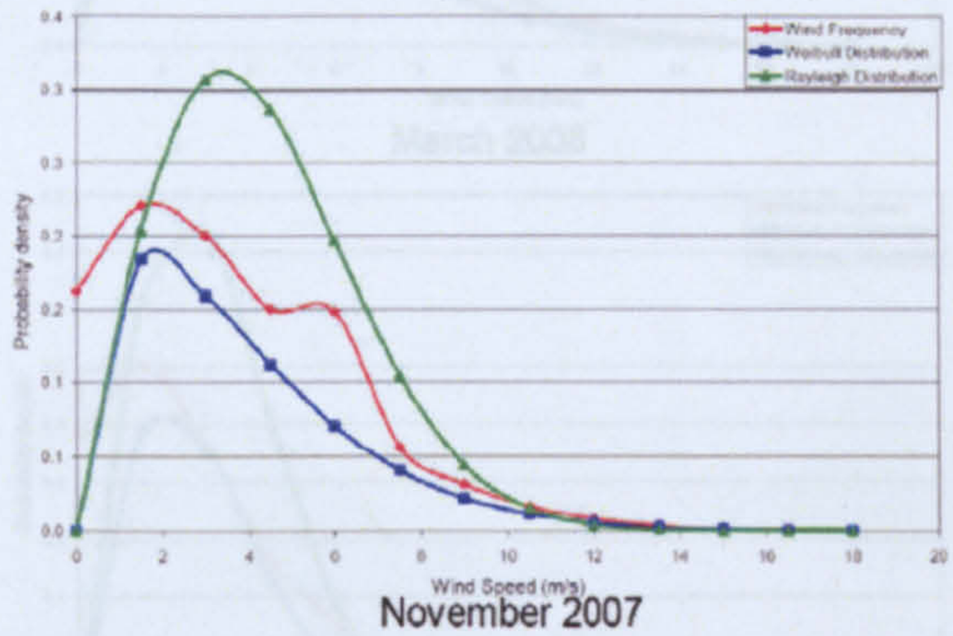

November 2007

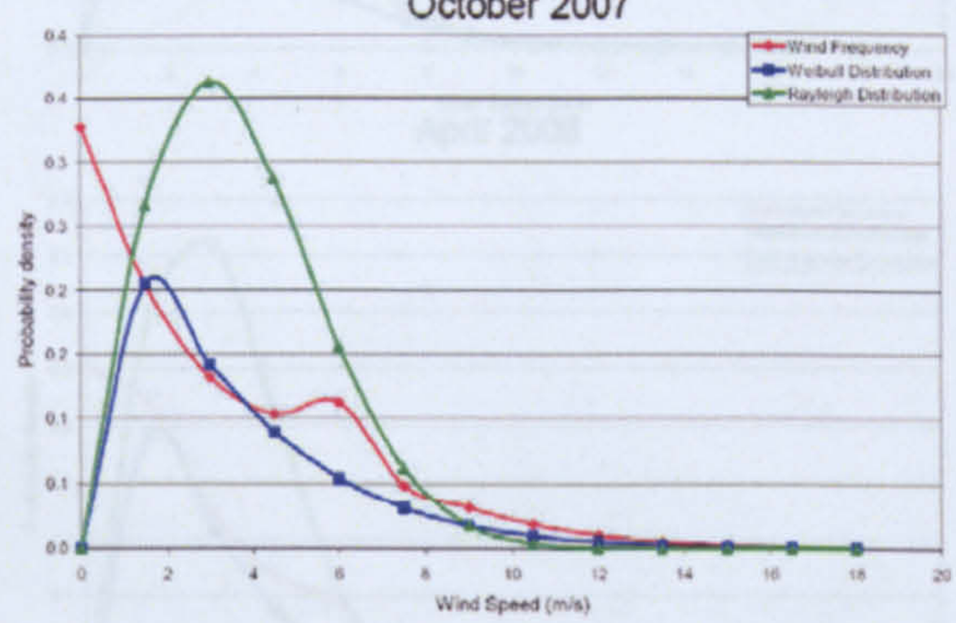

December 2007

Figure 6.8.7 Wind speed frequency distribution plots for Edinburgh Napier University. Note Red line: measured data, Blue line: Weibull fit, Green line: Rayleigh fit.

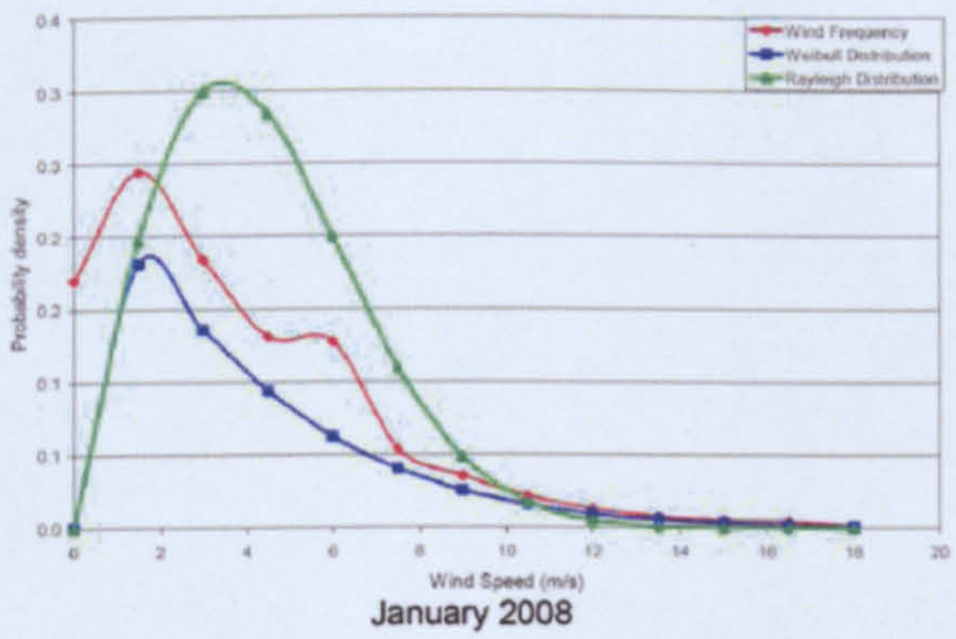

January 2008

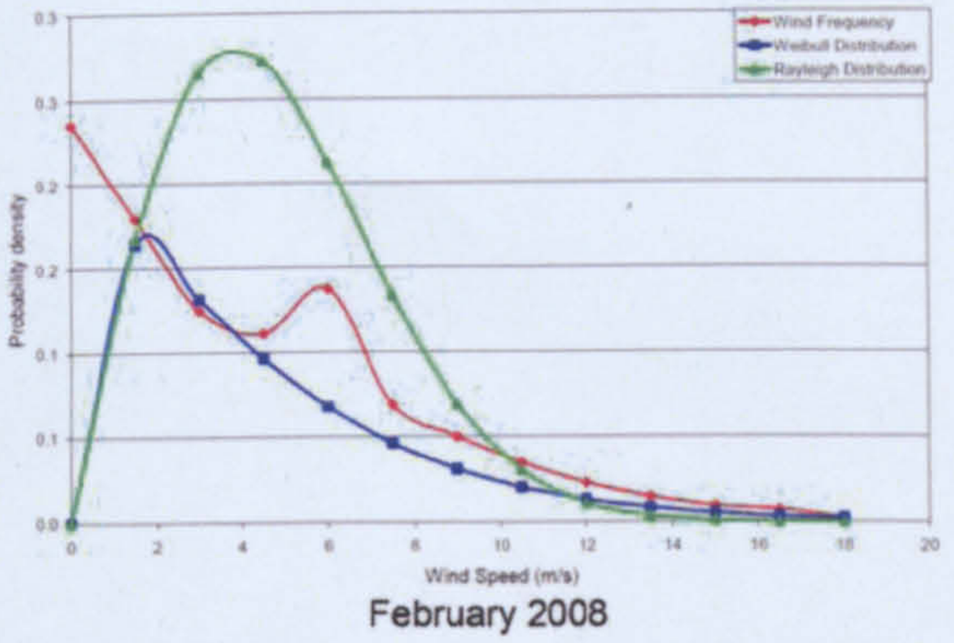

February 2008

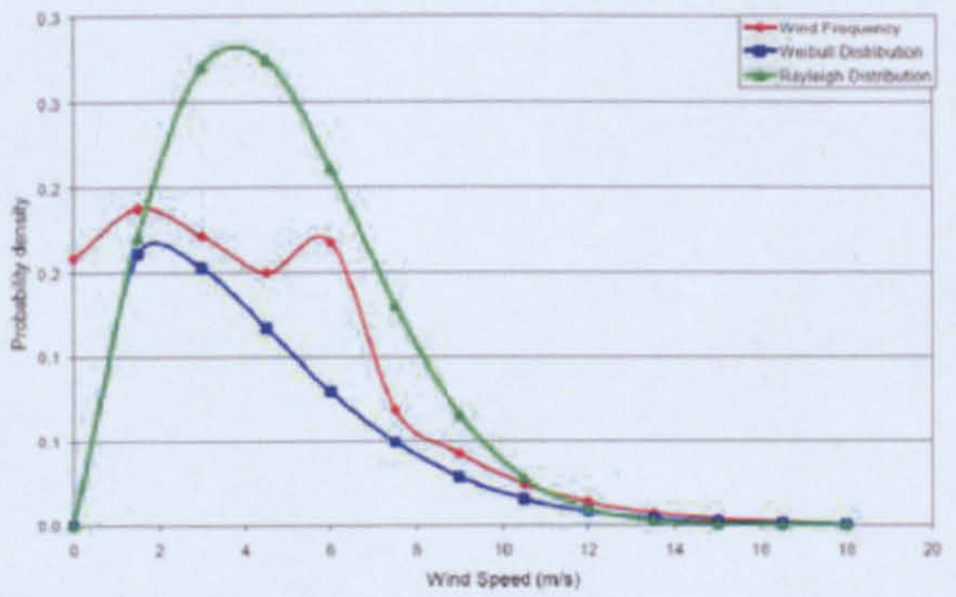

March 2008

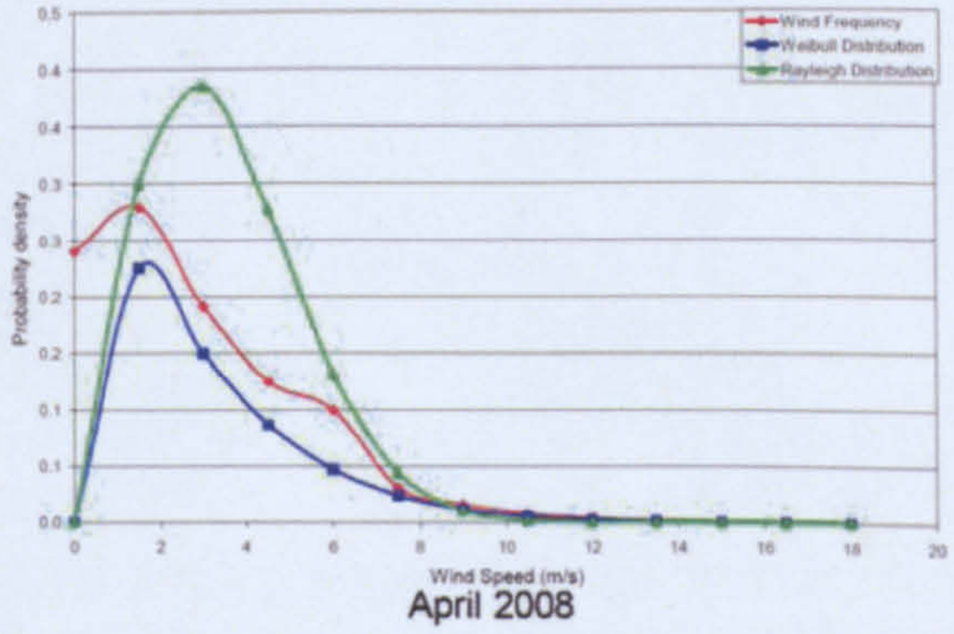

April 2008

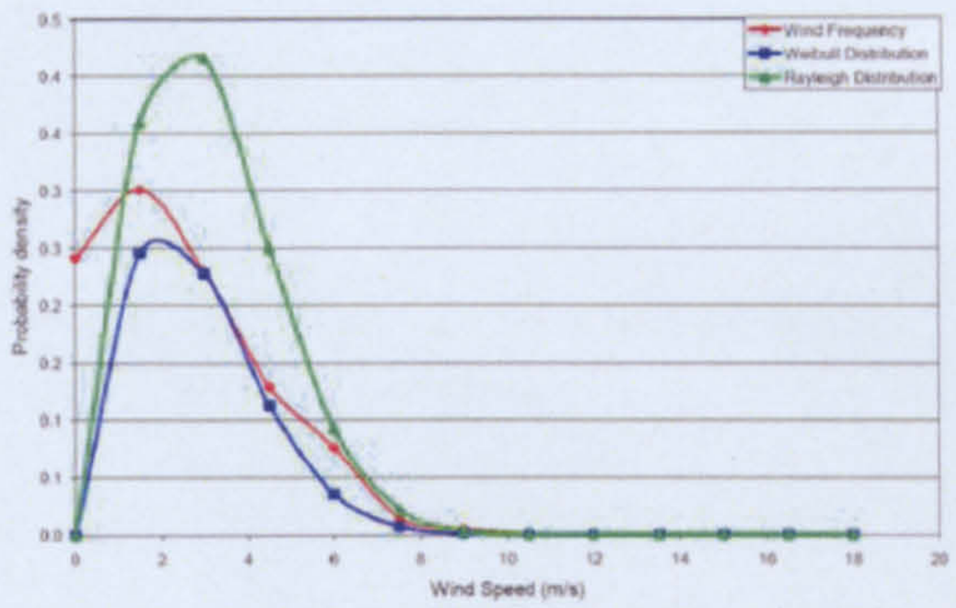

May 2008

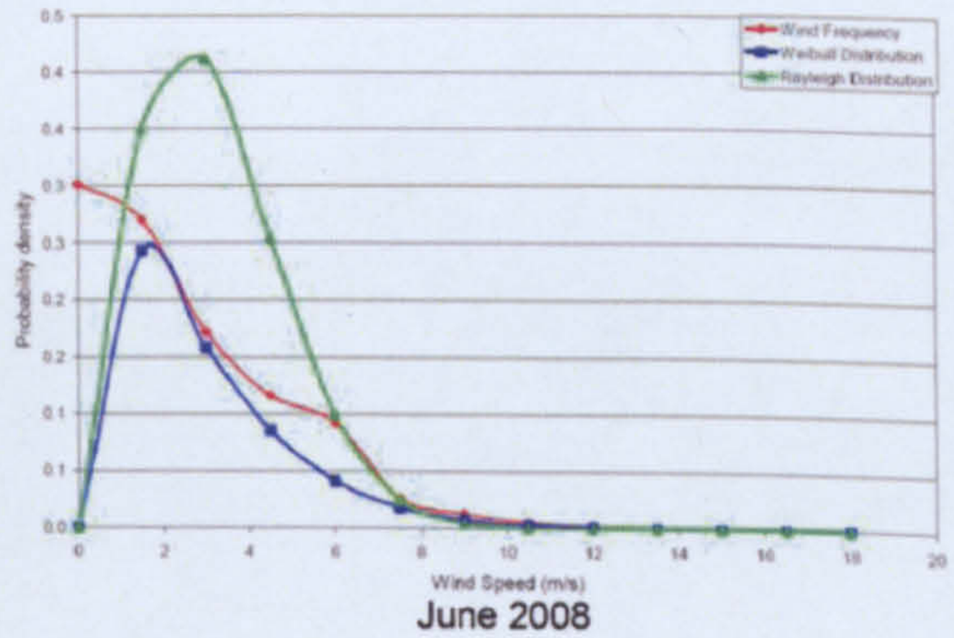

June 2008

Figure 6.8.7 (Continued) Wind speed frequency distribution plots for Edinburgh Napier University. Note Red line: measured data, Blue line: Weibull fit, Green line: Rayleigh fit.

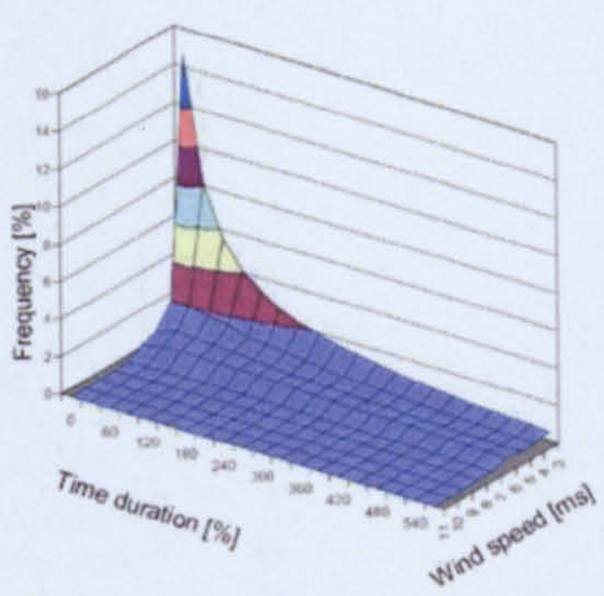

July 2007

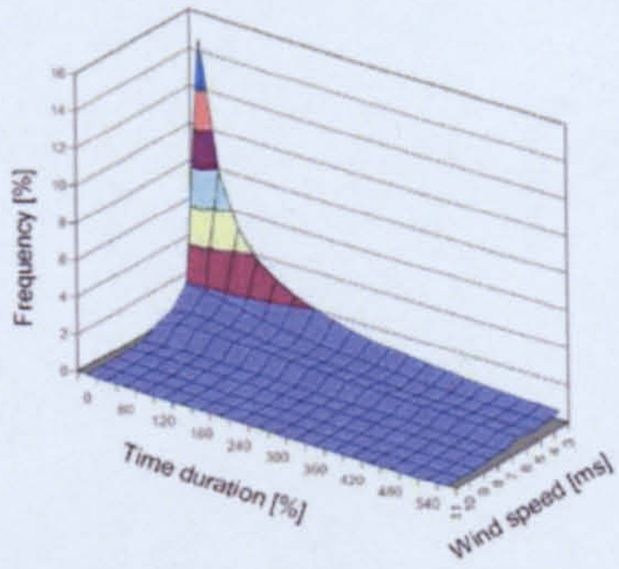

August 2007

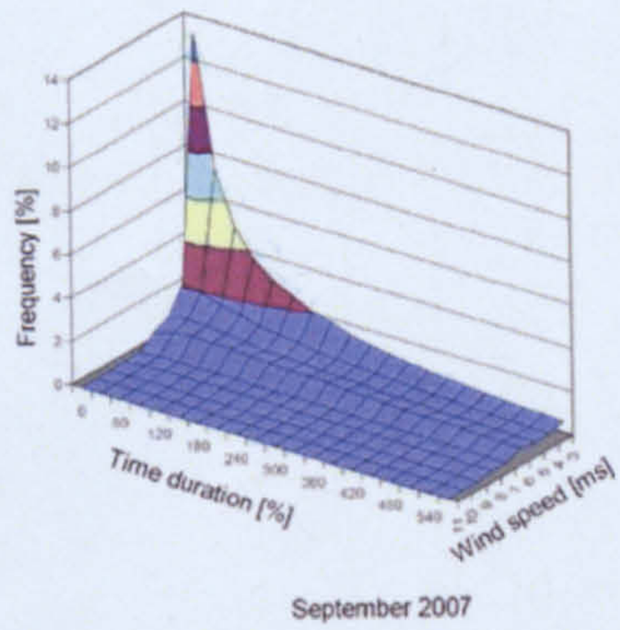

September 2007

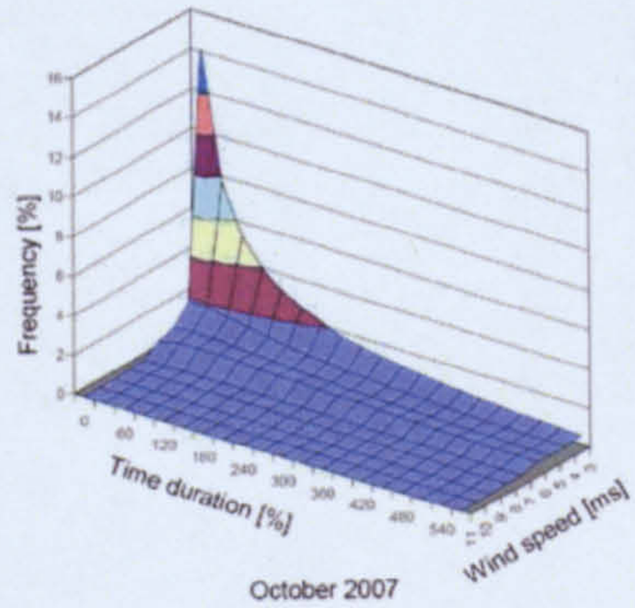

October 2007

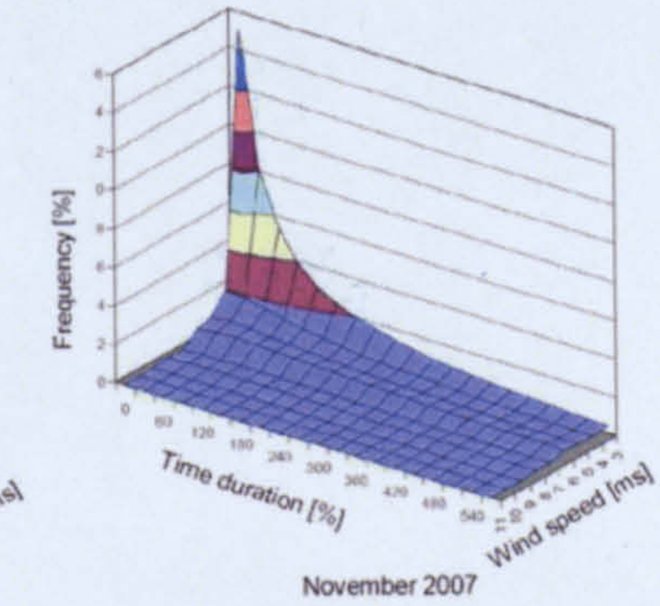

November 2007

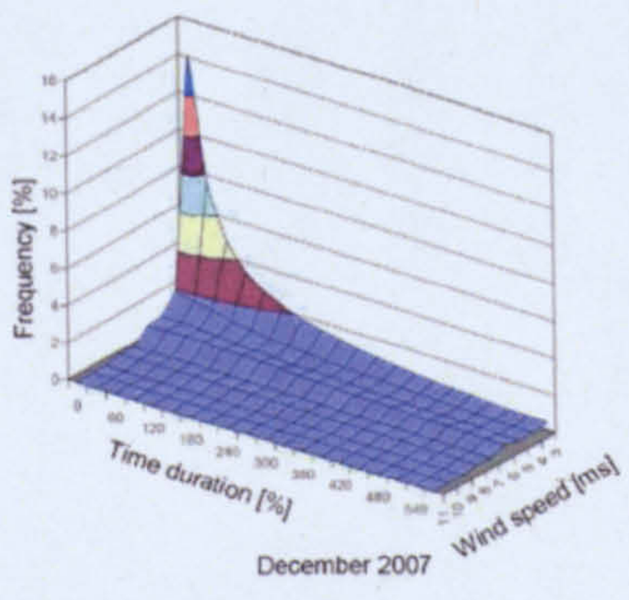

December 2007

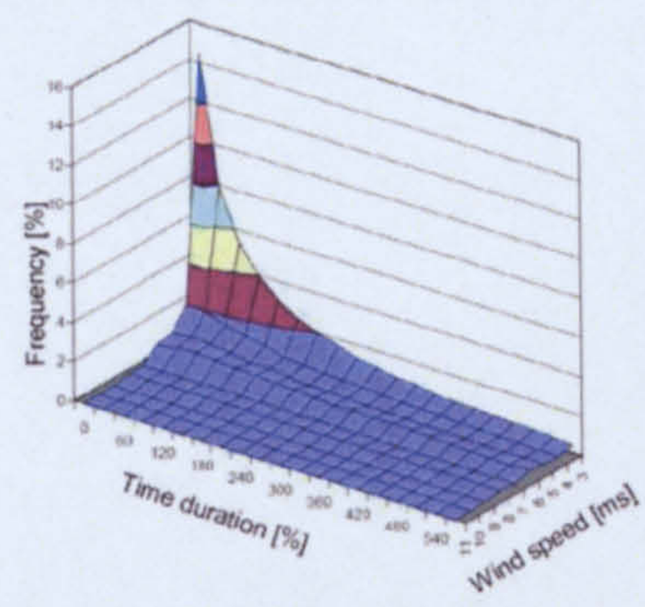

January 2008

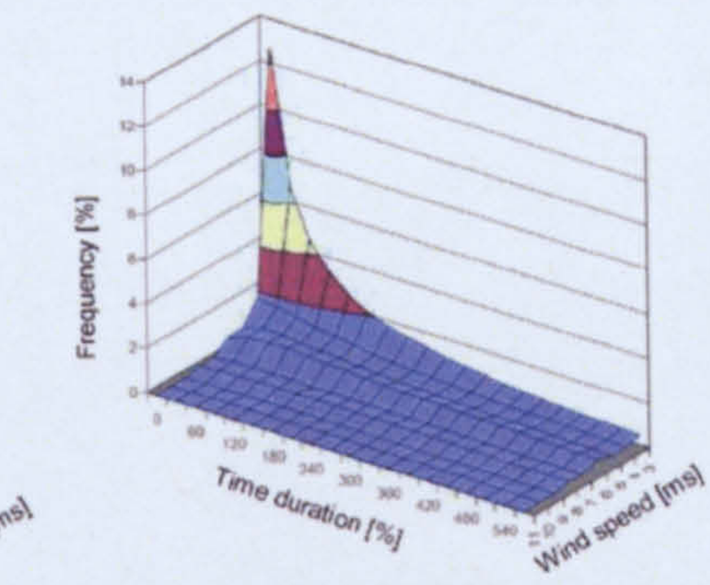

February 2008

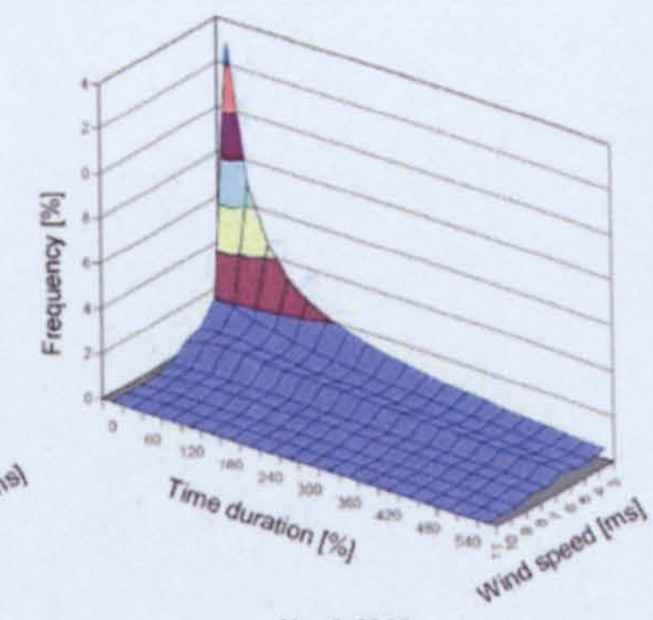

March 2008

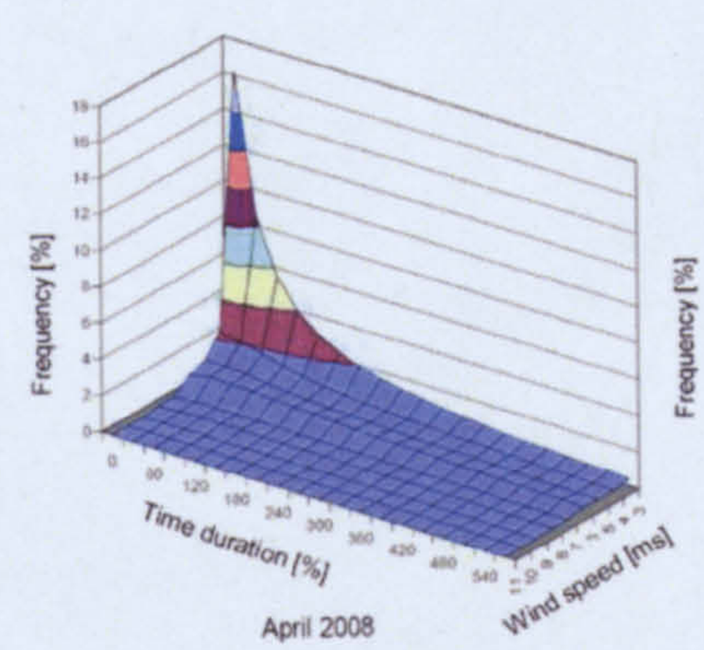

April 2008

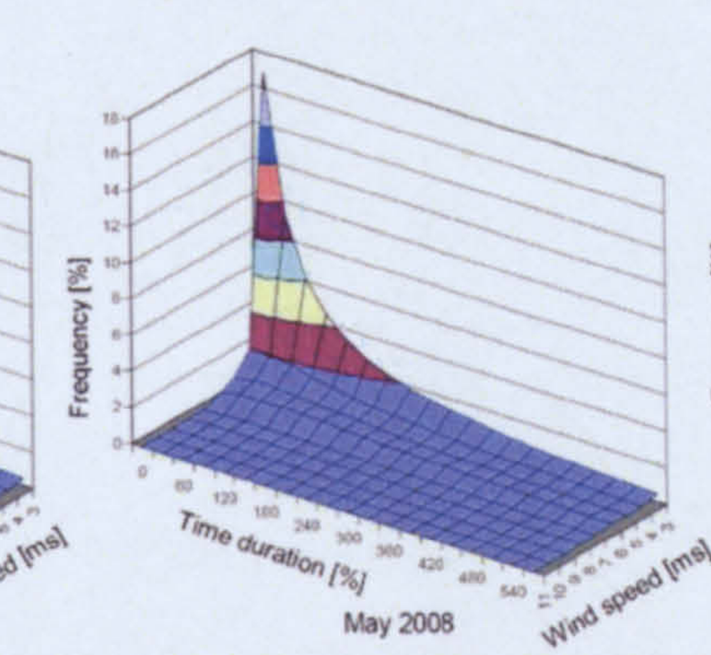

May 2008

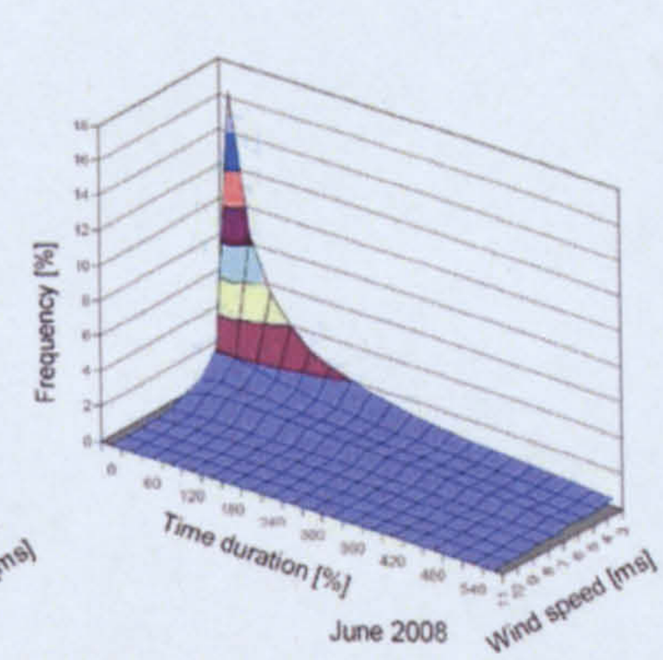

June 2008

Figure 6.8.8 Wind-gust frequency duration plots for Edinburgh Napier University.

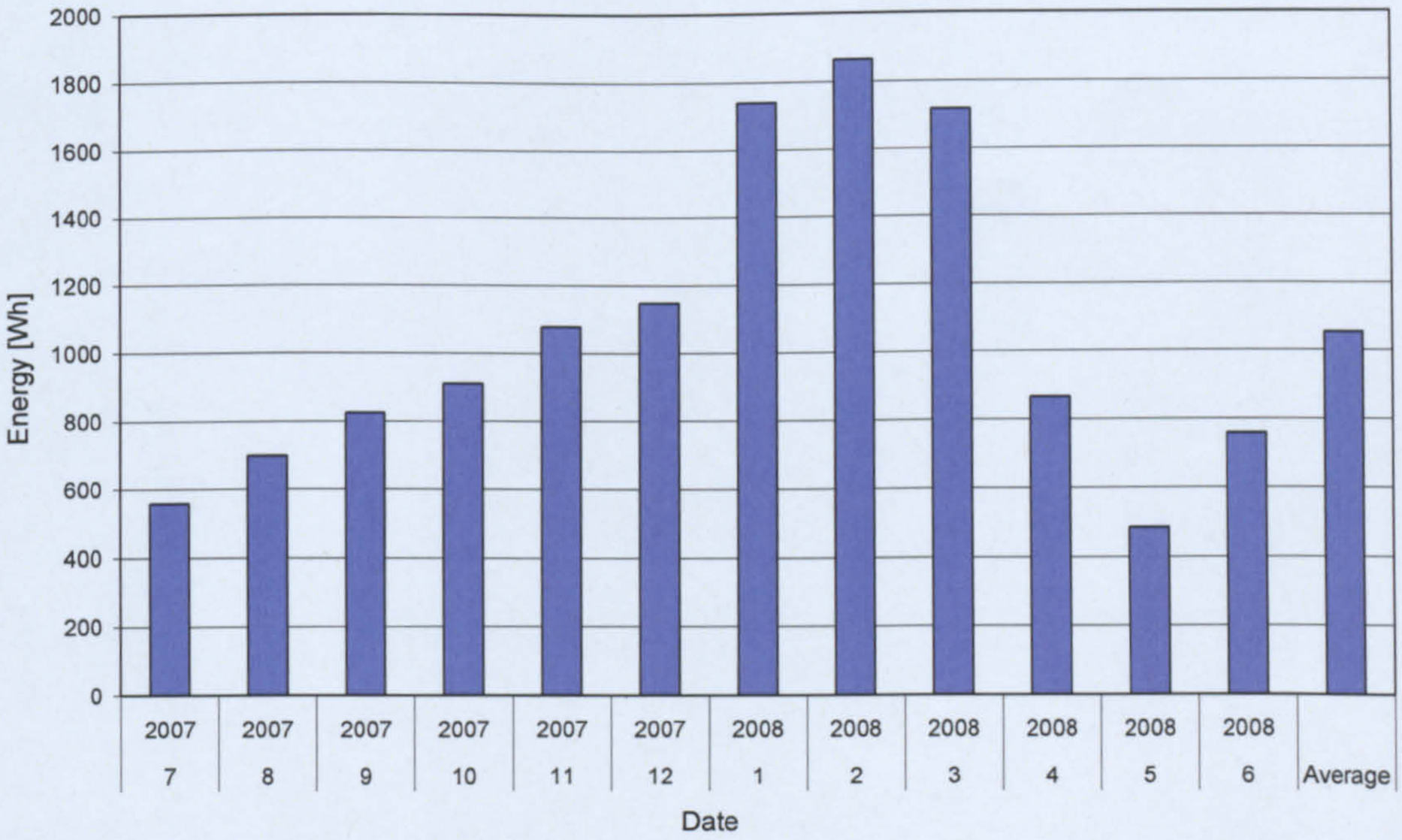

Figure 6.8.9 Airdolphin monthly-averaged daily energy output.

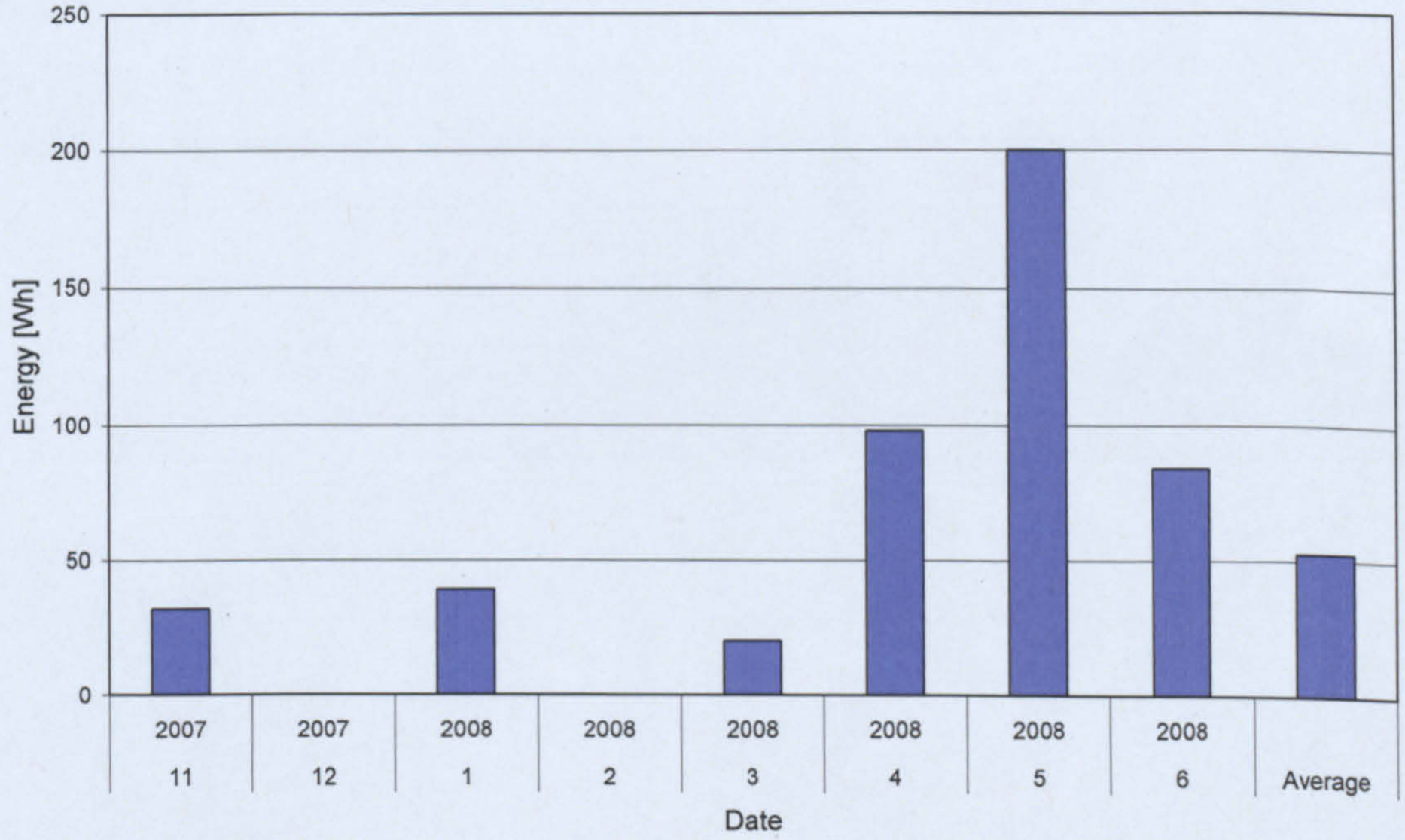

Figure 6.8.10 Ampair monthly-averaged daily energy output. Note: Months of December and February are missing due to turbine failure.

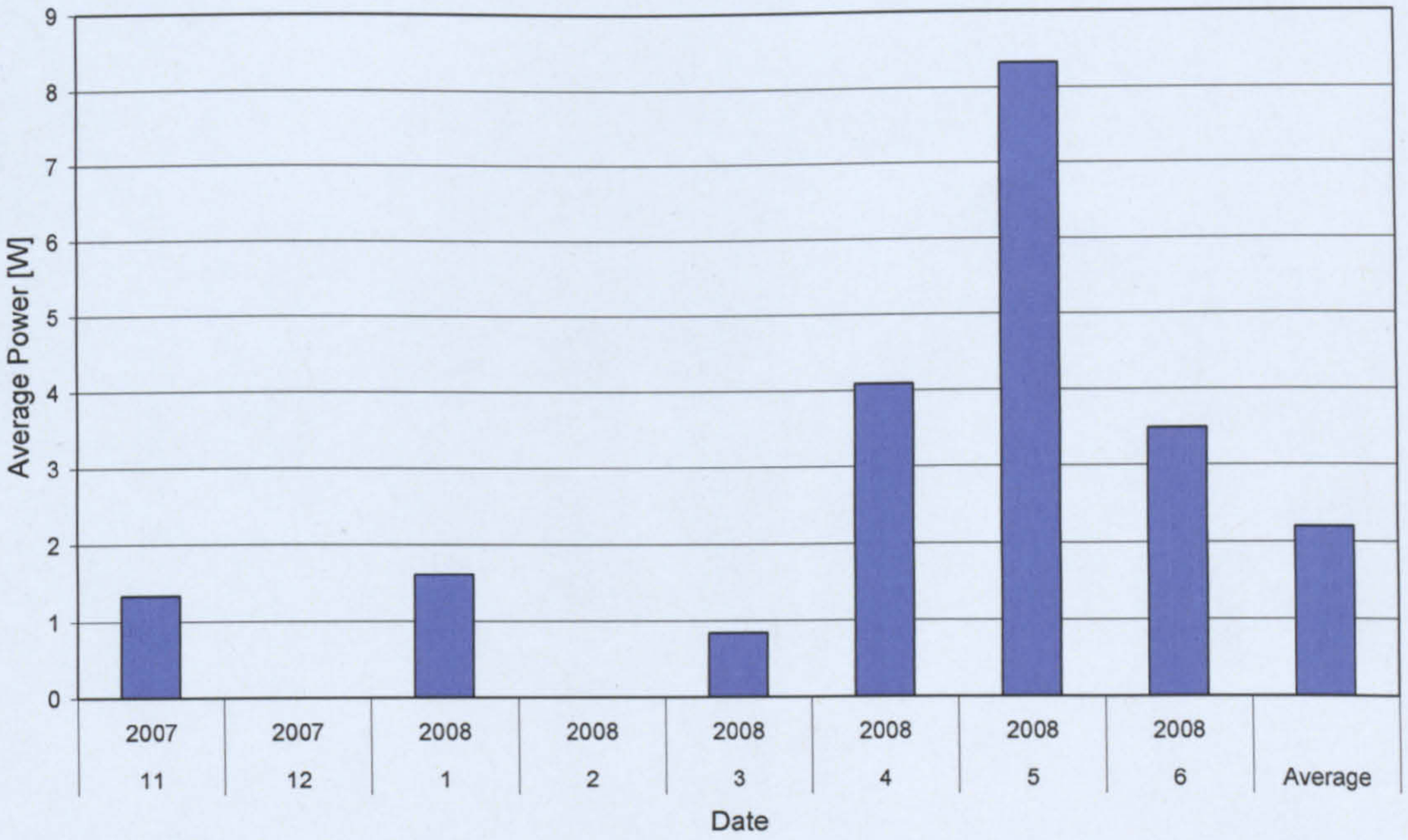

Figure 6.8.11 Ampair averaged monthly power. Note: Months of December and February are missing due to turbine failure.

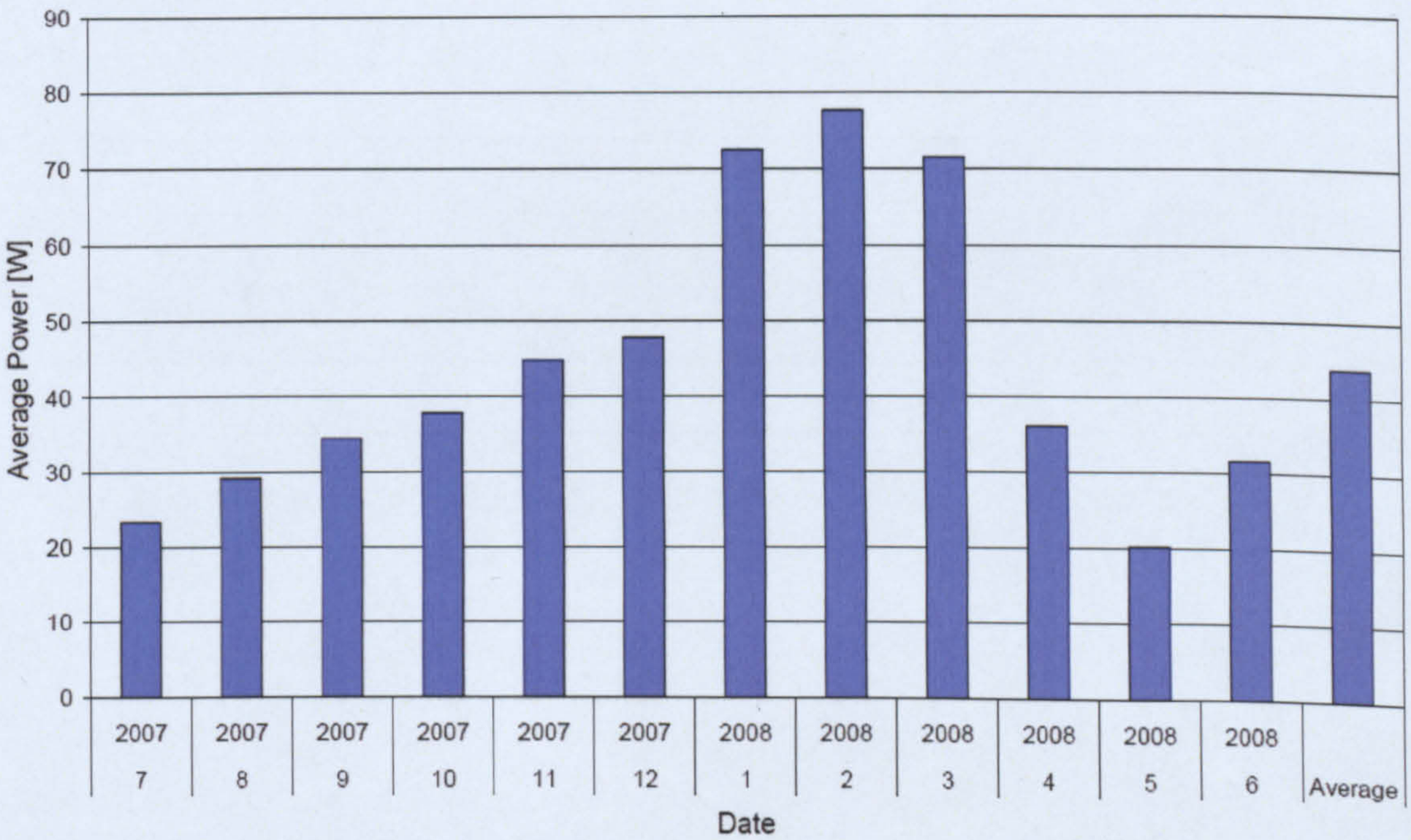

Figure 6.8.12 Airdolpin averaged monthly power.

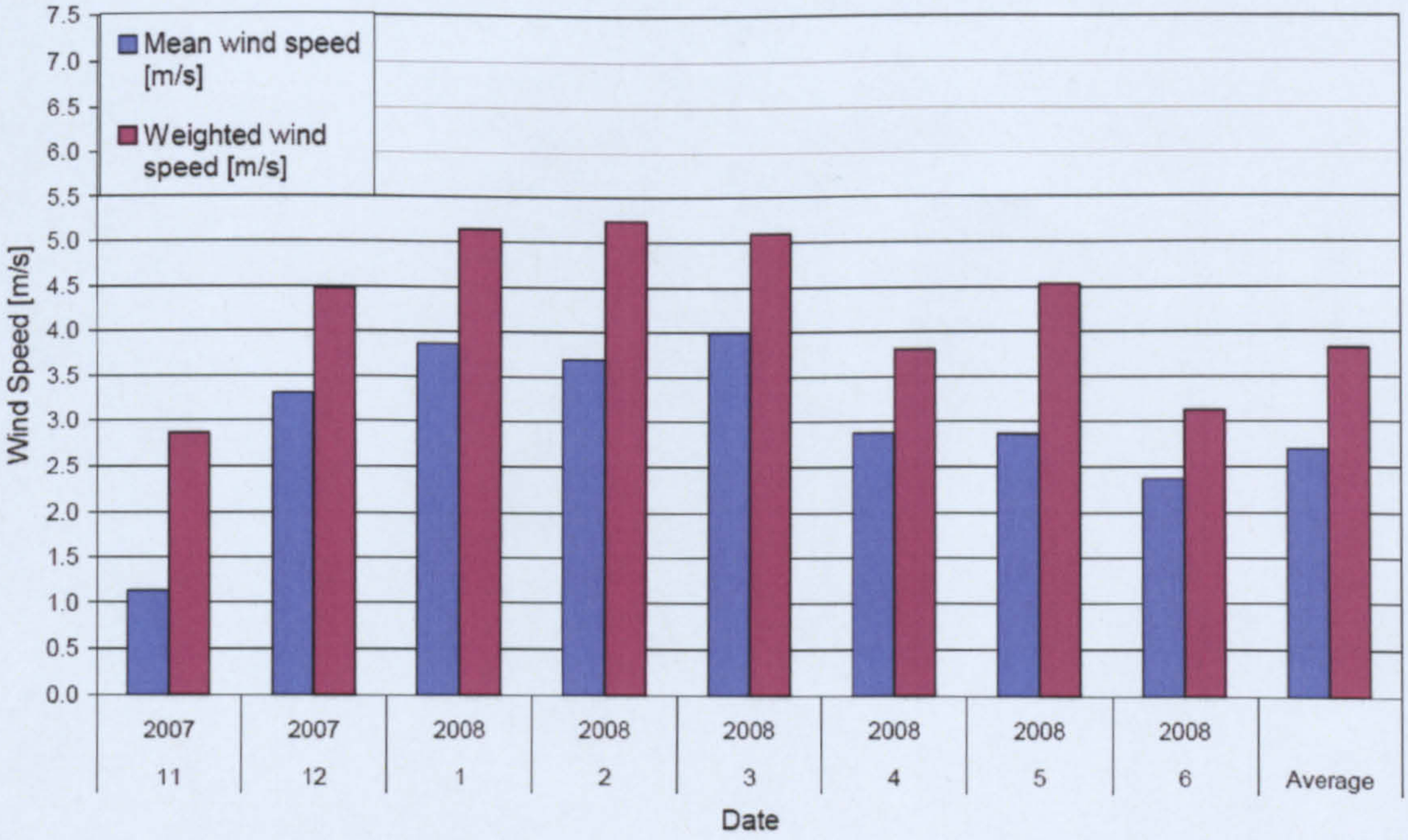

Figure 6.8.13 Ampair mean and weighted wind speed.

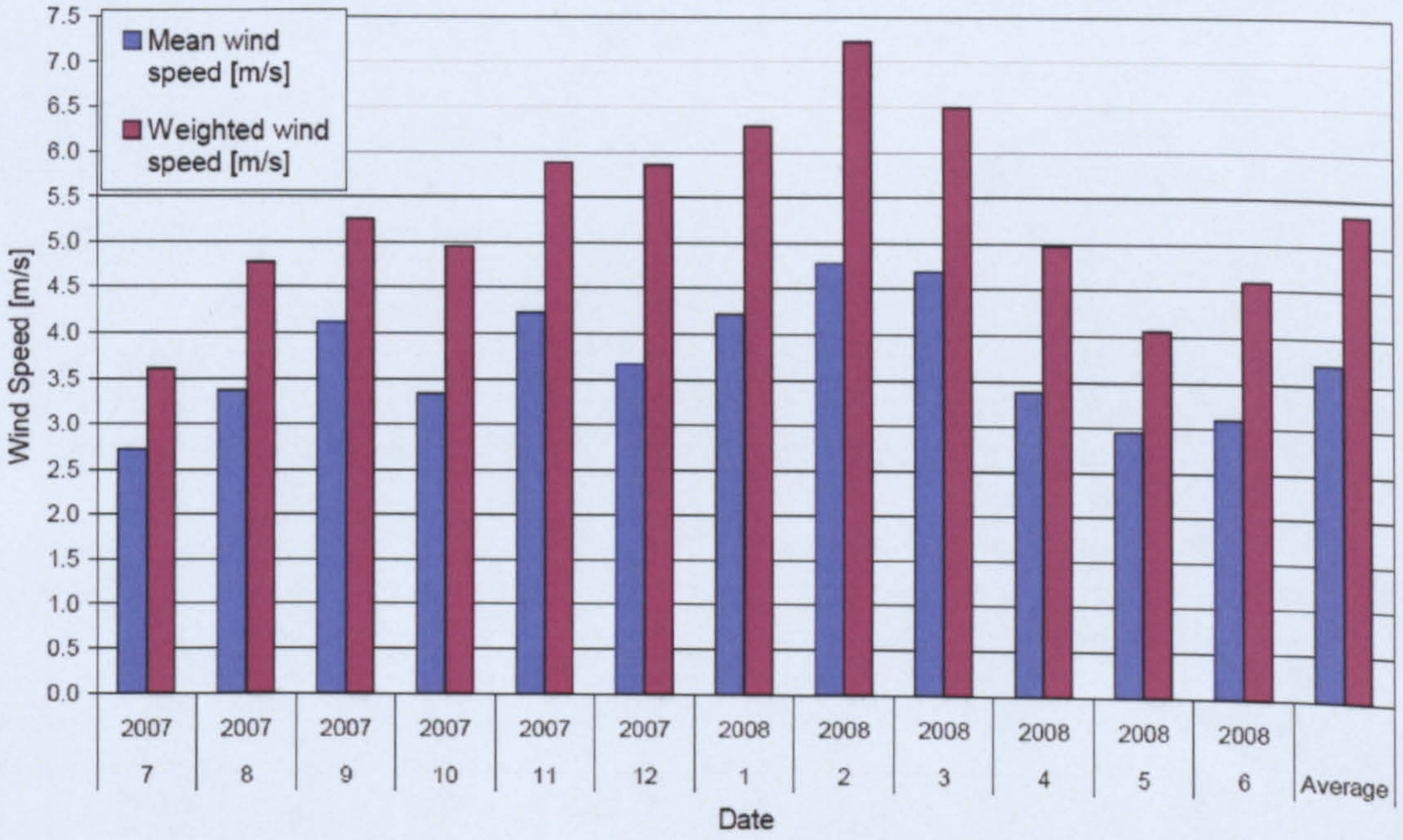

Figure 6.8.14 Airdolphin mean and weighted wind speed. Note: That weighed wind speed is the cubic root of the mean, of wind speed cubed. Weighted wind speed should be used for power calculations as the mean wind can lead to under estimation of potential wind power.

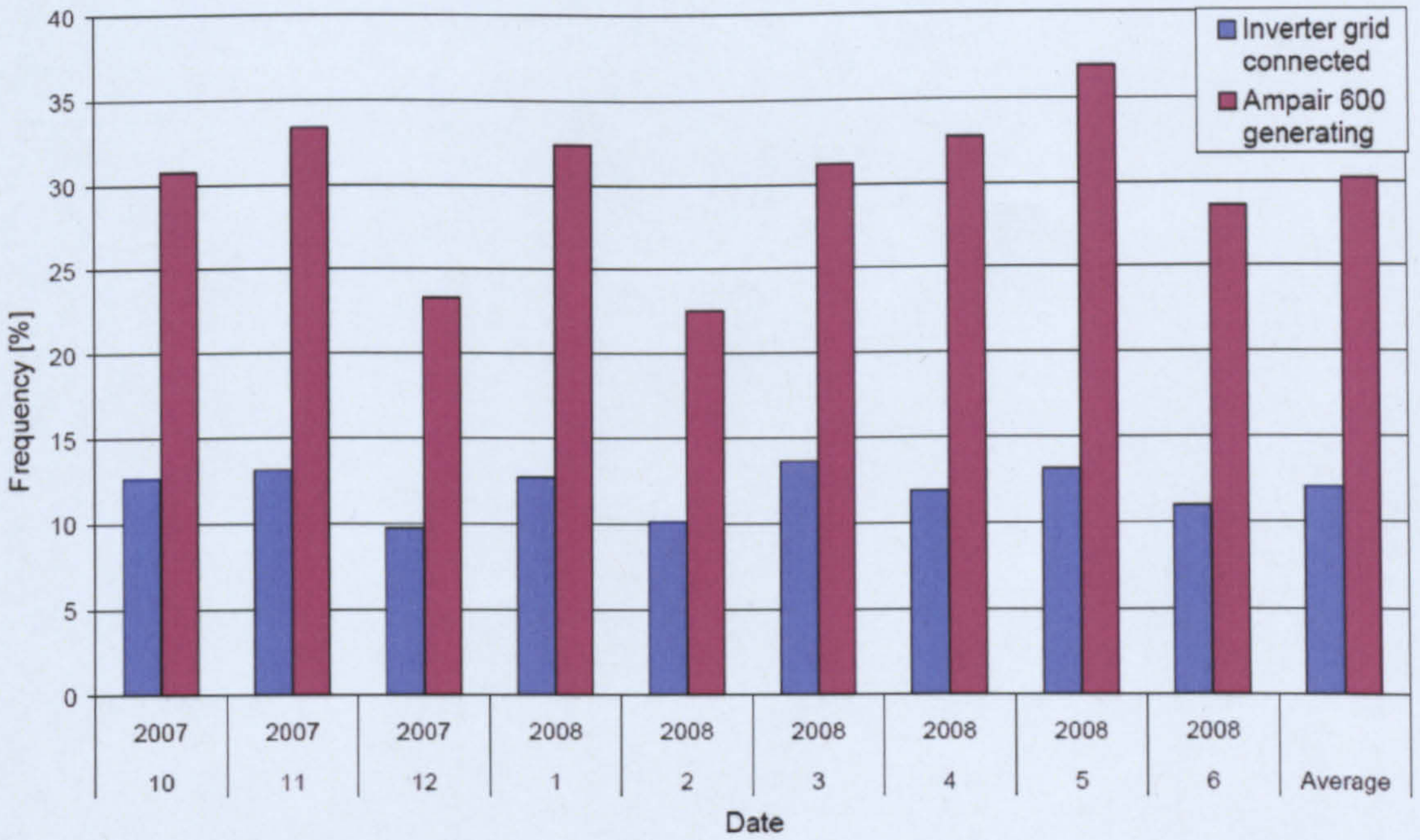

Figure 6.8.15 Shows the frequency which the Ampair turbine generator is producing power, and the frequency the turbine's export inverter is connected to the grid. Note: That when the inverter is not grid-connected, generated power is dissipated to dump load.

Table 6.8.1 Weibull and Rayleigh coefficients of wind regime observed at Airdolphin turbine and turbine capacity factor.

Month	Year	Number of seconds of data	Capacity factor ,%	Mean wind speed, m/s	Weibull, K	Weibull, C	Rayleigh, C
7	2007	986676	1.92	2.7	1.67	2.59	3.08
8	2007	2376820	2.91	3.4	1.39	3.12	3.81
9	2007	1045724	3.44	4.1	1.67	3.98	4.64
10	2007	2103420	3.79	3.3	1.23	3.05	3.77
11	2007	1854376	4.49	4.2	1.18	3.82	4.67
12	2007	2276776	4.79	3.7	1.11	3.26	4.14
1	2008	897216	7.25	4.2	1.13	3.90	4.76
2	2008	2270332	7.76	4.8	1.13	4.40	5.39
3	2008	2005020	7.14	4.7	1.39	4.47	5.29
4	2008	2076804	3.61	3.4	1.20	3.04	3.82
5	2008	2049728	2.02	3.0	1.42	2.71	3.33
6	2008	2037012	3.16	3.1	1.25	2.78	3.49
Average		**1831659**	**4.36**	**3.71**	**1.31**	**3.43**	**4.18**

Table 6.8.2 Airdolphin turbine outputs

Month	Year	Number of seconds of data	Weighted wind speed, m/s	Average Power, W	Monthly averaged energy output, kWh	Cumulative monthly averaged energy output, kWh
7	2007	986676	3.6	23.2	58	23
8	2007	2376820	4.8	29.1	27	50
9	2007	1045724	5.3	34.4	25	75
10	2007	2103420	5.0	37.9	28	103
11	2007	1854376	5.9	44.9	32	135
12	2007	2276776	5.9	47.9	36	171
1	2008	897216	6.3	72.5	54	225
2	2008	2270332	7.2	77.6	54	279
3	2008	2005020	6.5	71.4	53	332
4	2008	2076804	5.0	36.1	26	358
5	2008	2049728	4.1	20.2	15	373
6	2008	2037012	4.6	31.6	23	396
Average		**1831659**	**5.3**	**43.6**	**33.0**	
Total						**396**

Table 6.8.3 Weibull and Rayleigh coefficients of wind regime observed at Ampair turbine and turbine capacity factor.

Month	Year	Number of seconds of data	Capacity factor, %	Mean wind speed, m/s	Weibull, K	Weibull, C	Rayleigh, C
11	2007	2483400	0.22	1.1	0.82	1.21	1.28
12	2007	1236000	0.00	3.3	1.48	3.52	3.73
1	2008	2466800	0.22	3.9	1.47	4.49	4.37
2	2008	2401200	0.00	3.7	1.19	4.74	4.16
3	2008	2566800	0.14	4.0	1.69	4.44	4.51
4	2008	2592000	0.68	2.9	1.70	3.06	3.25
5	2008	2101800	1.39	2.9	1.61	8.83	3.24
6	2008	2484000	0.58	2.4	1.66	2.51	2.66
Average		**2060556**	**0.36**	**2.69**	**1.45**	**4.10**	**3.04**

Table 6.8.4 Ampair turbine outputs

Month	Year	Number of seconds of data	Weighted wind speed, m/s	Average Power, W	Monthly averaged energy output, kWh	Cumulative monthly averaged energy output, kWh
11	2007	2483400	1.1	1.3	1.0	1.0
12	2007	1236000	3.3	0.0	0.0	1.0
1	2008	2466800	3.9	1.6	1.2	2.2
2	2008	2401200	3.7	0.0	0.0	2.2
3	2008	2566800	4.0	0.8	0.6	2.8
4	2008	2592000	2.9	4.1	2.9	5.8
5	2008	2101800	2.9	8.3	6.2	12.0
6	2008	2484000	2.4	3.5	2.5	14.5
Average		**2060556**	**2.7**	**2.2**	**1.61**	**4.6**
Total						**14.5**

6.9 Findings and Conclusions

6.9.1 Edinburgh Napier University Merchiston Campus wind regime

The mean wind velocity at Napier Universities Merchiston campus has been found to be 3.5m/s, too low to provide any significant form of energy generation. This figure coincides well with figures published for similar sites throughout the UK taking part in the Warwick Wind Trials (Warwick Wind Trials, 2008).

The Edinburgh Napier University test site can be considered to be a near-optimum site for harnessing the wind within the urban environment, but it still cannot yield a useful amount of energy. The test site is located on top of a five-story building on the brow of a hill within the suburbs of Edinburgh. The site is approximately 120m above sea level and has a clear view to the prevailing south westerly winds.

There are two reasons for this poor wind resource. The first is due to the increased surface roughness of the urban landscape, which greatly increases the wind shear of the air stream flowing over urban areas. This results in the velocity of the air stream closer to the ground been greatly reduced, and its turbidity is also increased. The height of the free air stream boundary is greatly increased for urban locations.

The second reason is the presence of buildings within close proximity to the turbines.

An additional problem occurs when turbines are installed on buildings. As the air stream travels over the building, wind shear produced as airflows over the building creates a turbulence wake within the vicinity of the building as shown in Figure 6.4.2.1. The majority of rooftop turbines are installed within the wake of turbidity. To overcome this problem, the turbine should be sited as high as possible above the roofline. Research carried out by BRE suggests that rooftop turbines should be installed with a minimum hub height of 4.5m above the roofline for a domestic property to minimise the effects of the reduced wind speed (Blackmore, 2008). This height should be increased with the increased size of the building. However, increasing turbine hub height greatly increases the load force acting on the mast and support structure. Conventional domestic properties are not built to support the high load force required to support large turbine masts.

It has also been concluded that the design of the turbine is crucial in determining the available energy yield from the wind. There are two factors which have to be considered.

The turbine has to be designed to have a very low response time to enable it to react to any changes within the wind regime very rapidly. Due to the high intermittency of the urban wind regime, the power management system used to control the turbine must also have a very high response time to enable any energy generated to be used. Turbines have to be designed to be very robust to be able to survive very high turbulent winds.

This increased turbidity of winds has been observed at Edinburgh Napier University to cause increased loading and stress on the wind turbines, resulting in damage caused by fatigue. Failure of components has caused both the Airdolphin and Ampair turbines to stop working during the test survey. This agrees with findings for other turbines taking part in the Warwick Wind Trials. As of May 2008, there are 30 turbine sites throughout the UK taking part in these trials. 6 turbines are said to be switched off, either due to turbine failure or because they are awaiting modification (Warwick Wind Trials, 2008). Turbines have failed due to both mechanical and electrical failures.

At the Edinburgh Napier University site, the Ampair turbine failed twice because of overloading of the control unit as result of over-voltage. The poor quality of the national power grid within the UK has also caused grid-connected systems to fail. This seems to be a particular problem for remote rural sites. The poor quality of the grid supply causes inverters to shut down because the grid voltage and frequency fall outside regulated standards. The Department for Business Enterprise & Regulatory Reform (BERR) state that domestic grid supply voltage is maintained within 230 volts, minus 6% to plus 10%. From 2008 the supply standards are changing to harmonise with Europe to 230 volts +/- 10%. Grid frequency is limited to 50 Hz +/- 1% (BERR, 2008).

This was observed in the Warwick Wind Trials at the West Staddon site. The turbine failed when the inverter shut down at times of high grid voltage. The Nenthead case study previously mentioned within chapter 2 noted this same problem, when the grid voltage exceeded 260 volts.

The Warwick Wind Trials have also reported that turbines have also needed to be switched off due to concerns about noise and vibration issues when turbines are operating during times of high winds. Ten of the thirty turbines within the trials have been switched off for this reason.

When comparing stand-alone systems with grid-connected systems, it has been found that stand-alone systems give improved performance. This is due to stand-alone systems having very low start-up times, resulting in all the available energy generated being utilised to charge battery banks, whereas one type of grid-connected turbine requires three minutes of continuous power generation before the inverter connects to the grid and starts to export energy. Should the wind velocity drop below the turbine cut-in speed the inverter will disconnect from the grid. In the second type of turbine, the inverter is required to remain grid-connected continuously. This consumes energy supplied from the grid even when the turbine is not generating, thus over long periods of calm weather the turbine is not generating but the inverter still consumes energy. In the long term this can increase the household's energy bills. Thus rooftop wind turbines for the majority of urban sites will make little or no significant contribution towards reducing domestic carbon dioxide consumption.

6.9.2 Analysis of wind regime

To determine the wind regime at Edinburgh Napier University Merchiston Campus, it was decided that the regime should be assessed on a monthly resolution rather than annually, to give a better insight into how the wind characteristics change throughout the year. Four sets of wind roses have been produced, displaying power, energy, velocity and frequency for a twelve month period from July 2007 to June 2008 (Figures 6.8.1-6.8.4). The power and energy roses have been calculated using the sweep area of the Airdolphin turbine (1.8m diameter). The wind velocity and frequency roses are not dependent on blade diameter and are thus non-generic and suitable for use with any wind turbine. The energy rose is the most useful of all the wind roses as it shows the obtainable energy distribution for a site. Predominantly energy is generated from the west-south-west direction for the majority of the year. This is because of the high frequency of time that the wind blows from this direction as opposed to the high wind velocities from this direction.

Over the winter months of December to February, energy is increasingly generated from a westerly direction. This can be said to be an offshore wind. An examination of the frequency and velocity roses for this period (Figures 6.8.1 and 6.8.2) shows that the wind frequency from the westerly direction is not greatly increased, whereas higher velocity westerly winds are observed for this period, thus raising the wind energy yield.

The early summer months of April, May and July are a very different. It is observed that energy generated from both a west-south-westerly direction as well as the east. An onshore wind is coming directly off the east coast. This is also observed in the wind frequency roses (Figure 6.8.1).

The wind velocity probability distribution and cumulative distribution (Figures 6.8.7 and 6.8.6) are commonly used within the wind industry to describe the wind resource for a given site. The wind velocity probability distribution gives the probability of the wind's velocity occurring at a given rate. A narrow distribution centred about a high wind speed is most desired when selecting a site for a potential wind turbine. This would indicate that there is high wind velocity for the majority of the time.

Both the Raleigh and Weibull distributions have been fitted to the wind velocity distributions curves. By visual inspection it can be seen the Rayleigh distribution overestimates the measured for all months, whereas the Weibull distribution underestimates the measured but to a far lesser extent.
It should be noted that wind velocity data recorded below 1m/s should be discounted as is this below the calibrated measurement range of the anemometers used within this study. It should also be considered that winds below 1 m/s are of no interest in terms of wind energy potential.

As expected in the winter months, the distributions are more positively skewed due to the increased wind velocities observed. The distributions are more playkurtic-shaped overall as the distributions cover a larger range of wind speeds. The summer months have a narrower wind velocity distribution, and thus the distributions can be said to be more leptokurtic. Both parameters (the Rayleigh and Weibull distributions) are given in Table 6.8.1 for the Airdolphin turbine and in Table 6.8.3 for the Ampair turbine.

The capacity factor for the above-mentioned combined period was 0.3 percent lower than the capacity factor for the Airdolphin of 4.36%. On inspection, the mean wind velocities recorded at the Ampair 600 turbine are much lower than the wind velocities recorded at the Airdolphin. This could be for two reasons. The anemometer for the Ampair 600 turbine is installed two metres to the west of the turbine. The predominant wind blows from the south west and thus the anemometer may be sited within the turbine's wake, potentially reducing the wind velocities seen by the anemometer.

However, the low turbine outputs are in keeping with the low-recorded wind velocities. Thus the second explanation may be more useful. The turbine may well have been affected by four ventilation ducts protruding from the roof; these are approximately 10 metres to the west of the turbine. This was not an ideal location to mount the turbine. But due to space and planning restrictions on the roof, this was the only site where the turbine could be located.

6 .10 Airdolphin turbine

Micro-turbines are frequently described by their rated power output. The rated power output for the Zephyr Airdolphin turbine is 1kW at 12m/s wind velocity. However, for urban locations, the rated wind velocity is often greater than the mean weighted wind velocity. As a result, measured outputs are much lower than the figures claimed by the manufacturers. The performance of an Airdolphin was monitored for a period between July 2007 and July 2008 at Edinburgh Napier University. As expected, the highest averaged outputs were seen over the winter period of January, February and March 2008, yielding the highest average power outputs of 73W, 77W and 72W respectively. This is comparable with the daily averaged energy yields for each month, which for this period were calculated (for the month's output) as 1750Wh, 1840Wh and 1700Wh respectively.

The monthly energy outputs are reduced over the summer months. The month of May had the lowest: an annual daily average energy output of 1900Wh. The annual energy output was 395kWh and the capacity factor for this period was 4.36%. This is much lower than large-scale wind farms which have capacity factors typically around 25-30%.

Based on an annual output of 395kWh, the cost of the turbine (£3426 including VAT) and the current domestic electricity price of £0.10 per kWh, the economic payback period has been calculated as 86.7 years, although energy prices are set to increase and thus this payback period is predicted to reduce. However, this is still in keeping with other renewables such as Napier Universities PV facade which has an estimated payback period of 95 years (Muneer *et al.*, 2006). Embodied energy payback is a good method of estimating the turbine's environmental impact, as it estimates the energy consumed in the manufacture, assembly, transportation and installation of the turbine. Due to the in-depth analysis required, this was not estimated for this study.

6.11 Ampair 600 turbine

The months after the Ampair 600 was installed were fraught with technical problems caused by the control system. As a result, the inverter was damaged and had to be replaced. The failure of the control system to regulate the turbine's output also resulted in over-speeding, causing the destruction of the turbine. The turbine was replaced and the load controller was also replaced with an improved model. However, the problem in the Ampair 600 controller design is in its design strategy. The inverter has the above-mentioned problem of requiring three minutes grid connection time before generated power can be exported to the grid.

Figure 6.8.15 was generated using 4-second averaged wind data recorded at the Edinburgh Napier University site. The plot shows two columns for each month. One column shows the time frequency with which the wind velocity is blowing between the turbine's cut-in and cut-out speed. The second column shows the time frequency that the wind speeds between the cut-in and cut-out speed, but with a duration greater than three minutes. Thus this is the time required for the inverter to grid-connect, enabling power to be exported to the grid. Visual inspections of all months seem to show little correlation between seasonal variances. On average, for 30.5% of the time the wind velocity is within the turbine's operational limits, but due to the power management system energy can only be exported for 14% of the time. This significantly reduces the turbine's annual energy yield. Figures 6.8.3 and 6.8.4 show the Ampair 600 average monthly power and energy outputs. The turbine was installed in October 2007 but data was not collected until November 2007 due to an error made in wiring during the installation of the turbine. The monthly outputs have been monthly averaged to reduce the effects of the periods in which the turbine has been turned off for repairs. However, due to the turbine being turned off for the months of December and February, no outputs were recorded for this period. The average power output from November to March is unexpectedly low, not exceeding more than 2 Watts. The daily averaged power outputs are also very low for the period from November to March: the daily energy outputs were below 40Wh per day. From April, the turbine was replaced by a new reinforced turbine and modified control unit. The turbine has since been operating correctly and the power output has increased to an average output of 4W and daily

averaged energy yield of 100Wh. In May and June the daily average energy outputs were 200Wh and 80Wh, with an annual average of 55Wh for the whole period. Table 6.8.4 show the cumulative monthly averaged energy outputs and wind regime at Edinburgh Napier University's Merchiston campus. The table also gives the Weibull and Rayleigh wind regime coefficients for the Ampair 600 turbine. For the 8-month period that the turbine has been installed, the cumulative energy output was 41.6kWh and the turbine capacity factor 0.4%: ten times lower than that of the Airdolphin turbine.

An economic payback period was also calculated for the Ampair turbine. Due to its low annual energy yield of 28.8kWh and the high economic cost of the turbine (£4235.88 including VAT), the estimated economic payback period is 1471 years. It is concluded that this turbine installed in this location will never be economically viable.

6.12 Windsave WS1200 turbine

The Windsave turbine was installed in mid-June 2008 after a number of delays. The Windsave Company were hampered with technical problems at the launch of their product. For this reason the order was cancelled a number of times while modifications were made to the turbine, mast and inverter. Due to the length of delay it was not possible to collect any data for this turbine so no detailed study was carried out.

CHAPTER 7

Sustainable transport

7.1 Introduction

The work undertaken within the chapter is heavily based on the authors' work (Muneer & Clarke, 2008) pending publication.

The ever-increasing number of vehicles on the roads today is causing a significant contribution to the world's greenhouse emissions. There are currently more than 600 million vehicles on the world's roads, with a further 60 million new vehicles being added each year. Approximately two-thirds of the world's oil production is consumed by the transport sector, with road vehicles accounting for 40%. In terms of greenhouse gas emissions in the UK, the transport sector contributes 29%, and of that figure 40% is from cars (SMMT, 2008). The situation in relation to air pollution in the United Kingdom has improved dramatically over the past fifteen years, with the result that the air quality is better today than it has been at any point during the last hundred years. Despite this improvement there is still a long way to go until acceptable levels of quality are reached. "Air pollution is currently estimated to reduce the life expectancy of every person in the UK by an average of 7-8 months with estimated health costs of up to £20 billion each year" (DEFRA, 2007). Added to this is the UK's problem of ever-increasing emissions of CO_2 from the transport sector. For instance, between 1996 and 2006 private car registrations increased from 21 million to over 26 million, thus wiping out the efficiency gains acquired from tougher and more demanding legislation.

In 1998 the motor industry set a voluntary target of reducing vehicle fuel emissions to an average of 140g of CO_2/km by 2008. However, the latest statistics from motor industry trade association SMMT suggest that the average CO_2 emissions for new cars on the roads in 2008 were 159.7g of CO_2/km (IMechE, 2008a).

The European Commission is implementing mandatory targets for car manufacturers to produce vehicles with an average of less than 130 g of CO_2/km across their fleet range by 2012 and to 125g/km by 2015 (IMechE, 2008b). The Commission is set to increase emissions targets in the future to below 100g of CO_2/km by 2020 (IMechE, 2008a). Yet the rate of intended

reduction pales into insignificance when compared with the current 2.4% per annum rise in the car population.

To meet this long-term aim of lowering emissions of road vehicles, radical changes are required in both the technology used within vehicles as well as the attitude towards the uses of personal transportation.
Currently the majority of road vehicles are propelled via a petrol or diesel internal combustion engine. Vehicle manufacturers will continue to develop this technology within the foreseeable future, increasing fuel efficiency and lowering vehicle emissions. In addition, vehicle manufacturers will continue to improve vehicle aerodynamics as well as implementing new technologies such as hybrid technology.
Hybrid technology uses the addition of an electric motor to give additional propulsion and regenerative braking, thus reducing the engines power requirements and conserving potential energy during deceleration. The energy is stored within banks of batteries or ultra capacitors, which are able to rapidly deliver or absorb high charges over periods of acceleration and deceleration.
The current technologies being developed for the future are electric and hydrogen-fuelled vehicles, which will gradually replace petrol and diesel vehicles.

7.2 Hydrogen vehicle technology

There has been much research and development carried out in the field of hydrogen-fuelled vehicles. There are two areas of interest, hydrogen-fuelled internal combustion engines (ICE) and PEM fuel-celled vehicles.
BMW has opted to follow the route of internal combustion engines fuelled by hydrogen, as there has already been a great deal of research carried out on internal combustion engines, and so it is a matured technology. But due to the limited Carnot efficiency of around 25% for the internal combustion engine, this requires a much larger volume of stored hydrogen than if a more efficient fuel cell was used with an efficiency of around 50-60%.
Fuel cell technology will most likely supersede the internal combustion engine for this reason, although there are still many issues including life expectancy and cost which have to be addressed first.

PEM fuel cell technology operates at efficiencies of 50-60%, although there are additional losses which also need to be taken into account. Hydrogen electrolysers are used to convert water to hydrogen gas; these are 50-90% efficient. Depending on the type of hydrogen storage used there may also be up to a 30-40% energy loss during the storing process due to energy losses in compressing or liquefying hydrogen gas. Electric motor losses are fairly low, with efficiencies of 80 to 90%. The overall operating efficiency of a fuel-cell vehicle is likely to be limited to a maximum of 45%.

7.3 Electric vehicle technology

Electric vehicle technology has been around as long as the internal combustion engine vehicle. However, the internal combustion engine vehicle was preferred over the electric vehicle as batteries were heavy and could only provide a limited range before requiring a timely charge. Electric vehicles are similar in design to fuel-celled vehicles but instead of using a fuel cell a battery bank is used to drive an electric motor.

Recent developments in battery and ultra capacitor technology have led to vast improvements in electric vehicle performance. Batteries are becoming lighter and able to hold greater quantities of charge and have longer service lives. Battery recharge times are also greatly reduced from the early batteries requiring over night charging. New types of nanotechnology batteries from A123 Systems and Altair Nanotechnologies are capable of recharging in 5-15 minutes with high power charging stations.

This technology is rapidly developing, and it also brings increasingly long battery lifespans. Conventional batteries such as lead acid batteries were only capable of supplying 500-1000 discharge cycles at 60-80% depth of discharge (DOD) before needing to be replaced. New nanotechnology batteries are capable of operating with discharge cycles of 100% DOD without harm, minimising the size of battery capacity required and thus weight. These batteries also offer greatly improved life performance, being able to withstand 4,000-15,000 discharge cycles (Stone, 2008). The advantage of battery technology over that of fuel-cell technology are the higher overall operating efficiencies which can be achieved.

Altair Nanotechnologies have claimed that their batteries have cycle charge/discharge efficiencies, at 50% state of charge, varying between 91-97%

efficient (KEMA, 2008). When including other losses, such as AC to DC conversion, efficiency is typically 96%. With motor conversion efficiencies of 80-90%, overall system efficiencies of up to 75% are achievable and additional energy can be recovered with regenerative braking. Electric battery vehicles can offer greater energy efficiency than fuel-celled vehicles, which operate with an upper efficiency limit of 45%. EEStor technology has also being working in this field, and have developed an ultracapacitor which uses barium titanate as the dielectric. The ultracapacitor is capable of storing 52 kWh at much lower costs estimated to be $2,100. Ultracapacitors can offer several advantages over battery technology such as: greater power outputs than batteries providing improved acceleration, and longer lives typically over a millions cycles with out loss in performance. Ultracapacitors can also recharge rapidly in 5-10 minutes (The Energy Blog, 2006).

Figure 7.3.1 shows power and energy densities for various types and of energy storage and conversion systems which could potently be used in future road transport.

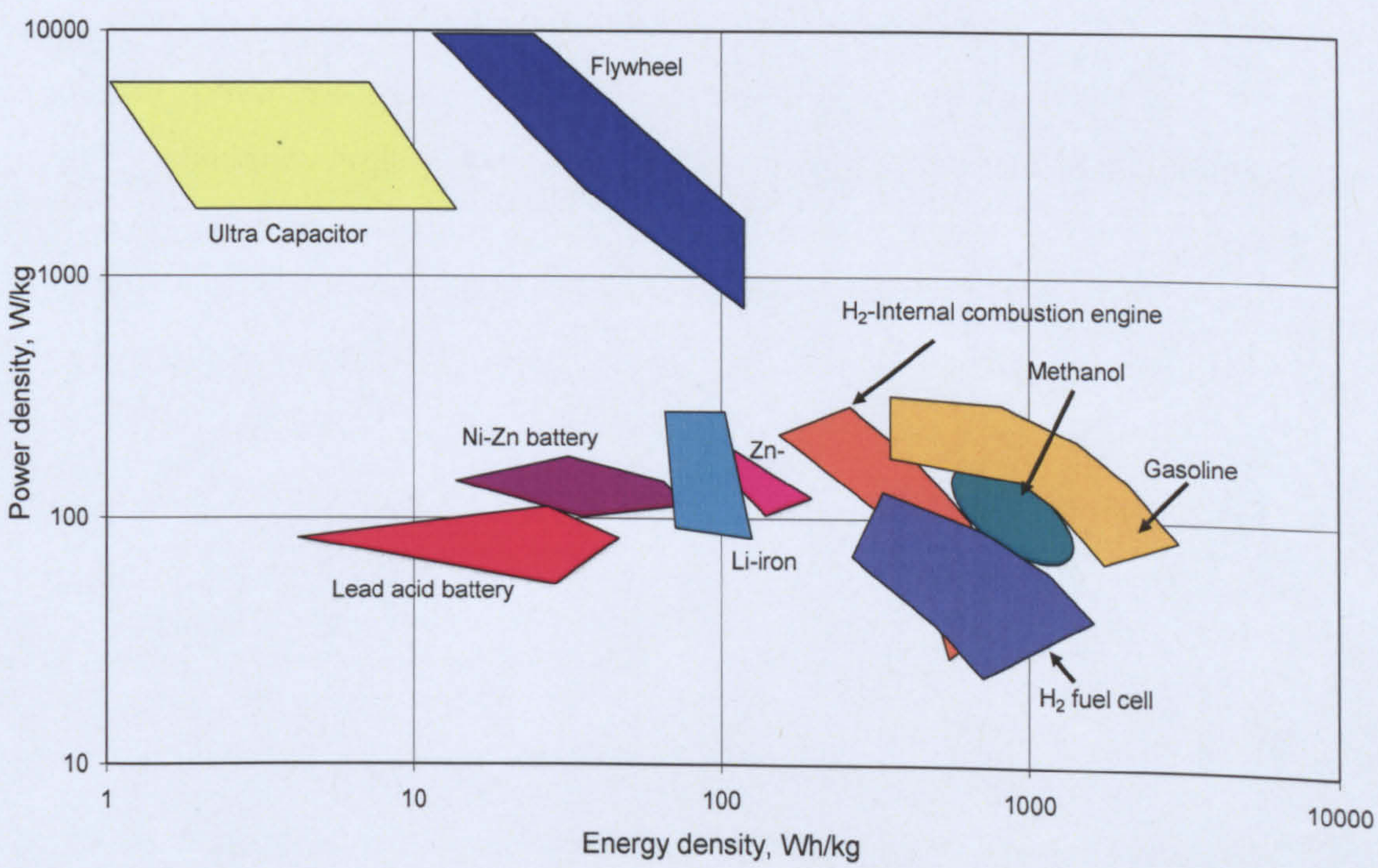

Figure 7.3.1 Specific power and energy densities of various energy storage and conversion methods. Source data: Fuhs, 2008.

7.4 Environmental impact of cars

A recent survey of 5,000 cars in Edinburgh, undertaken by this research team, indicated an average CO_2 emission of 208g/km. All-terrain vehicles (4x4s), such as the Porsche Cayenne Turbo S that emits 378g/km, are counteracting the emission reductions offered by technological innovation for smaller-engine cars. For the average new car on Britain's roads, 85% of its carbon footprint is attributed to fuel consumption during its operational life, 10% from its production of the vehicle and 5% from recycling the vehicle at the end of its life (SMMT, 2008).

Figure 7.4.1 shows an overall trend of CO_2 emissions reduction for new cars on the roads. It also shows the increase in the number of cars on the UK's roads each year. Figure 7.4.2 shows the reduction over time in car tail-pipe noxious gases made possible by technological developments.

It is becoming increasingly clear that unrestricted and unplanned growth in car ownership and use is unsustainable. Currently there are more than 600 million vehicles on roads across the world, with a further 60 million new vehicles being added each year.

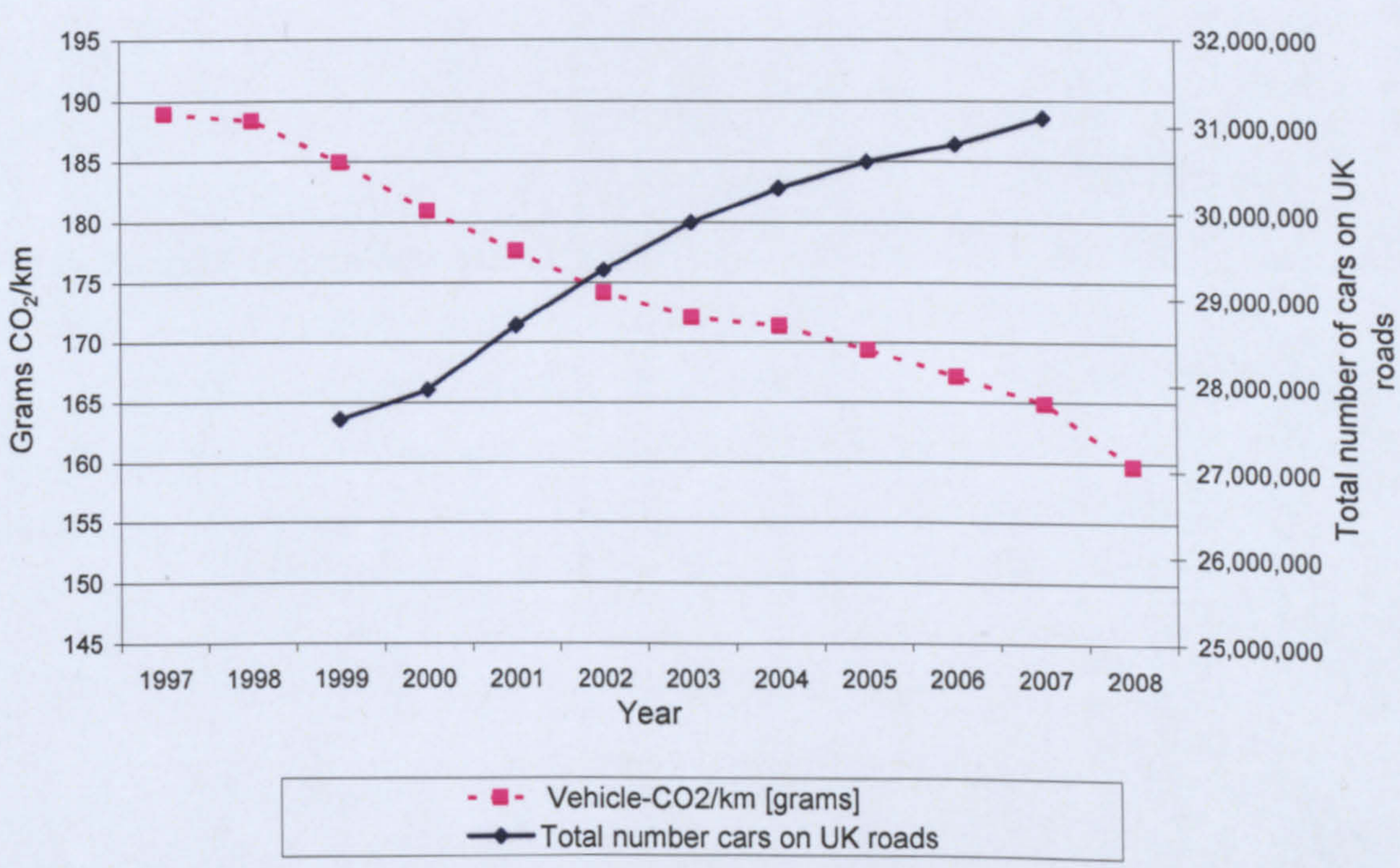

Figure 7.4.1 CO_2 emissions for new cars, and number of cars on the UK roads. Data source: SMMT, 2008.

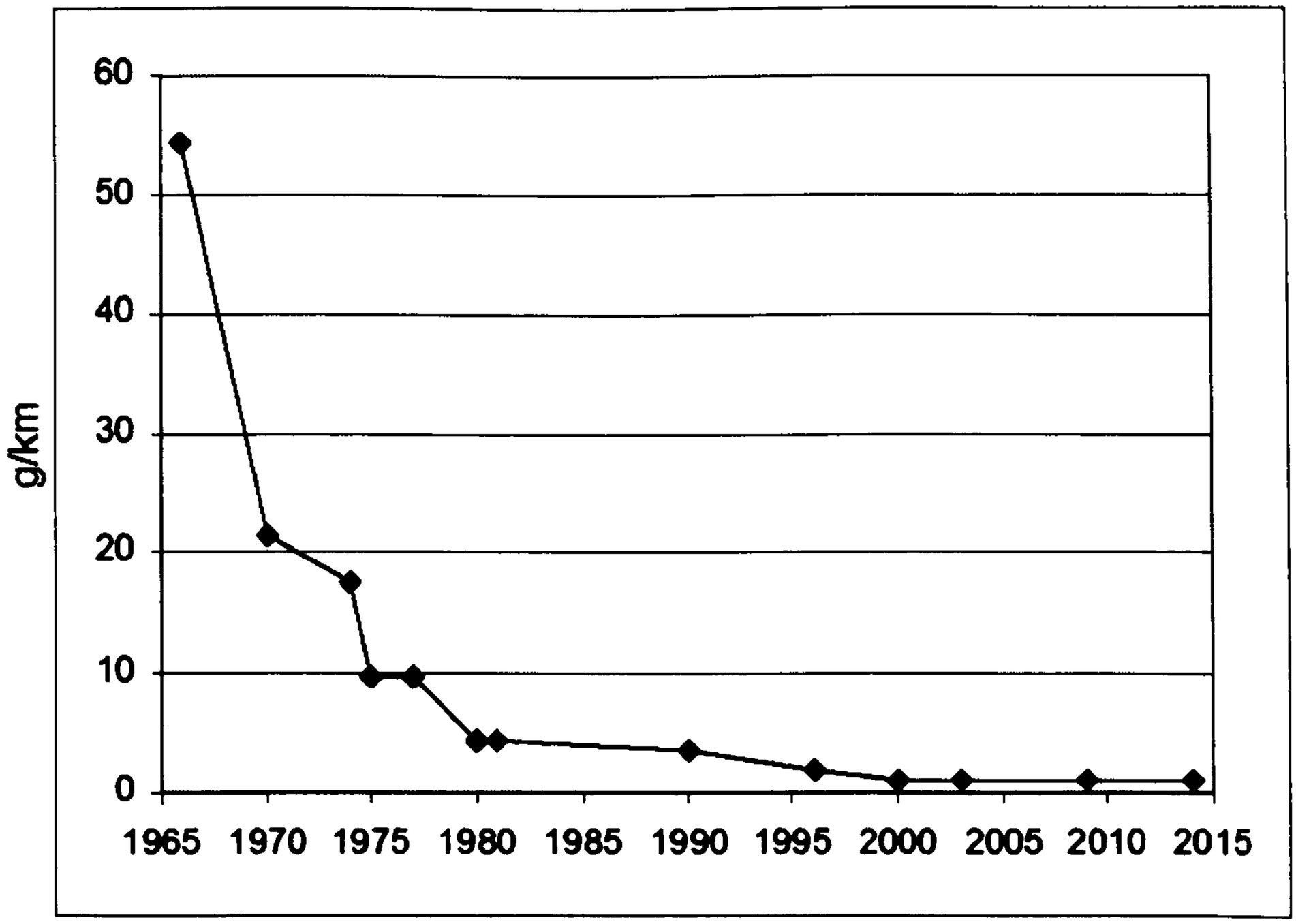

Figure 7.4.2 Historical reductions of tail-pipe noxious emissions achieved via technological developments, g/km.

In view of the unchecked rise of vehicle emissions, experiments are being undertaken at Edinburgh Napier University with a view to exploring the potential for reducing local and global air pollution by using more sustainable forms of urban transport. Hence, in the present work, an electric scooter that is charged by the University's own solar photovoltaic facility has been employed to investigate its emissions. Previous research has been carried out at Edinburgh Napier University to produce a definitive vehicle driving cycle for the city of Edinburgh (Booth *et al.*, 2001). That study was commissioned by the city council. It identified six principal routes that carry the bulk of the city's traffic flow.

Within the present research programme, and using measured and modelled data, the impact of electric scooters for urban commuting with respect to CO_2 emissions and vehicle parking space are investigated.

7.5 Pros and cons of cars and electric scooters

The car has been one of the greatest inventions of the twentieth century. Its overwhelming popularity itself is a proof of its usefulness to society. However,

as a choice for personal transport, it is increasingly coming into disfavour from local authorities and central governments across the world. Table 7.5.1 presents the advantages and disadvantages of cars.

Table 7.5.1 Why own a car?

Advantages	**Disadvantages**
Freedom of movement	Air pollution, major contributor towards climate change
Personal (driver/passenger) security	Road congestion
Large employment sector	Fossil fuel exhaustion
Personal or work space	Loss of building material
Ability to travel long distances	Space consumption on roads
Increased speed	Society stratification
Enjoining of communities	Accidents

Table 7.5.2 Merits and demerits of the use of electric scooters as opposed to cars

Merits	**Demerits**
Significant reduction in congestion	No network of recharging stations
Significant reduction in emissions	High insurance costs
Better flow of traffic	Road safety
Nil road tax	Difficulty in displaying parking tickets

It was pointed out above that the benefits from any technological advancement in achieving fuel economy and a reduction of pollutants such as carbon monoxide is undermined by the increasing population of cars. Hence, a step change is required in the choice of vehicle for personal transport, i.e. pollution-free two-wheelers may become much more of a necessity within urban areas. Furthermore, with accelerating fuel prices and parking costs for cars, the vehicle footprint of cars and their contribution to road congestion will bring them increasingly into disfavour. Once again, on the above three counts, the increased utilisation of scooters will be logical.

7.6 The Edinburgh driving cycle

Previous research carried out at Edinburgh Napier University developed the city driving cycle for the city of Edinburgh (Booth et al., 2001). In the research programme, a car-chasing technique was used to measure and obtain the driving pattern within Edinburgh's urban area. An instrumented car was used to chronologically log data pertaining to vehicle speed, engine rpm and parameters. That data was then used in conjunction with the city's traffic monitoring programme to produce the final driving cycle for the traffic flows along the principal routes of Edinburgh. Figure 7.6.1 presents details of the Edinburgh Driving Cycle (EDC). Table 7.6.1 provides information on the constituent driving modes for EDC and comparative figures for the European ECE-15 driving cycle.

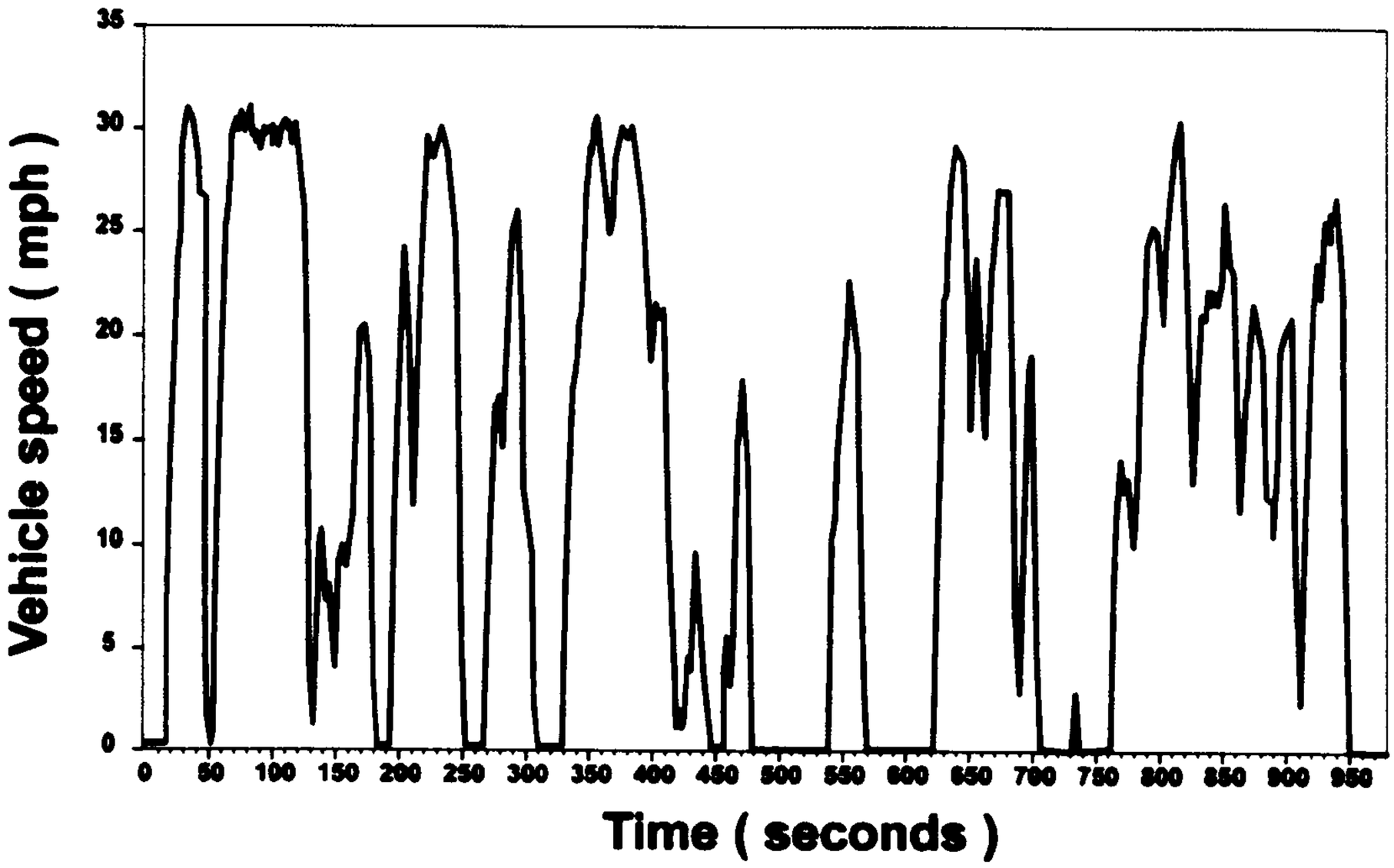

Figure 7.6.1 The City of Edinburgh car driving cycle. Source data: Booth *et al.*, 2001.

Table 7.6.1 Breakdown of the EDC and the ECE-15 driving cycles

	EDC		**ECE-15**	
Breakdown by driving mode	Time, s	Time fraction, %	Time, s	Time fraction, %
Idling	262	27	284	36
Acceleration	326	33	152	19
Steady-speed	44	5	236	30
Deceleration	242	35	108	15
Totals	974	100	780	100
General Information				
Average speed, kph	22	~	19	~
Distance covered, km	5.9	~	4.0	~

Note: figures stated above are for one-way journey. Source data: Booth *et al.*, 2001.

In the present work the cycle shown in Figure 7.6.1 has been used within purpose-built, MS Excel/VBA software to obtain the energy consumption for the journey undertaken by the scooter. Note that ample account is taken of the energy consumed during level cruising, acceleration and gradient-climbing modes of driving. For the purpose of auditing the latter driving mode, topography data was acquired from Ordinance Survey Sheet 350 drawn to a 1:25000 scale. For the purpose of comparing energy consumption between a car and scooter, a driving simulation was undertaken for one of the principal routes within Edinburgh (route number 4 of Both et al., 2008). That route has been identified as one that very closely resembles the composite Edinburgh Driving Cycle (Table 7.6.2).

Table 7.6.2 Route undertaken during driving simulation

Route undertaken
Morningside Rd
Bruntsfield Pl
Lothian Rd
S Charlotte St
Charlotte Sq
N Charlotte St
Queen St
York Lane
Leith Walk

7.7 Dynamic analyses for scooter

The analysis presented herein is largely based on the work of Rubin (Rubin, 2001). Figure 7.7.1 shows the electric scooter used with in the study.

Figure 7.7.1 Edinburgh Napier University electric demonstration scooter

7.8 Energy and power required for cruise mode

In this section the energy needed by a vehicle travelling along a horizontal surface at constant speed is presented. That energy is equal to the force of propulsion (F) multiplied by the distance (d) the vehicle travels,

$$E = Fd \tag{7.8.1a}$$

Equation 7.8.1b gives the required power, where v is the velocity.

$$P = Fv \tag{7.8.1b}$$

The two opposing forces on a vehicle are drag and friction. Drag is the aerodynamic force, which resists the vehicle as it travels through air. It can be approximated as

$$F_{drag} = \frac{1}{2} C_d A \rho v^2 \tag{7.8.2}$$

where C_d is the drag coefficient, A is the frontal cross-sectional area of the scooter and ρ the air density. The second opposing force is a due to rolling friction between the road surface and the vehicles tyres:

$$F_{friction} = \mu N = \mu W \tag{7.8.3}$$

Note that W = mg. The total force required to propel a vehicle at constant velocity over a smooth horizontal surface is therefore

$$F = \frac{1}{2} C_d A \rho v^2 + \mu W \tag{7.8.4}$$

Substituting the expression for F into equations 7.8.1a and 7.8.1b respectively gives the relationships for energy and power:

$$E = \left(\frac{1}{2} C_d A \rho v^2 + \mu W \right) d \tag{7.8.5}$$

$$P = \left(\frac{1}{2} C_d A \rho v^2 + \mu W \right) v \tag{7.8.6}$$

7.9 Energy and power for travel up a gradient

When the scooter is travelling up a gradient, a total of three forces are acting against the direction of motion – F_{drag}, $F_{friction}$ and $W\sin\theta$, where θ is the angle on inclination (see Figure 8.9.1). Thus the equations for E and P may be written as

$$E = \left(\frac{1}{2} C_d A \rho v^2 + \mu W \cos\theta + W \sin\theta \right) d \tag{7.9.1}$$

$$P = \left(\frac{1}{2} C_d A \rho v^2 + \mu W \cos\theta + W \sin\theta \right) v \tag{7.9.2}$$

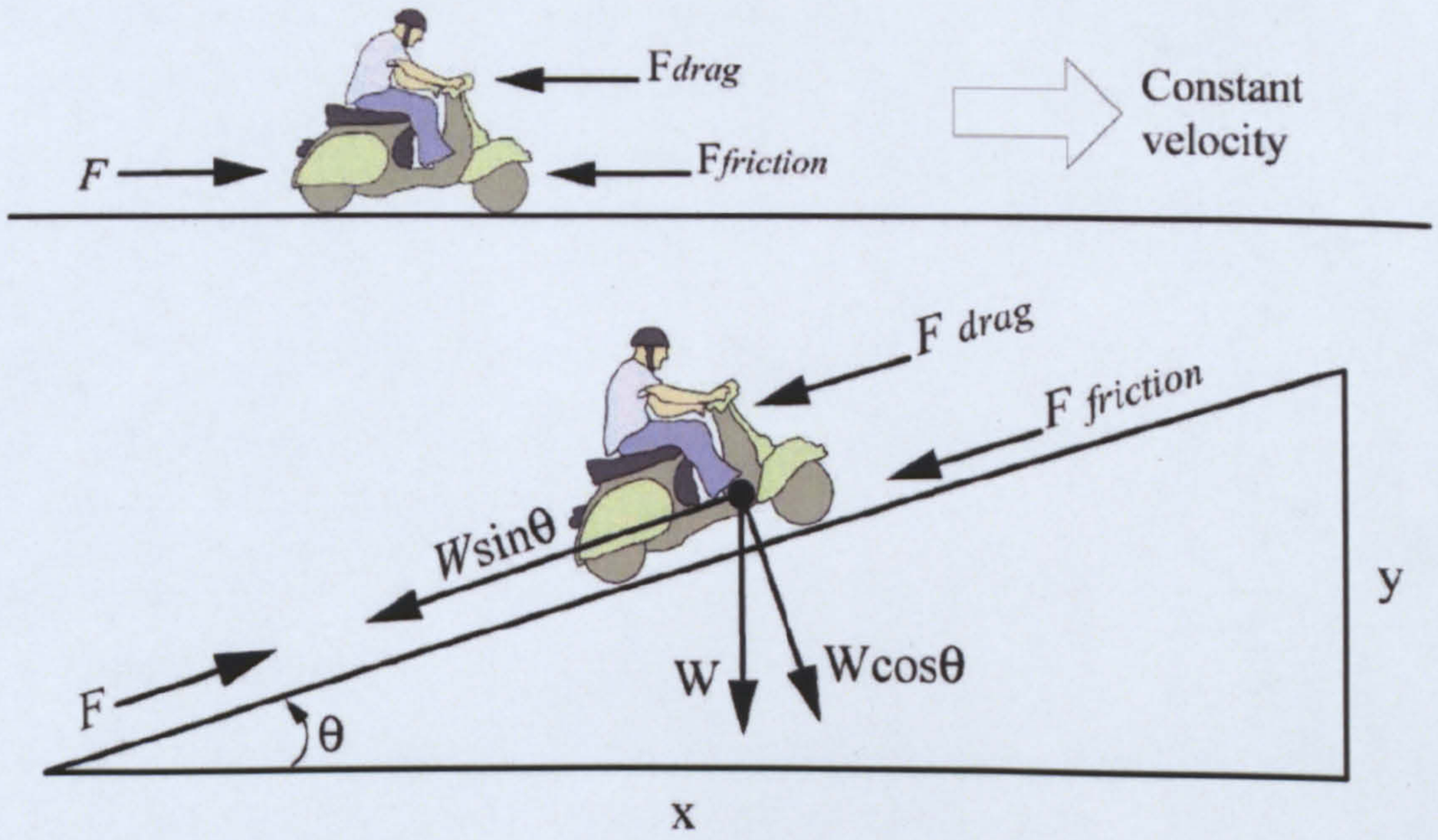

Figure 7.9.1 Free-body diagram for scooter on a level road surface (top) and travelling up a gradient (bottom)

7.10 Energy and power required for acceleration

The kinetic energy required to accelerate the scooter from an initial velocity of v_i to a final velocity of v_f is given by

$$E_{acceleration} = \frac{1}{2}mv_f^2 - \frac{1}{2}mv_i^2 \qquad (7.10.1)$$

Additional energy will however be required to overcome road friction and aerodynamic drag. Bearing in mind that the required energy needed for the latter component will change with changing velocity, the equations for E and P for a scooter that is accelerating from rest will be

$$E_{accel} = \frac{W}{2gf}v_f^2 + \mu Wd + \frac{1}{4}C_d A\rho v_d^2 d \qquad (7.10.2)$$

$$P = E/t \qquad (7.10.3)$$

7.11 Instrumentation, data collection, computer modelling and validation

Table 7.11.1 provides details of the scooter used in the trials and also provides a comparison with a medium-sized car.

Data on clock time, scooter speed, electric motor power demand, distance covered and route undertaken by the driver were recorded each second via the data-logger. One such image of the route undertaken on 15/05/2008 is shown in Figure 7.11.1, downloaded from the GPS sensors that were placed under the scooter's seat. At the end of each test drive, data was uploaded onto a PC and processed to obtain the key parameters such as chronological variation of speed and acceleration, distance covered, power demanded by the electric motor and energy drawn from the batteries.

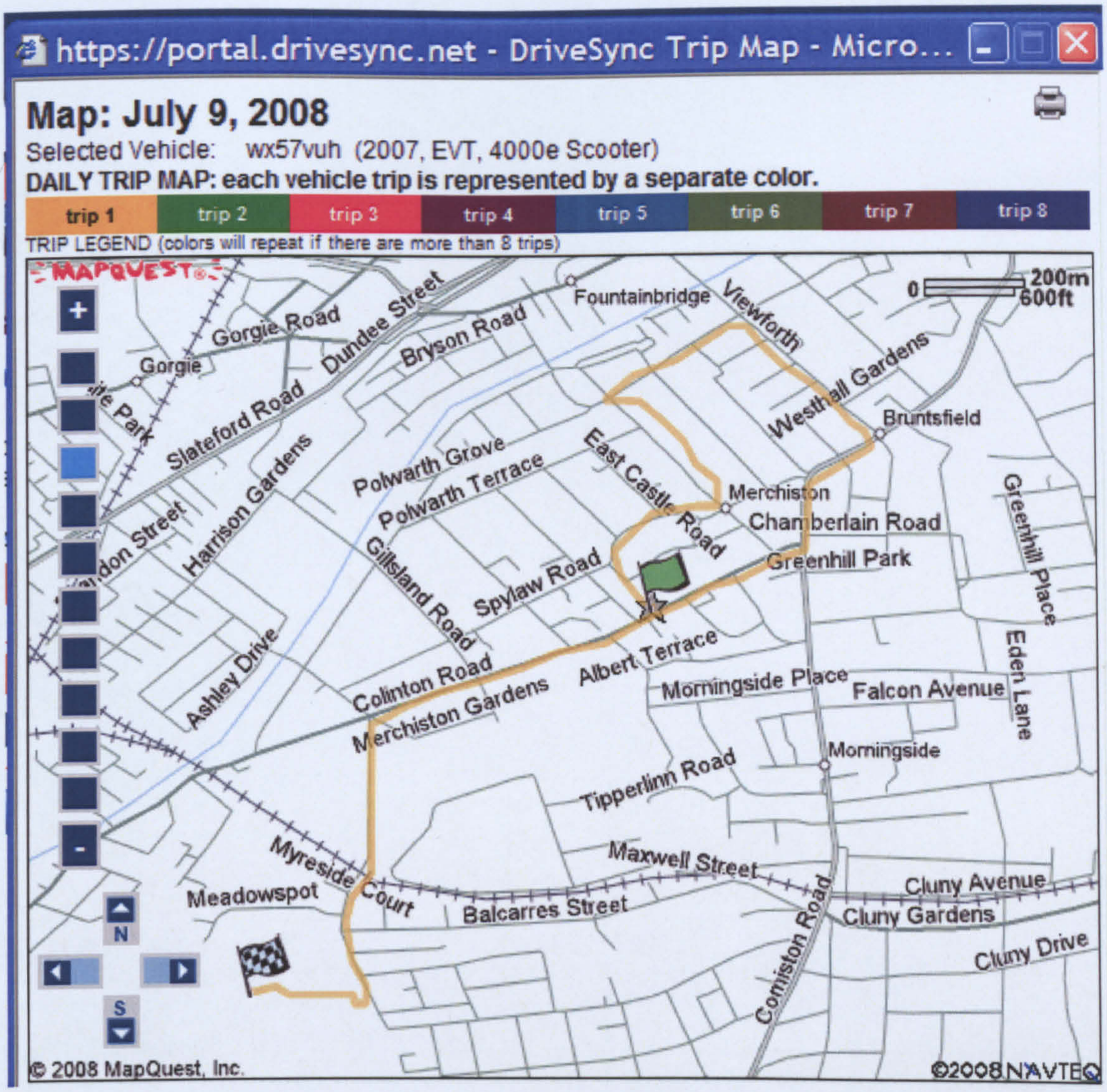

Figure 7.11.1 Trace of driven route obtained via on-board GPS sensor. Note that topographical details were obtained separately from the relevant 1:25,000 OS sheet.

Figure 7.11.2 shows a plot of measured speed, altitude and the total distance covered by the scooter during one of the test runs. The gradient climb is an important component of the energy estimation. This information is required within the MS-Excel/VBA simulation program and was keyed in manually after reading the relevant topographical details from OS sheet 350.

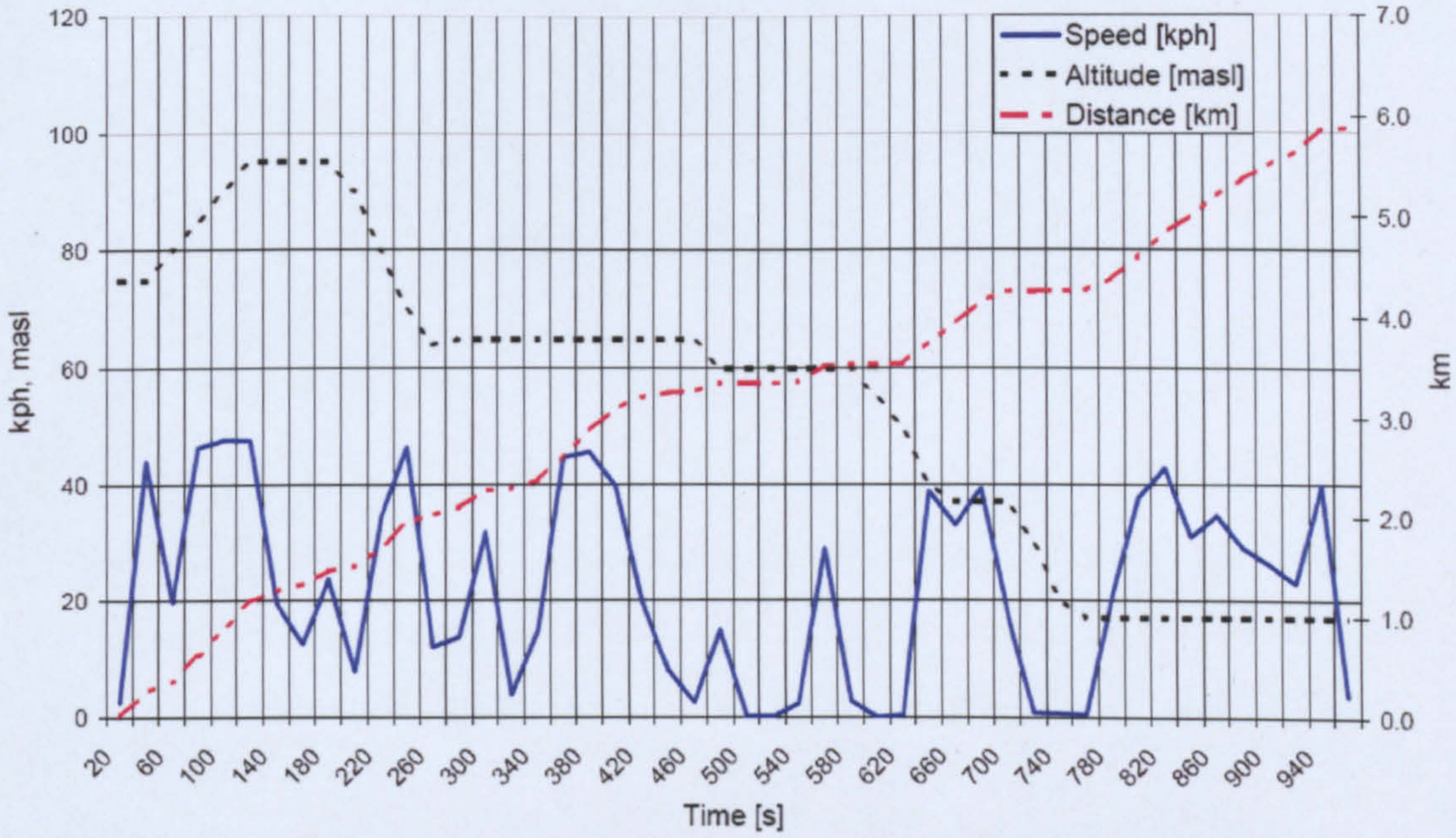

Figure 7.11.2 Plot of measured speed, altitude and total distance covered. Note that the gradient climb is an important component of the energy estimation within the MS-Excel/VBA simulation program.

Figure 7.11.3 presents the measured power and computed acceleration for the above test run. Note that the computed acceleration is also an important component of the energy estimation, as the main drain on the battery occurs during the hill-climbing and acceleration modes.

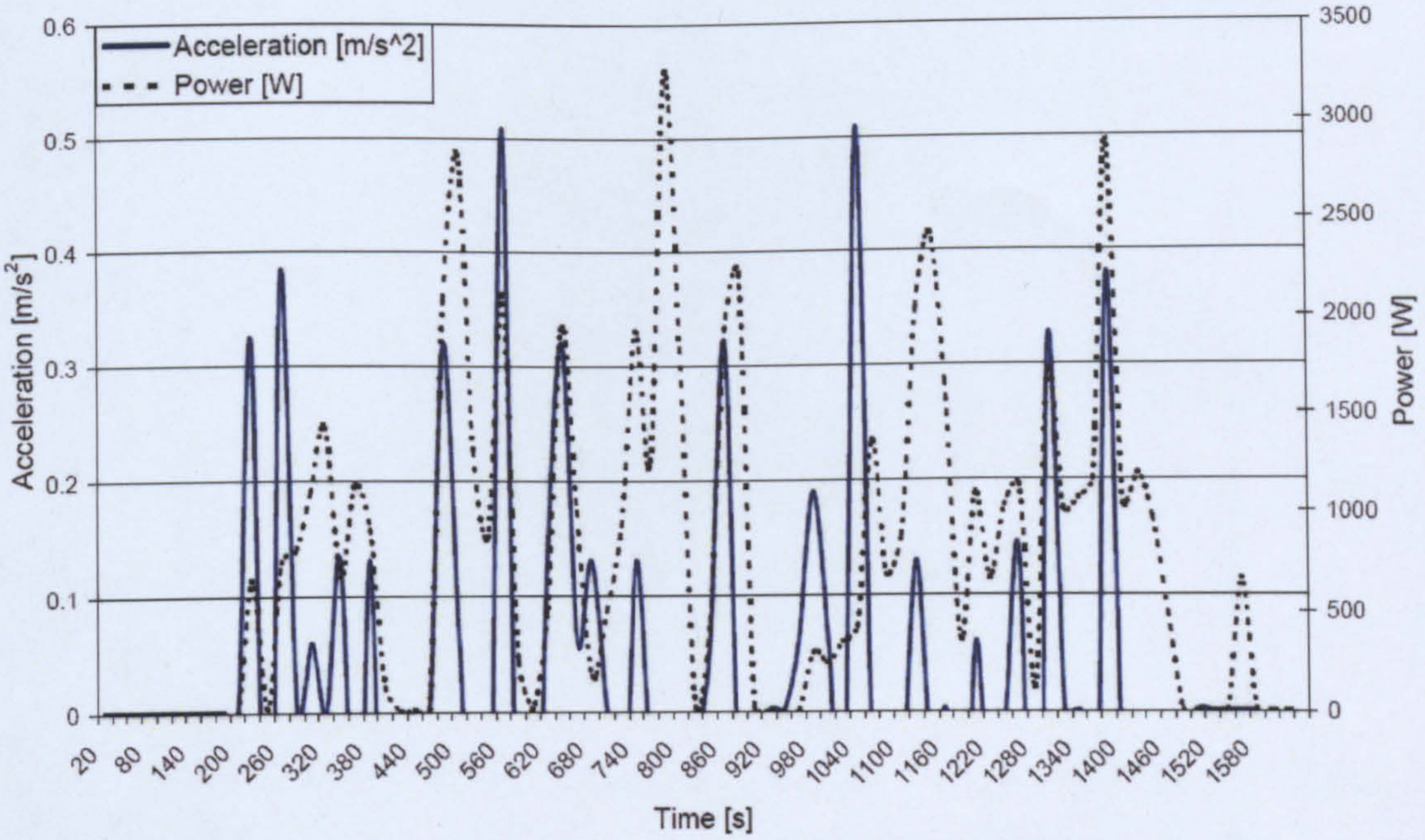

Figure 7.11.3 Measured power and computed acceleration. Note that the computed acceleration is an important component of the energy estimation within the MS-Excel/VBA simulation program.

Table 7.11.1 presents the validation results. The first two rows in Table 7.11.2 provide a comparison of energy required by daily commuters within Edinburgh using a car or an electric scooter respectively. Rows 3 and 4 provide a comparison of the required energy for two trial runs of the scooter. The scooter requires only a sixth of the energy used by a car. However, the CO_2 emissions from the electric scooter will be nil, as opposed to the 24g that will be emitted by the car. The daily trip CO_2 emissions from the above two sources of transport will be 322g for electric scooter and 2012g for the car. The CO_2 emission figure for scooter was obtained using a value of 587g CO_2/kWh of electrical energy that has been reported by Muneer *et al.*, 2006.

Table 7.11.1 Comparative data for the electric scooter and the chosen car

	Scooter	**Car**
Model	Moped, EVT	Renault, Megane
Length, m	1.64	3.87
Width, m	0.4	1.67
Footprint area, m^2	0.66	6.7
Frontal area, m^2	0.56	2.7
Purchase cost, £	£1,850	£11,170
Insurance cost/annum, £	£206	£240
MOT + maintenance cost/annum, £	£160	£285
Running cost for 4000 miles, £	£36	£536
Energy used for 4000 miles, kWh	68.5	469.4
CO2 emitted for 4000 miles, tonnes	0.21	0.67
CO emitted for 4000 miles, kg	0	23.4

Table 7.11.2 Validation results and comparison of energy requirements for the car and scooter*

Vehicle	**CO_2, g/trip**	**Driven distance, km**	**Measured value of energy consumed, Wh**	**Litres of petrol equivalent for return journey**	**Difference between measured and computed energy, %**
Car:Renault Megane	2012	11.8	2368	0.86	~
Scooter	322	11.8	384	0.14	~
Trial run 1	290	7.7	346	0.12	2.5
Trial run 2	205	5.9	245	0.09	3.3

* The first two rows in the above table provide a comparison of energy required by daily commuters within Edinburgh using a car or an electric scooter respectively. Note that the scooter requires only a sixth of the energy used by car. Rows 3 and 4 provide validation results for the presently developed MS-Excel/VBA simulation program.

7.12 Conclusions

An instrumented electric scooter was driven along selected routes within the City of Edinburgh with a view to measuring and recording key parameters such as clock time, scooter speed, electric motor power demand and the distance covered. The road gradient information was obtained from a detailed OS sheet. An MS-Excel/VBA simulation program was developed to simulate the three modes of driving that may be encountered on any given route, i.e. cruise on a level road, gradient climbing and acceleration, taking account of the road friction and aerodynamic drag. The simulation program returns the cumulative energy values with an accuracy of 96% or more. It was also found that, like with like, the scooter requires only a sixth of the energy used by an average-sized car. However, further reductions in the energy demand of scooters may be achieved

by technological improvements such as the use of electrical ultra capacitors that may be charged during downhill sections of a route and also the conservation of energy during braking modes. The ultra capacitors may then be used to prevent rapid discharge from the battery during acceleration and hill-climbing modes.

It was also noted that for the Edinburgh driving cycle, with an idling period that occupies a time fraction of 27% of the total journey time, the present fuel consumption of 0.86l for cars may be reduced by 9.6% to 0.62l, if engines were switched off during idle mode. The energy consumed for the scooter is 0.056kWh/km respectively, equating to monetary and environmental costs of cost of 0.56 pence and 33.3g CO_2 per km.

CHAPTER 8

Discussions conclusions and future work

8.1 Discussions

Energy is a crucial commodity that is essential to maintain a good quality of life. Energy dominates all aspects of modern living, and the global energy supply and consumption has reached a critical point in time. This is due to a number of contributing factors which has led humanity to revaluate its energy usage and reliance.

Global energy consumption is growing rapidly with global emissions spiralling out of control. A critical point has been reached where energy consumption is continually increasing. However, global fossil fuel production has reached its near maximum limit and is expected to start to fall into decline as the global reserves are rapidly depleted.

Environmental concerns about global emissions and the noticeable effects of climate change which are starting to be recognised has spurred governments around the world to tackle these global challenges. This research was carried out with the aim of reviewing and further developing the below-mentioned areas of renewable energy technology.

Chapter 1 gives the introduction to the thesis, which broadly covers the field of energy. The chapter begins with the global energy history before introducing and discussing energy sources such as fossil fuels, nuclear and renewable energy. The chapter also outlines the key areas of renewable energy which this thesis investigates.

Chapter 2, the literature review, covers the following areas of interest; the development of world renewable energy, solar energy and irradiation models; Edinburgh Napier University photovoltaic facade, wind energy and wind energy models, and micro and rooftop wind energy.

Chapter 3 examines the collection and quality control of the presently used solar database, and the development of solar energy regressions between

horizontal global and diffuse irradiation. It is concluded that a cubic curve developed between diffuse ratio and clearness index with linear cut-offs applied by visual inspection give superior performance over the quadratic regression. Monthly regressions gave an overall improved performance above both annual and seasonally developed regressions. However the increase in performance of monthly regressions over seasonal regressions is minimal. Thus it is considered that the increased simplicity of seasonal regressions makes it the optimal choice for the user.

Chapter 4 covers the development of solar irradiation models for use in urban environments, including the development of BIPVcalc software. The models have been developed to incorporate shading from trees and buildings. Statistical tests for the evaluation of solar models are also discussed in this chapter. Of the two models developed, statistical tests proved that the more complex SRDM model gave improved performance over ISRM model when estimating solar irradiance within a highly shaded urban environment. The SRDM model is also able to incorporate shading parameters with much greater accuracy.

Chapter 5 covers the validation of ISRM and SRDM model performance using measured data recorded from the Edinburgh Napier University PV facade and using statistical tests. This chapter also reviews the performance of the Edinburgh Napier University PV facade. The two models are used to simulate shading which occurs on the PV facade at various times throughout the day as a result of shading caused by the surrounding urban structures, such as buildings and trees.

Chapter 6 reviews wind energy within urban environments, the performance analysis of three micro turbines sited on the roof of Edinburgh Napier University, the rooftop wind regime and the development of Windcalc, a software which has been developed to analyse micro-turbine performances. The detailed study revealed the complexity of the observed urban wind regime. Design strategies used by turbine manufactures to optimise each of the turbines abilities to harness the wind also reviewed.

Chapter 7 compares a conventional petrol car with an electric scooter which is powered by renewably generated energy. The Edinburgh driving cycle has been used as the basis for comparison. The aim of the comparison is to determine what possible environmental improvements could be achieved with the adoption of clean and environmentally sustainable transport compared with a typical car.

Appendix A: covers the review of hydrogen technologies, and the development of the Napier hydrogen facility. To enable the development of the hydrogen research facility an in-depth review of hydrogen technology was undertaken. This included a review of hydrogen generation methods from both fossil fuels and sustainable methods as well as the status of current and future hydrogen storage methods. The review of available hydrogen fuel cell technology is also undertaken, including factors which prevent mass deployment of this technology. Finally, safety aspects and potential risks of hydrogen are reviewed.

8.2 Conclusions

The conclusions of the work under taken within this thesis are summarised below:

- The further development of sub-hourly regressions between the diffuse ratio, k, and clearness index, k_t, to enable the estimation of horizontal diffuse irradiation from its horizontal global counterpart. This is a further development of the work carried out by Liu & Jordon (1960) and Muneer & Saluja (1986) with the development and comparison of annual, seasonal and monthly regressions for the Edinburgh location being carried out.

- Solar energy within urban environments has long been recognised for its potential to provide a significant contribution towards building energy requirements. Although this potential has been recognised, there is a general lack of research being carried out within this area. The modelling of the availability of solar irradiation within the urban environment considering the affects of localised shading is required. There have been developments of specialised software which can be

used to simulate the effects of shading to a limited extent. However these software packages are limited by two factors, firstly their inability to adjust the diffuse component in highly built up environments and secondly their inability to incorporate shading parameters accurately. The two solar energy models mentioned below have been developed to address this issue.

- The development of the ISRM solar irradiation model incorporates simple one dimensional shading parameters to enable the simulation of global irradiation incident on a tilted surface for the detailed analysis of BIPV and other solar systems within the urban environment. The ISRM model is based on the integrated sloped irradiation model developed by Saluja & Muneer (1987).

- The development of the more complex SRDM solar irradiation model is a two dimensional model which is able to incorporate shading parameters with much greater accuracy. This model allows the simulation of shading on BIPV and other solar thermal energy systems within the urban environment with much greater accuracy than the ISRM model.

- The detailed analysis of the performance of Edinburgh Edinburgh Napier University PV facade has been carried out. The above-mentioned ISRM and SRDM models were also used to evaluate the affects of shading on the PV facade. In total, 45 months of data was analysed, system performances and monthly efficiencies were determined. The performances of the solar irradiance models were also evaluated.

- Micro rooftop wind turbines have received a great deal of media attention in recent years. There are a number of manufacturers marketing small turbines, typically rated at 2kW or less, with blade diameters ranging between 1-2m for the sole purpose of being mounted on the roofs of both domestic dwellings and commercial buildings. These systems can either be grid-tied or stand-alone. Manufacturers typically claim that building-mounted turbines can potentially generate 2000kWh annually (Renewable Devices, 2008). However, recent media attention and

reports from users state that micro rooftop turbines are not delivering their designed outputs. This thesis investigates the performance of three rooftop turbines and determines the precise reason why rooftop turbines are not meeting their design performance.

- In part of the above-mentioned research, the Windcalc analysis program was developed to analyse rooftop wind turbine performance and wind regimes in urban areas. The program is capable of combining separate wind velocity and turbine output datasets to carry out a range of statistical tests and performance modelling.

- Hydrogen and hydrogen fuel-cell technology is a rapidly growing area of research covering many different fields. A detailed review of this technology has been undertaken, covering areas such as hydrogen generation, storage media fuel-cell technology, as well as hydrogen safety.

- The development of the Edinburgh Napier University hydrogen research lab was also undertaken as part of this study. The laboratory has been designed to serve two purposes, for hydrogen generation and as a storage facility to allow energy generated by both solar PV and rooftop turbines to be stored and used at times of demand. This demonstrates the generation, storage and use cycle of renewable energy technology without the use of fossil fuel backup. The second use of the laboratory was to enable hydrogen research work to be carried out in a safe working environment.

- To demonstrate that renewables can be used to supply energy for transport, a detailed driving cycle analysis was carried out to evaluate and compare the energy consumption of an electric scooter with a typical petrol car. The analysis was based on the Edinburgh driving cycle to replicate typical driving patterns.

8.3 Future Work

Avenues open for possible future work are highlighted below:

SRDM model development of UK coefficients:

The SRDM model's performance could be further improved with the development of UK coefficients for Perez's all-sky model. The expression takes five coefficients which can be adjusted to produce a single model that can take account of the luminance distribution ranging from overcast to clear skies. The Coefficients are adjustable functions which have been based on more than 16,000 full-sky scans measured at Berkley, California covering all sky conditions. If a set of coefficients were developed for the UK this would most likely increase the model's performance significantly.

Development of BIPVcalc software for commercial purposes:

Currently the BIPVcalc software is only in prototype stage and thus is not very user-friendly. The software could be improved by making it easier to enter shading parameters, perhaps using a graphical user interface technique.

The optimisation of the Napier PV facade performance:

With careful analysis of shading throughout the day, Napier's PV module string layout could be reconfigured to minimise shading on PV strings, increasing the overall PV facade performance.

Development of Windcalc software for commercial purposes:

Currently the Windcalc software is only in a prototype stage and thus is not very user-friendly, If the software is to be commercialised it would require more user-friendly interfacing.

Investigation into the optimisation of micro-turbine blade mass and generator size:

Rooftop wind turbines operate in highly turbulent winds which are dynamically changing in both velocity and direction. As this occurs the turbine continually changes direction and the blades rapidly accelerate and decelerate. To optimise the turbine output the generator is required to rotate continuously at high speeds. Optimising the mass of the turbine blades and damping the yaw axis could lead to improved performances.

Investigation into the possible improvement of micro-turbine grid connection technology:

In evaluating the performance of the rooftop wind turbines, it was noted that the grid-connected turbines perform less well than the stand-alone turbines due to the inverter connection problems. Grid-connection inverters are required to monitor the state of the grid for three minutes before grid connecting. The inverters consume energy while been connected to the grid. Some turbine systems, such as the Windsave turbine, stay grid-connected continuously. Thus over long periods of no wind, the turbine will consume more energy than it generates. Other turbines such as the Ampair turbine only connect to the grid when generating power, but in turbulent wind conditions the inverter is continually disconnecting and connecting to the grid. Thus a large amount of potential of energy is lost. Research is required to optimise the frequency that the grid-connection inverter can connect to the grid.

Driving cycle analysis to optimise the size of the energy storage medium, to maximise the utilisation of energy recaptured during regenerative braking.

Research into the Edinburgh driving cycle showed that during normal driving operation typically a third of the energy consumed is lost during braking. A study could be carried out to quantify the energy lost during the vehicle's braking period with the aim of recovering this energy with regenerative braking. Energy conserved can be used during the vehicle acceleration period to reduce the vehicle's fuel consumption.

References

[Anon.], 2005. Solar PV. Refocus, May-June 2005. pp 21-24.

Bächler, M., 2006. Photovoltaics thin future. July-August 2006. pp 150-154.

BERR, 2008. Quality and Continuity of UK Electricity Supply. The Department for Business Enterprise & Regulatory Reform. Accessed online from. http://www.berr.gov.uk/energy/reliability/quality-continuity-supply/index.html. On 4th November 2008.

BERR, 2008. The Department for Business Enterprise & Regulatory Reform Wind speed Database. Accessed online from. http://www.berr.gov.uk/energy/sources/renewables/explained/wind/windspeed-database/page27326.html. On 3rd November 2008.

Blackmore, P., 2008 Siting micro-wind turbines on house roofs, BRE Trust. Accessed from www.BREbookshop.com. On June 10th 2008.

Booth, E.A., Muneer, T., Kirby, H., Kubie, J. and Hunter, J., 2001. The measurement of vehicular driving cycle within the city of Edinburgh, Transportation Research Part D, 6, pp. 209-220.

BP, 2008. The BP Statistical Review of World Energy, June 2008. British Petroleum. Accessed online from http://www.bp.com/liveassets/bp_internet/globalbp/globalbp_uk_english/reports_and_publications/statistical_energy_review_2008/STAGING/local_assets/downloads/pdf/renewable_table_solar_photovoltaic_power_2008.pdf. On October 22nd 2008.

BP, 2008a. Statistical Review of world energy. British Petroleum, June 2008. Accessed online from http://www.bp.com/liveassets/bp_internet/globalbp/globalbp_uk_english/reports_and_publications/statistical_energy_review_2008/STAGING/local_assets/downloads/pdf/statistical_review_of_world_energy_full_review_2008.pdf. On October 10th 2008.

BP, 2008b. The BP Statistical Review of World Energy, June 2008. British Petroleum. Accessed online from http://www.bp.com/sectiongenericarticle.do?categoryId=9023790&contentId=7044134. On October 22nd 2008.

BWEA, 2007.UK offshore wind: Moving up a gear. Accessed online from http://www.bwea.com/pdf/offshore/movingup.pdf. On October 30th 2008.

Çakanyıldırım, Çetin. Gürü, Metin., 2008. Hydrogen cycle with sodium borohydride. International Journal of Hydrogen Energy. Vol. 33, (Issue 17), pp4634-4639.

Celik, A, N. Muneer, T. Clarke, P., 2008. An analysis of installed solar photovoltaic and thermal collector capacities in the relation to solar potential for the EU-15. Renewable Energy, doi:10.1016/j.renene.2008.05.025.

Celik, A, N. Muneer, T. Clarke, P., 2009. A review of installed solar photovoltaic and thermal collector capacities in relation to solar potential for the EU-15. Renewable Energy, Vol 34, pp849-856.

CISBE Guide A., 2006. Chartered Institution of Building Services Engineers, London.

CISBE Guide J., 2004. Chartered Institution of Building Services Engineers, London.

Clarke, P. Munawaar, S. Davidson, A. Muneer, T. Kubie, J., 2007. An investigation of possible improvements in accuracy of regressions between diffused and global solar irradiation. Building Service Engineering Research Technology, Vol. 28 (Issues 2) pp1-9.

Clarke. P, Munawwar. S, Davidson. A, Muneer. T and Kubie. J., 2007. An investigation of possible improvements in accuracy of regressions between diffuse and global solar radiation. Building Services Engineering Research & Technology. Vol. 28 (Issue 2) pp189-197.

Commission International de l'Eclairage, 1973. Standardization of luminous distribution on clear skies. International Conference on Illumination, Paris, France. Dirnbirn, Austria: CIE.

DEFRA, 2005. Food and Rural Affairs. Annex B - Summary of Evidence Base (Demographics).Department for Environment, Accessed online from. http://www.defra.gov.uk/rural/strategy/annex_b.htm.Page last modified: 19 May, 2005. On 10th August 2008.

DEFRA, 2007. Air quality strategy for England, Scotland, Wales and Northern Ireland Vl.

Delta-T, 2002. BF3 Sunshine sensor data sheet. Accessed online from http://www.delta-t.co.uk/support-article.html?article=faq2005092822295. On October 22nd 2008.

Department for business enterprise & Regulations reform, July 2002. Energy consumption in the United Kingdom. Accessed online from http://www.berr.gov.uk/files/file11250.pdf. On October 17th 2008.

Department for business enterprise & Regulations reform, July 2008. UK energy in brief. Accessed online from http://www.berr.gov.uk/files/file46983.pdf. On October 11th 2008.

De Rosa, A. Ferraro, V. Kaliakatsos, D. and Marinelli, D., 2008. Predicting diffuse illuminance on vertical surfaces at Arcavacata di Rende (Italy) for various types of sky. Building and Environment. Vol. 43, (Issue 10), pp 1678-1686.

Efim, G, E. Avraham, I, K., 2008. The assessment of different models to predict the global solar radiation on a surface tilted to the south. Solar Energy. doi:10.1016/j.solener.2008.08.010.

ETSU NOABL, 2008. The Department of Trade and Industry wind speed database. Appendix MM1, Mini-manual 1, Accessed online from. http://edina.ac.uk/projects/mapscholar/casestudies/foley/MM1.pdf. On 3rd November 2008.

European Commission, 20th October 2000; GREEN PAPER: Towards a European strategy for the security of energy supply. Accessed online from http://www.europeanenergyforum.eu/background-and-references/background-and-reference-documents/green-paper-on-security-of-energy-supply. On October 10th 2008.

European Photovoltaic Industry Association, 2008. Report solar generation V-2008. Accessed online from http://www.epia.org/fileadmin/EPIA_docs/documents/EPIA_SG_V_ENGLISH_FULL_Sept2008.pdf. On October 20th 2008.

European Wind Energy Association, 2007. Stats 2007. Accessed online from http://www.ewea.org/fileadmin/ewea_documents/documents/Statistics/gwec/stats2007.pdf. On October 29th 2008.

FCH, 2004. Fuel Cell Handbook (Seventh Edition) By EG&G Technical Services, Inc. Under Contract No. DE-AM26-99FT40575. U.S. Department of Energy Office of Fossil Energy National Energy Technology Laboratory. Available from: National Technical Information Service, U.S. Department of Commerce, 5285 Port Royal Road, Springfield, VA 22161.

FRONIUS IG, 2005.Technical data brochure 40,000 6,2366-01.

Fuhs, A., 2008. Hybrid Vehicles: And the Future of Personal Transportation. New York, Taylor and Francis Group.

Grant, 2008. Grant squirrel 1000 series data logger 1000 series user. Accessed online from http://www.grant.co.uk/NR/rdonlyres/A4F8C9DB-EF4A-45E0-B46E-2447E0C5C6C9/0/1000SeriesManual.pdf. On October 22nd 2008.

Greif, J. Scharmer, K., 2000. European solar radiation atlas, 4th edition. France: Presses de l'Ecole, Ecole des mines de Paris.

Grimes, G., 2008. Onshore mid-year planning update: where are we now?. Real Power. Issue 13, pp14-15. Accessed online from http://www.bwea.com/pdf/realpower/realpower_13.pdf. On October 29th 2008.

Gueymard, C, A., 2008. From global horizontal to global tilted irradiance: How accurate are solar energy engineering predictions in practice. Proceedings of Solar 2008 Conference. San Diego, CA, American Solar Energy Society.

Gul, M. Muneer, T. Kambezdis, H., 1998. Models for obtaining solar radiation from other meteorological data. Solar Energy. Vol. 68, pp99-108.

Hankins, M., 2006. Rethinking Africa's Solar Market. International Rivers. December 2006. Accessed online from http://internationalrivers.org/en/node/1807. On October 31st 2008.

Hondo, H., 2005. Life cycle GHG emissions analysis of power generation systems: Japanese case. Energy. Vol. 30, pp2042-2056.

IMechE, 2008a. Professional Engineering: 23 July 2008, p.8.

IMechE, 2008b Professional Engineering: 27 February 2008, p.10.

INA, 2006. Hydrogen production and storage. International Energy Agency. Accessed online from: http://www.iea.org/textbase/papers/2006/hydrogen.pdf. On line from 4th November 2008.

Jalowiecki-Duhanel, L. Capentier, J. Payen, E. Heurtaux, F., 2007. Hydrogen charging/discharging systems with liquids organic compounds: A lacunar oxide catalyst to hydrogenate the unsaturated organic compound. International Journal of Hydrogen Energy. Vol. 32, pp2593-2597.

Jeong, S, U. Kim,R,K. Cho, E ,A. Kim, H, J. Nam, S. W. Oh, I, H. Hong, S, A. Kim, S, H., 2005. A study on hydrogen from NaBH4 solution using the high-performance Co-B catalyst. Journal of Power Sources. Vol. 144, pp129-134.

Joensen, F. Rostrup-Nielsen, J., 2002. Conversion of hydrogen and alcohols for fuel cells. Journal of Power and Energy Sources. Vol. 105, pp195-201.

Johnson, S,R. Anderson, P, A. Edwards, P ,P. Gameson, I. Prendergast, J, W. Al-Mamouri, M. Book, D. Harris, R, I. Speight, J, D and Walton, A., 2005. Chemical activation of MgH2; a new route to superior hydrogen storage materials. Chem. Commun. pp2823 - 2825, DOI: 10.1039/b503085d.

Karapinar, I. Kargi, F., 2005. Bio-hydrogen production from waste materials, Enzyme and microbial technology. Vol. 38, pp569-582.

KEMA., 2008. Summary of KEMA validation report two megawatt advanced lithium-ion BESS successfully demonstrates potential for utility applications, July 8, 2008. Accessed online from. http://www.b2i.cc/Document/546/KEMA_Carina_validation_report_public_final.pdf. On 3rd November 2008.

Kipp and Zonen., 2000. CM 11 Pyranometer / CM 14 Albedometer - Manual (English). Accessed online from http://www.kippzonen.com/?downloadcategory/38192/Discontinued+Solar+Instruments.aspx. On November 3rd 2008.

Kipp and Zonen, 2005. Pyranometers for atmosphere research and industry. Brochure 4414-470-W41.

Kondratyev ,K, Y.,1969. Radiation in the atmosphere. Academic Press, New York, pp 912.

Kovach, A. and Schmid, J., 1996. Determination of energy output losses due to shading of building-intergraded photovoltaic arrays using a retracing technique. Solar Energy. Vol. 57(Issue 2), pp117-124.

Lean, G. & Owen, J., 2008. Power cuts feared in UK nuclear plants crisis, The Independent, 5th October 2008.

Leggett, J., 1990. Global warming the Greenpeace report. Oxford, Oxford University Press.

Lin, S. Harada, M. Suzuki, Y. Hatano, H., 2002. Hydrogen production from coal by separating carbon dioxide during gasification, Fuelfirst. Vol. 81, pp2079-2085.

Liu, B,Y,H. and Jordan R,C., 1960. The interrelationship and characteristic distribution of direct, diffuse and total solar radiation. Solar Energy. Vol 4 (Issue 3), pp1-19.

Macias, E., 2007. An alliance for renewables: Private sector involvement in rural electrification. Renewable Energy world. January-February 2007.Vol 10

Marketbuzz, 2008. The leading annual world solar PV industry report. Accessed online from http://solarbuzz.com/Marketbuzz2008-into.htm. On October 24th 2008.

Mertens, S. Vries,E., 2008. Small wind turbines. Renewable Energy World, May-June 2008. pp130-139.

Mints, P., 2006. Photovoltaics PV in the US. Renewable Energy World. September-October 2006. pp 33-39.

Brown, G. 2005. Speech by the Rt Hon Gordon Brown MP, Chancellor of the Exchequer at the Energy and Environment Ministerial Roundtable. 15 March 2005. Accessed online from http://www.hm-treasury.gov.uk/1739.htm. On 27th October 2008.

Muneer, T. Abodahab, N. Weir, G. Kubie, J., 2000b. Windows in Buildings: Thermal, Acoustic, Visual and Solar Performance. Oxford, Architectural Press.

Muneer, T. and Clarke, P., 2008. The electric scooter as a vehicle of green transport. Pending publication.

Muneer, T. Angus, R, C., 1993. Daylight illuminance models for the United Kingdom. Lighting Research and Technology, Vol 25 (Issue 33), pp113-123.

Muneer, T. Gueymard, C. and Kambezidis, H., 1997. Solar Radiation and Daylight Models, (2nd ed 2004), Elsevier Butterworth-Heinemann Oxford.

Muneer, T. Gul, M., 2000. Evaluation of sunshine and cloud cover based models for generating solar irradiation data. Energy Conversion and Management. Vol. 41, pp461-482.

Muneer, T. Kubie, J. Grassie, T., 2003. Heat Transfer a problem solving approach. London, Taylor and Francis, pp286-187.

Muneer, T. Munawwar, S., 2006. Improved accuracy models for hourly diffused solar radiation. Transactions of the ASME. Vol. 128, pp105-117.

Muneer, T. Saluja, G, S., 1986. Correlations between hourly diffuse and global solar irradiation for the UK. Building Services Engineering Research & Technology. Vol.7, No.1. pp37-43.

Muneer, T. Younes, S. Munawwar, S., 2005. Discourses on solar radiation modelling, Renewable and Sustainable Energy Reviews. Vol. 11, pp551-602.

Muneer, T., 1987. Hourly diffuse and global irradiation: Further correlation. Building Services Engineering Research & Technology. Vol. 8, pp85-90.

Muneer, T., Younes, N., Lambert, N., Kubie, J., 2006. Life cycle assessment of a medium-sized photovoltaic facility at a high latitude location. IMechE, Part A:J. Power and Energy, 2005, 220, 517-524.

Myers, D, R., 2003. Solar radiation modelling and measurements for renewable energy applications: Data and model quality. National Renewable Energy Laboratory. International Expert Conference on Mathematical Modelling of solar radiation and daylight-challenges for the 21st century, Edinburgh, Scotland, September 15-16, 2003.

Najjari, M. Khemili, F. Nasrallah, S, B., 2007. The effects of the cathode flooding on the transient responses of a PEM fuel cell. Renewable Energy. Vol. 33, pp1824-1831.

Nakamura, H. Oki, M. Hayashi, Y., 1985. Luminance distribution of intermediate sky. Journal of light and visual environment. Vol. 9 (Issue1) pp6-13.

Nath, K. Das, D.,2003. Hydrogen from biomass, Current Science. Vol. 85, No. 3, pp265-271.

National Statistics, January 2004. Domestic energy consumption per household: by final use: Social Trends 34. Accessed online from http://www.statistics.gov.uk/STATBASE/ssdataset.asp?vlnk=7287. On October 17th 2008.

Newborough ,R., 2004. A report on electrolysers, future markets and the prospects for ITM power ltd's electrolyser technology. Accessed online from http://www.h2fc.com/Newsletter/PDF/ElectrolyserTechnologyReportFINAL.doc. On 4th November 2008.

O'Hayre, R. Cha, S. Colella, W. and Prinz, B., 2006 Fuel Cell fundamentals. New York: John Wiley & sons.

OS sheet 350 drawn to a 1:25000 scale

Page, J., 1997. Proposed quality control procedure for the Meteorological Office data tapes relating to global radiation, diffused solar radiation, sunshine and cloud in the UK. Report submitted to CIBSE Guide Solar Data Task group. 222 Balham High Road, London, UK: Chartered institute of Building Services Engineers.

Pearce, F, April 2005. Newscientist Environment. Squeaky clean fossil fuels. Accessed online from http://environment.newscientist.com/article.ns?id=mg18624976.500&print=true. On October 17th 2008.

Perez, R. Ineichen, P. Seals, R. Michalsky, J. Stewart, R., 1990. Modelling daylight availability and irradiance components from direct and global irradiance. Illuminating Engineering Society. Vol. 44, Pt 5, pp271-289.

Perez, R. Seals, R. Michalsky, J., 1993. Modelling skylight angular luminance distribution from routine irradiance measurements. Illuminating Engineering Society. Vol. 22, (1), pp10-17.

Perez. R, Ineichen. P, Seals, R. Michalsky, J. Stewart, R., 1990. Modelling daylight availability and irradiance components from direct and global irradiance. Illuminating Engineering Society. Vol. 44, Pt 5, pp271-289.

PVSYST 4.33., 2008. Software for photovoltaic Systems. Accessed online from. http://www.pvsyst.com/index.php. On November 3rd 2008.

Reidy, H.,2008. Change in the air. Professional Engineering. Vol 21, No 11, pp26-27.

Rubin, E.S., 2001. Introduction to engineering and the environment. McGraw-Hill, New York, 2001.

Saluja, G, S. Muneer, T., 1987. An anisotropic model for inclined surface solar irradiation. Proceedings of the Institution of Mechanical Engineers. Part C. Mechanical engineering science. Vol. 201 (Issue 11), pp11-20.

Sathyajith, M., 2006. Wind energy, fundamentals resource analysis and economics. Berlin Heidelberg: Springer-Verlag; 2006.

Schlapbach, L. Zuttel, A., 2001. Hydrogen-storage materials for mobile applications. Nature. Vol. 414, pp353-358.

SMMT, 2008. The ninth sustainability report. Accessed online from. http://lib.smmt.co.uk/articles/homepagearticle/HomePageArticles/9th%20SMMT%20suststainability%20report%20final.pdf. On October 28th 2008.

Sonntag, R, E. Borgnakke, C. Van Wylen, G, J., 2003. Fundamentals of thermodynamics, Sixth Edition. Hoboken. John Wiley & Sons.

Sorensen, B., 2005. Hydrogen and fuel cells emerging technologies and applications. London: Elsevier Academic Press; 2005.

Spencer, J, W., 1982. Comparison of methods for estimating hourly diffuse solar radiation from global solar radiation. Solar Energy Vol 29 (Issues 11), pp19-32.

Steven, M, D. Unsworth, M, H., 1979. The diffuse solar irradiance of slopes under cloudless skies. Quarterly Journal of the Royal Meteorological Society, Vol. 105, (Issue 445), pp 593-60.

Stone, A., 2008. How to Build A Quick-Charging Electric Battery. Accessed online from http://www.forbes.com/technology/2008/01/12/electric-cars-nanotech-tech-sciences-cz_as_0112nano.html. On 3rd November 2008.

Ströbel, R. Garche, J. Moseley, P.T. Jörissen, L. Wolf, G., 2006. Hydrogen storage by carbon materials. Journal of Power Sources. Vol. 159, (Issue 2,) pp781-801.

The Energy Blog, 2006. Ultracapacitor Shuns Publicity. January 27th, 2006. Accessed online from http://thefraserdomain.typepad.com/energy/2006/01/eestor_ultracap.html . On12th November 2008.

The National Energy Foundation. 2007. Energy advice, Accessed online from: http://www.nef.org .uk/energyadvice/co2emissions.html. On May 10th 2007.

Warwick Wind Trials, 2007. The first interim report on the trial March 2007, Accessed online from. http://www.warwickwindtrials.org.uk/resources/Warwick+Wind+Trials+Interim+Report+Final+2.pdf. On 4th November 2008.

Warwick Wind Trials, 2008. The first interim report on the trial May 2008, Accessed online from http://www.warwickwindtrials.org.uk/resources/Interim+Report+May+2008.pdf. On 4th November 2008.

Westwood, D., June 2008. Department for business enterprise & Regulations reform. Supply chain constraints on the deployment of renewable electricity technologies, Accessed online from http://www.berr.gov.uk/files/file46792.pdf. On October 12th 2008.

Wind Atlas Analysis and Application Program, 2008. Getting Started with WAsP 8. Accessed online from http://www.wasp.dk/Download/DownloadFiles/General/Archive/Getting%20Started%20with%20WAsP%208.pdf. On October 30th 2008.

Wood, J. Muneer, T. Kubie, J., 2003. Evaluation of a new photodiode sensor for measuring global and diffuse irradiance, and sunshine duration. Journal of Solar Energy Engineering.Vol.125 (Issue 1), pp43-48

World Wind Energy Association, 2008. Statistical report. Accessed online from http://www.wwindea.org/home/index.php?option=com_content&task=blogcategory&id=21&Itemid=43. On October 29th 2008.

Younes, S. Claywell, R. Muneer, T., 2005. Quality control of solar radiation data: Present status and proposed new approaches. Energy. Vol 30, pp1533-1549.

Zhou, L., 2004. Progress and problems in hydrogen storage methods. Renewable & Sustainable Energy Reviews. Vol. 9, pp395-408.

Zuttel, A., 2003. Materials for hydrogen storage. Materials today Vol. 6, (Issue 9), pp24-33.

APPENDICES

APPENDIX A

The development of the hydrogen research laboratory at Napier-lessons learnt

A.1 Introduction

Energy is one of the most basic human necessities, and the abundance of readily available energy has been crucial to the development of civilisation. Fossil fuels are predominately used, and supply over 80% of the world's energy needs. Ever-increasing energy demands are rapidly depleting finite fuel resources, and this is coupled with growing concerns about global warming. The rapidly increasing demand arising from the growth of the world's economy is putting unsustainable pressure on global resources. Until recent years the accessibility of carbon-based fuels made it an ideal energy source. With the increasingly noticeable effects of global warming, it is now time to find a suitable clean and sustainable fuel replacement. Hydrogen generated from sustainable resources will most likely be the energy carrier used to replace hydrocarbon-based fuels.

In this chapter a review of the status of hydrogen technology shall be undertaken which will be followed by a report on the aurthor's involvement with the respective hydrogen laboratory's development, the lessons that were learn from the above activity shall then be presented.

A.2 Hydrogen production

A cost-effective and efficient method of producing hydrogen is going to be a key part of introducing a successful hydrogen economy. There are many different routes which can be taken to produce hydrogen gas; each have there own merits and demerits and are at varying stages of development. These range from theoretical concepts to fully-developed commercialised products. Currently the most common technology used today is gas reforming and electrolysis. This would be the most likely technology for use in the early development of a hydrogen economy and infrastructure. This technology is already in wide use in the existing hydrogen infrastructure, where it is used to supply hydrogen to the petrochemical industry. However, the technology used is not a carbon-neutral process, as the most common method of producing

hydrogen is via reforming natural gas where carbon dioxide is a by-product. Electrolysis itself does not produce any greenhouse gases, as the only products of splitting water into its elements are hydrogen and oxygen. But the source of electricity used to supply energy to the electrolyser does produce greenhouse gases if not supplied from sustainable sources such as wind or solar. If non-renewable energy sources are used to supply electricity to the electrolyser then the carbon footprint will be greater than if the hydrogen was directly reformed from natural gas.

The most likely first step in the production of hydrogen for the transport infrastructure would be the use of reformed natural gas, as it can supply large quantities of hydrogen gas at low economic cost. This would not be carbon neutral unless it was used with carbon capture and sequestration. Electrolysis may be also used in areas with good renewable resources such as wind, solar and hydro power.

Once a hydrogen infrastructure was developed, a gradual changeover period would see reformed natural gas generation increasingly used with carbon capture and sequestration, and increased growth in renewable-based electrolysis. Looking further into the future, it is likely that photolysis and bio-photolysis will replace natural gas reforming with the depletion of gas reserves. A hydrogen gas infrastructure could also resolve the intermittency issues of renewables.

Currently hydro power is used for short durations, and gas-fired generation used for longer durations to flexibly accommodate the intermittency problem of renewables.

A.3 Hydrogen from fossil fuels

Hydrogen gas can be produced from nearly all types of fossil fuels; however, natural gas and coal are the most common fuels used for production today. Hydrogen generated from fossil fuels can only be said to be zero-emission if the by-product carbon dioxide can be carefully captured and sequestrated (INA, 2006).

A.3.1 Reforming hydrogen from natural gas

There are three methods commonly used in the production of hydrogen from natural gas. New technologies are currently been developed but are not commercially viable yet. The methods of reforming natural gas mentioned below are endothermic, requiring large energy inputs. A variety of processes have been developed aiming to achieve lower energy inputs and thus higher conversion efficiencies.

A.3.2 Steam reforming of methane

Steam reforming is used to convert methane (CH_4), the dominate component within natural gas, to hydrogen. The process is a strongly endothermic conversion of methane and water vapour into hydrogen and carbon monoxide (Equation A.3.2.1).

$$CH_4 + H_2O \rightarrow CO + 3H_2 - \Delta H^0$$

(A.3.2.1)

The enthalpy change ΔH^0 during this process equals 252kJ mol^{-1} at ambient pressure, 100kPa with a temperature of 298K and 206kJ mol^{-1} if the addition of water is in the form of vapour. The products of this reaction (Equation A.3.2.1) contain approximately 12% carbon monoxide. The process is then taken to completion with the conversion of carbon monoxide with addition of water vapour to the hydrogen gas mix (Equation A.3.2.2).

$$CO + H_2O \rightarrow CO_2 + H_2 - \Delta H^0 \qquad \text{(A.3.2.2)}$$

This step takes place at a temperature between 700°C and 850°C and at a pressure of 2500KPa, and the raised temperature is achieved by the combustion of the methane feed-gas. A catalyst is also required (commonly nickel or nickel-based catalysts). The enthalpy ΔH^0 equal to -41 kJ/mol where all the reactants are in a gaseous form (Sorensen, 2005). The combination of both reactions can be seen in Equation A.3.2.3. The overall efficiency for this process is typically around 80%.

$$CH_4 + 2H_2O + \Delta H^0 \rightarrow CO_2 + 4H_2 \qquad \text{(A.3.2.3)}$$

Hydrogen production by partial oxidation: Hydrogen can be produced from methane by means of partial oxidation which can be carried out in a number of ways, most commonly either by catalytic partial oxidation or auto-thermal reforming.

Non-catalytic partial oxidation is similar to the above-mentioned steam reforming process without the use of a catalyst to aid the oxidation process. Thus higher temperatures are required to ensure complete conversion takes place and minimum soot is produced. The small amount of soot which is produced is removed by scrubbers in a separate process afterwards.

Catalytic partial oxidation is a reaction which is initiated catalytically with no flame, thus producing no soot (Equation A.3.2.4). The use of a catalyst reduces the required temperature and increases the rate of reaction and overall conversion efficiency.

$$CH_4 + \frac{1}{2}O_2 \rightarrow CO + 2H_2 - \Delta H^0 \qquad \text{(A.3.2.4)}$$

Thermochemical reforming is a combination of both catalytic oxidation and steam reforming, and consists of a thermal and catalytic zone. In the thermal zone, methane is burnt with steam and sub-stoic metric volumes of oxygen from air so only partial combustion takes place (Equation A.3.2.5).

$$CH_4 + \frac{3}{2}O_2 \rightarrow CO + 2H_2O - \Delta H^0 \qquad \text{(A.3.2.5)}$$

The heat produced by the partial combustion in the thermal zone is used to supply heat for endothermic steam reforming (Equation A.3.2.5) in the catalytic zone. Where the above-mentioned reaction (Equation A.3.2.1) and the shift reaction (Equation A.3.2.2) take place, then soot precursors are broken down (Joensen & Rostrup-Nielsen, 2002). Table A.3.2.1 gives a comparison of all three technologies.

Table A.3.2.1. Comparison of technologies for H_2 production from natural gas

Technology	**Steam reforming**	**Partial oxidation or auto-thermal reforming**
Benefits	High efficiency Low emissions	Smaller plant size Low costs for smaller units Simpler system
Challenges	High costs for large units Complex systems Sensitive to natural gas quality	Lower efficiency Hydrogen purification required High emissions/flaring

Source: (INA, 2006)

A.3.3 Hydrogen production from coal

Hydrogen production from coal can only have zero carbon emissions if a carbon capturer and sequestration is used. It should be noted that the production of hydrogen from coal requires only half the energy compared with hydrogen generated by sustainable means. Hydrogen is produced by the gasification of coal. The primary reaction is shown in Equation A.3.3.1.

$$C_nH_m(coal) + nH_2O \rightarrow nCO + (n + m/2)H_2 \qquad \text{(A.3.3.1)}$$

The coal gasification process is highly endothermic, and requires a temperature of 1273K for the reaction to take place at a suitable rate. The product of this reaction is a mixture of gases containing carbon monoxide and hydrogen, known as the synthesis gas. The synthesis gas is then converted into hydrogen gas and carbon monoxide with a water shift reaction, as seen in Equation A.3.3.2. This reaction takes place at a much lower temperature and thus is carried out in a separate reactor. Carbon dioxide needs to be separated from the hydrogen at this stage. Calcium oxide is used as an absorbent to eliminate carbon dioxide from the synthesis gas leaving pure hydrogen Equation A.3.3.2 (Lin *et al.*, 2002).

$$CaO + CO_2 \rightarrow CaCO_3 \qquad \text{(A.3.3.2)}$$

A.4 Production of hydrogen by electrolysis

Electrolysis is the process which uses electricity to split water into hydrogen and oxygen. It should be noted that hydrogen produced by renewables is zero emission; however if the electricity supply is not from a renewable resource then the energy consumption and carbon dioxide emissions are much higher than that of reforming hydrogen from natural gas or coal.

The main use of electrolysis is for one of two applications, the conversion of renewable energy to hydrogen. The second reason is that hydrogen generated by electrolysis has a very high purity which is well suited for certain applications that require high purity hydrogen.

There are three main types of electrolyser technology in use: alkaline electrolysis, polymer electrolyte membrane electrolysis, and high-temperature electrolysis.

Electrolysers consist of two electrode plates made from inert metals such as platinum, which are placed in an aqueous solution as shown in Figure A.4.1. An electric potential difference across the solution will cause the decomposition of water, with hydrogen forming on the negatively charged cathode and oxygen forming on the positively charged anode. Water consists of two atoms of hydrogen and one of oxygen, so twice as much hydrogen is produced as oxygen in the electrolysis process. This is proportional to the total charge flowing through the electrolyte.

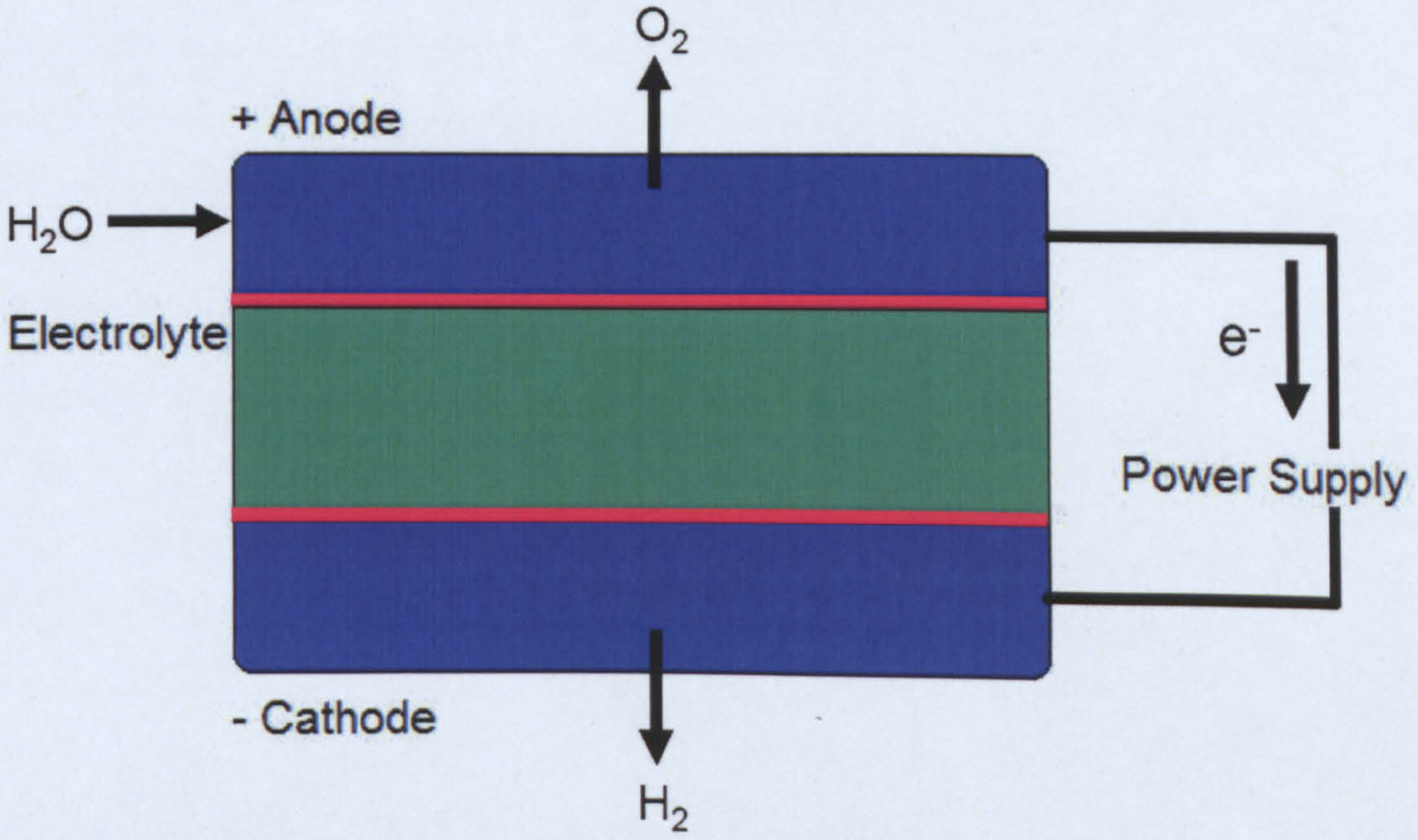

Figure A.4.1. Schematic of simple electrolyser.

At the cathode a reduction reaction takes place, with electrons (e^-) being transferred from the anode to the cathode by an external circuit and combining with hydrogen protons (H^+) to form hydrogen gas (Equation A.4.1).

$$2H^+ + 2e^- \rightarrow H_2 \qquad \text{(A.4.1)}$$

At the anode an oxidation reaction takes place, as electrons are stripped from the water molecules forming oxygen hydrogen ions, which pass through the electrolyte to the cathode (Equation A.4.2).

$$H_2O \rightarrow \frac{1}{2}O_2 + 2H^+ + 2e^- \qquad \text{(A.4.2)}$$

Both half reactions balance out, forming the overall reaction across the electrolyte. Water is decomposed into hydrogen and oxygen (Equation A.4.3).

$$2H_2O \rightarrow 2HO^- + 2H^+ \rightarrow H_2O + \frac{1}{2}O_2 + 2e^- + 2H^+ \qquad \text{(A.4.3)}$$

A.4.1 Alkaline electrolysers

Alkaline electrolysers use an aqueous electrolyte solution such as potassium hydroxide or sodium hydroxide. The role of the alkaline component within the electrolyte is to improve the ion conductivity of the water, enabling hydrogen ions to be more easily transported through the electrolyte by the electric potential difference.

The anode and the cathode are separated by a micro-porous diaphragm. Alkaline electrolysers have relatively low current densities of < 0.4A/cm^2 and conversion efficiencies typically between 60-90%. Current alkaline electrolysers can deliver gas at pressures up to 30 bars without additional compression. The purity of hydrogen produced is typically 99.8% without additional purification (Newborough, 2004).

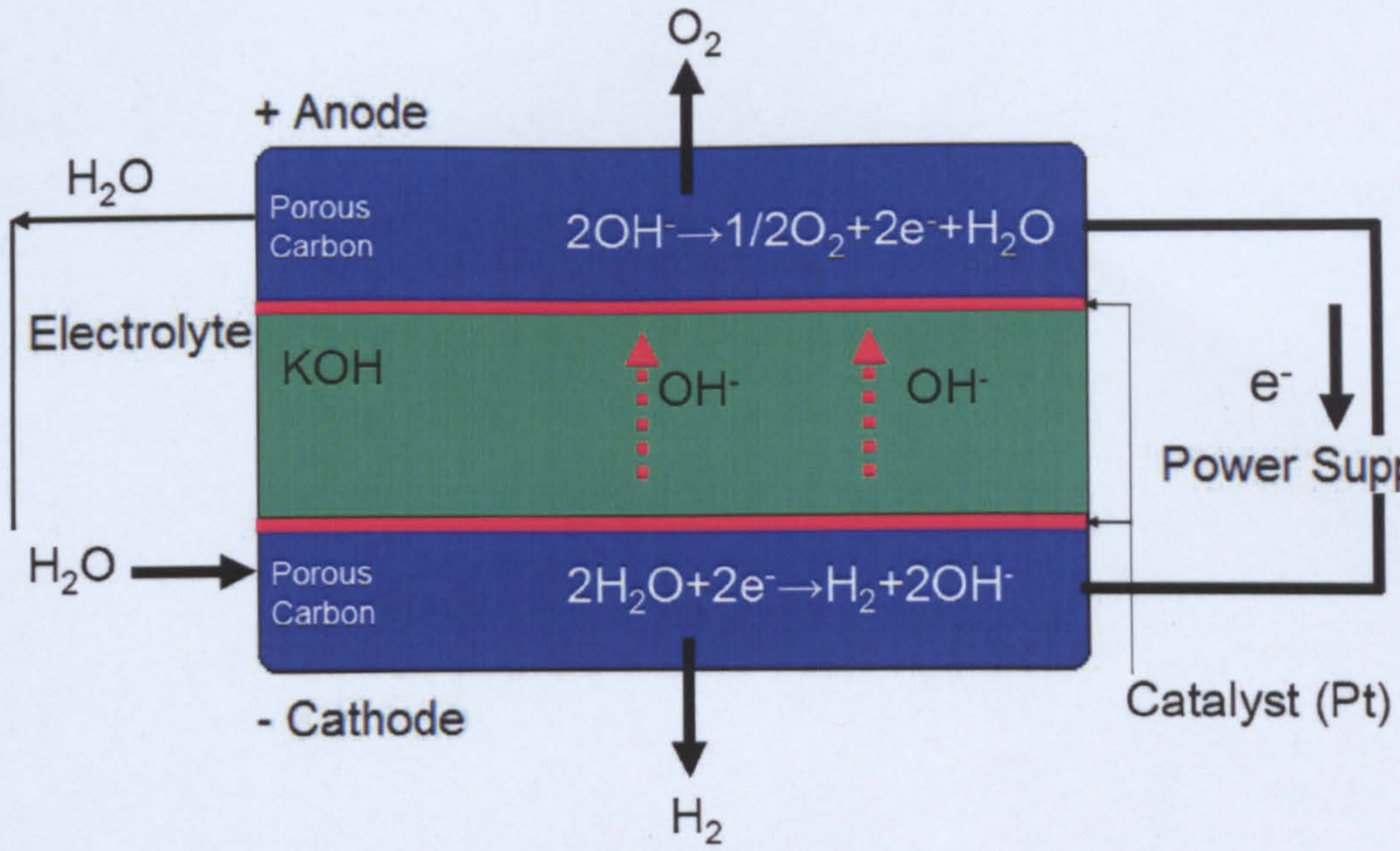

Figure A.4.1.1 Schematic of an alkaline electrolyser.

A.4.2 Proton-exchange membrane electrolysers

Proton exchange membrane (PEM) electrolysers use a proton exchange membrane as an electrolyte, which is a perfluorosulfonic acid polymer. The PEM electrolyser operates in a reverse process of the PEM fuel cell. Water is split into oxygen, hydrogen protons and electrons at the anode. The hydrogen protons pass through the polymer membrane to the cathode, combining with electrons and forming hydrogen. The conversion efficiencies range from 50-90%, and both hydrogen and oxygen gas can achieve very high purity (typically 99.9999%). PEM stacks can also operate at much higher pressure gradients than alkaline electrolysers, with pressures at up to 200 bars. However, both sides of the membrane require a balanced pressure to avoid damage. The increased pressure can reduce the requirements of having additional compressors, reducing the overall system size as well as cost, which is favourable. Figure A.4.2 shows a schematic layout of a PEM electrolyser.

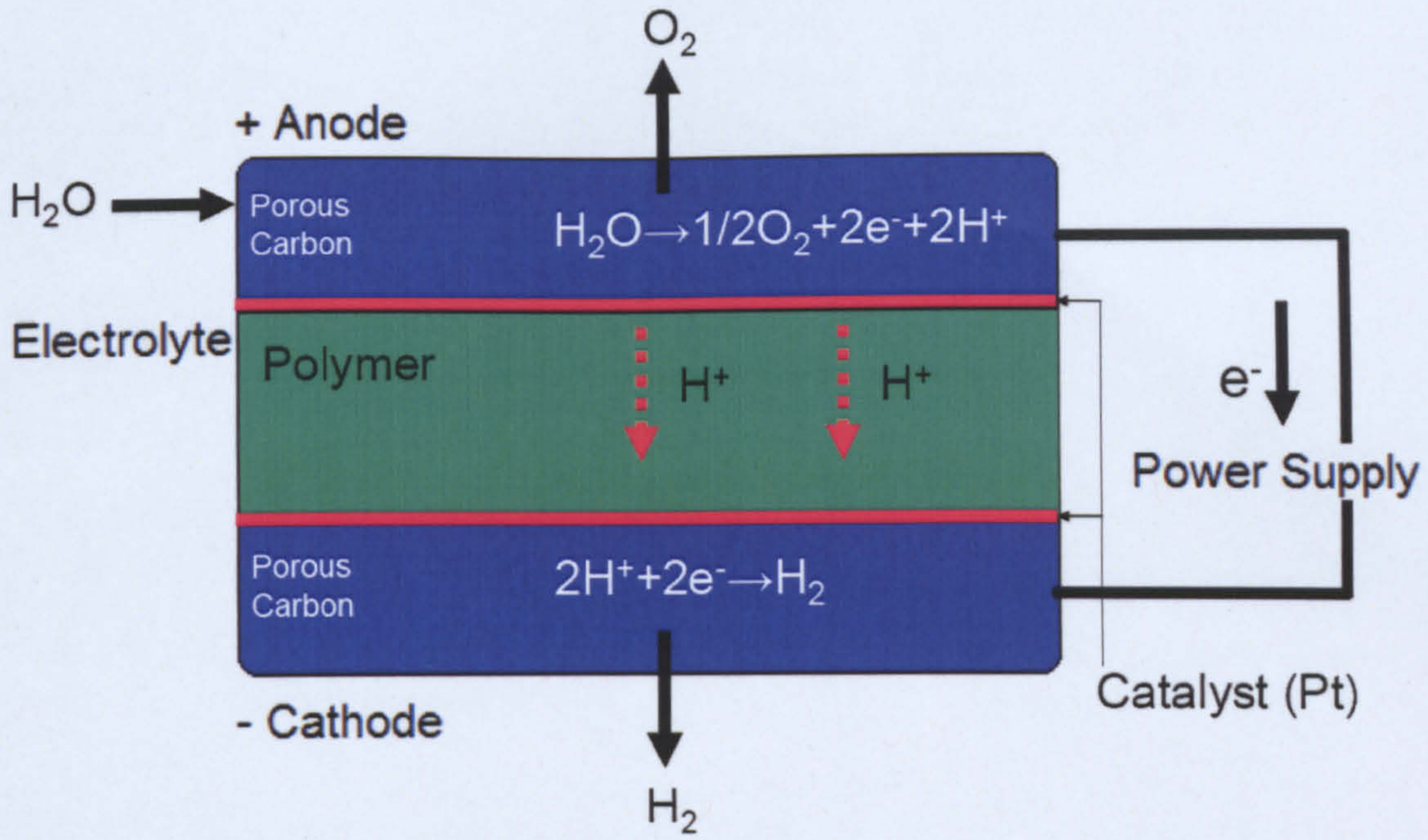

Figure A.4.2 Schematic of a proton exchange membrane electrolyser.

Another key advantage over alkaline electrolysers is that the PEM electrolyser offers increased flexibility with its ability to cope with variations in electrical power inputs. It is therefore ideally suited to renewable applications where power output is variable (Newborough, 2004).

A.4.3 Solid oxide electrolyser

Solid oxide electrolysers are high-temperature electrolysers based on the same technology as solid oxide fuel cells. The electrolyte is a solid ceramic, usually zirconia or ceria, and operates at much higher temperatures than PEM electrolysers (typically 800-1000°C). An external heat source is required; by operating at high temperatures the input heat energy meets some of the energetic electrical input requirements.

Solid oxide electrolyser technology, as shown in Figure A.4.3, is still in its infancy, with much work required to overcome issues of fatigue problems due to thermal cycling.

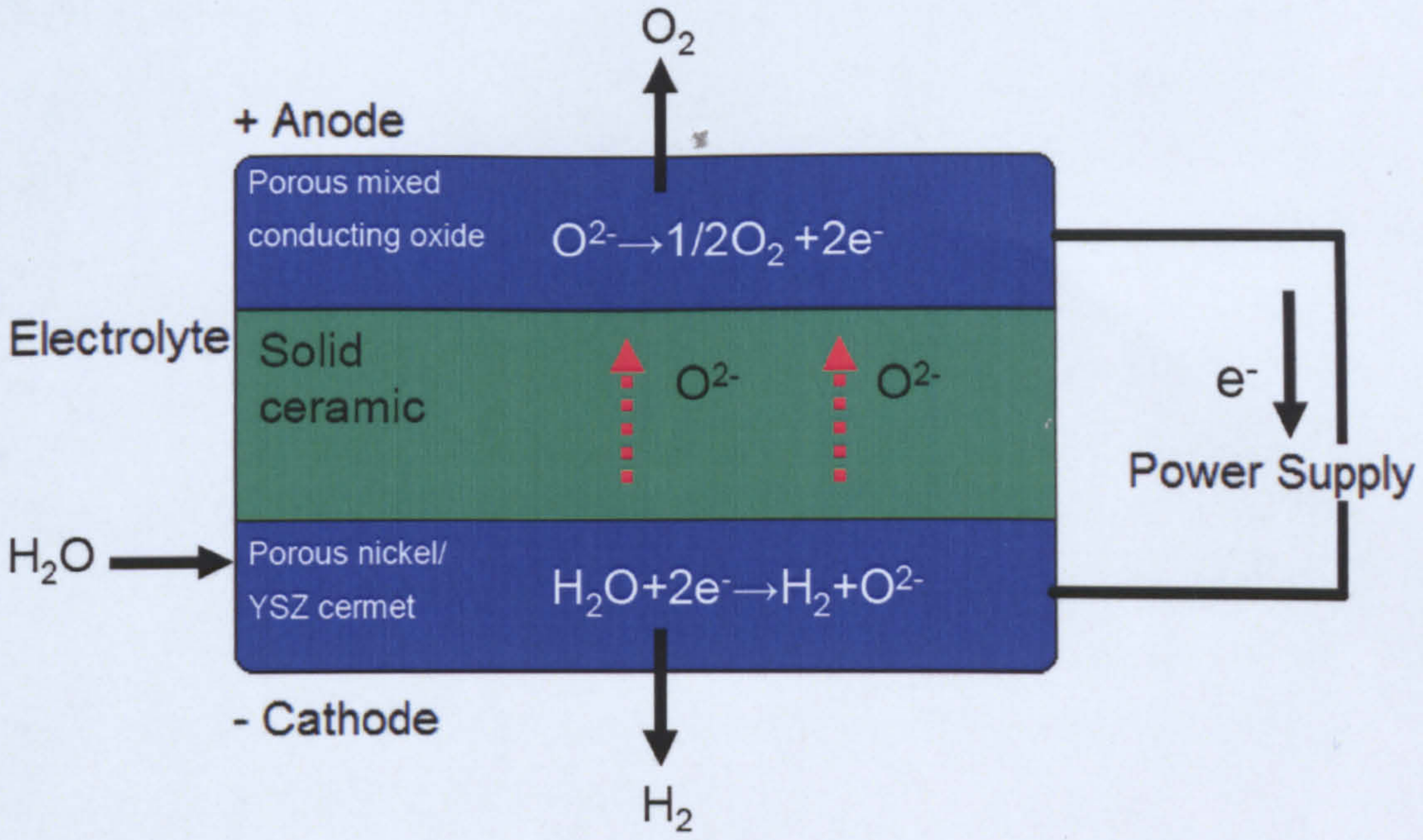

Figure A.4.3. Schematic of a solid oxide electrolyser.

A.5 Developing future technologies for hydrogen production

Biomass could potentially provide much of the world's hydrogen in an environmentally friendly and sustainable manner. There are several different technologies currently being developed to generate hydrogen from a variety of biological products, although there are currently no commercial facilities operating producing hydrogen from biomass. Biomass covers a whole range of biological matter, ranging from agricultural crops, aquatic plant life, wood and wood waste, effluents and rubbish, which can all be processed to generate hydrogen. The nature of these bio-resources are all very different, and therefore so are the processes required for their hydrogen production. These hydrogen production processes can broadly be classed as follows:

- Thermo-chemical gasification with a water shift reaction
- Pyrolysis coupled with reforming of hydrocarbons
- Supercritical conversion of biomass
- Microbiological conversion of biomass

Thermo-chemical gasification follows the same process as described in the above-mentioned thermo-chemical reforming of natural gas, where the feed of natural gas is replaced with biomass. Typically, thermo-chemical reforming is suitable for biomass feed stocks such as agricultural and forestry waste.

Pyrolysis is a high temperature process where the biomass feedstock is broken down into its constitute compounds in an anaerobic environment. The process produces a liquid known as bio-oil, which in turn can be converted to hydrogen by catalytic steam reforming.

Supercritical conversion of biomass is the aqueous conversion of biomass to hydrogen. Water at a pressure above 22MPa and temperature above 374 °C behaves like a solvent. In these harsh conditions the biomass degrades and dissolves within the supercritical water. In a separate process the aqueous biomass, known as synthesis gas and containing a mix of carbon monoxide, hydrogen and methane, is reformed by steam reforming to hydrogen and carbon dioxide (Nath and Das, 2003).

Microbiological conversion of biomass is the conversion of biomass into hydrogen, typically organic waste water and solid waste. A variety of bacteria break down carbon-based substrates such as carbohydrates by fermentation. They produce hydrogen and carbon dioxide; methane production can be suppressed with the introduction of a low voltage electric current through the fermented slurry (Nath and Das, 2003).

Bio-photolysis produces hydrogen from water by use of algae to break water molecules down into hydrogen ions and oxygen via photosynthesis. Hydrogen ions are then converted into hydrogen gas by the hydrogenase enzyme which can be found in marine green algae.

Production of hydrogen via microbiological conversion could potentially provide a low-cost, sustainable method of producing hydrogen from water. However, the limiting factor in the reaction which still needs to be addressed is the inhibition of gases which are present or produced by the reaction. The presence of oxygen, nitrogen and carbon dioxide all inhibit the reaction process of hydrogenase conversion.

Further work is still required to develop the anaerobic conditions required for sustainable production of hydrogen generation via algae (Karapinar and Kargi, 2005).

A.6 Hydrogen storage

Hydrogen can only be become the fuel of the future and replace fossil fuels if it can be stored safely in large quantities. Hydrogen gas will need to be produced by sustainable means with the use of renewable technology and stored to enable its use as a fuel for transport.

Hydrogen has a high chemical energy density of 143MJ kg^{-1}, which is more than three times greater then conventional hydrocarbon fuels such as gasoline, which has a chemical energy density of 45MJ kg^{-1} (Zuttel, 2003).

The problem which arises from using hydrogen is its storage, as it has a low density (0.0813kg/m^3) at normal atmospheric conditions (Sonntag *et al.*, 2003). Thus 1kg of hydrogen gas has a volume of 12m^3 (Zuttel, 2003), which is not desirable.

A modern family-sized vehicle fitted with a conventional internal combustion engine with a limited Carnot efficiency of 25% would require around 8kg of hydrogen to achieve a range of around 400km. Compare this to a petrol engine, which would require 24kg of petrol. If a hydrogen-fuelled vehicle used fuel cell technology, which operates with an efficiency of 50-60%, then only 4kg of hydrogen would be required (Schlapbach and Zuttel, 2001). Industry has therefore set itself the goal of producing a 110kg, 70MPa cylinder with a gravimetric storage density of 6% wt., enabling 6.6kg of hydrogen to be stored (Zuttel, 2003).

Hydrogen can be stored in three states: as a gas, as a liquid, or as a solid. Different types of storage medium offer different advantages in gravimetric storage densities; however this is not the only determining factor when considering storage media. The energy consumed in the process of filling the storage medium also needs to be addressed. For example, to compress hydrogen from 0.1 to 80MPa consumes 2.21kWh/kg of energy in theory, but in practice this figure is much higher. It is higher still for liquefying hydrogen (Zhou, 2004). Figure A.6.1 shows a plot of the gravimetric energy density to volume for various forms of stored hydrogen fossil fuels.

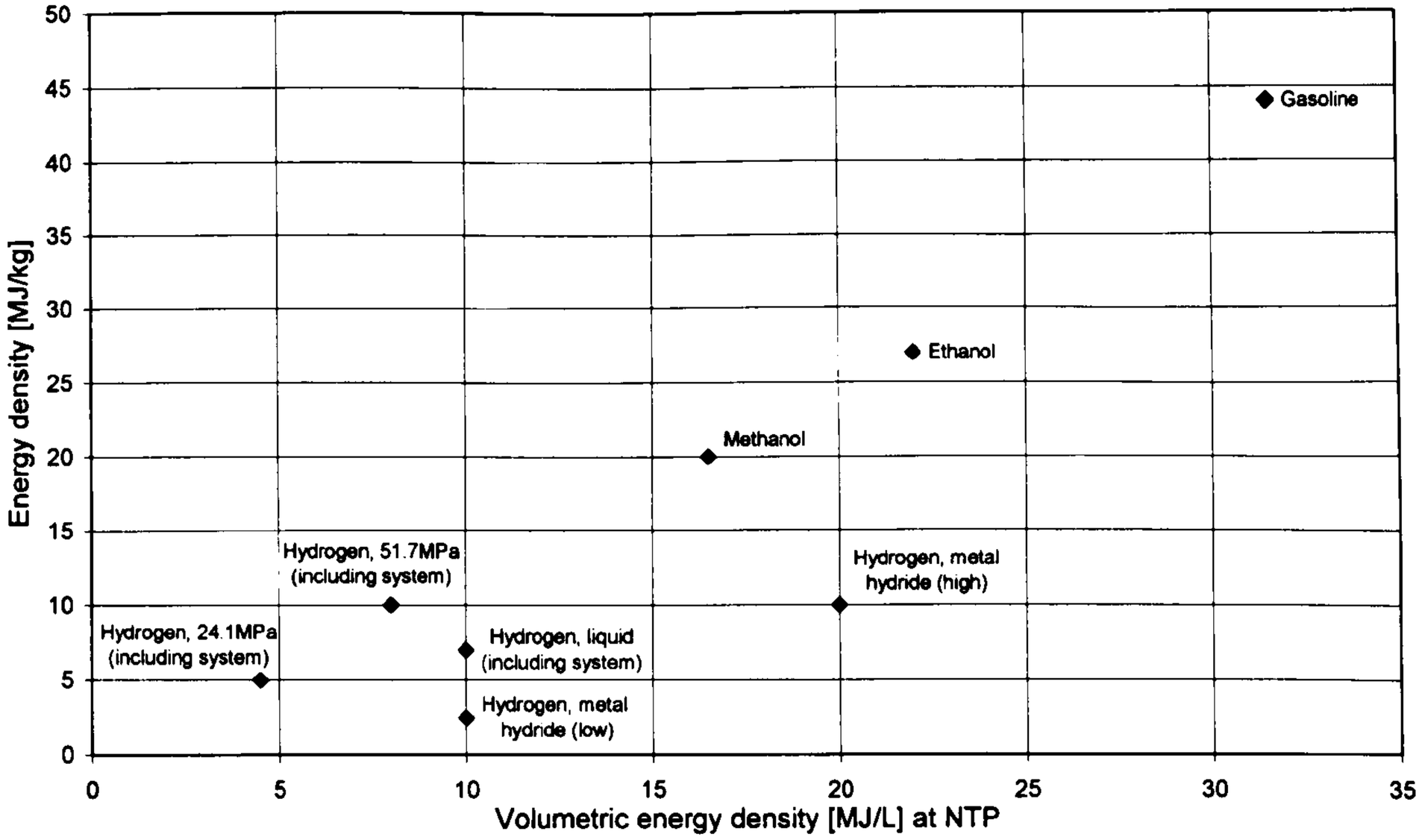

Figure A.6.1 Energy density comparison of select fuels (lower heating value) Source data: O'Hayre *et al.*, (2006).

A.6.1 High pressure gas storage

Traditionally gases have been stored in steel cylinders due to their low material cost and relatively high material strength. Steel cylinders can store gas up to 20MPa, but to achieve the design aim of storing 4kg of hydrogen gas, the cylinders would require a volume of 225 litres (Schlapbach & Zuttel, 2001). A higher pressure is required to enable a reduction in cylinder size. This can be achieved with use of composite materials in the construction of the cylinder. Composite cylinders under development currently use an inert aluminium inner liner to stop hydrogen from reacting with the reinforcing polymer. However development work is being carried out to develop polymer cylinder liners which can withstand corrosion and hydrogen enbrittlement. The cylinders are reinforced and strengthened with layers of carbon fibre to withstand the high stress loads. An additional impact and chemical absorbent coating protects the cylinder from the external environment.

Composite hydrogen cylinders are able to store hydrogen gas in excess of 70Mpa, thus achieving the design criteria of being able to store 4% hydrogen wt. Cylinder shape still make it difficult to store the cylinder within the vehicle's bodywork. There are still the disadvantages of the associated energy penalties of compressing the gas and the safety issues of handling pressurised gas, especially in vehicle collisions.

A.6.2 Glass microspheres

The use of glass microspheres is one potential method of reducing the required pressure of storing hydrogen gas. Glass microspheres are charged with hydrogen at high pressures and temperatures of 70MPa and 300°C. Once charged with hydrogen, the microspheres are cooled to ambient temperature and transferred to the vehicles low-pressure storage tank.

The microspheres can then be heated back up to 300°C to release hydrogen to the vehicle. The problems still to be overcome are mainly to do with the inherently low volumetric density of microspheres. Another issue is the durability of the microspheres under cycling (INA, 2006).

A.6.3 Liquid storage

There are three main methods of storing hydrogen as a liquid. The first and most common method is to cool it down to a very low temperature of -253°C. Other methods include storing hydrogen as a constituent in other liquids, which the hydrogen can then be released from and recharged.

A.6.4 Cryogenic storage

Hydrogen can be stored as a liquid if cooled to a temperature below its critical temperature of 33K. Above this temperature a liquid state cannot exist. Liquid hydrogen is stored in a cryogenic insulated vessel but this is not sealed, as even super-insulated cryogenic vessels suffer from heat ingression, and as a result hydrogen boil-off occurs. Hydrogen will evaporate over a period of time if it is not used. Boil-off losses are proportional to surface area, and the volume ratio of the storage vessel. Typically, for a vehicle-sized storage vessel, 3-5% loss per day can be expected (Sorensen, 2005). Liquid hydrogen has a high density of 70.8kg/m^3, which means a 100% gravimetric density can be stored. But only 20% by wt can be achieved, and a gravimetric density of 30 kg/m^3 is obtainable, making it the highest energy density storage medium for short time periods. This technology is well suited for space and air industry applications (INA, 2006). The disadvantage of using liquid hydrogen is that there is a 30-40% energy loss in the liquidation process.

The liquidation process uses the Joule-Thompson cycle. Hydrogen gas is first compressed and cooled with liquid nitrogen, via a heat exchanger. If the compressed hydrogen is below its inversion temperature of 202K, and allowed

to expand, its temperature will drop. The gas is then allowed to expand adiabatically through a throttle valve at constant enthalpy, causing the temperature to drop, resulting in a cooling effect and forming some liquid hydrogen. The liquid hydrogen is collected and the cooled compressed gas recycled and re-compressed (Zuttel, 2003).

A.6.5 Hydrogen storage in chemical hydride solutions

Hydrogen can be stored in a constituent borohydride solution. The catalytic hydrolysis is shown as a reaction in Equation A.6.5.1.

$$NaBH_4(aq) + 2H_2O \overset{Catalyst}{\rightarrow} 4H_2 + NaBO_2 9aq0 + heat(217kJ) \qquad \text{(A.6.5.1)}$$

The advantage of storing hydrogen in chemical hydride complexes is that they are non-flammable and stable in air, and have the ability to be recycled. They also provide high hydrogen storage efficiency. The maximum obtainable storage density of hydrogen within this reaction is 10.9% by weight.

To release the hydrogen from the solution a catalyst is required, such as, Ru, Pt or Ni.

The product of the hydrolysis reaction is that hydrogen gas is released and sodium metaborate ($NaBO_2$) is formed as a by-product. This can be recycled later.

The disadvantage of using sodium borohydride ($NaBH_4$) as a hydrogen storage medium is having to recycle the $NaBO_2$ back to $NaBH_4$. Further research is needed as the electrochemical techniques are costly, around 50$/kW (Çakanyıldırım and Gürü, 2008), (Jeong *et al.*, 2005).

A.6.6 Hydrogen storage in organic liquid hydrides

Organic liquids can also be used as liquid hydrogen storage media. The methylcyclohexane (C_7H_{14}) to toluene (C_7H_8) reaction can produce hydrogen by catalytic dehydrogenation when heated to 200-300°C, producing 6% by wt and 43kg of H_2/m^3. The dehydrogenation and hydrogenation of methylcyclohexane to toluene is shown in Equation A.6.7.

$$C_7H_{14}(l) \Leftrightarrow C_7H_{14}(l) + 3H_3(g) \qquad \text{(A.6.7)}$$

Toluene can then be recycled by hydrogenation in the presence of a catalyst. The reaction takes 20-50 minutes at 60°C in an excess of H_2. In these conditions the only product is methylcyclohexane (Jalowiecki-Duhanel *et al.*, 2007).

The disadvantage of using such organic liquids as rechargeable hydrogen storage media is the fact that they are highly volatile hydrocarbons, which make them a potential fire and explosion risk. It is also highly toxic, causing further safety concerns.

The relatively low energy storage density of organic liquids compared with other storage media may also limit their use within vehicles.

A.7 Solid hydrogen storage

A.7.1 Physisorption of hydrogen

Physisorption is the adsorption of a gas onto the surface of a solid. The force causing the adsorbate to adhere to the solid's surface is due to a weak intermolecular interaction between the adsorbate gas and the surface of the adsorbent solid, known as Van der Waal's force. This type of adsorption can only occur at ambient temperatures below the critical temperature of the adsorbate gas, which for hydrogen is below 273K. Molecules of hydrogen interact with molecules on the solid's surface. Once a monolayer of the adsorbate hydrogen molecules is formed, then additional hydrogen molecules interact with the monolayer of adsorbate molecules. The energy bonding this second layer of molecules is of similar magnitude to the latent heat of evaporation, where the energy adhering the monolayer to the solid's surface is equal or greater than that of the boiling point of the absorbate hydrogen (Zuttel, 2003).

A.7.2 Carbon and high surface area materials

Much research has been carried out on the use of carbon-based materials, such as carbon nanotubes, graphite nanofibres and graphene sheets, for hydrogen storage. Carbon technology could potentially be low-cost and available on an industrial scale. Compared with other storage media, carbon and high surface area materials offer a poor storage potential. Although graphite nanostructures have been found to store 7.4% by wt hydrogen, in practice hydrogen storage capacities in carbon materials is <3% by wt at

cryogenic temperatures (Ströbel *et al.* 2006). High-purity hydrogen can be liberated only at temperatures above 400°C. This technology is unlikely to be suitable for use in vehicles due to its low energy storage density and impractical hydrogen liberation temperatures.

A.8. Rechargeable hydrides

A.8.1 Metallic hydrides

Many metals and their alloys are capable of absorbing hydrogen into their structures. At elevated temperatures, hydrogen gas molecules form an electrolyte. On the surface of the metal hydrogen molecules are dissociated to form two hydrogen atoms, which can then be adsorbed by the metal's lattice structure, forming ionic or covalent-bonded compounds. Metallic hydrides are composed of two elements. The first is usually an alkaline earth metal which forms a stable hydride. The second element is usually a transition metal which only forms an unstable hydride; catalysts such as nickel are often used for hydrogen dissociation. High volumetric density of 115kg/m^3 are achieved but only low gravimetric hydrogen densities are obtainable, being less than 3% in wt. (Zhou, 2004).

A.8.2 Alanates and other light hydride

Alanates are compounds that contain aluminium and other compounds based on light metals found in Groups 1, 2, and 3. Lithium, boron, and sodium can all be used as hydrogen storage mediums. At elevated temperatures, hydrogen gas molecules form an electrolyte. On the surface of the metal hydrogen molecules are dissociated to form two hydrogen atoms, which can then be adsorbed by the metal's lattice structure. As the metal lattice adsorbs more hydrogen atoms, the lattice expands, as seen in Figure A.8.2 where the hydrogen is often located in the corner of the tetrahedron lattice. This complex will remain stable until decomposed at high temperatures. When the process is reversed, hydrogen is desorbed from the metal's lattice when heated. Hydrogen atoms recombine on the metal's surface, forming hydrogen gas.

The desorbed hydrogen is achieved only when heated typically from 80°C to 600°C. The addition of a titanium-based catalyst has been found to lower the desorption temperature. Alanates can only reversibly store 4-5% wt hydrogen,

but borohydrides have proven to give much improved performance (Schlapbach and Zuttel, 2001).

Borohydrides are generally more stable than alanates, making them less reversible. This increased stability also makes borohydrides safer than alanates. Currently $LiBH_4$ offers the highest hydrogen storage density of 18 % wt.

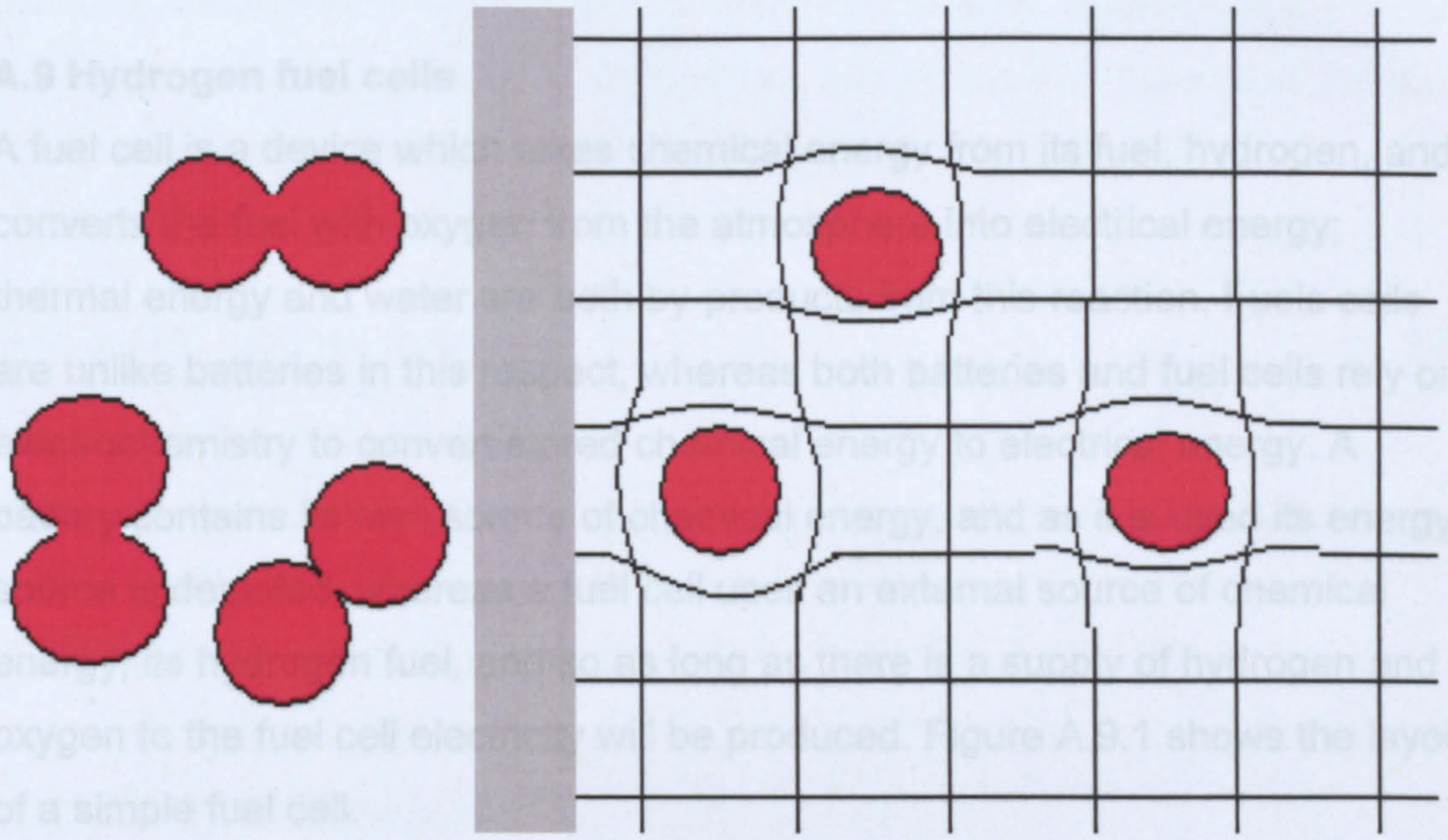

Figure. A.8.2 Hydrogen atoms stored in the lattice structure of a light metal hydride.

A.8.3 Chemical hydrides (H_2O reactive)

The advantage of a chemical hydride is in its ability to be handled as a fluid safely which make it suitable for pumping and thus simplifying the vehicle refuelling process compared with other hydrogen storage options. Typically, the chemical hydride is stored in mineral oil slurry, which makes the chemical hydride easier to handle. The oil also reduces the slurry's flammability and reduces the effects of moisture in the atmosphere. Hydrogen is liberated from the slurry via hydrolysis with the additional of water in an exothermic reaction. Chemical hydrides offer very good energy storage capabilities per unit weight. Magnesium hydrides offer the highest energy densities of all the reversible hydrides (Equation A.8.3) with a hydrogen storage density of 6.5% wt.

$$MgH_2 + 2H_2O \Rightarrow H_2 + Mg(OH)_2 \qquad \text{(A.8.3)}$$

However, hydrogen absorption/desorption kinetics is too slow for vehicle applications, but this can be improved with material handling and the preparing of nanocrystalline microstructures. The limiting factor in determining whether chemical hydrides will be viable as a hydrogen storage medium is the cost of reprocessing the spent hydroxide, which is an energy-intensive process (Johnson *et al*., 2005).

A.9 Hydrogen fuel cells

A fuel cell is a device which takes chemical energy from its fuel, hydrogen, and converts the fuel with oxygen from the atmosphere into electrical energy; thermal energy and water are both by-products from this reaction. Fuels cells are unlike batteries in this respect, whereas both batteries and fuel cells rely on electrochemistry to convert stored chemical energy to electrical energy. A battery contains its own source of chemical energy, and as it is used its energy source is depleted, whereas a fuel cell uses an external source of chemical energy, its hydrogen fuel, and so as long as there is a supply of hydrogen and oxygen to the fuel cell electricity will be produced. Figure A.9.1 shows the layout of a simple fuel cell.

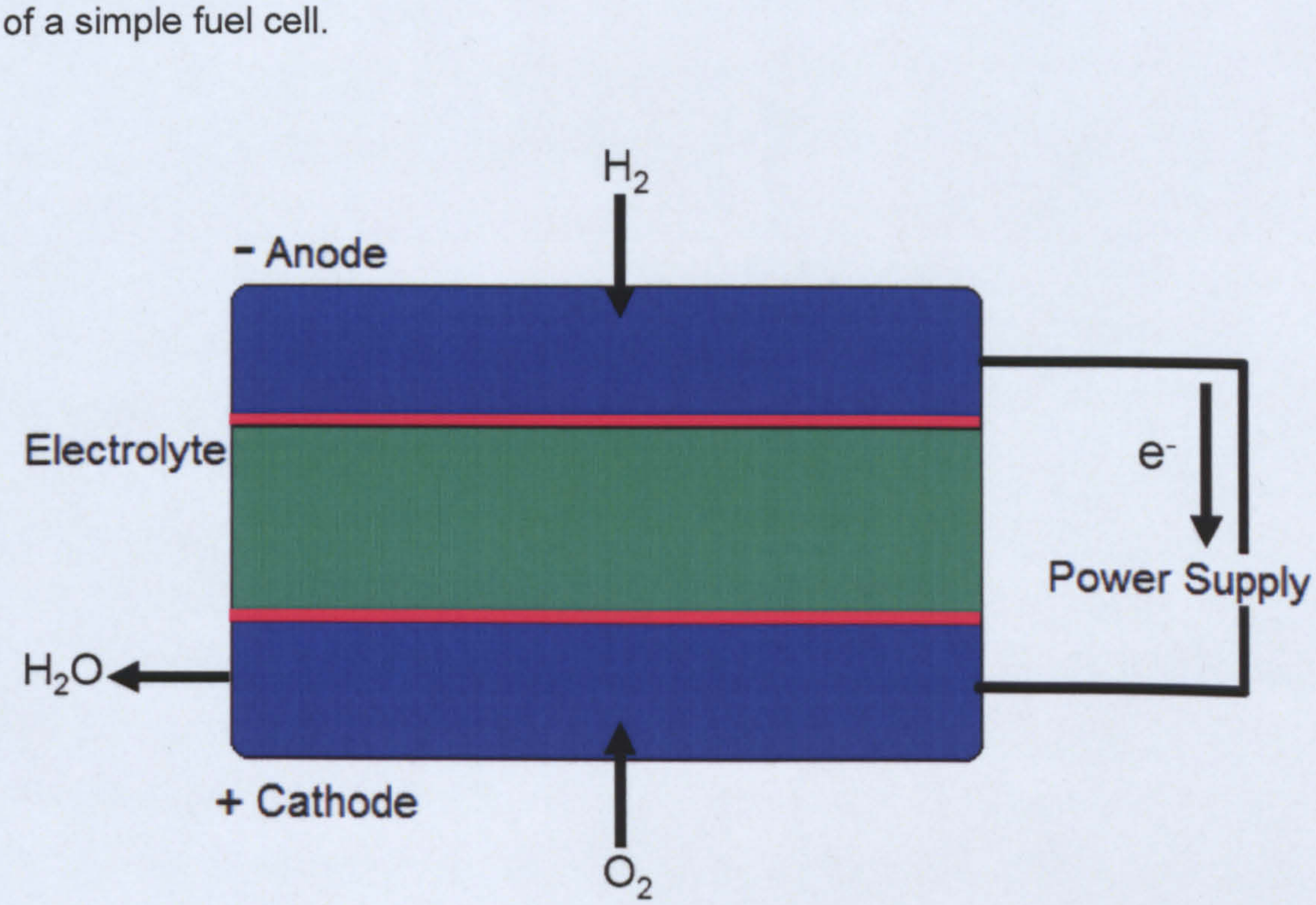

Figure A.9.1 Schematic of a simple fuel cell.

On a molecular scale, two half reactions are taking place which are separated by an electrolyte. The purpose of an electrolyte is allow ions (charged atoms) to be freely exchanged between the two half reactions but not to allow the free exchange of electrons between the reactions. The only way electrons may be transferred across the two half reactions is via an external circuit. An electrical load can then be placed within this circuit, thus the electrical current of electrons travelling between the two half reactions will do the work. Equation A.9.1 shows the half reaction taking place at the cathode and Equation A.9.2 shows the half reaction taking place at the anode.

$$H_2 \leftrightarrow 2H^+ + 2e^- \tag{A.9.1}$$

$$\frac{1}{2}O_2 + 2H^+ + 2e^- \leftrightarrow H_2O \tag{A.9.2}$$

There are five main types of fuel cells in development, although there are many further variations in each group. Fuel cells are classified by the types of electrolyte used. These are listed below.

- Molten carbonate cells
- Solid oxide cells
- Acid and alkaline cells
- Proton exchange membrane cells

A.9.1 Molten carbonate fuel cells (MCFC)

Molten carbonate fuel cells use a mixture of molten alkali carbonate as an electrolyte. This requires a high operating temperature of 650°C to achieve sufficient ionic conductivity of the molten electrolyte. The advantage of using high operating temperatures allows the use of low-cost electrolyte compounds. Typically these are Li_2CO_3 and K_2CO_3 supported in a $LiOAlO_2$ matrix (O'Hayre *et al.*, 2006). Traditionally these electrolyte tiles were made by a process of hot pressing, where $LiOAlO_2$ combined with alkali carbonates is pressed into thin tiles at high pressures, just below the melting point of the carbonates. However these tiles were difficult to process and handle, limiting the tile size, and the tiles were also relatively thick.

Tape casting is then used, increasing the size of tiles which could be manufactured and reducing the tile thickness. The electrolyte is supported with fibres or particulates to give increased rigidity.

The electrodes are commonly nickel-based, with the anode being a nickel chromium alloy and the cathode being lithiated nickel oxide. For both electrodes, the nickel provides catalytic function and conductivity.
In the molten carbonate fuel cell, instead of hydrogen protons being used as charge carriers, carbonate ions (CO_3^{2-}) act as the charge carriers for the reaction. The two half reactions taking place at the anode and cathode can be seen in Equation A.9.1.1 and Equation A.9.1.2, and the overall reaction in Equation A.9.1.3.

Anode: $$H_2 + CO_3^{2-} \rightarrow CO_2 + H_2O + 2e^- \quad \text{(A.9.1.1)}$$

Cathode: $$\frac{1}{2}O_2 + CO_2 + 2e^- \rightarrow CO_3^{2-} \quad \text{(A.9.1.2)}$$

$$H_2 + \frac{1}{2}O_2 + CO_2(Cathode) \rightarrow H_2O + CO_2(anode) \quad \text{(A.9.1.3)}$$

Unlike other fuel cells, carbon dioxide is used in the reaction as well as hydrogen and oxygen. The carbon dioxide is produced at the anode and consumed at the cathode. Typically the carbon dioxide produced at the anode is recycled and used at the cathode by taking waste steam produced at the anode and introducing it via a burner at the cathode, combusting any excess hydrogen, as seen in Figure A.9.1.1 Due to issues relating to stress cycling of melting the molten electrolyte, molten carbonate fuel cells are best suited to stationary applications where the fuel cell cycle can run continually after the fuel cell has been started. Electrical efficiency of up to 50% can be achieved, with a combined heat and power efficiency of up to 90% (O'Hayre *et al.*, 2006). Power densities of up to >150mW/cm^2 can be achieved, and since the reaction requires carbon dioxide to take place, the molten carbonate fuel is not damaged by the presence of carbon monoxide or carbon dioxide in the feed gas.

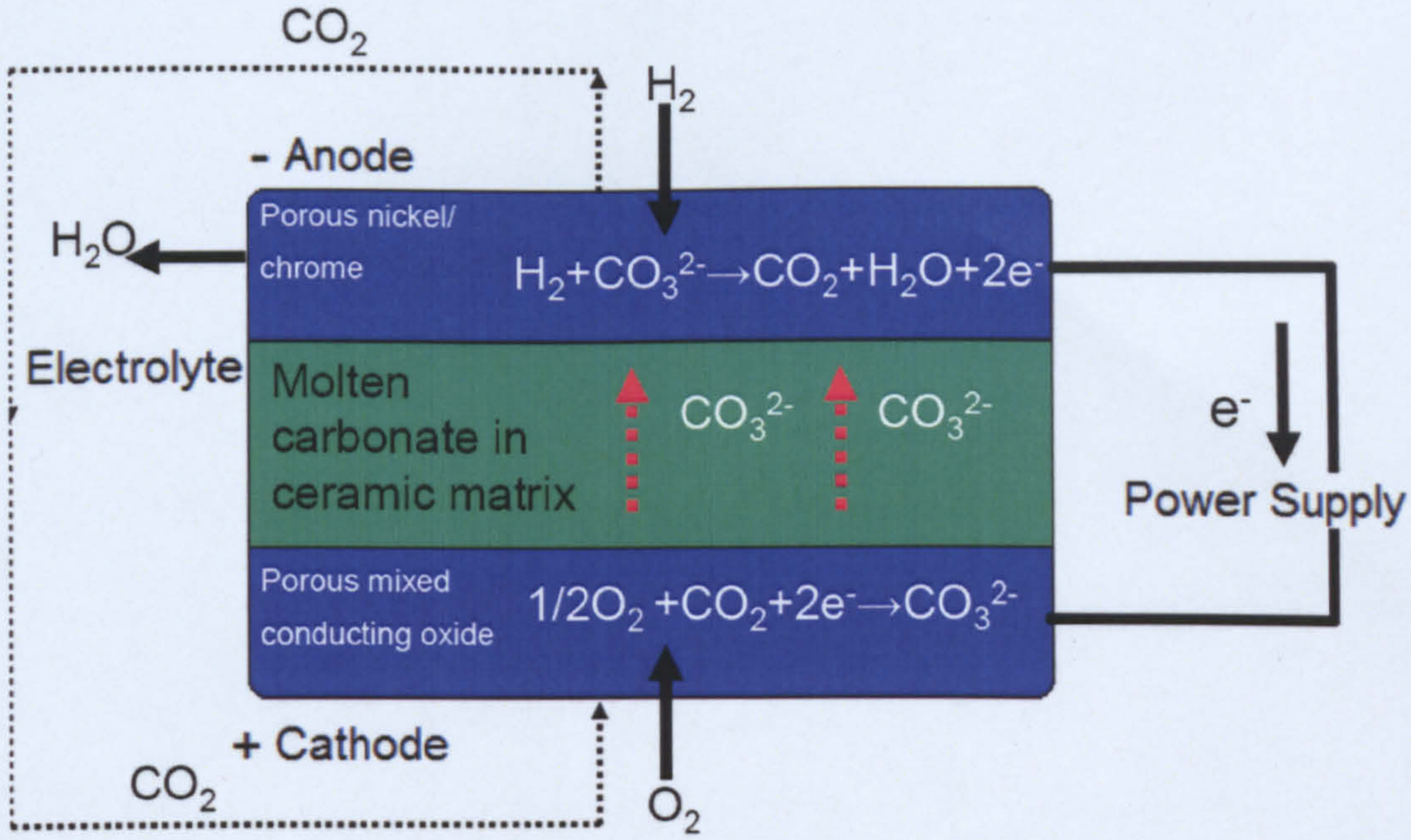

Figure A.9.1.1 Schematic molten carbonate fuel cell.

A.9.2 Solid oxide fuel cells (SOFC)

Solid oxide fuel cells use a solid non-porous metal oxide (ceramic) electrolyte. The most common electrolyte used in solid oxide fuel cells is yttria (Y_2O_3)-stabilized zirconia (ZrO_3), known as YSZ. High operating temperatures are required to achieve ionic conductivity of the electrolyte. In the case of solid oxide fuel cells, the oxygen ions are the charge carriers within the reaction, and the electrolyte is an oxygen-vacant conductor. This enables oxygen ions (O^{2-}) to be conducted across the electrolyte while remaining as a solid impermeable boundary, inhibiting the transfer of hydrogen and oxygen gas which flow across the surface of the electrolyte.

Since the oxygen ions travel across from the cathode to the anode, water is formed at the anode, unlike the process in other types of fuel cells. The two half reactions which take place at the anode and cathode can be seen in Equation A.9.2.1 and Equation A.9.2.2. This needs to be a thin as possible to maintain good ionic conductivity, yet thick enough to minimize any gas permeation or electrical conduction across its surfaces. The membrane's substrate is typically ziconia which is stabilized by doping with 3-8 mol % yttria (Sorensen, 2005).

Anode: $$H_2 + O^{2-} \rightarrow H_2O + 2e^- \quad \text{(A.9.2.1)}$$

Cathode: $$\frac{1}{2}O_2 + 2e^- \rightarrow O^{2-} \quad \text{(A.9.2.2)}$$

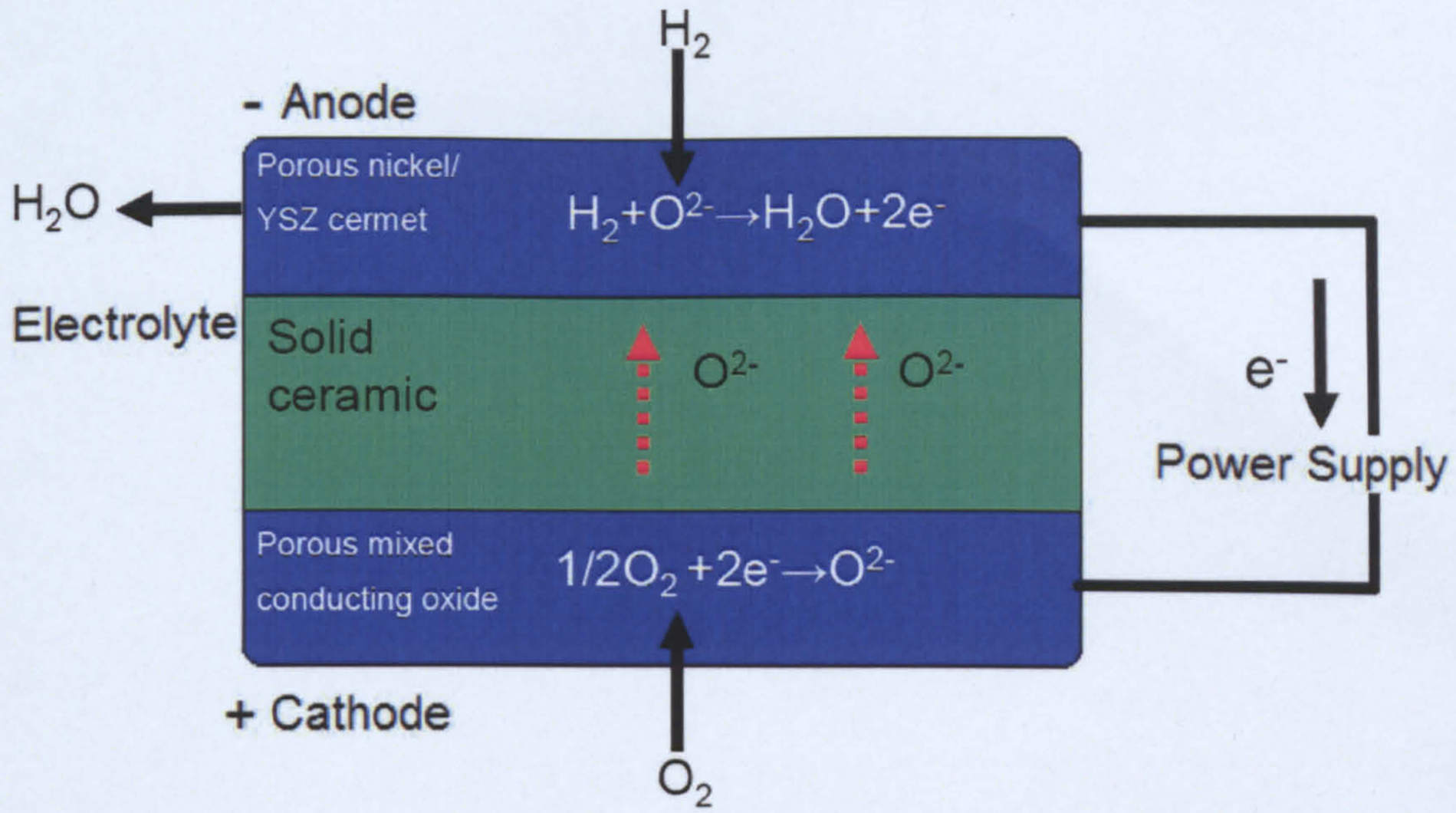

Figure A.9.2 Schematic of solid oxide fuel cell.

The anode and cathode materials are different; this is because the two environments are very different from each other. The anode is a highly reducing environment whereas the cathode is a highly oxidizing environment. Both environments operate at extremely high temperatures. The material commonly used in the anode is a cermet (metal and ceramic mix) consisting of nickel and YSZ, which provides the electrical conductivity required, as well as providing a catalyst area. The YSZ gives ionic conductivity and comparable thermal expansion, as well as being highly porous allowing good gas diffusion.
The cathode is made from highly oxidation-resistant ceramic materials, usually a mix of ceramics which are good electrical and ionic conductors. The ceramics used are typically strontium-doped lanthanum magnate (O'Hayre *et al.*, 2006). Current solid oxide fuels cells under development (seen in Figure A.9.2) operate at temperatures of 600°C to 1000°C, although work is being done to lower operating temperatures to allow a wider selection of materials to be used within the fuel cell and to reduce overall cost. This would also simplify the issues of interconnection and of sealing the fuel cell. The advantage of using high temperature operation allows the use of a variety of fuels, including hydrocarbon-based fuels (FCH, 2004). The electrical operating efficiency is 50-60%, but the addition of high-quality heat allows for a combined power and heat efficiency of up to 90%.

A.9.3 Phosphoric acid fuel cells (PAFC)

Phosphoric acid fuel cells were the first type of fuel cell to be produced commercially, and thus the technology has been well tested and proven reliable. A liquid phosphoric acid (H_3PO_4) electrolyte is used which is supported in a porous SiC matrix. The electrolyte is supported between two porous electrodes. These two electrodes have been coated with platinum, which acts as a catalyst, as seen in Figure A.9.3. The feed gases are supplied to the reverse sides of the electrodes and diffuse through the porous carbon. The reactions taking place at each electrode are given in Equation A.9.3.1 and Equation A.9.3.2.

Anode: $$H_2 \rightarrow 2H^+ + 2e^- \quad \text{(A.9.3.1)}$$

Cathode: $$\frac{1}{2}O_2 + 2H^+ + 2e^- \rightarrow H_2O \quad \text{(A.9.3.2)}$$

Since phosphoric acid forms a solid below 42°C, the phosphoric acid fuel cell is required to operate above this temperature, with an optimum performance at a temperature of 180°C to 210°C.

The phosphoric acid fuel cell is only used for stationary applications because of freeze-thaw stress cycling issues, thus the once the fuel cell is started it is not turned off. Since the electrolyte is a liquid, it is continuously replaced as it evaporates. The electrical efficiency is around 40% with a combined thermal efficiency of 70%. Due to the use of platinum electrodes, the phosphoric acid fuel cell is prone to carbon monoxide and sulphur poisoning.

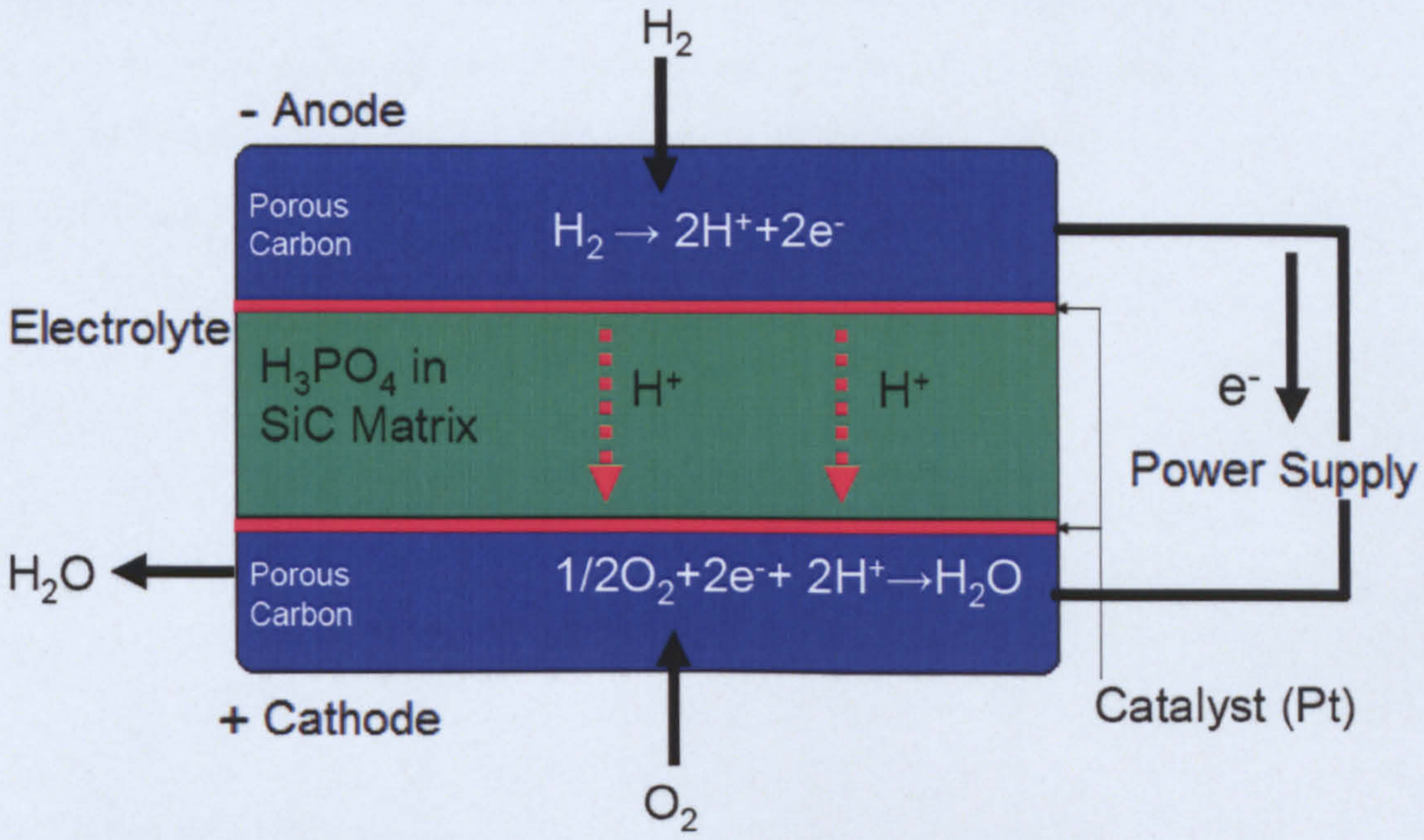

Figure A.9.3 Schematic of the phosphoric acid fuel cell.

A.9.4 Alkaline fuel cells (AFC)

In the alkaline fuel cell, an aqueous potassium hydroxide solution (KOH) is used as an electrolyte. The alkaline fuel cell differs to the phosphoric acid fuel cell in that instead of using the flow of hydrogen protons from the anode to the cathode, the alkaline fuel cell uses the OH^- ions which flow from the cathode to the anode, resulting in water being consumed at the anode and produced at the cathode.

Since the water is being processed as part of the overall reaction, and due to the ionic diffusion of the OH^- ions, twice the amount of water is processed at the anode. This water is removed at the anode by evaporation, as an excess of water at the anode dilutes the potassium hydroxide, reducing the reaction rate. A proportion of the water which is removed from the anode is used to replace the consumed water at the cathode. The two half reactions for the anode and cathode can be seen in Equation A.9.4.1 and Equation A.9.4.2.

Anode: $$H_2 + 2OH^- \rightarrow 2H_2O + 2e^- \quad \text{(A.9.4.1)}$$

Cathode: $$\frac{1}{2}O_2 + 2e^- + H_2O \rightarrow 2OH^- \quad \text{(A.9.4.2)}$$

The alkaline fuel cell is very sensitive to poisoning by carbon dioxide in both the hydrogen feed stock and from the ambient carbon dioxide within the air, which degrades the potassium hydroxide electrolyte. The use of scrubbers and continuous replenishment of the electrolyte can resolve this problem. This is considered too costly for terrestrial application, but alkaline fuel cells have been successfully used as a reliable power supply on board NASA space missions, where there are no issues of poisoning due to the use of pure cryogenic hydrogen and oxygen.

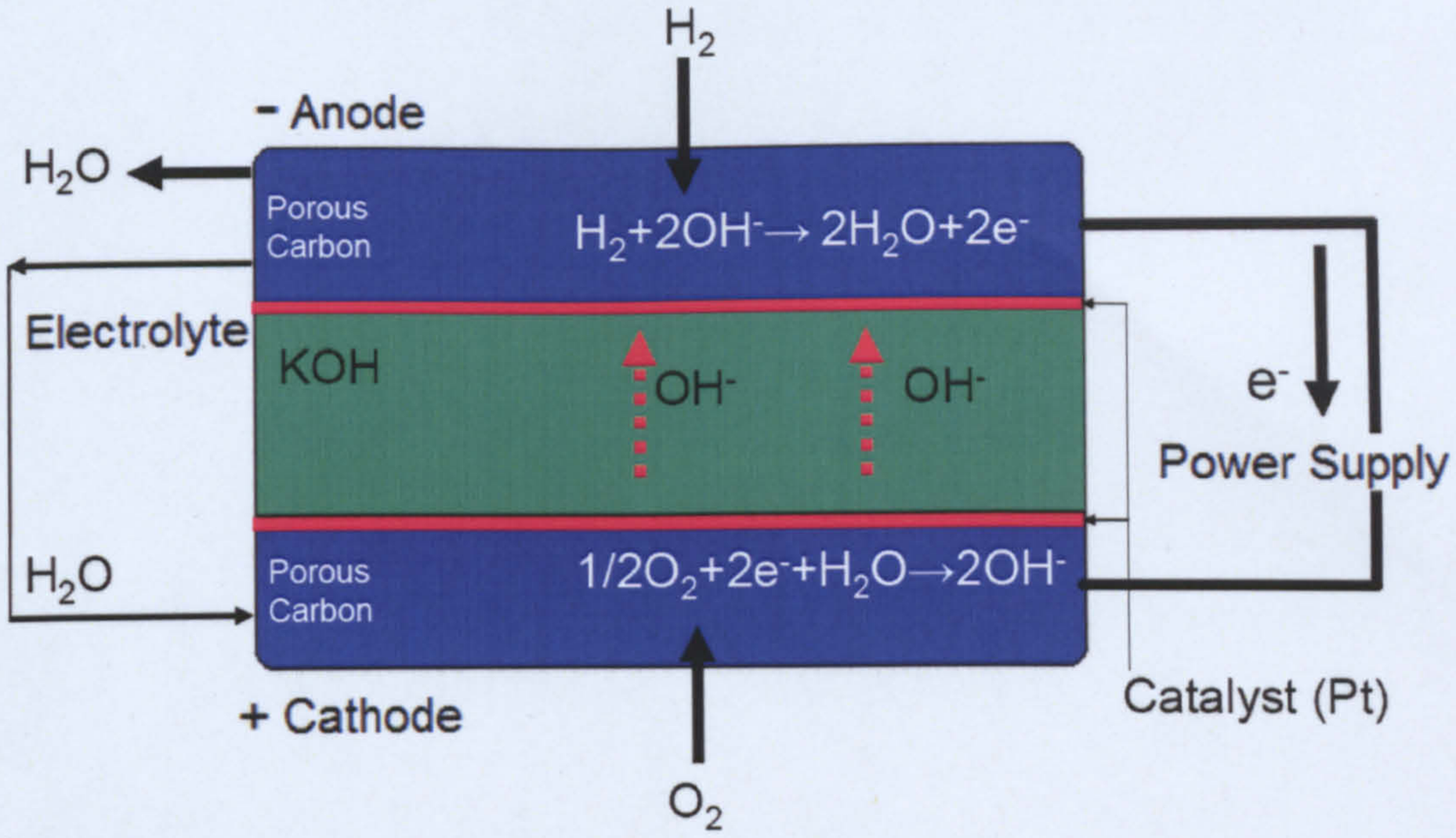

Figure A.9.4 Schematic of alkaline fuel cell.

The alkaline fuel cell has a simple construction, which uses porous carbon electrodes at both the anode and cathode, as seen in Figure A.9.4. Either a platinum or nickel-based catalyst can be used to increase reaction rates. Since the reaction is much more favourable than in the phosphoric acid fuel cell, only a third of the amount of catalyst is required (FCH, 2004). Alkaline fuel cells operate at around 60°C to 250°C, and due to high open circuit cell voltages give a high operating efficiency of 45-60% (Sorensen, 2005). Operating life is around 2,500 hours, which is suitable for short space missions but not suitable for terrestrial use.

A.9.5 Proton exchange membrane fuel cells (PEMFC)

Proton exchange membrane fuel cells are the newest fuel cell technology and are undergoing rapid development. They are aimed at mobile and portable applications, from telecommunications equipment such as mobile phones to transportation. They have a simple and robust construction ideally suited to such applications. PEM fuel cells differ from other types of fuel cell as they use a solid phase proton exchange membrane instead of the liquid electrolyte used by other types of fuel cells (as seen in Figure A.9.5). The membrane material used is a polymer, and although there have been variations in the materials used for membranes throughout the cell's development, typically polyperflourosulphonic acid is used.

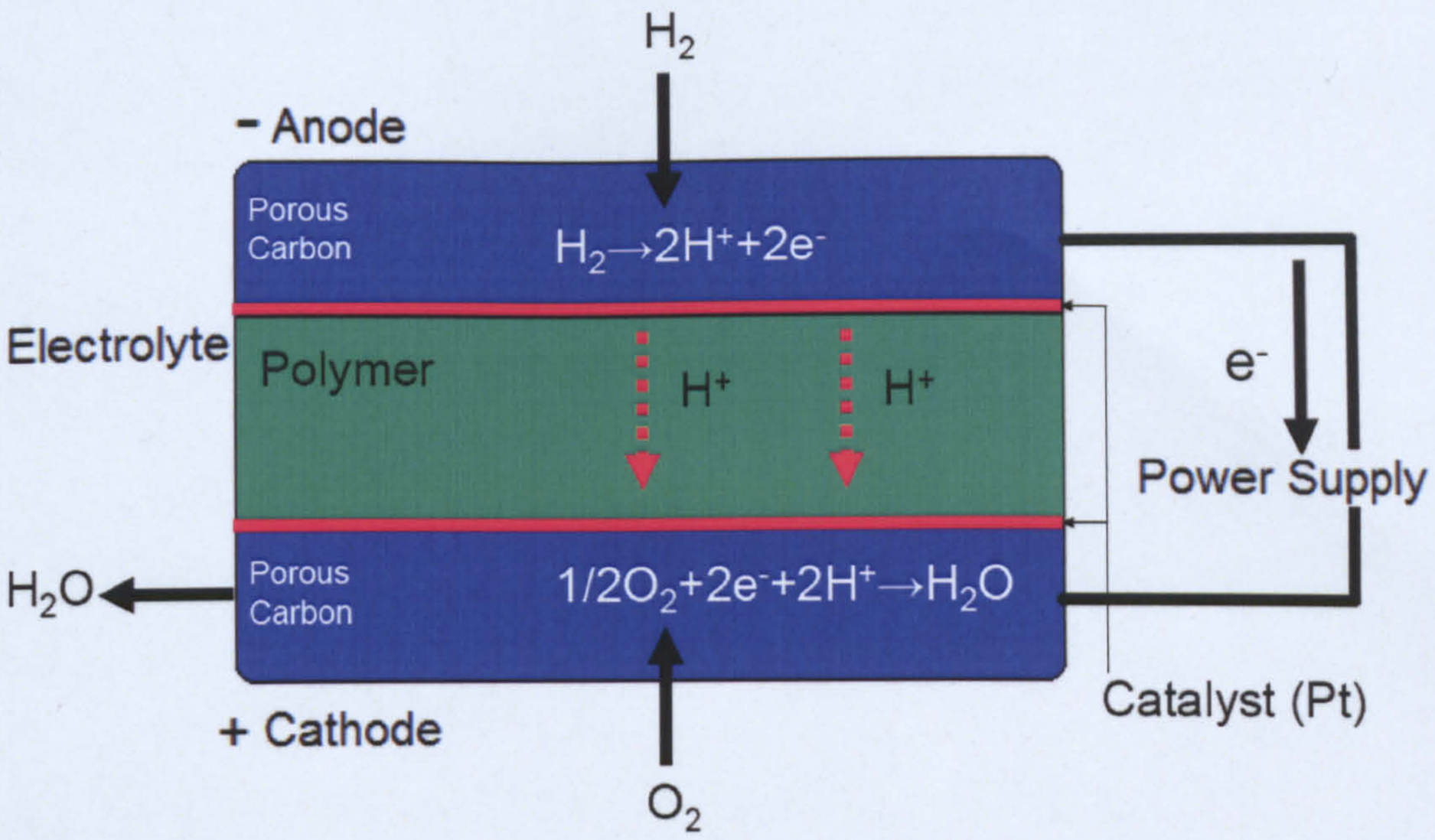

Figure A.9.5 Schematic of the proton exchange membrane fuel cell.

The advantage of PEM fuel cells over many other types of fuel cell is its low operating temperature of 60°C to 80°C, which is ideal for portable applications. The low temperature allows for fast start-up times, enabling the fuel cell to be easily stopped and started as required. Since the fuel cell is based around a solid membrane, which operates at low temperatures, this reduces the associated problems and costs of building and sealing the fuel cell stacks. Other fuel cells operate at high temperatures or use highly corrosive electrolytes, which require costly and complex sealing techniques. There are two factors which have been holding back the commercialisation of fuel cells, cost and reliability. PEM fuel cells are gradually dropping to an acceptable cost suitable for mass marketing. Duration of the cell life is also a problem, which is undergoing much development work.

A fuel cell needs a sufficiently long service life to make it acceptable for use in applications such as transport. Vehicles are required to be serviceable for up to hundreds of thousands of miles without a major overhaul being needed. Currently PEM fuel cells have been tested for over 20,000 hours of continuous operation, but their performance degrades over time. Current PEM fuel cells under operation degrade from 0.67 to 1.0% per 1000 hours. This needs to be reduced to around 0.1% per 1000 hours.

The electrical conversion efficiencies for PEM fuel cells range from 40 to 50% efficiency, if the by-product heat can be utilized to increase the overall efficiency (FCH, 2004).

At the fuel cell's centre lies the proton exchange membrane, made from a perfluorinated sulfonic acid polymer. The thickness of this membrane is around 20-200 μm. The purpose of the membrane is to create a good path for hydrogen protons to be exchanged, while keeping both the hydrogen and oxygen gases separated by the membrane. The membrane also has to be a good electrical insulator to ensure electrons are driven around the external electrical circuit.
The surfaces of this layer are coated with a porous layer of platinum-based catalyst with a binding agent that forms an electrode structure.
It is necessary that there is a good interaction between the catalyst layer and the membrane to ensure an easy route for hydrogen protons to be transferred across the membrane.
The purpose of the platinum catalyst is to increase the overall reaction speed for receiving the hydrogen gas (H_2) and splitting it into protons (H^+). The protons are then ionically transported through the membrane, combining with electrons and oxygen molecules to form water. The two half reactions taking place on both sides of the membranes can be seen in the above-mentioned Equations A.9.1 and A.9.2.
The quantity of water contained within the fuel cell's electrolyte membrane is also an important issue in maintaining optimum output. The membrane is required to remain saturated with water to ensure high ionic conductivity across the electrolyte. Should the membrane become dehydrated, the adherence of the membrane to the electrodes will become irreversibly damaged, since intimate contact between the electrode and membrane is required to ensure a low resistive electrical contact between the two surfaces. Unlike other types of fuel cells there is no liquid electrolyte to form a conductive bridge between the surfaces.

It is also important to reduce the effects of flooding. As protons diffuse across the membrane from the anode to the cathode, water molecules are also pulled across the membrane. As the concentration gradient between the electrodes increases, osmosis may occur to some extent, diffusing water molecules back

across the membrane to the anode (FCH, 2004). Water is removed from the fuel cell by evaporation at the electrodes. If the build-up of water is greater than the evaporation rate, the electrodes will become flooded. Flooding of the cathode is a particular problem, as liquid build-up blocks the porous diffusion layer, reducing the supply of oxygen to the reaction. Liquids build up on the surface of the catalyst layer, decreasing the catalyst's area, reducing its efficiency and slowing the overall reaction rate as oxygen is starved from the membrane (Najjari *et al.*, 2007).

PEM fuel cells offer good power densities of up to 1000 mW/cm^2, which is the highest of all types of fuel cells. Their disadvantage is their high cost due to the cost of the platinum catalysts (O'Hayre et al., 2006). Another disadvantage is the low operating temperature, which means that it is prone to poisoning by carbon monoxide which may be contained within the hydrogen supply, if the hydrogen is generated via steam reforming. The carbon monoxide attacks the anode platinum catalyst sites, reducing the ability of the catalysts to split the input hydrogen into protons, thus reducing the overall reaction rate. The effects of the catalyst poisoning can be reversed by passing pure carbon monoxide-free gas over the catalyst's electrodes. Increasing the electrode temperature to over 120°C minimises the effects of poising via carbon monoxide. At normal operating temperatures no more then one parts ppm of carbon monoxide may be tolerated.

The membrane itself is also sensitive to being poisoned by substances such as metal ions. The sources of these are usually either from the corrosion of metallic components within the fuel cell stack or via the feed fuel or oxidant gases (FCH, 2004).

A.10 Napier hydrogen research laboratory

Part of this PhD research project was to oversee and project-manage the development and installation of the hydrogen research laboratory. The laboratory has been designed and set up to serve two purposes within the University. Firstly, the integration of a hydrogen storage facility provides energy storage to the University's existing solar PV, wind energy and transport projects. Secondly, the laboratory provides a research centre for the development of hydrogen technologies.

A.11 The integration of a hydrogen storage facility into Edinburgh Napier University's sustainable energy and transport project

Installed at Napier's Merchiston Campus there is a 160 m^2 photovoltaic facade supplying 12MWh of electricity to the university campus annually. Further details of this can be seen in Chapter 2. Three building-mounted micro wind turbines are also installed on the campus buildings, supplying around 1MWh annually (for further details see Chapter 6). The sustainable energy systems installed are fully grid-connected, so that any energy generated which is not consumed by the campus power distribution board is exported to the national grid. However, this means that the sustainable energy system has to have a reliance on fossil-fuel-based power generation over the periods when there are no sustainable resources and at times when load outstrips supply. Power from the grid will supply any shortfall from the sustainable energy system.

The hydrogen storage facility is an integral part of the sustainable energy system, enabling any surplus electrical energy generated by sustainable means to be converted to chemical energy via the use of an electrolyser to hydrogen gas. Hydrogen gas can then be stored as compressed gas in the steel storage cylinders seen in Figure A.11.1. At times of intermittence sustainable generation, or when load is greater than the supply, the stored hydrogen can then be converted back to electrical energy via the use of hydrogen fuel cell technology. Thermal energy is also a by-product and may also be utilised for certain applications.

Hydrogen, as previously mentioned, can also be used as a high energy density storage medium which can be used as a zero carbon emission fuel for transport. Future work carried out at the university will look at zero carbon emission transport using fuel cell technology.

Figure A.11.1 Gas storage cylinder bank located on the University's roof behind the hydrogen lab. Note one nitrogen cylinder and 6 red hydrogen cylinders. Two high-level extraction fans can also be seen on the lab's roof.

A.12 Hydrogen research

The second application of the hydrogen research laboratory is to carry out much-needed research into a range of hydrogen technologies. The focus of this research will be on development work in solid oxide fuel cells and their electrodes.

A.13 Hydrogen safety

The key objective in designing a hydrogen research laboratory is to provide a working environment which is well-suited for carrying out hydrogen research work in a safe manner. Over the years the use of hydrogen has acquired the image in the public perception of being a high-risk and potentially dangerous gas. However research has shown that there is a wealth of information showing that hydrogen can be used, stored and handled safely.

Hydrogen has different properties to conventional hydrocarbon fuels and thus needs to be handled in a different manner. The difference in properties results in different safety issues. Some properties make hydrogen less safe, and other properties make dealing with hydrogen gas safer than conventional fuels. Table A.13 shows the properties of hydrogen gas compared with other commonly used fuels.

Table A.13 Properties of hydrogen and other hydrocarbons

Fuel	Hydrogen	Methane	Propane	Gasoline
Flammability limits				
Lower, (% fuel by volume)	4.0	5.3	2.1	1.0
Upper, (% fuel by volume)	75.0	15.0	10.4	7.8
Detonability limits				
Lower, (% fuel by volume)	18.3	6.3	3.4	1.1
Upper, (% fuel by volume)	59	13.5	-	3.3
Ignition energy, mJ	0.02	0.29	0.31	0.24
Minimum auto ignition, °C	520	630	450	-
Buoyancy (Density as a percent of air, %)	7	55	152	400
Diffusion Coefficient, cm/sec^2	0.61	0.16	0.10	0.05

(Source of data: Ringland, 1994)

The two critical issues in dealing with hydrogen gas are leak prevention and leak detection. Additional safety systems are also required to ensure that hydrogen gas can be safely vented in a controlled manner in emergencies, minimising risk of release of gas, and preventing the build-up of explosive fuel-air mixes in confined and poorly vented areas.

A.14 Laboratory safety

An analysis was carried out to determine all the potential risks of dealing with hydrogen gas and the risks which would be of concern within the hydrogen lab. These risks have been listed below, along with the required safety measures being taken to minimise these risks.

A.14.1 Hydrogen leaks

Eliminating leaks is key to maintaining a safe working environment. Hydrogen gas is the lowest density chemical element; it has a very low viscosity and a high diffusion coefficient. Its low viscosity can result in leaks occurring in plumbing joints, which may be gas-tight for other gases. Metal-to-metal jointing techniques such as compression joints should only be used. Other fitting such as threaded fittings with sealant or polymer-sealed fittings may result in sealants being displaced or hydrogen diffusing through seals and leaking.

Hydrogen embrittlement is another important factor to be considered when selecting materials to be used with hydrogen. Due to the small size of the gas molecules, hydrogen can permeate into materials such as metals and polymers. Gas molecules can permeate into cracks and voids within material structures, putting pressure on these small cracks and causing propagation. Hydrogen embrittlement can reduce a material's fracture toughness. High-strength steels are particularly prone, whereas low-strength steels, aluminium and most aluminium alloys, certain polymers and stainless steels are more resistant.

To reduce the above-mentioned risks within the laboratory, hydrogen gas is only stored at low pressures (8 bar) and high-grade 316 stainless steel piping is used. Piping and fittings are 316 stainless steel Swagelok compression joints, and all valves are of a sealant-free type. Hydrogen gas is stored in six high-pressure steel standard "K" type cylinders which are commonly used commercially for hydrogen storage. It should be noted that the cylinders are rated for use at 175 bar, however they will be only filled to a pressure of 8 bar with the Napier lab.

A.14.2 Leak detection and ventilation

Hydrogen gas has a very low density, 7% of the density of air, which results in any leakage rapidly rising to ceiling level and quickly diffusing. This poses a significant risk, as hydrogen-air mixtures have a broad range of flammability, ranging from 4 to 75% by volume concentration (Ringland, 1994).

To reduce the risk of any hydrogen gas build-up within the laboratory environment, the room is sealed with fire-rated sealant above the height of door level. The laboratory has also been located on the roof, minimising the risk of any hydrogen leaking into the rest of the University building.

Two high-level extraction fans have been installed at roof level, with the addition of floor-level ventilation, which enables the entire volume of air within the laboratory to be replaced twice a minute, removing any potentially dangerous gas build up. All high-level wiring and lighting are rated as intrinsically safe, limiting electrical spark ignition sources.

In the event of a hydrogen gas escape there are two hydrogen detectors installed at ceiling level above the electrolysers and fuel cell stack. The hydrogen detectors are set to activate the hydrogen alarm system should hydrogen levels within the lab exceed 0.4% by volume, ten times less than the lowest flammability limit of 4%.

If a hydrogen escape is detected then the following outcomes will be automatically activated: the hydrogen supply to the laboratory will be turned off, non-intrinsically safe power supplies will also be turned off, and high ventilation fans will start as well as emergency alarms sounding.

A naturally vented hood has also been installed over the fuel cell stack so any gas escape during the start-up procedure will be vented outside, minimising any risk.

A.15 The hydrogen research laboratory

Figures A.15.1 and A.15.2 show the completed laboratory with the key components labelled. In the lower right-hand corner in Figure A.15.1 can be seen the electrolyser (Figure A.15.3) which receives mains power and a purified water supply from the deioniser (Figure A.15.4). The oxygen produced is currently vented into the atmosphere; the hydrogen is fed into the membrane dryer. The electrolyser can produce hydrogen at a rate of up to 10 L/min at normal pressure.

The dryer (Figure A.15.5) uses a dry supply of nitrogen gas to dry the hydrogen gas. The purposes of this is to remove any humidity from the gas which could cause condensation and corrosion within the storage cylinders. Both the hydrogen and nitrogen cylinders are stored outside. The hydrogen storage cylinder bank is capable of storing 8.7kWh of chemical energy.
The nitrogen supply is controlled by the nitrogen regulator. The hydrogen is supplied from the cylinders to the laboratory via a safety shut-off solenoid valve to two hydrogen regulators, one supplying high-pressure gas and the other low-pressure gas.

The solid oxide fuel cell (Figures A.15.6 and A.15.7) is located in the centre of the room under the ventilation hood. Due to the seal-less design of the fuel cell being used, it is necessary to vent away any escaped hydrogen gas during the start-up process. The fuel cell is supplied air via an oil-less diaphragm compressor seen the right of the fuel cell.
Because solid oxide fuel cells cannot withstand the stress of thermal cycling, an additional solenoid valve (not shown) has been installed to switch the hydrogen supply to nitrogen when the fuel cell is operating in standby mode. This inhibits the poisoning or oxidization of the fuel cell stack from the ambient air. An internal electric heater is also used to keep the fuel cell stack at temperature while in standby mode. A schematic layout of the laboratory's hydrogen system is given Figure A.15.9 and the laboratory specifications are given in Table in A.15.

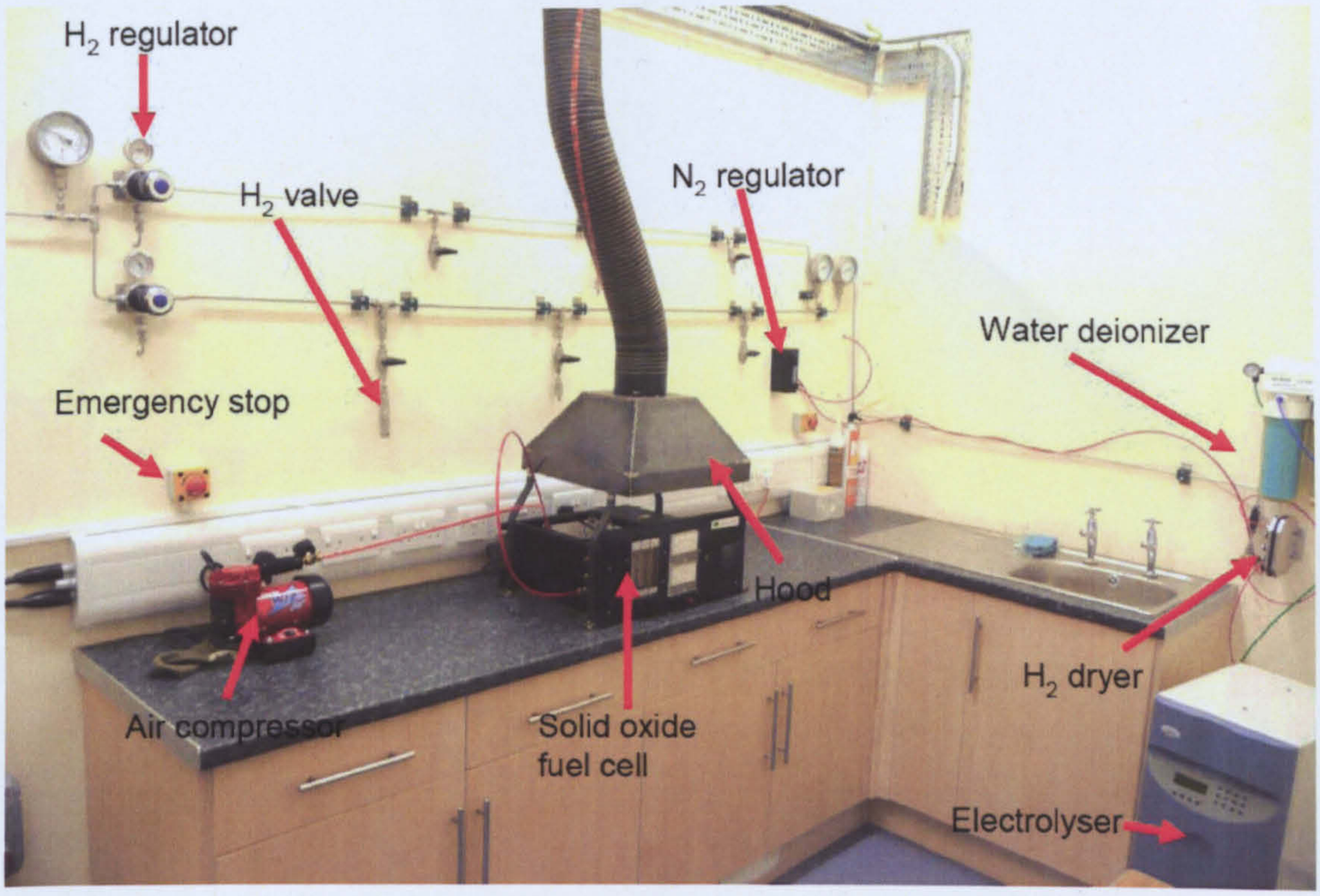

Figure A.15.1 View of hydrogen research laboratory showing key components.

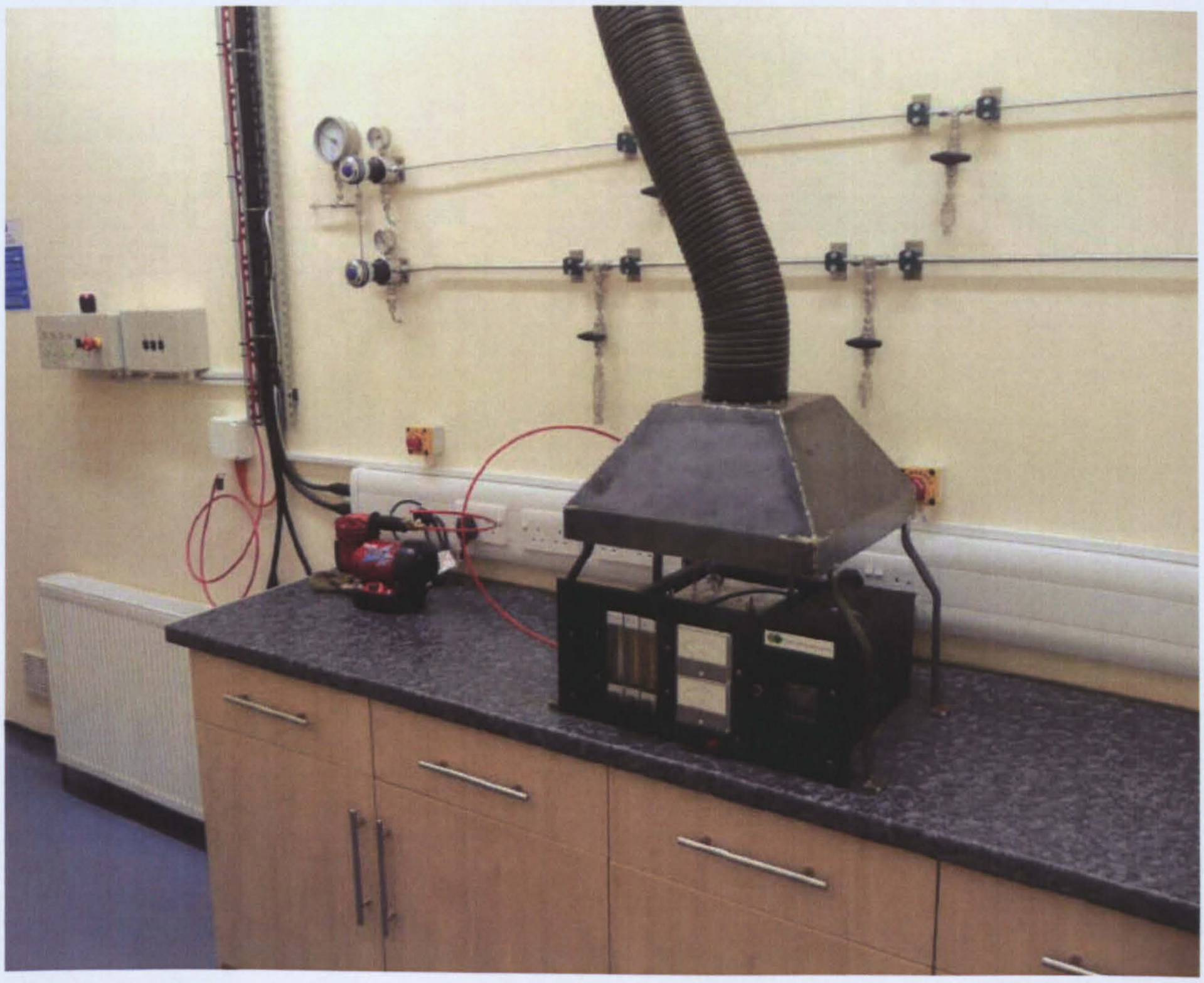

Figure A.15.2 Second view of hydrogen research laboratory, note hydrogen alarm safety system on left-hand side.

Table A.15 Hydrogen research laboratory specification

Storage type	
Rated system pressure	10 bar
Cylinder quantity	6 K-class steel cylinders
Cylinder volume	50l
Volume of stored gas:	456nl/cylinder
Volume of stored gas:	2.7 ncu.m (total)
Stored energy (chemical energy) hydrogen gas	8.7 kWh
Outlet pressure	0-10 bar
Pressure relief valve set to 10% above normal maximum	
Pipe work, metric 316 stainless steel, sizes 3mm, 6mm, 8mm, 10mm, 12mm	
Tape-thread joints, BSP, sizes 1/4" and 1/2"	
Compression joints are Parker or Swagelok	
Electrolyser	
LabGas PEM HFHG10L	
Output flow rate	10 normal L/Min
Gas purity (% H2 / O2)	99,995
Outlet pressure	8 bar
Power rating	3 kW at 230 Volts/ 50Hz
Water consumption (litres/hr)	0.5
Efficiency (%)	85
Dryer	
LabGas Palladium membrane	
Hydrogen purity (%)	99.999
Fuel cell	
Fuel cells (Scotland)	
Fuel cell type	Seal-less solid oxide
Max power output	600W
Stack size up to 10 cells	
Operating temperature	800°C

Figure A.15.3 LabGas PEM electrolyser.

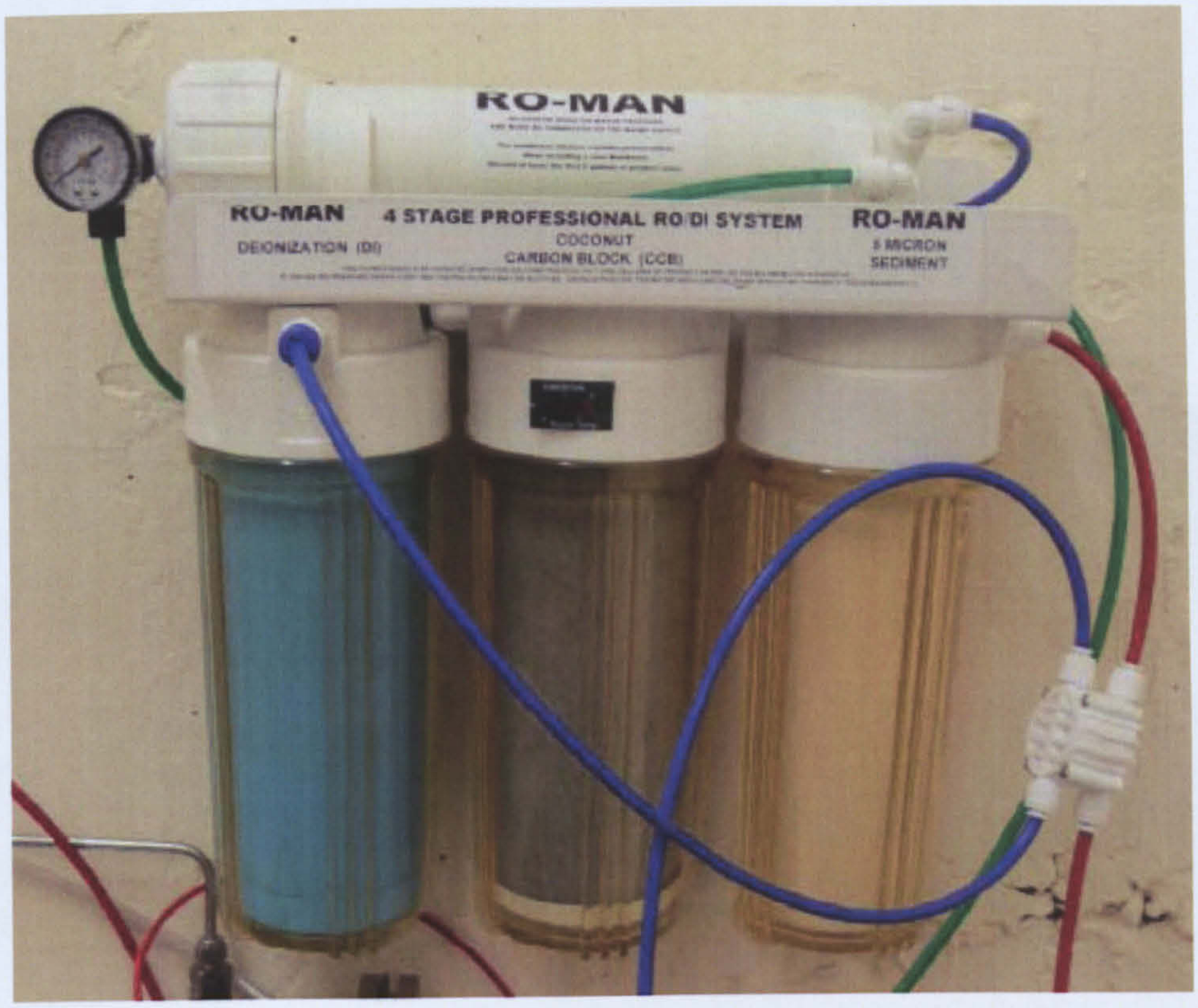

Figure A.15.4 Water purifying filter and deioniser.

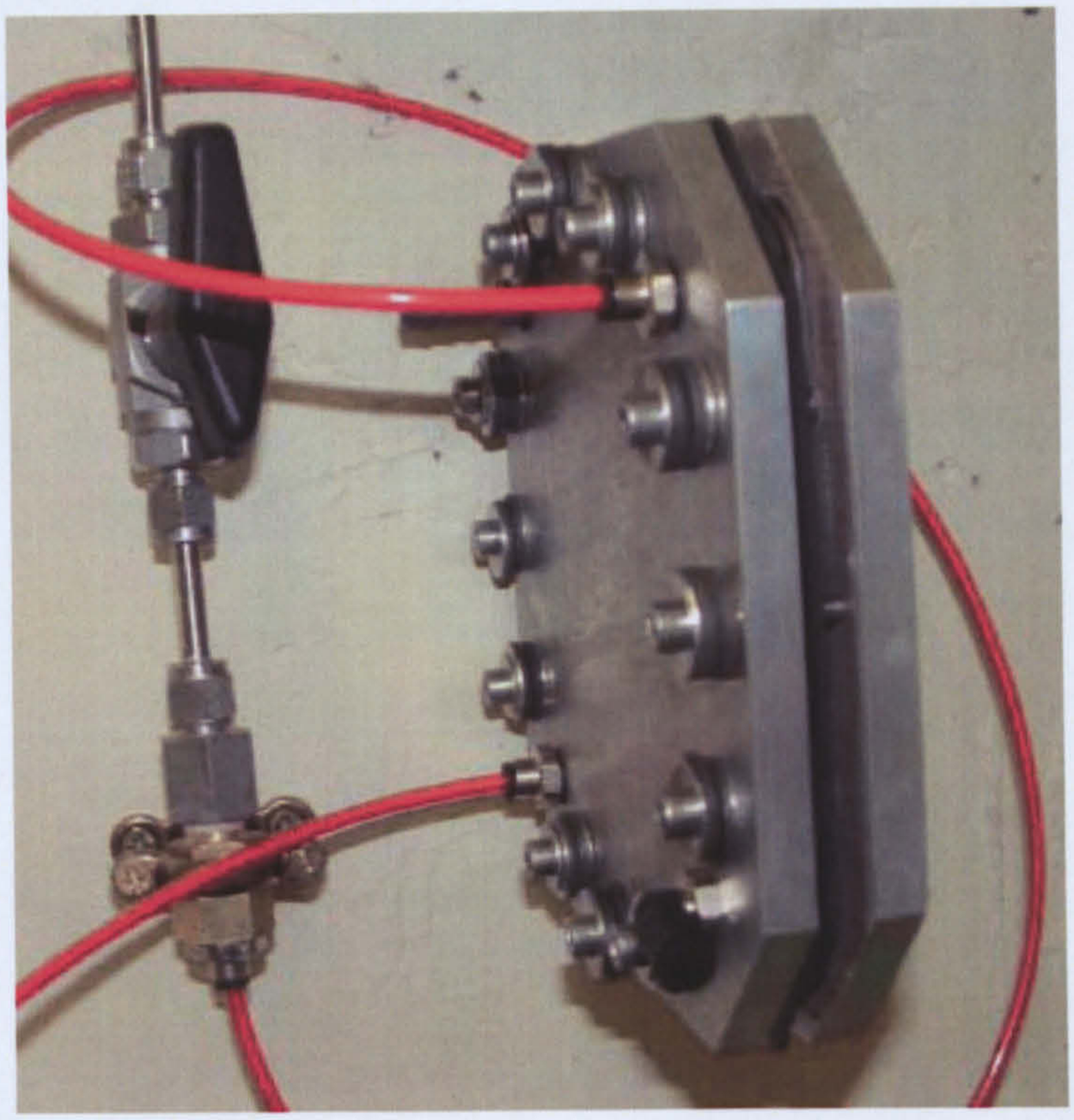

Figure A.15.5 LabGas Palladium membrane hydrogen gas dryer.

.

Figure A.15.6 Prototype solid oxide fuel cell used for research work and air compressor to supply air to fuel cell stack.

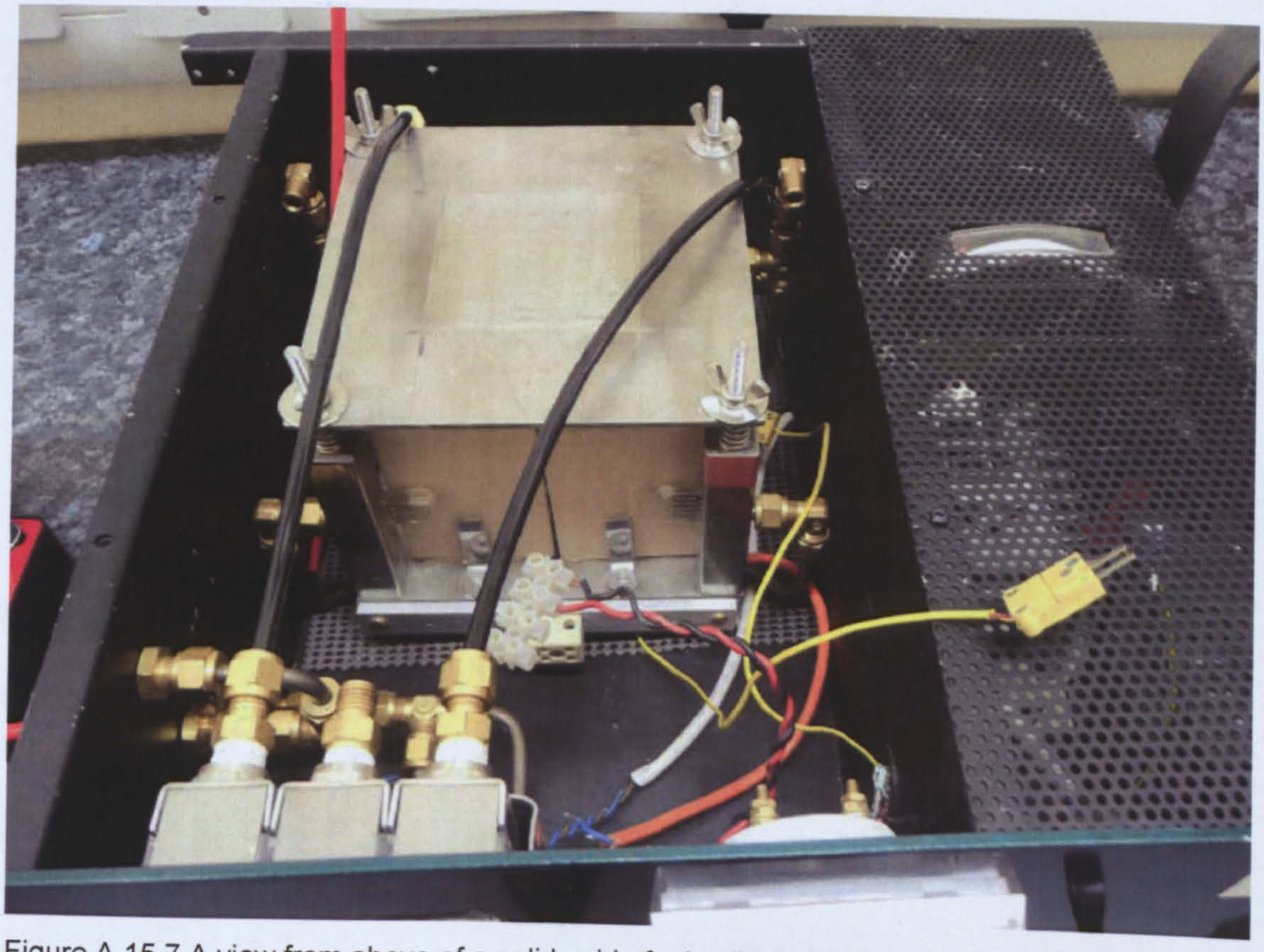

Figure A.15.7 A view from above of a solid oxide fuel cell, note novel seal-less design from fuel cell (Scotland).

Figure A.15.8 Hydrogen alarm and control panel.

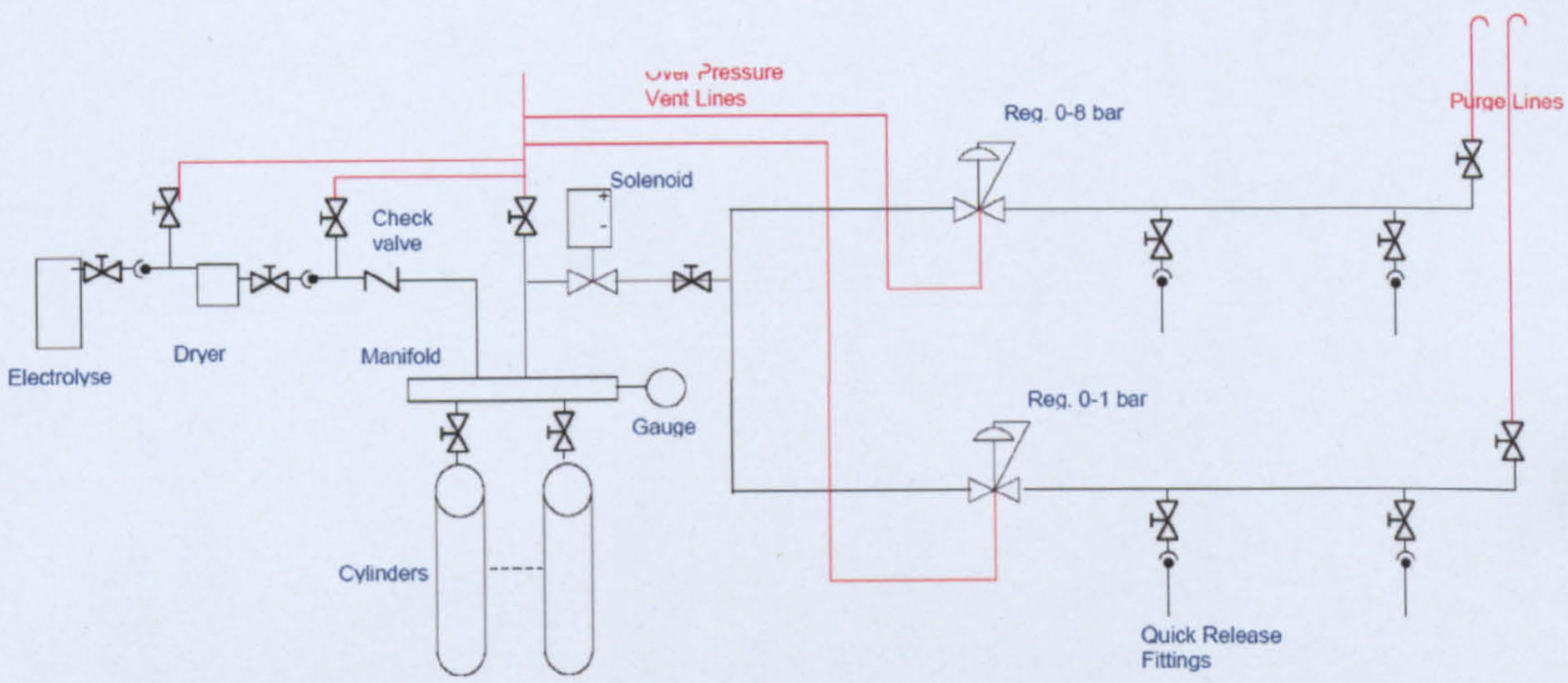

Figure A.15.9 Schematic of hydrogen system (Courtesy of SiGen Ltd).

APPENDIX B

List of Publications

Journal Articles

1. Clarke, P., Munawwar, S., Davidson, A., Muneer, T., and Kubie, J., 2007. Technical note: An investigation of possible improvements in accuracy of regressions between diffuse and global solar irradiation. Building Services Engineering Research and Technology, Vol. 28, pp189-197.

2. Clarke, P., Muneer, T Davidson, A., Kubie, J., 2008. Models for the estimation of building integrated photovoltaic systems in urban environments. Proceedings of the IMECHE Part A: Journal of Power and Energy, Vol. 222, Number 1, pp61-67.

3. Celik, A, N., Muneer, T., Clarke, P., 2007. An investigation into micro wind energy systems for their utilization in urban areas and their life cycle assessment. revision for publication on 17 July 2007. Proceedings of the IMECHE Part A: Journal of Power and Energy, Vol. 221, pp1107-1117.

4. Celik, A, N., Muneer, T., Clarke, P., 2009. A review of installed solar photovoltaic and thermal collector capacities in relation to solar potential for the EU-15. Renewable Energy, Vol.34, pp849–856.

Conference Articles

1. Clarke, P., and Muneer, T., 2008. Models for estimating building integrated photovoltaic system output in urban environments. World Renewable Energy Congress (WRECX) conference proceedings, pp1277-1281.

2. Clarke, P., Davidson, A., Kubie, J., and Muneer, T, 2007. Two years of measured performance of a medium-sized building integrated photovoltaic facility at Edinburgh Napier University, Edinburgh. Proceedings of 3rd International Conference on Solar Radiation and Day Lighting (SOLARIS 2007) conference proceedings, pp 397-401. Delhi, India, February 2007.

3. Muneer, T., Clarke, P., and Cullinane, K. 2008. The electric scooter as a vehicle of green transport. Pending publication.

4. Muneer, T., and Clarke, P., 2008. Evaluation of two solar energy models used to estimate building integrated photovoltaic systems in urban environments. Proceedings of 4rd International Conference on Solar Radiation and Day Lighting (SOLARIS 2008) conference proceedings. Hong Kong, December 2008.